Monoterpenes transformation using one-pot catalytic pathways with heterogeneous materials

Luis Alfonso Gallego Villada

Tesis doctoral presentada para optar al título de Doctor en Ingeniería Química

Director

Edwin Alexis Alarcón Durango, Doctor (PhD) en Ciencias Químicas

Universidad de Antioquia

Facultad de Ingeniería

Doctorado en Ingeniería Química

Medellín, Antioquia, Colombia

2025

UNIVERSIDAD DE ANTIOQUIA

DOCTORAL THESIS

MONOTERPENES TRANSFORMATION USING ONE-POT CATALYTIC PATHWAYS WITH HETEROGENEOUS MATERIALS

Author:
Luis Alfonso Gallego Villada

Advisor:
Edwin Alexis Alarcón Durango

A thesis submitted in fulfillment of the requirements for the degree of ***Doctor of Philosophy in Chemical Engineering***

Environmental Catalysis Research Group
Faculty of Engineering
Chemical Engineering Department

Medellin, Colombia
2025

To my mom and dad, whose unconditional support has allowed me to get this far

To my sister, who is the light of my life

To my wife, my greatest love and source of endless inspiration

"If you genuinely want something, don't wait for it – teach yourself to be impatient."

Gurbaksh Chahal

AND

"Success is not the key to happiness. Happiness is the key to success. If you love what you are doing, you will be successful."

Albert Schweitzer

Preface

This Ph.D. thesis contains the results of the incredible and passionate research conducted during my doctoral formation over the past four years. This journey has been full of ups and downs, but always trusted that the process would be successful. The research was developed within the Environmental Catalysis Research Group (Universidad de Antioquia, Medellín-Colombia) and at the Laboratory of Industrial Chemistry and Reaction Engineering (TKR), Process Chemistry Centre (Åbo Akademi University, Turku-Finland). I can confidently say that I have experienced a delightful journey, largely thanks to the support of many experts who supported me along the way.

I want to sincerely appreciate the time, discipline, patience, unconditional support, and friendship of my supervisor, Edwin Alarcón. I am incredibly grateful for his unwavering dedication and for always being there for me, in the moments when the research was progressing well, but also in those stressful times when there seemed to be no way forward.

I would like to express my sincere gratitude to Professor Aída Luz Villa for allowing me to carry out my doctoral studies at the Environmental Catalysis Research Group. Thanks to all the professors and co-workers in the research group. Their knowledge in their areas of expertise was essential to writing this thesis. Special thanks to my colleague, Alexander Quintero, for his constant willingness to listen to me and advise me when technical issues arose in the laboratory.

I am deeply grateful to Professors Dmitry Murzin and Päivi Mäki-Arvela from Åbo Akademi University (Turku-Finland) for hosting me during my research internship and providing an excellent environment for conducting research at the highest academic level. Their invaluable experience, kind guidance, and wisdom were of immense importance in helping me better understand the catalysis topics covered in this thesis. I am also grateful to them for teaching me invaluable lessons and for their genuine and authentic approach, which I believe serves as a role model for many. During those intense seven months, I underwent significant personal and professional growth.

Thanks to my colleagues at the TKR laboratory. Special mention to Professor Narendra Kumar, Kari Eränen, Wander Perez, and Mark Klimov for their technical and scientific support. Without their support, a big part of this thesis would not have been possible.

Thanks to the Universidad de Antioquia for providing financial support for this thesis through the Foundation for the Promotion of Research and Technology, Project 2022-56550, as well as Project 2022-53000 as a part of the 2021-2022 Programmatic Call: Engineering and Technology. Also, thanks for the support for my doctoral formation through the "Beca Doctoral Universidad de Antioquia" scholarship.

Special thanks to Dr. Julián Sánchez Velandia for his valuable advice on some of the reaction pathways investigated in this thesis. His passion for green organic synthesis is admirable. I offer my sincerest thanks to everyone who has been part of the collaborations in the published articles resulting from this thesis.

Last but not least, my deepest love and gratefulness to my family. My parents, Luis and Libia, and my sister, Ana María, were always beside me, supporting me and staying united as a family despite the difficulties. Thank you for all the sacrifices you have made on my behalf. Thank you to my wife, Isabel, for your love, kindness, and support throughout these four years. You and my family have always been the driving force in my life.

The past four years have truly transformed my life, and I am deeply grateful for the support I received along the way. I wish to express my heartfelt thanks to everyone who stood by me. Every detail is cherished in my heart.

Abstract

The valorization of biomass offers a sustainable approach to producing high-value-added chemicals. In particular, monoterpenes such as α- and β-pinene can be extracted from various types of pine trees, and limonene can be obtained from agro-industrial waste like fruit peels. These substrates contain highly reactive double bonds, which can be transformed into valuable chemicals through catalytic routes such as epoxidation. Subsequent reactions can yield epoxide isomers, including myrtanal, myrtenol, and perillyl alcohol from β-pinene epoxide, as well as dihydrocarvone (*cis* + *trans*) and carveol from limonene-1,2-epoxide. These products have numerous applications in medicinal chemistry due to their anti-inflammatory and anxiolytic-like effects, *in-vitro* inhibitory activity, and as intermediates in organic synthesis for the flavor and fragrance industry.

This thesis focuses on achieving two catalytic transformations of monoterpenes using the one-pot concept. The challenge of discovering new methodologies to synthesize these molecules has significantly motivated research efforts toward optimizing novel catalytic transformations. An attractive target is conducting one-pot reactions, where all consecutive and simultaneous transformations occur in a single reactor. This approach offers substantial advantages, including reduced operation time, maximized energy efficiency, simplified overall processes, and minimized material loss from multiple reaction and purification units. Despite the challenges in controlling multistep reactions and finding compatible reaction conditions, which limit the broad applicability of one-pot catalytic routes, this thesis addresses these issues. It begins by examining independent catalytic routes (epoxidation and isomerization) and subsequently explores one-pot routes. The primary challenge in the latter lies in identifying compatible reaction conditions.

The oxidation of monoterpenes over heterogeneous catalysts is one of the most important organic transformations, occurring through two competitive pathways: double bond epoxidation and allylic oxidation. The predominance of each route depends on the substrate´s nature, the oxidizing agent, reaction conditions, and the physicochemical properties of the catalysts. Additionally, the isomerization of monoterpene epoxides significantly depends on the acidity type of the catalyst (Lewis or Brønsted), the solvent type (polarity, donor number), and the architecture of the catalyst. Therefore, it is necessary to methodologically investigate the two independent pathways (epoxidation and epoxide isomerization) and then combine the insights to achieve the one-pot route.

The first part of this thesis (**Chapter 2** and **Chapter 3**) explores heterogeneous catalysts for the epoxidation of R-(+)-limonene. Two catalytic systems were evaluated: commercial magnesium oxide (**Chapter 2**) and catalysts based on metal-modified hierarchical zeolite Y (**Chapter 3**). For MgO, the epoxidation was conducted in a Payne reaction system using H_2O_2 and acetonitrile as an activator, achieving high yields of limonene epoxide (80%) and diepoxide (96%) under optimized conditions (50 °C, 30 min for epoxide, and 2 h for diepoxide). Particularly, limonene diepoxide has recently emerged for use in biomedical applications. Characterization of both fresh and spent MgO catalyst revealed their suitability over four cycles. Mechanistic insights included the description of peroxyacetimidic acid as an intermediate oxidant and modeling using reversible and Eley-Rideal models. For the zeolite Y catalyst, detailed characterization highlighted the superiority of Sn-modified dealuminated zeolite Y, showing a high turnover frequency (TOF) of 96 h^{-1}. This catalyst exhibited optimal

properties such as a low Brønsted to Lewis acidity ratio (0.1), significant mesoporosity (43%), and a specific surface area of 465 m^2 g^{-1}. Operational conditions yielding high limonene conversion (97%) and selectivity to monoepoxides (up to 96%) included 70 °C, H_2O_2: limonene molar ratio = 7, and acetonitrile as a solvent. The hydration of internal epoxides to limonene diol was favored under specific conditions, with H_2O_2 efficiency reaching 85%. A plausible reaction pathway for the epoxide formation was proposed over the dealuminated zeolite.

The second part (**Chapter 4** and **Chapter 5**) focuses on mesoporous catalysts derived from dendritic ZSM-5 zeolites for the isomerization of monoterpene epoxides, specifically α-pinene epoxide, β-pinene epoxide, and limonene-1,2-epoxide (LE). Among these, dendritic ZSM-5 synthesized with a crystallization time of 4 days exhibited exceptional catalytic activity, achieving a turnover frequency (TOF) of 4.4 min^{-1} for LE isomerization. Detailed characterization underscored its favorable properties, including a low Brønsted to Lewis acidity ratio (1.4), substantial mesopore/external surface area (360 m^2 g^{-1}), and a narrow mesopore size distribution. These attributed facilitated significant yields of campholenic aldehyde (72.4%, 70 °C, 5 min), myrtanal (47.7%, 50 °C, 5 min), and dihydrocarvone (63%, 70 °C, 2 h). The investigation delved into the kinetics and mechanisms governing LE isomerization using the highly active dendritic zeolite. The catalyst demonstrated superior efficiency in producing dihydrocarvone diastereoisomers. Ethyl acetate emerged as an optimal green solvent, promoting selective dihydrocarvone formation. Kinetic modeling, augmented by statistical analysis of a reaction network, elucidated activation energies for *cis*-dihydrocarvone and *trans*-dihydrocarvone formation, supported by DFT calculations. Notably, carbocation formation (ΔEact = 234 kJ mol^{-1}) was identified as the rate-determining step, highlighting the catalyst's efficacy in facilitating LE conversion under mild conditions.

The last part of the thesis (**Chapter 6**) investigates metal-modified mesoporous catalysts supported on MCM-41 and SBA-15, in conjunction with MgO, for the one-pot tandem transformation of β-pinene. This process involves epoxidation with H_2O_2 followed by isomerization to produce myrtanal as major product. Metals (Sn, Fe, Cu, and Co) were incorporated via wetness impregnation, and the resulting catalysts were characterized using several techniques. Among the catalysts, Fe/SBA-15 achieved the highest myrtanal yield (63%) with a H_2O_2 efficiency of 60%. This catalyst demonstrated a total acidity of 138 μmol g^{-1}, a surface area of 496 m^2 g^{-1}, and a pore volume of 0.96 cm^3 g^{-1}. While Sn-based catalysts also showed high selectivity for myrtanal, Cu-based catalysts performed poorly, and Co catalysts were ineffective due to H_2O_2 decomposition. Lewis acidity and acid site density were used as descriptors for catalytic performance. The most active catalysts exhibited excellent reusability and no detectable Fe leaching. A plausible reaction pathway for the β-pinene to myrtanal transformation was proposed based on the material characterization and the catalytic results.

The main contributions of this doctoral thesis are:

- The development of heterogeneous catalytic systems for the epoxidation of monoterpenes using commercial magnesium oxide and dealuminated zeolite Y-based catalysts, with H_2O_2 as a green oxidant.
- The kinetic modeling of R-(+)-limonene epoxidation using a Payne system, which considers a reaction network with three pathways. This modeling provides valuable insights for reactor design and process scaling.

- The use of novel heterogeneous catalysts based on dendritic ZSM-5 zeolites for the valorization of monoterpene epoxides through isomerization. This approach produces campholenic aldehyde from α-pinene epoxide, myrtanal from β-pinene epoxide, and dihydrocarvone from limonene-1,2-epoxide.
- Comprehensive kinetic and mechanistic studies of limonene-1,2-epoxide isomerization, including activation energy calculations and reaction pathways, supported by Density Functional Theory.
- The development of a one-pot catalytic system employing a tandem approach to convert β-pinene into myrtanal. This system integrates both epoxidation and isomerization in a single reactor, with a proposed reaction pathway using two heterogeneous catalysts.
- Insights into the relationship between the physicochemical properties of the catalysts and their catalytic performance across all studied systems.

Table of Contents

List of Figures

List of Tables

Acronyms

AA: Atmospheric air

ACS: Average crystal size

AIP: Aluminum isopropoxide

APS: Average pore size

ASAP: Accelerated Surface Area and Porosimetry

BAS: Brønsted acid sites

BET: Brunauer–Emmett-Teller method

BIAN: Bis(4-HOOC-phenyl)-acenaphthenequinonediimine

Biim: 2,2'-biimidazole ligands

Bipy: 2,2'-bipyridine-4.4'-dicarboxylato

BJH: Barrett-Joyner-Halenda method

CA: Campholenic aldehyde

CHP: Cumene hydrogen peroxide

CNE: Carvone

DBU: 1,8-Diazabicyclo(5.4.0)undec-7-ene

DHC: Dihydrocarvone

$D_{i,\,eff}$: Effective diffusivity of specie i through the catalyst

DMC: Dimethyl carbonate

DMF: Dimethylformamide

DMSO: Dimethyl sulfoxide

DN: Donor number

DRIFT: Diffuse Reflectance Infrared Fourier Transform

DRS: Diffuse Reflectance Spectroscopy

DTA: Differential Thermal Analysis

EDS: Energy-Dispersive X-Ray Spectroscopy

ee: Enantiomeric excess

E-factor: Environmental factor

EIM: Evaporation impregnation method

ELE: External limonene epoxide

EOs: Essential oils

FA: Fencholenic aldehyde

FID: Flame Ionization Detector

FTIR: Fourier Transform Infrared Spectroscopy

Hpytz: 5-(2-pyridyl)tetrazole

IBA: Isobutyraldehyde

ICP/OES: Inductively Coupled Plasma – Optical Emission Spectrometry

ILE: Internal limonene epoxide

INTRACEN: International Trade Centre

IUPAC: International Union of Pure and Applied Chemistry

LAS: Lewis acid sites

LE: Limonene epoxide

LD: Limonene diol

LDH: Layered double hydroxide

MAS: Magic Angle Spinning

MAUD: Material Analysis Using Diffraction – Analysis program

MCM-41: Mobil Composition of Matter No. 41

MCT: Mercury-Cadmium-Telluride detector

MTAB: Myristyltrimethylammonium bromide

MZ: Mesoporous beta zeolite

NBS: N-Bromosuccinimide

NL-DFT: Non-localized Density Functional Theory

NMR: Nuclear Magnetic Resonance

NRMSD: Normalized root mean square deviation

N_{W-P}: Weisz-Prater criterion

PA: Perillyl alcohol

PC: Pinocamphone

PCOL: Pinocarveol

PCY: P-Cymene

Ph-A: N-[3-(Trimethoxysilyl)propyl]aniline

Phttpy: Terpyridine-based catalyst

PMD: p-Menthadien-2-ol

R^2: Determination coefficient

R_{cat}: Average radius of the catalyst particle

RMSD: Root mean square deviation

SBA: Santa Barbara Amorphous

SEM: Scanning Electron Microscopy

SSE: Sum of squared errors

TBHP: tert-Butyl hydroperoxide

TC: Trans-carveol

TEA: Triethylamine

TEM: Transmission Electron Microscopy

TEOS: Tetraethyl orthosilicate

TFT: α, α, α-Trifluorotoluene

TGA: Thermogravimetric Analysis

THF: Tetrahydrofuran

TOF: Turnover frequency

TPAOH: Tetrapropylammonium hydroxide

TPC: Trans-pinocarveol

TPD: Temperature-Programmed Desorption

TPO: Temperature-Programmed Oxidation

TPOAC: Dimethyloctadecyl [3-(trimethoxysilyl) propil] ammonium chloride

TS: Trans-sobrerol

UHP: Urea hydrogen peroxide

UV-Vis: Ultraviolet-Visible Spectroscopy

VOCs: Volatile organic compounds

$[VO(sal2bz)]_2$: Vanadium complex

XPS: X-ray Photoelectron Spectroscopy

XRD: X-ray Diffraction

ZrP: Zirconium phosphate

ZSM-5: Zeolite Socony Mobil-5

d-ZSM-5: Dendritic zeolite based on ZSM-5

ε: Dielectric constant

μ: Dipole moment

σ_c: Constriction factor

φ_p: Catalyst porosity

τ: Tortuosity

Chapter 1. Overview

State of art in this chapter (**section 1.2**) corresponds to some sections of a review article published in ***Catalysis Reviews***, *2024, 1-126 – DOI: 10.1080/01614940.2024.2329553*.

Julián E. Sánchez-Velandia[a*], Luis A. Gallego-Villada[b,c], Päivi Mäki-Arvela[c], Alexander Sidorenko[d], Dmitry Yu. Murzin[c*]

a. Sustainable and supramolecular research group, Universidad Jaume I, Av. Vicent Sos Baynot, s/n, 12006, Castelló de la Plana, España.
b. Environmental Catalysis Research Group, Chemical Engineering Faculty, Universidad de Antioquia, Medellín, Colombia.
c. Laboratory of Industrial Chemistry, Process Chemistry Centre, Åbo Akademi University, Henriksgatan 2, 20500 Turku/ Åbo, Finland
d. Laboratory of Wood-Chemical products and technologies, institute of Chemistry of New Materials of NAS of Belarus, Belarus.

*Corresponding author: Dmitry Murzin (dmurzin@abo.fi), Julián E. Sánchez-Velandia (velandia@uji.es)

Graphical Abstract

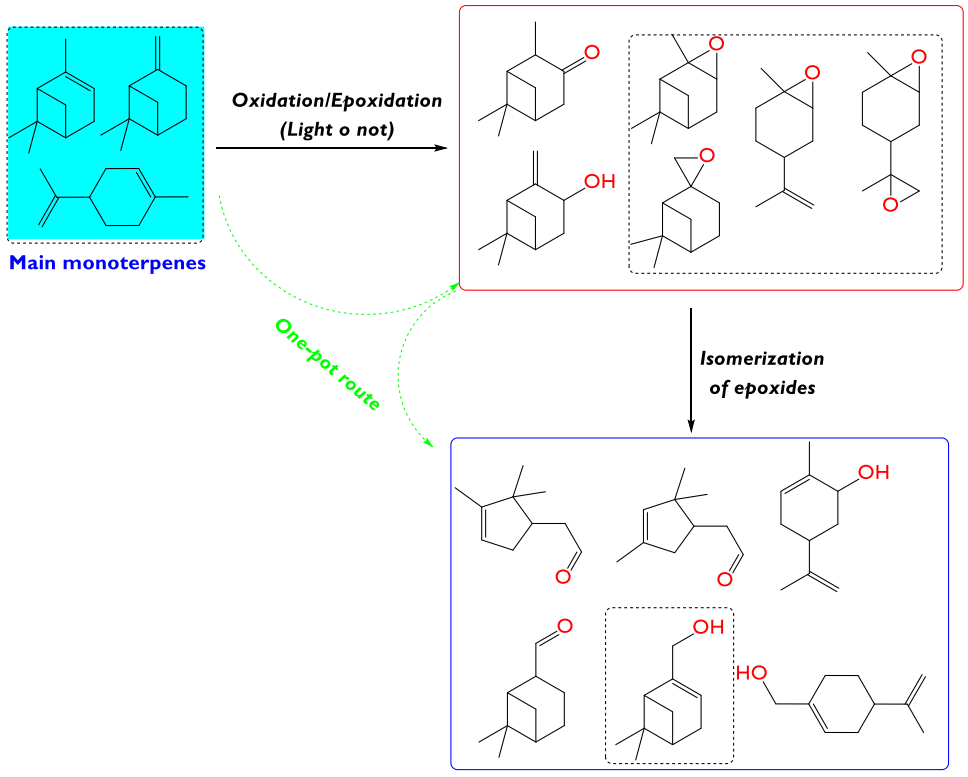

1.1. Introduction

Fine chemistry represents one of the most important industries that involve the production of molecules used as precursors of fragrances, pharmaceutical products, drugs, and related compounds. Generally, fine chemicals are produced in limited quantities (10000 metric t y^{-1}), their costs are high (8 € kg^{-1}) in comparison with other chemicals, and moreover, they are highly pure substances (>99% and <10 ppm metal residues and ee>98% in pharmaceuticals). Additionally, exhibit a relatively high E-factor ((kg waste) (kg product)$^{-1}$) with large amounts of unwanted products (**Table 1.1**) [1,2]. On the other hand, fine chemicals can be synthesized using flexible and multipurpose batch processes in relatively small amounts and with high-quality and purity products [3,4]. Fragrances, personal care, household products, or their precursors are fine chemical products that can be composed of natural organic substances or their derivatives such as monoterpenes, carboxylic acids, esters, ketones, and complex mixtures of these molecules [5].

Table 1.1. Production volume and E-factor of different industries [6].

Industry segment	Production volume (t y^{-1})	E-factor value*
Oil refining	10^6 - 10^8	< 0.1
Bulk chemicals	10^4 - 10^6	< 1-5
Fine chemicals	10^2 - 10^4	may-50
Pharmaceuticals	10 - 10^3	25-100

*E-factor value is defined as the ratio between kg of waste products to kg of the desired substance. A higher E-factor is associated with more waste and additionally, a larger negative environmental impact, while a lower E-factor corresponds to lower amounts of waste. In the calculation of the E-factor, water is excluded.

Essential oils (EOs) are products obtained from a natural raw material of plant origin, using dry or steam distillation or mechanical processes from the epicarp of citrus fruits [7,8]. EOs are composed of lipophilic and highly volatile secondary plant metabolites, reaching a mass 300 g/mol In general, the main components of essential oils are formed by monoterpenes and sesquiterpenes; one of example is the turpentine oil which basically is formed by monoterpenes such as α- and β-pinene [7]. Terpenes are hydrocarbons produced from a combination of several isoprene units $(C_5H_8)_n$. The classification of terpenes is given by the number of isoprene units: monoterpenes (n=2), sesquiterpenes (n=3), diterpenes (n=4), sesterpenoids (n=5), triterpenoids (n=6), carotenoids (n=8) and resinoids (n>8) [9,10].

Table 1.2 shows the monetary transactions related to imports and exports of the category of essential oils, as presented by the Trade Map tool [11], developed by the International Trade Centre (INTRACEN). This category includes i) concretes and absolutes, ii) resinoids, iii) extracted oleoresins, iv) concentrates of essential oils in fats, fixed oils, waxes, or similar substances obtained by enfleurage or maceration, v) terpenic by-products of the deterpenation of essential oils, vi) aqueous distillates, and vii) aqueous solutions of essential oils. World Imports and exports have varied between 5.2 and 6.1 billion US dollars, representing approximately 0.022 to 0.025% of the US gross domestic product in 2022 [12]. Furthermore, **Figure 1.1** illustrates the top importers and exporters of essential oils worldwide for the past five years, respectively. The United States stands out as the leading importer, accounting for

around 23% in 2022, but also as the leading exporter in 2022 with 13.5%, followed by India with 13.3% [11].

Table 1.2. World imports and exports (values in US Dollars thousand) of essential oils (Trade Map – Product: 3301 Essential oils, whether or not terpeneless [11]).

Year	2018	2019	2020	2021	2022
Imports	6,100,596	5,770,483	5,267,908	5,702,287	5,391,299
Exports	5,944,571	5,627,479	5,320,372	6,047,482	5,235,281

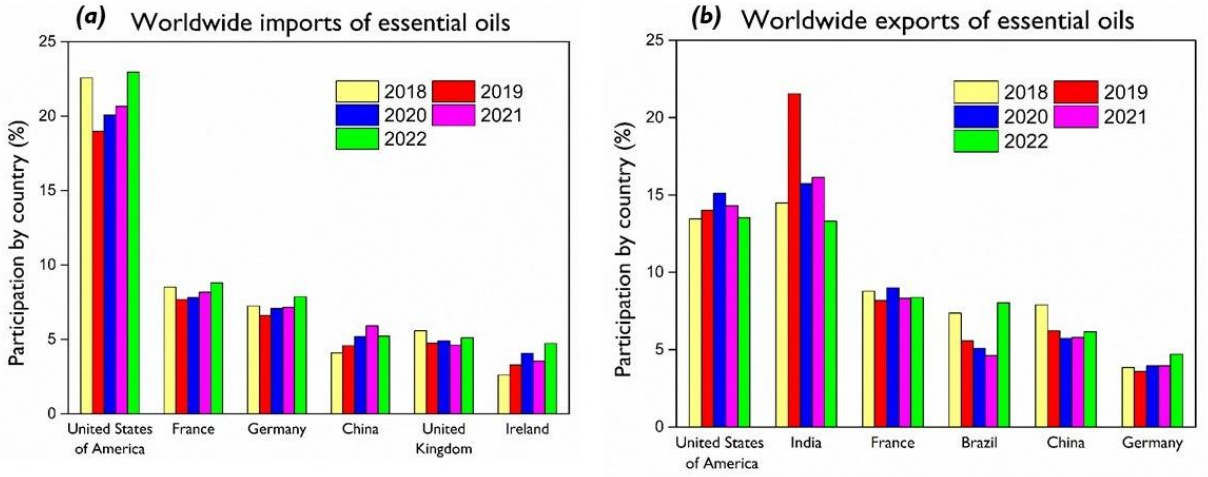

Figure 1.1. Imports (a) and exports (b) of the last five years of essential oils (Trade Map – Product: 3301 Essential oils, whether or not terpeneless [11]).

Monoterpenes are, interestingly, organic, and biomolecules derived from the isoprene unit and obtained by the plant's metabolic processes. They are cheap and abundantly available. Because of their odor and taste, monoterpenes are useful in cosmetic materials, food additives, and attractant drugs, among others. Oxygenated monoterpenes (monoterpenoids) are distributed in higher plants, algae, fungi, and even some insects [13]. Currently, isoprene monoterpenes represent a significant percentage of biomass and they are also included as volatile organic compounds (VOCs) in which more than 55000 different isoprenoids are well known [14]. There are a lot of classifications of monoterpenes which include the type of structure and its disposition in the geometrical space. For example, monoterpenes can be classified into three groups: lineal, monocyclic terpenes, and bicyclic monoterpenes (with strained structures).

Catalytic conversion of monoterpenes and different derivatives is still a way to synthetize different medicines [15,16], cosmetics [17], fragrances [18], etc. Furthermore, polysulfides derived from renewable natural product-based monomers such as terpenes, terpenoids and essential oils [19] can be used in many fields such as infrared imaging [20], energy storage [21,22], heavy metal adsorbents [23,24], oil adsorbents [25,26], fertilizers [27] and antibacterial agents [28,29].

Among a lot of applications of monoterpenes in the field of medicine, it has been reported that different essential oils of aromatic plants exhibit anti-inflammatory action, for example, limonene and 1,8-cineole [30]. Several reviews about the analgesic and anti-inflammatory activity of monoterpenes have been published [30,31], which provided detailed information

about acyclic monoterpenes (linalool, linalyl acetate, myrcene, neral, geranial, citronellal, citronellol), monocyclic monoterpenes (menthol, pulegone, R-(+)-limonene, α-phellandrene, thymoquinone, thymol, thymol acetate, carvacrol, p-cymene, carvone, carvone, hydroxydihydrocarvone, α-terpineol), and bicyclic monoterpenes (1,8-cineol, α-pinene, β-pinene, fenchone, rotundefolone, limonene oxide, carvone epoxide, and pulegoneoxide). On the other hand, the cardiovascular effects of 16 monoterpenes (carvacrol, citronellol, *p*-cymene, 1,8-cineole, linalool, menthol, myrtenal, myrtenol, α-pinene, rotundifolone, sobrerol, thymol, limonene, α-terpinen-4-ol, α-terpineol, and perillyl alcohol) have been reported, observing vasorelaxation as the main effect, which decreased the heart rate and blood pressure, showing applicability of monoterpenes for prevention or treatment of cardiovascular diseases [32].

1.2. State of the art

The primary goal of this doctoral thesis is to develop a one-pot transformation process for monoterpenes. To achieve this, it is crucial to understand the independent routes involved in the process, specifically: the oxidation/epoxidation of monoterpenes (**section 1.2.1**), and the isomerization of monoterpene epoxides (**section 1.2.2**). Therefore, the state-of-the-art review is divided into three relevant sections, including a discussion of the limited information available on one-pot transformations of monoterpenes (**section 1.2.3**).

1.2.1. Oxidation and epoxidation

1.2.1.1. General aspects

Among transformations of monoterpenes, oxidation reactions of terpenes have been widely studied focusing on two routes: the first one related to the typical oxidation by radical pathways and using oxidizing agents, and the second associated with the epoxidation of the C=C bond to achieve the corresponding cyclic ether. Selective oxidation of monoterpenes under mild conditions is currently of great interest because of the valuable intermediates used for the synthesis of fine chemicals. In the case of monoterpenes, bioderived biomass, recent development of epoxidation routes has featured several catalysts (homogeneous, heterogeneous, and enzymatic) to be highly selective at the laboratory scale, however, many of them cannot be scaled up or used in a continuous mode. Then, the practical implementation is still unexplored. In fact, the synthesis of biomass-derived epoxides is tremendously important in the modern era as they lead to a series of important chemicals which can be used for the production of polymers, fragrances, formulations in manufacture, pharmaceuticals, cosmetics, etc.

1.2.1.2. Reactivity of some monoterpenes in oxidation and epoxidation

Figure 1.2 shows the main oxidized and epoxidation products obtained from the most abundant and commercially available monoterpenes: Limonene, α-pinene, and β-pinene. Conventionally, limonene (in their two stereochemical configurations *R-(+)* and *S-(-)*) is extracted from the peels of citric fruits such as lemon and orange, respectively. In the case of lemon, the peel contains a sole isomer, S- (-)-limonene, while for orange the main stereoisomer corresponds to R- (+)-limonene. Both contain two C=C bonds which are susceptible to oxidation and epoxidation. Interestingly, location of both alkene bonds drastically affects selectivity of the final product. Several factors such as the type of catalyst, reaction conditions, the oxidizing agent, and location of the C=C are the most reported factors to drive the selectivity to desired target. Because of the presence of an external C=C bond for limonene and with the use of thermal initiators, biodegradable polymers can be

achieved. In many of these cases, the formation of oligomers (up to 40 of polymerization degree) has been reported [33]. Epoxidation of limonene is an interesting chemical route to obtain derived biomass substances for applications in fine chemistry, synthesis of intermediates used in disease treatments, building blocks in the polymeric industry, etc. The oxygen-rich epoxides are susceptible to replacing many common monomers such as bisphenol A, and they can also be used for the fabrication of new biodegradable materials [34]. In addition, epoxides can react together with other substrates to produce polyesters, polycarbonates, and copolymers with vinyl and non-vinyl monomeric units.

Limonene contains two C=C bonds susceptible to epoxidation: one of them is localized in the *endo* location while the other is in the *exo* position. From the chemical point of view, the *endo* C=C is epoxidized faster than *exo* C=C because of its reactivity. More rigid double bonds tend to be more reactive because of the strain. Then, the strained is the most reactive in epoxidation. Several factors influence epoxidation selectivity and yield, namely reaction conditions (temperature, pressure, and additive) and the oxidizing agent nature. However, the reactivity of the olefin together with the type of catalyst and the oxidizing agent could be determined as the most critical factors in driving selectivity toward the epoxide product.

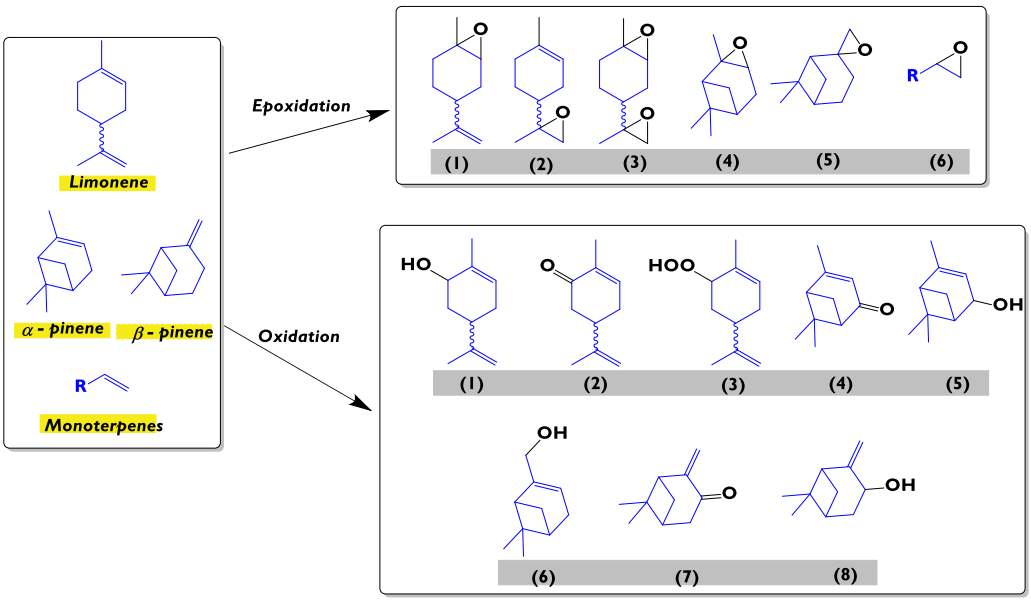

Figure 1.2. The most relevant oxidized and epoxidized products from commercial monoterpenes: ***Epoxidation***: (1) 1,2-limonene-epoxide, (2) 8,9-epoxy-limonene, (3) limonene diepoxide, (4) α-pinene epoxide, (5) β-pinene epoxide, (6) other monoterpenes epoxides. ***Oxidation***: (1) carveol, (2) carvone, (3) limonene-2-hydroperoxide, (4) verbenone, (5) verbenol, (6) myrtenol, (7) pinocamphone, (8) pinocarveol. *limonene-1.2-diol and 4-terpineol can be also obtained but after opening of limonene-1,2-epoxide by water.

1.2.1.3. Recent literature involving heterogeneous catalysts

Similarly, several olefins including monoterpenes and monoterpenoids were converted into epoxides by using a one-pot procedure dissolving the olefin into DMSO (anhydrous grade) and adding NBS to the reaction mixture [35]. However, this strategy requires adding DBU at the final step, otherwise it won't work. By using this procedure, the yields of the desired epoxides with camphene and α-terpineol as the starting materials were up to 76% in both cases. Other monoterpenoids were also used to achieve the epoxides giving up to 88% yield of carvenone.

With limonene, the yield of limonene epoxide did not exceed 69%. Interestingly, it appears that sterically hindered alcohols are oxidized more rapidly and give better results than less hindered substrates. This fact could be attributed to various factors: I) capacity of the oxidizing agent to produce radicals which then attack the C=C II) steric hindrance III) reactivity of the alkene.

On the other hand, microporous zeolites have also been reported for the synthesis of epoxides starting from monoterpenes such as α-pinene, β-pinene, and limonene. For example, with the composite ZSM-5@Co-MOF (**Table 1.3, *entry 1***) and using a green oxidizing agent (air), selectivity to the cyclic ether was up to 96.2% in the case of α-pinene. Because of the presence of bicyclic structure, both α- and β-pinene are more reactive in comparison with limonene which did not exhibit a similar structure. Then, in these cases, reactivity will depend on the type of monoterpene structure and ability of the catalyst for the adsorption and activation of the oxidizing agent. Well-known methodology for the homogeneous synthesis of epoxides starting from hydrogen peroxide and acetonitrile has been used for several decades which is comparable with those reported for the composite of zeolite-MOF. The use of air as the oxidizing agent drastically decreases the E-factor, improving the green metrics and making it more sustainable. Comparatively, a complex based on Co (**Table 1.3, *entry 2***) achieved promising results with selectivity up to 99% to limonene epoxide albeit at mediocre conversion (less than 10%). Again, α-pinene as starting the monoterpene achieved almost complete conversion and total selectivity to α-pinene epoxide. The same order of reactivity as for ZSM-5@Co-MOF was obtained. The use of this kind of complex catalyst makes the process difficult to reuse and scale up.

In the same way, the 5-(2-pyridyl) tetrazole complex of molybdenum (VI) (**Table 1.3, *entry 3***) was tested as an active catalyst for the synthesis of limonene epoxide in different stereochemical configurations and using TBHP as an oxidizing agent. Relative low selectivity to the desired epoxide was achieved, which is related to ability of TBHP to form radicals and generate polymerization reactions of C=C in limonene. It is well known that many of these reactions (polymerization or oligomerization) depend on the initiator, solvation, and the intermediate carbocation. Control of epoxidation over oligomerization (or polymerization) is associated with the amount of the oxidizing agent, temperature, and the type of solvent. For radical polymerization, the use of non-polar solvents (such as benzene and toluene) generates a co-lateral chain transfer reaction which affects the overall kinetics.

Among complexes covalently attached to solids supports, β-tetra-brominated meso-tetraphenylporphyrinatomanganese(III) acetate [MnTPPBr4(OAc)] (MnPor) [36] was anchored onto a magnetite imidazole-modified graphene oxide nanosheet (Fe_3O_4.GO.Im) (**Table 1.3, *entry 4***). The catalyst was successfully applied for epoxidation of different alkenes using urea hydrogen peroxide (UHP) and acetic acid (HOAc) as oxidant activators under mild conditions. Olefins were oxidized efficiently to their corresponding epoxide with 63–100% selectivity in the presence of Fe_3O_4.GO.Im@MnPor. Moreover, a remarkable turnover frequency (93) was achieved for the oxidation of α-pinene. The graphene oxide-bound Mn-porphyrin was recovered from the reaction mixture by magnetic decantation and reused several times. Similarly, tungsten complexes were used as active catalysts for oxidation of commercial and naturally available limonene (including other natural-based compounds) (**Table 1.3, *entry 5***). The molybdenum (II) catalyst precursors are very active, reaching 100% of conversion and 98% of selectivity to the epoxide. However, their heterogenization seems to be beneficial with to

improve the sustainability. In general, W complexes exhibit better activity than Mo complexes, however when supported on MCM-41, activity decreased substantially. This could be related to poor anchoring, dispersion, and size of the crystallite. The authors [37] performed DFT (Density Functional Theory) calculations to elucidate the reaction mechanism and the difference between the W and Mo centers. Surprisingly, in the catalytic cycle, tungsten complexes and iodide ligands can be oxidized from W(II) to W(VI) more readily than molybdenum complexes, even though the energies of the relevant species involved in the cycle are very comparable across all complexes. Furthermore, it appears that iodide complexes were more easily oxidized by ROOH, but the catalytic reaction was less favored than for bromides. In general, tungsten complexes serve as effective catalysts; however, their performance was not improved when supported on MCM-41. Due to the challenging synthesis process compared to molybdenum analogues, such complexes are not promising. On the other hand, certain molybdenum heterogeneous catalysts show activity, higher than the complexes and offer the advantages typical of heterogeneous catalysts.

In comparison with the previous reports [36–40], a series of composites materials composed of WOx and SiO_2 (**Table 1.3, entry 6**) were synthetized by using a novel, template-free sol-gel method [41]. The effectiveness of the synthesis method lies in its custom-designed reactor, which enables interactions of the reactants exclusively in the presence of $scCO_2$ (supercritical carbon dioxide). Various synthetic parameters were carefully examined to optimize the performance of the resulting materials as heterogeneous catalysts in epoxidation reactions using H_2O_2 as an environmentally friendly oxidant.

On the other hand, modification of zeolite Y with a complex of the type $[VO(Sal_2bz)]_2$ [42] was successfully applied as a heterogeneous catalyst for the synthesis of allylic products from the two renewables molecules such as limonene and α-pinene. Relatively mild conditions (**Table 1.3, *entry 7***) has allowed to achieve conversion close to 99% and selectivity up to 70% to the desired products. The decrease of the steric hindrance increases the formation of the olefinic product at the expense of the formation of allylic oxidation products. Formation of a specific product (epoxide vs allylic or diols) can be explained by coordination of the C=C bond (electron-rich) to the oxo vanadium active species (**Figure 1.3**).

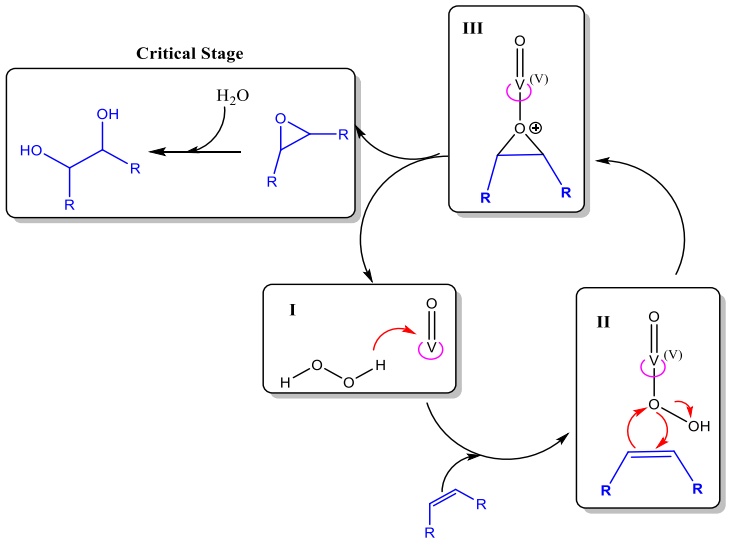

Figure 1.3. Proposed reaction mechanism for epoxidation and ring-opening of some epoxides. Steps: (I) Activation of hydrogen peroxide by coordination of the oxo-vanadium unit (II) back donation of the oxygen to the olefin (III) formation of the oxirane ring.

On the other hand, two double layer hydroxides ZnAl-LDH and MgAl-LDH were functionalized with *bis*(4- HOOC-phenyl)-acenaphthenequinonediimine) (H2BIAN) [43] (**Table 1.3**, ***entry 8***), and then tested for the selective synthesis of epoxides starting from limonene. The rational design of this catalyst was based on the idea that π-based ligands exhibit high activity in the transition metal chemistry. In this way, the material was evaluated as a possible catalyst for the transformation of limonene with TBHP as the oxidizing agent. In comparison with the previously discussed reports [36–42], the temperature was as high as 110°C in toluene as a solvent. From the green chemistry point of view, the use of toluene as the solvent is deemed undesirable due to its toxicity and potential negative effects. ZnAl-LDH-BIAN-MgI_2 was the most active catalyst resulting in 94% of conversion with almost 97% selectivity to the epoxide [43]. Stereoselectivity was also assessed for R-(+)-limonene-1,2-epoxide which was found to be crucial to achieve one diastereomer over another other and comparing homogeneous and heterogeneous catalysts. Homogeneous catalysts clearly favor the *trans* diastereomer contrary to heterogeneous counterparts. Three catalysts did not show any preference, producing both diastereomers in approximately equal amounts (around 50/50 ratio). However, the ZnAl-LDH-BIAN-MoBr2 catalyst displays an intermediate behavior, favoring the trans diastereomer with a ratio of 28-to-72.

Table 1.3. Heterogeneous catalyst for the oxidation/epoxidation of monoterpenes.

Entry	Catalyst	Substrate	Reaction conditions	Oxidizing agent	X (%)	S[b] (%)	Ref
1	ZSM-5@Co-MOF	α-pinene	10 mg ZSM-5@Co-MOF-150 catalyst, 3 mmol olefin, 5 h	Air	98.2	96.2	[39]
		β-pinene			72.6	78.3	
		Limonene			48.1	98.0	
2	$[Co(NH_3)_6]Cl_3$	α-pinene	5 mg of catalyst, 3 mol of pinene, 10 g of solvent, 90°C, 0.3 mmol of TBHP, 5 h, flow rate of air 40 mL min^{-1}.	Air	98	99	[40]
		β-pinene			43	55	
		Limonene			9	>99	
3	5-(2-pyridyl) tetrazole complex of molybdenum (VI)	Limonene	TFT, 70°C, ratio Mo:monoterpene: TBHP: 1:100:210, 24 h.	TBHP	>99	51 to monoepoxides**	[38]
4	Fe_3O_4.O.Im@MnPo r	α-pinene	Molar ratios catalyst: substrate: UHP: HOAc of 1:100:200:300 in CH_2Cl_4, 1 h, room temperature.	UHP with acetic acid (HOAc)	93	95 to epoxide	[36]
		Limonene			67	95% exo-epoxide and 5% endo-epoxide	
5	MCM-$MoIL_2$	S-Limonene	2 eq. of oxidant, 3 mL of dichloromethane, and 175 mg of catalyst at 328 K and 24 h.	TBHP	100	98	[37]
6	WO_3-SiO_2	Limonene	1 eq. of oxidant and 20 mg catalyst in 1-4-dioxane+isopropanol, at 80 °C for 4 h.	H_2O_2	54	53 epoxide 33 glycol 9 allylic products	[41]
7	$[VO(sal_2bz)]_2$-Y	Limonene	2 eq. of oxidant, 15 mf of catalyst, 3 mL acetonitrile as solvent, at 80 °C for 24 h.	H_2O_2	90	39 glycol 49 allylic products	[42]
		α-pinene			100	70 allylic products	
8	ZnAl-LDH-BIAN-MoI_2	Limonene	2 eq. of oxidant, toluene as solvent, at 110 °C for 24 h	TBHP	94.0	97.0 epoxides	[43]

	ZnAl-LDH-BIAN-$MoBr_2$				80.0	89.0 epoxides	
	MgAl-LDH-BIAN-MoI_2				64.0	93.0 epoxides	
	MgAl-LDH-BIAN-$MoBr_2$				79.0	93.0 epoxides	
9	Co/SBA-16	Limonene	3.6 mmol of substrate, 170 mg of catalyst, 10 mL min^{-1} of O_2, 12 mmol Isobutyraldehyde, and 10 mL of ethyl acetate, at 301 K for 200 min.	O_2	99 (Co/Si = 1.1 %) 99 (Co/Si = 8.8 %)	44 epoxide 41 diepoxide 41 epoxide 25 diepoxide	[44]
10	W/SiO_2	Limonene	1 mmol of substrate, 2 mmol of oxidant, 5 mL of acetonitrile, 10 mg of catalyst, at 90 °C for 6 h.	H_2O_2	68	53% 1,2-epoxide 11% 8,9-epoxide	[45]
11	$[VO(L).H_2O]$-Y	α-Pinene	10 mmol substrate, 20 mmol of oxidant, 70 mg of catalyst, 2 mL of acetonitrile, at 75 °C for 24 h.	H_2O_2	85.4	46.5 verbenone 7.7 verbenol 44.2 α-campholenic aldehyde 1.5 epoxide	[46]
		Limonene			87.4	40.6 carvone 32.0 carveol 9.1 glycol 6.5 1,2-epoxide 11.8 4-terpineol	
12	ZnCo-MOF	α-Pinene	3 mmol of substrate, 40 mL min^{-1} of oxidant, 30 mg of catalyst, 10 g of DMF as solvent, at 90 °C for 5 h.	Air	95.5	96.7 epoxide	[47]
		β-Pinene			70.8	62.5 epoxide	
		Limonene			42.4	80.3 epoxide	
13	Pd/HPA-300/SBA-15	β-Pinene	1 mmol of substrate, 6.8 mmol of oxidant, 15 mg of catalyst, 1 mL of acetone as solvent, 50 °C, 18 h, 450 rpm.	H_2O_2	99	63 trans-pinocarveol 12 pinocamphone 16 myrtenol	[48]
	Pd(0.5)/HPA/SBA-15				90	67 trans-pinocarveol 13 pinocamphone 15 myrtenol	
14	Co(II) complex	α-Pinene	20 g of α-pinene, 100 mg of catalyst, volumetric flow ratio 5:5 for mixture: CO_2, 160 atm, at 260 °C in a tubular reactor of 7 cm^3.	Atmospheric O_2	59.8	21.1 camphene 3.0 tricyclene 5.5 α-fenchene 4.0 verbenone 6.2 β-pinene 19.4 limonene 5.7 p-cymene 4.2 bornyl acetate 4.2 α-fenchyl acetate	[49]
15	MgO	Limonene	0.1 mmol substrate, mass ratios for substrate/MgO/H_2O/acetone/acetonitrile:H_2O_2 of 1:1.20:30.3:19.7:15.7:1.20, 50 °C, 1000 rpm	Peroxyacetimidic acid[a]	80 (0.5 h) 100 (2 h)	100 epoxides (1,2 + 8,9) 96 diepoxide	[50]

*Reported as the isolated yield. **Molar ratio of diepoxide/monoepoxides was 0.3. ***BIAN*:** bis(4-HOOC-phenyl)-acenaphthenequinonediimine. ***LDH*:** Layered double hydroxide. Bipy: 2,2'-bipyridine-4,4'-dicarboxylate. [a]*In-Situ*

production from H_2O_2 with acetonitrile. [b] The epoxidized double bond is at the 1,2 position unless otherwise indicated.

Materials containing special textural properties e.g.: silica, zeolites, etc. can be of interest for the selective synthesis of organic reactions because of their ability to distribute active sites in confined spaces. In many cases, they can be highly dispersed increasing catalytic activity. A particular example of these kind of materials is Co/SBA-16 (**Table 1.3, *entry 9***) in which Co can be located inside of the pores of the well-defined structure of SBA-16. Interestingly, the catalyst was used as heterogeneous material for aerobic Mukaiyama epoxidation of limonene in the presence of isobutyraldehyde, under mild conditions (28°C, ethyl acetate as the solvent, and 200 min). Synthesis of these catalysts by adjusting the pH was performed with the aim to obtain isolated tetrahedrally coordinated Co^{2+} ions in the support which could act as the active species. The reported methodology affords materials with larger pore volumes and with larger pore sizes making them very attractive for the diffusion of relatively large molecules such as limonene. In general, these new materials displayed high reactivity for epoxidation of limonene yielding different epoxides in both the *endo* and *exo* positions. In addition, the authors [44] suggested that $Co^{3+}OO^{-}$ peroxo intermediate could be critical for the formation of the epoxides which was rigorously analyzed by kinetic analysis.

In a similar way, tungstenocene (IV) dichloride (**Table 1.3, *entry 10***) was deposited and grafted on an amorphous silica by using two approaches: liquid-phase and dry impregnation. The results suggest that W-containing systems were active in the epoxidation of limonene when hydrogen peroxide was used as an oxidizing agent. Only WO_3 displayed mediocre activity because of the amount of tungsten in the bulk of pure tungsten oxide samples. In fact, selectivity to epoxide was good (for both 1,2- and 8,9- C=C bonds) while formation of carveol (and their isomers) was low. As no menthenediols were formed as side products, it is possible to suggest that with this catalyst oxidation via the homolytic pathway did not play a role. In comparison, when TBHP was used as the oxidant agent, limonene indeed underwent oxidation with a very large number of minor side-products which are related with the radical species generated by TBHP decomposition [51].

In comparison with the previous catalytic system, transition metals containing complexes with Schiff-base ligands (**Table 1.3, *entry 11***) were entrapped and deposited in the cages of zeolite-Y and then were tested in the catalytic oxidation of limonene and α-pinene. Zeolite-Y [46] have gained attention because of their properties such as a high surface area, large pore volume as well as the typical channels and cavities which made it possible for entrapment of large size complexes [52,53]. Nevertheless, the post-activation of the complex for further uses is still a challenge. Because of the organic counterpart, typical calcination of these kind of materials is not possible. On the other hand, several steps required for the covalent anchoring of the complex to the zeolite, make this alternative not too simple. With respect to catalytic activity, the material was successfully applied as an active catalyst for oxidation of both α-pinene and limonene monoterpenes and using hydrogen peroxide as a green oxidizing agent. The ratio monoterpene to the oxidizing agent was 1:2. Oxidation was performed at relatively mild conditions (75°C, 24 h and acetonitrile as a solvent). Interestingly, after such a long time, the conversion was not complete, achieving values up to close to 90% and with mediocre selectivity to verbenone (46.5%) in the case of α-pinene and carvone (40.6%) for limonene. Interestingly for oxidation of α-pinene, campholenic aldehyde was obtained in almost in the same amounts as verbenone. It is well known that campholenic aldehyde (campholenal) is one of the main products of α-pinene epoxide isomerization with Lewis acidic sites. This suggests

that a large amount of this epoxide is converted totally to campholenic aldehyde in the presence of Lewis acid sites. On the other hand, oxidation of limonene also gave limonene-1,2-diol (glycol) and 4-terpineol as the main subproducts, which also suggesting that an intermediate epoxide is obtained thereafter being consumed by reacting with water. Diols can be obtained in a one-pot two steps in which the first step is formation of the epoxide and then, the ring-opening using water as the nucleophile. The stereochemistry of these diols remained unexplored.

ZnCo-MOF catalyst (**Table 1.3, *entry 12)*** was tested as an efficient material for the air epoxidation of monoterpenes (including also other cycloalkenes) [47]. Activation of oxygen is as well a very difficult process requiring energy or at least a sacrificial reducing agent and initiator to obtain the singlet-state atomic oxygen. The use of the sacrificial agent has been reported to have a negative effect on the epoxidation because of the large quantity of low-value secondary products. Metal organic frameworks which are porous, crystalline materials, with a high surface area and adjustable structure, were successfully modified with Zn and Co by using the dry-gel method. Synthesis of the material was performed in only one vessel containing the desired amounts of the ligand (dicarboxylic acid), precursors of Zn and Co, HF and water. Exceptionally, synthesis of MOF does not require high temperature and pressure and usually the synthetic protocols are reproducible. A typical crystal structure and functional groups were identified by TEM and Raman spectroscopy (**Figure 1.4**). Growing crystalline MOFs together with Zn and Co, avoids the use of a sacrificial agent in the epoxidation of olefines. Almost complete conversion with 96.7% selectivity to α-pinene epoxide was achieved after 5 h of reaction time (**Figure 1.4**) [47]. Detected by-products such as campholenic aldehyde illustrate the nature of the Lewis acid sites in the catalyst.

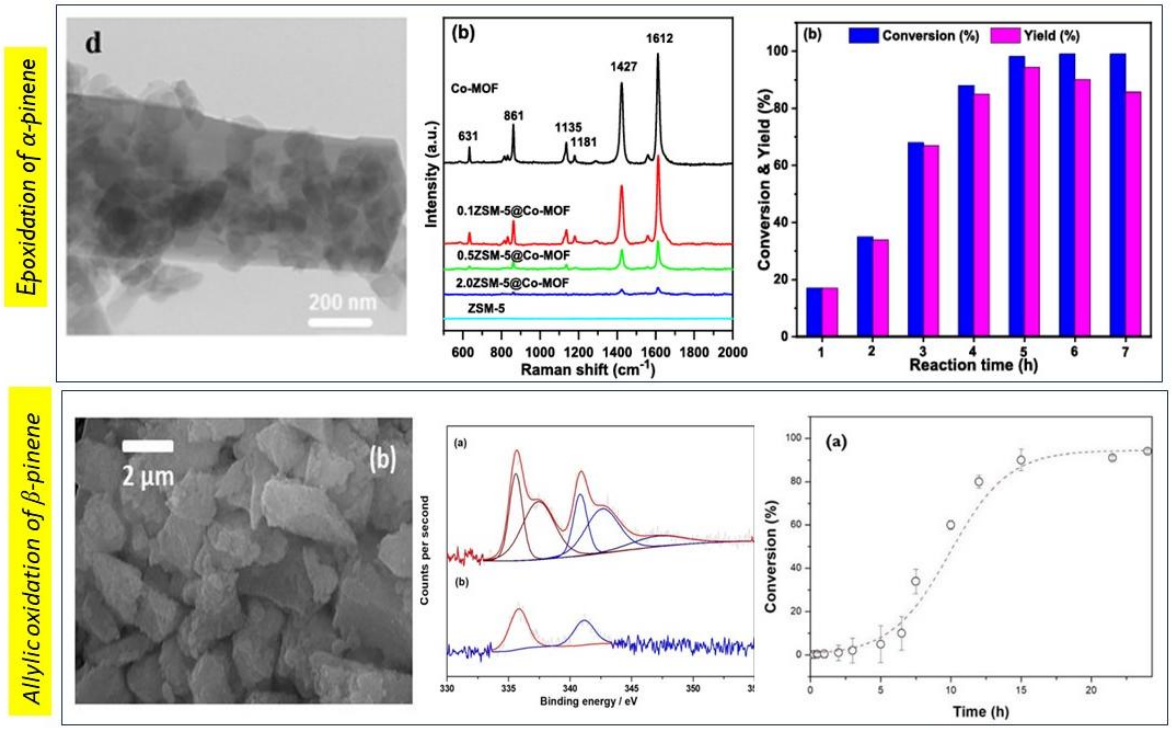

Figure 1.4. Some selected characterization and catalytic activity of materials active in oxidation or epoxidation of terpenes: a) epoxidation of α-pinene with ZnCo-MOF b) allylic oxidation of β-pinene with Pd/HPA/SBA-15. Images reproduced with permission of ref [39] (a) and [48] (b).

The last example, i.e.: combination of metal/acid sites for selective epoxidation, demonstrates that nature the of the metal center, together with the distribution of acid/basic sites can promote epoxidation rather than isomerization and allylic oxidation. Sometimes, the solvent also plays a critical role together with the oxidizing agent. Then, a combination of these all factors can drive the reaction to the desired epoxide/oxidized product. Considering these facts, recently a Pd supported on a modified heteropolyacid-silica (HPA/SBA-15, **Table 1.3, *entry 13***) [48] was reported to be active in the allylic oxidation of β-pinene into *trans*-pinocarveol as the main product and myrtenol/pinocamphone as the byproducts. Multifunctional heterogeneous materials containing both a metal and an acid function were prepared by using wetness impregnation, showing typical laminar geometry together with Pd in oxidation state +2 (**Figure 1.4**). In this case, the material containing Pd with a heteropolyacid supported on SBA-15 (Pd/HPA-300/SBA-15) was one of the best materials to give *trans*-pinocarveol with the yield of 65% (total conversion of β-pinene). Independent on the Pd loading (0.5 wt% or 1.0 wt%) and calcination temperature, selectivity to the desired trans-pinocarveol was not affected. At the same time the calcination temperature influenced conversion, Pd dispersion, acidity, and the surface area. It appears that when the support was changed to amorphous silica, the selectivity changed drastically (pinocarveol decreased to 53%, with only 17% of conversion). Then, distribution, dispersion and location of the metal and acid functions drive selectivity to the desired product. The catalyst was successfully reused, and the process was scaled up to 10 mL with no negative implication for selectivity or conversion.

$CoBr_2$ complex with 2,6-lutidine [$Co(2,6\text{-}Me_2C_5H_3N)_2Br_2$] (**Table 1.3, *entry 14***) was prepared and tested for the oxidation of α-pinene in a flow reactor using a supercritical solvent (mixture of CO_2 and ethyl acetate) [49]. The range of temperature and pressure varied between 190-230°C and 110-125 atm, giving isomerization products with partial racemization under these conditions. Oxidized products such as verbenone and pinocamphone were also obtained which selectivity seems to be lower (<20%). The authors suggest the presence of campholenic aldehyde which is formed by the ring-opening of α-pinene epoxide. Formation of acetoxylated products was also observed (up to 6%). The studied reaction conditions with the Co-complex seem not to be favorable either for oxidation or epoxidation.

Recently, commercial MgO (**Table 1.3, *entry 15***) has been reported as a versatile catalyst for the selective synthesis of limonene epoxides and diepoxide, depending on the reaction conditions [50]. The epoxidation catalytic route was carried out with H_2O_2 in a Payne system, which used acetonitrile as an oxidant activator, and water and acetone as solvents. The highest yields for limonene epoxide (80%) and diepoxide (96%) were achieved after 30 min and 2 h, respectively, at a low temperature (50 °C). The catalyst exhibited a composition of 82.6 wt.% of the periclase phase (mineral form of MgO) and 17.4% of the brucite phase (mineral form of $Mg(OH)_2$). After the reaction, a slight phase transition was observed from periclase to brucite, explained by the hydration under the reaction conditions, which had a negative effect on the selectivity to diepoxide after three reuses (a decrease from 97% to 76%). In general, the authors [50] reported that diepoxide is favored with high concentrations of MgO and H_2O_2, high temperatures, and long reaction times, while epoxide is favored mainly with low temperatures and short reaction times. A successful kinetic modeling was reported for the first time for the epoxidation of R-(+)-limonene using a Payne reaction system, with a set of three reactions describing the formation of intermediate oxidant, the H_2O_2 decomposition, and the epoxidation reaction of limonene with intermediate.

1.2.2. Isomerization of monoterpene epoxides

1.2.2.1. Reactivity of monoterpenes epoxides and main factors that affecting it

Isomerization of monoterpene epoxides refers to the rearrangement of the epoxy group within a monoterpene molecule, resulting in the formation of different isomers with altered chemical structures and properties. During isomerization of monoterpene epoxides, the epoxy group undergoes intramolecular rearrangement, leading to high-added value chemicals of interest in the field of natural product chemistry and has implications in various industries such as fragrance, flavor, and pharmaceuticals. Because epoxides are highly strained (strain energy, SE, of 27.9 kcal mol^{-1}) due to the bond angle distortion [36], they react with nucleophiles and electrophiles that rearrange their structure in thermodynamically stable substances such as aldehyde, alcohols, ketones among other compounds. In the case of monoterpene epoxides such as α- and β-pinene epoxides (**Figure 1.5**) can rearrange using an acidic or basic medium onto oxygenated compounds. These epoxides contain a cyclohexane ring as a part of their structure. For α-pinene epoxide the epoxy group is in the endo-position being for β pinene epoxide in the *exo*-position, which is the cause of their different reactivity. α-Pinene epoxide acquires more stress in comparison to β-pinene epoxide (**Figure 1.5**). It is attributed to lower β-pinene epoxide torsional strain in comparison with α-pinene epoxide and for this reason, its arrangement energy is higher [36].

Both epoxides are usually starting materials for the synthesis of chemicals of interest in the fragrance industry. For example, from α-pinene epoxide, it is possible to achieve campholenic aldehyde, *trans*-carveol, *trans*-sobrerol, pinocarveol, and pinocamphone, among others. Campholenic aldehyde and *trans*-carveol are the main products when the epoxide is in contact with an acidic catalyst. Selectivity is dependent on the specific reaction conditions and also on the type of catalyst. In general, the most important factors that drive selectivity to a specific target starting from these epoxides are the type of acid sites (Brønsted, Lewis or their ratio) and the solvent (polar or non-polar, e.g.: toluene, DMSO, DMF, etc.). **Figure 1.5** shows the most relevant products obtained from the isomerization of both epoxides.

Isomerization of α-pinene epoxide, one of the most studied monoterpene epoxides, can give two main products: campholenic aldehyde and *trans*-carveol with *trans*-sobrerol, pinocamphone, pinocarveol, and *p*-cymene as the secondary products. Campholenic aldehyde can be selectively obtained using a Lewis acid catalyst and non-polar solvents such as toluene. Ring-opening of the epoxide was described by coordination to the Lewis acid site and then rearrangement of the internal cyclobutene finally giving the desired isomerization products. Interestingly, the C-C shift to give a secondary carbocation in the second step can be carried out because of the internal tension of cyclobutene. This kind of bicyclic compound tends to relax their internal stress to give more favorable energetic products. The most relevant references for the synthesis of both industrially important commodities such as *trans*-carveol and campholenic aldehyde are mentioned in **Table 1.4.**

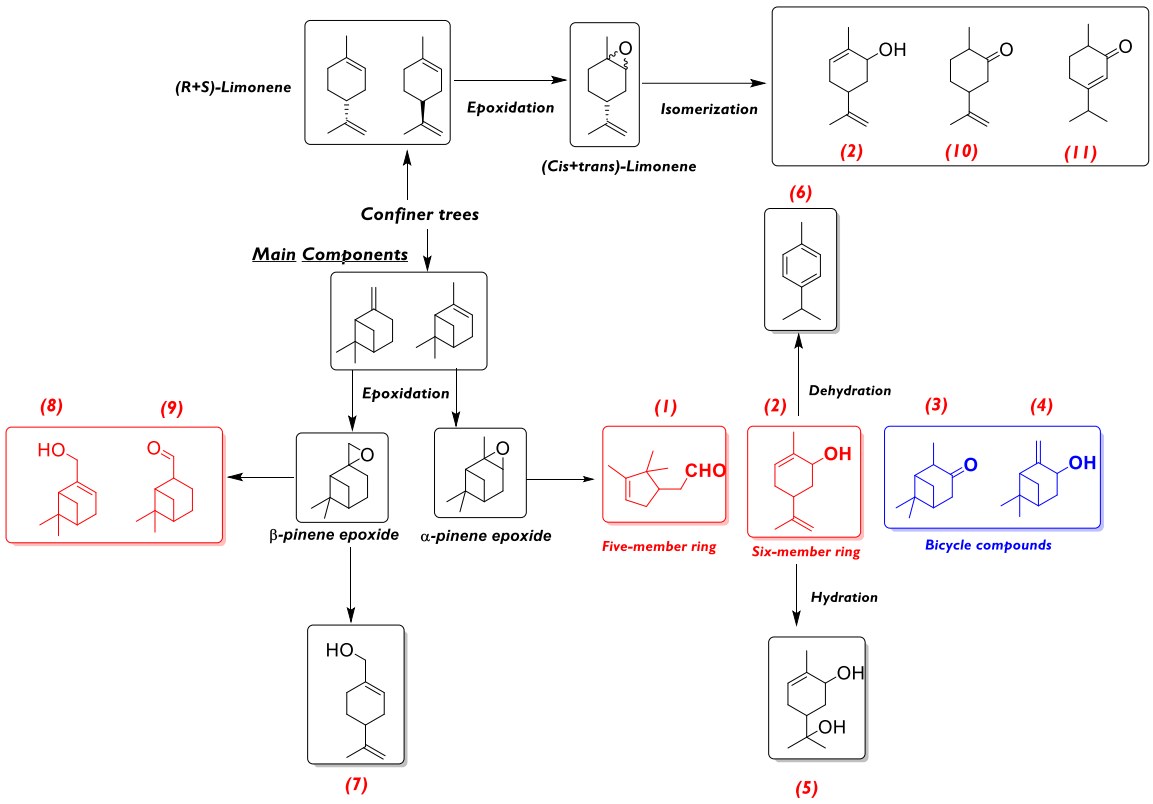

Figure 1.5. The most relevant isomerization products from α-, β-pinene and limonene epoxides by using acidic heterogeneous and homogeneous catalysts. 1=Campholenic aldehyde, 2=Carveol, 3=Pinocamphone, 4=Pinocarveol, 5=*trans*-sobrerol, 6=*p*-cymene, 7=Perillyl alcohol, 8=myrtenol, 9=Myrtanal, 10= Dihydrocarvone, 11= Carvenone.

1.2.2.2. Analysis of the most relevant heterogeneous catalysts for the synthesis of aldehydes and alcohols

A selective catalyst based on zirconium phosphate was used as an inexpensive, efficient, and cost-effective material for synthesis of *trans*-carveol from α-pinene epoxide. *Trans*-carveol has been widely reported as a precursor for the synthesis of fragrances, shampoo, toilet soaps and non-cosmetics products. It is the main constituent of spearmint essential oil. In addition, carveol as a phytochemical together with other monoterpenes was demonstrated to be active in the cloned α7 subunit of the human nicotinic acetylcholine receptor [54].

It is well known that Zr-phosphate catalysts comprising Zr-framework together with the covalently anchoring Zr-P can be effective for the ring-opening of epoxides (**Table 1.4, *entry 1).*** The acidic nature of the catalyst can be controlled by tuning Zr to P ratios. In [55], the authors claimed that exceptional activity is attributed to broad functionality of the phosphate groups which give the Brønsted acidic nature this together with DMA as a solvent provided the best results reported up to now for the synthesis of the six-member ring product (*trans*-carveol). A similar yield of carveol (73%) has been reported using task-specific ionic liquids (TSILs) which act as both eco-friendly catalysts and reusable solvents in numerous industrial reaction [56]. The authors successfully correlated the reaction behavior with physical properties such as conductivity, density, molecular volume, standard entropy, and lattice energy. In addition, the designed process complies with the green metrics criteria having 100 % of atom economy and E-factor of 1 [56].

Fe supported catalysts [57,58] were reported to be selective in isomerization of α and β-pinene epoxides and also in the rearrangement of limonene epoxide with solvent polarity playing a critical role (**Table 1.4, *entries 2-4***). As mentioned previously, this is a very sensitive reaction which can give a variety of aldehydes, alcohols, alkenes, etc. Then, controlling the type and strength of the acid sites as well as the solvent type can change the distribution of products. In the case of Fe/MCM-41, a decrease in selectivity to campholenic aldehyde was observed when the solvent was changed from toluene to tert-butanol, while selectivity to trans-carveol was apparently increased. The same trend was observed with Fe/SBA-15; however, the effect was more prominent. At total conversion of α-pinene oxide, selectivity decreased from 64% (for toluene) to 48% when tert-butanol was used as the solvent. When the authors [57] compared the same support with another metal (Cu), lower yields (in terms of conversion and selectivity) to the desired aldehyde and alcohol were achieved. For example, in the case of Cu/MCM-41, the maximum conversion was 20% while selectivity to campholenic aldehyde was 82%. An increase of conversion (46%) resulted in lower selectivity to the aldehyde (71%). The ability of Cu to coordinate *tert*-butanol is an explanation offered at such reaction conditions. The total Lewis acidity of Cu materials in comparison with Fe counterparts is the reason Cu being more selective to campholenic aldehyde. In the same way, thermodynamics of the isomerization of both epoxides at the reported reaction conditions showed that all the isomers (campholenic aldehyde, trans-carveol, isopinocamphone, fencholenic aldehyde from α-pinene oxide and myrtanal, myrtenol and perillyl alcohol from β-pinene oxide) are thermodynamically favorable, but it is more spontaneous for the synthesis of campholenic aldehyde and myrtanal. No significant effect in different solvents and temperatures were found to be critical in thermodynamics [59].

The same Fe catalysts were also active in isomerization of limonene and β-pinene epoxides (**Table 1.4, *entries 3-4***) [57,58], however in the first case poor activity and selectivity was obtained. Changing polarity of the solvent (from toluene to acetonitrile) induces a slight increase of conversion, however, selectivity to isomers was in all the cases lower than 50%. Competition between isomerization and hydrolysis is expected to be one of the most important factors to control. Remaining water (in the solvent, catalyst, or the additive) can produce limonene-1,2-diol rather than typical isomers (dihydrocarvone, trans-carveol, etc). Although the undesired diol finds applications in fine chemistry, formation of the isomers is more attractive because of their annual costs and direct implications in factory processes. On the other hand, isomerization of β-pinene epoxide which typically produces myrtanal, myrtenol and perillyl alcohol as the major products, was also tested with Fe catalysts showing that in all the cases and changing the polarity of the solvent, the major product is myrtanal [60]. However, modification of catalyst as well as the solvent can give perillyl alcohol as the main target; some examples are described in ***Entries 6-7*** (**Table 1.4**). In the case of zeolite-beta [61], the use of DMSO as a polar basic solvent improves selectivity to perillyl alcohol over myrtanal and myrtenol while for Ti- and Mo- based silica materials (MCM-41 and SBA-15) [60] the same main target was obtained but with a non-polar solvent. It is well known that, generally, perillyl alcohol is favored with a polar basic solvent whereas myrtanal is obtained with non-polar ones. This exceptional case in which Ti or Mo materials were selective to perillyl alcohol using n-hexane as a non-polar solvent is due to I) the typical texture and distribution of the active sites and II) the stabilization of the transition state. Myrtanal requires less steps from the opening of β-pinene epoxide, and the energetic barrier of the two transition states (TS) can be unfavored because of solvation and its interaction with TS. For

perillyl alcohol, more steps are necessary in addition to a conformation change in which a Csp^3 rotates to favor a hydrogen transfer [62].

In the same way, MoO_3 modified beta zeolite was also tested for the selective ring-opening of α-pinene epoxide at relatively mild conditions (**Table 1.4, *entry 8***). In this case, the authors reported that the effect of different solvents (cyclohexane, toluene, nitromethane, propan-1-ol, dichlorobenzene, cyclohexanone, cyclohexanol, ethyl acetate and N,N'-dimethylformamide) slightly influenced selectivity to campholenic aldehyde and trans-carveol. The highest selectivity (44.9%) to the aldehyde was achieved when nitromethane was used as a non-polar solvent while N,N'-dimethylformamide (polar basic) favored *trans*-carveol. In the latter case, conversion was just 27%. As mentioned previously, the synergy between acidity (strength and type) and the solvent type can favor the formation of a specific product in the isomerization of α-pinene epoxide. The use of alcohols of a low molecular weight can induce formation of high-molecular weight substances which result from the nucleophilic attack of the alcohol to the epoxide. A typical example is the methanolysis of α-pinene epoxide in an acid medium which can yield sobrerol ethers [63]. The proposed reaction pathways are depicted in **Figure 1.6**. As the first step, α-pinene oxide is coordinated to the acid site (Brønsted or Lewis which will change the strength of the non-covalent bond) leading to an intermediate carbocation. Then different rearrangement of the carbocation to have a more thermodynamically favorable cation occurs. At this point, simple proton elimination can give pinocarveol and pinocamphone while the C-C shift in the two routes can eliminate the strain of the internal cyclobutene generating two different carbocations. Thereafter carveol and its optical configurations, and campholenic aldehyde are formed as more favorable products. Kinetics (which could be affected by temperature, the type of solvent, and the catalyst) is crucial to obtain a specific target. Thermodynamics also is crucial in this rection but is less critical with respect to kinetics.

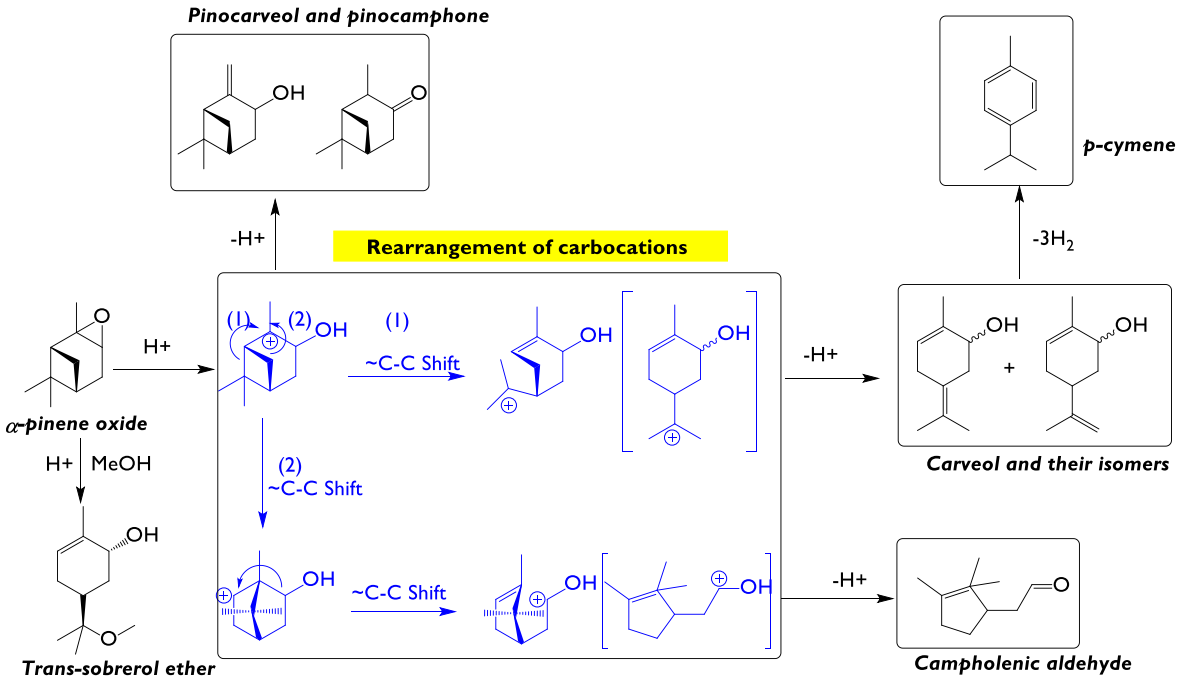

Figure 1.6. Schematic representation of the main reaction pathways in isomerization of α-pinene epoxide into various products. 1=Campholenic aldehyde, 2=carveol and their isomers, 3=p-cymene, 4=pinocarveol, 5=pinocamphone, 6=trans-sobrerol ether.

With the aim of investigating the oxidation state of iron in Fe/MCM-41, different precursor salts were tested and then compared with the heterogeneous catalysts (**Table 1.4, *entry 9***). For this, iron nitrate, chloride, sulfate, and iron oxide were tested at the same reaction conditions and the results suggest a crucial effect on the role of the oxidation state of both Fe^{3+} and Fe^{2+}. Although the amount of Fe active sites was not the same, the excess (almost 7-10-fold with respect to iron in Fe/MCM-41) showed that, apparently, the most active site was Fe^{3+} rather than Fe^{2+}. Only 7% of conversion was achieved when $FeSO_4.7H_2O$ was used as the catalyst Fe_2O_3 was completely inactive. In fact, it was evident that the nature and the oxidation state of the metal site play an important role in determining the conversion and selectivity of α-pinene epoxide isomerization. This fact could be explained by the acidic nature of Fe^{3+} with respect to Fe^{2+}; In the first case, more available free d-orbital is present enhancing Lewis acidity.

On the other hand, heteropolytungstate based on Cs [64] was selectively tested in biomass derived α-pinene epoxide yielding mainly trans-carveol, *trans*-sobrerol and pinol in 60-80%, exceeding the yields reported previously for the synthesis of pinol (**Table 1.4, *entry 10***). For this case, different reaction conditions were tested (mainly time, temperature, and polarity of the solvent) highlighted that relatively short reaction times (<180 min) and low temperature enhance formation of pinol over campholenic aldehyde and *trans*-sobrerol. Further optimization of the reaction temperature and catalyst loading enabled the pinol yield up to 80% while the combined selectivity with campholenic aldehyde was *ca.* 95%. In addition, low temperatures are favorable for the intermediate carbocation to form *trans*-carveol. Interestingly, decreasing the amount of residual water during the reaction (when acetone solutions were used) favors the intramolecular cyclization for the intermediate carbocation giving pinol as the main product.

On the other hand, a series of silicas modified chemically with Al were tested in the isomerization α-pinene oxide pointing out in the effect of Al amount (**Table 1.4, *entry 11***) [65]. Particularly, the silica modification was performed by using a one-pot two steps synthesis in which the first step was activation of silica while in the second step, TEA (tetraethyl aluminum) was added with subsequent drying and calcination [65]. The best result was achieved for Al-SiO_2 containing 12 wt% of Al with 80% of conversion and 72% selectivity to campholenic aldehyde. In comparison with previously discussed literature, the relatively mild conditions used in this work (only 30°C and 30 min) enhanced formation of the desired aldehyde. However, under these conditions the catalysts could not be reused. The expected activity was attributed mainly to the oligomeric species of Al_2O_3 present in the catalyst and to an increase in the textural properties. Among many heterogeneous catalysts reported for selective synthesis of campholenic aldehyde starting from α-pinene oxide, Ti-MCM-22 (**Table 1.4**, ***entry 12***) [66] has been the most effective catalyst yielding up to 96% of the aldehyde with 4% of other isomers. Excellent performance of this catalyst was associated with the presence of isolated tetrahedrally coordinated Ti, which acts as a Lewis acid without undesired Brønsted acidity, together with the typical MWW shape which can favor the transition state to for aldehyde formation. Finally, phosphotungstated based catalyst ($Cs_{2.5}H_{0.5}PW_{12}O_{40}$ and HPW/SiO_2) was reported for isomerization of limonene epoxide yielding mainly dihydrocarvone as the major product (**Table 1.4, *entry 13-14***). Exceptional acidity together with utilization of the green solvent (in case of HPA/SiO_2) can lead to a feasible method for synthesis of such isomer.

Recently [67], the reusable biomass-derived phosphonate carbon was used for the synthesis of *trans*-carveol from α-pinene oxide at relatively mild conditions indicating the role of the amounts and distribution of the phosphonate groups in the selective synthesis of this alcohol (**Table 1.4, *entry 15***). The use of DMF as a polar basic solvent confirms the hypothesis previously that such solvents favor formation of the alcohol over aldehydes (campholenic and fencholenic aldehydes). Although the process is in line with the typical green processes, the remaining issue is removal of DMF from the reaction mixture.

Ionic liquid-supported indenyl-molybdenum (II) bipyridine complexes as an organometallic and robust catalyst were used for the selective synthesis of campholenic aldehyde starting from α-pinene epoxide (**Table 1.4, *entry 16)*** [68]. Interestingly, only one minute is enough to obtain 94% of the desired aldehyde which is comparable with Fe/MCM-41 (**Table 1.4, *entry 2***). The authors [68] claimed that a change of the ligand during the synthesis of the complexes can alter the Lewis acidity of the metal center. For the mentioned complex, introduction of electron-donating or electron-withdrawing groups can modify the overall reactivity of the catalysts, decreasing the electronic density and changing the catalytic activity and robustness of the material.

Finally, the mordenite-based natural zeolite (TECHNOSA-H_2) [69] coming from volcanic islands in Greek Islands (**Table 1.4, *entry 17***) achieved up to 57% of selectivity to campholenic aldehyde at total conversion with only 10 min of the reaction. Although the authors did not measure the acidity of the material by using TPD of ammonia or FTIR of pyridine, they suggested, for this case, that active sites on the mordenite-based catalyst are mostly Brønsted one because of selectivity. Despite these results, the catalyst was not tested in this reaction in additional cycles.

Table 1.4. Some heterogeneous catalysts for isomerization of monoterpene epoxides.

Entry	Catalyst	Monoterpene epoxide	Reaction conditions	X (%)	S (%)	Ref
1	ZrP[a] (0.6 M)	α-Pinene epoxide	3.28 mmol substrate, 50 mg catalyst, 2 mL N, N Dimethylacetamide, 160 °C, 5 h.	45	72 TC 21 CA 7 Others	[55]
	ZrP[a] (1.2 M)			60	71 TC 20 CA 9 Others	
	ZrP[a] (2.4 M)			100	73 TC 19 CA 8 Others	
2	Fe/MCM-41 (1.7 wt%)	α-Pinene epoxide	0.25 mmol substrate, 1 mL solvent, 10 mg catalyst, 70 °C, 2.5 h, 750 rpm	100 (Toluene)	66 CA 34 Others	[57]
				100 (Ethyl acetate)	58 CA 42 Others	
				100 (*tert*-Butanol)	53 CA 47 Others	
	Cu/MCM-41 (1.3 wt%)			20 (Toluene)	82 CA 18 Others	
				5 (Ethyl acetate)	80 CA 20 Others	
				0 (*tert*-Butanol)	-	
	Fe/SBA-15 (3.9 wt%)			100 (Toluene)	64 CA 36 Others	
				100 (Ethyl acetate)	58 CA 42 Others	

	Cu/SBA-15 (1.2 wt%)			98 (*tert*-Butanol)	48 CA 52 Others	
				46 (Toluene)	71 CA 29 Others	
				5 (Ethyl acetate)	79 CA 21 Others	
				1 (*tert*-Butanol)	72 CA 28 Others	
3	Fe/SBA-15 (3.9 wt%)	Limonene epoxide	0.25 mmol substrate, 1 mL solvent, 10 mg catalyst, 70 °C, 1 h, 750 rpm	21 (Toluene)	15 LD 3 CC 35 TC 42 DHC 5 Others	[57]
				15 (Ethyl acetate)	6 LD 35 CC 15 TC 44 DHC	
				5 (Acetonitrile)	50 LD 50 DHC	
				17 (Acetone)	84 LD 16 CC	
				5 (THF)	48 DHC 52 Others	
				8 (1,4-Dioxane)	74 LD 26 Others	
				5 (*tert*-Butanol)	71 LD 13 DHC 16 Others	
				12 (Cyclohexane)	86 LD 7 TC 7 DHC	
				10 (Hexane)	86 LD 7 CC 3 TC 2 DHC 2 Others	
4	Fe/MCM-41	β-pinene epoxide	0.25 mmol substrate, 1 mL solvent, 26% of catalyst, 70 °C, 1 h, 750 rpm	18 (Hexane)	34 PA 63 Myrtanal 3 Myrtenol	[58]
				23 (Acetonitrile)	8 PA 90 Myrtanal 2 Myrtenol	
				14 (tert-Butanol)	14 PA 81 Myrtanal 5 Myrtenol	
				27 (Hexane)	26 PA 68 Myrtanal 6 Myrtenol	
	Fe/SBA-15			20 (Acetonitrile)	13 PA 82 Myrtanal 5 Myrtenol	
				7 (tert-Butanol)	6 PA 87 Myrtanal 7 Myrtenol	
5	MZ-5 (1.5)	α-Pinene epoxide[b]	2 mmol substrate, 100 mL of N, N-dimethylacetamide (solvent), 75 mg catalyst, 140 °C, 3 h.	92	45 TC 27 CA	[70]

6	Zeolite beta 25	β-pinene epoxide	0.8 mL substrate, 25 wt% based on the weight of substrate, volume ratio substrate: DMSO = 1:5, demineralized water (molar ratio substrate: H_2O = 1:8), 70 °C, 2 h.	100	36 PA 19 Myrtanal 10 Myrtenol 9 p-Menth-1-en-7,8-diol	[61]
7	SBA-15	β-pinene epoxide	0.25 mmol substrate, 0.5 mL hexane, 10 mg catalyst, 80 °C, 1 h.	70	45 PA 9 Myrtanal 46 Others	[60]
	Ti/SBA-15			> 99	45 PA 20 Myrtanal 35 Others	
	Mo/SBA-15			> 99	63 PA 37 Others	
	MCM-41			50	34 PA 20 Myrtanal 7 Myrtenol 39 Others	
	Ti/MCM-41			60	47 PA 2 Myrtanal 51 Others	
	Mo/MCM-41			98	20 PA 2 Myrtanal 5 Myrtenol 73 Others	
	SiO_2			14	5 PA 95 Others	
	Ti/SiO_2			64	15 PA 55 Myrtanal 4 Myrtenol 26 Others	
	Mo/SiO_2			> 99	32 PA 12 Myrtanal 2 Myrtenol 54 Others	
8	MoO_3-Modified Beta zeolite	α-Pinene epoxide	1.25 g substrate, 6 mL solvent, 125 mg catalyst, 70 °C, 3 h.	99 (Cyclohexane)	34.6 CA 17.4 TC 13.9 PMD	[71]
				100 (Toluene)	34.2 CA 14.8 TC 14.0 PMD	
				86 (Nitromethane)	44.9 CA 10.7 TC 12.3 PMD	
				100 (Propan-1-ol)	3.3 CA 6.4 TC 2.7 PMD	
				100 (Dichlorobenzene)	42.1 CA 13.3 TC 13.1 PMD	
				100 (Cyclohexanone)	37.4 CA 15.0 TC 16.6 PMD	
				100 (Cyclohexanol)	24.1 CA 21.1 TC 5.1 PMD	
				97 (Ethyl acetate)	37.1 CA 15.8 TC 13.9 PMD	
				27 (N, N'-Dimethylformamide)	26.5 CA 43.8 TC 14.0 PMD	

9	Fe/MCM-41	α-Pinene epoxide	0.25 mmol substrate, 1 mL toluene, 15 mg catalyst, 70 °C, 750 rpm, 2.5 h.	> 99	65 CA 14 Carveol 5 FA 16 Others	[62]
	$Fe(NO_3)_3 \cdot 9H_2O$			97	59 CA 10 Carveol 6 FA 28 Others	
	$FeCl_3 \cdot 4H_2O$			99	61 CA 9 Carveol 3 FA 27 Others	
	$FeSO_4 \cdot 7H_2O$			7	40 CA 45 Carveol 5 FA 10 Others	
	Fe_2O_3			0	-	
10	$Cs_{2.5}H_{0.5}PW_{12}O_{40}$	α-Pinene epoxide	0.75 mmol substrate, 7.50 µmol catalyst, 5 mL of reaction volume with acetone as solvent.	100 (5 min, 25 °C)	17 CA 22 TC 9 TS 45 Pinol	[64]
				100 (180 min, 25 °C)	19 CA 5 TC 70 Pinol	
				100 (5 min, 40 °C)	17 CA 11 TS 62 Pinol	
				100 (120 min, 40 °C)	17 CA 75 Pinol	
11	SiO_2[c]	α-Pinene epoxide	0.25 mmol substrate, 2 mL dichloroethane, 5 mg catalyst, 30 °C, 30 min.	3	50 CA 6 FA 10 TC 6 TS 28 Others	[65]
	Al-SiO_2[c] (12 wt%)			80	72 CA 2 FA 15 TC 8 TS 3 Others	
12	Ti/MCM-22	α-Pinene epoxide	Toluene, 70 °C	100	96 CA 1 TC 1 FA 1 PC	[66]
13	$Cs_{2.5}H_{0.5}PW_{12}O_{40}$	Limonene epoxide	1.5 mmol substrate, 5 mg Catalyst, 10 mL total volume with dichloromethane as solvent, 25 °C, 240 min	100	69 DHC 20 MICC 8 LD	[72]
14	HPW/SiO_2	Limonene epoxide	0.45 mmol substrate, 14.29 mg catalyst µmol^{-1} HPW, 25 °C, 15 min, 3 mL of total volume with dimethyl carbonate as solvent	100	84 DHC 8 MICC 7 LD	[73]
15	Phosphonate/Carbon	α-Pinene epoxide	3.28 mmol substrate, 50 mg catalyst, 2 mL DMF, 140 °C, 1 h	100	67 TC 22 CA 9 TPC	[67]
16	Ionic liquid-supported indenyl-molybdenum(II)-bipyridine complexes	α-Pinene epoxide	0.9 M initial substrate concentration, 0.044M Mo, [Ch][NTf_2] as solvent, 35 °C, 1 min.	100	79 CA 6 TCV	[68]
17	TECHNOSA-H2 mordenite	α-Pinene epoxide	25 °C, 10 min	100	57 CA	[69]

[a]Values in parenthesis refer to the concentration of H_3PO_4 employed in the synthesis of the catalyst. [b]Selectivities at 70 % conversion. [c]Values in parenthesis refer to the aluminum loading. **ZrP:** Zirconium phosphate. **CA:** Campholenic aldehyde. **CC:** *cis*-Carveol. **TC:** *trans*-Carveol. **LD:** Limonene diol. **DHC:** Dihydrocarvone. **PA:** Perillyl alcohol. **MZ:** Hierarchical beta zeolites, where the value in parenthesis denotes the Brønsted-to-Lewis acid site ratio. **CB-1:** Conventional beta zeolite. **PMD:** *p*-methadien-2-ol. **FA:** Fencholenic aldehyde. **TS:** *trans*-sobrerol. **MICC:** 1-methyl-3-isopropenyl-cyclopentyl-1-carboxaldehyde. **PC:** pinocamphone. **TPC:** trans-pinocarveol.

1.2.3. One-pot synthesis

A significant contemporary challenge in organic chemistry is the search for alternative cleaner, safer, and environmentally friendly technologies [74], which are addressed to contribute to the goals of sustainable development and the principles of green chemistry. Therefore, the reduction of waste together with the use of renewable feedstocks, environmentally friendly reagents, and catalysts are significant to achieving more sustainable processes [74]. An effective approach is to synthesize the target molecule in a single reaction vessel, which is often termed 'one-pot', being able to apply to a multi-step reaction, method, or synthesis. This approach is promising and effective because the transformations can be carried out in a single pot, avoiding several intermediate purification processes, minimizing chemical waste, saving time, and simplifying practical aspects [75]. Considering these principles, the rational design of heterogeneous catalysts for the synthesis of aldehydes or alcohols from biomass-derived α-pinene, β-pinene, and limonene represents one important challenge for valorizing wastes.

In this way, the synthesis of campholenic aldehyde from α-pinene has been evaluated using bi-functional PrAlPO-5 materials [76]. They found that when the ratio of (Al + P)/Pr decreased, an increase of Lewis acidity can be achieved and increasing the selectivity to the desired target up to 90% at total conversion (70°C, 12 h, chloroform as solvent and air as oxidizing agent). Furthermore, they studied the effect of several solvents additional to chloroform such as dichloroethane, acetonitrile, acetone, dimethylacetamide, n-hexane, and cyclohexane and they found that weakly basic and non-polar solvents favored the isomerization of α-pinene epoxide to campholenic aldehyde. Zeolite Y encaged Ru (III) and Fe(III) complexes [77], prepared by the "flexible ligand" method, showed complete conversion of α-pinene towards campholenic aldehyde (35.9%), α-pinene epoxide (34.1%), and verbenone (20.7%) after 18 h at 80 °C, and using H_2O_2 as oxidizing agent and acetonitrile as solvent. Mesoporous material such as V-MCM-41 [78], synthesized by direct hydrothermal method, has been tested in the one-pot reaction from α-pinene achieving a conversion of 12.8% with selectivities up to 13.4% to campholenic aldehyde, 15.9% to 1,2 pinanediol, 36.3% to *trans*-sobrerol, and 11.4% to verbenol (70 °C, 7 h, H_2O_2 as oxidizing agent and acetonitrile as solvent). A study of the effect of vanadium content in V-VSB-5 zeolites on activity and selectivity [79], showed that the increase of V content leads to the increase in isomerization of α-pinene epoxide to *trans*-carveol and decrease into campholenic aldehyde, i.e., the strength of Brönsted acid sites was increased; specifically, 12% of α-pinene conversion was reached with selectivities of 21%, 8%, and 9% for epoxide, campholenic aldehyde and *trans*-carveol, respectively (60 °C, 5 h, molecular oxygen as oxidant and acetonitrile as solvent). Co/SiO_2 catalyst prepared by sol-gel method [80] gives only 5% to campholenic aldehyde and 34% to verbenol, using molecular oxygen as an oxidizing agent at 60 °C and 24 h, under solvent-free conditions. Over Ti-HMS catalyst and TBHP as

oxidant [81,82], a selectivity to campholenic aldehyde around 80% and α-pinene conversion around 30% were reached at 77 °C, 24 h, and acetonitrile as the solvent, which was possible because the removal of water contained in the oxidizing agent, to decrease the allylic oxidation products as verbenol and verbenone and in this way, increasing the accessibility to catalytic sites. Then, the authors evaluated again the reaction under nitrogen atmosphere generated by N_2 purge throughout the reaction and with TBHP previously dried with $MgSO_4$, whose results showed clearly that the catalytic activity turned out to be improved and also, only two products, α-pinene epoxide, and its isomerized aldehyde, were observed.

The previous literature review evidences the importance of proposing heterogeneous catalytic systems that could be promising for the transformation of monoterpenes contained in essential oils by one-pot reactions. Due to the significant challenge in researching these transformations, explained by the need to find reaction conditions compatible with both epoxidation and the subsequent isomerization, it is crucial to first study the independent routes to gain knowledge that will ultimately lead to the proposal of viable heterogeneous catalytic systems for one-pot processes.

1.3. Research question

How are efficient heterogeneous catalysts used to obtain high-added value products from monoterpenes contained in essential oils through one-pot reactions?

1.4. Objectives

1.4.1. General

Evaluate the effect of heterogeneous mesoporous catalysts on the selective synthesis of high-added value products from monoterpenes contained in essential oils, through one-pot reactions.

1.4.2. Specific

- Evaluate mesoporous materials as supports of heterogeneous catalysts.
- Establish the best one-pot reaction conditions to obtain the highest yields in the transformation of monoterpenes towards high-added value products.
- Determine the effect of the solvent, temperature, and type of catalyst on the selective synthesis of fine chemicals from at least one monoterpene.
- Establish the relationship between the physicochemical properties of catalysts with the one-pot reactions.

1.5. Thesis structure

This doctoral thesis is divided into eight chapters, mainly consisting of an integration of six scientific manuscripts (**Chapter 1** to **Chapter 6**) according to the specific regulations of the faculty of engineering: ACUERDO DE FACULTAD 797/2017 – Universidad de Antioquia (Article 17, Paragraph 2). Manuscripts included in the first six chapters of this thesis were formatted in the document's style and provided with corresponding sections of abstract (and graphical), keywords, introduction, experimental methodology, results and discussion, conclusions, acknowledgments, and references. The thesis methodologically presents the results of two independent pathways: epoxidation (**Chapter 2** and **Chapter 3**) and epoxide isomerization (**Chapter 4** and **Chapter 5**). These results are then integrated into the development of a heterogeneous catalytic system aimed at achieving a one-pot route (**Chapter 6**).

In **Chapter 1**, a general contextualization of fine chemistry and essential oils is provided to understand the importance of synthesizing the target compounds in this thesis. A detailed state-of-the-art review on the oxidation/epoxidation of monoterpenes, isomerization of monoterpene epoxides, and the corresponding one-pot transformation (epoxidation + isomerization) of monoterpenes are then presented. The research question and the general and specific objectives that guided this thesis are outlined, followed by a summary of the scientific products divided into international articles, national/international conferences, publications resulting from scientific cooperation, and financial support for this doctoral research.

Chapter 2 covers the epoxidation of R-(+)-limonene into limonene epoxide (endo and exo) and limonene diepoxide using magnesium oxide as a commercial heterogeneous catalyst. This catalyst is highly active in a Payne system where the epoxidizing intermediate is formed from acetonitrile with hydrogen peroxide. The effects of several reaction conditions (temperature and concentration of catalyst, H_2O_2, and limonene) are investigated in the epoxidation route of limonene. The characterization of the catalyst was conducted using XRD, TGA, N_2 adsorption-desorption isotherms, FTIR, and SEM-EDX. Kinetic modeling was performed for the production of limonene epoxides using the tested reaction conditions over a time interval of 0-30 min. To our knowledge, this is the first report on the kinetic study of a Payne system for the epoxidation of a monoterpene, addressing a research gap necessary for reactor design and scaling up fine chemical processes. The H_2O_2 efficiency is calculated based on quantification using cerimetric titration, and the catalyst stability is investigated through reuse and leaching tests.

Chapter 3 presents zeolite Y-based catalysts for efficient epoxidation of R-(+)-limonene, showing insights into the structure-activity relationship. These kinds of mesoporous materials have not been extensively explored as heterogeneous catalysts for the valorization of limonene towards its monoepoxides. The aim is to investigate the epoxidation route using H_2O_2 as a green oxidizing agent, studying the physicochemical properties of the catalysts including crystalline phases (XRD), morphology (TEM and SEM), textural properties, acidity (pyridine-FTIR and NH_3-TPD), basicity (CO_2-TPD), and environment of the species in the zeolitic materials (UV-Vis-DRS, ^{27}Al-NMR, ^{29}Si-NMR), and correlating them with the catalytic performance. Spent materials are investigated by TPO-MS and TGA to determine coke formation. The effect of various parameters such as the initial concentration, catalyst loading,

oxidant/substrate feed ratio, and temperature are evaluated. The role of the solvent is explained using its polarity and donor capacity. The product distribution is presented, including limonene-1,2-epoxide (endo, *cis* and *trans*), limonene-8,9-epoxide (exo), limonene diepoxide, limonene diol, carveol, carvone, and dihydrocarvone. The heterogeneity and reusability of the catalysts are investigated. The H_2O_2 efficiency is determined using cerimetric titration, and a plausible reaction mechanism is proposed for the most active catalyst based on the experimental findings.

Chapter 4 deals with mesoporous materials based on ZSM-5 dendritic zeolites as highly active catalysts for the valorization of monoterpene epoxides such as α-pinene epoxide, β-pinene epoxide, and limonene epoxide into high-added value products including campholenic aldehyde, myrtanal, and dihydrocarvone. These zeolites considered the "rising stars" among mesoporous solids, possess 3D branched superstructures characterized by exceptional accessibility due to the highly interconnected network of radially oriented mesopores, which is suitable for exploiting them for these isomerization reactions. All fresh catalysts are characterized using XRD, Ar physisorption, pyridine-FTIR, and TEM, whereas spent materials are studied using TPO-MS. The aim is to understand the correlation between the physicochemical properties of the zeolites and their catalytic performance using mild reaction conditions and employing more benign solvents than previously employed in the literature. The role of substrate, solvent polarity, and catalyst robustness are investigated. This is the first contribution regarding the use of dendritic zeolites for valorization of monoterpene epoxides.

Chapter 5 concisely explores the isomerization of limonene-1,2-epoxide from kinetic and mechanistic viewpoints using the most active dendritic zeolite presented in Chapter 4. Ethyl acetate is used as a green solvent, and mild reaction conditions are tested to study the synthesis of dihydrocarvone isomers. Kinetic modeling was performed using a detailed reaction network based on the experimental findings reported in Chapter 4, with reaction rates derived from the assumption of rate-limiting surface reactions. Statistical tools are implemented to refine the kinetic model. Moreover, Density Functional Theory reveals the pathway for converting limonene-1,2-epoxide (*cis* + *trans*) into dihydrocarvone and carveol as typical products.

Chapter 6 presents a one-pot catalytic system using a tandem approach, which involves the use of two heterogeneous catalysts: MgO and acidic materials based on mesoporous catalysts (Me/Support, where Me = Sn, Fe, Cu, Co, and Support = MCM-41, SBA-15). This chapter integrates the epoxidation of monoterpenes (**Chapter 2** and **Chapter 3**), followed by the subsequent isomerization of monoterpene epoxides (**Chapter 4** and **Chapter 5**) to obtain high-value-added compounds using a one-pot catalytic pathway. In particular, the synthesis of myrtanal is investigated using these catalysts. All catalysts are characterized using ICP/OES, XRD, N_2 physisorption, TEM-EDX, pyridine-FTIR, NH_3-TPD, and XPS. The catalytic tests are conducted under mild reaction conditions. Additionally, total Lewis acidity and acid site density are identified as suitable kinetic descriptors of catalytic data, due to their crucial role in the ring-opening of monoterpene epoxides. Catalyst stability is successfully examined, and a plausible reaction pathway for the formation of myrtanal is proposed based on the tandem catalysis approach.

Finally, **Chapter 7** covers the general conclusions and future work, while **Chapter 8** presents the supporting information.

1.6. Academic products

1.6.1. List of publications

I. Julián E. Sánchez-Velandia, **Luis A. Gallego-Villada**, Päivi Mäki-Arvela, Alexander Sidorenko, Dmitry Yu. Murzin, Upgrading Biomass to High-Added Value Chemicals: Synthesis of Monoterpenes-based Compounds using Catalytic Green Chemical Pathways, *Catalysis Reviews* (2024), 1-126. 10.1080/01614940.2024.2329553.

II. **Luis A. Gallego-Villada**, Edwin A. Alarcón, Aída Luz Villa, Versatile Heterogeneous Catalytic System for the Selective Synthesis of Limonene Epoxide and Diepoxide, *Industrial & Engineering Chemistry Research* (2023), 62, 20152-20169. 10.1021/acs.iecr.3c02633.

III. **Luis A. Gallego-Villada**, Päivi Mäki-Arvela, Narendra Kumar, Edwin A. Alarcón, Zuzana Vajglová, Teija Tirri, Ilari Angervo, Robert Lassfolk, Mika Lastusaari, Dmitry Yu. Murzin, Zeolite Y-Based Catalysts for Efficient Epoxidation of R-(+)-Limonene: Insights into the Structure-Activity Relationship, *Microporous and Mesoporous Materials* (2024), 372, 113098. 10.1016/j.micromeso.2024.113098.

IV. **Luis A. Gallego-Villada**, Jennifer Cueto, María del Mar Alonso-Doncel, Päivi Mäki-Arvela, Edwin A. Alarcón, David P. Serrano, Dmitry Yu. Murzin, Dendritic ZSM-5 Zeolites as Highly Active Catalysts for the Valorization of Monoterpene Epoxides, *Green Chemistry* (2024), 27. https://doi.org/10.1039/D4GC04003A.

V. **Luis A. Gallego-Villada**, Wander Y. Perez-Sena, Julián E. Sánchez-Velandia, Jennifer Cueto, María del Mar Alonso-Doncel, Johan Wärnå, Päivi Mäki-Arvela, Edwin A. Alarcón, David P. Serrano, Dmitry Yu. Murzin, Synthesis of Dihydrocarvone over Dendritic ZSM-5 Zeolite: A Comprehensive Study of Experimental, Kinetics, and Computational Insights, *Chemical Engineering Journal* (2024), 498, 155377. https://doi.org/10.1016/j.cej.2024.155377.

VI. **Luis A. Gallego-Villada**, Edwin A. Alarcón, Felipe Bustamante, Aída Luz Villa, One-Pot Tandem Catalysis: Green Synthesis of β-Pinene Derivatives with MgO and Mesoporous Catalysts, Journal of Catalysis (2024), 438, 115698. https://doi.org/10.1016/j.jcat.2024.115698.

VII. Pascal Demuth, **Luis A. Gallego-Villada**, Päivi Mäki-Arvela, Ramin Majidov, Zuzana Vajglová, Narendra Kumar, Ilari Angervo, Mika Lastusaari, Kari Eränen, Dmitry Yu. Murzin, Micro and Mesoporous Materials Based on Zeolite Y for the Florol Synthesis Via the Prins Cyclization of Isoprenol, *Catalysis Today* (2024), 433, 114695. 10.1016/j.cattod.2024.114695.

Contribution of the author to the publications

I. Conceptualization, Supervision, Writing - Original Draft.

II. Conceptualization, Methodology, Investigation, Software, Formal Analysis, Writing - Original Draft.

III. Conceptualization, Methodology, Investigation, Formal Analysis, Writing - Original Draft.

IV. Conceptualization, Methodology, Investigation, Formal Analysis, Writing - Original Draft.

V. Conceptualization, Methodology, Investigation, Software, Formal Analysis, Writing - Original Draft.

VI. Conceptualization, Methodology, Investigation, Formal Analysis, Writing - Original Draft.

VII. Conceptualization, Investigation, Writing - Original Draft.

1.6.2. Conference proceedings

I. Luis A. Gallego-Villada, Edwin A. Alarcón, Transformation of monoterpenes through one-pot pathways over heterogeneous catalysts, 2nd International Engineering Congress (IC EXPOI 2022), Medellín – Colombia, Oral presentation.

II. Luis A. Gallego-Villada, Edwin A. Alarcón, Aída Luz Villa, Nanomaterials as catalysts for the transformation of β-pinene through a one-pot reaction, 31st International Materials Research Congress (2023), Cancún-Mexico, Oral presentation.

III. Luis A. Gallego-Villada, Edwin A. Alarcón, Aída Luz Villa, Kinetic study for the synthesis of limonene epoxide using a Payne-type system with commercial magnesium oxide as a heterogeneous catalyst, 13th Colombian Catalysis Symposium (2023), Bucaramanga-Colombia, Oral presentation.

Award: *Best oral presentation at the XIII Colombian Symposium on Catalysis, Universidad Industrial de Santander, 2023.*

IV. Luis A. Gallego-Villada, Päivi Mäki-Arvela, Narendra Kumar, Edwin A. Alarcón, Zuzana Vajglová, Teija Tirri, Ilari Angervo, Robert Lassfolk, Mika Lastusaari, Dmitry Yu. Murzin, Hierarchical Zeolite Y-Based Catalysts for Efficient Epoxidation of Limonene, XXIX Ibero-American Catalysis Congress (2024), Bilbao-Spain, Oral presentation.

V. Luis A. Gallego-Villada, Jennifer Cueto, María del Mar Alonso-Doncel, Julián E. Sánchez-Velandia, Johan Wärnå, Päivi Mäki-Arvela, Wander Y. Perez-Sena, Edwin A. Alarcón, David P. Serrano, Dmitry Yu. Murzin, Kinetic Study of Limonene-1,2-Epoxide Isomerization over a Dendritic ZSM-5 Zeolite, XXIX Ibero-American Catalysis Congress (2024), Bilbao-Spain, Oral presentation.

1.6.3. Other publications

Other publications were completed during my PhD studies (2021-2024) as a result of research collaboration:

I. Luis A. Gallego-Villada, Edwin A. Alarcón, Diego M. Ruiz, Gustavo P. Romanelli, Kinetic study of the esterification of t-cinnamic acid over Preyssler structure acid, *Molecular Catalysis* (2022), 528, 112507. 10.1016/j.mcat.2022.112507.

II. Luis A. Gallego-Villada, Edwin A. Alarcón, Gustavo P. Romanelli, Chapter 27 – Nanofuel additives, Nanotechnology in the Automotive Industry, *Elsevier* (2022), pp. 561-578. 10.1016/B978-0-323-90524-4.00027-X.

III. **Luis A. Gallego-Villada**, Edwin A. Alarcón, Claudio Cerruti, Guillermo Blustein, Ángel G. Sathicq, Gustavo P. Romanelli, Levulinic Acid Esterification with n-Butanol over a Preyssler Catalyst in a Microwave-Assisted Batch Reactor: A kinetic Study, *Industrial & Engineering Chemistry Research* (2023), 62, 10915-10929. 10.1021/acs.iecr.3c00893.

IV. **Luis A. Gallego-Villada**, Edwin A. Alarcón, Ángel G. Sathicq, Gustavo P. Romanelli, Kinetic Modeling of Microwave-Assisted Esterification for Biofuel Additive Production: Conversion of Levulinic Acid with Pentanol using Dowex® 50WX8 Catalyst, *Reaction Kinetics, Mechanisms and Catalysis* (2024), 1-23. 10.1007/s11144-024-02657-3.

1.7. Financial support

- ✓ This doctoral thesis was performed with the financial support of the project 2022-53000: "Transformación de monoterpenos mediante reacciones 'one-pot' sobre catalizadores heterogéneos", as part of the 2021-2022 Programmatical Call: Engineering and Technology – Universidad de Antioquia, and project 2022-56550: "Transformación de monoterpenos mediante rutas catalíticas one-pot con catalizadores heterogéneos" with the Foundation for the Promotion of Research and Technology – Banco de la República.

- ✓ Scholarship for PhD program in Chemical Engineering, "Beca Doctoral Universidad de Antioquia". Medellín, Colombia (2021-2025).

- ✓ Research stay: Laboratory of Industrial Chemistry and Reaction Engineering (TKR), Åbo Akademi University, Turku, Finland, June 1st, 2023 – December 30th, 2023.

- ✓ Grant for International Postgraduate studies of the "Programa Único de Acceso y Permanencia en la Educación Post-secundaria (PUAP)", period 2023-02, granted by Alcaldía de Medellín.

1.8. References

[1] C. Lucarelli, A. Vaccari, Examples of heterogeneous catalytic processes for fine chemistry, Green Chem. 13 (2011) 1941. https://doi.org/10.1039/c0gc00760a.

[2] H.-U. Blaser, Heterogeneous catalysis for fine chemicals production, Catal. Today. 60 (2000) 161–165. https://doi.org/10.1016/S0920-5861(00)00332-1.

[3] V. Garcia, M. Cabassud, M.V. Le Lann, L. Pibouleau, G. Casamatta, Constrained optimization for fine chemical productions in batch reactors, Chem. Eng. J. Biochem. Eng. J. 59 (1995) 229–241. https://doi.org/10.1016/0923-0467(94)02949-0.

[4] M. Le Lann, Modeling, optimization and control of batch chemical reactors in fine chemical production, Annu. Rev. Control. 23 (1999) 25–34. https://doi.org/10.1016/S1367-5788(99)00004-8.

[5] S. Herman, Fragrance, in: K. Sakamoto, R.Y. Lochhead, H.I. Maibach, Y. Yamashita (Eds.), Cosmet. Sci. Technol. Theor. Princ. Appl., United States, 2017: pp. 1–835.

[6] R.A. Sheldon, The E Factor: fifteen years on, Green Chem. 9 (2007) 1273–1283. https://doi.org/10.1039/b713736m.

[7] J.-L. Ríos, Essential Oils: What They Are and How the Terms Are Used and Defined, in: Essent. Oils Food Preserv. Flavor Saf., Elsevier, 2016: pp. 3–10.

https://doi.org/10.1016/B978-0-12-416641-7.00001-8.

[8] M. Hyldgaard, T. Mygind, R.L. Meyer, Essential Oils in Food Preservation: Mode of Action, Synergies, and Interactions with Food Matrix Components, Front. Microbiol. 3 (2012) 1–24. https://doi.org/10.3389/fmicb.2012.00012.

[9] G. de J. Montoya-Cadavid, Aceites esenciales: una alternativa de diversificación para el eje cafetero, 2010. http://bdigital.unal.edu.co/50956/7/9588280264.pdf.

[10] E.E. Stashenko, Aceites Esenciales, Bucaramanga, Colombia, 2009.

[11] T. Map, Trade Map, (n.d.). https://www.trademap.org/Country_SelProduct_TS.aspx?nvpm=1%7C%7C%7C%7C%7C3301%7C%7C%7C4%7C1%7C1%7C1%7C2%7C1%7C2%7C1%7C1%7C1 (accessed June 19, 2023).

[12] Gross Domestic Product, Fourth Quarter and Year 2022 (Third Estimate), GDP by Industry, and Corporate Profits | U.S. Bureau of Economic Analysis (BEA), (2023). https://www.bea.gov/news/2023/gross-domestic-product-fourth-quarter-and-year-2022-third-estimate-gdp-industry-and (accessed June 19, 2023).

[13] Y. Noma, Y. Asakawa, Biotransformation of Monoterpenoids, in: Compr. Nat. Prod. II, Elsevier, 2010: pp. 669–801. https://doi.org/10.1016/B978-008045382-8.00742-5.

[14] R. Marmulla, J. Harder, Microbial monoterpene transformations-a review, Front. Microbiol. 5 (2014) 1–14. https://doi.org/10.3389/fmicb.2014.00346.

[15] L.A. Baltina, N.G. Komissarova, Transformations of pentacyclic triterpenoids as a route to the future medicines, in: Stud. Nat. Prod. Chem., Elsevier, 2023: pp. 331–407. https://doi.org/10.1016/B978-0-323-91296-9.00001-0.

[16] A. Wawoczny, D. Gillner, The Most Potent Natural Pharmaceuticals, Cosmetics, and Food Ingredients Isolated from Plants with Deep Eutectic Solvents, J. Agric. Food Chem. 71 (2023) 10877–10900. https://doi.org/10.1021/acs.jafc.3c01656.

[17] T.M. Bennett, J. Portal, V. Jeanne-Rose, S. Taupin, A. Ilchev, D.J. Irvine, S.M. Howdle, Synthesis of model terpene-derived copolymers in supercritical carbon dioxide for cosmetic applications, Eur. Polym. J. 157 (2021) 110621. https://doi.org/10.1016/j.eurpolymj.2021.110621.

[18] S.D. Tetali, Terpenes and isoprenoids: a wealth of compounds for global use, Planta. 249 (2019) 1–8. https://doi.org/10.1007/s00425-018-3056-x.

[19] Y. Zhang, F. Seidi, M. Ahmad, L. Zheng, L. Cheng, Y. Huang, H. Xiao, Green and sustainable natural derived polysulfides for a broad range of applications, Green Chem. (2023). https://doi.org/10.1039/D3GC02005C.

[20] W. Cho, J. Hwang, S.Y. Lee, J. Park, N. Han, C.H. Lee, S. Kang, A. Urbas, J.O. Kim, Z. Ku, J.J. Wie, Highly Sensitive and Cost-Effective Polymeric-Sulfur-Based Mid-Wavelength Infrared Linear Polarizers with Tailored Fabry–Pérot Resonance, Adv. Mater. 35 (2023) 2209377. https://doi.org/10.1002/adma.202209377.

[21] A. Manthiram, Y. Fu, S. Chung, C. Zu, Y. Su, Rechargeable Lithium–Sulfur Batteries, Chem. Rev. 114 (2014) 11751–11787. https://doi.org/10.1021/cr500062v.

[22] Z.W. Seh, Y. Sun, Q. Zhang, Y. Cui, Designing high-energy lithium–sulfur batteries, Chem. Soc. Rev. 45 (2016) 5605–5634. https://doi.org/10.1039/C5CS00410A.

[23] F.G. Müller, L.S. Lisboa, J.M. Chalker, Inverse Vulcanized Polymers for Sustainable Metal Remediation, Adv. Sustain. Syst. 7 (2023). https://doi.org/10.1002/adsu.202300010.

[24] N.A. Lundquist, Y. Yin, M. Mann, S.J. Tonkin, A.D. Slattery, G.G. Andersson, C.T. Gibson, J.M. Chalker, Magnetic responsive composites made from a sulfur-rich polymer, Polym. Chem. 13 (2022) 5659–5665. https://doi.org/10.1039/D2PY00903J.

[25] S.K. Bajpai, D. Dubey, Removal of Oil from Oil-in-Water Emulsion by Poly (Sulfur/Soya Bean Oil) Composite Adsorbent: An Equilibrium Study, J. Polym. Environ. 29 (2021) 2385–2396. https://doi.org/10.1007/s10924-020-02032-y.

[26] M.J.H. Worthington, C.J. Shearer, L.J. Esdaile, J.A. Campbell, C.T. Gibson, S.K. Legg, Y. Yin, N.A. Lundquist, J.R. Gascooke, I.S. Albuquerque, J.G. Shapter, G.G. Andersson, D.A. Lewis, G.J.L. Bernardes, J.M. Chalker, Sustainable Polysulfides for Oil Spill Remediation: Repurposing Industrial Waste for Environmental Benefit, Adv. Sustain. Syst. 2 (2018) 1800024. https://doi.org/10.1002/adsu.201800024.

[27] M. Mann, J.E. Kruger, F. Andari, J. McErlean, J.R. Gascooke, J.A. Smith, M.J.H. Worthington, C.C.C. McKinley, J.A. Campbell, D.A. Lewis, T. Hasell, M. V. Perkins, J.M. Chalker, Sulfur polymer composites as controlled-release fertilisers, Org. Biomol. Chem. 17 (2019) 1929–1936. https://doi.org/10.1039/C8OB02130A.

[28] J.A. Smith, R. Mulhall, S. Goodman, G. Fleming, H. Allison, R. Raval, T. Hasell, Investigating the Antibacterial Properties of Inverse Vulcanized Sulfur Polymers, ACS Omega. 5 (2020) 5229–5234. https://doi.org/10.1021/acsomega.9b04267.

[29] R.A. Dop, D.R. Neill, T. Hasell, Antibacterial Activity of Inverse Vulcanized Polymers, Biomacromolecules. 22 (2021) 5223–5233. https://doi.org/10.1021/acs.biomac.1c01138.

[30] R. De Cássia Da Silveira E Sá, L.N. Andrade, D.P. De Sousa, A review on anti-inflammatory activity of monoterpenes, Molecules. 18 (2013) 1227–1254. https://doi.org/10.3390/molecules18011227.

[31] A.G. Guimarães, J.S.S. Quintans, L.J. Quintans-Júnior, Monoterpenes with Analgesic Activity-A Systematic Review, Phyther. Res. 27 (2013) 1–15. https://doi.org/10.1002/ptr.4686.

[32] M.R. V. Santos, F. V. Moreira, B.P. Fraga, D.P. de Souza, L.R. Bonjardim, L.J. Quintans-Junior, Cardiovascular effects of monoterpenes: a review, Rev. Bras. Farmacogn. 21 (2011) 764–771. https://doi.org/10.1590/S0102-695X2011005000119.

[33] M.P. Stevens, Polymer Chemistry: An Introduction, (1999).

[34] E. Louisy, V. Khodyrieva, S. Olivero, V. Michelet, A. Mija, Use of Limonene Epoxides and Derivatives as Promising Monomers for Biobased Polymers, Chempluschem. 87 (2022) 1–9. https://doi.org/10.1002/cplu.202200190.

[35] G. Majetich, J. Shimkus, Y. Li, Epoxidation of olefins by β-bromoalkoxydimethylsulfonium ylides, Tetrahedron Lett. 51 (2010) 6830–6834. https://doi.org/10.1016/j.tetlet.2010.10.068.

[36] R. Hajian, E. Bahrami, Mn(III)-Porphyrin Immobilized on the Graphene Oxide-Magnetite Nanocomposite as an Efficient Heterogeneous Catalyst for the Epoxidation of Alkenes, Catal. Letters. 152 (2022) 2445–2456. https://doi.org/10.1007/s10562-021-03827-x.

[37] M. Vasconcellos-Dias, C.D. Nunes, V. Félix, P. Brandão, M.J. Calhorda, New heptacoordinate tungsten(II) complexes with α-diimine ligands in the catalytic oxidation of multifunctional olefins, Inorganica Chim. Acta. 519 (2021) 120263. https://doi.org/10.1016/j.ica.2021.120263.

[38] M.S. Nunes, D.M. Gomes, A.C. Gomes, P. Neves, R.F. Mendes, F.A.A. Paz, A.D. Lopes, A.A. Valente, I.S. Gonçalves, M. Pillinger, A 5-(2-Pyridyl)tetrazolate Complex of Molybdenum(VI), Its Structure, and Transformation to a Molybdenum Oxide-Based Hybrid Heterogeneous Catalyst for the Epoxidation of Olefins, Catalysts. 11 (2021) 1407. https://doi.org/10.3390/catal111111407.

[39] H. Guo, X. Lu, J. He, H. Zhang, H. Zhang, Y. Dong, D. Zhou, Q. Xia, Co-MOF nanosheet supported on ZSM-5 with an improved catalytic activity for air epoxidation

of olefins, Mater. Chem. Phys. 294 (2023) 127001. https://doi.org/10.1016/j.matchemphys.2022.127001.

[40] C. Wang, H. Zhan, X. Lu, R. Jing, H. Zhang, L. Yang, X. Li, F. Yue, D. Zhou, Q. Xia, A recyclable cobalt(iii)-ammonia complex catalyst for catalytic epoxidation of olefins with air as the oxidant, New J. Chem. 45 (2021) 2147–2156. https://doi.org/10.1039/d0nj05466f.

[41] Y. Tao, O. De Luca, B. Singh, A.J. Kamphuis, J. Chen, P. Rudolf, P.P. Pescarmona, WO3–SiO2 nanomaterials synthesized using a novel template-free method in supercritical CO2 as heterogeneous catalysts for epoxidation with H2O2, Mater. Today Chem. 18 (2020) 100373. https://doi.org/10.1016/j.mtchem.2020.100373.

[42] D.K. Parmar, P.M. Butani, N.J. Thumar, P.M. Jasani, R. V. Padaliya, P.R. Sandhiya, H.D. Nakum, M.N. Khan, D. Makwana, Oxy-functionalization of olefins with neat and heterogenized binuclear V(IV)O and Fe(II) complexes: Effect of steric hindrance on product selectivity and output in homogeneous and heterogeneous phase, Mol. Catal. 474 (2019) 110424. https://doi.org/10.1016/j.mcat.2019.110424.

[43] J. Marreiros, M. Diaz-Couce, M.J. Ferreira, P.D. Vaz, M.J. Calhorda, C.D. Nunes, Synthesis and catalytic activity of Mo(II) complexes of α-diimines intercalated in layered double hydroxides, Inorganica Chim. Acta. 486 (2019) 274–282. https://doi.org/10.1016/j.ica.2018.10.062.

[44] S. Madadi, J.-Y. Bergeron, S. Kaliaguine, Kinetic investigation of aerobic epoxidation of limonene over cobalt substituted mesoporous SBA-16, Catal. Sci. Technol. 11 (2021) 594–611. https://doi.org/10.1039/D0CY01700K.

[45] C. Bisio, A. Gallo, R. Psaro, C. Tiozzo, M. Guidotti, F. Carniato, Tungstenocene-grafted silica catalysts for the selective epoxidation of alkenes, Appl. Catal. A Gen. 581 (2019) 133–142. https://doi.org/10.1016/j.apcata.2019.05.027.

[46] C.K. Modi, R.S. Vithalani, D.S. Patel, N.N. Som, P.K. Jha, Zeolite-Y entrapped metallo-pyrazolone complexes as heterogeneous catalysts: Synthesis, catalytic aptitude and computational investigation, Microporous Mesoporous Mater. 261 (2018) 275–285. https://doi.org/10.1016/j.micromeso.2017.10.043.

[47] H. Zhang, X. Lu, L. Yang, Y. Hu, M. Yuan, C. Wang, Q. Liu, F. Yue, D. Zhou, Q. Xia, Efficient air epoxidation of cycloalkenes over bimetal-organic framework ZnCo-MOF materials, Mol. Catal. 499 (2021) 111300. https://doi.org/10.1016/j.mcat.2020.111300.

[48] J.E. Sánchez-Velandia, L.M. Valdivieso, F. Martínez O, S.M. Mejía, A.L. Villa, J. Wärnå, D.Y. Murzin, Synthesis of trans-pinocarveol from oxidation of β-pinene using multifunctional heterogeneous catalysts, Mol. Catal. 541 (2023) 113104. https://doi.org/10.1016/j.mcat.2023.113104.

[49] V.I. Anikeev, I. V. Il'ina, S.Y. Kurbakova, A.A. Nefedov, K.P. Volcho, N.F. Salakhutdinov, Oxidation of α-pinene by atmospheric oxygen in the supercritical CO2—ethyl acetate system in the presence of Co(II) complexes, Russ. J. Phys. Chem. A. 86 (2012) 190–195. https://doi.org/10.1134/S0036024412010049.

[50] L.A. Gallego-Villada, E.A. Alarcón, A.L. Villa, Versatile Heterogeneous Catalytic System for the Selective Synthesis of Limonene Epoxide and Diepoxide, Ind. Eng. Chem. Res. 62 (2023) 20152–20169. https://doi.org/10.1021/acs.iecr.3c02633.

[51] J.-A. Becerra, L.-M. González, A.-L. Villa, A bio-inspired heterogeneous catalyst for the transformation of limonene from orange peel waste biomass into value-added products, Catal. Today. 302 (2018) 250–260. https://doi.org/10.1016/j.cattod.2017.07.012.

[52] S. Hajimirzaee, G.A. Leeke, J. Wood, Modified zeolite catalyst for selective dialkylation

of naphthalene, Chem. Eng. J. 207–208 (2012) 329–341. https://doi.org/10.1016/j.cej.2012.06.134.

[53] M. Salavati-Niasari, Synthesis, characterization and liquid-phase hydroxylation of phenol with hydrogen peroxide over host (nanopores of zeolite-Y)/guest (oxovanadium(IV) complexes of tetraaza macrocyclic ligands) nanocatalyst, Inorganica Chim. Acta. 362 (2009) 2159–2166. https://doi.org/10.1016/j.ica.2008.09.043.

[54] Y. Lozon, A. Sultan, S.J. Lansdell, T. Prytkova, B. Sadek, K.-H.S. Yang, F.C. Howarth, N.S. Millar, M. Oz, Inhibition of human α7 nicotinic acetylcholine receptors by cyclic monoterpene carveol, Eur. J. Pharmacol. 776 (2016) 44–51. https://doi.org/10.1016/j.ejphar.2016.02.004.

[55] A.S. Singh, D.R. Naikwadi, K. Ravi, A. V. Biradar, Chemoselective isomerization of α-Pinene oxide to trans-Carveol by robust and mild Brønsted acidic zirconium phosphate catalyst, Mol. Catal. 521 (2022) 112189. https://doi.org/10.1016/j.mcat.2022.112189.

[56] S. Mehra, D.R. Naikwadi, K. Singh, A. V Biradar, A. Kumar, Selective isomerization of α-pinene oxide to trans -carveol by task-specific ionic liquids: mechanistic insights via physicochemical studies, Green Chem. (2023). https://doi.org/10.1039/D3GC01757E.

[57] J.E. Sánchez-Velandia, A. Luz Villa, Selective Synthesis of High-Added Value Chemicals from α-pinene epoxide and Limonene epoxide Isomerization over Mesostructured Catalysts: Effect of the metal loading and solvent, Catal. Today. (2021). https://doi.org/10.1016/j.cattod.2021.09.011.

[58] M. Chaves-Restrepo, A. Viloria, J.E. Sánchez-Velandia, A.L. Villa, Effect of reaction conditions and kinetics of the isomerization of β-pinene epoxide to myrtanal in the presence of Fe/MCM-41 and Fe/SBA-15, React. Kinet. Mech. Catal. 135 (2022) 2013–2029. https://doi.org/10.1007/s11144-022-02220-y.

[59] J.E. Sánchez-Velandia, J.-A. Becerra, S.M. Mejía, A.L. Villa, F. Martínez O, Thermodynamics of the Isomerization of Monoterpene Epoxides, ACS Omega. 6 (2021) 34206–34218. https://doi.org/10.1021/acsomega.1c03049.

[60] M.C. Cruz, J.E. Sánchez-Velandia, S. Causíl, A.L. Villa, Selective Synthesis of Perillyl Alcohol from β-Pinene Epoxide over Ti and Mo Supported Catalysts, Catal. Letters. 151 (2021) 2279–2290. https://doi.org/10.1007/s10562-020-03489-1.

[61] K. Zítová, E. Vyskočilová, L. Červený, Preparation of α-terpineol and perillyl alcohol using zeolites beta, Res. Chem. Intermed. 47 (2021) 4297–4310. https://doi.org/10.1007/s11164-021-04515-6.

[62] J.E. Sánchez-Velandia, S.M. Mejía, A.L. Villa, Reaction Mechanism of the Isomerization of Monoterpene Epoxides with Fe 3+ as Active Catalytic Specie: A Computational Approach, J. Phys. Chem. A. 124 (2020) 3761–3769. https://doi.org/10.1021/acs.jpca.9b09622.

[63] S.I. Erdagi, F.G. Boztas, C. Uyanik, The Formation of Sobrelol Ethers by the Alcoholysis of Pinene Epoxides, J. Chem. Res. 40 (2016) 318–319. https://doi.org/10.3184/174751916X14615863512197.

[64] C.J.A. Ribeiro, M.M. Pereira, E.F. Kozhevnikova, I. V. Kozhevnikov, E. V. Gusevskaya, K.A. da Silva Rocha, Heteropoly acid catalysts in upgrading of biorenewables: Synthesis of para-menthenic fragrance compounds from α-pinene oxide, Catal. Today. 344 (2020) 166–170. https://doi.org/10.1016/j.cattod.2018.12.023.

[65] V.N. Panchenko, V.L. Kirillov, E.Y. Gerasimov, O.N. Martyanov, M.N. Timofeeva, Isomerization of α-pinene oxide to campholenic aldehyde in the presence of Al-SiO2 and magnetic Al-SiO2/Fe3O4 catalysts, React. Kinet. Mech. Catal. 130 (2020) 919–934.

https://doi.org/10.1007/s11144-020-01811-x.

[66] M. Pitínová-Štekrová, P. Eliášová, T. Weissenberger, M. Shamzhy, Z. Musilová, J. Čejka, Highly selective synthesis of campholenic aldehyde over Ti-MWW catalysts by α-pinene oxide isomerization, Catal. Sci. Technol. 8 (2018) 4690–4701. https://doi.org/10.1039/C8CY01231H.

[67] A.S. Singh, J.H. Advani, A. V. Biradar, Phosphonate functionalized carbon spheres as Brønsted acid catalysts for the valorization of bio-renewable α-pinene oxide to trans - carveol, Dalt. Trans. 49 (2020) 7210–7217. https://doi.org/10.1039/D0DT00921K.

[68] S.M. Bruno, M. Pillinger, A.A. Valente, I.S. Gonçalves, Selective isomerization of α-pinene oxide to campholenic aldehyde by ionic liquid-supported indenyl-molybdenum(II)-bipyridine complexes, J. Organomet. Chem. 970–971 (2022) 122372. https://doi.org/10.1016/j.jorganchem.2022.122372.

[69] D. Makarouni, C. Dimitriadi Evgenidi, C. Kordulis, V. Dourtoglou, Catalytic conversion of biomass-derived compounds to high added value products using an acid treated natural mordenite, Sustain. Chem. Pharm. 33 (2023) 101125. https://doi.org/10.1016/j.scp.2023.101125.

[70] R. Barakov, N. Shcherban, P. Mäki-Arvela, P. Yaremov, I. Bezverkhyy, J. Wärnå, D.Y. Murzin, Hierarchical Beta Zeolites As Catalysts in α-Pinene Oxide Isomerization, ACS Sustain. Chem. Eng. 10 (2022) 6642–6656. https://doi.org/10.1021/acssuschemeng.2c00441.

[71] E. Vrbková, E. Vyskočilová, M. Lhotka, L. Červený, Solvent Influence on Selectivity in α-Pinene Oxide Isomerization Using MoO3-Modified Zeolite BETA, Catalysts. 10 (2020) 1244. https://doi.org/10.3390/catal10111244.

[72] V. V. Costa, K.A. Da Silva Rocha, I. V. Kozhevnikov, E.F. Kozhevnikova, E. V. Gusevskaya, Heteropoly acid catalysts for the synthesis of fragrance compounds from biorenewables: Isomerization of limonene oxide, Catal. Sci. Technol. 3 (2013) 244–250. https://doi.org/10.1039/c2cy20526b.

[73] R.F. Cotta, R.A. Martins, M.M. Pereira, K.A. da Silva Rocha, E.F. Kozhevnikova, I. V. Kozhevnikov, E. V. Gusevskaya, Heteropoly acid catalysis for the isomerization of biomass-derived limonene oxide and kinetic separation of the trans-isomer in green solvents, Appl. Catal. A Gen. 584 (2019) 117173. https://doi.org/10.1016/j.apcata.2019.117173.

[74] M.J. Climent, A. Corma, S. Iborra, Heterogeneous Catalysts for the One-Pot Synthesis of Chemicals and Fine Chemicals, Chem. Rev. 111 (2011) 1072–1133. https://doi.org/10.1021/cr1002084.

[75] Y. Hayashi, Pot economy and one-pot synthesis, Chem. Sci. 7 (2016) 866–880. https://doi.org/10.1039/C5SC02913A.

[76] B. Sundaravel, C.M. Babu, R. Vinodh, W.S. Cha, H.-T. Jang, Synthesis of campholenic aldehyde from α-pinene using bi-functional PrAlPO-5 molecular sieves, J. Taiwan Inst. Chem. Eng. 63 (2016) 157–165. https://doi.org/10.1016/j.jtice.2016.02.028.

[77] D.R. Godhani, H.D. Nakum, D.K. Parmar, J.P. Mehta, N.C. Desai, Zeolite Y encaged Ru(III) and Fe(III) complexes for oxidation of styrene, cyclohexene, limonene, and α-pinene: An eye-catching impact of H2SO4 on product selectivity, J. Mol. Catal. A Chem. 426 (2017) 223–237. https://doi.org/10.1016/j.molcata.2016.11.020.

[78] C.M. Chanquía, A.L. Cánepa, E.L. Winkler, E. Rodríguez-Castellón, S.G. Casuscelli, G.A. Eimer, Nature of active vanadium nanospecies in MCM-41 type catalysts for olefins oxidation, Mater. Chem. Phys. 175 (2016) 172–179.

https://doi.org/10.1016/j.matchemphys.2016.03.014.

[79] M.N. Timofeeva, Z. Hasan, V.N. Panchenko, I.P. Prosvirin, S.H. Jhung, Vanadium-containing nickel phosphate molecular sieves as catalysts for α-pinene oxidation with molecular oxygen: A study of the effect of vanadium content on activity and selectivity, J. Mol. Catal. A Chem. 363–364 (2012) 328–334. https://doi.org/10.1016/j.molcata.2012.07.008.

[80] P.A. Robles-Dutenhefner, M.J. da Silva, L.S. Sales, E.M.B. Sousa, E. V. Gusevskaya, Solvent-free liquid-phase autoxidation of monoterpenes catalyzed by sol–gel Co/SiO2, J. Mol. Catal. A Chem. 217 (2004) 139–144. https://doi.org/10.1016/j.molcata.2004.03.007.

[81] Y.-W. Suh, N.-K. Kim, W.-S. Ahn, H.-K. Rhee, One-pot synthesis of campholenic aldehyde from α-pinene over Ti-HMS catalyst II: effects of reaction conditions, J. Mol. Catal. A Chem. 198 (2003) 309–316. https://doi.org/10.1016/S1381-1169(02)00733-1.

[82] Y.-W. Suh, N.-K. Kim, W.-S. Ahn, H.-K. Rhee, Redox-mesoporous molecular sieve as a bifunctional catalyst for the one-pot synthesis of campholenic aldehyde from α-pinene, J. Mol. Catal. A Chem. 174 (2001) 249–254. https://doi.org/10.1016/S1381-1169(01)00192-3.

Chapter 2. Versatile Heterogeneous Catalytic System for the Selective Synthesis of Limonene Epoxide and Diepoxide

This chapter corresponds to an article published in ***Industrial & Engineering Chemistry Research***, *2023, 62, 47, 20152-20169 – DOI: 10.1021/acs.iecr.3c02633*.

Luis A. Gallego-Villada[a]*, Edwin A. Alarcón[a], Aída Luz Villa[a]

[a]Chemical Engineering Department, Environmental Catalysis Research Group, Universidad de Antioquia, Calle 70 No. 52-21, Medellín 050010, Colombia

*Corresponding author: alfonso.gallego@udea.edu.co.

Graphical Abstract

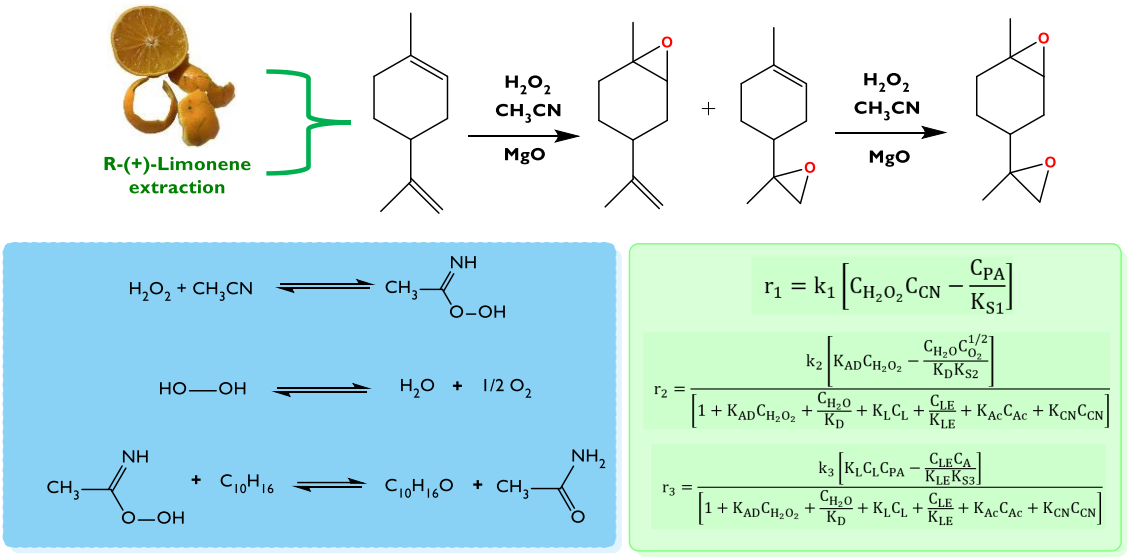

$$r_1 = k_1\left[C_{H_2O_2}C_{CN} - \frac{C_{PA}}{K_{S1}}\right]$$

$$r_2 = \frac{k_2\left[K_{AD}C_{H_2O_2} - \frac{C_{H_2O}C_{O_2}^{1/2}}{K_D K_{S2}}\right]}{\left[1 + K_{AD}C_{H_2O_2} + \frac{C_{H_2O}}{K_D} + K_L C_L + \frac{C_{LE}}{K_{LE}} + K_{Ac}C_{Ac} + K_{CN}C_{CN}\right]}$$

$$r_3 = \frac{k_3\left[K_L C_L C_{PA} - \frac{C_{LE}C_A}{K_{LE}K_{S3}}\right]}{\left[1 + K_{AD}C_{H_2O_2} + \frac{C_{H_2O}}{K_D} + K_L C_L + \frac{C_{LE}}{K_{LE}} + K_{Ac}C_{Ac} + K_{CN}C_{CN}\right]}$$

2.1. Abstract

The products obtained from limonene epoxidation can be used as intermediates or precursors in organic and pharmaceutical synthesis. Commercial magnesium oxide was evaluated as a heterogeneous catalyst in the epoxidation of R-(+)-limonene using H_2O_2 in a Payne reaction system, using acetonitrile as an oxidant activator, and water and acetone as solvents. The effect of temperature and the concentration of catalyst, H_2O_2, and limonene, was evaluated; the highest yields for limonene epoxide (80%, endo + exo) and diepoxide (96%), were found at 50 °C and 30 min and 2 h, respectively. Fresh and spent catalysts were characterized by XRD, TGA, N_2 adsorption-desorption isotherms, FTIR, and SEM-EDX. The efficiency of H_2O_2 in the epoxidation reaction varied between 100 and 20% in the time range of 0 to 30 min, for all tested reaction conditions. The production of peroxyacetimidic acid as an intermediate oxidant in the limonene epoxide synthesis was described using a pseudo-homogeneous reversible model (E = 58.61 kJ mol^{-1}), while the Eley-Rideal model describes both the decomposition of H_2O_2 (E = 29.06 kJ mol^{-1}) and the epoxidation of limonene with the intermediate (E = 52.28 kJ mol^{-1}). Leaching tests verified the heterogeneity of MgO which was used in four consecutive cycles.

2.2. Introduction

Limonene is a monoterpene that possesses both ring and external double bonds, and it is the main component of the essential oil extracted from biomass found in the peel of citrus fruits such as limes (*Citrus aurantiifolia*), lemons (*Citrus limon*), mandarins (*Citrus reticulate*), grapefruits (*Citrus paradisi*), and oranges (*Citrus Sinensis*) [1]. The citrus fruit production in 2021 was estimated at 162 million metric tons, with approximately 20% utilized by the processing industry; China (28.8%) is the top country in worldwide production, followed by Brazil, India, Mexico, and Spain, which together account for 58.8% [2,3]. In addition, the rapid increase in the use of citrus fruits has led to an increase in the amount of generated waste. Specifically, 50% of the fresh fruit mass is wasted during citrus juice production, including peels (55% of the fruit mass), seeds (20-40% of the fruit mass), pomace, and wastewater [4]. Furthermore, citrus waste contains vitamins, active phytochemicals, and folic acid, among other beneficial compounds that can help to protect human health against serious illnesses [5,6]; it is also known for its anti-inflammatory, anti-infective, antioxidative, anti-cancer, and neuroprotective properties [7]. Although the physicochemical characteristics of citrus peel waste, such as high water content and low pH, make it difficult to handle [8], its valorization through essential oil extraction with R-(+)-limonene the main compound, is a promising green process. More than 15 million tons of orange peel waste is generated annually, from which approximately 60,000 tons of R-(+)-limonene can be extracted [9,10].

Limonene can be used directly in industrial applications such as aromas, cosmetics, additive foods, and cleaning materials, but it has also been extensively used as a precursor for the synthesis of high-added-value products based on oxygenated compounds such as epoxides, diepoxides, ketones, alcohols, aldehydes and acids [11]. The oxidation route of limonene can occur towards two competitive pathways (**Figure 2.1**): i) double bond epoxidation yielding limonene-1,2-epoxide, limonene-8,9-epoxide, limonene diepoxide, and limonene glycol, and ii) allylic oxidation yielding carveol, carvone, and perillyl alcohol; the predominance of each pathway depends on the reaction conditions [12]. Specifically, the catalytic epoxidation of monoterpenes has been a research hotspot in heterogeneous catalysis because epoxides are very useful intermediates or precursors in organic and pharmaceuticals synthesis, such as the

production of compounds that exhibit antinociceptive and antitumoral activity [13,14]. Furthermore, limonene-1,2-epoxide (LE) and limonene diepoxide (LD) as primary and secondary epoxidation products of limonene, respectively, have been extensively studied in the last years as versatile building blocks for the production of bio-based polycarbonates with attractive thermal and optical properties [15–21]. Great research efforts are brought with the development of these renewable routes, which are aimed at looking for sustainable alternatives to reduce the demand for petroleum-based polymers. This is because the conventional production (condensation of bisphenol-A with phosgene) involves a highly toxic volatile compound, phosgene, which can be replaced by CO_2, the most abundant greenhouse gas, making it a greener route. For instance, limonene-based carbonates can be used to perform non-isocyanate polyurethanes, which have similar properties to commercially available polyurethanes with the advantage of avoiding the use of toxic isocyanates [22–24].

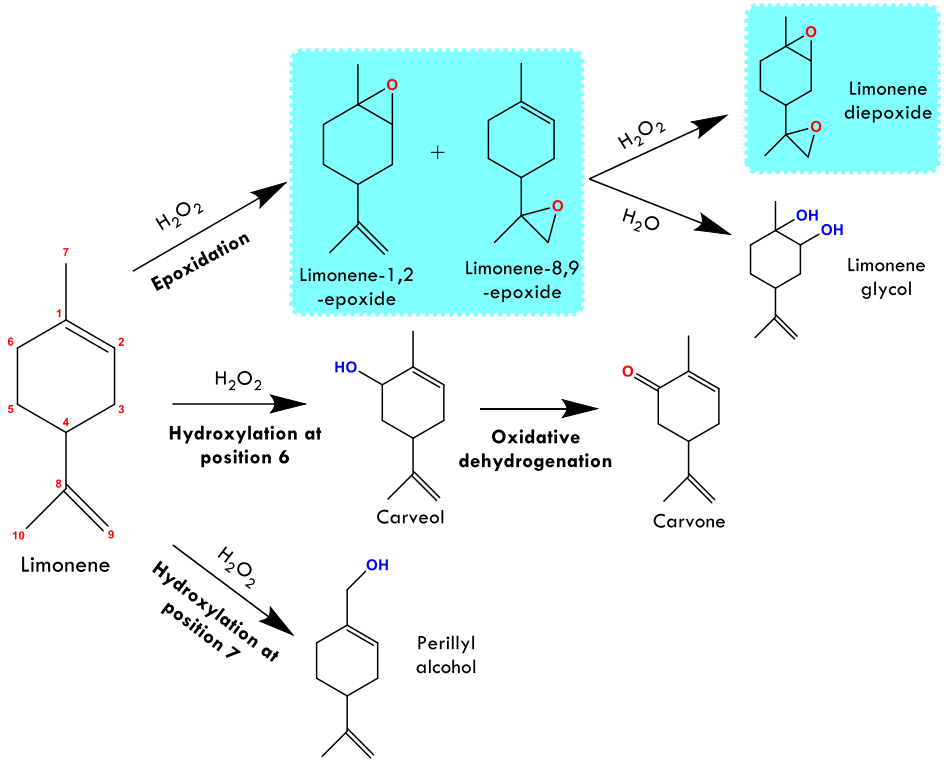

Figure 2.1. Scheme of routes for limonene oxidation with an aqueous solution of hydrogen peroxide.

The product distribution of the limonene epoxidation route with an aqueous solution of H_2O_2 is presented in **Figure 2.1**. Limonene-1,2-epoxide (internal epoxide) and limonene-8,9-epoxide (external epoxide) are often obtained as a mixture of both *cis* and *trans* epoxides, and the epoxidation of the two double bonds of limonene can lead to the formation of four limonene diepoxide diastereoisomers [25]. In addition, the diol or glycol can be obtained due to the hydration of the epoxides ring. On the other hand, the oxidation reaction in which the C-H bond is oxidized into C-OH (hydroxylation) produces carveol or perillyl alcohol depending on the oxidation position. Carvone can also be obtained from the oxidative dehydrogenation of carveol as well [26]. A wide variety of heterogeneous catalysts have been tested in the R-(+)-limonene oxidation using different oxidizing agents under a broad range of reaction conditions, as shown in **Table 2.1**. These catalysts

Table 2.1. Heterogeneous catalytic systems for R-(+)-limonene oxidation.

Entry	Catalyst	T (°C)	t (h)	Oxidizing agent	Solvent	Oxidant/R-limonene (molar)	Catalyst/R-limonene (mg/mmol)	X (%)	$S_{epoxides}$ (%)	$S_{diepoxide}$ (%)	S_{glycol} (%)	$S_{allylic}$ (%)	S_{NR} (%)	Ref.
1	Al_2O_3	80	10	H_2O_2	Ethyl acetate	15.89	287.8	99.0	0.0	100.0	0.0	0.0	0.0	[25]
2	Mo/Hf-MOF	70	24	TBHP	TFT	1.52	34.5	85.0	91.0	4.0	5.0	0.0	0.0	[27]
3	Mo-TUD-1	70	24	TBHP	TFT	1.53	5.6	95.0	60.0	15.8	0.0	0.0	24.2	[28]
4	ZnCo-MOF	90	10	Air	DMF	40[a]	10.0	42.4	80.3	0.0	0.0	0.0	19.7	[29]
5	$PMo_{11}Co$@UiO-66	60	24	TBHP	Chloroform	2.00	10.0	50.0	64.0	10.0	0.0	26.0	0.0	[30]
6	$MnFe_2O_4$/Phttpy-MoO_2	95	0.5	TBHP	Solvent-free	4.00	0.0100	99.0	63.0	37.0	0.0	0.0	0.0	[31]
7	[MoO_3(Hpytz)]	70	5	TBHP	TFT	2.10	10 µmol Mo/mmol	100.0	73.0	27.0	0.0	0.0	0.0	[32]
8	[MoO_3(biim)]	70	6	TBHP	TFT	2.26	10 µmol Mo/mmol	97.0	80.0	12.0	1.0	7.0	0.0	[33]
9	Ru/Darco-G60	80	6	O_2	Solvent-free	3 bar O_2	4.9	35.0	38.0	19.0	0.0	25.5	17.5	[34]
10	V/MCM-41	70	7	H_2O_2	Acetonitrile	2	NR	18.9	35.7	2.8	0.0	61.5	0.0	[35]
11	Nanoporous carbon	140	6	H_2O_2	Methanol	2.00	NR	42.0	13.4	0.0	21.4	65.2	0.0	[36]
12	Cu/MCM-41	70	5	H_2O_2	Acetonitrile	2	NR	8.5	37.2	15.9	5.6	41.3	0.0	[37]
13	Cu/MCM-41	70	5	TBHP	Acetonitrile	2	4 wt%	19.3	6.7	0.0	0.0	93.3	0.0	[37]
14	WO_3-SiO_2	80	4	H_2O_2	1,4-Dioxane + Isopropanol	1	20.0	54.0	53.0	0.0	33.0	9.0	5.0	[38]
15	Co/SBA-16	28	3.33	O_2 – IBA	Ethyl acetate	10[a] - 3.33	47.2	99.0	50.0	33.0	0.0	0.0	17.0	[39]
16	Ni/SBA-16	28	3.33	O_2 – IBA	Ethyl acetate	10[a] - 3.33	47.2	88.0	58.0	10.0	0.0	0.0	32.0	[39]
17	Fe/SBA-16	28	3.33	O_2 – IBA	Ethyl acetate	10[a] - 3.33	47.2	46.0	48.0	0.0	0.0	0.0	52.0	[39]
18	Mn/SBA-16	28	3.33	O_2 – IBA	Ethyl acetate	10[a] - 3.33	47.2	97.0	42.0	0.0	0.0	0.0	58.0	[39]
19	Co/SBA-16	28	3.33	O_2 – IBA	Acetonitrile	10[a] - 3.33	47.2	99.0	20.0	34.0	0.0	0.0	46.0	[39]
20	TiO_2/SiO_2-Mn	60	6	O_2 – IBA	Dichloroethane	5 bar O_2 - 2	71.0	80.5	56.0	0.0	0.0	0.0	44.0	[40]
21	PMo/SiO_2	80	24	TBHP	Solvent-free	1.5	5.0	91.0	0.0	0.0	47.0	7.0	46.0	[41]

22	PW/SiO_2	80	24	TBHP	Solvent-free	1.5	5.0	58.0	3.0	0.0	14.0	16.0	67.0	[41]
23	$[VO(sal_2bz)]_2$-Y	80	24	H_2O_2	Acetonitrile	2	1.5	90.0	0.0	0.0	39.0	49.0	12.0	[42]
24	$[Fe(sal_2bz)(H_2O)_2]_2$ -Y	80	24	H_2O_2	Acetonitrile	2	1.5	80.0	0.0	0.0	43.0	46.0	11.0	[42]
25	CoOx/mordenite	90	4	Air - CHP	DMF	40[a] - 0.1	16.7	28.7	88.3	0.0	0.0	0.0	11.7	[43]
26	γ-AlO(OH)-nanorods	80	4	H_2O_2	Ethyl acetate	2	20.0	42.0	97.0	0.0	0.0	0.0	3.0	[44]
27	ZnAl-LDH-BIAN-MoI_2	110	24	TBHP	Toluene	2	1.5	94.0	97.0	0.0	0.0	0.0	3.0	[45]
28	ZnAl-LDH-BIAN-$MoBr_2$	110	24	TBHP	Toluene	2	1.5	80.0	89.0	0.0	0.0	0.0	11.0	[45]
29	MgAl-LDH-BIAN-MoI_2	110	24	TBHP	Toluene	2	1.5	64.0	93.0	0.0	0.0	0.0	7.0	[45]
30	MgAl-LDH-BIAN-$MoBr_2$	110	24	TBHP	Toluene	2	1.5	79.0	93.0	0.0	0.0	0.0	7.0	[45]
29	W/SiO_2-Liq	90	6	H_2O_2	Acetonitrile	2	100.0	55.0	56.4	0.0	0.0	0.0	43.6	[46]
30	W/SiO_2-Imp	90	6	H_2O_2	Acetonitrile	2	100.0	68.0	63.2	0.0	0.0	0.0	36.8	[46]
31	HT-cys-Au	80	96	Air - TBHP	Toluene	AA - 0.05	1 mol% Au	100.0	81.0	0.0	0.0	19.0	0.0	[47]
32	HT-met-Au	80	96	Air - TBHP	Toluene	AA - 0.05	1 mol% Au	100.0	69.0	0.0	0.0	31.0	0.0	[47]
33	^{Ex}HT-cys-Au	80	96	Air - TBHP	Acetonitrile	AA - 0.05	1 mol% Au	67.0	80.0	0.0	0.0	20.0	0.0	[47]
34	^{Ex}HT-met-Au	80	96	Air - TBHP	Acetonitrile	AA - 0.05	1 mol% Au	83.0	73.0	0.0	0.0	27.0	0.0	[47]
35	$Mo_{72}Fe_{30}$	75	6	H_2O_2	Ethanol	3	2 μmol/mmol	65.0	0.0	45.0	0.0	0.0	55.0	[48]
36	$PMo_{12} \subset Mo_{72}Fe_{30}$	75	6	H_2O_2	Ethanol	3	2 μmol/mmol	76.0	0.0	54.0	0.0	0.0	46.0	[48]
37	$SiMo_{12} \subset Mo_{72}Fe_{30}$	75	6	H_2O_2	Ethanol	3	2 μmol/mmol	92.0	0.0	46.0	0.0	0.0	54.0	[48]
38	$BW_{12} \subset Mo_{72}Fe_{30}$	75	6	H_2O_2	Ethanol	3	2 μmol/mmol	89.0	0.0	58.0	0.0	0.0	42.0	[48]
39	Ti/KIT-6	50	7	TBHP	Acetonitrile	1.00	63.1	23.0	60.0	0.0	0.0	0.0	40.0	[49]
40	Ti/SBA-16	75	24	TBHP	Acetonitrile	1.81	48.39	80.0	79.0	0.0	0.0	0.0	21.0	[50,51]
41	Ti/SBA-15	80	0.25	H_2O_2	Acetonitrile	1.00	NR	19.8	43.8	0.0	10.6	45.6	0.0	[52]

X: Limonene conversion**. S_i:** Selectivity to specie i**. NR:** Not reported**. Phttpy:** terpyridine-based catalyst. **Hpytz:** 5-(2-pyridyl)tetrazole. **biim:** 2,2'-biimidazole ligands. ***sal_2bz:*** Schiff base ligand (Z)-2-[4'-Methyleneamin-biphenyl-4-ylimino)-methyl]-phenol. **BIAN:** bis(4-HOOC-phenyl)-acenaphthenequinonediimine. **LDH:** Layered double hydroxide. **Liq:** Liquid-phase grafting. **Imp:** Dry impregnation. **HT:** Hydrotalcite. **cys:** Cysteine. **met:** Methionine. **Ex:** Exfoliated. **DMF:** Dimethylformamide. **TFT:** α, α, α-Trifluorotoluene. **TBHP:** *Tert*-butyl hydroperoxide. **CHP:** Cumene hydroperoxide. **IBA:** Isobutyraldehyde. **AA:** Atmospheric air. [a] Volumetric flow of oxidizing agent (air or O_2) in mL min^{-1}.

include materials such as oxides (entries 1, 14, 26, 29-30), mesoporous materials (entries 3, 10, 12-13, 15-19, 20, 39-41), microporous materials (entry 25), hybrid composites (entries 5, 8, 31-34), complexes (entries 6, 7, 23-24, 27-30), metal-organic frameworks (entries 2, 4), activated carbons (entries 9, 11), and supported heteropolyacids (entries 21-22, 35-38). Among these, a two-layered double hydroxide ZnAl-LDH functionalized with bis(4-HOOC-phenyl)-acenaphthenequinonediimine (entry 27), a molybdenum oxide-based polymeric hybrid material (entry 8), and $Mo(CO)_6$ species inside UiO-66 (zirconium and hafnium) MOF (entry 2) have shown to be the most active catalysts for the synthesis of limonene monoepoxides, with yields of 91.2%, 77.6%, and 77.4%, respectively. On the other hand, alumina (entry 1) has been the most active material to produce limonene diepoxide, outperforming other materials by far with yields close to 100% under the tested reaction conditions. However, those catalytic systems require relatively long reaction times (between 6 and 24 h), and temperatures above 70 °C to achieve those yields.

Magnesium oxide has been reported as a suitable heterogeneous catalyst for the epoxidation route of β-pinene [53], and styrene [54] under mild reaction conditions (50 °C and 2 h) via a Payne system with water and acetone as solvents; the reaction involves the formation of peroxyacetimidic acid as the active intermediate oxidant, which is formed by activating H_2O_2 with acetonitrile through a nucleophilic attack by perhydroxyl anion species (HOO^-) on the nitrile, acting as basic OH^- groups [54–56]. The efficiency of H_2O_2 can be calculated by quantification of the oxidant after reaction, which has been determined using classical methods such as the direct measurement of the absorbance at 240 nm of the H_2O_2 molecule, and through the reaction of H_2O_2 with ferrous iron, monitored via a subsequent reaction with the dye xylenol orange and subsequent measurement of the absorbance of the solution at 550 nm [57,58]. Other reported methods include colorimetric detection [59], spectrophotometry [60,61], a technique using leuco crystal violet [62], iodometric titration [27,33,35], and cerimetric titration [63].

This study aims to evaluate the use of magnesium oxide as a highly selective catalyst for the R-(+)-limonene epoxidation using a versatile Payne reaction system towards monoepoxides and diepoxide, depending on the reaction conditions. Furthermore, kinetic equations based on pseudo-homogeneous and heterogeneous models are proposed and detailed characterizations of the fresh and spent catalysts are presented.

2.3. Experimental

2.3.1. Materials

Commercial materials were used as received. Magnesium oxide (MgO, 99.6 wt. %, J.T. Baker), R-(+)-limonene (97 wt. %, Sigma-Aldrich), hydrogen peroxide (H_2O_2, 30 % w/v, PanReac AppliChem), acetone (99.9 wt. %, PanReac AppliChem), acetonitrile (99.5 wt. %, Merck), cerium (IV) sulfate solution ($Ce(SO_4)_2 \cdot 4H_2O$, 0.1 N, Titripur®, Merck), manganese (IV) oxide (MnO_2, ≥ 99 wt. %, Sigma-Aldrich), magnesium hydroxide ($Mg(OH)_2$, 95%, Carlo Erba) and deionized water.

2.3.2. Catalyst characterization

Powder X-ray diffraction patterns (XRD) were recorded using a Malvern-PANalytical Empyrean 2012 diffractometer equipped with a PIXcel3D detector and a copper source (λ = 1.541874 Å) operating at 45 kV and 40 mA, in the range 2θ = 5 – 80°. The goniometer was set to perform

Omega/2 theta scans, and the platform was configured for reflection transmission spinner mode with a 4-second rotation period. The scan step size was set to 0.05° with a time per step of 50 s. The textural properties of the samples were determined using nitrogen adsorption-desorption isotherms at 77 K in a Micromeritics ASAP 2020 PLUS instrument. The samples were pre-treated at 180 °C for 4 h under high vacuum conditions for degassing. Surface areas were calculated using the Brunauer-Emmett-Teller (BET) model, and the pore size was determined using the Barrett-Joyner-Halenda (BJH) model. Thermogravimetric analysis (TGA) was performed using a TGA/DTA 5500 TA instrument equipped with a platinum sample holder. The samples were heated in air atmosphere from 30 to 1000 °C at 10 °C min^{-1}. Fourier transform-infrared spectroscopy (FTIR) analysis was conducted using a Frontier FT-IR PerkinElmer instrument, model Spectrum 65, equipped with a Mercury-Cadmium-Telluride (MCT) detector, with pellets prepared with controlled amounts of sample and KBr at room temperature. The measurements were performed at wavenumbers ranging from 4000 to 800 cm^{-1} with a resolution of 4 cm^{-1}. Scanning electron microscopy (SEM) images were collected using a JEOL JSM-6490LV microscope, with an electron acceleration voltage of 20 kV; the samples were fixed onto a graphite tape, coated with a thin layer of gold using a DENTON VACUUM Desk IV equipment, and analyzed using the high vacuum microscope to obtain high-resolution images. The secondary electron detector was used to evaluate the morphology of the samples. The elemental analysis was performed using an X-ray Energy Dispersive Spectroscopy Microprobe (INCA PentaFETx3 Oxford Instruments).

2.3.3. Catalytic tests

The oxidation reactions of R-(+)-limonene with H_2O_2 were carried out in 2 mL capped vials, covered with silicone septa, as batch reactors. A well-stirred oil bath equipped with an EKT Hei-Con Heidolph controller was used to maintain the reaction temperature. Reactions were stopped by immediate cooling with an air stream at room temperature to subsequently separate the catalyst by centrifugation at 3200 rpm for 10 min. Typical reaction conditions were 0.10 mmol of R-(+)-limonene and 1: 1.2: 30.2: 19.7: 15.6: 0.8 as weight ratios for R-(+)-limonene: MgO: H_2O: acetone: acetonitrile: H_2O_2, at 50 °C and 1000 rpm. An aliquot of the centrifuged mixture was used for the quantification of H_2O_2, and the rest of the mixture was decomposed using MnO_2, before the analysis by GC-MS.

The products of the reaction were identified by gas chromatography coupled with mass spectrometry using a GC-MS Agilent 7890N with a DB-1 capillary column (30 m x 0.32 mm x 0.25 µm), equipped with an FID detector and autosampler. The chromatographic method used He as carrier gas (30.462 cm s^{-1} and 2.2912 mL min^{-1}), a split ratio of 15:1, a detector temperature of 250 °C, and two injections of 1 µL. The oven temperature was kept at 70 °C for 2 min, then raised to 130 °C (10 °C min^{-1}) for 1 min, and finally heated up to 180 °C (10 °C min^{-1}). Each GC-MS analysis was replicated at least twice. The R-(+)-limonene conversion (X_L), and the selectivity (S_j) towards monoepoxides were calculated based on **Eqs. (2.1)** and **(2.2)**, respectively.

$$X_L(\%) = \frac{(A_i - A_f)_{Limonene}}{A_{i,Limonene}} * 100 \quad \textbf{(2.1)}$$

$$S_j(\%) = \frac{A_{f,j}}{\sum A_{f,products}} * 100 \quad \textbf{(2.2)}$$

Where A_i and A_f correspond to FID areas at the initial and final time, respectively.

2.3.4. Reusability and leaching tests

For reusing tests, the catalyst was separated from the reaction mixture by centrifugation (3200 rpm, 10 min), then it was washed with acetone at 50 °C for 2 h; subsequently, the solid was dried at 100 °C overnight. This resulting solid was called "spent catalyst". Leaching tests were conducted to evaluate the heterogeneity of the catalytic system with MgO using the hot-filtration method to remove the catalyst from the reaction mixture. The reaction was carried out for 25 min, and then the catalyst was separated from the liquid at the reaction temperature using Acrodisc® PSF syringe filters. A liquid aliquot was analyzed by GC-MS to quantify the limonene conversion, while the remaining mixture was allowed to react for 1 h and 2 h; finally, the sample was analyzed by GC-MS to determine the conversion after removing the catalyst.

2.3.5. Quantification of hydrogen peroxide

The concentration of H_2O_2 in the reaction mixture was determined by cerimetric titration using a $Ce(SO_4)_2$ standardized aqueous solution [64]. The reaction of the colored cerium (IV) sulfate to the colorless cerium (III) sulfate proceeds in the presence of H_2O_2 to yield sulfuric acid and oxygen as is shown in **Figure 2.2** [65]. The sample (100 µL of the reaction mixture) in a beaker containing 5 mL of deionized water was titrated using a Metrohm 775 Dosimat equipment; the endpoint of the titration (V_T) was reached when the solution changed from colorless to yellow. The blank test (5 mL of deionized water) was carried out to determine the volume spent of the titrant (V_b). The concentration of H_2O_2 was calculated according with **Eq. (2.3)**, where θ_{SF} refers to the stoichiometric factor of H_2O_2: $Ce(SO_4)_2$ with a value of 1/2, C_T is the concentration of the titrant (0.1 mol L^{-1}), $M_{H_2O_2}$ is the molecular weight of H_2O_2 (34.01 g mol^{-1}), and W_s is the sample weight. The quantification of each catalytic run was analyzed twice.

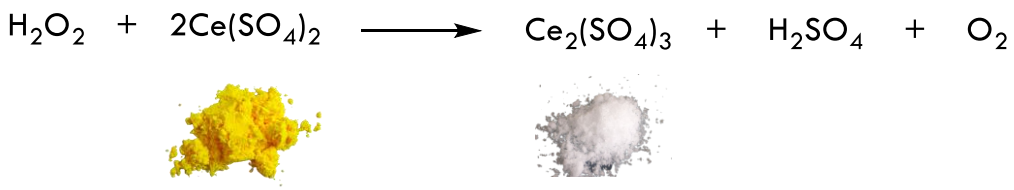

Figure 2.2. Scheme of cerimetric titration of hydrogen peroxide (H_2O_2).

$$C_{H_2O_2}(\text{wt.}\%) = \frac{\theta_{SF}(V_T - V_b)C_T M_{H_2O_2}}{W_s} * 100 \quad \textbf{(2.3)}$$

The H_2O_2 conversion was calculated using the **Eq. (2.4)**, with the initial molar concentration ($C_{H_2O_2,0}$) and the molar concentration after the reaction ($C_{H_2O_2}$).

$$X_{H_2O_2} = \frac{C_{H_2O_2,0} - C_{H_2O_2}}{C_{H_2O_2,0}} \quad \textbf{(2.4)}$$

2.3.6. Kinetic study

2.3.6.1. General considerations

A kinetic study was conducted with reaction times ranging from 0 to 30 min under experimental conditions presented in **Table 2.2**, where mainly the formation of limonene monoepoxides (selectivities greater than 96%) was observed. The formation of an active intermediate oxidant is a key aspect of the Payne system for the catalytic epoxidation route [53]. Although H_2O_2 is readily available, environmentally friendly, and relatively inexpensive, it is not a very reactive oxidant for some substrates such as olefins and aromatic hydrocarbons [66–68]; therefore, a highly effective oxidant such as peroxyacetimidic acid is formed from the reaction between H_2O_2 and acetonitrile under mild reaction conditions. The series and parallel reactions carried out during R-(+)-limonene oxidation with H_2O_2 over MgO are represented in **Figure 2.3**.

Table 2.2. Tested experimental conditions in the R-(+)-limonene transformation with H_2O_2 over MgO as a heterogeneous catalyst.

Entry	L (mmol)	Weight ratios					T (°C)
		MgO/L	H_2O_2/L	H_2O/L	Acetone/L	CH_3CN/L	
1	0.10	1.20	0.80	30.30	19.70	15.70	50
2	0.10	0.90	0.80	30.30	19.70	15.70	50
3	0.10	0.60	0.80	30.30	19.70	15.70	50
4	0.10	1.20	1.20	30.30	19.70	15.70	50
5	0.10	1.20	0.80	30.30	19.70	15.70	40
6	0.20	0.60	0.80	16.22	9.85	7.85	50
7	0.15	0.80	0.80	20.91	13.13	10.47	50

L refers to R-(+)-limonene.

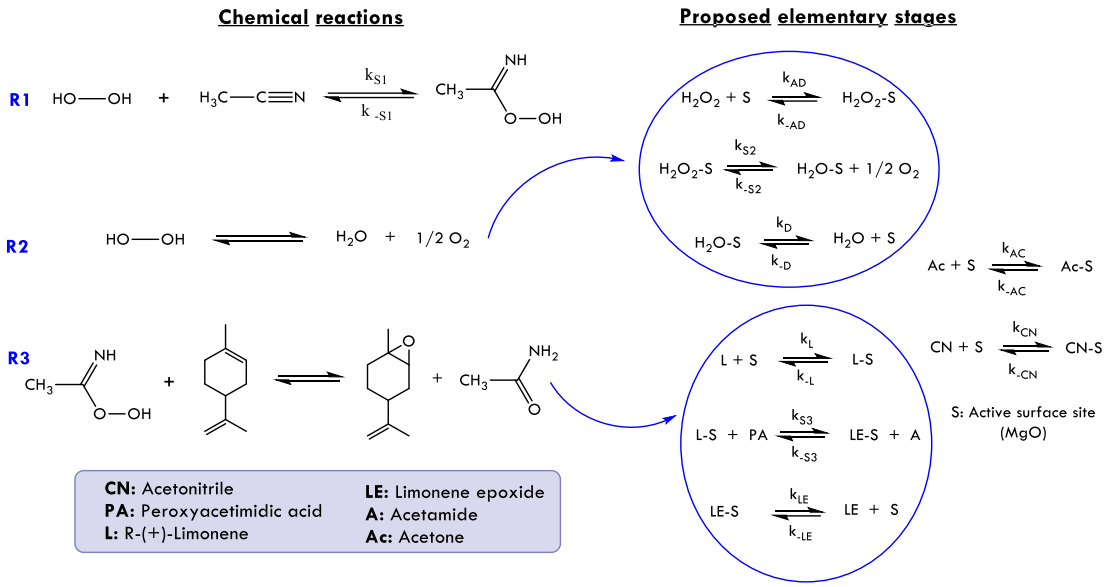

Figure 2.3. Set of reactions and proposed reaction pathway to produce limonene monoepoxide through a Payne system with water and acetone, and MgO as a heterogeneous catalyst.

Concentrations of limonene (C_L) and limonene epoxide (C_{LE}) were calculated with **Eqs. (2.5)-(2.6)**, respectively, which depend on the initial limonene concentration ($C_{L,0}$), limonene conversion (X_L), and limonene epoxide selectivity (S_{LE}).

$$C_L = C_{L,0}(1 - X_L) \quad \textbf{(2.5)}$$

$$C_{LE} = C_{L,0} X_L S_{LE} \quad \textbf{(2.6)}$$

2.3.6.2. Kinetic modeling

The proposed kinetic model was based both on a pseudo-homogeneous reversible model for the formation of the peroxyacetimidic acid (R1) and Eley-Rideal mechanisms, assuming the surface reactions as the rate-limiting step for the decomposition of H_2O_2 (R2) and the formation of limonene epoxide (R3). The rate law for each one of the three reactions is shown in **Table 2.3** and the detailed math treatment can be found in the **section 8.1.1**. k_i are the reaction rate constants for each reaction, which are described by the Arrhenius equation, **Eq. (2.7)**, where A_i is the pre-exponential factor of reaction i, E_i is the activation energy of reaction i, R is the universal gas constant and T is the absolute temperature, and K_{Si} are the equilibrium constants that can be considered constants due to the small evaluated temperature range (40 °C - 50 °C) [69,70].

Table 2.3. Kinetic models for the R-(+)-limonene transformation with H_2O_2.

Reaction	Description	Reaction rate (r_i)
R1	Pseudo-Homogeneous reversible model	$r_1 = k_1\left[C_{H_2O_2}C_{CN} - \frac{C_{PA}}{K_{S1}}\right]$
R2	Heterogeneous mechanism assuming the surface reaction as rate-limiting step	$r_2 = \frac{k_2\left[K_{AD}C_{H_2O_2} - \frac{C_{H_2O}C_{O_2}^{1/2}}{K_D K_{S2}}\right]}{\left[1 + K_{AD}C_{H_2O_2} + \frac{C_{H_2O}}{K_D} + K_L C_L + \frac{C_{LE}}{K_{LE}} + K_{Ac}C_{Ac} + K_{CN}C_{CN}\right]}$
R3	Heterogeneous mechanism with limonene as adsorbed specie and assuming the surface reaction as rate-limiting step	$r_3 = \frac{k_3\left[K_L C_L C_{PA} - \frac{C_{LE}C_A}{K_{LE}K_{S3}}\right]}{\left[1 + K_{AD}C_{H_2O_2} + \frac{C_{H_2O}}{K_D} + K_L C_L + \frac{C_{LE}}{K_{LE}} + K_{Ac}C_{Ac} + K_{CN}C_{CN}\right]}$

$$k_i = A_i \exp\left(-\frac{E_i}{RT}\right) \quad \textbf{(2.7)}$$

The mole balance for the specie i in a liquid-phase batch reactor is given by **Eq. (2.8)**, which assumes that the mixture is well stirred and thus there are no concentration gradients in the reactor, and the volume remains constant. This expression shows a relationship between the concentration of specie i (C_i) with the catalyst weight (W), the reaction volume (V), the reaction time (t), and the production rate for the specie i per mass of catalyst (R_i), which are evaluated according to relations given in **Table 2.4**.

$$\frac{dC_i}{dt} = \frac{W}{V}R_i \quad \textbf{(2.8)}$$

Table 2.4. Production rate for each of the i species.

Specie	Production rate (R_i)
Hydrogen peroxide	$R_{H_2O_2} = -(r_1 + r_2)$
Acetonitrile	$R_{CN} = -r_1$
Peroxyacetimidic acid	$R_{PA} = r_1 - r_3$
Water	$R_{H_2O} = r_2$
Oxygen	$R_{O_2} = \frac{1}{2}r_2$
Limonene	$R_L = -r_3$
Limonene epoxide	$R_{LE} = r_3$
Acetamide	$R_A = r_3$
Acetone	$R_{Ac} = 0$

2.3.6.3. Parameters optimization

The kinetic parameters were determined by a minimization of the sum of squared errors (SSE), between the experimental ($C_{j,i,Exp}$) and modeled ($C_{j,i,Mod}$) concentrations of the specie j (limonene, limonene epoxide, and H_2O_2) for each run i (**Table 2.2**), according with **Eq. (2.9)**, where N_{run} = 7 and N_{com} = 3. The optimization was performed using the *fmincon subroutine* from Matlab® software. Some stats parameters defined by **Eqs. (2.10)-(2.12)**, such as the root mean square deviation (RMSD), the normalized root mean square deviation (NRMSD), and the determination coefficient (R^2) can be calculated to conclude the goodness of fit of the proposed kinetic models [71]. Here, N_t refers to the total of the fitted experimental data (3 concentrations x 7 runs x 3 times, N_t = 63), $\max(C_{j,i,Exp})$ and $\min(C_{j,i,Exp})$ refers to the largest and smallest experimental concentration values, respectively, and $\bar{C}_{j,i,Exp}$ refers to the mean of the experimental concentration data.

$$SSE = \sum_{j}^{N_{com}} \sum_{i=1}^{N_{run}} \left(C_{j,i,Exp} - C_{j,i,Mod}\right)^2 \quad \textbf{(2.9)}$$

$$RMSD = \sqrt{\frac{\sum_{j}^{N_{com}} \sum_{i=1}^{N_{run}} \left(C_{j,i,Exp} - C_{j,i,Mod}\right)^2}{N_t}} \quad \textbf{(2.10)}$$

$$NRMSD = \frac{RMSD}{\max(C_{j,i,Exp}) - \min(C_{j,i,Exp})} \quad \textbf{(2.11)}$$

$$R^2 = 1 - \frac{\sum_{j}^{N_{com}} \sum_{i=1}^{N_{run}} \left(C_{j,i,Exp} - C_{j,i,Mod}\right)^2}{\sum_{j}^{N_{com}} \sum_{i=1}^{N_{run}} \left(C_{j,i,Exp} - \bar{C}_{j,i,Exp}\right)^2} \quad \textbf{(2.12)}$$

2.4. Results and discussion

2.4.1. Catalyst characterization

2.4.1.1. Powder X-ray diffraction

The XRD patterns for the fresh and spent MgO catalysts are shown in **Figure 2.4**, revealing the presence of brucite and periclase phases corresponding to the minerals forms of $Mg(OH)_2$ and MgO, respectively [72]. The diffraction peaks with the crystallographic planes (hkl) for both phases are listed in **Table 2.5**, with periclase and brucite phases corresponding to cubic and hexagonal crystal systems, respectively [73,74]. Indexing the pattern involves assigning the correct Miller indices to each peak and determining the unit cell parameters (a = b = c for a cubic system and a = b ≠ c for a hexagonal system). Thus, Bragg's law (**Eq. (2.13)**) can be solved, along with the expressions for the interplanar spacing (d) for cubic (**Eq. (2.14)**) and hexagonal (**Eq. (2.15)**) structures [75].

$$n\lambda = 2d\sin(\theta) \quad \textbf{(2.13)}$$

$$d^2 = \frac{a^2}{h^2 + k^2 + l^2} \quad \textbf{(2.14)}$$

$$\frac{1}{d^2} = \frac{4}{3}\left(\frac{h^2 + hk + k^2}{a^2}\right) + \frac{l^2}{c^2} \quad \textbf{(2.15)}$$

Where h, k, and l are the Miller indices, θ is the incidence angle (which is half the Bragg angle), and λ is the wavelength of the incident X-ray beam (0.154 nm for copper lamp).

Table 2.5 present the interplanar spacings for each diffraction peak for both phases, as well as the unit cell parameters. The unit cell parameter "a" for periclase was determined from each diffraction peak, with very close values calculated, thus validating the successful indexing of the periclase phase in the MgO catalyst. The mean value of a was found to be 4.2 Å, which is in good agreement with the reference data available in the Crystallography Open Database (COD ID 1000053) [76]. In contrast, the parameters for the brucite crystal system (a and c) were calculated by minimizing the mean squared error for $1/d^2$ for the five peaks presented in **Table 2.5**. The obtained values were a = b = 3.14 Å and c = 4.76 Å, which are in accordance with the reference data in the COD ID 1000054.

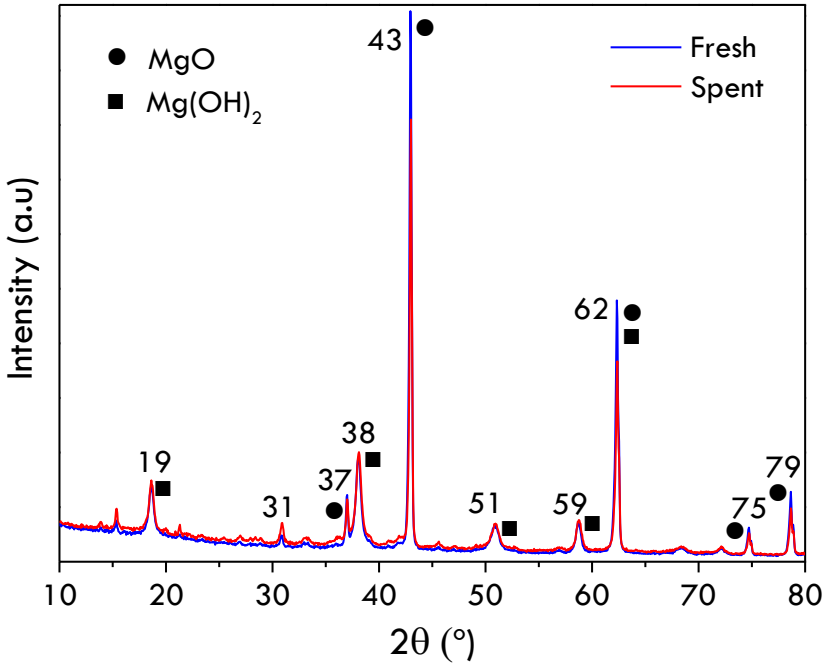

Figure 2.4. XRD patterns of fresh and spent MgO catalyst.

Table 2.5. Indexing of diffraction peaks for the brucite and periclase phases.

Phase	(hkl)	θ (°)	d (nm)	a = b (nm)	c (nm)
Brucite (Hexagonal)	(001)	9.50	0.4671	0.3142	0.4762
	(011)	19.00	0.2368		
	(012)	25.50	0.1791		
	(110)	29.50	0.1566		
	(111)	31.00	0.1497		
Periclase (Cubic)	(111)	18.50	0.2430	0.4208	
	(200)	21.50	0.2104	0.4207	
	(220)	31.00	0.1497	0.4234	
	(311)	37.50	0.1266	0.4200	
	(222)	39.50	0.1212	0.4199	

Quantitative phase analysis is a method that involves determining and calculating the absolute intensities of the two identified phases in MgO [77]. In this study, a semi-automatic Rietveld analysis was conducted using HighScore Plus software to quantify the two phases in the MgO catalyst. The analysis showed that the periclase composition was 82.6 wt. % and 78 wt. %, and the brucite composition was 17.4 wt. % and 22 wt. % for the fresh and spent catalyst, respectively. This slight difference in phase composition can be observed by the change in the diffraction peaks intensity between the fresh and spent catalyst. These results suggest a slight phase transition from MgO to $Mg(OH)_2$ due to the hydration of MgO with water present in the reaction mixture. The small transition (4.6 wt. %) can be explained by the relatively low temperature (50 °C) used in the reaction [78].

2.4.1.2. Thermal stability

The TGA curves for the fresh and spent catalysts are shown in **Figure 2.5**, with three stages identified for both materials. The first stage between room temperature and 200 °C [79], can be associated to physisorption on the surface of the material, of water for the fresh material and of water, acetone, and acetonitrile for the spent material, as well as the elimination of hydroxide groups. The second stage begins at 200 °C and ends around 480 °C, corresponding to the elimination of chemisorbed species and the decomposition of $Mg(OH)_2$ present in the materials to form MgO [80]. The no significant weight loss after 480 °C shows the high stability of MgO. More pronounced losses are observed in the profile of the spent material than in the fresh material. In the first stage, this is probably because there is more adsorption of substances after the reaction, compared to the fresh material that only contains moisture. However, in the second stage, the greater losses can be explained by the more significant presence of $Mg(OH)_2$ (brucite) which is decomposed to periclase MgO as the most stable form. Furthermore, the DTG curves exhibit the maximum weight losses at around 300-480 °C, consistent with the TGA curves [81]. For fresh and spent catalysts, approximately 2.5% and 5% of losses were observed for stage 1, 17.5% and 23% for stage 2, and only 1% for stage 3, respectively.

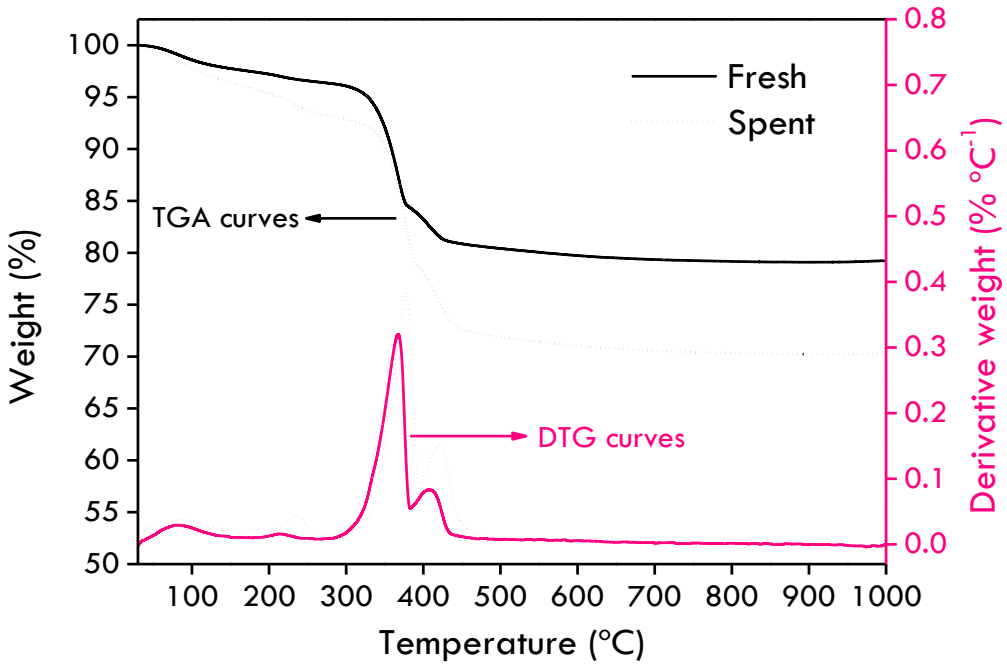

Figure 2.5. TGA and DTG curves of fresh and spent MgO catalyst.

2.4.1.3. Textural properties

The N_2 adsorption-desorption isotherms of the materials are shown in **Figure 2.6**, which exhibit a type IV isotherm according to the IUPAC classification, with a typical hysteresis loop (type H4) for mesoporous materials. This loop is often associated with capillary condensation inside the narrow slit-like pores [77,82]. The BET area for the fresh material was 124 ± 1.8 $m^2\ g^{-1}$, consistent with a previously reported value for MgO [53]. Meanwhile, the area for the spent catalyst showed a slight increase, with a value of 169 ± 2.2 $m^2\ g^{-1}$, which can be attributed to the largest presence of brucite. The pore volume is significantly higher for the spent catalyst (0.36 $cm^3\ g^{-1}$) than for the fresh material (0.19 $cm^3\ g^{-1}$), which is expected due to its direct relationship with the surface area. On the other hand, the average pore diameter was very similar for two materials (3.5 nm), which is evidenced in the pore size distribution (**Figure 2.6**) according to the maximum point of the curves, which confirms the solids as mesoporous materials, according to the IUPAC definition.

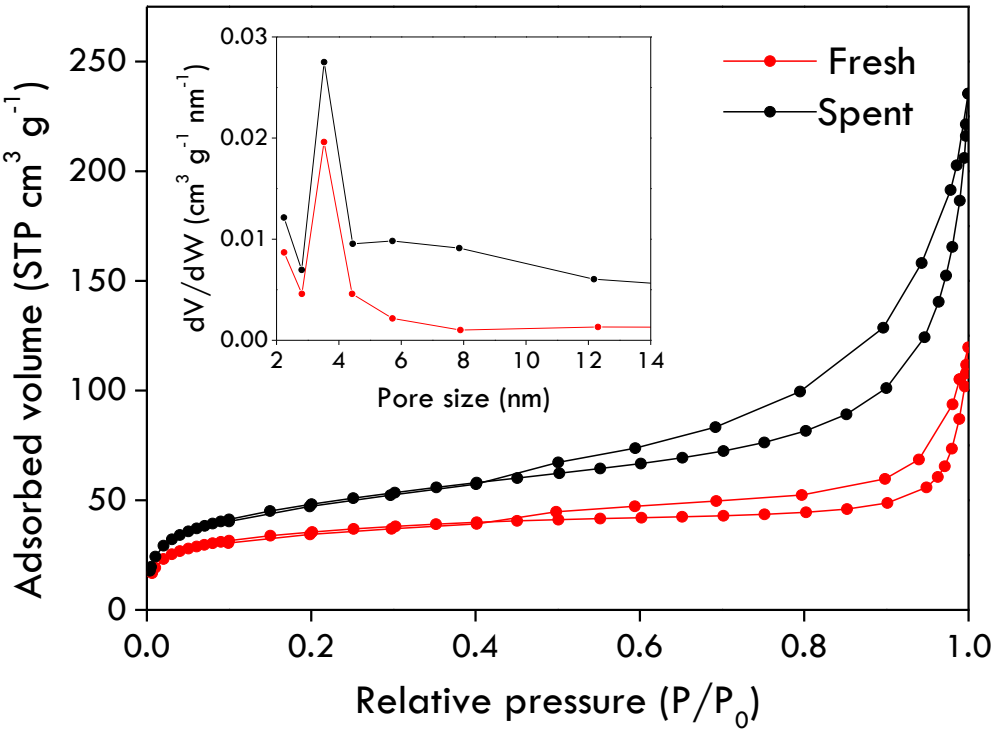

Figure 2.6. N_2 adsorption-desorption isotherms and pore size distribution for the materials.

2.4.1.4. FTIR analysis

Figure 2.7 shows the FTIR bands of both fresh and spent catalysts. The sharp band at 3698 cm^{-1}, as well as the bands at 3650, 3515, and 3450 cm^{-1}, are attributed to the hydroxyl stretching vibration of brucite [83–85]. A very broad band within the range of 4000-3000 cm^{-1} is assigned to the vibration mode of the lamellar OH group and H_2O molecules, which may be either inserted in the interlamellar space or physisorbed on the surface [84,86]. It is widely known that H_2O and CO_2 molecules can be easily chemisorbed onto the surface of MgO when exposed to the atmosphere. In both spectra, the broad vibration band at 1420 cm^{-1} is associated with the stretching of CO_3^{2-} molecules, which has been previously reported for studies of MgO [53,87]. The band observed at 1480 cm^{-1} is assigned to the presence of -OH stretching due to the adsorption of water on the surface of the metal [88]. The bands appearing at low frequencies of 857 and 690 cm^{-1} are attributed to the stretching vibration of -Mg-O-Mg-O- bonding [89,90]. An additional slight band is observable in the spectrum of the spent material, appearing at approximately 2920 cm^{-1}. This band can be attributed to the vibrations of C-H bonds present in acetone and/or acetonitrile structures, two compounds employed in the reaction mixture. This observation aligns with the findings from TGA, which suggested the presence of adsorbed species.

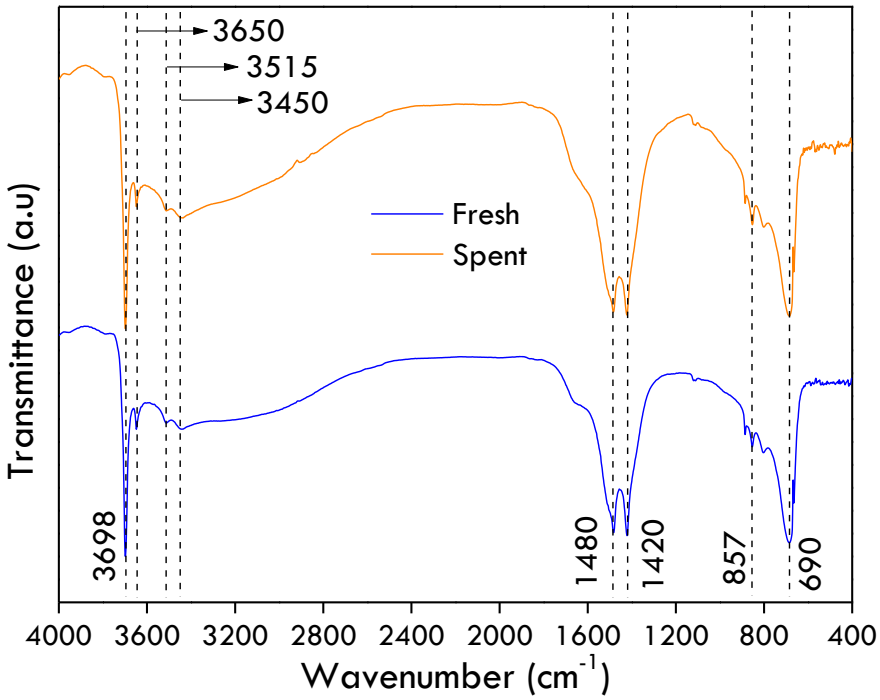

Figure 2.7. FTIR spectra of fresh and spent MgO catalyst.

2.4.1.5. SEM images

As the MgO commercial catalyst is composed of periclase (MgO) and brucite ($Mg(OH)_2$) phases, the SEM images for the pure two phases are presented in **Figure 2.8**. MgO commercial material was calcined at 600 °C (1 °C min^{-1} for 1 h) to obtain high-purity MgO, as was evidenced by TGA analysis. **Figure 2.8.A** shows the rod-like pure MgO crystals with definite boundaries (without agglomeration), and arranged randomly with different sizes; $Mg(OH)_2$ displays morphology in spherical-like structures, which are smaller than MgO particles, but more homogeneous sizes distribution (**Figure 2.8.B**). **Figure 2.8.C-D** show micrographs with higher magnification (X7000) for pure MgO and $Mg(OH)_2$, respectively. The surface of the MgO nanoparticles exhibits considerable surface roughness, while $Mg(OH)_2$ consists mainly of thin flakes, which look like the nanopetals of rose flowers composed of thinner nanoplates [79]. The EDS spectra of pure MgO and $Mg(OH)_2$ (**Figure 8.30** and **Figure 8.31**, **section 8.1**) show that samples contain only Mg and O. Peaks related to C and Au are owing to the sample preparation for SEM analysis.

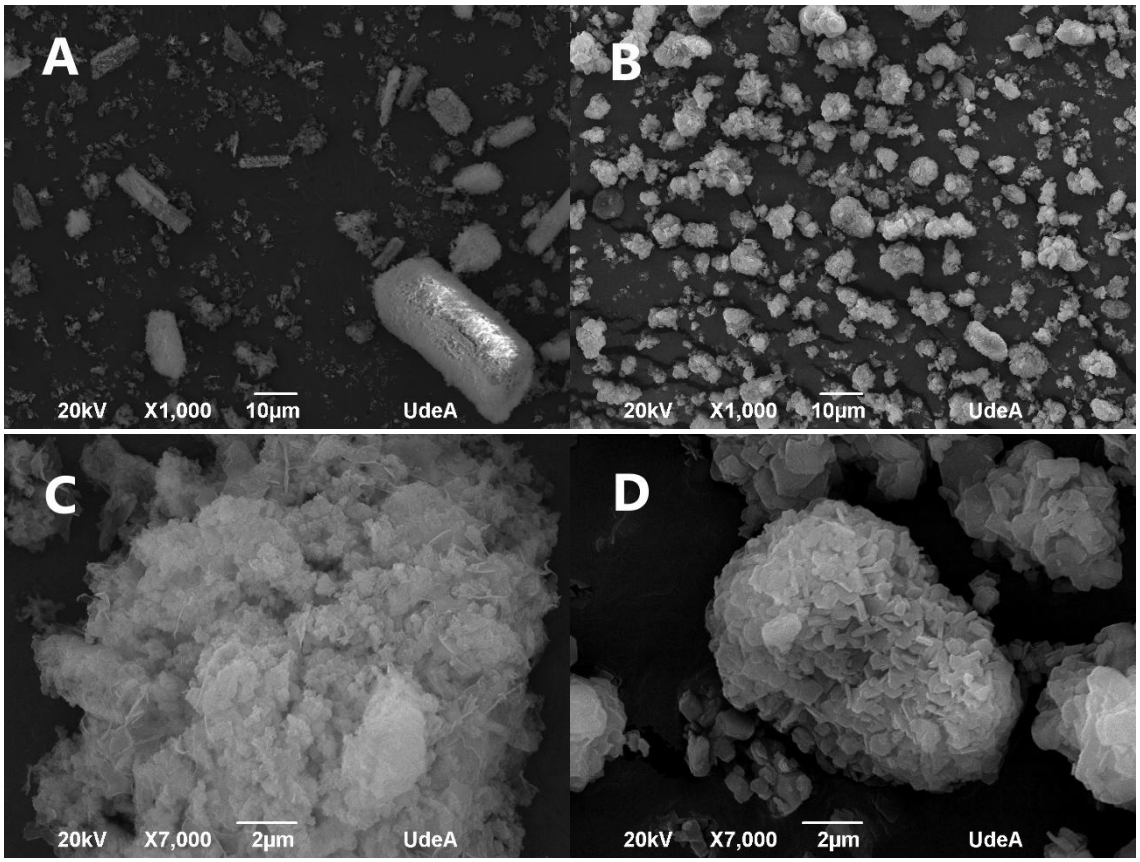

Figure 2.8. SEM images of **A)** MgO calcined at 600 °C (X1000), **B)** $Mg(OH)_2$ (X1000), **C)** MgO calcined at 600 °C (X7000), **D)** $Mg(OH)_2$ (X7000).

The SEM images for the fresh (**Figure 2.9.A** and **Figure 2.9.C**) and spent (**Figure 2.9.B** and **Figure 2.9.D**) MgO catalysts show a contribution of two structures of different sizes with the lowest magnification (**Figure 2.9.A-B**), rod-like pure MgO and spherical-like $Mg(OH)_2$, as was seen in the micrographs for each independent phase in **Figure 2.8**. On the other hand, the images with the highest magnification (X15000) in **Figure 2.9.C-D**, display the presence of thin flakes and surface roughness nanoparticles, which are features of $Mg(OH)_2$ and MgO, respectively. Therefore, it agrees with the crystalline phases characterized previously by XRD. The EDS spectrum of materials (**Figure 8.32** and **Figure 8.33**, **section 8.1**) shows only the presence of Mg and O.

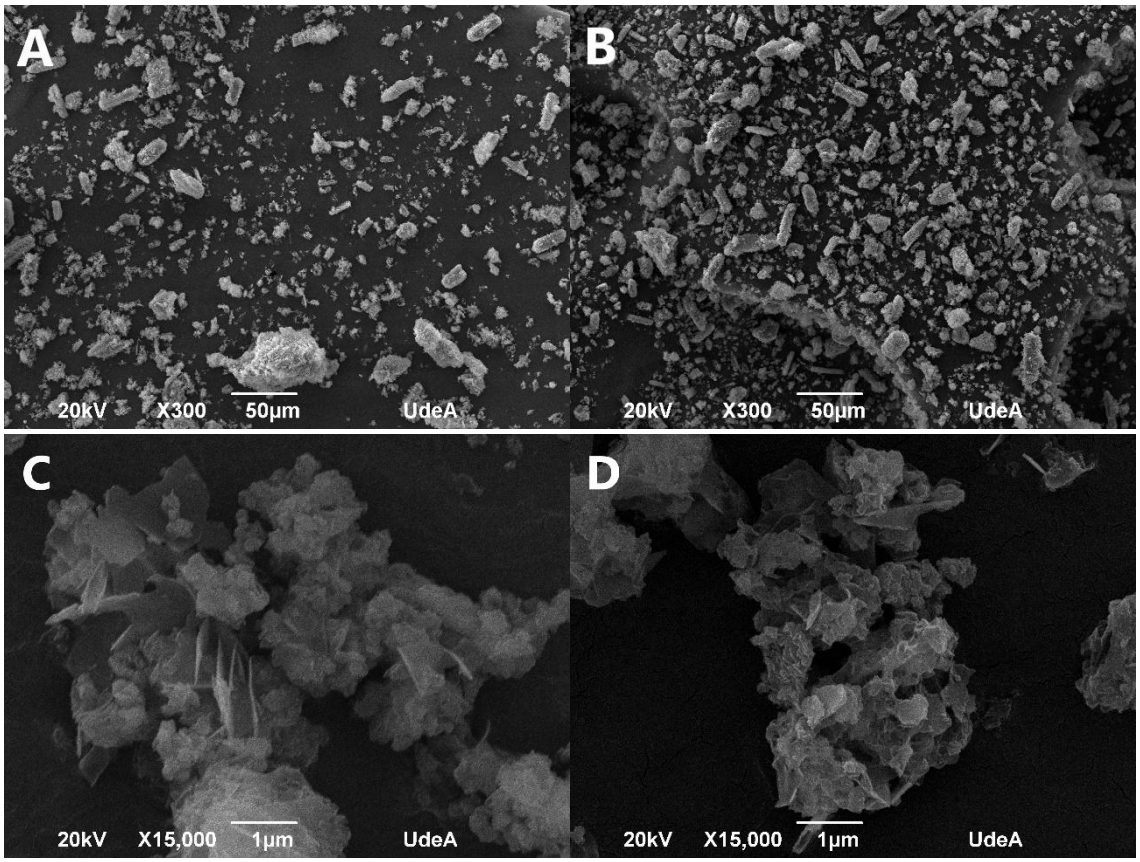

Figure 2.9. SEM images of **A)** MgO fresh catalyst (X300), **B)** MgO spent (X300), **C)** MgO fresh catalyst (X15000), **D)** MgO spent (X15000).

The SEM/EDS image with elemental maps presents the physical structure more clearly in **Figure 2.10**. **Figure 2.10.A** and **Figure 2.10.D** show the images of materials regions where EDS analyses were performed. Mg (**Figure 2.10.B** and **Figure 2.10.E**) and O (**Figure 2.10.C** and **Figure 2.10.F**) were very well distributed in the materials without any concentrated region of specific element, and without the presence of impurities.

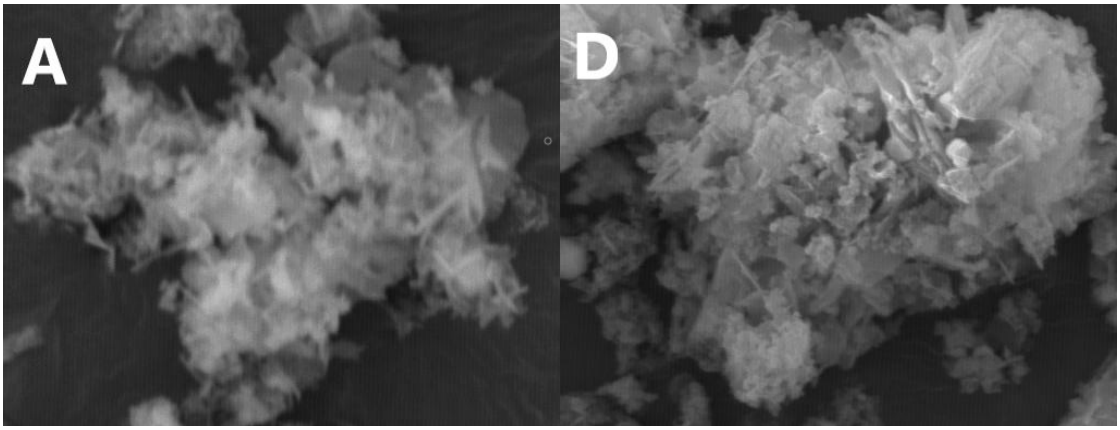

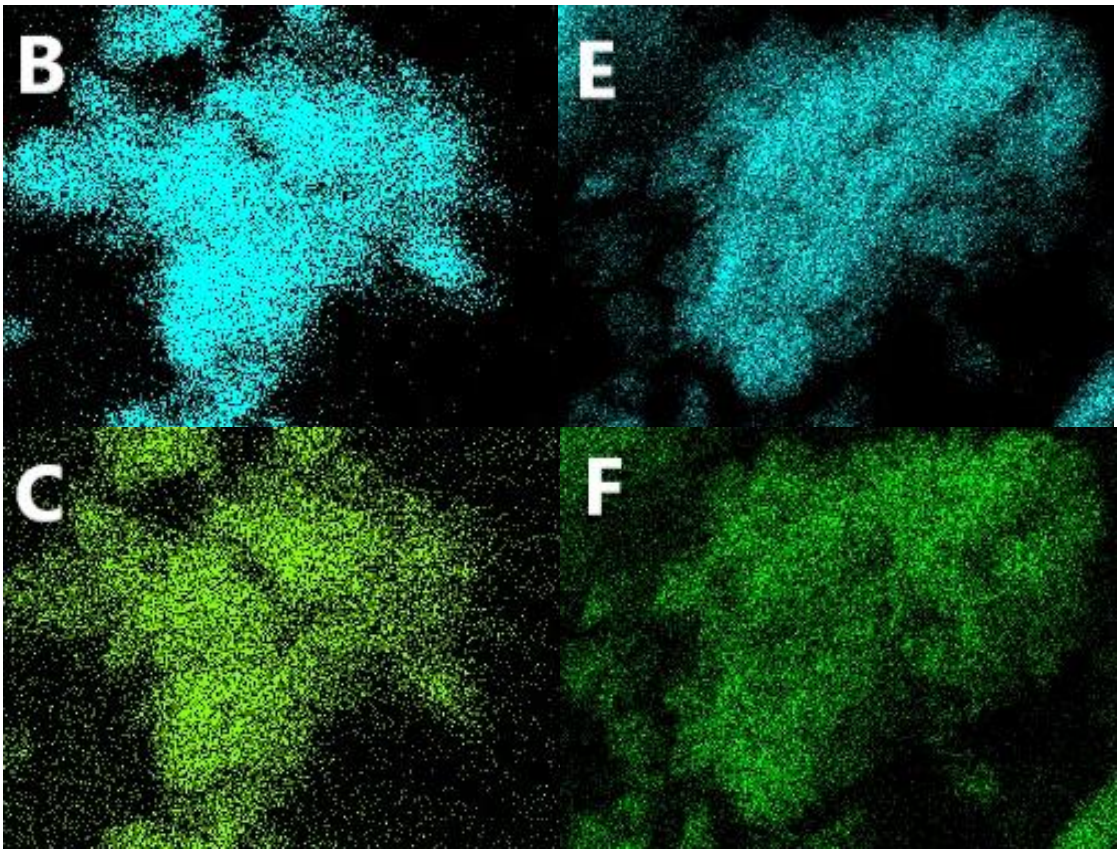

Figure 2.10. SEM-EDS images with elemental maps: **A)** SEM image for MgO fresh catalyst, **B)** Mg elemental map for fresh MgO, **C)** O elemental map for fresh MgO, **D)** SEM image for MgO spent catalyst, **E)** Mg elemental map for spent MgO, **F)** O elemental map for spent MgO.

2.4.2. Catalytic performance

Figure 2.11 shows the profiles for limonene conversion and selectivities to limonene monoepoxides and limonene diepoxide with different MgO: limonene mass ratios. Before 30 min, only limonene monoepoxides was formed, for the three concentrations of MgO. Complete conversion of limonene was achieved after 90 min of reaction for the three concentrations; however, before 90 min, the conversion increased as the MgO concentration increased, which can be explained by the greater availability of catalytic sites in the reaction mixture. As the MgO concentration increased, the selectivity towards the diepoxide is improved and the selectivity towards the monoepoxides is decreased. It occurs because there are consecutive reactions where the limonene epoxide is formed first, but simultaneously, it is transformed into limonene diepoxide (**Figure 2.1**). Therefore, results suggest that the production of limonene diepoxide is favored with high concentrations of MgO, achieving selectivities higher than 85% after 90 min and higher than 96% after 120 min, with a MgO: limonene mass ratio of 1.20. The balance (around 4%) were by-products that could not be identified by mass spectrometry. Perhaps these products correspond to diols resulting from the opening of the endocyclic and/or exocyclic ring.

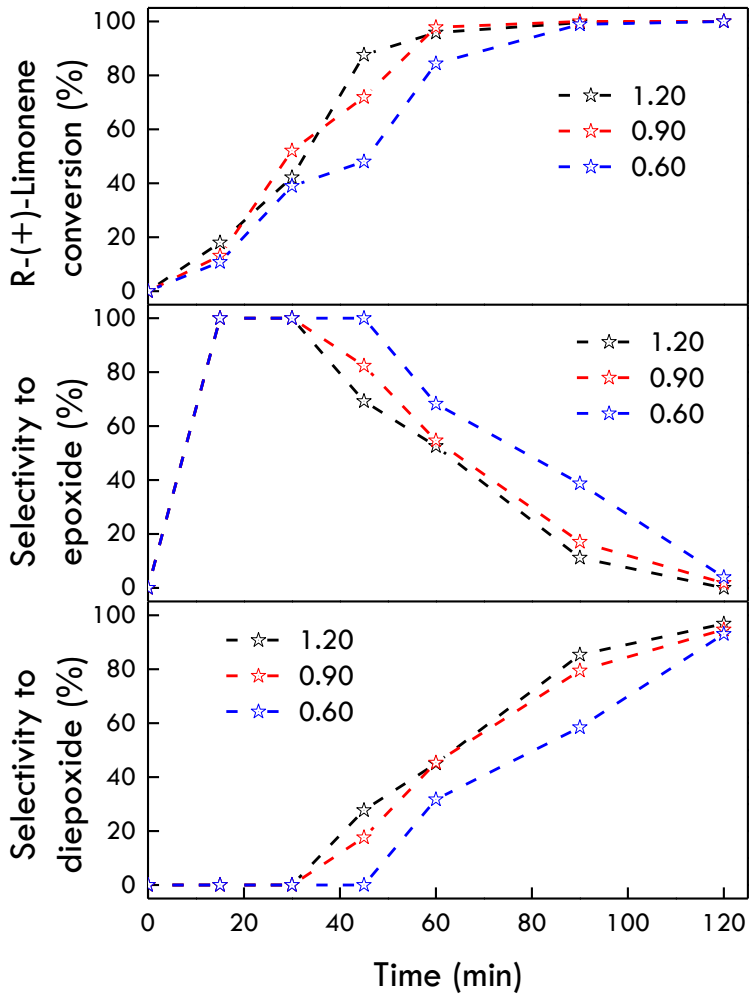

Figure 2.11. Effect of MgO concentration (MgO: limonene mass ratio) in the oxidation of R-(+)-limonene. **Reaction conditions:** 0.1 mmol limonene, mass ratios for limonene: H_2O: acetone: acetonitrile: H_2O_2 of 1: 30.3: 19.7: 15.7: 0.8, 50 °C, 1000 rpm.

The effect of the oxidant agent (H_2O_2) was evaluated in the oxidation of limonene at different reaction times, **Figure 2.12**. Three H_2O_2: limonene mass ratios were tested, which showed a maximum limonene conversion of around 25% when a mass ratio of 0.40 (mole ratio of 1.6) was used; the limonene conversion profiles with mass ratios of 0.80 (mole ratio of 3.2) and 1.20 (mole ratio of 4.8) were quite similar. Selectivities to limonene monoepoxides and diepoxide close to 100% and 0%, respectively, were obtained with the lowest H_2O_2: limonene mass ratio, for all times. With H_2O_2: limonene mass ratios of 0.80 and 1.20, selectivities to limonene diepoxide highest to 95% can be obtained after 120 min.

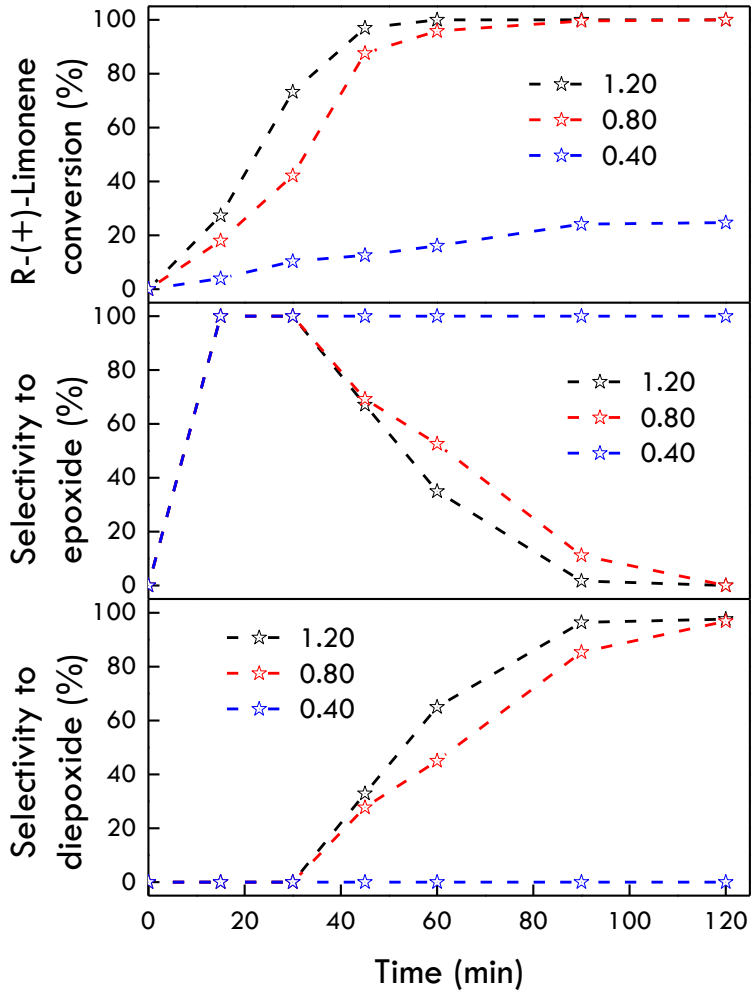

Figure 2.12. Effect of H_2O_2 concentration (H_2O_2: limonene mass ratio) in the oxidation of R-(+)-limonene. **Reaction conditions:** 0.1 mmol limonene, mass ratios for limonene: MgO: H_2O: acetone: acetonitrile of 1: 1.20: 30.3: 19.7: 15.7, 50 °C, 1000 rpm.

Figure 2.13 shows the effect of the initial concentration of limonene in the reaction mixture, which was achieved by varying the amounts of the substrate, water, acetone, and acetonitrile keeping constant the mass content of MgO and the H_2O_2: limonene mass ratio (0.80). Almost complete conversions (higher than 96%) of limonene can be achieved after 90 min for the three concentrations. The highest selectivities towards the monoepoxide are reached between 15 and 30 min of reaction, while the highest selectivities towards the diepoxide are reached after 120 min, obtaining the maximum (96%) with an initial concentration of limonene around 0.095 M. Furthermore, although the mole ratio between H_2O_2 and limonene remained constant, the monoepoxide selectivity increased as the limonene initial concentration increased.

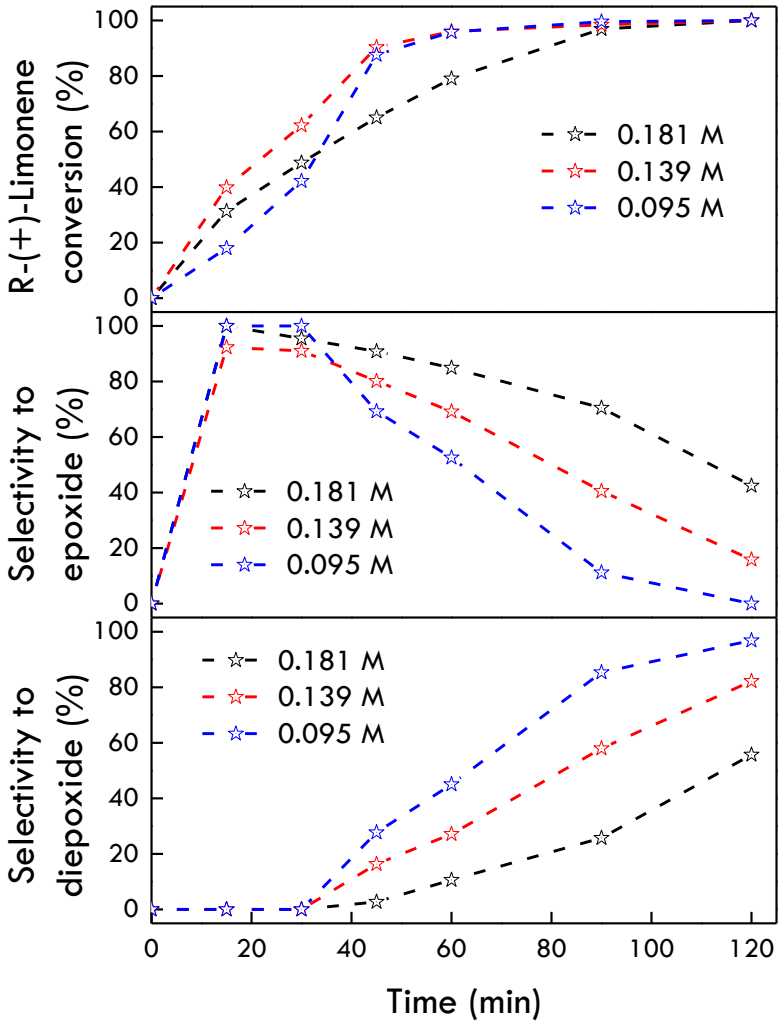

Figure 2.13. Effect of initial concentration of limonene in the oxidation of R-(+)-limonene. **Reaction conditions:** (0.10, 0.15, 0.20) mmol limonene, mass ratios for limonene: MgO: H_2O: acetone: acetonitrile: H_2O_2 of 1: (1.20, 0.80, 0.60): (30.3, 20.9, 16.22): (19.7, 13.13, 9.85): (15.7, 10.47, 7.85): 0.8, 50 °C, 1000 rpm.

The effect of temperature in the oxidation of limonene with H_2O_2 was evaluated at three temperatures (40 °C, 50 °C, and 60 °C), as is shown in **Figure 2.14**. It is observed that the reaction rate increased as the temperature increased, which is evidenced in the conversion profiles since the values are higher as the reaction temperatures increased. Almost complete conversions can be reached after 120 min, 60 min, and 45 min at 40 °C, 50 °C, and 60 °C, respectively. At 40 °C, the maximum reached selectivity to diepoxide is around 44%, while selectivities higher than 96% can be reached at 50 °C and 60 °C. Furthermore, at 60°C is observed the formation of monoepoxide in 15 min of reaction, but it is rapidly transformed to diepoxide (notice the pronounced changes in the black curve in the selectivity to the monoepoxide).

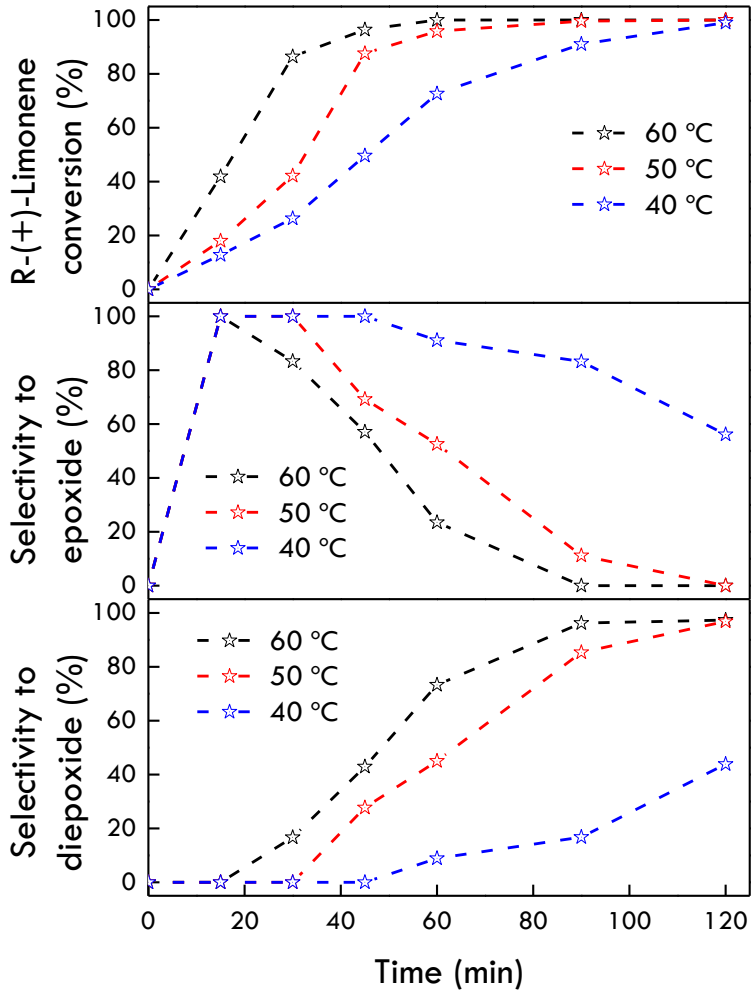

Figure 2.14. Effect of temperature in the oxidation of R-(+)-limonene. **Reaction conditions:** 0.1 mmol limonene, mass ratios for limonene: MgO: H_2O: acetone: acetonitrile: H_2O_2 of 1: 1.20: 30.3: 19.7: 15.7: 0.8, 1000 rpm.

Figure 2.15 shows the consumption of H_2O_2 during the epoxidation reaction of limonene for the reactions presented in **Figure 2.11**-**Figure 2.14**. H_2O_2 is consumed through the production of peroxyacetimidic acid (PA) from the reaction between H_2O_2 and acetonitrile but also its decomposition. The lowest MgO: limonene mass ratio (0.60) allowed to obtain lower conversions in comparison with the other two mass ratios (0.90 and 1.20), which suggested that the greater availability of MgO active sites improves both the production of PA and the H_2O_2 decomposition. With the highest H_2O_2: limonene mass ratios (0.80 and 1.20), quite similar profiles were obtained, which showed lower conversion values than the corresponding one with 0.40, indicating that the H_2O_2 conversion is favored with low amounts in the reaction medium. On the other hand, as the reaction temperature increases, the H_2O_2 conversion increases significantly, which was expected because the H_2O_2 decomposition can be promoted at high temperatures. Contrarily, the initial limonene concentration seems to have not a significant effect on the H_2O_2 conversion, which can be explained because the H_2O_2: limonene mass ratio was 0.80, which remained constant for those

catalytic tests. Finally, all the experimental catalytic tests showed that the H_2O_2 conversion reached values higher than 80% after 2 h, excepting the tests at 40 °C.

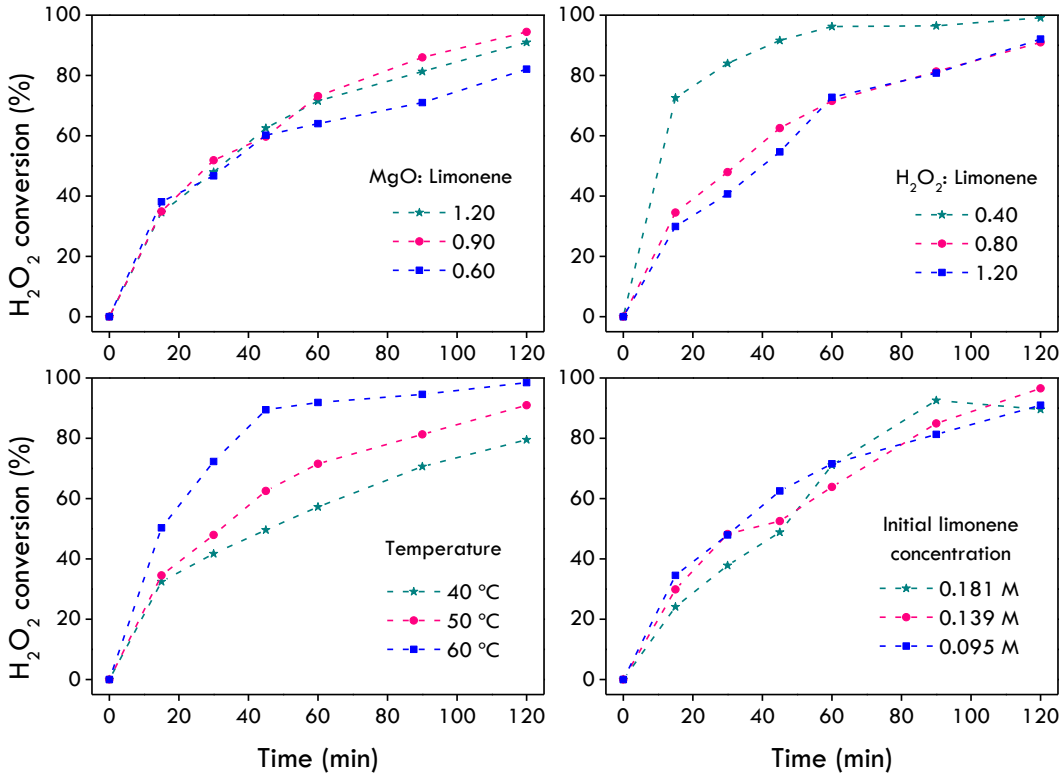

Figure 2.15. Profiles of H_2O_2 conversion in the oxidation of R-(+)-limonene. Reaction conditions were reported previously in **Figure 2.11**-**Figure 2.14**.

As the commercial catalyst is a mixture of brucite and periclase, the catalytic performance of these materials was evaluated in the oxidation of R-(+)-limonene with H_2O_2 and compared with the results achieved with the commercial material. **Figure 2.16** illustrates the conversion profiles for periclase and MgO, revealing their remarkable similarity. On the other hand, brucite demonstrated a slower activity during the initial 90 min but eventually attained complete conversion afterward. Furthermore, it is observed that the pure phases are more selective towards the monoepoxide, as this selectivity is better maintained over time, while the commercial catalyst significantly enhances selectivity towards the diepoxide as time goes by, showing a synergistic effect between the two phases.

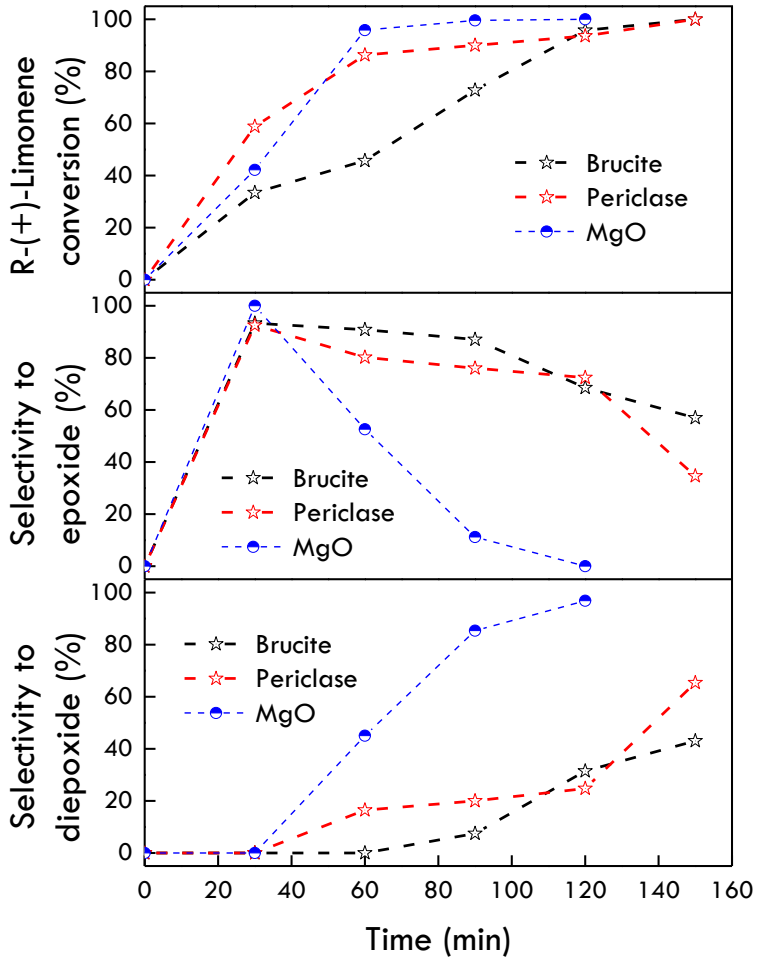

Figure 2.16. Comparison of catalytic performance using brucite ($Mg(OH)_2$), periclase (MgO calcined at 600 °C), and commercial catalyst (MgO). **Reaction conditions:** 0.1 mmol limonene, mass ratios for limonene: catalyst: H_2O: acetone: acetonitrile: H_2O_2 of 1: 1.20: 30.3: 19.7: 15.7: 0.8, 50 °C, 1000 rpm.

The results of two leaching tests over MgO as a heterogeneous catalyst are shown in **Figure 2.17**, which were performed using the hot-filtration method to separate the catalyst from the medium at the reaction temperature. After the catalyst removal, the reaction mixtures were allowed to continue for 1 h (L1 test) and 2 h (L2 test) to observe a possible change in the limonene conversion. The results indicated that the limonene conversion is maintained at around 33-35% after the removal of the catalyst, which indicates the absence of MgO leaching in the reaction mixture. On the other hand, a typical conversion profile for the limonene transformation with MgO as catalyst (Entry 1), in the range of 0-120 min, was presented in **Figure 2.17** which showed the behavior of a regular reaction. Furthermore, the reaction without catalyst (Blank), showed a limonene conversion of around 3% at 120 min, which evidences the importance of MgO as a heterogeneous catalyst. Therefore, these results evidence the heterogeneity of the catalytic reaction.

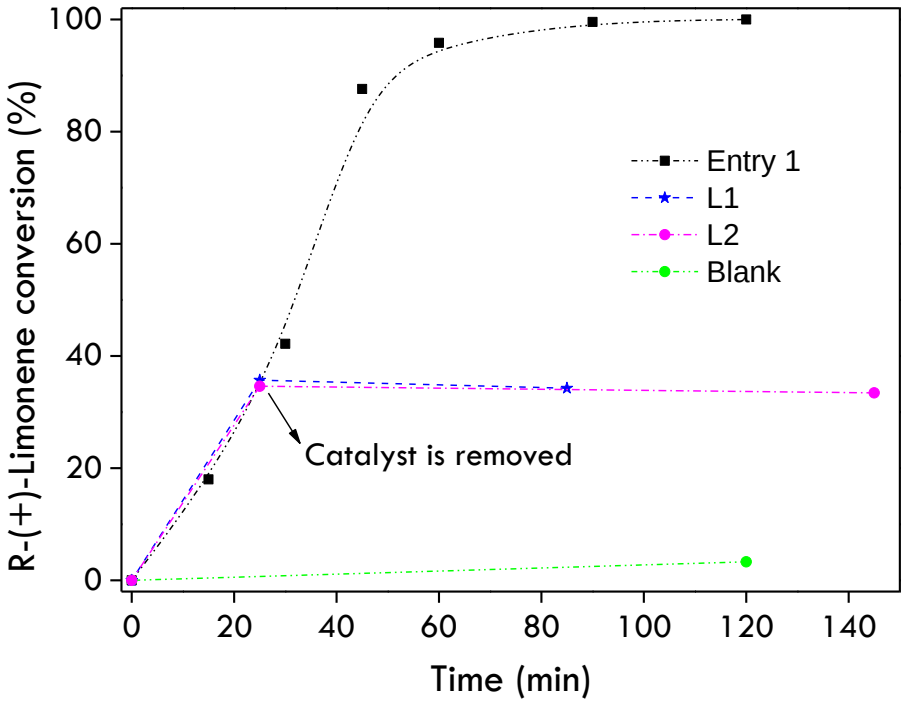

Figure 2.17. Leaching tests over MgO in the oxidation of R-(+)-limonene with H_2O_2. **Reaction conditions:** 0.1 mmol limonene, mass ratios for limonene: MgO: H_2O: acetone: acetonitrile: H_2O_2 of 1: 1.20: 30.3: 19.7: 15.7: 0.8, at 50 °C and 1000 rpm. Leaching tests were performed for 1 h (L1) and 2 h (L2) after the catalyst is removed. Entry 1 refers to a regular reaction and Blank to a reaction without catalyst.

The reuse tests (**Figure 2.18**) show a complete limonene conversion for the four cycles, but a slight decrease in the selectivity to diepoxide was observed (97% for cycle 1 and 76% for cycle 4). This indicates a reduction in the reaction rate of monoepoxide towards diepoxide, which can be explained by the slight phase change that occurs in the catalyst (from periclase to brucite) as discussed previously. However, these results are promising because it suggests that increasing the reaction time slightly could help in recovering the high selectivity towards the diepoxide, with complete conversion of the substrate.

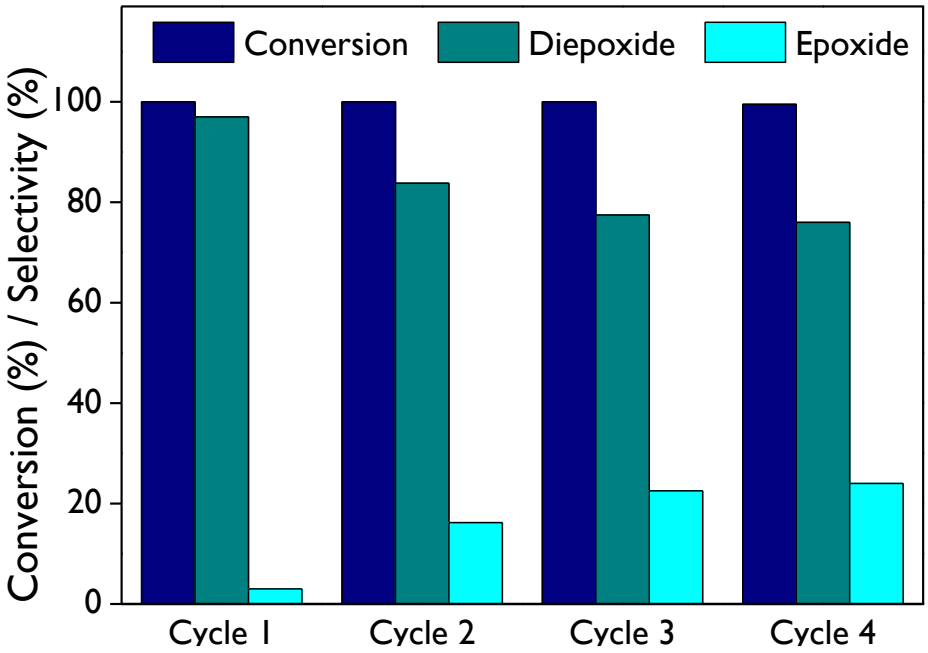

Figure 2.18. Reusability of commercial MgO in the oxidation of R-(+)-limonene with H_2O_2. **Reaction conditions:** 0.1 mmol limonene, mass ratios for limonene: MgO: H_2O: acetone: acetonitrile: H_2O_2 of 1: 1.20: 30.3: 19.7: 15.7: 1.6, 50 °C, 3 h and 1000 rpm.

2.4.3. Kinetics

2.4.3.1. Limitations by internal mass transfer

The Weisz-Prater criterion ($N_{W\text{-}P}$), given by **Eq. (2.16)**, is a dimensionless number widely used to check if the reaction is limited or not by internal diffusion, which requires some parameters that are either measured or known. If $N_{W-P} \ll 1$, the internal diffusion is negligible but if $N_{W-P} \gg 1$, internal diffusion limits the reaction severely [91,92]. Furthermore, a more concise criterion is $N_{W\text{-}P} \leq 3b$, where b depends on the reaction order, with values of 0.1, 0.2, and 2 for the second, first, and zero-order reactions, respectively. On the other hand, if $N_{W\text{-}P}$ is greater than 6, internal pore diffusion limitations definitely exist [92].

$$N_{W-P} = \frac{-r_i^{exp} \rho_{cat} R_{cat}^2}{D_{i,eff} C_{i,cat}} \quad \textbf{(2.16)}$$

Where $-r_i^{exp}$ (mol g^{-1} min^{-1}) is the reaction rate of specie i, R_{cat} is the average radius of the catalyst particle (31.5 µm, taken as an average of the particle size for the 230-mesh), ρ_{cat} is the catalyst density (3.58 g cm^{-3}), $D_{i,eff}$ is the effective diffusivity of specie i through the catalyst given by **Eq. (2.17)**, and $C_{i,cat}$ is the concentration of specie i at the catalyst surface which can be taken as the bulk concentration (C_i) when the absence of external mass transfer limitations is ensured through high stirring in the catalytic tests (1000 rpm).

$$D_{i,eff} = \frac{\varphi_p \sigma_c D_{i,L}}{\tau} \quad \textbf{(2.17)}$$

Here, φ_p is the catalyst porosity (0.82 [93]), σ_c is the constriction factor (0.8 [91]), τ is the tortuosity (3.0 [91]), and $D_{i,L}$ is the diffusion coefficient of specie i in the reaction mixture at the specific temperature, which was estimated using the Aspen Plus software (details in **section 8.1.4**). On the other hand, r_i^{exp} was calculated from the experimental data, and the detailed procedure is illustrated in the **section 8.1.2**. It is important to notice that the $N_{W\text{-}P}$ criterion gives an upper bound to avoid internal mass transfer limitations, which indicates that is enough to use the maximum value of $-r_i^{exp}$, corresponding to $-r_{i0}^{exp}$.

Table 8.3 and **Table 8.4** (**section 8.1**) show the results of the Weisz-Prater criterion for both limonene and H_2O_2, observing that it is satisfied for all experimental runs because $N_{W\text{-}P} \ll 1$. These results indicate the absence of limitations by internal mass transfer, which means there is no existence of concentration gradients within the catalyst. Therefore, it is concluded that the transformation of R-(+)-limonene with H_2O_2 over MgO as a catalyst, is controlled by the surface-rate steps.

2.4.3.2. Kinetic modeling

The kinetic study was performed using a pseudo-homogeneous reversible model to describe the production of peroxyacetimidic acid (PA) as the active oxidant intermediate (R1), and heterogeneous kinetics models based on Eley-Rideal mechanism for describing the decomposition of H_2O_2 towards H_2O and O_2 (R2) and the production of limonene monoepoxide (R3). **Table 2.6** reports the optimized kinetic parameters found according to the objective function given by **Eq. (2.9)**. The activation energies for each one of the three reactions were found, noticing that the energy barrier for the decomposition of H_2O_2 (E_2 = 29.06 kJ mol^{-1}) is the smallest, which was to be expected due to its ease decomposition at temperatures higher than ambient, and the presence of catalysts. Furthermore, the activation energies to produce PA and monoepoxide were E_1 = 58.61 kJ mol^{-1} and E_3 = 52.28 kJ mol^{-1}, respectively. A very suitable adjustment of the kinetics models to the concentration experimental data of limonene, H_2O_2, and limonene monoepoxide, was achieved, which is reflected in a high determination coefficient (R^2) of 99.38%. On the other hand, the adsorption equilibrium constant values suggested that the adsorption strength over MgO decreases in the following order: H_2O_2, limonene, acetone, and acetonitrile. This perspective of the kinetic study constitutes a significant advance in heterogeneous catalysis for the transformation of R-(+)-limonene with H_2O_2 through a Payne system. It demonstrates a lower energy barrier (52.3 kJ mol^{-1}) for monoepoxide production compared to other catalytic systems, such as PW-Amberlite under triphasic conditions (76 kJ mol^{-1}) [63] and Al_2O_3 for external monoepoxides (54 kJ mol^{-1}) [94]. This highlights the versatility of MgO as a material for the valorization of limonene through the epoxidation route.

Table 2.6. Kinetic and stats parameters for the kinetic modeling.

Parameter	Value	Parameter	Value
A_1 (L^2 mol^{-1} g^{-1} min^{-1})	5.0230E+06	K_D (mol L^{-1})	1.1082E+04
A_2 (mol g^{-1} min^{-1})	9.8121E+00	K_L (L mol^{-1})	9.7947E+06
A_3 (L g^{-1} min^{-1})	8.2703E+06	K_{LE} (mol L^{-1})	3.6969E+05
E_1 (kJ mol^{-1})	58.61	K_{Ac} (L mol^{-1})	2.2423E-01
E_2 (kJ mol^{-1})	29.06	K_{CN} (L mol^{-1})	5.4546E-02
E_3 (kJ mol^{-1})	52.28	R^2	0.9938
K_{S1} (L mol^{-1})	4.3315E-02	SSE	0.0067
K_{S2} ($mol^{0.5}$ $L^{-0.5}$)	1.3566E+04	RMSD	0.0103
K_{S3}	1.0057E+05	NRMSD	0.0180
K_{AD} (L mol^{-1})	2.8105E+07		

2.4.3.3. Efficiency of H_2O_2

As H_2O_2 is consumed through two reactions of the catalytic pathway (**Figure 2.3**), the hydrogen peroxide efficiency (or selectivity) is calculated as the fraction of moles of H_2O_2 that are converted into peroxyacetimidic acid (PA) [52]. The H_2O_2 selectivity ($S_{H_2O_2,Ri}$) for each one of the reactions R1 (production of PA) and R2 (decomposition of H_2O_2) can be calculated by **Eq. (2.18)**, in terms of the reaction rates of H_2O_2 for each step (r_1 and r_2) and the H_2O_2 production rate ($R_{H_2O_2}$). On the other hand, the selectivity varies between 0 and 1, suggesting the use of the conversion definition as a helpful parameter to describe how is the consumption distribution of H_2O_2 ($X_{H_2O_2,Ri}$) into the two routes given by **Eq. (2.19)**.

$$S_{H_2O_2,Ri} = \frac{-r_i}{R_{H_2O_2}} \qquad (i = 1, 2) \tag{2.18}$$

$$X_{H_2O_2,Ri} = S_{H_2O_2,Ri} X_{H_2O_2} \qquad (i = 1, 2) \tag{2.19}$$

Figure 2.19 shows the predominance of H_2O_2 to be consumed for either the production of the oxidant intermediate (R1) or the decomposition into water and oxygen (R2) during the catalytic reaction from 0 up to 30 min. At the beginning of the reaction (0 – 5 min), the R1 reaction is significantly favored over the R2 reaction, which was expected due to the formation of limonene monoepoxide can be observed at noticeably short reaction times, which requires the presence of PA for reacting with R-limonene. As the reaction proceeded, a greater selectivity of H_2O_2 to its decomposition was observed due to higher temperatures than ambient and the presence of MgO as the catalyst. Similar behavior was observed for all experimental runs. This finding can be

validated considering the values of the activation energies obtained previously in the kinetic modeling since the energy barrier for the H_2O_2 decomposition was the lowest. On the other hand, the global H_2O_2 conversion profiles for each experimental run, in the range of 0-30 min, are shown in **Figure 2.20**. At 30 min, $X_{H_2O_2}$ presented the extreme values between 36.5 and 54% corresponding to the entries 3 and 1, respectively. Furthermore, the H_2O_2 consumption through each one of the reactions is presented through the H_2O_2 conversions in each step, observing that the contribution to the H_2O_2 decomposition increases as the reaction proceeds, while the consumption of H_2O_2 for the formation of PA remains almost constant which is enough for the transformation of PA with limonene. A maximum consumption is observed in the period 0-5 min for all experimental runs, which corresponds to the maximum production of PA.

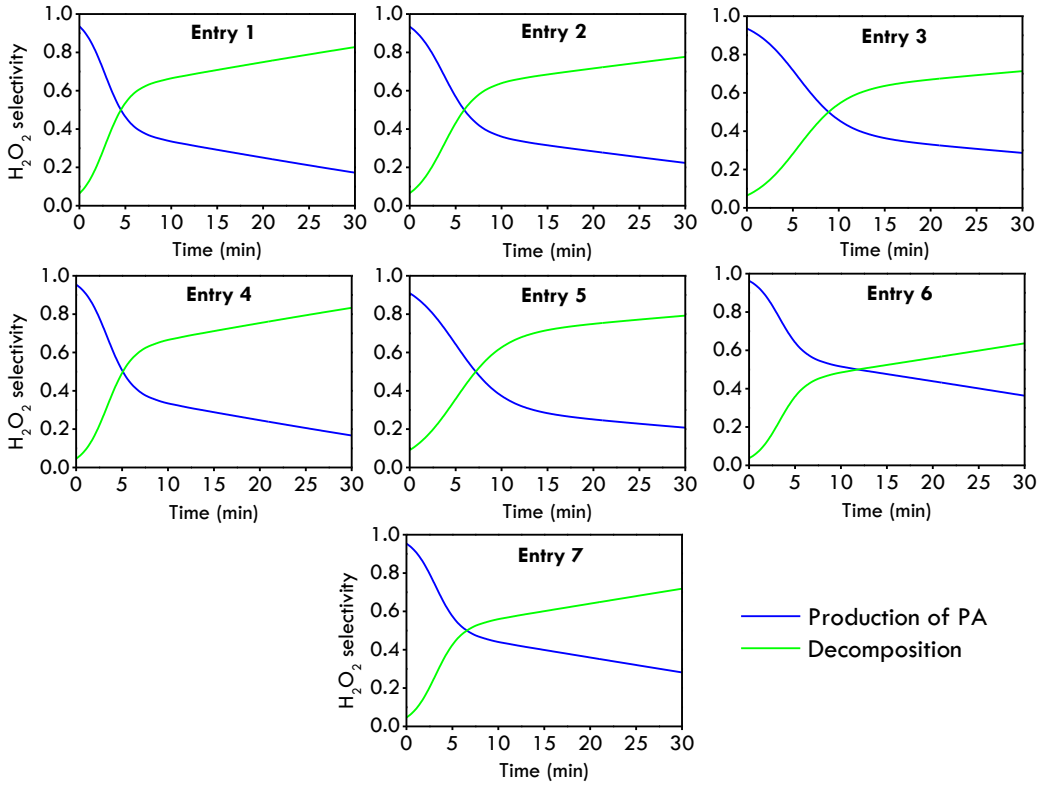

Figure 2.19. H_2O_2 selectivity through two catalytic routes: production of PA (R1) and decomposition of H_2O_2 (R2). Information of each entry is reported in **Table 2.2**.

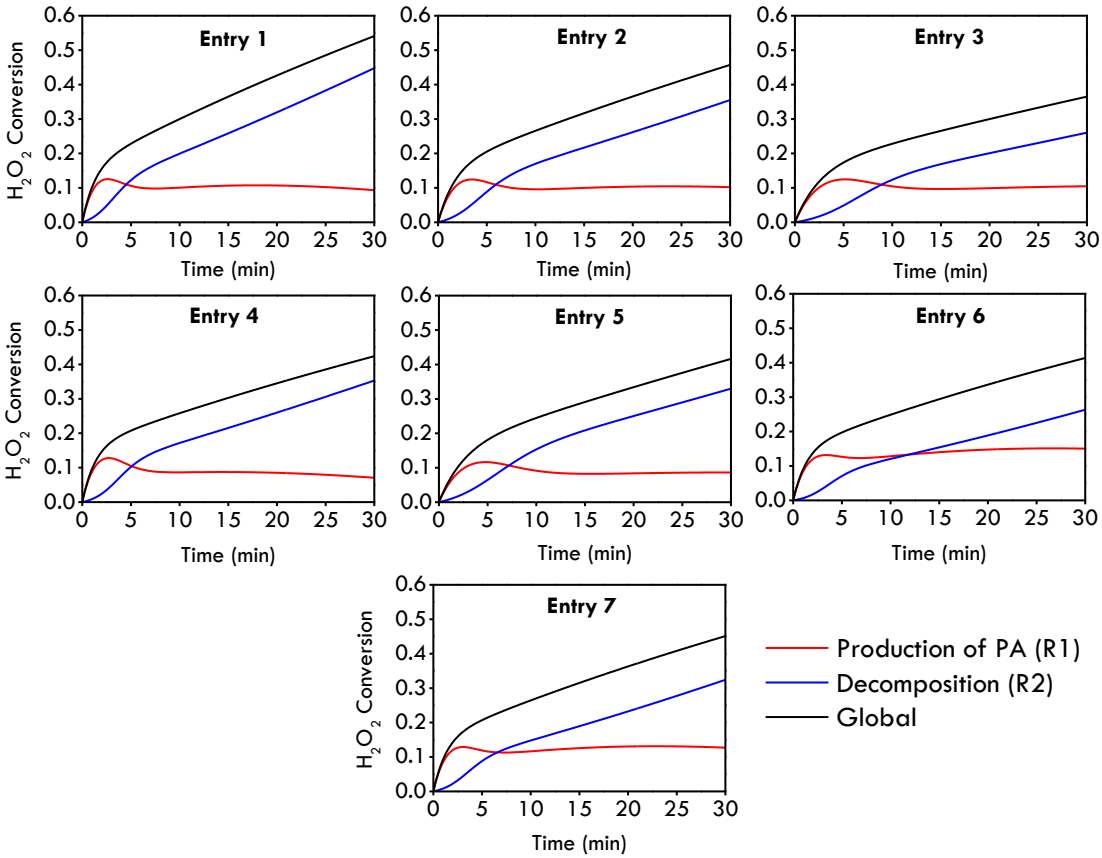

Figure 2.20. Global H_2O_2 conversion and its contribution to the production of PA (R1) and the decomposition of H_2O_2 (R2). Information of each entry is reported in **Table 2.2**.

2.5. Conclusions

MgO is a catalyst with basic sites, which showed a composition of 82.6 wt. % of periclase phase (the mineral form of MgO) and 17.4 wt. % of brucite phase (the mineral form of $Mg(OH)_2$). A slight phase transition (4.6 wt. %) from periclase to brucite was observed after the reaction, probably because of hydration at the reaction conditions, which involved a slight decrease of the selectivity to diepoxide (97% for fresh use and 76% for the third reuse); thermal analysis showed weight loss owing to physisorbed and chemisorbed species, and the transformation of $Mg(OH)_2$ to MgO. Additionally, MgO did not show a very high BET surface area (124 $m^2\ g^{-1}$), which prioritizes the basic sites as a key point in the limonene epoxidation route. SEM images showed thin flakes and surface roughness nanoparticles, which are characteristics of brucite and periclase phases, respectively. MgO was highly active for the epoxidation reaction of R-(+)-limonene with H_2O_2 through a Payne reaction system with acetonitrile as oxidant activator and acetone and water as solvents. Additionally, the system is significantly versatile because it is also highly selective to the production of both limonene monoepoxide and diepoxide, depending on mild reaction conditions. Diepoxide is favored with high concentrations of MgO and H_2O_2, and high temperatures and reaction times, while monoepoxide is favored mainly with low temperatures and reaction times. At temperatures above 50 °C, weight ratios of MgO: R-(+)-limonene higher than 0.90 and weight ratios of H_2O_2: R-(+)-limonene higher than 0.80 lead to complete limonene conversion after 1 h and selectivity close to 100% to diepoxide after 2 h. Meanwhile, the highest yield (80%) towards

limonene monoepoxide was achieved using 1: 1.20: 30.3: 19.7: 15.7: 1.20 as weight ratios for limonene: MgO: H_2O: acetone: acetonitrile: H_2O_2, at 50 °C. The conversion of H_2O_2, increases with an increase of temperature and lower initial concentrations of H_2O_2, reaching values higher than 80% after 2 h for all conditions, except for reactions carried out at 40 °C.

The kinetic modeling for the epoxidation of R-(+)-limonene in the Payne reaction system was proposed using a set of three reactions, under reaction conditions where only the production of limonene monoepoxide was guaranteed. The high goodness-of-fit (R^2 = 99.38%) of the kinetic modeling to the experimental data validated the choice of the three reaction rates laws. A pseudo-homogeneous reversible model was employed to describe the formation of the intermediate oxidant (E = 58.61 kJ mol^{-1}), which does not require the presence of a catalyst. Two heterogeneous kinetic models based on the Eley-Rideal approach, where the surface reaction was assumed as the rate-limiting step, were used to describe the decomposition of H_2O_2 (E = 29.06 kJ mol^{-1}) and the epoxidation reaction between limonene and the intermediate (E = 52.28 kJ mol^{-1}). Additionally, internal mass transfer limitations were ruled out using the Weisz-Prater criterion for all experimental runs of both limonene and H_2O_2, and the high stirring rate ensured the absence of external mass transfer limitations. MgO is a promising very low-cost commercial catalyst for a green catalytic route with high activity in the formation of limonene monoepoxide and diepoxide. It does not require any type of modification of the commercial material that is used as catalyst, which is a great advantage for scaling-up the process.

Supporting Information

The Supporting Information (**section 8.1**) contains details on the deduction of the reaction rate equations, the calculations of the reaction rate for the kinetic study, SEM-EDS analysis, estimation of diffusion coefficient, results of the Weisz-Prater criterion, and chromatographic analysis for the reusability tests. **Table 8.1** and **Table 8.2** provide the parameters of the adjusted mathematical model for the molar concentration of limonene and H_2O_2, respectively. **Table 8.3** and **Table 8.4** show the evaluation of the Weisz-Prater criterion for limonene and H_2O_2, respectively. **Figure 8.1** depicts the proposed reaction pathway to produce limonene monoepoxide. **Figure 8.2**-**Figure 8.8** and **Figure 8.9**-**Figure 8.15** depict the fitting of the concentration of limonene and H_2O_2, respectively, for the 7 experimental runs, while **Figure 8.16** to **Figure 8.22** and **Figure 8.23** to **Figure 8.29** show the profiles of the reaction rate of limonene and H_2O_2, respectively. **Figure 8.30**-**Figure 8.33** depict the SEM-EDS analysis for the materials. **Figure 8.34** shows the chromatograms for the reusability tests.

2.6. Acknowledgments

The authors thank CODI-Universidad de Antioquia for providing financial support through projects 2022-56550 and 2022-53000. They also acknowledge funding from the Ministry of Science, Technology, and Innovation, the Ministry of Education, the Ministry of Industry, Commerce and Tourism and ICETEX, programme Ecosistema Científico-Colombia Científica, from the Francisco José de Caldas Fund, Grant RC-FP44842-212-2018. Luis A. Gallego-Villada is also grateful to Universidad de Antioquia for supporting his PhD studies through the ¨Beca Doctoral Universidad d Antioquia¨ scholarship.

2.7. References

[1] M.A. Ardagh, D.T. Bregante, D.W. Flaherty, J.M. Notestein, Controlled Deposition of Silica on Titania-Silica to Alter the Active Site Surroundings on Epoxidation Catalysts, ACS Catal. 10 (2020) 13008–13018. https://doi.org/10.1021/acscatal.0c02937.

[2] Knoema, Citrus fruit production quantity, (2021). https://knoema.com/atlas/topics/Agriculture/Crops-Production-Quantity-tonnes/Citrus-fruit-production (accessed January 29, 2023).

[3] V. Yadav, A. Sarker, A. Yadav, A.O. Miftah, M. Bilal, H.M.N. Iqbal, Integrated biorefinery approach to valorize citrus waste: A sustainable solution for resource recovery and environmental management, Chemosphere. 293 (2022) 133459. https://doi.org/10.1016/j.chemosphere.2021.133459.

[4] S. Suri, A. Singh, P.K. Nema, Current applications of citrus fruit processing waste: A scientific outlook, Appl. Food Res. 2 (2022) 100050. https://doi.org/10.1016/j.afres.2022.100050.

[5] P. Sharma, R. Vishvakarma, K. Gautam, A. Vimal, V. Kumar Gaur, A. Farooqui, S. Varjani, K. Younis, Valorization of citrus peel waste for the sustainable production of value-added products, Bioresour. Technol. 351 (2022) 127064. https://doi.org/10.1016/j.biortech.2022.127064.

[6] S. Rafiq, R. Kaul, S.A. Sofi, N. Bashir, F. Nazir, G. Ahmad Nayik, Citrus peel as a source of functional ingredient: A review, J. Saudi Soc. Agric. Sci. 17 (2018) 351–358. https://doi.org/10.1016/j.jssas.2016.07.006.

[7] C. Russo, A. Maugeri, G.E. Lombardo, L. Musumeci, D. Barreca, A. Rapisarda, S. Cirmi, M. Navarra, The Second Life of Citrus Fruit Waste: A Valuable Source of Bioactive Compounds, Molecules. 26 (2021) 5991. https://doi.org/10.3390/molecules26195991.

[8] A. Christofi, D. Tsipiras, D. Malamis, K. Moustakas, S. Mai, E.M. Barampouti, Biofuels production from orange juice industrial waste within a circular economy vision, J. Water Process Eng. 49 (2022) 103028. https://doi.org/10.1016/j.jwpe.2022.103028.

[9] J.R. Ayala, G. Montero, M.A. Coronado, C. García, M.A. Curiel-Alvarez, J.A. León, C.A. Sagaste, D.G. Montes, Characterization of Orange Peel Waste and Valorization to Obtain Reducing Sugars, Molecules. 26 (2021) 1348. https://doi.org/10.3390/molecules26051348.

[10] E. Louisy, V. Khodyrieva, S. Olivero, V. Michelet, A. Mija, Use of Limonene Epoxides and Derivatives as Promising Monomers for Biobased Polymers, Chempluschem. 87 (2022). https://doi.org/10.1002/cplu.202200190.

[11] J.-A. Becerra, Ó.F. Arbeláez, A.-L. Villa, Transformation of monoterpenes and monoterpenoids using gold-based heterogeneous catalysts, Brazilian J. Chem. Eng. 37 (2020) 1–27. https://doi.org/10.1007/s43153-020-00013-1.

[12] L.M. González, A. Villa de P., C. Montes de Correa, A. Sorokin, Oxidación alílica de monoterpenos con metaloftalocianinas, Sci. Tech. XIII (2007) 111–115. https://doi.org/10.22517/23447214.6135.

[13] A. Corma, S. Iborra, A. Velty, Chemical Routes for the Transformation of Biomass into Chemicals, Chem. Rev. 107 (2007) 2411–2502. https://doi.org/10.1021/cr050989d.

[14] A.A.C. de Almeida, J.P. Costa, R.B.F. de Carvalho, D.P. de Sousa, R.M. de Freitas, Evaluation

of acute toxicity of a natural compound (+)-limonene epoxide and its anxiolytic-like action, Brain Res. 1448 (2012) 56–62. https://doi.org/10.1016/j.brainres.2012.01.070.

[15] O. Hauenstein, S. Agarwal, A. Greiner, Bio-based polycarbonate as synthetic toolbox, Nat. Commun. 7 (2016) 11862. https://doi.org/10.1038/ncomms11862.

[16] O. Hauenstein, M. Reiter, S. Agarwal, B. Rieger, A. Greiner, Bio-based polycarbonate from limonene oxide and CO2 with high molecular weight, excellent thermal resistance, hardness and transparency, Green Chem. 18 (2016) 760–770. https://doi.org/10.1039/C5GC01694K.

[17] V. Schimpf, B.S. Ritter, P. Weis, K. Parison, R. Mülhaupt, High Purity Limonene Dicarbonate as Versatile Building Block for Sustainable Non-Isocyanate Polyhydroxyurethane Thermosets and Thermoplastics, Macromolecules. 50 (2017) 944–955. https://doi.org/10.1021/acs.macromol.6b02460.

[18] T. Stößer, C. Li, J. Unruangsri, P.K. Saini, R.J. Sablong, M.A.R. Meier, C.K. Williams, C. Koning, Bio-derived polymers for coating applications: comparing poly(limonene carbonate) and poly(cyclohexadiene carbonate), Polym. Chem. 8 (2017) 6099–6105. https://doi.org/10.1039/C7PY01223C.

[19] S. Kernbichl, B. Rieger, Aliphatic polycarbonates derived from epoxides and CO2: A comparative study of poly(cyclohexene carbonate) and poly(limonene carbonate), Polymer (Guildf). 205 (2020) 122667. https://doi.org/10.1016/j.polymer.2020.122667.

[20] V. Sessini, M. Palenzuela, J. Damián, M.E.G. Mosquera, Bio-based polyether from limonene oxide catalytic ROP as green polymeric plasticizer for PLA, Polymer (Guildf). 210 (2020) 123003. https://doi.org/10.1016/j.polymer.2020.123003.

[21] S. Neumann, S.B. Däbritz, S.E. Fritze, L.-C. Leitner, A. Anand, A. Greiner, S. Agarwal, Sustainable block copolymers of poly(limonene carbonate), Polym. Chem. 12 (2021) 903–910. https://doi.org/10.1039/D0PY01685C.

[22] K.A. Maltby, M. Hutchby, P. Plucinski, M.G. Davidson, U. Hintermair, Selective Catalytic Synthesis of 1,2- and 8,9-Cyclic Limonene Carbonates as Versatile Building Blocks for Novel Hydroxyurethanes, Chem. – A Eur. J. 26 (2020) 7405–7415. https://doi.org/10.1002/chem.201905561.

[23] A. Rehman, E. Russell, F. Saleem, F. Javed, S. Ahmad, V.C. Eze, A. Harvey, Synthesis of trans-limonene bis-epoxide by stereoselective epoxidation of (R)-(+)-limonene, J. Environ. Chem. Eng. 9 (2021) 104680. https://doi.org/10.1016/j.jece.2020.104680.

[24] A. Rehman, A.M. López Fernández, M.F.M. Gunam Resul, A. Harvey, Highly selective, sustainable synthesis of limonene cyclic carbonate from bio-based limonene oxide and CO2: A kinetic study, J. CO2 Util. 29 (2019) 126–133. https://doi.org/10.1016/j.jcou.2018.12.001.

[25] A.J. Bonon, J.O. Bahú, B.C. Klein, D. Mandelli, R.M. Filho, Green production of limonene diepoxide for potential biomedical applications, Catal. Today. 388–389 (2022) 288–300. https://doi.org/10.1016/j.cattod.2020.06.030.

[26] D. Grajales, L. González, A. Villa, Catalytic oxidative dehydrogenation of carveol to carvone over the phthalocyanine complex FePcCl 16 immobilized on the mesoporous silica SBA-15, Appl. Catal. A Gen. 541 (2017) 15–24. https://doi.org/10.1016/j.apcata.2017.04.019.

[27] D.P. Gomes, A.F. Silva, A.C. Gomes, P. Neves, A.A. Valente, I.S. Gonçalves, M. Pillinger, Epoxidation catalysts prepared by encapsulation of molybdenum hexacarbonyl in UiO-66(Zr/Hf)-type metal-organic frameworks, Microporous Mesoporous Mater. 330 (2022) 111603. https://doi.org/10.1016/j.micromeso.2021.111603.

[28] D.M. Gomes, P. Neves, M.M. Antunes, A.J.S. Fernandes, M. Pillinger, A.A. Valente, Post-Synthesis Strategies to Prepare Mesostructured and Hierarchical Silicates for Liquid Phase Catalytic Epoxidation, Catalysts. 12 (2022) 1513. https://doi.org/10.3390/catal12121513.

[29] H. Zhang, X. Lu, L. Yang, Y. Hu, M. Yuan, C. Wang, Q. Liu, F. Yue, D. Zhou, Q. Xia, Efficient air epoxidation of cycloalkenes over bimetal-organic framework ZnCo-MOF materials, Mol. Catal. 499 (2021) 111300. https://doi.org/10.1016/j.mcat.2020.111300.

[30] D. Hu, X. Song, S. Wu, X. Yang, H. Zhang, X. Chang, M. Jia, Solvothermal synthesis of Co-substituted phosphomolybdate acid encapsulated in the UiO-66 framework for catalytic application in olefin epoxidation, Chinese J. Catal. 42 (2021) 356–366. https://doi.org/10.1016/S1872-2067(20)63665-8.

[31] M. Fadaei Sarabi, A. Bezaatpour, A. Mahmoudi, Anchoring of a terpyridine-based Mo(VI) complex on manganese ferrite as a recoverable catalyst for epoxidation of olefins under solvent-free conditions, J. Coord. Chem. 74 (2021) 1597–1612. https://doi.org/10.1080/00958972.2021.1904507.

[32] M.S. Nunes, D.M. Gomes, A.C. Gomes, P. Neves, R.F. Mendes, F.A.A. Paz, A.D. Lopes, A.A. Valente, I.S. Gonçalves, M. Pillinger, A 5-(2-Pyridyl)tetrazolate Complex of Molybdenum(VI), Its Structure, and Transformation to a Molybdenum Oxide-Based Hybrid Heterogeneous Catalyst for the Epoxidation of Olefins, Catalysts. 11 (2021) 1407. https://doi.org/10.3390/catal11111407.

[33] T.R. Amarante, P. Neves, F.A. Almeida Paz, A.C. Gomes, M. Pillinger, A.A. Valente, I.S. Gonçalves, Heterogeneous catalysis with an organic–inorganic hybrid based on MoO 3 chains decorated with 2,2′-biimidazole ligands, Catal. Sci. Technol. 11 (2021) 2214–2228. https://doi.org/10.1039/D1CY00055A.

[34] S. Madadi, S. Kaliaguine, Activated Carbon-Supported Ruthenium as a Catalyst for the Solvent- and Initiator-Free Aerobic Epoxidation of Limonene, ACS Sustain. Chem. Eng. 9 (2021) 10557–10568. https://doi.org/10.1021/acssuschemeng.1c02597.

[35] V.M. Vaschetti, G.A. Eimer, A.L. Cánepa, S.G. Casuscelli, Catalytic performance of V-MCM-41 nanocomposites in liquid phase limonene oxidation: Vanadium leaching mitigation, Microporous Mesoporous Mater. 311 (2021) 110678. https://doi.org/10.1016/j.micromeso.2020.110678.

[36] A. Wróblewska, J. Serafin, A. Gawarecka, P. Miądlicki, K. Urbaś, Z.C. Koren, J. Llorca, B. Michalkiewicz, Carbonaceous catalysts from orange pulp for limonene oxidation, Carbon Lett. 30 (2020) 189–198. https://doi.org/10.1007/s42823-019-00084-2.

[37] V.M. Vaschetti, A.L. Cánepa, D. Barrera, K. Sapag, G.A. Eimer, S.G. Casuscelli, Limonene oxyfunctionalization over Cu-modified silicates employing hydrogen peroxide and t-Butyl hydroperoxide: Reaction pathway analysis, Mol. Catal. 481 (2020) 110234. https://doi.org/10.1016/j.mcat.2018.11.005.

[38] Y. Tao, O. De Luca, B. Singh, A.J. Kamphuis, J. Chen, P. Rudolf, P.P. Pescarmona, WO3–SiO2 nanomaterials synthesized using a novel template-free method in supercritical CO2 as

heterogeneous catalysts for epoxidation with H2O2, Mater. Today Chem. 18 (2020) 100373. https://doi.org/10.1016/j.mtchem.2020.100373.

[39] S. Madadi, L. Charbonneau, J.-Y. Bergeron, S. Kaliaguine, Aerobic epoxidation of limonene using cobalt substituted mesoporous SBA-16 Part 1: Optimization via Response Surface Methodology (RSM), Appl. Catal. B Environ. 260 (2020) 118049. https://doi.org/10.1016/j.apcatb.2019.118049.

[40] A. Gottuso, A. Köckritz, M.L. Saladino, F. Armetta, C. De Pasquale, G. Nasillo, F. Parrino, Catalytic and photocatalytic epoxidation of limonene: Using mesoporous silica nanoparticles as functional support for a Janus-like approach, J. Catal. 391 (2020) 202–211. https://doi.org/10.1016/j.jcat.2020.08.025.

[41] Y. Wang, F. Gayet, P. Guillo, D. Agustin, Organic Solvent-Free Olefins and Alcohols (ep)oxidation Using Recoverable Catalysts Based on [PM12O40]3− (M = Mo or W) Ionically Grafted on Amino Functionalized Silica Nanobeads, Materials (Basel). 12 (2019) 3278. https://doi.org/10.3390/ma12203278.

[42] D.K. Parmar, P.M. Butani, N.J. Thumar, P.M. Jasani, R. V. Padaliya, P.R. Sandhiya, H.D. Nakum, M.N. Khan, D. Makwana, Oxy-functionalization of olefins with neat and heterogenized binuclear V(IV)O and Fe(II) complexes: Effect of steric hindrance on product selectivity and output in homogeneous and heterogeneous phase, Mol. Catal. 474 (2019) 110424. https://doi.org/10.1016/j.mcat.2019.110424.

[43] P. Tao, X. Lu, H. Zhang, R. Jing, F. Huang, S. Wu, D. Zhou, Q. Xia, Enhanced activity of microwave-activated CoOx/MOR catalyst for the epoxidation of α-pinene with air, Mol. Catal. 463 (2019) 8–15. https://doi.org/10.1016/j.mcat.2018.11.006.

[44] W. Lueangchaichaweng, B. Singh, D. Mandelli, W.A. Carvalho, S. Fiorilli, P.P. Pescarmona, High surface area, nanostructured boehmite and alumina catalysts: Synthesis and application in the sustainable epoxidation of alkenes, Appl. Catal. A Gen. 571 (2019) 180–187. https://doi.org/10.1016/j.apcata.2018.12.017.

[45] J. Marreiros, M. Diaz-Couce, M.J. Ferreira, P.D. Vaz, M.J. Calhorda, C.D. Nunes, Synthesis and catalytic activity of Mo(II) complexes of α-diimines intercalated in layered double hydroxides, Inorganica Chim. Acta. 486 (2019) 274–282. https://doi.org/10.1016/j.ica.2018.10.062.

[46] C. Bisio, A. Gallo, R. Psaro, C. Tiozzo, M. Guidotti, F. Carniato, Tungstenocene-grafted silica catalysts for the selective epoxidation of alkenes, Appl. Catal. A Gen. 581 (2019) 133–142. https://doi.org/10.1016/j.apcata.2019.05.027.

[47] S.R. Leandro, A.C. Mourato, U. Łapińska, O.C. Monteiro, C.I. Fernandes, P.D. Vaz, C.D. Nunes, Exploring bulk and colloidal Mg/Al hydrotalcite–Au nanoparticles hybrid materials in aerobic olefin epoxidation, J. Catal. 358 (2018) 187–198. https://doi.org/10.1016/j.jcat.2017.12.014.

[48] H. Taghiyar, B. Yadollahi, New perspective to catalytic epoxidation of olefins by Keplerate containing Keggin polyoxometalates, Polyhedron. 156 (2018) 98–104. https://doi.org/10.1016/j.poly.2018.09.015.

[49] E. Niño-Arrieta, A.L. Villa-Holguín, E.A. Alarcón-Durango, A. Talavera-López, S.A. Gómez-Torres, G.A. Fuentes-Zurita, Limonene epoxidation in aqueous phase over TiKIT-6, Rev. Fac. Ing. Univ. Antioquia. (2018) 74–79. https://doi.org/10.17533/udea.redin.n88a08.

[50] L. Charbonneau, X. Foster, D. Zhao, S. Kaliaguine, Catalyst-Free Epoxidation of Limonene to Limonene Dioxide, ACS Sustain. Chem. Eng. 6 (2018) 5115–5121. https://doi.org/10.1021/acssuschemeng.7b04782.

[51] L. Charbonneau, S. Kaliaguine, Epoxidation of limonene over low coordination Ti in Ti-SBA-16, Appl. Catal. A Gen. 533 (2017) 1–8. https://doi.org/10.1016/j.apcata.2017.01.001.

[52] A. Wróblewska, M. Malko, M. Walasek, Environmental friendly method of the epoxidation of limonene with hydrogen peroxide over the Ti-SBA-15 catalyst, Polish J. Chem. Technol. 20 (2018) 6–12. https://doi.org/10.2478/pjct-2018-0047.

[53] D. García, M. Jaramillo, F. Bustamante, A.L. Villa, E. Alarcón, Epoxidation of β-pinene with a highly-active and low-cost catalyst, Brazilian J. Chem. Eng. 38 (2021) 89–100. https://doi.org/10.1007/s43153-020-00078-y.

[54] I. Kirm, F. Medina, X. Rodríguez, Y. Cesteros, P. Salagre, J. Sueiras, Epoxidation of styrene with hydrogen peroxide using hydrotalcites as heterogeneous catalysts, Appl. Catal. A Gen. 272 (2004) 175–185. https://doi.org/10.1016/j.apcata.2004.05.039.

[55] O. V. Bakhvalov, V. V. Fomenko, N.F. Salakhutdinov, Modern Methods for the Epoxidation of α- and β-Pinenes, 3-Carene and Limonene, Chem. Sustain. Dev. 16 (2008) 633–691.

[56] K. Yamaguchi, K. Mori, T. Mizugaki, K. Ebitani, K. Kaneda, Epoxidation of α,β-Unsaturated Ketones Using Hydrogen Peroxide in the Presence of Basic Hydrotalcite Catalysts, J. Org. Chem. 65 (2000) 6897–6903. https://doi.org/10.1021/jo000247e.

[57] National Diagnostics, Hydrogen Peroxide Detection: The Methods, (n.d.). https://www.nationaldiagnostics.com/2011/10/10/hydrogen-peroxide-detection-methods/ (accessed February 12, 2023).

[58] A.G. Hildebrandt, I. Roots, Reduced nicotinamide adenine dinucleotide phosphate (NADPH)-dependent formation and breakdown of hydrogen peroxide during mixed function oxidation reactions in liver microsomes, Arch. Biochem. Biophys. 171 (1975) 385–397. https://doi.org/10.1016/0003-9861(75)90047-8.

[59] G. Su, Y. Wei, M. Guo, Direct Colorimetric Detection of Hydrogen Peroxide Using 4-Nitrophenyl Boronic Acid or Its Pinacol Ester, Am. J. Anal. Chem. 02 (2011) 879–884. https://doi.org/10.4236/ajac.2011.28101.

[60] A. Rubio Clemente, C. Cardona, G. Peñuela, Sensitive spectrophotometric determination of hydrogen peroxide in aqueous samples from advanced oxidation processes: Evaluation of possible interferences, Afinidad. 74 (2017) 161–168. https://raco.cat/index.php/afinidad/article/view/328470.

[61] C.-C. Hsu, Y.-R. Lo, Y.-C. Lin, Y.-C. Shi, P.-L. Li, A Spectrometric Method for Hydrogen Peroxide Concentration Measurement with a Reusable and Cost-Efficient Sensor, Sensors. 15 (2015) 25716–25729. https://doi.org/10.3390/s151025716.

[62] C.A. Cohn, Quantifying hydrogen peroxide in iron-containing solutions using leuco crystal violet, Geochem. Trans. 6 (2005) 47. https://doi.org/10.1063/1.1935449.

[63] R. Barrera Zapata, A.L. Villa, C. Montes de Correa, Kinetic Modeling of Limonene Epoxidation over PW-Amberlite, Ind. Eng. Chem. Res. 48 (2009) 647–653. https://doi.org/10.1021/ie800822n.

[64] R. Barrera Zapata, Doctoral Thesis: Modeling, simulation, and design of a reactor and product separation process for the production of limonene epoxide., University of Antioquia, 2010.

[65] K.S. Putt, R.B. Pugh, A High-Throughput Microtiter Plate Based Method for the Determination of Peracetic Acid and Hydrogen Peroxide, PLoS One. 8 (2013) e79218. https://doi.org/10.1371/journal.pone.0079218.

[66] A.K. Liubymova, T. V. Bezbozhnaya, V.L. Lobachev, Activation of Hydrogen Peroxide by Acetonitrile in the Oxidation of Thioethers: Reaction Kinetics and Mechanism, Kinet. Catal. 62 (2021) 342–349. https://doi.org/10.1134/S002315842103006X.

[67] R.D. Bach, Peroxyacetimidic Acid, in: Encycl. Reagents Org. Synth., John Wiley & Sons, Ltd, Chichester, UK, 2001: pp. 1–2. https://doi.org/10.1002/047084289X.rp038.

[68] R. Curci, J.O. Edwards, Activation of Hydrogen Peroxide by Organic Compounds, in: 1992: pp. 45–95. https://doi.org/10.1007/978-94-017-0984-2_3.

[69] L.A. Gallego-Villada, E.A. Alarcón, V. Palermo, P.G. Vázquez, G.P. Romanelli, Kinetics for the biodiesel production from lauric acid over Keggin heteropolyacid loaded in silica framework, J. Ind. Eng. Chem. 92 (2020) 109–119. https://doi.org/10.1016/j.jiec.2020.08.030.

[70] L.A. Gallego-Villada, E.A. Alarcón, D.M. Ruiz, G.P. Romanelli, Kinetic study of the esterification of t-cinnamic acid over Preyssler structure acid, Mol. Catal. 528 (2022) 112507. https://doi.org/10.1016/j.mcat.2022.112507.

[71] L.A. Gallego-Villada, E.A. Alarcón, C. Cerrutti, G. Blustein, Á.G. Sathicq, G.P. Romanelli, Levulinic Acid Esterification with n -Butanol over a Preyssler Catalyst in a Microwave-Assisted Batch Reactor: A Kinetic Study, Ind. Eng. Chem. Res. 62 (2023) 10915–10929. https://doi.org/10.1021/acs.iecr.3c00893.

[72] M.A. Aramendía, J.A. Benítez, V. Borau, C. Jiménez, J.M. Marinas, J.R. Ruiz, F. Urbano, Study of MgO and Pt/MgO Systems by XRD, TPR, and 1 H MAS NMR, Langmuir. 15 (1999) 1192–1197. https://doi.org/10.1021/la9808972.

[73] C.W. Wong, Y.S. Chan, J. Jeevanandam, K. Pal, M. Bechelany, M. Abd Elkodous, G.S. El-Sayyad, Response Surface Methodology Optimization of Mono-dispersed MgO Nanoparticles Fabricated by Ultrasonic-Assisted Sol–Gel Method for Outstanding Antimicrobial and Antibiofilm Activities, J. Clust. Sci. 31 (2020) 367–389. https://doi.org/10.1007/s10876-019-01651-3.

[74] G. Fiquet, P. Richet, G. Montagnac, High-temperature thermal expansion of lime, periclase, corundum and spinel, Phys. Chem. Miner. 27 (1999) 103–111. https://doi.org/10.1007/s002690050246.

[75] C. Suryanarayana, M.G. Norton, X-Ray Diffraction: A Practical Approach, Springer US, New York, 1998. https://doi.org/10.1007/978-1-4899-0148-4.

[76] Crystallography Open Database, (2004). http://www.crystallography.net/cod/ (accessed April 2, 2023).

[77] G. Ertl, H. Knozinger, F. Schuth, J. Weitkamp, Handbook of Heterogeneous Catalysis, Wiley-VCH Verlag GmbH, Germany, 2008. https://onlinelibrary.wiley.com/doi/book/10.1002/9783527610044.

[78] Y. Xia, K. Dong, X. Xiang, W. Li, Y. Gong, Z. Li, Phosphorus hyperaccumulation in nano-

MgO using a circular recovery process based on multiple phase transitions from periclase to brucite, Sci. Total Environ. 727 (2020) 138510. https://doi.org/10.1016/j.scitotenv.2020.138510.

[79] M.H. Zahir, M.M. Rahman, K. Irshad, M.M. Rahman, Shape-Stabilized Phase Change Materials for Solar Energy Storage: MgO and Mg(OH)2 Mixed with Polyethylene Glycol, Nanomaterials. 9 (2019) 1773. https://doi.org/10.3390/nano9121773.

[80] A.A. Hanna, A.S. Abdelmoaty, M.A. Sherief, Synthesis, Characterization, and Thermal Behavior of Nanoparticles of Mg(OH) 2 to Be Used as Flame Retardants, J. Chem. 2019 (2019) 1–6. https://doi.org/10.1155/2019/1805280.

[81] K.S. Sánchez-Zambrano, M. Hernández-Reséndiz, C. Gómez-Rodríguez, L.V. García-Quiñonez, J.A. Aguilar-Martínez, E.A. Rodríguez-Castellanos, L.F. Verdeja, D. Fernández-González, G.A. Castillo-Rodríguez, XPS Study on Calcining Mixtures of Brucite with Titania, Materials (Basel). 15 (2022) 3117. https://doi.org/10.3390/ma15093117.

[82] K.S.W. Sing, Reporting physisorption data for gas/solid systems with special reference to the determination of surface area and porosity (Recommendations 1984), Pure Appl. Chem. 57 (1985) 603–619. https://doi.org/10.1351/pac198557040603.

[83] L. Xiaoji, S. Tsutomu, O. Einstine, Y. Tetsuro, Adsorption and Co-Precipitation Behavior of Fluoride Onto Mg-Bearing Minerals in Si-Al-Mg Mineral System At Hyperalkaline Conditions, Clay Sci. 16 (2012) 49–57.

[84] J.T. Kloprogge, R.L. Frost, Fourier Transform Infrared and Raman Spectroscopic Study of the Local Structure of Mg-, Ni-, and Co-Hydrotalcites, J. Solid State Chem. 146 (1999) 506–515. https://doi.org/10.1006/jssc.1999.8413.

[85] R.L. Frost, J.T. Kloprogge, Infrared emission spectroscopic study of brucite, Spectrochim. Acta Part A Mol. Biomol. Spectrosc. 55 (1999) 2195–2205. https://doi.org/10.1016/S1386-1425(99)00016-5.

[86] L. Châtelet, J.Y. Bottero, J. Yvon, A. Bouchelaghem, Competition between monovalent and divalent anions for calcined and uncalcined hydrotalcite: anion exchange and adsorption sites, Colloids Surfaces A Physicochem. Eng. Asp. 111 (1996) 167–175. https://doi.org/10.1016/0927-7757(96)03542-X.

[87] N.C.S. Selvam, R.T. Kumar, L.J. Kennedy, J.J. Vijaya, Comparative study of microwave and conventional methods for the preparation and optical properties of novel MgO-micro and nano-structures, J. Alloys Compd. 509 (2011) 9809–9815. https://doi.org/10.1016/j.jallcom.2011.08.032.

[88] R. Mahadevaiah, H.S. Lalithamba, S. Shekarappa, R. Hanumanaika, Synthesis of Nα-protected formamides from amino acids using MgO nano catalyst: Study of molecular docking and antibacterial activity, Sci. Iran. 24 (2017) 3002–3013. https://doi.org/10.24200/sci.2017.4491.

[89] A.-T. Vu, S. Jiang, K. Ho, J.B. Lee, C.-H. Lee, Mesoporous magnesium oxide and its composites: Preparation, characterization, and removal of 2-chloroethyl ethyl sulfide, Chem. Eng. J. 269 (2015) 82–93. https://doi.org/10.1016/j.cej.2015.01.089.

[90] A. Ansari, A. Ali, M. Asif, S. Shamsuzzaman, Microwave-assisted MgO NP catalyzed one-pot multicomponent synthesis of polysubstituted steroidal pyridines, New J. Chem. 42 (2018) 184–197. https://doi.org/10.1039/C7NJ03742B.

[91] H.S. Fogler, Elements of Chemical Reaction Engineering, 5th ed., Prentice Hall, 2016.

[92] M.A. Vannice, Kinetics of catalytic reactions, 1st ed., Springer New York, NY, 2005.

[93] U.R. Nanomaterials, Magnesium Oxide Powder (MgO, 99.5%), (n.d.). https://www.us-nano.com/inc/sdetail/23081 (accessed February 21, 2023).

[94] A.J. Bonon, Y.N. Kozlov, J.O. Bahú, R.M. Filho, D. Mandelli, G.B. Shul'pin, Limonene epoxidation with H2O2 promoted by Al2O3: Kinetic study, experimental design, J. Catal. 319 (2014) 71–86. https://doi.org/10.1016/j.jcat.2014.08.004.

Chapter 3. Zeolite Y-Based Catalysts for Efficient Epoxidation of R-(+)-Limonene: Insights into the Structure-Activity Relationship

This chapter corresponds to an article published in ***Microporous and Mesoporous Materials,*** *2024, 372, 113098 – DOI: 10.1016/j.micromeso.2024.113098.*

Luis A. Gallego-Villada[a,b,*], Päivi Mäki-Arvela[b], Narendra Kumar[b], Edwin A. Alarcón[a], Zuzana Vajglová[b], Teija Tirri[b], Ilari Angervo[c], Robert Lassfolk[d], Mika Lastusaari[e], Dmitry Yu. Murzin[b,*]

e. Environmental Catalysis Research Group, Chemical Engineering Faculty, Universidad de Antioquia, Medellín, Colombia.
f. Laboratory of Industrial Chemistry and Reaction Engineering, Johan Gadolin Process Chemistry Centre, Åbo Akademi University, Henriksgatan 2, 20500 Turku/ Åbo, Finland
g. Wihuri Physical Laboratory, Department of Physics and Astronomy, FI-20014 University of Turku, Finland
h. Laboratory of Molecular Science and Engineering, Åbo Akademi University, Finland
i. University of Turku, Department of Chemistry, FI-20014 Turku, Finland

* Corresponding author: E-mail address: alfonso.gallego@udea.edu.co (Luis A. Gallego-Villada), dmitry.murzin@abo.fi (Dmitry Yu. Murzin)

Graphical Abstract

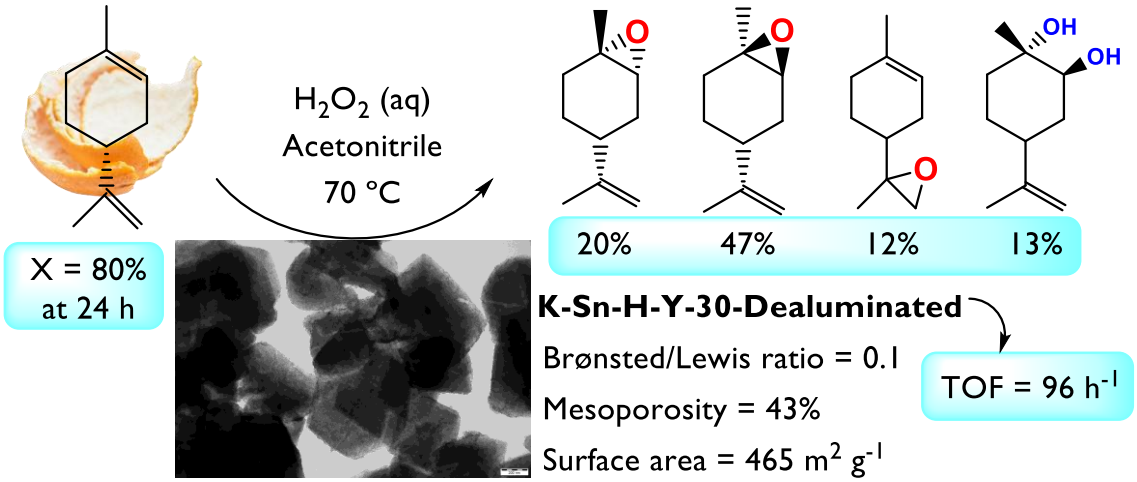

3.1. Abstract

Parent, hierarchical, and metal-modified hierarchical zeolite Y were investigated as heterogeneous catalysts in the R-(+)-limonene epoxidation, a catalytic route for synthesizing precursors of bio-polycarbonates, an alternative to isocyanate polyurethanes. The fresh catalysts underwent detailed characterization using XRD, N_2 physisorption, TEM, SEM-EDX, pyridine-FTIR, NH_3-TPD, CO_2-TPD, UV-Vis-DRS, and solid-state NMR. Spent materials were investigated by TPO-MS and TGA, confirming low coke formation on the catalytic surface. The most active material was K-Sn-modified dealuminated zeolite Y, reflected in a high turnover frequency (TOF) of 96 h^{-1}. This material exhibited the lowest Brønsted to Lewis acidity ratio (0.1), the highest mesoporosity fraction (43%), and the lowest total surface area (465 m^2 g^{-1}). Aprotic polar solvents with high polarity and medium donor capacity appeared suitable for limonene epoxidation. Limonene conversion of ca. 97% was reached at 70 °C, H_2O_2: limonene molar ratio = 7, and acetonitrile as a solvent, while selectivity to total monoepoxides exhibited values up to 96% under different reaction conditions. Hydration of internal epoxides to limonene diol was favored at high temperatures and high H_2O_2/limonene molar ratios. The efficiency of H_2O_2 reached maximum values of about 85% at low H_2O_2 amounts, while no significant influence was observed for temperature, catalyst amount, and the initial concentration of limonene. A plausible reaction mechanism was proposed for the R-(+)-limonene epoxidation with H_2O_2 based on the experimental findings.

Keywords:

Zeolite Y, Hierarchical zeolite, Epoxidation, Limonene, Catalyst.

3.2. Introduction

Molecular sieves refer to crystalline materials with a variety of compositions that exhibit shape-selective adsorption and reaction properties [1]. Zeolites, a specific type of molecular sieve, are crystalline aluminosilicates with a three-dimensional framework structure that creates uniformly sized pores of molecular dimensions, ranging from angstroms (Å) to a couple of nanometers (nm) [2]. These pores selectively adsorb molecules that fit easily within their confines while excluding larger molecules [3]. The remarkable and highly exploitable properties of zeolitic materials, including their ion-exchange capacity, strong acidic sites, large surface area, high thermal stability, sorption capacity, shape selectivity, catalytic activity, and their role as hosts in advanced materials, are primarily governed by their unique structures [4]. However, the microporosity of zeolites limits their applicability for transforming relatively large organic molecules due to the pore diffusion limitations imposed by the microporous network structure [5]. To overcome these limitations, various synthesis methods have been employed to produce zeolites with mesoporous (2-50 nm) [6,7] and macroporous (> 50 nm) [8,9] dimensions, which are generally preferred and well-known as hierarchical zeolites.

Zeolites are extensively used in applications of gas separation [10,11] and adsorption [12–14], but also as heterogeneous catalysts in different areas such as the petrochemical industry [15–17], the production of biofuels [18–21], and the synthesis of fine chemicals [22–27]. Fine chemistry represents one of the most important industries with a projected estimated market of ca. US $ 185×10^3 million in 2023, covering perfumes, intermediates in the synthesis of active pharmaceutical

ingredients (APIs), and various green chemicals [28]. Zeolites as heterogeneous catalysts offer the advantage of being relatively inexpensive, easy to recover, and recyclable. These aspects are closely aligned with the objectives of green chemistry, aiming to minimize or, ideally, eliminate waste generation in chemical processes. As a result, there has been a growing awareness of the importance of green chemistry metrics in catalysis studies, making the research of efficient heterogeneous materials as catalysts imperative [29].

Limonene is a monoterpene ($C_{10}H_{16}$) with two double bonds (ring and external), which is typically the major constituent of essential oils derived from various biomass found in citrus fruit peels, such as lemons, limes, grapefruits, mandarins, and oranges. The citrus fruit production in 2021 was estimated at 162 million tons, being China (28.8%) the top country in worldwide production, followed by Brazil, India, Mexico, and Spain [30]. The citrus waste during juice production is about 50%, which includes peels, seeds, pomace, and wastewater [31]. Specifically, about 15 million tons of orange peel waste are generated annually where 60,000 metric tons correspond to extracted R-(+)-limonene [32,33].

Limonene finds extensive use in various industrial applications, serving as a flavor and fragrance additive in cleaning and cosmetic products, food, beverages, and pharmaceuticals. Additionally, it plays a crucial role in the manufacturing of resins, acts as a wetting and dispersing agent, and contributes to the insect control. Moreover, limonene has been employed as a sorption promoter or accelerant to enhance transdermal drug delivery and works by penetrating the skin, effectively reducing barrier resistance in a reversible manner [34]. On the other hand, limonene is an important precursor in the synthesis of oxygenated compounds such as monoepoxides (*cis* and *trans* of internal and external configurations) and diepoxides (*cis* and *trans*). Recently, these epoxides products have been considered promising building blocks in the production of bio-polycarbonates which have shown attractive thermal and optical properties [35–40]. Limonene-based carbonates offer a versatile option for producing non-isocyanate polyurethanes (NIPUs) with properties comparable to those of commercially available polyurethanes, without the utilization of toxic isocyanates in their synthesis [41,42].

The reaction pathways of limonene with H_2O_2 as the oxidizing agent (**Figure 3.1**) can yield various products depending on the reaction conditions such as catalyst, the solvent, the H_2O_2: limonene ratio, H_2O_2 concentration, amount of solvent, and temperature. The synthesis of allylic products, such as carveol and carvone, has been favored over epoxides and hydration products using V/MCM-41 [43], nanoporous carbon [44], Ti/SBA-15 [45], and Cu/MCM-41 [46] as heterogeneous catalysts and H_2O_2 as an oxidizing agent, reaching selectivities about 61.5%, 65.2%, 45.6% and 41.3%, respectively, but with low limonene conversions (< 42%), under the tested reaction conditions. More active systems with H_2O_2 have been reported based on zeolite Y immobilized with heterogenized binuclear V(IV)O ([VO(*sal*$_2$*bz*)]$_2$-Y) and Fe(II) ([Fe(*sal*$_2$*bz*)(H$_2$O)$_2$]$_2$-Y) complexes [47] with limonene conversions larger than 80% and selectivities to allylic products of ca. 49.0% and 46.0%, respectively, using acetonitrile as a solvent and 80 °C for 24 h. Furthermore, limonene glycol was observed as the main byproduct with these catalysts, reaching selectivity of 39.0% and 43%, respectively. A Keggin heteropolyacid ($H_3PMo_{12}O_{40}$) supported on SiO_2 has been reported as a catalyst in a solvent-free system, with TBHP as an oxidizing agent, showing limonene conversion of 91% and selectivity to glycol of ca. 47.0% [48].

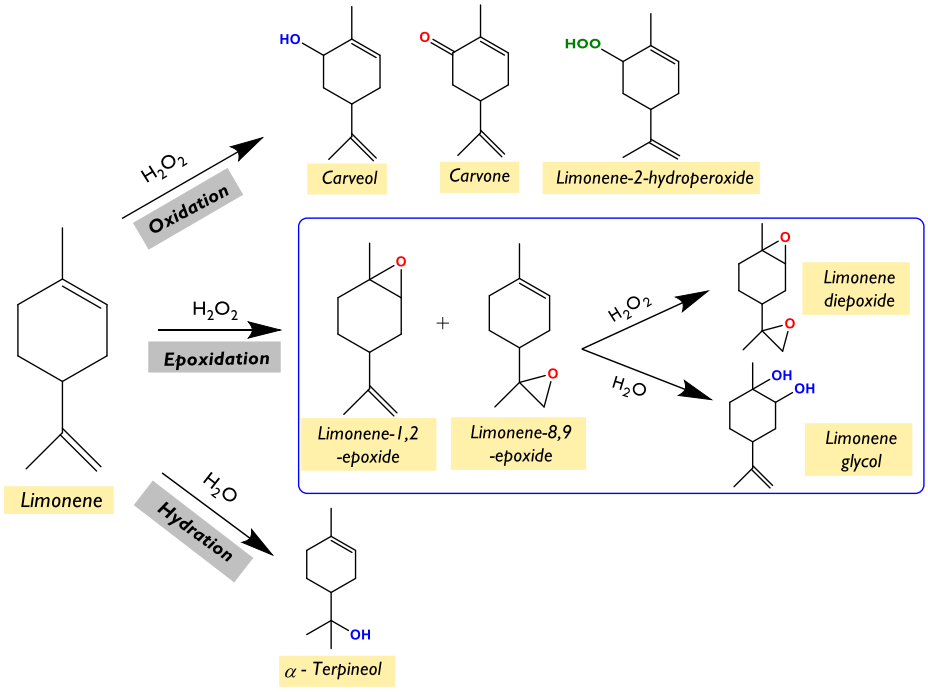

Figure 3.1. Reaction pathways for the catalytic transformation of limonene via oxidation.

Many heterogeneous catalytic systems yield limonene monoepoxides as the main products, which are based on oxides such as MgO [49], WO_3/SiO_2 [50], γ-AlO(OH)-nanorods [51], and W/SiO_2 [52]; hybrid composites such as a Co-substituted phosphomolybdate acid encapsulated in the UiO-66 framework (PMo11Co@UiO-66) [53], an organic-inorganic hybrid based on MoO_3 chains with 2,2'-biimidazole ligands ([MoO_3(biim)]) [54], and Mg/Al hydrotalcites-Au nanoparticles [55]; complexes-based catalysts such as a terpyridine-based Mo(VI) complex on manganese ferrite ($MnFe_2O_4$/Phttpy-MoO_2) [56], a 5-(2-pyridyl)tetrazolate complex of Mo(VI) (MoO_3(Hpytz)) [57], and two layered double hydroxides ZnAl-LDH and MgAl-LDH functionalized with bis(4-HOOC-phenyl)-acenaphthenequinonediimine (BIAN) [58]; MOFs-based catalysts such as Mo/Hf-MOF [59] and Zn/Co-MOF [60]; activated carbons as Ru/Darco-G60 [61]; mesoporous materials such as Co/SBA-16 [62], Ni/SBA-16 [62], TiO_2/SiO_2-Mn [63], Ti/SBA-16 [64,65], Mo-TUD-1 [66], and Ti/KIT-6 [67]; and microporous materials such CoO_x/mordenite [68]. The ZnAl-LDH-BIAN-MoI_2 catalyst has been reported to exhibit the highest selectivity for limonene monoepoxides (97%) with a remarkable limonene conversion (94%) when using TBHP as the oxidizing agent and toluene as the solvent at 110 °C for 24 h [58]. The [MoO_3(biim)] catalyst is another promising material, which yielded limonene conversion of 97% with selectivity of 80% towards monoepoxides when TBHP and α, α, α-trifluorotoluene (TFT) were employed as the oxidant and the solvent, respectively.

Despite a wide range of catalytic materials reported in the literature, mesoporous zeolitic materials (hierarchical zeolites) with appealing morphological, textural, and acidic properties have not been extensively explored as heterogeneous catalysts for the valorization of limonene towards its monoepoxides. Herein, this study aims to investigate the limonene epoxidation route using

H_2O_2 as a green oxidizing agent over hierarchical zeolite Y-based catalysts. The research will focus on studying the physicochemical properties of the catalysts, including crystalline phases, morphology, textural properties, acidity, and environment of the species in the zeolitic materials, and correlating them with the catalytic performance. The effect of various parameters such as the solvent nature, substrate initial concentration, catalyst loading, oxidant/substrate feed ratio, reaction temperature, and catalyst stability will be evaluated.

3.3. Materials and Methods

3.3.1. Reagents

Commercial materials were used in the experiments without further processing. Reagents for the synthesis of catalysts were UHY zeolite (CBV 720, SiO_2/Al_2O_3 molar ratio = 30, Zeolyst International), nitric acid solution (HNO_3, 70 wt. %, Fischer Scientific), tin (IV) chloride pentahydrate ($SnCl_4 \cdot 5H_2O$, 98 wt. %, Sigma-Aldrich), triethylamine (TEA, 99 wt. %, Alfa Aesar), and potassium chloride (KCl, ≥ 99.5 wt. %, Merck). Reagents for the catalytic tests were R-(+)-limonene ($C_{10}H_{16}$, 97 wt. %, Sigma-Aldrich), hydrogen peroxide solution (H_2O_2, 30 wt. %, Sigma-Aldrich), acetonitrile (CH_3CN, gradient grade for liquid chromatography, Merck), N-N-dimethylformamide (DMF, ≥ 99.5 wt. %, VWR Chemicals), ethyl acetate ($C_4H_8O_2$, ≥ 99.5 wt. %, Sigma-Aldrich), dimethyl carbonate (DMC, 99 wt.%, Sigma-Aldrich), cyclohexane (99.9 wt.%, Thermo Scientific), tetrahydrofuran (THF, 99.9 wt.%, Sigma-Aldrich), and 2-butanol (99 wt.%, Acros Organics). Reagents used as standards for the quantification through the multipoint calibration curves were *cis*-(-)-limonene oxide ($C_{10}H_{16}O$, 98 wt. %, Sigma-Aldrich), *trans*-limonene-1,2-epoxide ($C_{10}H_{16}O$, 97.5 wt. %, Sigma-Aldrich), (4R, 8RS)-limonene-8,9-epoxide ($C_{10}H_{16}O$, 95 wt. %, Biosynth), D-dihydrocarvone ($C_{10}H_{16}O$, ≥ 97 wt. %, mixture of isomers, Sigma-Aldrich), L-carveol ($C_{10}H_{16}O$, mixture of *cis* and *trans*, ≥ 95 wt. %, Sigma-Aldrich), R-(-)-carvone ($C_{10}H_{14}O$, 98 wt. %, Sigma-Aldrich), α-terpineol ($C_{10}H_{18}O$, ≥ 95 wt. %, Sigma-Aldrich), dipentene dioxide ($C_{10}H_{16}O_2$, 95 wt. %, Sigma-Aldrich), and (1*S*,2*S*,4*R*)-(+)-limonene-1,2-diol (≥ 97 wt.%, Sigma-Aldrich). Reagents for the quantification of H_2O_2 concentration were ammonium cerium (IV) sulfate solution ($Ce(NH_4)_4(SO_4)_4$, 0.1 mol L^{-1}, VWR Chemicals), ferroin solution indicator (1,10-phenanthroline iron (II) sulfate, VWR Chemicals) and sulfuric acid (H_2SO_4, 95-98 wt. %, Fluka).

3.3.2. Synthesis of Catalysts

The catalysts were prepared following the procedure outlined by Jimenez-Martin et al. [69] with some modifications (**Table 3.1**). Commercial CBV 720 zeolite (H-Y-30), designated as HY, was dealuminated treating it with a 10 M aqueous HNO_3 solution (20 mL g^{-1} of zeolite) for 1 h at room temperature with continuous stirring (120–150 rpm). The resulting solid was recovered via filtration, washed thoroughly with distilled water until reaching a neutral pH, and subsequently dried at 105 °C overnight. This dealumination procedure was repeated twice to ensure the effective removal of a substantial amount of the initial aluminum loading. The resulting material was denoted as HYD.

Table 3.1. Description of the catalytic materials.

Entry	Catalyst	Description
1	HY	H-Y-30
2	HYD	H-Y-30-DA
3	SnHYD1	2 wt% Sn-H-Y-30-DA
4	KSnHYD1	K-2 wt% Sn-H-Y-30-DA
5	SnHYD2	15.8 wt% Sn-H-Y-30-DA
6	KSnHYD2	K-15.8 wt% Sn-H-Y-30-DA

DA refers to the dealumination procedure.

Sn was introduced by combining $SnCl_4 \cdot 5H_2O$ (2 or 15.8 wt. % Sn) with 250 mL of distilled water, followed by stirring the suspension at room temperature (120-150 rpm) for 5 h. The objective of extending the contact time was to enhance the diffusion of the tin source within the porous structure of the zeolite, fostering a close interaction between the metal precursor and the zeolite support. Subsequently, TEA was introduced with stirring (120-150 rpm) for 2 h to chemically facilitate Sn incorporation, maintaining a TEA: $SnCl_4 \cdot 5H_2O$ molar ratio of 4. During this stage, TEA acted as an activator for the grating of the metal, activating the silanol groups in the dealuminated zeolite. These active groups readily attracted the tin species, resulting in the formation of Sn-O-Si bonds. Simultaneously, TEA acted as a neutralizer for the hydrogen chloride generated in the reaction, leading to the formation of a soluble adduct in water, such as triethylamine hydrochloride. The zeolite was subsequently recovered by filtration and dried at 105 °C before undergoing calcination in static air through a stepwise procedure. This involved heating the catalyst from room temperature to 250 °C for 75 min, maintaining this temperature for 40 min, raising the temperature to 550 °C within 120 min, holding it for 240 min, and finally cooling the catalyst to 25 °C over 100 min. The resulting solid was designated as SnHYDx, with x = 1 for a Sn loading of 2 wt. % and x = 2 for 15.8 wt. %.

The calcined material is modified by the alkaline ion exchange method. The procedure consisted of suspending the SnHYDx material in an aqueous solution of KCl (0.5 M, 100 mL g^{-1} of zeolite) with stirring (120-150 rpm) for 2 h at room temperature. The final catalyst (KSnHYDx) was filtered, dried at 105 °C overnight, and calcined with the same previous step calcination procedure.

3.3.3. Catalysts Characterization

The prepared metal-modified zeolite Y-based catalysts were characterized by employing several characterization techniques. The textural properties were determined by nitrogen physisorption using a Micromeritics 3Flex-3500 at -196 °C using 50-100 mg of the catalysts. First, the sample was degassed ex-situ in a Micromeritics VacPrep 061 Sample Degas System under vacuum at 180 °C overnight, followed by *in-situ* degassing in the physisorption equipment under vacuum for 4 h at 250 °C. The specific surface area was calculated using the BET and Dubinin-Radushkevich methods and the pore size, pore volume, and pore size distribution were calculated with the Horvath-Kawazoe and the non-local density functional theory (N_2-Tarazona NLDFT) methods.

The phase purity and identification of the crystal phases were determined by powder X-ray diffraction (XRD), whose patterns were recorded using a PANalytical Empyrean diffractometer

with five axis goniometers. The incident beam optics consisted of Bragg-Brentano HD x-ray mirror, fixed 1/4° divergence slit, 10 mm mask, 0.04 rad soller slit and 1° antiscatter slit. The diffracted beam optics consisted of 7.5 mm divergence slit, 0.04 rad soller slit and PIXcel detector array. The used x-ray tube was Empyrean Cu LFF. The X-ray radiation was filtered to include only $CuK_{\alpha 1}$ and $CuK_{\alpha 2}$ components. The results were analyzed with MAUD (Material Analysis Using Diffraction) analysis program [70]. Instrumental broadening was evaluated with Si standard sample. The results were obtained with 2θ scan range from 5° to 120°.

The strength and concentrations of both Brønsted and Lewis acid sites were measured using Fourier Transform Infrared Spectroscopy (FTIR) and pyridine as the probe molecule. Pyridine-FTIR spectra were acquired with an IRTracer-100 (Shimadzu) spectrophotometer pressing the solid catalysts into thin wafers and placed into the FTIR cell, which was outgassed and heated to 450 °C for 1 h. After that, the cell was cooled to 100 °C and the background spectrum was recorded. Pyridine (>99 wt. %, Acros Organics) was adsorbed on the solid surface for 30 min followed by measurements after desorption at 250 °C, 350 °C, and 450 °C under vacuum for 1 h at each temperature. Brønsted acid sites (BAS) and Lewis acid sites (LAS) were identified using the spectral bands at 1545 cm^{-1} and 1450 cm^{-1}, respectively, and the corresponding concentrations were calculated using the extinction coefficients reported by Emeis [71].

The catalyst morphology was investigated by transmission electron microscopy (TEM) with a JEM-1400Plus (JEOL, Japan) instrument. Prior to analysis, the catalyst samples were suspended in ethanol and affixed to a copper grid. To determine the average size of metal particles, the diameter of more than 200 particles was measured using ImageJ software. Additionally, the crystal morphology of the catalysts was examined through scanning electron microscopy (SEM) using a Zeiss Leo Gemini 1530 instrument, which was equipped with a Thermo Scientific UltraDry Silicon Drift Detector (SDD).

The total acidity strength was measured using NH_3-Temperature Programmed Desorption (NH_3-TPD) on a BELCAT II analyzer (Microtrac MRB). Initially, approximately 50 mg of the sample underwent *in-situ* activation at 500 °C for 1 h (ramping at 10 °C min^{-1}). Subsequently, the sample was cooled to 50 °C under a helium flow (30 mL min^{-1}) and saturated with a gas mixture of 5 vol % NH_3/He (30 mL min^{-1}) for 1 h. Physisorbed ammonia was then flushed with helium (30 mL min^{-1}) at 50 °C for 1 h. Finally, the sample underwent heating to 600 °C at a rate of 10 °C min^{-1} under a helium flow of 30 mL min^{-1} for the desorption of NH_3.

Basicity was measured using CO_2-Temperature Programmed Desorption (CO_2-TPD), which was carried out on a BELCAT II analyzer (Microtrac MRB). First, around 50 mg of sample was activated *in-situ* at 500 °C for 2 h (10 °C min^{-1}). Then, the sample was cooled down at 50 °C while flowing helium (30 mL min^{-1}) and saturated with 30 mL min^{-1} of a gas mixture of 5 vol % CO_2/He for 1 h. Physisorbed CO_2 was flushed with 30 mL min^{-1} He at 50 °C for 1 h. Finally, the sample was heated up to 900 °C with a heating rate of 10 °C min^{-1} under a helium flow of 30 mL min^{-1} for the desorption of CO_2.

UV-Vis reflectance spectra were obtained using an Avantes Avaspec HS-TEC CCD spectrometer, coupled with an Avantes FC-UV600-1-SR fiber optic cable of 600 μm diameter. The light source

employed was the Avantes Ava-Light-DHc, which utilized deuterium and halogen lamps. A $BaSO_4$ disc from Edinburgh Instruments served as the reference.

The ^{29}Si and ^{27}Al MAS NMR spectra were recorded on a Bruker AVANCE-III spectrometer operating at 79.50 MHz (^{29}Si) and 104.26 MHz (^{27}Al) using a CP-MAS 4 mm solid state probe. The ^{27}Al spectra were obtained with a 90° pulse (zg0) and a recycle delay of 0.05 s at a spinning speed of 14 kHz, while the ^{29}Si spectra were acquired with a 90° pulse (zg) and a recycle delay of 100 s at a spinning speed of 14 kHz.

The characterization of the spent catalyst also included powerful techniques to detect and quantify the coke formation such as temperature-programmed oxidation (O_2-TPO)-mass spectrometry (MS) and thermogravimetric (TGA) analysis. O_2-TPO was carried out on a BELCAT II analyzer (Microtrac MRB) coupled with a mass spectrometer (Pfeiffer OmniStar GSD 350). First, around 200 mg of the sample was pre-treated at 120 °C for 2 h (10 °C min^{-1}), followed by cooling to 35 °C. The analysis was carried out by heating up to 900 °C at 5 °C min^{-1} using a 30 mL min^{-1} of a mixture of 5 vol% O_2/Ar. The holding time of the target temperature was 10 min. TGA was performed using an SDT650 TA Instrument equipped with a 90 µL alumina sample cup. About 5 mg of the samples were heated in an air flow of 100 mL min^{-1} from room temperature up to 800 °C at 10 °C min^{-1} and held for 6 s. The results obtained for the spent catalyst were compared to the results for the fresh one.

3.3.4. Catalytic Tests

The epoxidation reaction of R-(+)-limonene with H_2O_2 as the oxidizing agent was carried out in the liquid phase using a 100 mL three-neck glass flask as a batch reactor. The flask was equipped with a thermocouple, a sampling valve, and a condenser that utilized glycol as the coolant fluid (at 1 °C). The setup also included an oil-heating jacket (ECO E4 Silver immersion thermostat) and mechanical stirring (Heidolph RZR-2041 instrument) for precise temperature control and mixing. In a typical experiment, 1.9611 g (14.40 mmol) of limonene and 43 mL of the solvent were loaded into the reactor. The solution was then preheated to a reaction temperature of 70 °C while stirring at 750-800 rpm. Next, 2.4483 g (71.98 mmol) of H_2O_2 was added to the reactor. After a few minutes, when the reactor temperature stabilized, the catalyst (648 mg) was rapidly introduced, marking the start time of the reaction. Approximately 0.6 mL samples were taken at specific time intervals and analyzed using a Shimadzu Nexis GC-2030 equipment equipped with a DB-225 capillary (30 m length x 320 µm internal diameter x 0.25 µm film thickness), an FID detector, and an autosampler. Helium was used as the carrier gas (24 mL min^{-1}) with a split ratio of 10:1. The detector temperature was set to 250 °C, and the injection volume was 1 µL. The oven-temperature program ramped from 50 °C to 220 °C at a rate of 10 °C min^{-1} and was held for 1 min. The nature of the products was further confirmed with an Agilent GC/MS 6890N/5973N equipped with a DB-1 capillary column (30 m length x 250 µm internal diameter x 0.5 µm film thickness).

The R-(+)-limonene conversion (X_L), the selectivity to the product i (S_i), and the yield to the product (Y_i) were calculated based on the **Eqs. (3.1)-(3.3)**.

$$X_L(\%) = \frac{n_{L,0} - n_{L,t}}{n_{L,0}} * 100 \quad \textbf{(3.1)}$$

$$S_i(\%) = \frac{n_{i,t}}{n_{L,0} - n_{L,t}} * 100 \quad \textbf{(3.2)}$$

$$Y_i(\%) = \frac{n_{i,t}}{n_{L,0}} * 100 = \frac{X_L * S_i}{100} \quad \textbf{(3.3)}$$

Where $n_{L,0}$, $n_{L,t}$, and $n_{i,t}$ represent the initial moles of limonene, the moles of limonene after a time t, and the moles of the product i after a time t, in the reaction mixture, respectively. The concentrations of limonene as the substrate and different oxidation products such as cis(-)-1,2-epoxide, trans(-)-1,2-epoxide, (4R, 8RS)-limonene-8,9-epoxide, dihydrocarvone, carveol, carvone, limonene diepoxide, and limonene diol were determined from the multipoint calibration curves.

The initial reaction rate ($-r_{L,0}$) and turnover frequency (TOF) for limonene can be calculated using **Eqs. (3.4)-(3.5)**, where $C_{L,0}$ corresponds to the initial molar concentration of limonene, V is the total reaction volume, X is the conversion, m is the catalyst mass, Δt is the time interval (2 h), and TA is the total acidity measured by pyridine-FTIR.

$$-r_{L,0} = \frac{C_{L,0} * V * X}{m * \Delta t} \quad \textbf{(3.4)}$$

$$TOF = \frac{-r_{L,0}}{TA} \quad \textbf{(3.5)}$$

For the reusability test, the catalyst was recovered from the reaction mixture through filtration, followed by abundant washing with acetone. Subsequently, the solid was dried at 105 °C overnight. This resulting solid was labeled as "spent catalyst". Leaching tests were conducted using the hot-filtration method to remove the catalyst from the reaction mixture. The reaction proceeded for 4 h, after which the catalyst was separated from the liquid at the reaction temperature. A liquid aliquot was then analyzed by GC to quantify limonene conversion and product selectivity, while the remaining mixture continued to react for an additional 20 h. Finally, the sample was analyzed by GC to determine the conversion after removing the catalyst.

3.3.5. Quantification of H_2O_2

The H_2O_2 concentration was followed in the reaction via titration using a cerium sulfate solution as has been reported in the literature [72]. An aliquot of the reaction sample was accurately weighed and placed in an Erlenmeyer flask containing 50 mL of H_2SO_4 (10 % w/v) and sufficient amount of ice to maintain the temperature between 0 and 10 °C. Two drops of the ferroin indicator were added and the flask solution was titrated with 0.1 N ammonium cerium (IV) sulfate solution until the disappearance of the salmon color by formation of a light blue. The H_2O_2 concentration ($C_{H_2O_2}$) and conversion ($X_{H_2O_2}$) can be calculated according to **Eqs. (3.6)** and **(3.7)**, respectively.

$$C_{H_2O_2}(\text{wt.}\%) = \frac{V_T C_T MW_{H_2O_2}}{\theta_{SF} W_s} * 100 \quad \textbf{(3.6)}$$

$$X_{H_2O_2} = \frac{C_{H_2O_2,0} - C_{H_2O_2}}{C_{H_2O_2,0}} \quad (3.7)$$

Where θ_{SF} refers to the stoichiometric factor of $(NH_4)_4Ce(SO_4)_4$:H_2O_2 with a value of 2, C_T is the concentration of the titrant (0.1 mol L^{-1}), V_T is the volume of the spent titrant, $MW_{H_2O_2}$ is the molecular weight of H_2O_2 (34.01 g mol^{-1}), W_S is the sample weight, and $C_{H_2O_2,0}$ is the H_2O_2 initial concentration.

3.4. Results and Discussion

3.4.1. Catalyst Characterization

3.4.1.1. X-Ray Diffraction (XRD) Patterns

The XRD patterns for the prepared catalysts are illustrated in **Figure 3.2**. All diffraction patterns can be adequately explained by the presence of faujasite (ICSD 24869) and SnO (ICSD 92552) phases. In all samples, ordered structures are evident, as indicated by the narrow diffraction peaks corresponding to the main crystallographic planes (111), (220), (311), (331), (511), (440), (533), (642), and (555) located at 2θ = 6.2°, 10.1°, 11.9°, 15.6°, 18.6°, 20.3°, 23.6°, 26.9°, and 31.3°, respectively [73,74]. The ordered structures are clearly visible in all samples, as shown in **Figure 8.35** to **Figure 8.41**.

Concerning the Sn species, some broad diffraction peaks are observed at 33°, associated with the SnO phase [75], and at 26.5° and 51.7°, associated with SnO_2 [76], in SnHYD2, KSnHYD2, and spent KSnHYD2 materials (**Figure 8.38**, **Figure 8.40**, and **Figure 8.41**). Although the refinement of the diffraction models suggests minor SnO traces in the SnHYD1 and KSnHYD1 catalysts (**Figure 8.37** and **Figure 8.39**), their identification from the XRD patterns is more speculative.

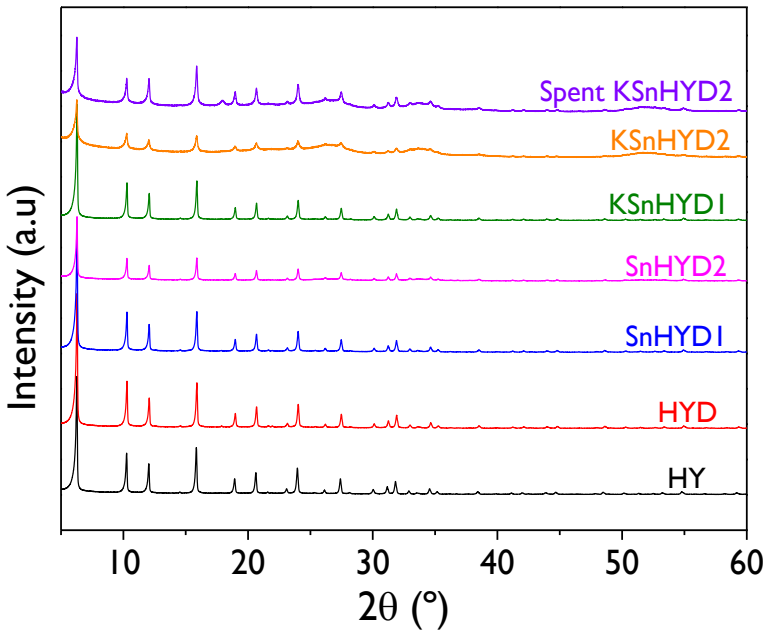

Figure 3.2. XRD patterns of the catalysts.

3.4.1.2. Textural Properties

The textural properties of the catalytic materials were measured using N_2 adsorption-desorption isotherms and are illustrated in **Figure 3.3** and **Table 3.2**. The presence of mesopores in all materials, including the parent zeolite (HY), is confirmed by **Figure 3.3.A**, whose isotherms exhibited type IV hysteresis associated with the capillary condensation that occurs inside the pores [77]. The plots of the cumulative pore volumes as a function of the pore width (**Figure 3.3.B**) increase more rapidly in the microporosity range than the mesoporosity range for all the materials, indicating that the volume of micropores is larger than the volume of mesopores (V_{mic}/V_{mes} >1), as displayed in **Table 3.2**. The pore size distributions (**Figure 3.3.C**) illustrate average pore sizes (APS) for the catalysts ranging from 6.6 to 8.5 Å (**Table 3.2**), with the lowest values for the parent (HY) and dealuminated (HYD) zeolites. The catalysts modified with Sn and/or K did not exhibit appreciable differences regarding the metals loading. Therefore, the results suggest that the post-incorporation of Sn (either 2% or 15.8% nominal loading) to the dealuminated zeolite as the support led to an increase in the APS of materials, although modification of tin-modified zeolites with K by the alkaline ion exchange method did not lead to any dependence on the pore size since the values were similar (8.4 – 8.5 Å). It is worth mentioning, according to **Figure 3.3.D**, that spent KSnHYD2 did not exhibit any change in the APS compared to the fresh one, even with two methods such as NLDFT and Horvath-Kawazoe, yielding values of 8.5 and 7.5 Å, respectively.

On the other hand, the specific surface areas, reported in **Table 3.2**, were calculated by the conventional Brunauer-Emmett-Teller (BET) method but also with a powerful method deduced from the micropore filling theory like the Dubinin-Radushkevich method [78], perfectly applicable for these hierarchical zeolites Y-based catalysts. The first observation is that the Dubinin areas are ca. 34-41% larger than BET areas. The parent zeolite (HY) exhibited the highest surface area of about 1115 $m^2\ g^{-1}$, while the dealuminated zeolite (HYD) possessed a specific area of around 753 $m^2\ g^{-1}$, resulting from a successful nitric acid treatment forming mesopores in the zeolitic structures. Incorporation of 2% Sn nominal loading (SnHYD1) and K (KSnHYD1) did not exhibit appreciable changes in the surface areas, with values ranging from 753 to 816 $m^2\ g^{-1}$, while a higher Sn loading (nominal 15.8%) showed a decrease in the surface area of around 10% (SnHYD2) compared to the dealuminated support, explained by possible pore blocking or clogging. When this tin-modified zeolite was further modified with K (KSnHYD2), an appreciable decrease in the area was observed, around 31% (465 $m^2\ g^{-1}$), suggesting that potassium incorporation into the tin-modified zeolites can tune the total surface area. On the other hand, the surface area for spent KSnHYD2 showed a decrease concerning the fresh one of around 13% (407 $m^2\ g^{-1}$). The mesoporosity, calculated as the ratio between the mesoporous and total volumes, is shown in **Table 3.2**, indicating the lowest value (20%) for the parent zeolite (HY) and the higher values for KSnHYD2 (43%). It is worth noting that mesoporosity did not change significantly after their use in the reaction (45%).

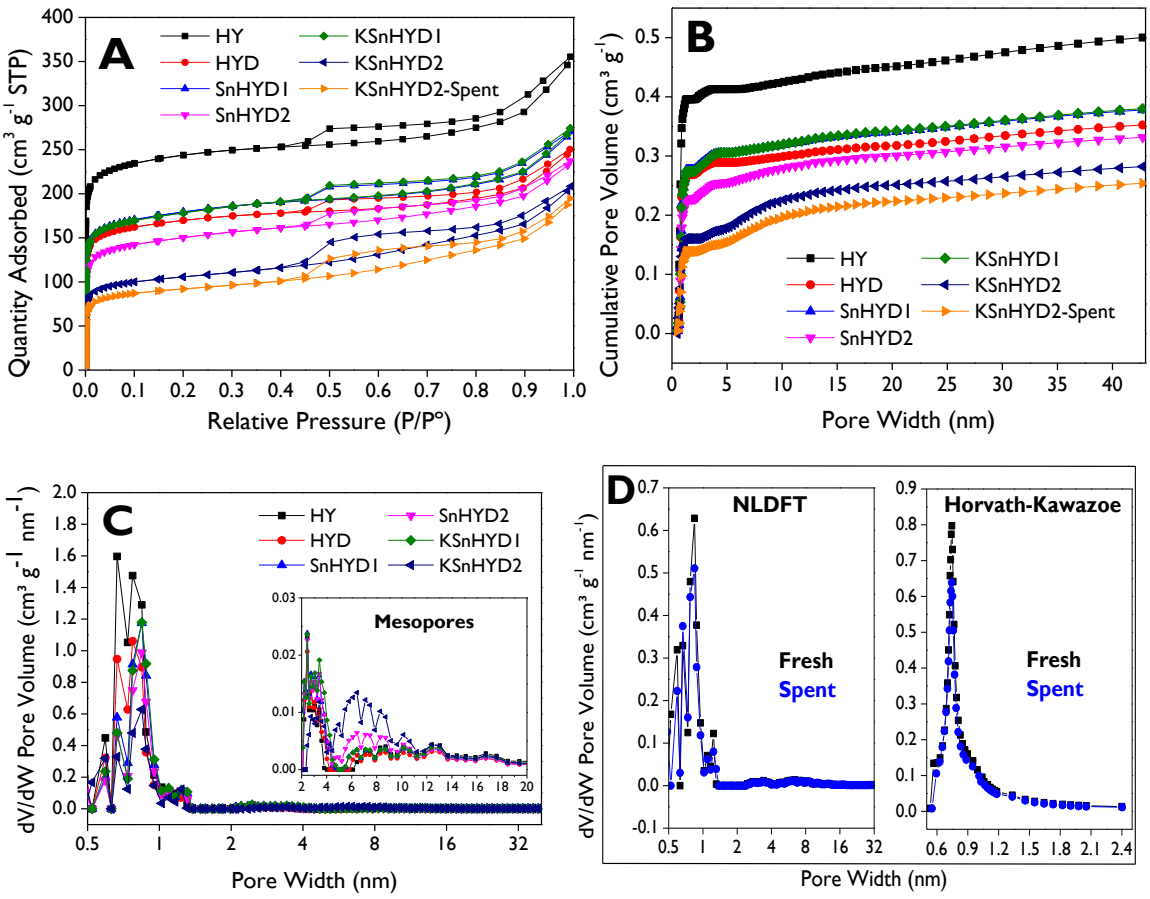

Figure 3.3. N_2 adsorption-desorption isotherms **(A),** cumulative pore volume **(B),** pore size distribution of the fresh materials **(C)**, and pore size distribution of the fresh and spent KSnHYD2 **(D)**.

Table 3.2. Textural properties of the prepared catalysts.

Catalyst	SA_{BET} ($m^2\ g^{-1}$)	$SA_{Dubinin}$ ($m^2\ g^{-1}$)	APS[b] (Å)	V_{mic} ($cm^3\ g^{-1}$)	V_{mes} ($cm^3\ g^{-1}$)	V_T ($cm^3\ g^{-1}$)	Mesoporosity[c] (%)	V_{mic}/V_{mes}
HY	789	1115	6.6	0.40	0.10	0.50	20	3.8
HYD	553	753	7.7	0.27	0.08	0.35	23	3.2
SnHYD1	586	816	8.4	0.28	0.10	0.38	26	2.7
KSnHYD1	584	809	8.5	0.27	0.11	0.38	28	2.6
SnHYD2	493	674	8.4	0.23	0.10	0.33	31	2.2
KSnHYD2	348	465	8.5 (7.5)	0.16	0.12	0.28	43	1.3
KSnHYD2S[a]	302	407	8.5 (7.5)	0.14	0.12	0.26	45	1.2

SA: surface area. **APS:** Average pore size estimated from the pore size distribution with the NLDFT method (**Figure 3.3**). **V_{mic}:** Micropores volume. **V_{mes}:** Mesopores volume. **V_T:** Total pore volume. [a] S denotes spent catalyst. [b] Value in parenthesis was estimated by Horvath-Kawazoe method. [c] Mesoporosity is calculated as the V_{mes}/V_T ratio.

3.4.1.3. Transmission Electron Microscopy (TEM)

The TEM images for the fresh catalysts and the spent KSnHYD2 are shown in **Figure 3.4** and **Figure 8.42** to **Figure 8.48**. Micrographs of the dealuminated zeolite (**Figure 3.4.B** and **Figure 3.4.C**) exhibited large cavities, clearly indicating the successful creation of mesopores in the structure, at the same time the nitric acid treatment did not cause a collapse in the structure. Additionally, the parent zeolite also exhibited some cavities (**Figure 3.4.A**) corresponding to mesopores but in a lesser extent than the dealuminated one, which was confirmed by the N_2 physisorption results (**Table 3.2**) with 20% of mesoporosity for that material. On the other hand, TEM images for Sn-modified zeolites (**Figure 3.4.D** and **Figure 3.4.F**) and K-Sn-modified zeolites (**Figure 3.4.E** and **Figure 3.4.G**) show well-dispersed metal particles over the support. Additionally to the previous qualitative information obtained from the TEM analysis, the distribution of metal particle sizes (**Figure 3.5**) can be plotted from at least 200 measurements for each catalyst image. All fresh metal catalysts exhibited an APS ranging from 4.9 nm to 6.1 nm, indicating a direct relationship between the tin loading and the particle size, as the lowest values were obtained for the catalysts with the lower tin loading (SnHYD1 and KSnHYD1, **Figure 3.5.A** and **Figure 3.5.C**, respectively) and the highest values for the higher tin loading (SnHYD2 and KSnHYD2, **Figure 3.5.B** and **Figure 3.5.D**, respectively). Notice that the obtained distributions are unimodal, indicating that it is not possible to discern the average particle size for K and Sn individually from the TEM images due to their similar sizes.

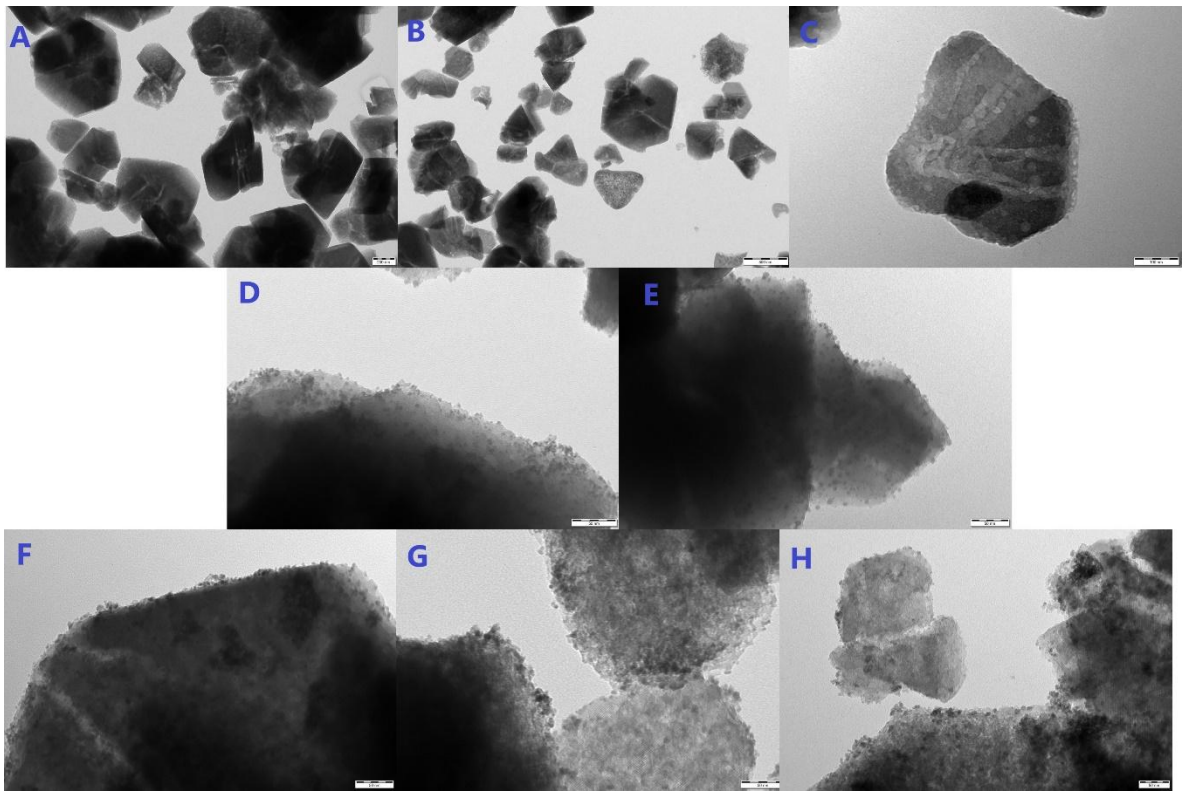

Figure 3.4. TEM images of **(A)** HY, **(B)** HYD (x12000), **(C)** HYD (x60000), **(D)** SnHYD1, **(E)** KSnHYD1, **(F)** SnHYD2, **(G)** KSnHYD2, **(H)** KSnHYD2-Spent. The ruler sizes for the images are 50 nm (**D, E, F, G, H**), 100 nm (**C**), 200 nm (**A**), and 500 nm (**B**).

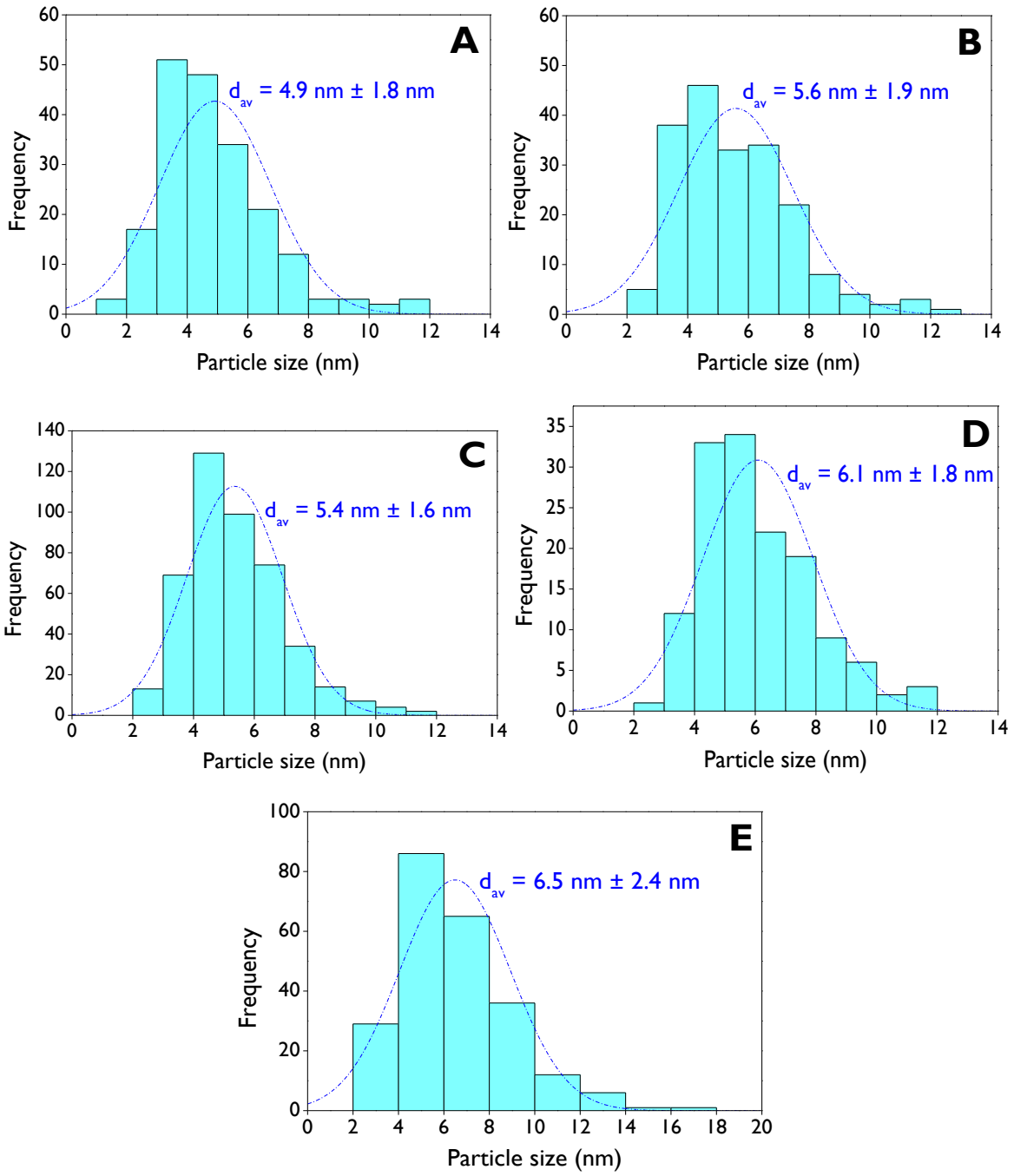

Figure 3.5. Particle size distribution of **(A)** SnHYD1, **(B)** SnHYD2, **(C)** KSnHYD1, **(D)** KSnHYD2, **(E)** KSnHYD2-Spent.

3.4.1.4. Scanning Electron Microscopy – Energy Dispersive X-Rays (SEM-EDX)

The SEM micrographs of the synthesized catalysts are presented in **Figure 3.6**. All materials exhibit various crystal shapes such as pyramidal, rectangular, hexagonal, triangular, and agglomerates with crystal sizes ranging from 100 to 600 nm (**Figure 8.49** to **Figure 8.55**). However, the materials do not show a visibly uniform distribution of the metal particles over the

dealuminated support. This could be attributed to the use of $SnCl_4 \cdot 5H_2O$ as the precursor, as observed recently in our group. The most important observation from the SEM images is that the dealumination procedure of the HY zeolite was successful, as evidenced by the absence of the structure collapse. Conversely, larger particles were broken to create more mesoporosity (**Table 3.2**).

On the other hand, the elemental composition was determined by EDX and is reported in **Table 3.3** in weight percentage for both atomic and oxides. As the parent zeolite (HY) was investigated without further treatment, the SiO_2/Al_2O_3 molar ratio of ca. 28.0 was expected, given the nominal SiO_2/Al_2O_3 ratio of 30. The dealuminated zeolite (HYD) and metal-modified catalysts showed that this ratio was larger than 28.0, easily explained by creation of mesopores resulting from the removal of aluminum from the starting zeolite. The nominal Sn loading can be compared with the experimental values obtained by EDX, resulting in 2.65% and 2.39% of Sn for SnHYD1 and KSnHYD1, respectively, while obtaining 15.08% and 13.02% for SnHYD2 and KSnHYD2, respectively. The K loadings presented a maximum of 2.21% for KSnHYD2.

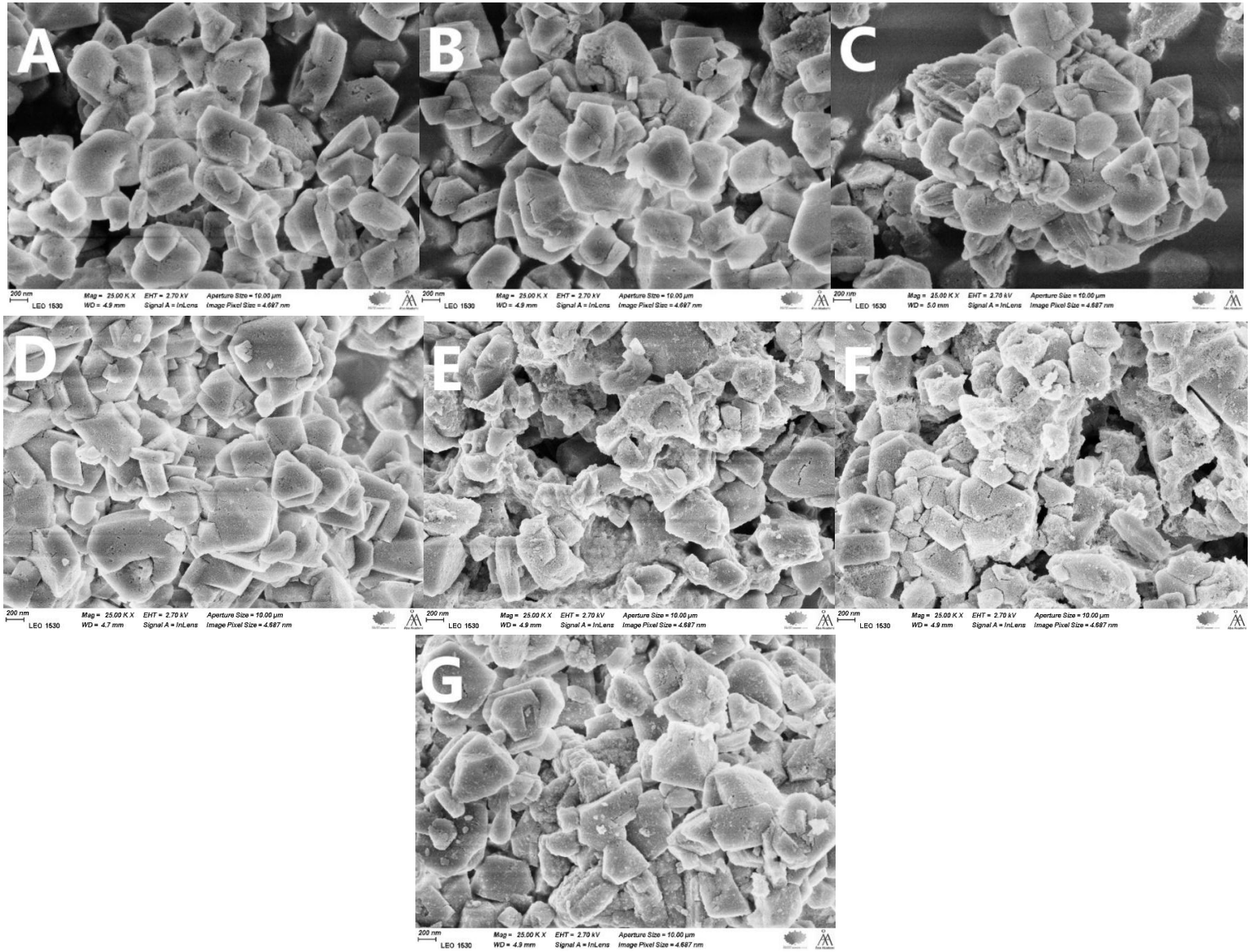

Figure 3.6. SEM images of **(A)** HY, **(B)** HYD, **(C)** SnHYD1, **(D)** KSnHYD1, **(E)** SnHYD2, **(F)** KSnHYD2, **(G)** KSnHYD2-Spent.

Table 3.3. Elemental composition of the materials using SEM-EDX analysis.

Catalyst	Weight %									SiO_2/Al_2O_3 mole ratio
	SiO_2	Al_2O_3	SnO_2	K_2O	Si	Al	O	Sn	K	
HY	94.29	5.71	0.00	0.00	44.07	3.02	52.90	0.00	0.00	28.0
HYD	97.74	2.26	0.00	0.00	45.69	1.19	53.12	0.00	0.00	73.4
SnHYD1	94.96	1.68	3.37	0.00	44.39	0.89	52.07	2.65	0.00	95.9
KSnHYD1	93.56	2.90	3.04	0.51	43.73	1.53	51.92	2.39	0.42	54.8
SnHYD2	78.53	2.32	19.14	0.00	36.71	1.23	46.98	15.08	0.00	57.4
KSnHYD2[a]	78.28	1.98	16.54	2.66	36.59	1.05	46.58	13.02	2.21	67.09

[a]The balance (0.55) corresponds to Cl.

3.4.1.5. Catalysts Acidity and Basicity

The quantification of Brønsted (BA) and Lewis (LA) acid sites (**Table 3.4**, **Figure 8.56**) in the catalytic materials was performed using pyridine as a probe molecule in the adsorption-desorption FTIR analysis. The parent zeolite (HY) exhibited the highest total acidity (275 μmol g^{-1}) and the highest BA/LA ratio (4.0), associated with the highest aluminum amount (**Table 3.3**). After dealumination, the materials showed significantly lower Brønsted acidity reflected in both total acidity and the BA/LA ratios. When Sn was anchored on the dealuminated zeolite, an increase in total acidity was observed, primarily associated with an increase in Lewis acidity, resulting in values of 62 and 81 μmol g^{-1} for SnHYD1 and SnHYD2, respectively. The difference between them can be explained by variations in the loading of Sn onto the catalysts (2.65% and 15.08%, respectively, **Table 3.3**). On the other hand, incorporation of K into the catalysts led to a decrease in total acidity and the BA/LA ratio, mainly associated with lower Brønsted acidity. The spent KSnHYD2 exhibited acidity values similar to the fresh one. The lowest BA/LA ratios were obtained with the highest tin loadings (SnHYD2 and KSnHYD2).

Table 3.4. Acidity of the catalysts by FTIR using pyridine as probe molecule.

Catalyst	Brønsted acidity (μmol g^{-1})				Lewis acidity (μmol g^{-1})				BA/LA ratio	Total (μmol g^{-1})
	Weak	Medium	Strong	Total	Weak	Medium	Strong	Total		
HY	10	20	190	220	19	10	26	55	4.0	275
HYD	17	2	10	29	19	2	6	27	1.1	56
SnHYD1	9	8	9	26	21	5	10	36	0.7	62
KSnHYD1	3	6	6	15	12	6	7	25	0.6	40
SnHYD2	10	3	6	19	38	14	10	62	0.3	81
KSnHYD2	1	0	3	4	20	2	6	28	0.1	32
KSnHYD2S[a]	2	1	1	4	14	9	3	26	0.2	30

[a] S denotes spent catalyst.

The acidity strength of the catalysts was also studied by NH_3-TPD, quantified according to **Eq. (3.8)** [79,80], where n_{Des} are the desorbed moles of ammonia, $\dot{V}_{He}$ is the volumetric flow of carrier gas, V_m is the molar volume of one mole of an ideal gas at standard conditions (22.4 L mol^{-1}), β is the heating rate and C_i is the ammonia concentration (% vol).

$$n_{Des} = \frac{\dot{V}_{He}}{V_m}\frac{1}{\beta}\int_{T_0}^{T_f} C_i dT \qquad (3.8)$$

The acidity strength is classified as weak, medium, and strong acidity, related with the bands of the deconvoluted TCD signal in the different temperature ranges of < 150 °C, < 250 °C, and > 250 °C, as is shown in **Figure 3.7**. Parent zeolite (HY) and tin-dealuminated zeolites (SnHYD1 and SnHYD2) exhibited weak, medium, and strong acid sites, while potassium-modified catalysts showed the absence of strong acidity due to the lack of a band at high temperatures. **Table 3.5** shows the acidity strength values measured by NH_3-TPD, observing a close relationship between these results with the pyridine-FTIR (**Figure 8.57**).

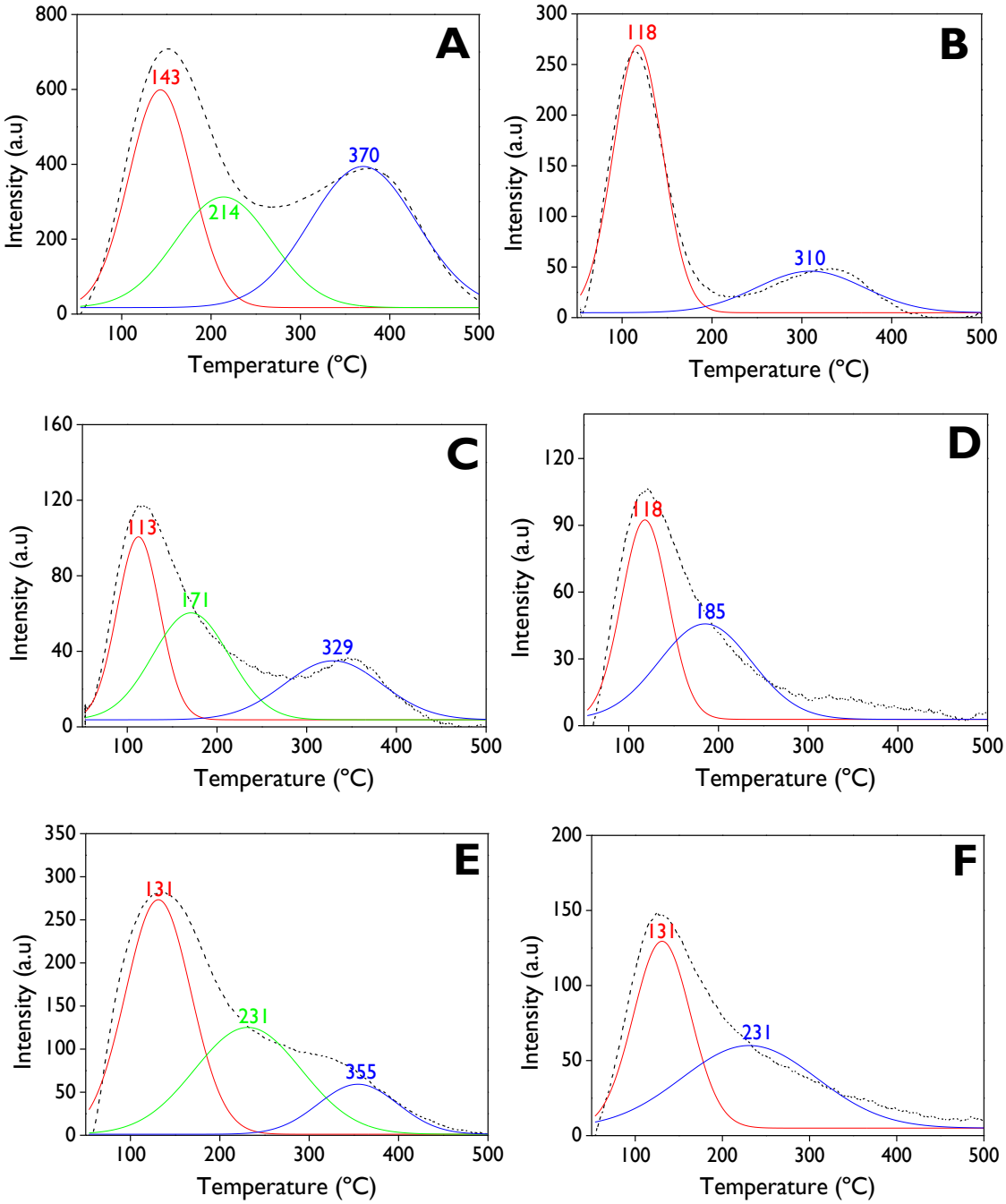

Figure 3.7. NH_3-TPD profiles for the fresh catalysts: **(A)** HY, **(B)** HYD, **(C)** SnHYD1, **(D)** KSnHYD1, **(E)** SnHYD2, **(F)** KSnHYD2.

Table 3.5. Acidity of the catalysts by NH_3-TPD.

Catalyst	Acidity (mmol g^{-1})			
	Weak	Medium	Strong	Total
HY	64	45	53	162
HYD	23	0	11	34
SnHYD1	6	6	4	16
KSnHYD1	7	7	0	14
SnHYD2	32	14	11	57
KSnHYD2	12	11	0	23

Basicity of the potassium-modified catalysts was investigated using CO_2-TPD analysis coupled with mass spectrometry. Results showed absence of basic sites as no signal was observed in desorption of CO_2, as shown in **Figure 8.58**. Furthermore, these results were expected according to the EDX analysis (**Table 3.3**).

3.4.1.6. UV-Vis-DRS Analysis

The UV-Vis-DRS analysis (**Figure 3.8**) is one of the most widely used methods for assessing the environment of the metal Lewis-acid center in zeolites [81]. The peak at ca. 210 nm observed in materials with the highest Sn loading (SnHYD2, KSnHYD2, and spent KSnHYD2) is attributed to the absorption of isolated Sn^{4+} species in tetrahedral coordination located inside the channels of the mesopores of hierarchical zeolites [82]. The wide band observed between 200 and 300 nm for all materials has been assigned to extra-framework Sn species, namely octahedrally coordinated and/or oligomeric Sn species [81,83,84], which could be present in synthesized catalysts with Sn (IV) centers located outside the zeolite pores [79,85]. Spectra for the parent (HY) and dealuminated (HYD) zeolites exhibited no bands, as expected. On the other hand, the spent KSnHYD2 showed a shoulder around 450 nm, which can be associated with impurities after the reaction.

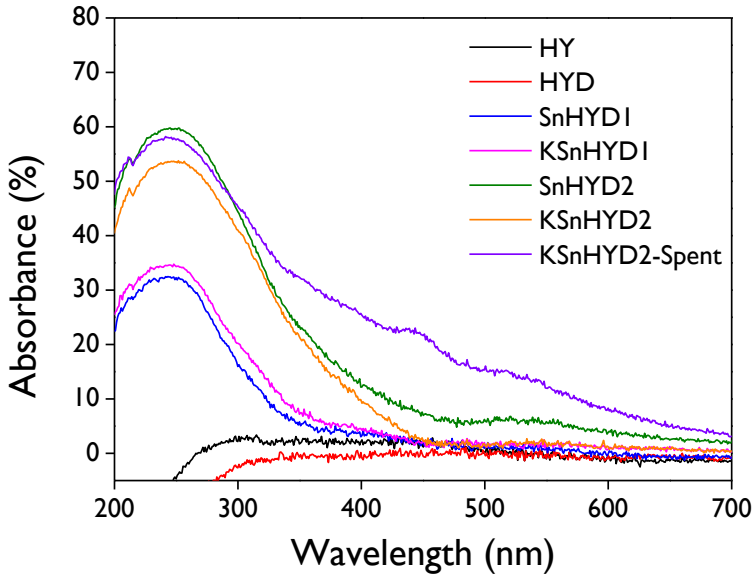

Figure 3.8. UV-Vis-DRS spectra of the catalysts.

3.4.1.7. Solid-state NMR

This technique has been established as an efficient method to determine the coordination and local structure of Si and Al species in zeolites [86]. **Figure 3.9** illustrates the ^{27}Al spectra (**Figure 3.9.A** and **Figure 3.9.B**) and the ^{29}Si spectrum (**Figure 3.9.C**) for all synthesized catalysts. Two well-defined ^{27}Al resonances around 60 and 0 ppm are observed for all the samples, attributed to the four-coordinated framework Al and six-coordinated extra-framework Al, respectively [86,87], although some authors have recently assigned the resonance at 0 ppm to aluminum entities with octahedral coordination [88]. The absence of resonance around 30 ppm indicates the absence of five-coordinated extra-framework Al [89]. Specifically, materials with potassium displayed a slight resonance at 0 ppm, as shown clearly in **Figure 3.9.B**. On the other hand, the resonance observed around -110 ppm for ^{29}Si NMR (**Figure 3.9.C**) is due to Si[4Si] environments and reflects the unique local geometries within the zeolite Y unit cell [90,91].

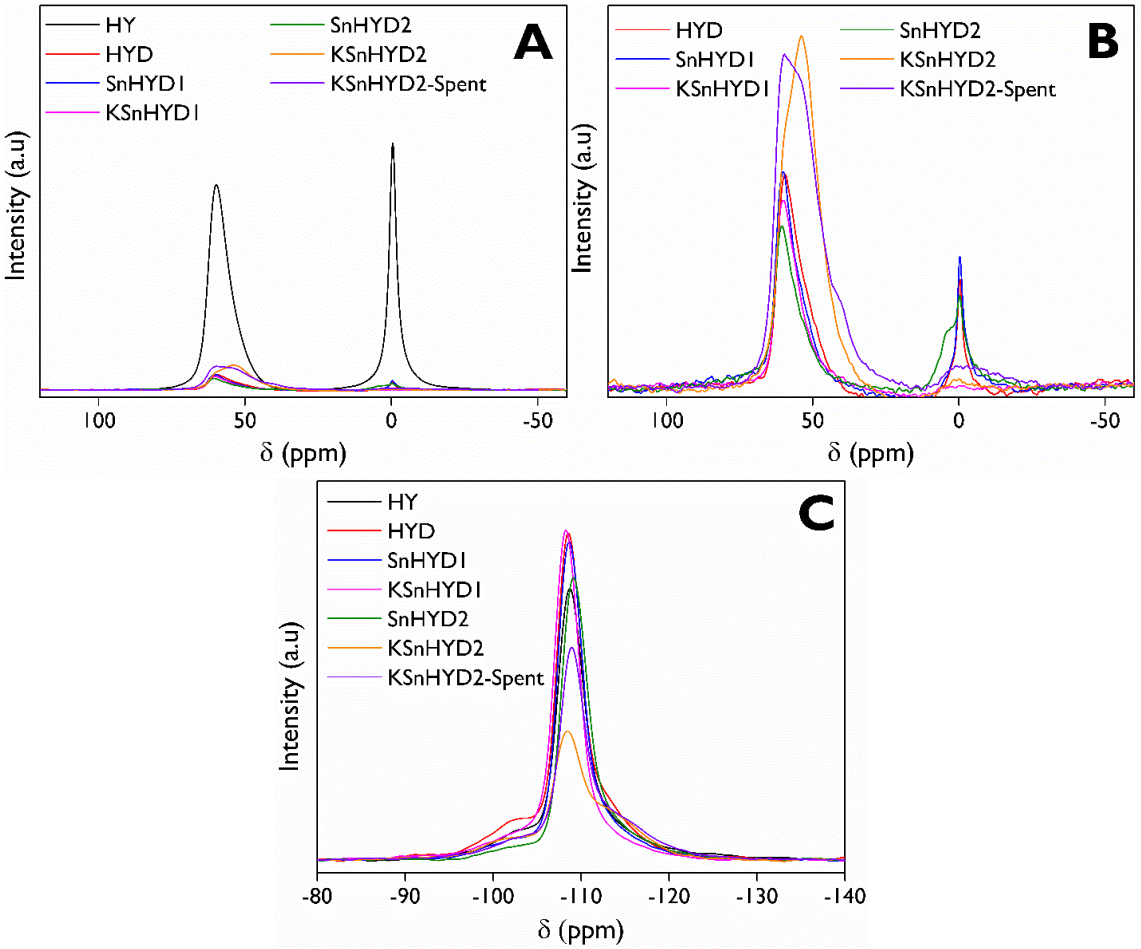

Figure 3.9. (A, B) ^{27}Al MAS NMR and **(C)** ^{29}Si MAS NMR spectra of catalysts.

3.4.2. Catalytic Performance

A preliminary study of heterogeneous catalysts, in which micro and mesoporous materials based on zeolites were investigated, revealed the modified materials on hierarchical zeolite Y as promising for the epoxidation reaction of R-(+)-limonene (**Figure 8.59**). Therefore, these materials are further examined in this contribution. Furthermore, the repeatability of the

experimental procedure was confirmed using the KSnHYD2 catalyst, as depicted in **Figure 8.60**.

3.4.2.1. Initial reaction rate and turnover frequency

The initial reaction rate ($-r_{L,0}$) of R-(+)-limonene transformation and the turnover frequency (TOF) were correlated with the Brønsted/Lewis acidity mole ratio (BA/LA) and the mesoporosity fraction, as shown in **Figure 3.10**. **Figure 3.10.A** demonstrates an inverse relationship between $-r_{L,0}$ and the BA/LA ratio, where the highest initial rates were obtained with the catalysts exhibiting the highest Sn loadings and the lowest BA/LA ratios, such as KSnHYD2 (BA/LA = 0.1) and SnHYD2 (BA/LA = 0.3), with values of 3.1 and 2.5 mmol g^{-1} h^{-1}, respectively. In contrast, the hierarchical support (HYD, BA/LA = 1.1) exhibited the lowest value, corresponding to 0.1 mmol g^{-1} h^{-1}. On the other hand, $-r_{L,0}$ exhibited a direct relationship with the mesoporosity fraction (MES), as observed in **Figure 3.10.B**. KSnHYD2 (MES = 43%) followed by SnHYD2 (MES = 31%) were the materials with the highest mesoporosity values. The other catalysts with mesoporosity between 20% and 30% exhibited the initial rates below 1.1 mmol g^{-1} h^{-1}. For TOF, similar observations regarding the BA/LA ratio (**Figure 3.10.C**) and mesoporosity (**Figure 3.10.D**) can be made, with the highest values of 96.1 and 30.2 h^{-1} for KSnHYD2 and SnHYD2, respectively. It is noteworthy that the parent zeolite (HY), while exhibiting a higher initial rate than HYD (7 times), demonstrates TOF values that are remarkably similar for both materials (2.4 and 1.3 h^{-1}). In general, high TOF and $-r_{L,0}$ values can be observed at low surface areas (**Figure 8.61.A** and **Figure 8.61.E**), and low Brønsted acidity (**Figure 8.61.D** and **Figure 8.61.H**). These trends are consistent, except for the hierarchical zeolite (HYD), which exhibits almost negligible activity despite its high surface area of approximately 753 m^2 g^{-1}. Furthermore, there is no clear relationship between $-r_{L,0}$ and TOF with either the total acidity of the materials (**Figure 8.61.B** and **Figure 8.61.F**) or Lewis acidity (**Figure 8.61.C** and **Figure 8.61.G**).

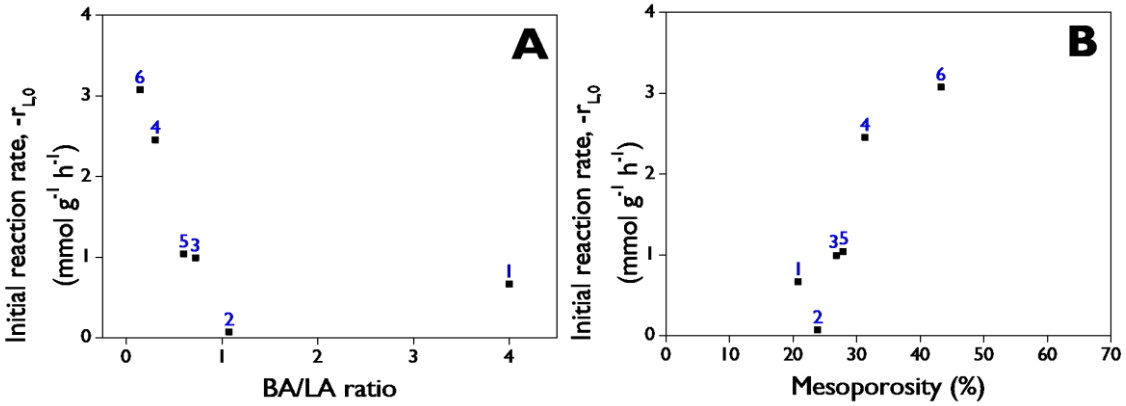

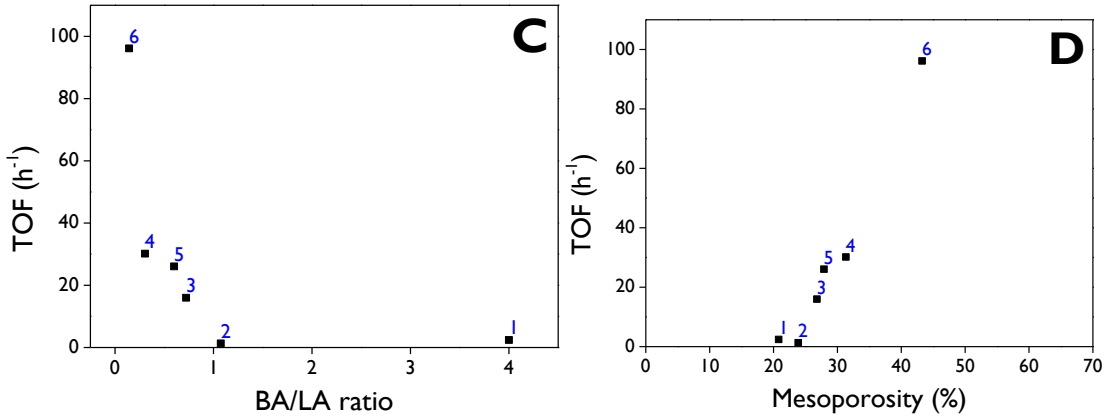

Figure 3.10. Initial reaction rate (A, B) and turnover frequency (C, D) as functions of Brønsted (BA)/Lewis (LA) acidity ratio and mesoporosity fraction. (1) HY, (2) HYD, (3) SnHYD1, (4) SnHYD2, (5) KSnHYD1, (6) KSnHYD2.

3.4.2.2. Conversion and product distribution

Conversion and selectivity toward the main products were investigated with the prepared heterogeneous catalysts, as illustrated in **Figure 3.11**. At the same reaction time, the increasing order of catalytic activity, based on conversion (**Figure 3.11.A**), was as follows: HYD < HY < SnHYD1 < KSnHYD1 < SnHYD2 < KSnHYD2. This trend aligns with the behavior of $-r_{L,0}$ and TOF represented in **Figure 3.10**. Under the tested conditions, a conversion of ca. 76% was achieved with KSnHYD2 after 24 h. The reaction was also conducted without a catalyst (Blank), resulting in approximately 5% conversion after 24 h, attributed to the non-catalytic reaction. This emphasizes the importance of using a heterogeneous catalyst for successful epoxidation of R-(+)-limonene.

The results clearly indicate that the parent and hierarchical supports are not very active per se for the catalytic reaction. When the hierarchical support is modified with Sn and K, the activity is significantly enhanced due to the modification of the physicochemical properties, as discussed previously. Selectivity to the internal epoxides with hierarchical-based catalysts exhibited values of ca. 70-80% at low conversions (**Figure 3.11.B**), which decreases as the reaction progresses, explained by the formation of limonene diol (**Figure 3.11.D**) in a consecutive reaction of epoxides with water present in the commercial oxidant. In contrast, the parent zeolite (HY) exhibited the opposite behavior, increasing selectivity from 7% to 25% in the conversion range of 4-20%. Regarding selectivity to diol, it varies from 24% to 28% throughout the conversion range. On the other hand, selectivity to the external epoxides (**Figure 3.11.C**) shows very similar values of ca. 10% for all materials during the entire conversion range, except for KSnHYD2, which displayed maximum values of ca. 21% at low conversions (20%), decreasing to 12% at 80% conversion. **Figure 3.11.E** illustrates that *trans* internal epoxide is preferable compared to the *cis* configuration for the Sn- and K-modified catalyst, while for HY and HYD, the profile stabilizes at 0.33 and 0.43, respectively. **Figure 3.11.F** demonstrates that selectivity to diol is favored with high BA/LA ratios, as previously shown in the literature with hierarchical zeolites [92]. Conversely, **Figure 3.11.G** illustrates that the *cis*/*trans*-1,2-LE ratio decreases as the BA/LA ratio increases but exhibits a maximum at a BA/LA of ca. 0.3. **Figure 8.62** shows the concentration of diol as a function of the concentration of limonene-1,2-epoxide, exhibiting a typical behavior of a consecutive reaction corresponding to the hydration of epoxides (**Figure 3.1**).

The results obtained with metal-modified hierarchical zeolites are comparable to those reported in the literature using two double-layer hydroxides, such as ZnAl-LDH functionalized with *bis*(4- HOOC-phenyl)-acenaphthenequinonediimine) (H2BIAN) as catalysts [58], along with TBHP as the oxidizing agent. The authors reported 94% of conversion with 97% selectivity to monoepoxides after 24 h, as opposed to 76% and 90% achieved with KSnHYD2 in this contribution, respectively. It is worth noting that the former study employed a significantly higher temperature (110 °C) compared to 70 °C used in this contribution. Additionally, conversion and selectivity results in this study surpass those reported with other recent heterogeneous catalysts [47,50,52,62]. A catalytic system with WO_3-SiO_2 as the catalyst, dioxane and isopropanol as solvents, and H_2O_2 as the oxidant, exhibited 54% conversion after 4 h at 80 °C, with selectivity values of 53%, 33%, and 9% to monoepoxides, glycol, and allylic products, respectively [50]. The modification of zeolite Y with a complex of the type $[VO(Sal_2bz)]_2$ produced high limonene conversion (90%) after 24 h at 80 °C, using acetonitrile as a solvent, but the main products corresponded to allylic compounds and limonene glycol with selectivity values of 49% and 39%, respectively [47]. Co/SBA-16 with ethyl acetate as a solvent, and O_2 and isobutyraldehyde as oxidants, yielded almost complete limonene conversion with selectivity to monoepoxides below 50% and to diepoxide between 25% and 41% [62]. Tungstenocene (IV) dichloride was anchored on amorphous silica (W/SiO_2) and was tested on limonene oxidation using H_2O_2 as the oxidant and acetonitrile as a solvent, producing 68% conversion and 63% selectivity to monoepoxides after 6 h at 90°C [52].

On the other hand, MgO was reported as a successful heterogeneous catalyst for the selective synthesis of monoepoxides and diepoxides, depending on the reaction conditions [49]. High yields of monoepoxides (80%) and diepoxides (96%) can be achieved after 30 min and 2 h, respectively, at 50 °C. However, the catalytic system corresponds to a Payne system, which is more complex than the one used in this contribution. In this system, the oxidant intermediate, peroxyacetimidic acid, is produced from acetonitrile and H_2O_2, and the presence of water and acetone is required as solvents.

Therefore, the heterogeneous catalysts reported in this contribution, prepared based on hierarchical zeolite Y, showed to be promising for limonene epoxidation. Thus, as KSnHYD2 was the most active material for the epoxidation reaction, different reaction conditions were studied as discussed below.

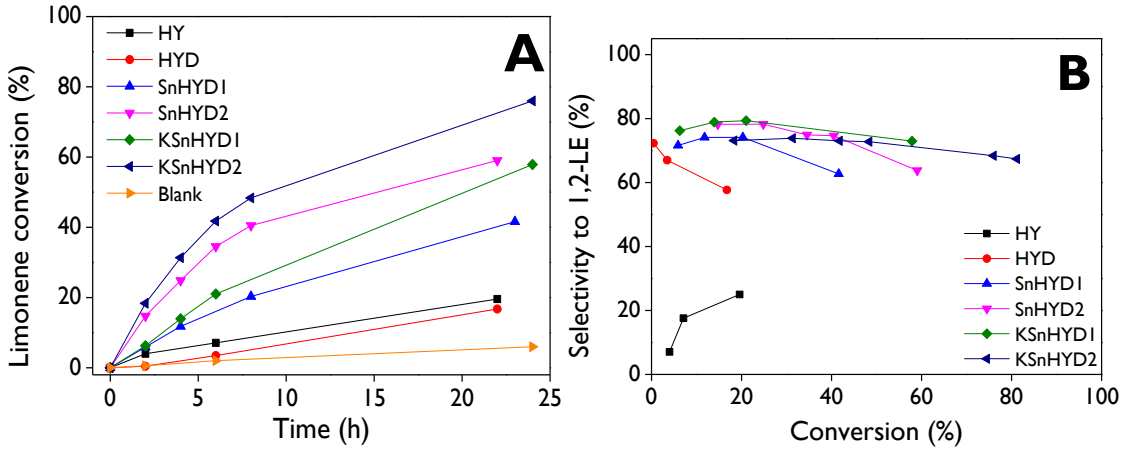

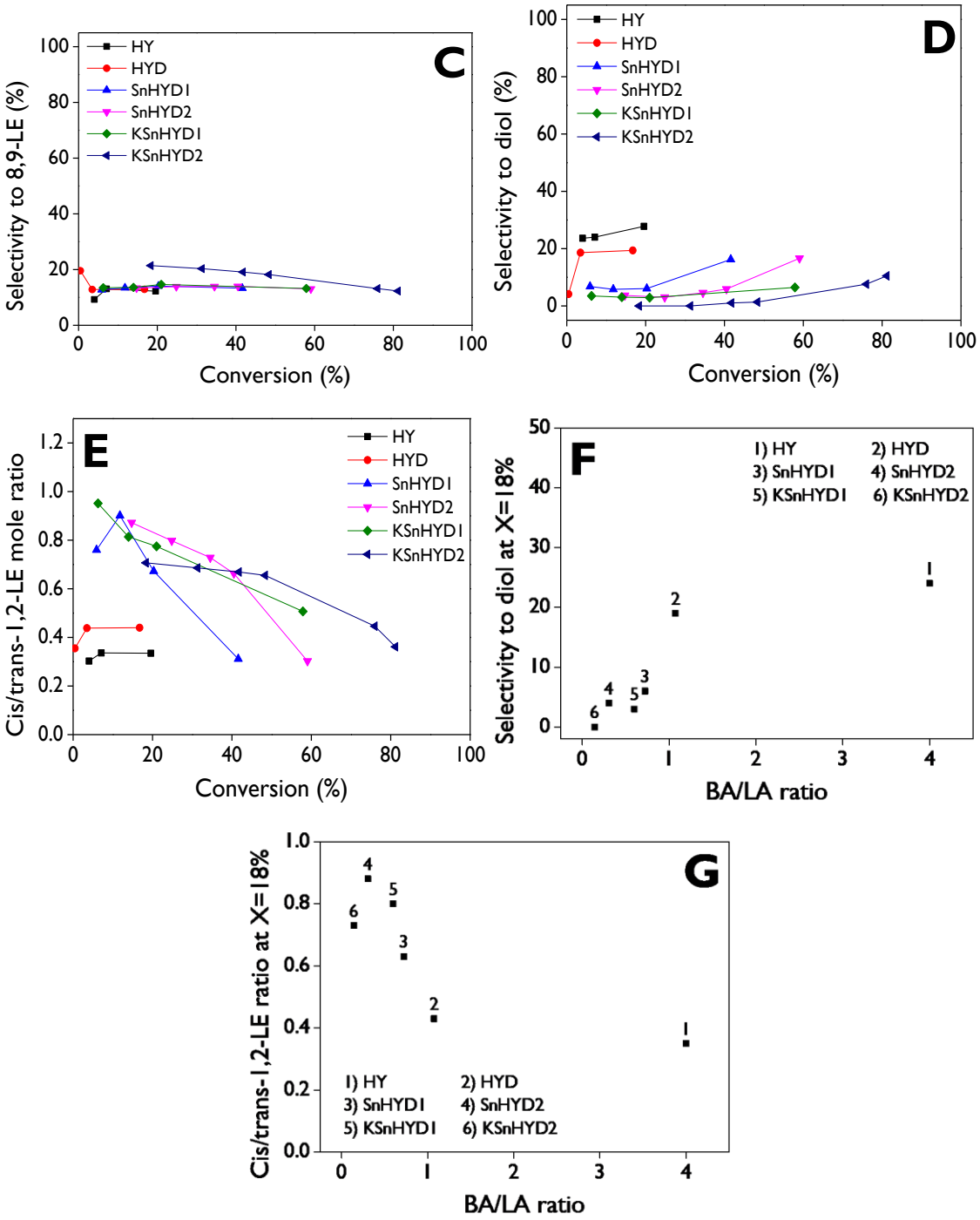

Figure 3.11. Role of catalyst in the R-(+)-limonene conversion and product distribution: Limonene conversion as a function of the reaction time **(A)**; selectivity to limonene-1,2-epoxides **(B)**, selectivity to limonene-8,9-epoxides **(C)**, selectivity to limonene diol **(D),** and *cis*/*trans*-limonene-1,2-epoxide molar ratio **(E)** as a function of the conversion; selectivity to diol **(F)** and *cis*/*trans*-1,2-LE molar ratio **(G)** at 18% conversion as a function of the BA/LA ratio. **Reaction conditions:** $C_{L,0}$ = 0.27 M, acetonitrile as a solvent, H_2O_2/limonene molar ratio = 5:1, 432 mg of catalyst, 70 °C, 800 rpm.

3.4.2.3. Effect of the reaction conditions

The feed molar ratio of the oxidant to the substrate plays a crucial role in the epoxidation of monoterpenes, gaining even more importance when aqueous solutions of the oxidizing agent, such as H_2O_2, are used. This makes sense due to the production of limonene diepoxide is favored by higher concentrations of the oxidant in the reaction medium [49]. Additionally, higher concentration of water can lead to the undesired hydration of the internal limonene epoxides toward limonene diol, as illustrated in **Figure 3.1**. Conversion profiles with varying the H_2O_2/limonene molar ratio at 3:1, 5:1, and 7:1 are shown in **Figure 3.12.A**. These profiles exhibit the expected behavior, with limonene conversion increasing as the oxidant amount in the reaction medium increases, reaching values of 75%, 84%, and 97%, respectively, after 30 h. The plot between $\ln(-r_0)$ and $\ln(C_{H2O2,0})$, illustrated in **Figure 8.63**, exhibits a fractional reaction order of ~0.5, similar to previously reported [93], which suggest a complex mechanism in the transformation of limonene. Selectivity to the internal epoxides (*cis*-1,2-LE + *trans*-1,2-LE) as a function of conversion (**Figure 3.12.B**) showed that, at the same conversion, selectivity is favored at the lowest reactant ratio, yielding values of ca. 76-84% in the entire conversion range.

The selectivity profiles of external epoxides (*cis*-8,9-LE + *trans*-8,9-LE) are shown in **Figure 3.12.C**, with values below 20%, indicating no significant effect of the reactants molar ratio. Resul et al. [93] reported similar trends in the yield of monoepoxides (1,2-LE + 8,9-LE) as a function of the oxidant amount, demonstrating a preference for monoepoxides with a low amount of oxidant in the system. In coherence with the decrease of selectivity to 1,2-LE as the reaction progresses, the selectivity to diol (**Figure 3.12.D**) is favored with the highest molar ratio (7:1), reaching values of about 39% at almost complete conversion, while only 7% is observed with the 3:1 ratio at 74% conversion. Similar observations were reported using a tungsten-based catalyst at 50 °C and toluene as a solvent [93]. **Figure 3.12.E** displays the molar ratio of the two isomers of the internal epoxides as a function of conversion, showing a notable predominance of the *trans* configuration over the *cis* one. Almost zero value is observed for the highest reactant ratio (7:1) at 97% conversion, and around 0.5 for the lowest one (3:1) at 74% conversion. These results could suggest a different dependence on the reaction order for the hydration of *cis* and *trans* isomers. The balance of the products corresponds to traces of allylic products such as carveol and carvone, limonene diepoxide, and dihydrocarvone as an isomer of the internal epoxides. The highest selectivity to diepoxide (~5%) was reached with the 5:1 ratio after 30 h.

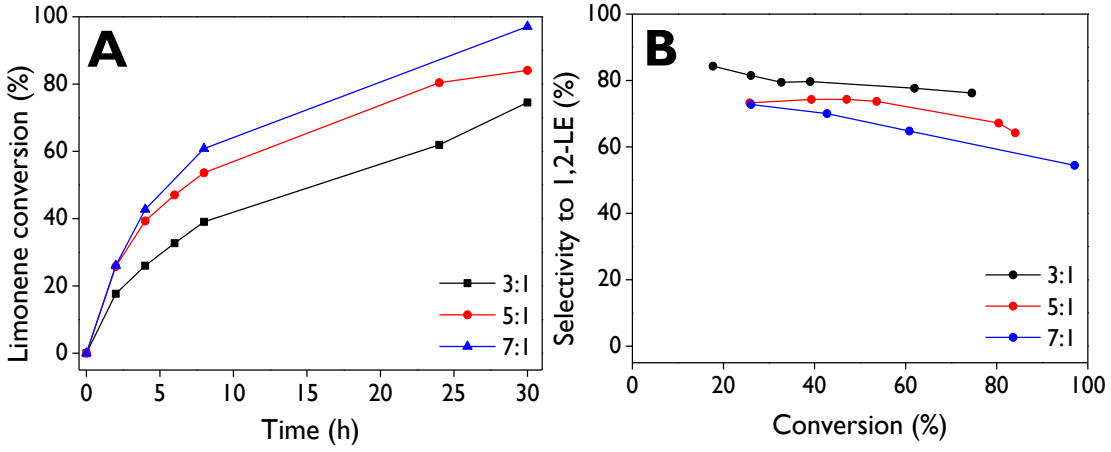

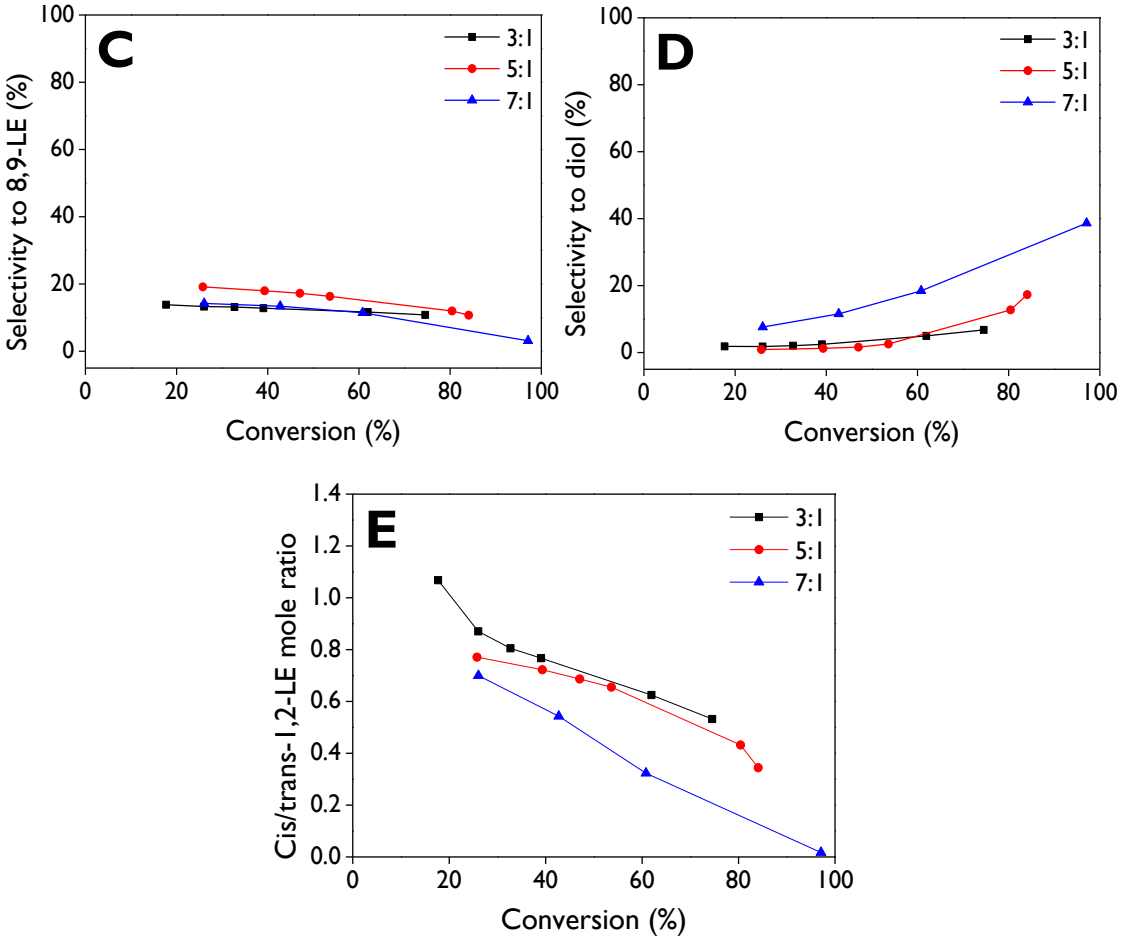

Figure 3.12. Effect of the H_2O_2/limonene molar ratio in the R-(+)-limonene conversion and product distribution over KSnHYD2 as a catalyst: Limonene conversion as a function of the reaction time **(A)**; selectivity to limonene-1,2-epoxides **(B)**, selectivity to limonene-8,9-epoxides **(C)**, selectivity to limonene diol **(D),** and *cis*/*trans*-limonene-1,2-epoxide molar ratio **(E)** as a function of the conversion. **Reaction conditions:** $C_{L,0}$ = 0.27 M, acetonitrile as a solvent, 648 mg of catalyst, 70 °C, 800 rpm.

Investigation of the initial concentration of limonene was done using the H_2O_2/limonene ratio of 5:1, chosen to prevent hydration of the internal epoxides and achieve a high yield of monoepoxides. The reaction rate generally increases as the initial substrate concentration rises, providing a straightforward explanation for the observed behavior in **Figure 3.13.A**. Limonene conversion is notably enhanced with increasing initial molar concentrations, reaching values of ca. 86% and 63% after 24 h with 0.32 M and 0.21 M, respectively. The plot between $\ln(-r_0)$ and $\ln(C_{L,0})$, as illustrated in **Figure 8.64.A**, reveals a fractional reaction order of ~1.7, differing from the first-order dependence reported with a tungsten-based catalyst [93]. This once again supports the conclusion of a complex mechanism for the limonene epoxidation route over KSnHYD2 as a catalyst.

Selectivity to internal epoxides (**Figure 3.13.B**) exhibits slightly higher values at the lowest initial concentration and maintains almost constant values of ca. 74-76% across the conversion range. For concentrations of 0.27 M and 0.32 M, a similar trend is observed, with a decreasing selectivity attributed to the transformation of internal epoxides with water, leading to the formation of the diol. This is clearly depicted in **Figure 3.13.D**, where the maximum values of ca. 18% are observed. In contrast, selectivity to the external epoxides (**Figure 3.13.C**)

demonstrates almost complete independence from the initial concentration, consistently remaining below 20% throughout the entire conversion range. Similar trends are evident in **Figure 3.13.E** for the *cis*/*trans* molar ratio, where values of around 0.34 are reached at 86% conversion for 0.27 M and 0.32 M, while the lowest value (0.6) corresponds to 63% conversion for 0.21 M. The maximum selectivity to limonene diepoxide (11%) was achieved with an initial concentration of 0.32 M after 24 h.

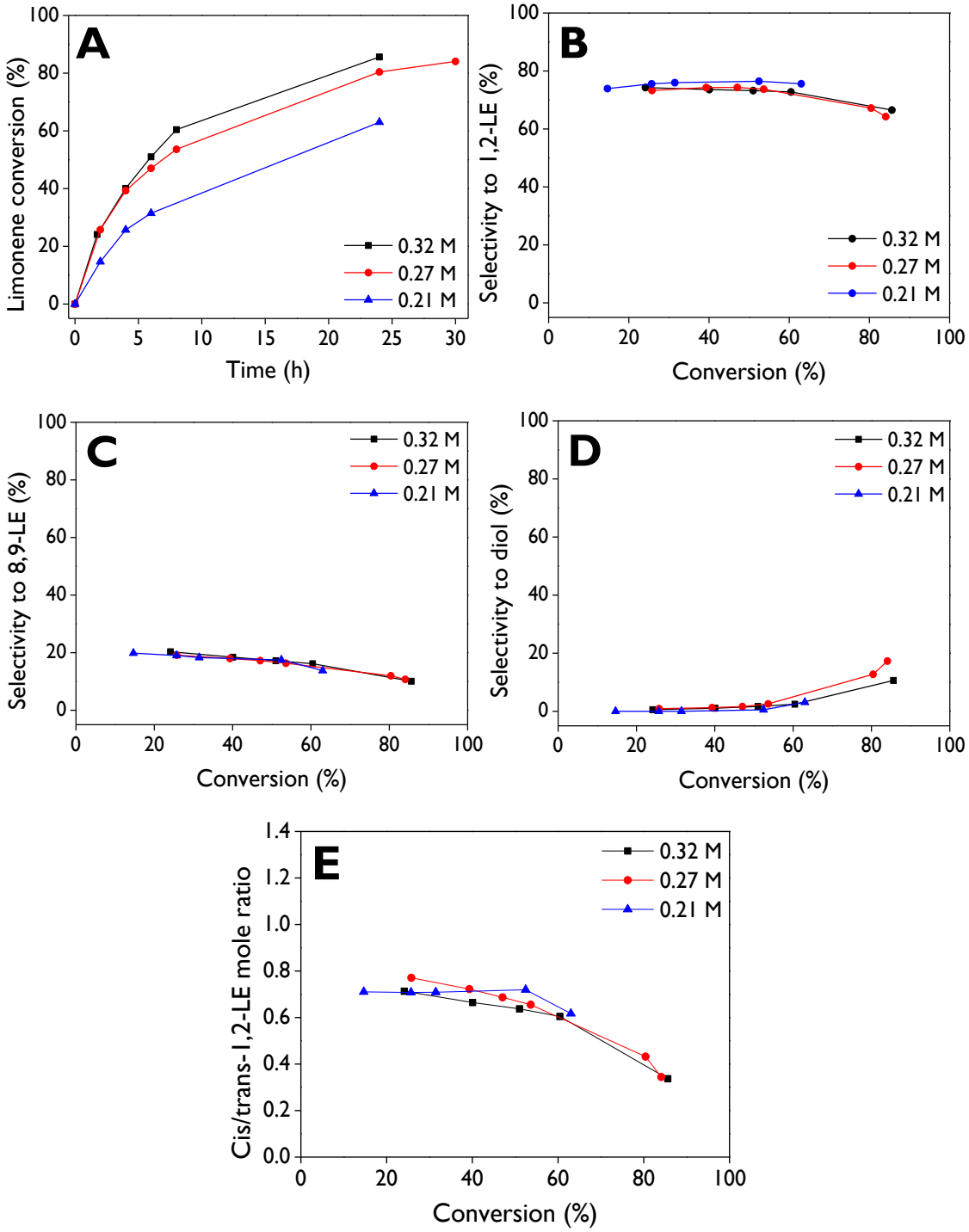

Figure 3.13. Effect of the limonene initial concentration in the conversion and product distribution over KSnHYD2 as a catalyst: Limonene conversion as a function of the reaction time **(A)**; selectivity to limonene-1,2-epoxides **(B)**, selectivity to limonene-8,9-epoxides **(C)**, selectivity to limonene diol **(D),** and *cis*/*trans*-limonene-1,2-epoxide molar ratio **(E)** as a

function of the conversion. **Reaction conditions:** H_2O_2/limonene molar ratio = 5:1, acetonitrile as a solvent, 648 mg of catalyst, 70 °C, 800 rpm.

The effect of the number of active sites, directly related to the catalyst amount, was studied using different ratios of the catalyst (mg) to limonene (mmol), ranging from 30:1 to 60:1, as shown in **Figure 3.14**. Limonene conversion of ca. 92%, 80%, and 76% was reached after 24 h using ratios of 60:1, 45:1, and 30:1, respectively, exhibiting the profiles demonstrated in **Figure 3.14.A**. On the contrary, selectivity profiles for internal epoxides (**Figure 3.14.B**), external epoxides (**Figure 3.14.C**), and diol (**Figure 3.14.D**) showed to be almost independent of catalyst mass. **Figure 3.14.E** displays that the formation of *trans*-1,2-LE is more significant than *cis*-1,2-LE, which is explained by the thermodynamic favorability of the *trans* configuration compared to the *cis* configuration. This is established with the binding energy of adsorption on the active sites of each configuration, with values of -2.1 kJ mol^{-1} and 5.4 kJ mol^{-1}, respectively [92]. **Figure 3.14.F** confirms that non-catalytic routes are not relevant in this system due to the linear dependence of the initial reaction rate of the substrate and the catalyst mass.

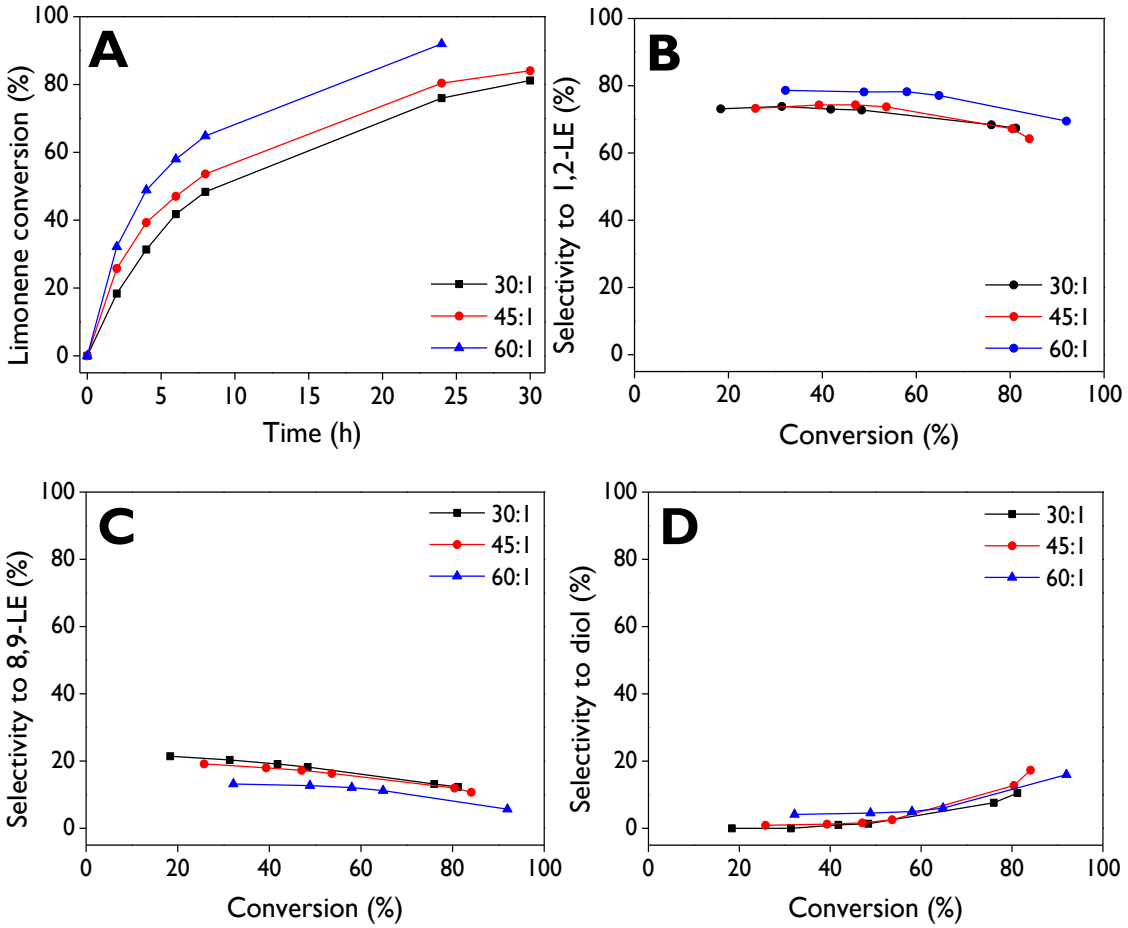

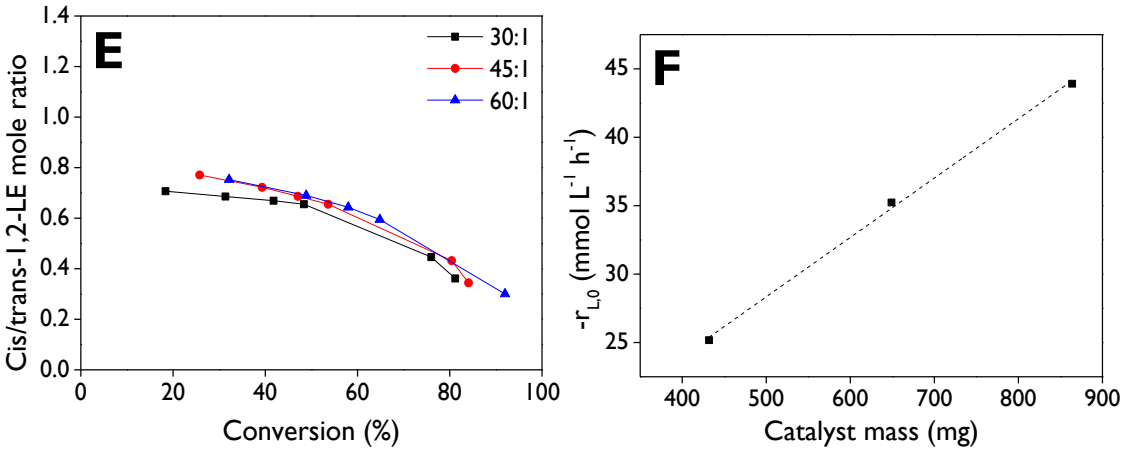

Figure 3.14. Effect of the catalyst amount (catalyst (mg):limonene (mmol) ratio) in the R-(+)-limonene conversion and product distribution over KSnHYD2 as a catalyst: Limonene conversion as a function of the reaction time **(A)**; selectivity to limonene-1,2-epoxides **(B)**, selectivity to limonene-8,9-epoxides **(C)**, selectivity to limonene diol **(D),** and *cis*/*trans*-limonene-1,2-epoxide molar ratio **(E)** as a function of conversion; initial reaction rate of limonene as a function of the catalyst mass **(F)**. **Reaction conditions:** $C_{L,0}$ = 0.27 M, acetonitrile as a solvent, H_2O_2/limonene molar ratio = 5:1, 70 °C, 800 rpm.

The effect of the temperature on R-(+)-limonene epoxidation was investigated within the range of 60 to 80 °C, as depicted in **Figure 3.15**. **Figure 3.15.A** clearly illustrates higher limonene conversion at high temperatures, reaching 67%, 80%, and 93% after 24 h for 60 °C, 70 °C, and 80 °C, respectively. Selectivity to 1,2-LE (**Figure 3.15.B**) is negatively impacted by temperature, as selectivity decreases with the progress of the reaction. This is explained by subsequent conversion of these epoxides towards diol, as depicted in **Figure 3.15.D**. Maximum selectivity to 1,2-LE and diol correspond to 80% (33% conversion) and 35% (93% conversion), respectively, achieved at 60 °C and 80 °C. **Figure 3.15.C** reveals that selectivity to 8,9-LE remains below 20% for the three temperatures in the conversion range, with the maximum values observed at 70 °C. Similarly, in line with the profile of *cis*/*trans*-1,2-LE molar ratio with the highest H_2O_2/limonene ratio (7:1) in **Figure 3.12.E**, the reaction at 80 °C demonstrates a possibility of achieving a ratio close to zero at high limonene conversions (**Figure 3.15.E**). This is attributed to the preferential hydration of *cis*-1,2-LE into diol. On the other hand, estimation of the activation energy of limonene epoxidation can be done using the plot of the initial reaction rate as a function of 1/T, as shown in **Figure 3.15.F**, resulting in a value of 38.1 kJ mol^{-1}. **Table 3.6** displays the activation energy previously reported for limonene oxidation using different heterogeneous catalysts. Notably, the estimated value in this work closely resembles two previous systems that used a homogeneous tungsten-based catalyst (36.0 kJ mol^{-1}) and Al_2O_3 (33.5 kJ mol^{-1}).

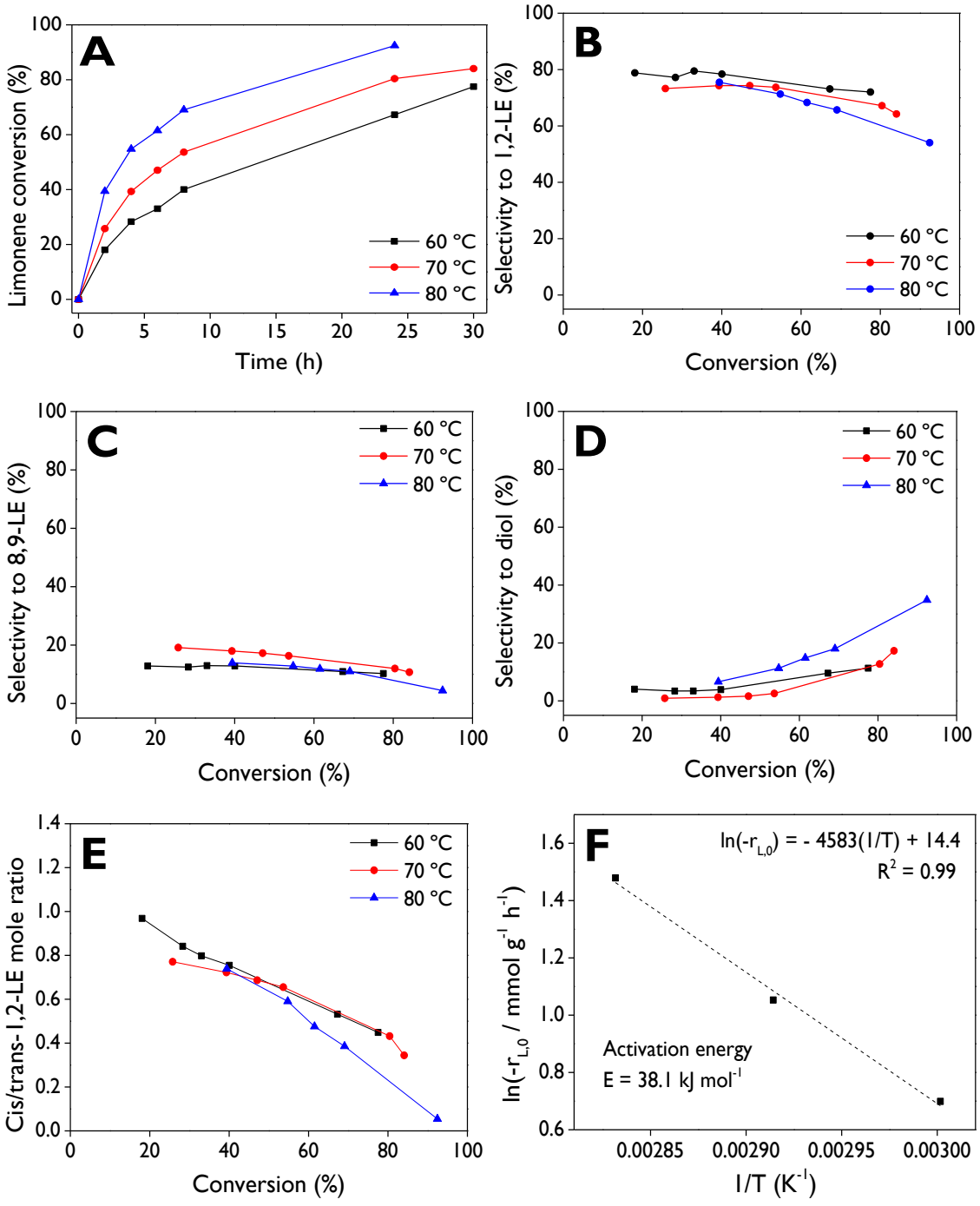

Figure 3.15. Effect of the reaction temperature in the R-(+)-limonene conversion and product distribution over KSnHYD2 as a catalyst: Limonene conversion as a function of the reaction time **(A)**; selectivity to limonene-1,2-epoxides **(B)**, selectivity to limonene-8,9-epoxides **(C)**, selectivity to limonene diol **(D),** and *cis*/*trans*-limonene-1,2-epoxide molar ratio **(E)** as a function of conversion; estimation of the activation energy **(F)**. **Reaction conditions:** $C_{L,0}$ = 0.27 M, acetonitrile as a solvent, H_2O_2/limonene molar ratio = 5:1, 648 mg of catalyst, 800 rpm.

Table 3.6. Activation energy with different heterogeneous catalysts for limonene oxidation.

Catalyst	E (kJ mol^{-1})	Reference
PW-Amberlite	76.0	[94]
MgO	52.3	[49]
Al_2O_3 (ILE)[a]	33.5	[95]
Al_2O_3 (ELE)[a]	54.4	[95]
Tungsten-based catalyst (LE)[b]	36.0	[93]
Tungsten-based catalyst (LG)[b]	79.0	[93]
Tungsten-based catalyst (LD)[b]	43.0	[93]
KSnHYD2	38.1	This work

[a]Activation energy for the transformation of limonene to internal (ILE) or external (ELE) epoxides. [b] Activation energy for the transformation of limonene to monoepoxides (LE), limonene glycol (LG) or limonene diepoxide (LD).

3.4.2.4. Role of the solvent

Different solvents were tested in the R-(+)-limonene epoxidation to investigate the solvent features that favor selective formation of the monoepoxides. Non-polar solvents such as cyclohexane, protic polar solvents like 2-butanol, and aprotic polar solvents including DMC, ethyl acetate, THF, acetonitrile, and DMF, were evaluated. **Figure 3.16.A** shows that acetonitrile is by far the solvent allowing the highest limonene conversion (76%) after 24 h, followed by ethyl acetate with 26%. The initial reaction rate for limonene was plotted as a function of the inverse of the dielectric constant (1/ε), as shown in **Figure 3.16.C**, which clearly displays the highest catalytic activity with acetonitrile, followed by ethyl acetate. The other solvents exhibited conversion values below 20%, indicating their limitations for this heterogeneous epoxidation system. On the other hand, selectivity to the total monoepoxides (*cis*-1,2 + *trans*-1,2 + *cis*-8,9 + *trans*-8,9) as a function of conversion, given in **Figure 3.16.B**, shows values above 90% with acetonitrile for low conversions, which decreases as the reaction proceeds. This is explained by the consecutive reaction of internal monoepoxides towards diol (**Figure 3.12.D**, **Figure 3.13.D**, **Figure 3.14.D**, **Figure 3.15.D**). Additionally, the selectivity to monoepoxides at 18% conversion was plotted as a function of the dielectric constant, as shown in **Figure 3.16.D**. It exhibits a minimum around the value corresponding to 2-butanol, demonstrating a strong dependency of selectivity on solvent polarity, as has been discussed [96]. Cyclohexane, DMC, and DMF appeared to be highly selective to the reaction, being, however, not suitable solvents due to their low reactivity. THF and ethyl acetate display a wide range of selectivity values between 25% and 75% during the conversion range obtained for those solvents. Specifically, hydrophobic limonene was not easily diffused to the active site in the cyclohexane, explained by the formation of two phases with the commercial H_2O_2.

Table 3.7 displays the initial reaction rate of limonene, TOF, conversion, and product distribution with the studied solvents, as well as their main properties such as dielectric constant (ε), dipole moment (μ), and donor number (DN) developed by Gutmann in 1976 [97]. Limonene diol was mainly observed using 2-butanol with selectivity of 43%, making this solvent the least selective to monoepoxides (**Figure 3.16.B**). A crucial aspect to observe is the appreciable difference between the catalytic activity using acetonitrile and DMF as solvents, with TOF values of 96.1 and 6.6 h^{-1}, respectively. Both are aprotic polar solvents with very

similar polarity (ε = 36.6 and 38.3 and μ = 3.5D and 3.8D); however, this difference in reactivity can be explained by the appreciable difference in the DN values, being 14.1 and 26.6 for acetonitrile and DMF, respectively, indicating that acetonitrile is a much weaker Lewis base than DMF. Furthermore, DMF is bulkier than acetonitrile, i.e., it has a larger size and more steric hindrance in comparison with acetonitrile [98]. On the other hand, the second-best solvent was ethyl acetate (**Figure 3.16.C),** which has significantly lower polarity than acetonitrile, but the DN values are quite similar (17.1 and 14.1). Therefore, these results suggest that R-(+)-limonene epoxidation over KSnHYD2 as a catalyst requires aprotic polar solvents with high polarity as well as medium donor capacity.

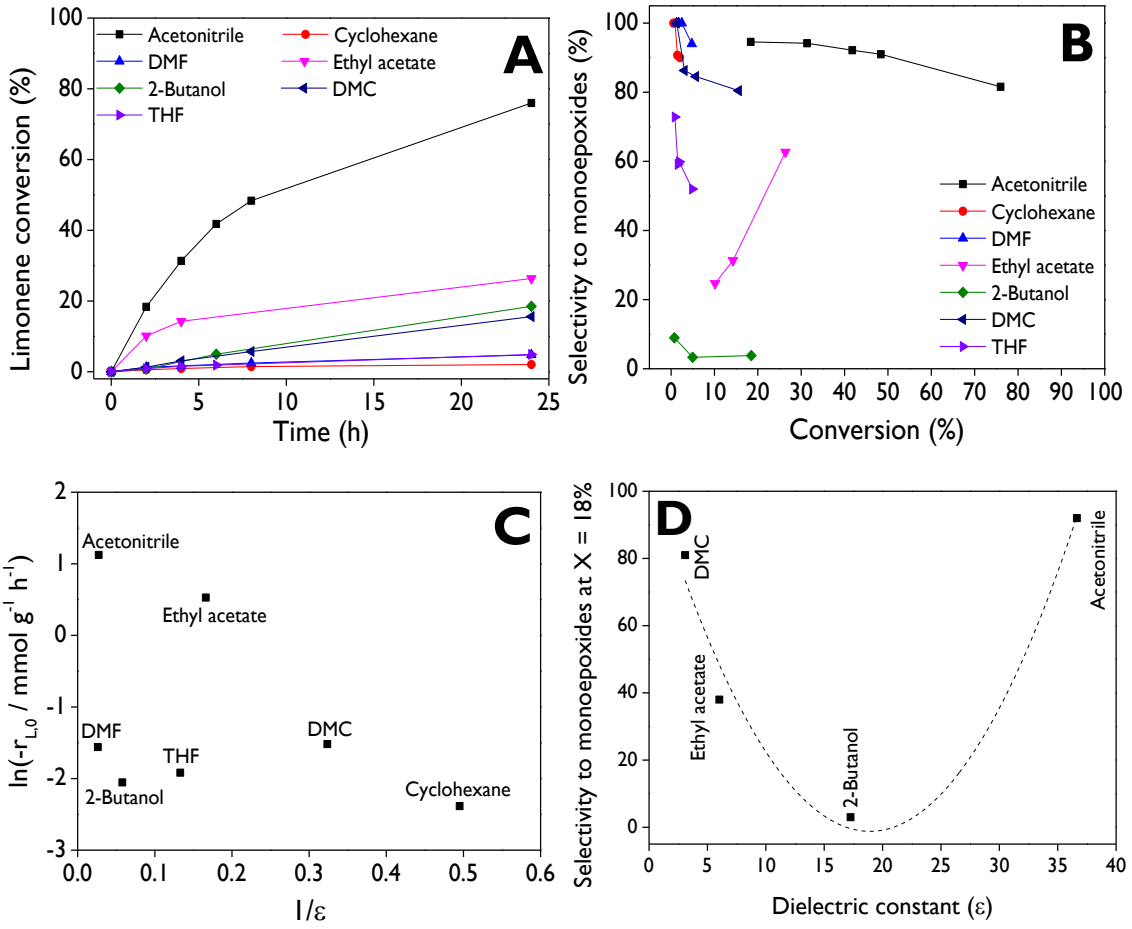

Figure 3.16. Role of the solvent in the R-(+)-limonene conversion and product distribution over KSnHYD2 as a catalyst: Limonene conversion as a function of the reaction time **(A)**; selectivity to monoepoxides (internal + external) **(B)**; ln(-r_{L0}) of limonene as a function of 1/ε **(C);** selectivity to monoepoxides at 18% conversion as function of the dielectric constant **(D). Reaction conditions:** C_{L0} = 0.27 M, H_2O_2/limonene molar ratio = 5:1, 648 mg of catalyst, 70 °C (66 °C for THF), 800 rpm.

Table 3.7. Effect of different solvents in the oxidation reaction of R-(+)-limonene. Conversion and product distribution after 24 h.

Solvent	Structure	Dielectric constant[a] [99]	Dipole moment (D) [100,101]	DN (kcal mol^{-1}) [97]	$-r_{L,0}$ (mmol g^{-1} h^{-1})	TOF (h^{-1})	Limonene conversion (%)	Product distribution (%)
Cyclohexane		2.02	0.00	0.0	0.1	2.9	2.1	12.4 cis-ILE 72.2 trans-ILE 15.4 ELE
Dimethyl carbonate (DMC)	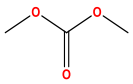	3.09[b]	0.93	17.2	0.2	6.8	15.6	36.6 cis-ILE 31.9 trans-ILE 11.9 ELE 4.1 CL 3.6 CNE 4.9 LG
Ethyl acetate	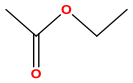	6.02[b]	1.78	17.1	1.7	53.0	26.4	24.7 cis-ILE 29.7 trans-ILE 8.3 ELE 1.4 DHC 1.6 CL 1.5 CNE 8.7 LG
Tetrahydrofuran (THF)		7.52	1.63	20.0	0.1	4.6	4.9	15.6 cis-ILE 21.1 trans-ILE 15.3 ELE 1.7 DHC 8.8 CL 5.9 CNE
2-Butanol	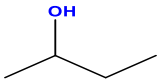	17.26	1.7	n.a	0.1	4.0	18.5	0.3 cis-ILE 1.6 trans-ILE 1.9 ELE 3.6 CL 2.9 CNE 4.5 LD 43.2 LG
Acetonitrile		36.64	3.5	14.1	3.1	96.1	76.0	17.9 cis-ILE 49.5 trans-ILE 12.3 ELE 0.7 DHC 1.2 CL 0.6 CNE 7.3 LD 10.5 LG
N-N-Dimethylformamide (DMF)	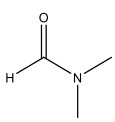	38.25	3.8	26.6	0.2	6.6	4.8	36.3 cis-ILE 41.5 trans-ILE 16.2 ELE 6.0 CNE

DN: Donor number. **Reaction conditions:** $C_{L,0}$ = 0.27 M, H_2O_2/limonene molar ratio = 5:1, 648 mg of catalyst, 70 °C (66 °C for THF), 800 rpm. Dielectric constant reported at [a]20 °C or [b]25 °C. n.a: not available. **ILE:** Internal limonene epoxide, **ELE:** External limonene epoxide, **CL:** Carveol, **CNE:** Carvone, **DHC:** Dihydrocarvone, **LD:** Limonene diepoxide, **LG:** Limonene glycol.

3.4.3. Efficiency of the Oxidizing Agent

H_2O_2 is consumed through two parallel reactions: its consumption in the epoxidation reaction with limonene (**Eq. (3.9)**) and its decomposition into water and oxygen (**Eq. (3.10)**).

$$C_{10}H_{16} + H_2O_2 \rightarrow \text{Products} \quad \textbf{(3.9)}$$

$$H_2O_2 \rightarrow H_2O + \frac{1}{2}O_2 \quad \textbf{(3.10)}$$

Assigning X_L as the limonene conversion (**Eq. (3.1)**), X_{ep} as the partial conversion of H_2O_2 through epoxidation reaction (**Eq. (3.9)**), and X_{dec} as the partial conversion of H_2O_2 through decomposition (**Eq. (3.10)**), **Eq. (3.11)** is used to calculate X_{ep}:

$$C_{L,0}X_L = C_{H_2O_2,0}X_{ep} \rightarrow X_{ep} = \frac{C_{L,0}X_L}{C_{H_2O_2,0}} \quad \textbf{(3.11)}$$

X_{dec} is calculated using the overall conversion of H_2O_2 determined by cerimetric titration (**Eq. (3.7)**), as indicated in **Eq. (3.12)**:

$$X_{H_2O_2} = X_{ep} + X_{dec} \quad \textbf{(3.12)}$$

The efficiency of H_2O_2 ($E_{H_2O_2}$) in the epoxidation reaction is defined according to **Eq. (3.13)**:

$$E_{H_2O_2} = \frac{X_{ep}}{X_{H_2O_2}} \quad \textbf{(3.13)}$$

The profiles of H_2O_2 conversion are shown in **Figure 8.65**, reflecting the expected behavior. The overall conversion increases with the feed H_2O_2/limonene molar ratio, limonene initial concentration, catalyst amount, and temperature, as previously reported [49]. From **Figure 8.65.D**, the activation energy for the H_2O_2 decomposition was estimated to be 45.3 kJ mol^{-1}. The results concerning the efficiency of H_2O_2, presented in **Figure 3.17**, do exhibit a strong dependence on the feed H_2O_2/limonene ratio (**Figure 3.17.A**), while not significantly affected by the initial concentration of limonene (**Figure 3.17.B**), catalyst amount (**Figure 3.17.C**), and temperature (**Figure 3.17.D**). The highest efficiency values were achieved with an H_2O_2/limonene molar ratio of 3:1, resulting in approximately 85% efficiency at low conversions, gradually decreasing to ca. 65% at 40% conversion. Under other conditions, efficiency ranged between 40% and 60%. Similar results for the efficiency of H_2O_2 in the epoxidation of R-(+)-limonene have been reported using MgO as a heterogeneous catalyst in a Payne system [49].

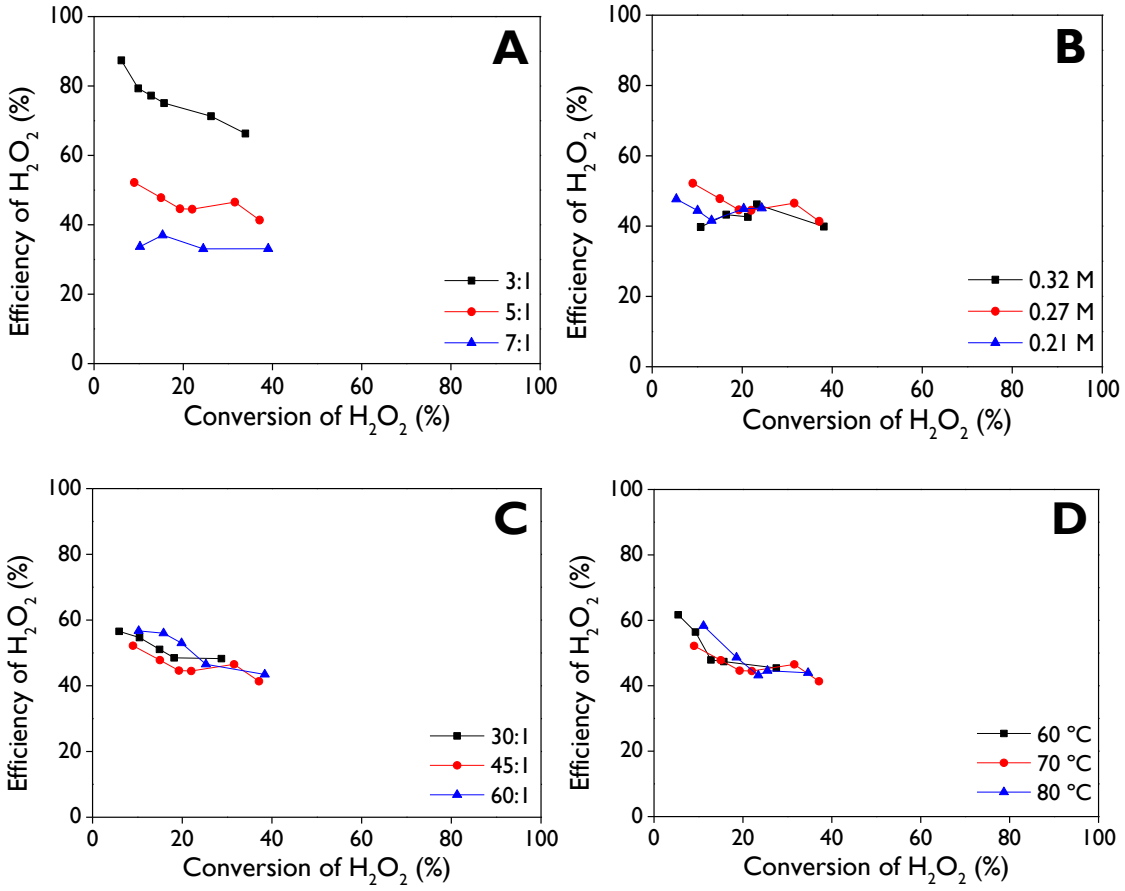

Figure 3.17. Efficiency of H_2O_2: **(A)** effect of the H_2O_2/limonene molar ratio, **(B)** effect of the limonene initial concentration, **(C)** effect of the catalyst (mg): limonene (mmol) ratio, and **(D)** effect of the reaction temperature. The reaction conditions were reported in the labels of **Figure 3.12** to **Figure 3.15**.

3.4.4. Catalyst Stability

The robustness of the KSnHYD2 catalyst was investigated through reusability and leaching tests. The reuse of the catalyst was tested in the reaction after washing with acetone and regenerating the spent catalyst at 550 °C. The profiles of limonene conversion are shown in **Figure 3.18.A**. The results demonstrated conversion of ca. 68% with the reuse run after 24 h, which is slightly lower than the fresh run, corresponding to 80%. This loss of activity can be explained by the leaching test. When the catalyst was removed after 4 h of the reaction medium by the hot-filtration method and the reaction was allowed to continue, an increase of ca. 11% in conversion was obtained after 24 h. Therefore, there is a slight leaching of Sn into the reaction medium. However, the main contribution to the reaction is through heterogeneous catalysis, as depicted in the profile with the fresh run reaching high conversions compared to the leaching test.

Selectivity to total monoepoxides (**Figure 3.18.B**) looks very similar for fresh and reuse runs, although its value decays significantly when the catalyst is removed, which makes sense considering the heterogeneous catalytic nature of the reaction. Regeneration of the spent catalyst by calcination was required because TPO-MS results (**Figure 3.18.C** and **Figure 3.18.D**) confirmed coke formation, specifically a peak at 256 °C is associated with soft coke, while two peaks associated with hard coke were observed at 432 and 524 °C [102]. Similar results were obtained for the TPO-MS analysis of the spent SnHYD1 (**Figure 8.66**), spent

SnHYD2 (**Figure 8.67**), and KSnHYD1 (**Figure 8.68**). Once the catalyst was regenerated, no signals were observed by TPO-MS, showing the success of the procedure (**Figure 8.69**). Furthermore, around 5.5 wt.% of coke formed on the surface of spent KSnHYD2 was estimated from the TGA analysis (**Figure 3.18.E**).

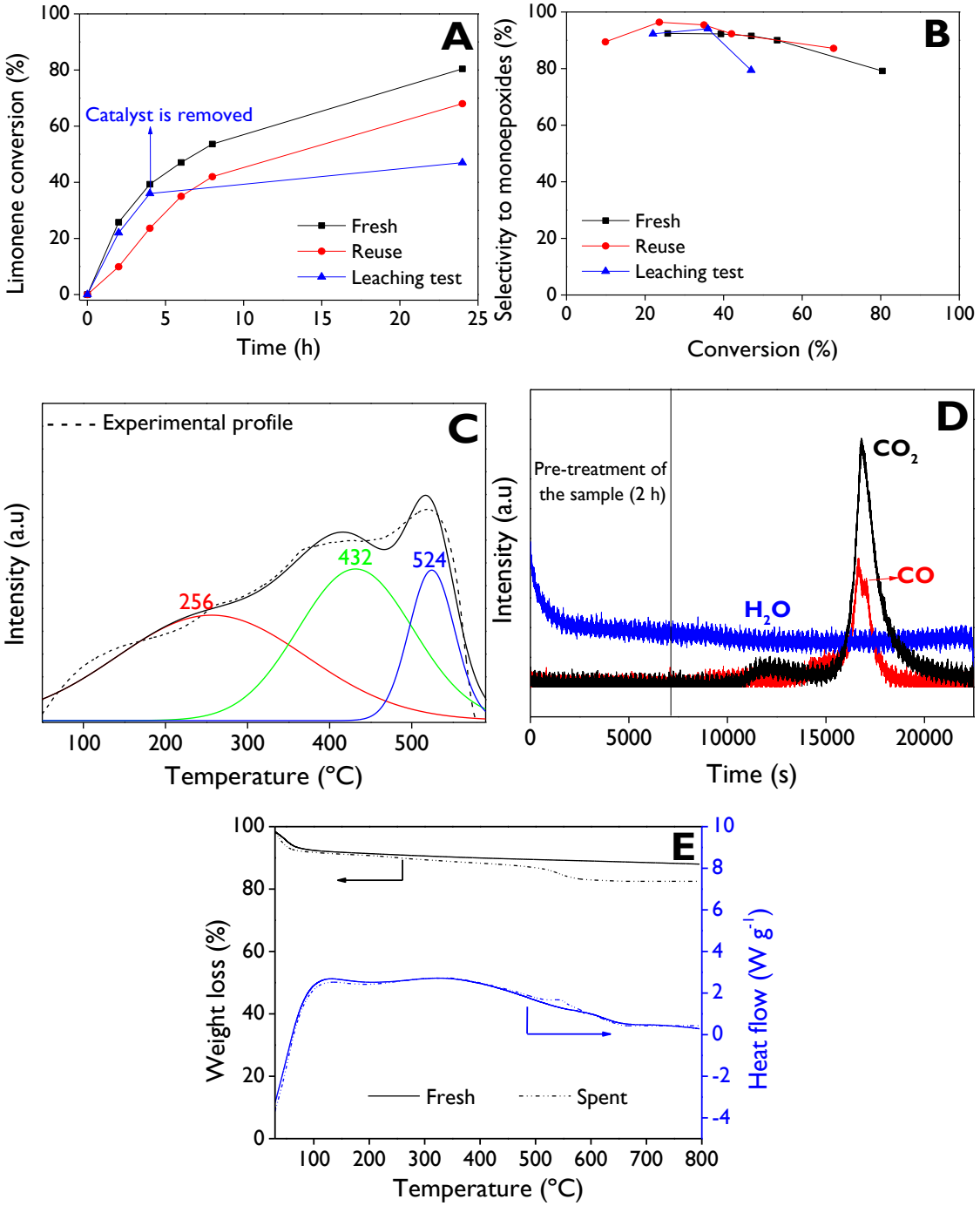

Figure 3.18. (A) Limonene conversion as a function of time, **(B)** Selectivity to monoepoxides as a function of conversion, **(C)** O_2-TPO profile for spent KSnHYD2 catalyst, **(D)** *In-situ* mass spectrometry coupled with TPO, **(E)** TGA analysis for the fresh and spent KSnHYD2 catalysts.

3.4.5. Reaction pathway

A plausible reaction pathway for the epoxidation of R-(+)-limonene with H_2O_2 is proposed in **Figure 3.19**. Three different active sites (AS1, AS2, and AS3) **(1)** are suggested based on a

previous report that identified similar sites [103]. Although the presence of silanol (AS3) and internal siloxane groups is typical, they lack sufficient acidic strength to address the reaction. Consequently, the most active sites are the superficial Sn-OH groups (AS1), which exhibit lower steric hindrance than the Sn network (AS2). Therefore, AS1 was chosen as the active site for proposing the reaction pathway. Initially, acetonitrile is adsorbed in AS1 **(2),** followed by the adsorption of hydrogen peroxide **(3).** The catalyst assists in the formation of peroxyacetimidic acid as an epoxidizing agent through hydrogen bonding [49,104] **(4).** Then, limonene is adsorbed onto either the internal or external double bond **(5)** and undergoes a concerted epoxidation with a syn addition-type, producing limonene monoepoxide (1,2 or 8,9). It is important to note that when H_2O_2 cedes the oxygen for the epoxidation, water is produced. Subsequently, the catalyst is regenerated, along with the solvent **(6).** It is noteworthy that **Figure 3.19** represents the mechanistic scheme of the epoxidation of limonene by the internal double bond, producing limonene-1,2-epoxide. The pathway for the diepoxide is essentially the same, but in stage (5), the corresponding monoepoxide is adsorbed to produce diepoxide. Finally, limonene glycol is formed through the hydration of limonene-1,2-epoxide.

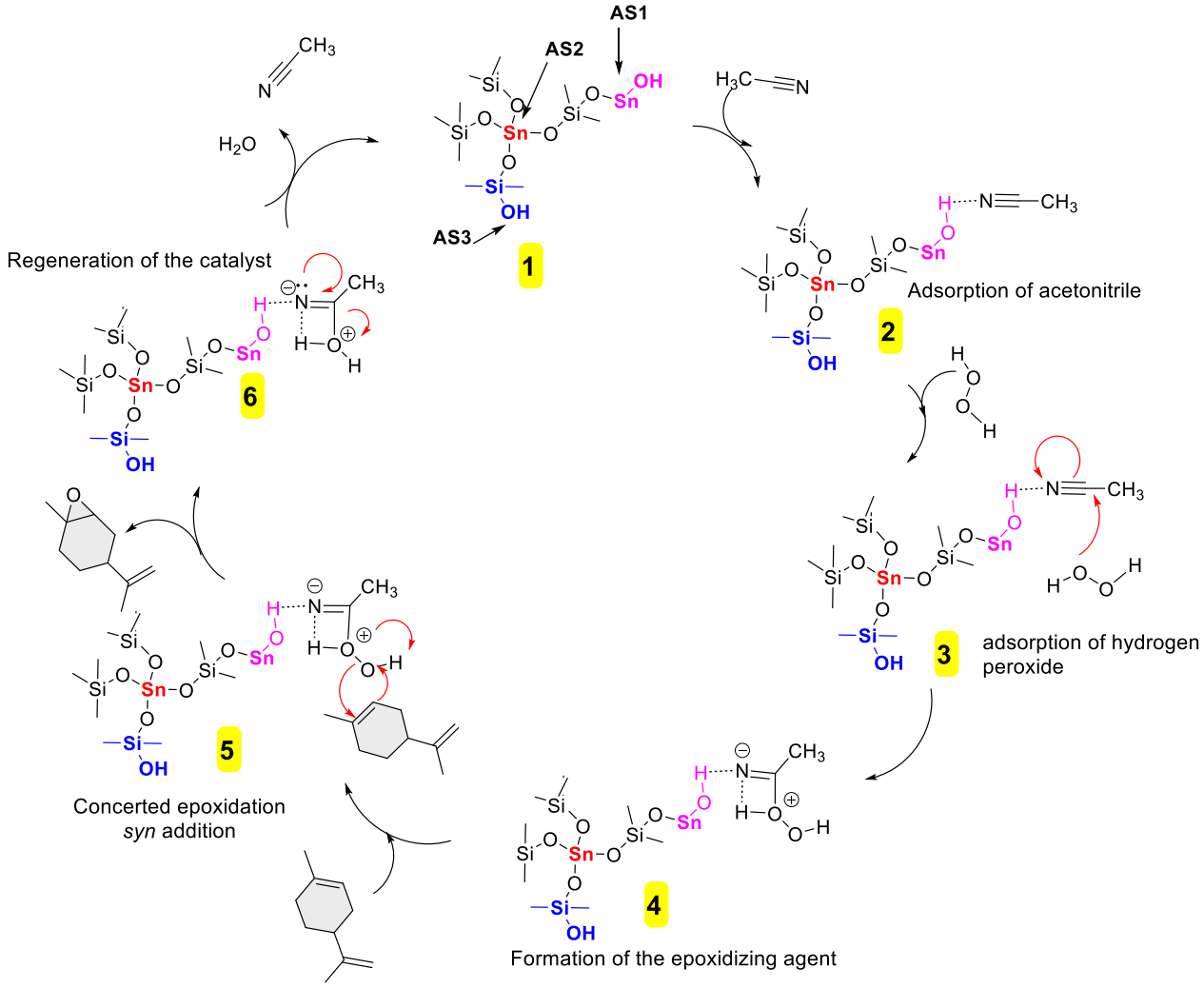

Figure 3.19. Plausible reaction pathway for the R-(+)-limonene epoxidation with H_2O_2.

3.5. Conclusions

Heterogeneous catalysts based on zeolite Y were successfully evaluated for the epoxidation of R-(+)-limonene, including parent, dealuminated, Sn-modified zeolite Y, and K-Sn-modified zeolite Y with a nominal SiO_2/Al_2O_3 ratio of 30. These epoxides have gained importance due to their use as excellent building blocks in the production of bio-polycarbonates, offering attractive thermal and optical properties and avoiding the need for commercially available polyurethanes that may require toxic isocyanates for their synthesis.

Sn was incorporated using the impregnation method with $SnCl_4 \cdot 5H_2O$ as the salt precursor, and modification with K was carried out through the alkaline ion exchange method using KCl. Ordered structures were observed in all materials by XRD, with no loss of crystallinity in the hierarchical catalysts due to the dealumination process with nitric acid. SnO and SnO_2 phases were detected in the materials with the highest Sn loading (SnHYD2 and KSnHYD2). The total surface area in the catalysts decreased as the Sn loading increased, as well as when K was incorporated, suggesting pore blocking by the metal species. No structural collapse due to dealumination was confirmed by TEM and SEM analysis. The Brønsted to Lewis acidity ratio increased in the order KSnHYD2 < SnHYD2 < KSnHYD1 < SnHYD1 < HYD < HY. The total acidity of the catalysts was directly correlated using NH_3-TPD and pyridine-FTIR, while no basicity was observed in the K-modified catalysts. Isolated Sn^{4+} species in tetrahedral coordination inside the mesoporous channels were observed only in materials with high Sn loadings, while extra-framework Sn species were observed in all catalysts. Al entities with four-coordinated framework and six-coordinated extra-framework were observed by NMR.

The highest initial reaction rate (3.1 mmol g^{-1} h^{-1}) and the highest turnover frequency (96.1 h^{-1}) were obtained with KSnHYD2 zeolite, exhibiting the lowest Brønsted to Lewis acidity ratio (0.1), the highest mesoporosity fraction (43%), and the lowest total surface area (465 m^2 g^{-1}). However, no direct relationship was observed with the total surface area. The parent and dealuminated zeolites exhibited low catalytic activity, as reflected in the reaction rate and TOF. Limonene conversion increased with a higher H_2O_2/limonene molar ratio or temperature, but the opposite effect was observed for the selectivity to limonene-1,2-epoxides, indicating a preference for their hydration towards limonene diol under those conditions. Additionally, conversion was positively affected by the initial concentration of the substrate, although selectivity to the main products did not change significantly. The activation energy for the R-(+)-limonene epoxidation was estimated to be 38.1 kJ mol^{-1}. The solvent played a critical role in the epoxidation route, showing a preference for aprotic polar solvents with high polarity and medium donor capacity, such as acetonitrile, and to a lesser extent, ethyl acetate.

The efficiency of H_2O_2 in the epoxidation reaction reached maximum values of up to 85% when employing low H_2O_2/limonene molar ratios (3:1). However, a weak dependence was observed with other parameters such as temperature, initial concentration of limonene, and the catalyst amount. The activation energy for the H_2O_2 decomposition was estimated in 45.3 kJ mol^{-1}. A coke layer, constituting 5.5 wt.%, formed on the catalyst surface after reaction at 70 °C. Regeneration was achieved through calcination at 550 °C. The regenerated catalyst was reused in the limonene epoxidation, demonstrating a conversion loss of ca. 12% after 24 h of the reaction, attributed to slight Sn leaching of the catalyst into the reaction medium. In summary, valuable insights have been gained into the intricate correlation between the structure and catalytic activity of heterogeneous catalysts prepared based on hierarchical zeolite Y, which are easily synthesized being also rather robust. Moreover, these materials

produced high limonene conversion (> 80%) and high selectivity to monoepoxides (> 90%) under different conditions, surpassing the results reported previously in the literature with many heterogeneous catalysts. Those catalysts often showed a competitive transformation between epoxidation (to monoepoxides as well as diepoxides), hydration, and the allylic route.

3.6. Acknowledgments

The authors thank the Universidad de Antioquia for providing financial resources for this work through the project 2022-53000: "Transformation of monoterpenes through one-pot reactions over heterogeneous catalysts", as part of the 2021-2022 Programmatic Call: Engineering and Technology. They also thank the Foundation for the Promotion of Research and Technology, project 2022-56550. Additionally, Luis A. Gallego-Villada is grateful to the Universidad de Antioquia for supporting his Ph.D. studies through the "Beca Doctoral Universidad de Antioquia" scholarship. The authors would like to express their gratitude to Dr. Julián Sánchez for his valuable advice on the reaction pathway.

3.7. References

[1] C.H. Bartholomew, R.J. Farrauto, Fundamentals of Industrial Catalytic Processes, 1997.

[2] G. Aguirre-Cruz, F. Legorreta-Garcia, G. Aguirre-Cruz, L. Stanciu, G. Aguirre-Alvarez, Synthesis of hierarchical silica zeolites for heterogenous catalysis and adsorption, Microporous Mesoporous Mater. 345 (2022) 112274. https://doi.org/10.1016/j.micromeso.2022.112274.

[3] T. Maesen, The Zeolite Scene - An Overview, in: J. Cejka, H. Van Bekkum, A. Corma, F. Schüth (Eds.), Introd. to Zeolite Sci. Pract., 3rd ed., Elsevier, 2007: p. 455.

[4] L.B. McCusker, C. Baerlocher, Zeolite Structures, in: J. Cejka, H. Van Bekkum, A. Corma, F. Schüth (Eds.), Stud. Surf. Sci. Catal., 3rd ed., Elsevier, 2007: pp. 13–37. https://doi.org/10.1016/S0167-2991(07)80790-7.

[5] R. Srivastava, Synthesis and applications of ordered and disordered mesoporous zeolites: Present and future prospective, Catal. Today. 309 (2018) 172–188. https://doi.org/10.1016/j.cattod.2017.08.017.

[6] B.K. Singh, Y. Kim, S. Kwon, K. Na, Synthesis of Mesoporous Zeolites and Their Opportunities in Heterogeneous Catalysis, Catalysts. 11 (2021) 1541. https://doi.org/10.3390/catal11121541.

[7] J. Liu, H. Zhang, N. Lu, X. Yan, B. Fan, R. Li, Influence of Acidity of Mesoporous ZSM-5-Supported Pt on Naphthalene Hydrogenation, Ind. Eng. Chem. Res. 59 (2020) 1056–1064. https://doi.org/10.1021/acs.iecr.9b04411.

[8] T. Weissenberger, R. Leonhardt, B.A. Zubiri, M. Pitínová-Štekrová, T.L. Sheppard, B. Reiprich, J. Bauer, R. Dotzel, M. Kahnt, A. Schropp, C.G. Schroer, J. Grunwaldt, J.L. Casci, J. Čejka, E. Spiecker, W. Schwieger, Synthesis and Characterisation of Hierarchically Structured Titanium Silicalite-1 Zeolites with Large Intracrystalline Macropores, Chem. – A Eur. J. 25 (2019) 14430–14440. https://doi.org/10.1002/chem.201903287.

[9] V. Smeets, E.M. Gaigneaux, D.P. Debecker, Hierarchical micro-/macroporous TS-1 zeolite epoxidation catalyst prepared by steam assisted crystallization, Microporous

Mesoporous Mater. 293 (2020) 109801. https://doi.org/10.1016/j.micromeso.2019.109801.

[10] S.P. Nandala, A. Tallam, N. Roy Choudhary, S. Sundergopal, S.K. Bhargava, Design and optimization of multilayer composite membrane for biomethane enrichment: Process simulations and economics, Sep. Purif. Technol. 319 (2023) 124073. https://doi.org/10.1016/j.seppur.2023.124073.

[11] R. Wijiyanti, I.S. Caralin, A.R. Widyanto, T. Gunawan, Z.A. Karim, A.F. Ismail, M. Nomura, N. Widiastuti, Evaluation of different carbon-modified zeolite derivatives preparation methods as a filler in mixed matrix membrane on their gas separation performance, Microporous Mesoporous Mater. 359 (2023) 112650. https://doi.org/10.1016/j.micromeso.2023.112650.

[12] B. Yu, H. Deng, Y. Lu, T. Pan, W. Shan, H. He, Adsorptive interaction between typical VOCs and various topological zeolites: Mixture effect and mechanism, J. Environ. Sci. 136 (2024) 626–636. https://doi.org/10.1016/j.jes.2023.02.015.

[13] Y. Tadayon, M.E. Bahrololoom, S. Javadpour, An experimental study of sunflower seed husk and zeolite as adsorbents of Ni(II) ion from industrial wastewater, Water Resour. Ind. 30 (2023) 100214. https://doi.org/10.1016/j.wri.2023.100214.

[14] A.M. Alotaibi, A.F. Ismail, E.S. Aziman, Ultra-effective modified clinoptilolite adsorbent for selective thorium removal from radioactive residue, Sci. Rep. 13 (2023) 9316. https://doi.org/10.1038/s41598-023-36487-5.

[15] W. Liu, X. Liu, Y. Gu, Y. Liu, Z. Yu, Y. Lyu, Y. Tian, A new composite consisting of Y zeolite and ZrO2 for fluid catalytic cracking reaction, Compos. Part B Eng. 200 (2020) 108317. https://doi.org/10.1016/j.compositesb.2020.108317.

[16] K. Wang, F. Wang, Y. Zhai, J. Wang, X. Zhang, M. Li, L. Jiang, X. Fan, C. Bing, J. Zhang, X. Zhang, Application of zeolite in Beckmann rearrangement of cyclohexanone oxime, Mol. Catal. 535 (2023) 112881. https://doi.org/10.1016/j.mcat.2022.112881.

[17] S.-W. Cao, P. Xiao, J. Wang, Y. Sun, Y.-S. Shang, Y.-F. Ge, Q. Liu, Y.-J. Gong, G. Mo, Z.-H. Li, Active precursor promoting nucleation/growth of MWW zeolite and controlling its morphology, Pet. Sci. 20 (2023) 1922–1933. https://doi.org/10.1016/j.petsci.2023.01.005.

[18] A.A. Zaidi, A. Khan, H. AlMohamadi, M.W. Anjum, I. Ali, S.R. Naqvi, S. Kokuryo, K. Miyake, N. Nishiyama, Catalytic pyrolysis of rice husk over defect-rich beta zeolites for biofuel production, Fuel. 348 (2023) 128624. https://doi.org/10.1016/j.fuel.2023.128624.

[19] Q. Deng, H. Peng, Z. Yang, T. Wang, J. Wang, Z. Zeng, S. Dai, A one-pot synthesis of high-density biofuels through bifunctional mesoporous zeolite-encapsulated Pd catalysts, Appl. Catal. B Environ. 337 (2023) 122982. https://doi.org/10.1016/j.apcatb.2023.122982.

[20] W. Hunsiri, N. Chaihad, C. Ngamcharussrivichai, D.N. Tungasmita, P. Reubroycharoen, N. Hinchiranan, Branched-chain biofuels derived from hydroisomerization of palm olein using Ni/modified beta zeolite catalysts for biojet fuel production, Fuel Process. Technol. 248 (2023) 107825. https://doi.org/10.1016/j.fuproc.2023.107825.

[21] G. Papanikolaou, D. Chillè, S. Perathoner, G. Centi, M. Migliori, G. Giordano, P. Lanzafame, Use of zeolites in green chemicals and bio-fuel production via HMF valorisation, Microporous Mesoporous Mater. 358 (2023) 112330. https://doi.org/10.1016/j.micromeso.2022.112330.

[22] Z. Vajglová, N. Kumar, P. Mäki-Arvela, K. Eränen, M. Peurla, L. Hupa, M. Nurmi, M. Toivakka, D.Y. Murzin, Synthesis and Physicochemical Characterization of Shaped Catalysts of β and Y Zeolites for Cyclization of Citronellal, Ind. Eng. Chem. Res. 58 (2019) 18084–18096. https://doi.org/10.1021/acs.iecr.9b02829.

[23] P. Mäki-Arvela, I. Simakova, Z. Vajglová, D.Y. Murzin, One-Pot Synthesis of Menthol from Citral and Citronellal Over Heterogeneous Catalysts, Catal. Surv. from Asia. 27 (2023) 2–19. https://doi.org/10.1007/s10563-022-09376-6.

[24] M. Laluc, R. Barakov, P. Mäki-Arvela, N. Shcherban, D.Y. Murzin, Catalytic activity of hierarchical beta zeolites in the Prins cyclization of (−)-isopulegol with acetone, Appl. Catal. A Gen. 618 (2021) 118131. https://doi.org/10.1016/j.apcata.2021.118131.

[25] R. Barakov, N. Shcherban, P. Mäki-Arvela, P. Yaremov, I. Bezverkhyy, J. Wärnå, D.Y. Murzin, Hierarchical Beta Zeolites As Catalysts in α-Pinene Oxide Isomerization, ACS Sustain. Chem. Eng. 10 (2022) 6642–6656. https://doi.org/10.1021/acssuschemeng.2c00441.

[26] N. Shcherban, R. Barakov, B. Lasne, P. Mäki-Arvela, M. Shamzhy, I. Bezverkhyy, J. Wärnå, D.Y. Murzin, Florol synthesis via Prins cyclization over hierarchical beta zeolites, Mol. Catal. 531 (2022) 112683. https://doi.org/10.1016/j.mcat.2022.112683.

[27] B. Lasne, P. Mäki-Arvela, A. Aho, Z. Vajglova, K. Eränen, N. Kumar, J.E. Sánchez-Velandia, M. Peurla, C. Mondelli, J. Pérez-Ramírez, D.Y. Murzin, Synthesis of Florol via Prins cyclization over heterogeneous catalysts, J. Catal. 405 (2022) 288–302. https://doi.org/10.1016/j.jcat.2021.12.008.

[28] I. , Future Market Insights, Fine Chemicals Market Outlook (2023 to 2033), (2023). https://www.futuremarketinsights.com/reports/fine-chemicals-market (accessed July 14, 2023).

[29] R.A. Sheldon, M.L. Bode, S.G. Akakios, Metrics of green chemistry: Waste minimization, Curr. Opin. Green Sustain. Chem. 33 (2022) 100569. https://doi.org/10.1016/j.cogsc.2021.100569.

[30] Knoema, Citrus fruit production by country, (2021). https://knoema.com/atlas/topics/Agriculture/Crops-Production-Quantity-tonnes/Citrus-fruit-production (accessed July 19, 2023).

[31] S. Suri, A. Singh, P.K. Nema, Current applications of citrus fruit processing waste: A scientific outlook, Appl. Food Res. 2 (2022) 100050. https://doi.org/10.1016/j.afres.2022.100050.

[32] E. Louisy, V. Khodyrieva, S. Olivero, V. Michelet, A. Mija, Use of Limonene Epoxides and Derivatives as Promising Monomers for Biobased Polymers, Chempluschem. 87 (2022) 1–9. https://doi.org/10.1002/cplu.202200190.

[33] J.R. Ayala, G. Montero, M.A. Coronado, C. García, M.A. Curiel-Alvarez, J.A. León, C.A.

Sagaste, D.G. Montes, Characterization of Orange Peel Waste and Valorization to Obtain Reducing Sugars, Molecules. 26 (2021) 1348. https://doi.org/10.3390/molecules26051348.

[34] S. Nikfar, A.F. Behboudi, Limonene, in: Encycl. Toxicol., Elsevier, 2014: pp. 78–82. https://doi.org/10.1016/B978-0-12-386454-3.00628-X.

[35] O. Hauenstein, S. Agarwal, A. Greiner, Bio-based polycarbonate as synthetic toolbox, Nat. Commun. 7 (2016) 11862. https://doi.org/10.1038/ncomms11862.

[36] O. Hauenstein, M. Reiter, S. Agarwal, B. Rieger, A. Greiner, Bio-based polycarbonate from limonene oxide and CO2 with high molecular weight, excellent thermal resistance, hardness and transparency, Green Chem. 18 (2016) 760–770. https://doi.org/10.1039/C5GC01694K.

[37] V. Schimpf, B.S. Ritter, P. Weis, K. Parison, R. Mülhaupt, High Purity Limonene Dicarbonate as Versatile Building Block for Sustainable Non-Isocyanate Polyhydroxyurethane Thermosets and Thermoplastics, Macromolecules. 50 (2017) 944–955. https://doi.org/10.1021/acs.macromol.6b02460.

[38] T. Stößer, C. Li, J. Unruangsri, P.K. Saini, R.J. Sablong, M.A.R. Meier, C.K. Williams, C. Koning, Bio-derived polymers for coating applications: comparing poly(limonene carbonate) and poly(cyclohexadiene carbonate), Polym. Chem. 8 (2017) 6099–6105. https://doi.org/10.1039/C7PY01223C.

[39] S. Kernbichl, B. Rieger, Aliphatic polycarbonates derived from epoxides and CO2: A comparative study of poly(cyclohexene carbonate) and poly(limonene carbonate), Polymer (Guildf). 205 (2020) 122667. https://doi.org/10.1016/j.polymer.2020.122667.

[40] S. Neumann, S.B. Däbritz, S.E. Fritze, L.-C. Leitner, A. Anand, A. Greiner, S. Agarwal, Sustainable block copolymers of poly(limonene carbonate), Polym. Chem. 12 (2021) 903–910. https://doi.org/10.1039/D0PY01685C.

[41] A. Rehman, A.M. López Fernández, M.F.M. Gunam Resul, A. Harvey, Highly selective, sustainable synthesis of limonene cyclic carbonate from bio-based limonene oxide and CO2: A kinetic study, J. CO2 Util. 29 (2019) 126–133. https://doi.org/10.1016/j.jcou.2018.12.001.

[42] K.A. Maltby, M. Hutchby, P. Plucinski, M.G. Davidson, U. Hintermair, Selective Catalytic Synthesis of 1,2- and 8,9-Cyclic Limonene Carbonates as Versatile Building Blocks for Novel Hydroxyurethanes, Chem. – A Eur. J. 26 (2020) 7405–7415. https://doi.org/10.1002/chem.201905561.

[43] V.M. Vaschetti, G.A. Eimer, A.L. Cánepa, S.G. Casuscelli, Catalytic performance of V-MCM-41 nanocomposites in liquid phase limonene oxidation: Vanadium leaching mitigation, Microporous Mesoporous Mater. 311 (2021) 110678. https://doi.org/10.1016/j.micromeso.2020.110678.

[44] A. Wróblewska, J. Serafin, A. Gawarecka, P. Miądlicki, K. Urbaś, Z.C. Koren, J. Llorca, B. Michalkiewicz, Carbonaceous catalysts from orange pulp for limonene oxidation, Carbon Lett. 30 (2020) 189–198. https://doi.org/10.1007/s42823-019-00084-2.

[45] A. Wróblewska, M. Malko, M. Walasek, Environmental friendly method of the

epoxidation of limonene with hydrogen peroxide over the Ti-SBA-15 catalyst, Polish J. Chem. Technol. 20 (2018) 6–12. https://doi.org/10.2478/pjct-2018-0047.

[46] V.M. Vaschetti, A.L. Cánepa, D. Barrera, K. Sapag, G.A. Eimer, S.G. Casuscelli, Limonene oxyfunctionalization over Cu-modified silicates employing hydrogen peroxide and t-Butyl hydroperoxide: Reaction pathway analysis, Mol. Catal. 481 (2020) 110234. https://doi.org/10.1016/j.mcat.2018.11.005.

[47] D.K. Parmar, P.M. Butani, N.J. Thumar, P.M. Jasani, R. V. Padaliya, P.R. Sandhiya, H.D. Nakum, M.N. Khan, D. Makwana, Oxy-functionalization of olefins with neat and heterogenized binuclear V(IV)O and Fe(II) complexes: Effect of steric hindrance on product selectivity and output in homogeneous and heterogeneous phase, Mol. Catal. 474 (2019) 110424. https://doi.org/10.1016/j.mcat.2019.110424.

[48] Y. Wang, F. Gayet, P. Guillo, D. Agustin, Organic Solvent-Free Olefins and Alcohols (ep)oxidation Using Recoverable Catalysts Based on [PM12O40]3− (M = Mo or W) Ionically Grafted on Amino Functionalized Silica Nanobeads, Materials (Basel). 12 (2019) 3278. https://doi.org/10.3390/ma12203278.

[49] L.A. Gallego-Villada, E.A. Alarcón, A.L. Villa, Versatile Heterogeneous Catalytic System for the Selective Synthesis of Limonene Epoxide and Diepoxide, Ind. Eng. Chem. Res. 62 (2023) 20152–20169. https://doi.org/10.1021/acs.iecr.3c02633.

[50] Y. Tao, O. De Luca, B. Singh, A.J. Kamphuis, J. Chen, P. Rudolf, P.P. Pescarmona, WO3–SiO2 nanomaterials synthesized using a novel template-free method in supercritical CO2 as heterogeneous catalysts for epoxidation with H2O2, Mater. Today Chem. 18 (2020) 100373. https://doi.org/10.1016/j.mtchem.2020.100373.

[51] W. Lueangchaichaweng, B. Singh, D. Mandelli, W.A. Carvalho, S. Fiorilli, P.P. Pescarmona, High surface area, nanostructured boehmite and alumina catalysts: Synthesis and application in the sustainable epoxidation of alkenes, Appl. Catal. A Gen. 571 (2019) 180–187. https://doi.org/10.1016/j.apcata.2018.12.017.

[52] C. Bisio, A. Gallo, R. Psaro, C. Tiozzo, M. Guidotti, F. Carniato, Tungstenocene-grafted silica catalysts for the selective epoxidation of alkenes, Appl. Catal. A Gen. 581 (2019) 133–142. https://doi.org/10.1016/j.apcata.2019.05.027.

[53] D. Hu, X. Song, S. Wu, X. Yang, H. Zhang, X. Chang, M. Jia, Solvothermal synthesis of Co-substituted phosphomolybdate acid encapsulated in the UiO-66 framework for catalytic application in olefin epoxidation, Chinese J. Catal. 42 (2021) 356–366. https://doi.org/10.1016/S1872-2067(20)63665-8.

[54] T.R. Amarante, P. Neves, F.A. Almeida Paz, A.C. Gomes, M. Pillinger, A.A. Valente, I.S. Gonçalves, Heterogeneous catalysis with an organic–inorganic hybrid based on MoO 3 chains decorated with 2,2′-biimidazole ligands, Catal. Sci. Technol. 11 (2021) 2214–2228. https://doi.org/10.1039/D1CY00055A.

[55] S.R. Leandro, A.C. Mourato, U. Łapińska, O.C. Monteiro, C.I. Fernandes, P.D. Vaz, C.D. Nunes, Exploring bulk and colloidal Mg/Al hydrotalcite–Au nanoparticles hybrid materials in aerobic olefin epoxidation, J. Catal. 358 (2018) 187–198. https://doi.org/10.1016/j.jcat.2017.12.014.

[56] M. Fadaei Sarabi, A. Bezaatpour, A. Mahmoudi, Anchoring of a terpyridine-based Mo(VI) complex on manganese ferrite as a recoverable catalyst for epoxidation of olefins under solvent-free conditions, J. Coord. Chem. 74 (2021) 1597–1612. https://doi.org/10.1080/00958972.2021.1904507.

[57] M.S. Nunes, D.M. Gomes, A.C. Gomes, P. Neves, R.F. Mendes, F.A.A. Paz, A.D. Lopes, A.A. Valente, I.S. Gonçalves, M. Pillinger, A 5-(2-Pyridyl)tetrazolate Complex of Molybdenum(VI), Its Structure, and Transformation to a Molybdenum Oxide-Based Hybrid Heterogeneous Catalyst for the Epoxidation of Olefins, Catalysts. 11 (2021) 1407. https://doi.org/10.3390/catal11111407.

[58] J. Marreiros, M. Diaz-Couce, M.J. Ferreira, P.D. Vaz, M.J. Calhorda, C.D. Nunes, Synthesis and catalytic activity of Mo(II) complexes of α-diimines intercalated in layered double hydroxides, Inorganica Chim. Acta. 486 (2019) 274–282. https://doi.org/10.1016/j.ica.2018.10.062.

[59] D.P. Gomes, A.F. Silva, A.C. Gomes, P. Neves, A.A. Valente, I.S. Gonçalves, M. Pillinger, Epoxidation catalysts prepared by encapsulation of molybdenum hexacarbonyl in UiO-66(Zr/Hf)-type metal-organic frameworks, Microporous Mesoporous Mater. 330 (2022) 111603. https://doi.org/10.1016/j.micromeso.2021.111603.

[60] H. Zhang, X. Lu, L. Yang, Y. Hu, M. Yuan, C. Wang, Q. Liu, F. Yue, D. Zhou, Q. Xia, Efficient air epoxidation of cycloalkenes over bimetal-organic framework ZnCo-MOF materials, Mol. Catal. 499 (2021) 111300. https://doi.org/10.1016/j.mcat.2020.111300.

[61] S. Madadi, S. Kaliaguine, Activated Carbon-Supported Ruthenium as a Catalyst for the Solvent- and Initiator-Free Aerobic Epoxidation of Limonene, ACS Sustain. Chem. Eng. 9 (2021) 10557–10568. https://doi.org/10.1021/acssuschemeng.1c02597.

[62] S. Madadi, L. Charbonneau, J.-Y. Bergeron, S. Kaliaguine, Aerobic epoxidation of limonene using cobalt substituted mesoporous SBA-16 Part 1: Optimization via Response Surface Methodology (RSM), Appl. Catal. B Environ. 260 (2020) 118049. https://doi.org/10.1016/j.apcatb.2019.118049.

[63] A. Gottuso, A. Köckritz, M.L. Saladino, F. Armetta, C. De Pasquale, G. Nasillo, F. Parrino, Catalytic and photocatalytic epoxidation of limonene: Using mesoporous silica nanoparticles as functional support for a Janus-like approach, J. Catal. 391 (2020) 202–211. https://doi.org/10.1016/j.jcat.2020.08.025.

[64] L. Charbonneau, X. Foster, D. Zhao, S. Kaliaguine, Catalyst-Free Epoxidation of Limonene to Limonene Dioxide, ACS Sustain. Chem. Eng. 6 (2018) 5115–5121. https://doi.org/10.1021/acssuschemeng.7b04782.

[65] L. Charbonneau, S. Kaliaguine, Epoxidation of limonene over low coordination Ti in Ti-SBA-16, Appl. Catal. A Gen. 533 (2017) 1–8. https://doi.org/10.1016/j.apcata.2017.01.001.

[66] D.M. Gomes, P. Neves, M.M. Antunes, A.J.S. Fernandes, M. Pillinger, A.A. Valente, Post-Synthesis Strategies to Prepare Mesostructured and Hierarchical Silicates for Liquid Phase Catalytic Epoxidation, Catalysts. 12 (2022) 1513. https://doi.org/10.3390/catal12121513.

[67] E. Niño-Arrieta, A.L. Villa-Holguín, E.A. Alarcón-Durango, A. Talavera-López, S.A. Gómez-Torres, G.A. Fuentes-Zurita, Limonene epoxidation in aqueous phase over TiKIT-6, Rev. Fac. Ing. Univ. Antioquia. (2018) 74–79. https://doi.org/10.17533/udea.redin.n88a08.

[68] P. Tao, X. Lu, H. Zhang, R. Jing, F. Huang, S. Wu, D. Zhou, Q. Xia, Enhanced activity of microwave-activated CoOx/MOR catalyst for the epoxidation of α-pinene with air, Mol. Catal. 463 (2019) 8–15. https://doi.org/10.1016/j.mcat.2018.11.006.

[69] J.M. Jimenez-Martin, A. Orozco-Saumell, H. Hernando, M. Linares, R. Mariscal, M. López Granados, A. García, J. Iglesias, Efficient Conversion of Glucose to Methyl Lactate with Sn-USY: Retro-aldol Activity Promotion by Controlled Ion Exchange, ACS Sustain. Chem. Eng. 10 (2022) 8885–8896. https://doi.org/10.1021/acssuschemeng.2c01987.

[70] L. Lutterotti, Total pattern fitting for the combined size–strain–stress–texture determination in thin film diffraction, Nucl. Instruments Methods Phys. Res. Sect. B Beam Interact. with Mater. Atoms. 268 (2010) 334–340. https://doi.org/10.1016/j.nimb.2009.09.053.

[71] C.A. Emeis, Determination of Integrated Molar Extinction Coefficients for Infrared Absorption Bands of Pyridine Adsorbed on Solid Acid Catalysts, J. Catal. 141 (1993) 347–354. https://doi.org/10.1006/jcat.1993.1145.

[72] F.P. Greenspan, D.G. MacKellar, Analysis of Aliphatic Per Acids, Anal. Chem. 20 (1948) 1061–1063. https://doi.org/10.1021/ac60023a020.

[73] IZA Structure Commission, FAU: Framework Type, (n.d.). https://europe.iza-structure.org/IZA-SC/framework.php?STC=FAU (accessed November 26, 2023).

[74] A. Mekki, A. Benmaati, A. Mokhtar, M. Hachemaoui, F. Zaoui, H. Habib Zahmani, M. Sassi, S. Hacini, B. Boukoussa, Michael Addition of 1,3-Dicarbonyl Derivatives in the Presence of Zeolite Y as an Heterogeneous Catalyst, J. Inorg. Organomet. Polym. Mater. 30 (2020) 2323–2334. https://doi.org/10.1007/s10904-019-01424-5.

[75] P. Mäki-Arvela, N. Kumar, S.F. Diáz, A. Aho, M. Tenho, J. Salonen, A. Leino, K. Kordás, P. Laukkanen, J. Dahl, I. Sinev, T. Salmi, D.Y. Murzin, Isomerization of β-pinene oxide over Sn-modified zeolites, J. Mol. Catal. A Chem. 366 (2013) 228–237. https://doi.org/10.1016/j.molcata.2012.09.028.

[76] M.A. Farrukh, H.B. Teck, R. Adnan, Surfactant-controlled aqueous synthesis of SnO2 nanoparticles via the hydrothermal and conventional heating methods, Turkish J. Chem. 34 (2010) 537–550. https://doi.org/10.3906/kim-1001-466.

[77] K.S.W. Sing, Reporting physisorption data for gas/solid systems with special reference to the determination of surface area and porosity (Recommendations 1984), Pure Appl. Chem. 57 (1985) 603–619. https://doi.org/10.1351/pac198557040603.

[78] V. Palomba, A. Frazzica, Modeling of sorption systems for thermal energy storage, in: Adv. Therm. Energy Storage Syst., Elsevier, 2021: pp. 453–475. https://doi.org/10.1016/B978-0-12-819885-8.00015-2.

[79] L.A. Gallego-Villada, E.A. Alarcón, A.L. Villa, Effect of Colombian raw materials on the Prins condensation reaction over Sn/MCM-41, Catal. Today. 372 (2021) 36–50.

https://doi.org/10.1016/j.cattod.2020.10.040.

[80] F. Arena, R. Dario, A. Parmaliana, A characterization study of the surface acidity of solid catalysts by temperature programmed methods, Appl. Catal. A Gen. 170 (1998) 127–137. https://doi.org/10.1016/S0926-860X(98)00041-6.

[81] P.Y. Dapsens, C. Mondelli, J. Pérez-Ramírez, Design of Lewis-acid centres in zeolitic matrices for the conversion of renewables, Chem. Soc. Rev. 44 (2015) 7025–7043. https://doi.org/10.1039/C5CS00028A.

[82] P. Wolf, C. Hammond, S. Conrad, I. Hermans, Post-synthetic preparation of Sn-, Ti- and Zr-beta: a facile route to water tolerant, highly active Lewis acidic zeolites, Dalt. Trans. 43 (2014) 4514. https://doi.org/10.1039/c3dt52972j.

[83] L.A. Gallego-Villada, E.A. Alarcón, A.L. Villa, Evaluation of nopol production obtained from turpentine oil over Sn/MCM-41 synthesized by wetness impregnation using the Central Composite Design, Mol. Catal. 498 (2020) 111250. https://doi.org/10.1016/j.mcat.2020.111250.

[84] W. Dai, Q. Lei, G. Wu, N. Guan, M. Hunger, L. Li, Spectroscopic Signature of Lewis Acidic Framework and Extraframework Sn Sites in Beta Zeolites, ACS Catal. 10 (2020) 14135–14146. https://doi.org/10.1021/acscatal.0c02356.

[85] M. Sánchez-Sánchez, R. van Grieken, D.P. Serrano, J.A. Melero, On the Sn(II) and Sn(IV) incorporation into the AFI-structured AlPO4-based framework: the first significantly acidic SnAPO-5, J. Mater. Chem. 19 (2009) 6833. https://doi.org/10.1039/b905057d.

[86] S. Li, A. Zheng, Y. Su, H. Fang, W. Shen, Z. Yu, L. Chen, F. Deng, Extra-framework aluminium species in hydrated faujasite zeolite as investigated by two-dimensional solid-state NMR spectroscopy and theoretical calculations, Phys. Chem. Chem. Phys. 12 (2010) 3895. https://doi.org/10.1039/b915401a.

[87] C.A. Fyfe, J.L. Bretherton, L.Y. Lam, Solid-State NMR Detection, Characterization, and Quantification of the Multiple Aluminum Environments in US-Y Catalysts by 27 Al MAS and MQMAS Experiments at Very High Field, J. Am. Chem. Soc. 123 (2001) 5285–5291. https://doi.org/10.1021/ja003210k.

[88] S.R. Batool, V.L. Sushkevich, J.A. van Bokhoven, Correlating Lewis acid activity to extra-framework aluminum species in zeolite Y introduced by Ion-exchange, J. Catal. 408 (2022) 24–35. https://doi.org/10.1016/j.jcat.2022.02.010.

[89] F. Deng, Y. Yue, C. Ye, Observation of Nonframework Al Species in Zeolite β by Solid-State NMR Spectroscopy, J. Phys. Chem. B. 102 (1998) 5252–5256. https://doi.org/10.1021/jp9801929.

[90] C.A. Fyfe, J.H. O'Brien, H. Strobl, Ultra-high resolution 29Si MAS NMR spectra of highly siliceous zeolites, Nature. 326 (1987) 281–283. https://doi.org/10.1038/326281a0.

[91] D.H. Brouwer, Applications of silicon-29 NMR spectroscopy, in: Compr. Inorg. Chem. III, Elsevier, 2023: pp. 107–137. https://doi.org/10.1016/B978-0-12-823144-9.00032-7.

[92] J.E. Sánchez-Velandia, J.A. Castañeda-Olarte, C.F. Imbachí-Gamba, F. Martínez-Ortega, A.L. Villa, Hydrolysis of Limonene Epoxide over Hierarchical Zeolites, Catal. Letters.

153 (2023) 150–166. https://doi.org/10.1007/s10562-022-03963-y.

[93] M.F.M. Gunam Resul, A.M. López Fernández, A. Rehman, A.P. Harvey, Development of a selective, solvent-free epoxidation of limonene using hydrogen peroxide and a tungsten-based catalyst, React. Chem. Eng. 3 (2018) 747–756. https://doi.org/10.1039/C8RE00094H.

[94] R. Barrera Zapata, A.L. Villa, C. Montes de Correa, Kinetic Modeling of Limonene Epoxidation over PW-Amberlite, Ind. Eng. Chem. Res. 48 (2009) 647–653. https://doi.org/10.1021/ie800822n.

[95] A.J. Bonon, Y.N. Kozlov, J.O. Bahú, R.M. Filho, D. Mandelli, G.B. Shul'pin, Limonene epoxidation with H2O2 promoted by Al2O3: Kinetic study, experimental design, J. Catal. 319 (2014) 71–86. https://doi.org/10.1016/j.jcat.2014.08.004.

[96] D.Y. Murzin, Solvent effects in catalysis: implementation for modelling of kinetics, Catal. Sci. Technol. 6 (2016) 5700–5713. https://doi.org/10.1039/C6CY00495D.

[97] V. Gutmann, Solvent effects on the reactivities of organometallic compounds, Coord. Chem. Rev. 18 (1976) 225–255. https://doi.org/10.1016/S0010-8545(00)82045-7.

[98] P.K. Chattopadhyay, B. Kratochvil, Ligand substitution kinetics of nickel(II) ion in N,N - dimethylformamide , Can. J. Chem. 55 (1977) 3449–3455. https://doi.org/10.1139/v77-483.

[99] D.R. Joshi, N. Adhikari, An Overview on Common Organic Solvents and Their Toxicity, J. Pharm. Res. Int. 28 (2019) 1–18. https://doi.org/10.9734/jpri/2019/v28i330203.

[100] C.L. Yaws, Yaws' Thermophysical Properties of Chemicals and Hydrocarbons, Electronic, Knovel, 2010. https://app.knovel.com/hotlink/toc/id:kpYTPCHE02/yaws-thermophysical-properties/yaws-thermophysical-properties.

[101] S. Murov, Properties of Solvents Used in Organic Chemistry, (2020). http://murov.info/orgsolvents.htm (accessed July 30, 2023).

[102] M. Díaz, E. Epelde, J. Valecillos, S. Izaddoust, A.T. Aguayo, J. Bilbao, Coke deactivation and regeneration of HZSM-5 zeolite catalysts in the oligomerization of 1-butene, Appl. Catal. B Environ. 291 (2021) 120076. https://doi.org/10.1016/j.apcatb.2021.120076.

[103] M. Boronat, P. Concepción, A. Corma, M. Renz, S. Valencia, Determination of the catalytically active oxidation Lewis acid sites in Sn-beta zeolites, and their optimisation by the combination of theoretical and experimental studies, J. Catal. 234 (2005) 111–118. https://doi.org/10.1016/j.jcat.2005.05.023.

[104] G. Casella, S. Carlotto, A.P.C. Ribeiro, L.M.D.R.S. Martins, The reaction of acetonitrile with hydrogen peroxide in alkaline medium: a DFT mechanistic study of green production of amides, Phys. Chem. Chem. Phys. 25 (2023) 22775–22781. https://doi.org/10.1039/D3CP02024J.

Chapter 4. Dendritic ZSM-5 Zeolites as Highly Active Catalysts for the Valorization of Monoterpene Epoxides

This chapter corresponds to an article published in ***Green Chemistry**, 2024, 27 – DOI: 10.1039/D4GC04003A.*

Luis A. Gallego-Villada[a,b,*], Jennifer Cueto[c], María del Mar Alonso-Doncel[c], Päivi Mäki-Arvela[a], Edwin A. Alarcón[b], David P. Serrano[c,d*], Dmitry Yu. Murzin[a,*]

a. Laboratory of Industrial Chemistry and Reaction Engineering, Johan Gadolin Process Chemistry Centre, Åbo Akademi University, Henriksgatan 2, 20500 Turku/ Åbo, Finland
b. Environmental Catalysis Research Group, Chemical Engineering Faculty, Universidad de Antioquia, Medellín, Colombia
c. Thermochemical Processes Unit, IMDEA Energy Institute, Avda. Ramón de la Sagra, 3, 28935, Móstoles, Madrid, Spain
d. Chemical and Environmental Engineering Group, Rey Juan Carlos University, c/Tulipán s/n, 28933, Móstoles, Madrid, Spain

* Corresponding author, e-mail address: alfonso.gallego@udea.edu.co (Luis A. Gallego-Villada), david.serrano@imdea.org (David P. Serrano), dmitry.murzin@abo.fi (Dmitry Yu. Murzin)

Graphical Abstract

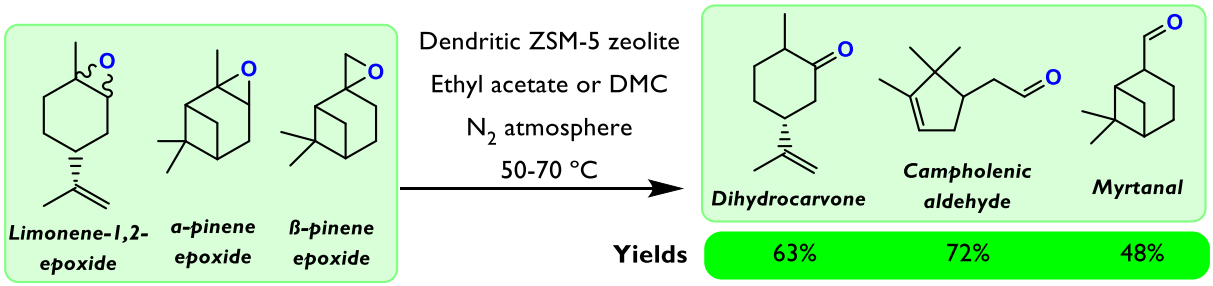

4.1. Abstract

Dendritic ZSM-5 zeolites were synthesized and investigated in the isomerization of monoterpene epoxides, including limonene-1,2-epoxide (LE), α-pinene epoxide, and β-pinene epoxide, which yields high-value compounds used in fragrances, cosmetics, and pharmaceuticals. The fresh catalysts were thoroughly characterized using XRD, Ar physisorption, pyridine-FTIR, TEM, FTIR/DTBPy, and ^{27}Al MAS NMR. In comparison with conventional and hierarchical ZSM-5 materials, the dendritic zeolite with a crystallization time of 4 days (d-ZSM-5/4d) was the most active material, with a turnover frequency value of 4.4 min^{-1} for LE isomerization. Likewise, remarkable yields of dihydrocarvone (DHC, 63%, 70 °C, 2 h), campholenic aldehyde (72.4%, 70 °C, 5 min), and myrtanal (47.7%, 50 °C, 5 min) were obtained with this material that exhibited the lowest Brønsted to Lewis acidity ratio (1.4) and the largest mesopore/external surface area (360 m^2 g^{-1}), also showing the narrowest mesopore size distribution. A direct relationship was observed between the TOF values and the concentration of external Brønsted acid sites, showing presence of strong steric/diffusional limitations that are greatly overcome with the dendritic zeolites. Lower reactivity of *trans*-LE compared to *cis*-LE was attributed to the larger steric hindrance of the oxygen atom. Exploration of the solvent influence revealed that the reaction rate of LE was favored by non-polar solvents, while highly selective DHC formation occurred in the solvents of medium polarity. The d-ZSM-5/4d sample was shown to be robust because catalytic activity could be completely recovered by air calcination.

Keywords: Dendritic Zeolite, ZSM-5, Isomerization, Monoterpene Epoxides, Dihydrocarvone.

4.2. Introduction

The valorization of renewable feedstock has particularly attracted a lot of attention as one of the main areas of chemistry for the production of a wide range of valuable chemicals [1–4], searching always for greener systems to contribute to the twelve principles of Green Chemistry [5]. Among various feedstock, terpenoids constitute one of the most numerous and structurally diverse natural products, which can be extracted by distillation such as α- and β-pinene from turpentine oil, but also utilizing mechanical treatment such as limonene from the peels of citrus fruits [6–8]. Selective partial oxidation of these platform molecules has been widely investigated through two well-known routes: allylic oxidation involving often free-radical pathways [9,10], and the epoxidation of the double carbon-carbon bond to obtain the corresponding cyclic ether [11–18]. Synthesis of monoterpene epoxides like limonene-1,2-epoxide (LE) presents an enormous significance because these are intermediates for the production of bio-based polymers [19–21] or can be transformed, often by isomerization (**Figure 4.1**), into a series of important chemicals used in fragrances, cosmetics, and pharmaceuticals such as dihydrocarvone (DHC) and carveol [22,23]. DHC is a monoterpenoid compound that can be naturally found in caraway oil, being a key building block to synthesize sesquiterpenes [24,25]. It can be used in the synthesis of i) dispiro 1,2,4,5-tetraoxanes, which show potent anti-malarial activity [26], ii) an epoxylactone, which can undergo copolymerization with ε-caprolactone to form cross-linked copolymers with shape memory properties [25], and iii) α-cyperone, which is a eudesmane type sesquiterpenoid compound with potent insecticidal activity [27].

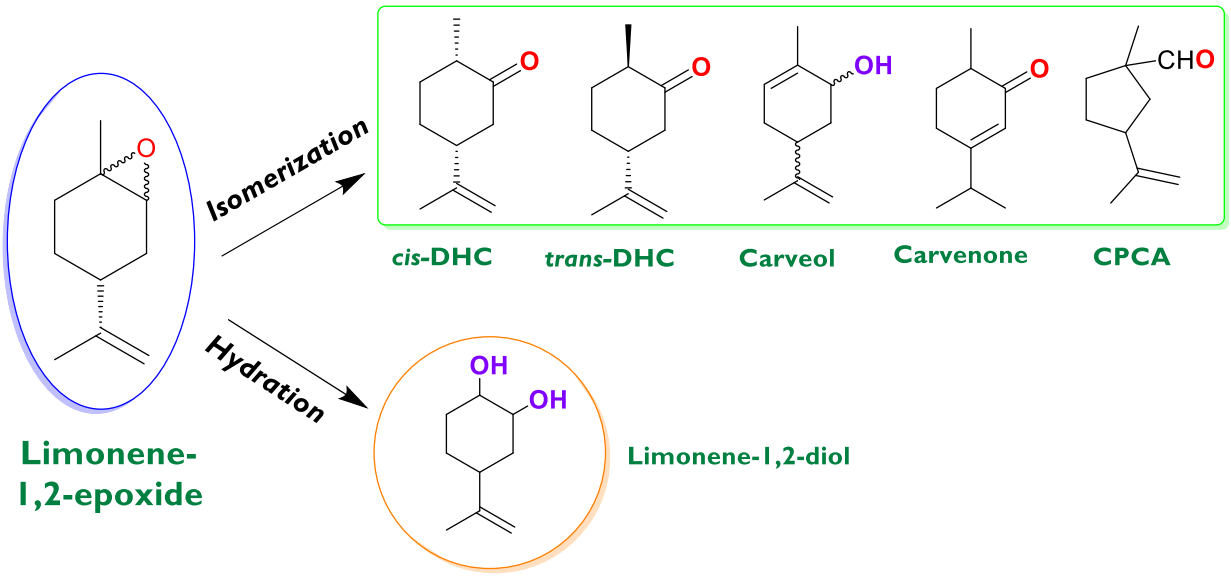

Figure 4.1. Transformation of limonene-1,2-epoxide into *cis*-dihydrocarvone (*cis*-DHC), *trans*-dihydrocarvone (*trans*-DHC), carveol, carvenone, cyclopentyl-carboxaldehyde (CPCA), and (1*S*,2*S*,4*R*)-limonene-1,2-diol.

There is considerable recent literature on the development of efficient heterogeneous catalytic systems for the isomerization of α-pinene [28–37] and β-pinene [38,39] epoxides, including also some homogeneous ones [40–43]. These studies have mainly focused on the production of campholenic aldehyde and myrtanal, respectively. However, there is a noticeable research gap regarding selective heterogeneous catalysts for the synthesis of DHC via the isomerization of internal limonene epoxide (LE). This route (**Figure 4.1**) involves the intramolecular rearrangement of the epoxy group, yielding thermodynamically stable isomers with distinct structures and properties. Specifically, DHC is formed by a hydride shift, whereas other products are generated by alkyl fragment migration [44]. The major homogeneous catalyst reported for the isomerization of LE is $ZnBr_2$, with the main products of the reaction being cyclopentanecarboxyaldehyde (CPCA) and DHC [45]. In general, LE can be converted in the presence of acidic heterogeneous catalysts [22]. Amorphous silica-alumina gave CPCA and DHC with selectivities up to 77% and 7 % (room temperature, 1 h and toluene as the solvent), respectively, indicating that CPCA formation is favored on the Lewis acid sites [46]. On the other hand, carvenone was produced from LE over montmorillonite under solvent-free conditions, at a high temperature (140 °C) and short reaction time (60 min), with a yield of ca. 80 %. Additionally, the same yield can be obtained using microwave-assisted heating in only 6 min [47].

Heteropolyacids of the Keggin type, which possess Brønsted acid sites, were investigated in the isomerization of limonene epoxide, leading to DHC as the main product with a yield of 82%, in the presence of a toxic and rigorously regulated aprotic solvent such as 1,4-dioxane under ambient conditions [48]. The nature of the aprotic solvent (dichloromethane and 1,2-dichloroethane besides 1,4-dioxane) was found to significantly affect both the reaction rate and selectivity towards DHC. A similar catalyst, silica-supported tungstophosphoric acid, demonstrated the potential to produce DHC and carvenone with yields up to 90 % by adjusting the reaction conditions (although with temperatures below 40 °C in all cases) using dimethylcarbonate and diethylcarbonate as benign and green solvents [22]. Recently, a Fe-containing ordered mesoporous catalyst (Fe/SBA-15) was tested in the reaction, showing that

the product distribution (DHC, limonene-1,2-diol, and *trans*-carveol) depends on the polarity of the solvent [49]. It was reported that an increase in polarity appears to enhance the selectivity to DHC, while limonene-1,2-diol is favored with solvents of lower polarity. Nevertheless, at the tested reaction conditions, the limonene epoxide conversion was lower than 30%, and the selectivity to isomers did not exceed 50%. Competition between isomerization and hydrolysis (**Figure 4.1**) is expected to be one of the most important factors to control the products distribution. The remaining water in the system (moisture in the solvent or the catalyst) can produce limonene-1,2-diol rather than typical isomers [50]. Although this diol finds applications in fine chemistry, the formation of the isomers is more attractive due to their high commercial value and direct implications in chemical processes. Selectivity depends on the specific reaction conditions as well as on the catalyst and solvent type. In general, the most critical factors influencing selectivity towards a specific target from limonene epoxide are the type of acid sites (Brønsted, Lewis, or their ratio) and the solvent (polar or non-polar).

Zeolites have garnered significant interest over the last decades in numerous fields, such as catalysis, adsorption, gas purification, wastewater treatment, and biomedical applications, among others [51,52]. ZSM-5 is one of the most relevant zeolites due to its exceptional properties and versatility in industrial applications. However, the relatively small size of its micropores restricts the access of bulky molecules to the active sites leading to strong steric and diffusional hindrances in many applications [53]. In this way, recent research has focused on developing ZSM-5 zeolites with improved accessibility, typically by generating a secondary porosity in the mesopore range. Interestingly, in a recent work, the synthesis of ZSM-5 zeolite showing a dendritic nanoarchitecture has been reported by Serrano et al. [54]. The zeolitic materials so obtained display 3D branched and radially oriented superstructures characterized by exceptional accessibility, attributed to the existence of a highly interconnected network of pores encompassing different scales [54]. Therefore, dendritic ZSM-5 zeolites are expected to overcome those drawbacks, exploiting their high porosity and accessibility, in a large variety of reactions involving bulky species.

Hence, this study aims to evaluate the use of dendritic ZSM-5 zeolite-based catalysts, in comparison with conventional and hierarchical samples, as highly selective catalysts for the isomerization of limonene-1,2-epoxide toward *cis*/*trans*-dihydrocarvone, using mild reaction conditions and more benign solvents than previously reported in the literature, such as ethyl acetate and dimethyl carbonate. The focus of this contribution was to gain an understanding of how the physicochemical properties of the zeolites are correlated with their catalytic performance in limonene-1,2-epoxide isomerization. Moreover, this study investigated the effects of substrate (*cis*-LE, *trans*-LE, and mixture-LE), solvent polarity, and catalyst robustness, and extended the scope of catalytic performance with other epoxides as substrates, such as α- and β-pinene epoxides.

4.3. Experimental section

4.3.1. Reagents

Commercial reagents were used in the experiments without further processing. Reagents for the synthesis of hierarchical and dendritic materials were aluminum isopropoxide (AlP, Sigma-Aldrich, 98 wt.%); tetrapropylammonium hydroxide (TPAOH, Sigma-Aldrich, 40 wt.% in water); tetraethyl orthosilicate (TEOS, Sigma-Aldrich, 98 wt.%); dimethyloctadecyl [3-(trimethoxysilyl) propil] ammonium chloride (TPOAC, Sigma-Aldrich, 42 wt.% in methanol);

N-[3-(Trimethoxysilyl)propyl]aniline (Ph-A, Sigma-Aldrich, 98%). Commercial ZSM-5 catalyst in H^+ form was purchased from Zeolyst (H-CVB-80) and used as a reference (coded as ZSM-5). Reagents for the catalytic tests were (+)-limonene-1,2-epoxide (mixture of *cis*/*trans*-isomers, ≥97 wt.%, Sigma-Aldrich), *cis*-(-)-limonene-1,2-epoxide (98 wt. %, Sigma-Aldrich), *trans*-limonene-1,2-epoxide (97.5 wt. %, Sigma-Aldrich), α-pinene epoxide (97 wt.%, Sigma-Aldrich), β-pinene epoxide (80 wt.%, International Laboratory USA), dimethyl carbonate (DMC, 99 wt.%, Sigma-Aldrich), ethyl acetate (anhydrous, 99.8 wt.%, Sigma-Aldrich), toluene (grade for liquid chromatography, Merck), acetonitrile (CH_3CN, gradient grade for liquid chromatography, Merck), and nitrogen (99.999%, Woikoski). Other reagents used as standards for the quantification through the multipoint calibration curves were D-dihydrocarvone (≥ 97 wt.%, mixture of isomers, Sigma-Aldrich), L-carveol (mixture of *cis* and *trans*, ≥ 95 wt.%, Sigma-Aldrich), (1*S*,2*S*,4*R*)-(+)-limonene-1,2-diol (≥ 97 wt.%, Sigma-Aldrich), *p*-cymene (≥90 wt.%, Fluka), campholenic aldehyde (97 wt.%, Hangzhou Grascent Co.), (1*R*)-(-)-myrtenal (Kosher, 97 wt.%, SAFC), (S)-(-)-perillyl alcohol (≥90 wt.%, SAFC), and (1*R*)-(-)-myrtenol (Kosher, ≥95 wt.%, SAFC).

4.3.2. Synthesis of catalysts

Dendritic and hierarchical ZSM-5 materials were prepared based on the experimental methodology reported previously [54,55]. Briefly, dendritic ZSM-5 samples were synthesized first by mixing fined milled AlP with TPAOH and distilled water at 300 rpm and room temperature, in a round bottom flask until complete dissolution of AlP. Then, a proper amount of silicon source (TEOS) was added dropwise submerging the flask in an ice bath, being then stirred at room temperature for 42 h until complete hydrolysis of TEOS. The molar composition of the initial precursor solution was 1 Al_2O_3: 60 SiO_2: 11 TPAOH: 1500 H_2O. Then, the alcohols produced as hydrolysis by-products were removed using a rotatory evaporator at 100 mbar and 50 °C. The clear precursor solution was pre-crystallized under reflux and stirred at 300 rpm and 90 °C for 20 h. Subsequently, the round bottom flask was cooled in an ice bath and a 5 mol% of TPOAC regarding to the initial Si content was added dropwise to the synthesis gel. The mixture was maintained under stirring in the ice bath for 6 hours. After that, the hydrothermal crystallization of the synthesis gel was performed loading it in a Teflon-lined reactor. The sealed reactor was subjected to 150 °C for two different times (4 and 7 days). After crystallization, the autoclaves were cooled down by immersion into an ice bath to suddenly interrupt the process. Two solid phases from the dendritic synthesis gel were obtained after 4 and 7 days of crystallization: a whitish supernatant phase and a white solid in the bottom of the Teflon container. The white solid phase contained the dendritic zeolite sample, and it was mechanically separated, washed with distilled water, centrifuged at 11000 rpm three times, and dried at 100 °C overnight. The obtained solid was designated as d-ZSM-5/Xd where d refers to the dendritic zeolite and X indicates the crystallization time in days (4 or 7).

A similar procedure was performed to obtain the hierarchical zeolite with some modifications. In this case, once the pre-crystallization was completed, 5 mol% of Ph-A was added to the synthesis gel, maintained at 90 °C, and stirred under reflux for 6 h. Also, to obtain the hierarchical sample, its synthesis gel was hydrothermally crystallized at 170 °C for 7 days, after which a solid phase and a transparent supernatant were obtained. The solid phase was recovered following the same procedure as for the dendritic samples and designated as h-ZSM-5.

Both hierarchical and dendritic samples were calcined in a two-step process using Ar and synthetic air as carrier gases for the first and second steps, respectively, following the procedure reported elsewhere [56], to prevent the generation of hot points during the combustion of the organic components present in the as-synthesized zeolites.

After crystallization of the dendritic ZSM-5 samples, three different phases are obtained: solid down phase in the synthesis reactor (it is the dendritic ZSM-5 material), slid upper phase in the synthesis reactor (it is a nano-crystalline ZSM-5 material), and the liquid solution obtained by water washing of the two former phases. At the commercial scale, the nano-crystalline ZSM-5 solid would be a co-product of the crystallization process having also practical applications. The share between both zeolitic products varies along the crystallization process, hence the dendritic ZSM-5 represents about 80% and 60% of the overall ZSM-5 yield in the synthesis performed with a duration of 4 and 7 days, respectively.

CHON and TGA analyses of the solid zeolitic samples allow their content in organic components (TPA^+ and TPOAC species) to be determined. Based on these results and considering the yield of the solid phases, it has been possible to estimate that the overall (Si+Al) atom economy during the transformation of the amorphous gel into the crystalline zeolite samples is 77%, distributed as 45% and 32% for the down and upper zeolitic phases, respectively. The remaining raw inorganic components (23%) remain as soluble aluminosilicate species that, in an industrial process, could be recovered and reused in subsequent crystallization batches. Regarding the organic reagents, a great part of them can also be recovered and reused after water washing and ethanol extraction treatments of the zeolites. The organic components that cannot be recovered are those strongly trapped within the zeolitic materials, being finally removed by combustion. The non-recovered (combusted) organic species represent about 16% of TPA^+ and 36% of TPOAC of the amounts added to the synthesis gel. Accordingly, the difference (84% TPA^+ and 64% TPOAC) could be used back in the crystallization process. Finally, the alcohols (mainly ethanol containing some isopropanol) released from the TEOS and IPA hydrolysis, are recovered by vacuum evaporation, so they could also find applications when scaling up the process, thus contributing to minimizing the generation of waste streams in agreement with green chemistry principles.

4.3.3. Catalysts characterization

X-ray diffraction patterns of calcined samples were recorded covering 2θ range between 0° and 5° for low-angle, and between 5° and 50° for wide angle with an Empyrean PANalytical diffractometer using Cu (Kα = 1.54 Å). Argon (-186 °C) adsorption-desorption isotherms were measured in a 3Flex instrument. Calcined samples were outgassed under vacuum at 300 °C for 5 h before adsorption analyses. The NL-DFT model was employed for calculating the pore size distribution and the cumulative pore volume over the isotherm adsorption branch. Also, the specific surface area was obtained by applying the BET model. The total pore volume (V_T) was estimated at the isotherm final relative pressure (0.99), and the micropore volume (V_{mic}) was calculated from the NL-DFT cumulative pore volume data. Finally, the external volume (V_{ext}) was determined as the subtraction of V_T and V_{mic}. The mesopore/external surface area ($S_{MES-EXT}$) was determined as a difference between the S_{BET} and the microporous surface area S_{MIC}. The latter was calculated following the procedure described elsewhere based on the application of the NL-DFT model [57]. In addition, the BJH method was applied, using the Harkins and Jura equation, to the adsorption branch of the dendritic zeolite isotherms.

Micrographs of the calcined zeolite samples were captured using JEOL JEM 1400 transmission electron microscopes (TEM) at 120 kV. Moreover, High-Resolution Transmission Electron Microscopy (HR-TEM) and High-Angle Annular Dark Field Scanning TEM (HAADF-STEM) images were collected using a JEOL F200 CF (200 kV) microscope. Additionally, scanning electron microscopy (SEM) images of the calcined samples were obtained using a JEOL microscope operating at 1 kV in the GSBH mode. To quantify the Si/Al ratio of the calcined zeolites, ICP-OES analyses were performed using a Perkin Elmer Optima 7300 DV equipment. Calcined samples were previously subjected to sealed acid digestion with an HNO_3 and HF solution (2:1 v/v) in an Anton Paar Multi-wave 3000 equipment. Solid-state ^{27}Al MAS NMR spectra of the calcined zeolite samples were obtained at 104.26 MHz in a Bruker Avance III/HD 400 MHz spectrometer.

To determine the concentrations of Brønsted and Lewis acid sites (BAS and LAS), pyridine served as a probe molecule, and the assessment was conducted through FTIR in a custom-built system. Self-supported wafers, weighing 15 mg cm^{-2}, were fabricated and subjected to activation under a vacuum (10^{-4} mbar) at 525 °C for 1 hour before measurements. Subsequently, pyridine was introduced into the system at 150 °C, and it was sealed for 20 minutes. Thermal desorption was performed under high vacuum, with temperatures escalating within the range of 150 to 450 °C (heating rate: 10 °C min^{-1}), including a 20-min equilibrium period before obtaining the spectrum at each designated temperature. Spectra were recorded utilizing a Jasco-4600 instrument equipped with a TGS detector, with a resolution of 4 cm^{-1} and 128 scans. The molar extinction coefficients used for quantifying BAS and LAS concentrations were sourced from Zholobenko et al. [58] for the ZSM-5 zeolite: ξ_{BAS} = 1.09 cm μmol^{-1} and ξ_{LAS} = 1.71 cm μmol^{-1}. Similarly, the concentration of external Brønsted acid sites was assessed by adsorbing 2,6-di-tert-butylpyridine (DTBPy) as a probe molecule (ε_{Bext} = 5.3 cm·μmol^{-1}) [59], following the same procedure described earlier and maintaining adsorption-desorption equilibrium intervals of 60 minutes.

The spent catalysts were characterized using temperature-programmed oxidation (TPO) coupled with mass spectrometry (MS) to detect the coke formation. TPO was carried out on a BELCAT II analyzer (Microtrac MRB) coupled with a mass spectrometer (Pfeiffer OmniStar GSD 350). First, around 75 mg of the sample was pre-treated at 120 °C for 2 h (10 °C min^{-1}), followed by cooling to 35 °C. The analysis was carried out by heating up to 900 °C (5 °C min^{-1}) using a mixture of 5 vol% O_2/Ar (30 mL min^{-1}). The holding time of the target temperature was 10 min. Additionally, thermogravimetric analysis (TGA) was performed with a NETZSCH STA 449 thermobalance. These assays were performed under air flow and heating the samples to 900 °C at 10 °C/min, followed by an isothermal step of 10 min.

4.3.4. Catalytic tests

The isomerization of limonene-1-2-epoxide over ZSM-5 zeolites was performed in a batch glass reactor with a total liquid volume of 75 mL and under a nitrogen atmosphere. The flask was equipped with a thermocouple, a N_2 feeding, a sampling valve, and a condenser (**Figure 8.70**). Catalytic tests were performed using a sufficiently high liquid volume-to-catalyst mass ratio and vigorous agitation (520-530 rpm) to overcome external mass-transfer limitations [60,61]. Furthermore, small catalyst particles (< 75 μm) were used to suppress the internal mass transfer limitations. In a typical experiment, 115 mg of catalyst was heated at 250 °C for 30 min under a N_2 atmosphere to ensure the removal of physisorbed water. Subsequently, 152 mg (1 mmol) of epoxide was added to the pre-heated solvent at 70 °C to reach 75 mL as the

total liquid volume. Samples of approximately 0.4 mL were collected at various time intervals using a syringe equipped with 0.45 µm filters to analyze the reaction kinetics using an Agilent Technologies GC-6890N equipment provided with a DB-1 column (30 m length x 250 µm internal diameter x 0.50 µm film thickness), a FID detector, and an autosampler. Helium was used as the carrier gas (1.5 mL min^{-1}, 0.12 MPa) with a split ratio of 10:1. The detector temperature was set to 280 °C, and the injection volume was 1 µL. The oven-temperature program ramped from 60 °C to 100 °C at a rate of 20 °C min^{-1}, followed by an increase to 200 °C at 10 °C min^{-1} and was held for 1 min. The nature of the products was further confirmed with an Agilent GC/MS 6890N/5973N equipped with a DB-1 capillary column (30 m length x 250 µm internal diameter x 0.5 µm film thickness).

The limonene-1,2-epoxide conversion (X_{LE}), the selectivity to the product i (S_i), and the yield to the product (Y_i) were calculated based on the **Eqs. (4.1)-(4.3).**

$$X_{LE}(\%) = \frac{n_{LE,0} - n_{LE,t}}{n_{LE,0}} * 100 \quad \textbf{(4.1)}$$

$$S_i(\%) = \frac{n_{i,t}}{n_{LE,0} - n_{LE,t}} * 100 \quad \textbf{(4.2)}$$

$$Y_i(\%) = \frac{n_{i,t}}{n_{LE,0}} * 100 = \frac{X_{LE} * S_i}{100} \quad \textbf{(4.3)}$$

Where $n_{LE,0}$, $n_{LE,t}$, and $n_{i,t}$ refer to the initial moles of epoxide, the moles of epoxide after time *t*, and the moles of the product i after time *t* in the reaction mixture, respectively. The concentrations of limonene-1,2-epoxide as the substrate, isomeric products such as dihydrocarvone and carveol, and limonene-1,2-diol as the hydration product were determined from multipoint calibration curves.

The initial reaction rate and TOF for limonene-1,2-epoxide were calculated using **Eqs. (4.4)-(4.5):**

$$r_{0,LE} = \frac{n_{i,LE} - n_{f,LE}}{\Delta t * W} \quad \textbf{(4.4)}$$

$$TOF = \frac{n_{i,LE} - n_{f,LE}}{\Delta t * TA * W} \quad \textbf{(4.5)}$$

Where $n_{i,LE}$ and $n_{f,LE}$ correspond to moles of limonene-1,2-epoxide at time 0 min and 5 min, respectively, Δt is the time interval, W is the catalyst weight, and TA is the total acidity referred to the sum of Brønsted and Lewis acidity of the catalyst.

4.4. Results and discussion

4.4.1. Catalyst characterization

4.4.1.1. X-ray diffraction

X-ray diffraction patterns of calcined ZSM-5 catalyst are shown in **Figure 4.2.A**. All samples display the characteristic peaks of a well-crystallized MFI zeolitic structure [62]. However, conventional ZSM-5 zeolite shows the highest diffraction intensity due to the larger zeolitic domains of the commercial sample compared with the synthesized materials, which are formed by aggregates of very small zeolite nanounits [55,63]. A slight enhancement in the diffraction intensity is also observed for the dendritic samples when the crystallization time is increased from 4 to 7 days. In addition, to probe the presence of porosity in the mesoscale, low-angle X-ray diffraction was performed over hierarchical and dendritic samples (**Figure 8.71**). A broad diffraction signal is detected for the d-ZSM-5/4d sample between 1.2° and 2.2°, suggesting the presence of some degree of mesoscopic order in the sample obtained after 4 days of hydrothermal crystallization, that disappears when increasing the crystallization time up to 7 days. This signal is not detected for the h-ZSM-5 sample, being in good agreement with previous work [63].

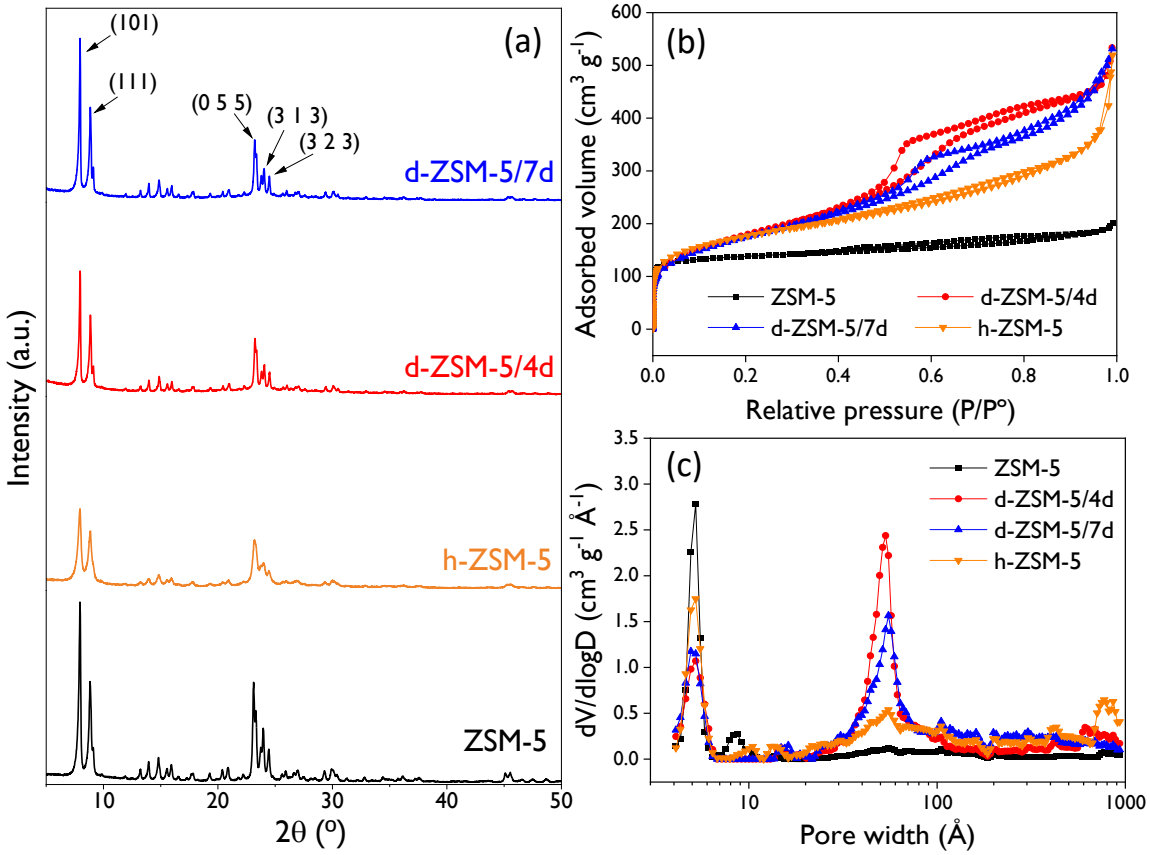

Figure 4.2. (a) XRD patterns of the ZSM-5 samples, and textural properties by argon physisorption of the ZSM-5 samples: **(b)** Adsorption-desorption isotherms and **(c)** NL-DFT pore size distribution.

4.4.1.2. Argon physisorption

Figure 4.2.B and **Figure 4.2.C** display the argon adsorption-desorption isotherms and the pore size distribution, respectively. The reference ZSM-5 zeolite exhibits a type I(a) isotherm, characteristic of microporous materials [64]. On the other hand, h-ZSM-5 and d-ZSM-5 samples present isotherms with contributions from both micro- and mesopores, but with

significant differences among them. The hierarchical ZSM-5 zeolite (h-ZSM-5) shows adsorption in the range (P/P_0 = 0.2 – 0.9) due to the presence of a broad mesoporosity with pore sizes between 20 and 200 Å, as illustrated in **Figure 4.2.C**. These findings align well with other hierarchical samples synthesized under similar conditions [55]. Concerning the dendritic zeolites, both samples exhibit hybrid type I(a) and IV(a) isotherms due to the presence of well-defined micro- and mesopores. Notably, there are differences in the mesopore size distribution between them. The d-ZSM-5/4d sample displays a narrower distribution centered at 51.4 Å, whereas the d-ZSM-5/7d sample exhibits less uniform mesopores centered at 61 Å (both sizes being determined by applying the BJH model to the adsorption branch of the isotherms). This fact indicates variations in the mesoporosity during the crystallization process at 150 °C, as previously reported [54].

The textural properties of the catalysts (**Table 4.1**) are in good agreement with the pore size distributions and cumulative pore volumes calculated with the NL-DFT model. In general, both the BET and the mesopore/external surface areas increase with the mesoporosity share. As expected, a direct correlation exists between the reduction in micropore volume (V_{mic}) and the extent of mesoporosity introduced in the zeolitic structure. In this context, the conventional ZSM-5 sample exhibits the highest micropore volume (0.201 $cm^3\ g^{-1}$), whereas the most extensively modified catalyst, the d-ZSM-5/4d zeolite, displays the lowest microporosity (0.131 $cm^3\ g^{-1}$) and the highest BET and mesopore/external surface areas (570 and 360 $m^2\ g^{-1}$, respectively). It is also remarkable that the dendritic samples exhibit the highest levels of mesoporosity share (c.a. 80%). This underscores the exceptional accessibility of these samples, being much higher than the pore volume of the conventional ZSM-5 sample. Therefore, it is expected that these great differences in terms of textural properties and accessibility between the four ZSM-5 samples will have a strong effect on their catalytic behavior in reactions that may suffer from strong steric and/or transport limitations due to the bulky size of the involved species, as it is the case of the limonene-1,2-epoxide isomerization here investigated.

Table 4.1. Al content and textural properties of the ZSM-5 samples.

Catalyst	Si/Al	S_{BET} ($m^2\ g^{-1}$)	$S_{MES/EXT}$ ($m^2\ g^{-1}$)	V_{mic} ($cm^3\ g^{-1}$)	V_T ($cm^3\ g^{-1}$)	Mesoporosity[a] (%)
ZSM-5	40	426	77	0.20	0.26	21.8
h-ZSM-5	40	557	279	0.17	0.66	73.8
d-ZSM-5/4d	42	570	360	0.13	0.68	80.7
d-ZSM-5/7d	41	553	330	0.14	0.68	79.5

Si/Al: Molar ratio, **S_{BET}:** BET surface area, **$S_{MES/EXT}$:** Mesopore/external surface area**; V_{mic}:** Micropore volume, **V_T:** Total pore volume. [a] Calculated as V_{Ext}/V_T*100

4.4.1.3. Catalyst acidity

Table 4.2 presents the acid properties of the calcined catalysts as determined by pyridine-FTIR measurements. Although all the samples present quite similar Al content (**Table 4.1**), significant differences can be appreciated in their acidic features. Specifically, both ZSM-5 and h-ZSM-5 samples exhibit a high concentration of Brønsted acid sites. Conversely, the dendritic ZSM-5 materials show a substantial reduction in the Brønsted acid site population at the expense of an increase in that of Lewis acid sites. These findings establish a trend in the BA/LA concentration ratio as follows: ZSM-5 > h-ZSM-5 > d-ZSM-5/7d > d-ZSM-5/4d, mirroring the

mesoporosity and mesopore/external surface area contributions outlined in **Table 4.1**. Interestingly, the large concentration of Lewis acid sites in the dendritic samples can be mainly related to Al framework species since ^{27}Al MAS NMR measurements indicate that the share of extra-framework Al atoms is just about 6-7% for both d-ZSM-5 samples. Another remarkable finding is the high concentration of external Brønsted acid sites for the dendritic materials, and in particular for the d-ZSM-5/4d sample, denoting the presence of a high accessibility acidity.

Table 4.2. Acidic properties of the ZSM-5 samples determined with pyridine-FTIR.

Catalyst	Brønsted acidity (μmol g^{-1})				Lewis acidity (μmol g^{-1})				Total	BA/LA	$C_{B,\,ext}$
	Weak	Medium	Strong	Total	Weak	Medium	Strong	Total	(μmol g^{-1})	ratio	(μmol g^{-1})
ZSM-5	40	52	97	189	10	7	14	31	220	6.1	16
h-ZSM-5	47	53	99	199	11	5	49	65	264	3.1	41
d-ZSM-5/4d	33	32	58	123	21	9	58	88	211	1.4	97
d-ZSM-5/7d	32	34	65	131	22	11	53	86	217	1.5	61

BA and LA: Brønsted and Lewis acid sites concentration calculated from pyridine-FTIR tests. Measurements at 250 °C: weak + medium + strong; measurements at 350 °C: medium + strong; measurements at 450 °C: strong.

$C_{B,\,ext}$: BA external concentration measured at 250 °C by FTIR/DTBPy.

4.4.1.4. TEM analyses

TEM micrographs in **Figure 4.3** highlight distinct morphological variations among the calcined catalysts. The ZSM-5 sample exhibits the characteristic coffin-like particles of the MFI structure, ranging in size from 70 - 100 nm for the smallest dimension to approximately 400 nm for the largest. In contrast, the h-ZSM-5 sample consists of 250 – 300 nm-sized globular aggregates composed of nanoparticles measuring about 5-10 nm. This random aggregative structure creates mesopores with a broad pore size distribution. On the other hand, the dendritic samples showcase oval-shaped particles measuring c.a. 400 nm x 250 nm. These particles are formed by nanounits of about 5 nm, arranged in rod-like spikes that extend from the inner to the outer part of the particle, giving rise to the radially oriented and branched morphology distinctive of dendritic ZSM-5 zeolites. Notably, some large vesicles, previously reported for this morphology [54], are also visible within the particles of both d-ZSM-5 samples in the HAADF-STEM images. All these features denote the high connectivity existing between the different types of porosities present in the d-ZSM-5 samples.

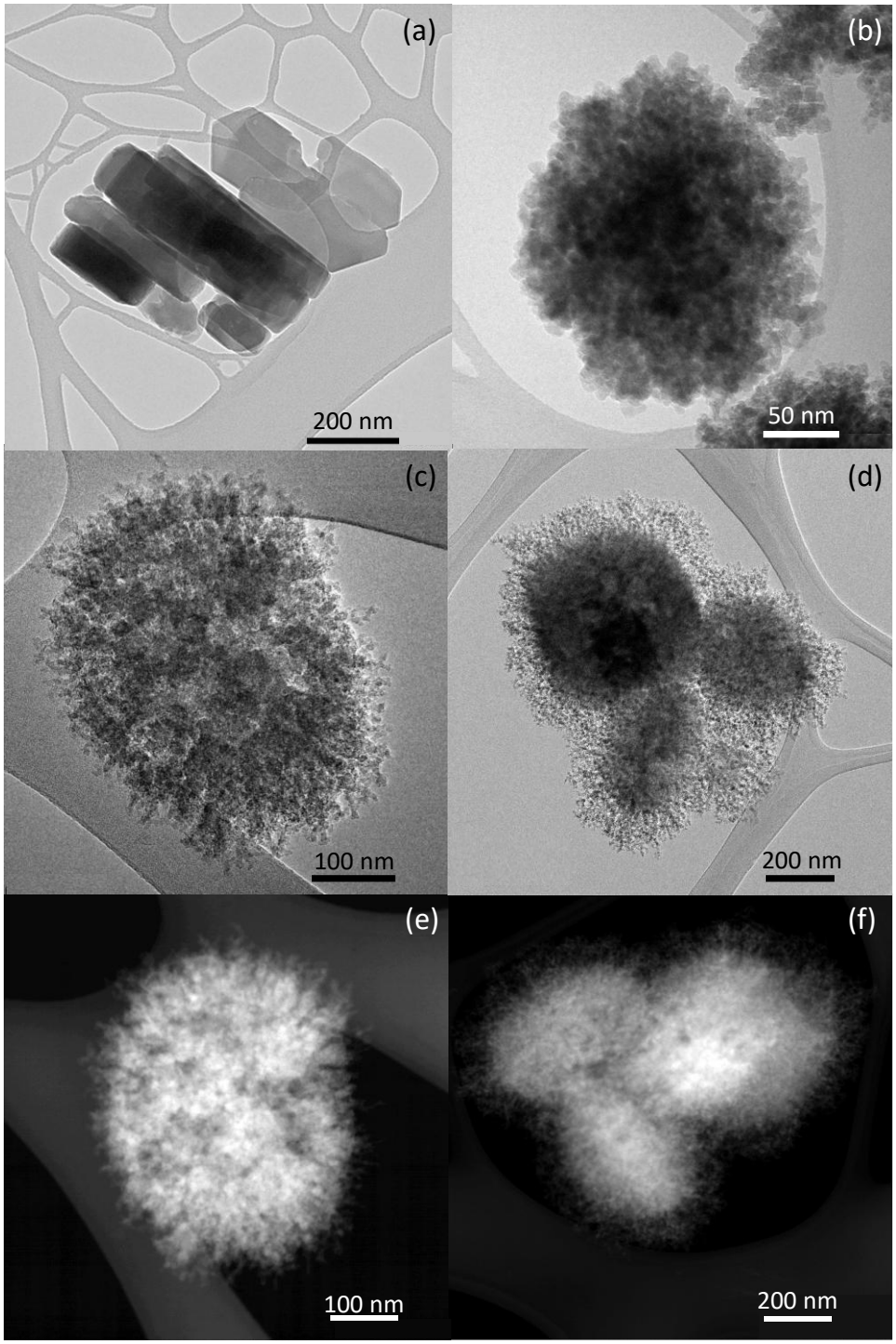

Figure 4.3. TEM images of ZSM-5 (a), and h-ZSM-5 (b) samples. HR-TEM and HAADF-STEM micrographs of d-ZSM-5/4d (c, e), and d-ZSM-5/7d (d, f) samples.

4.4.2. Catalytic activity

4.4.2.1. General aspects

Figure 8.73 shows a general scheme of the products that were identified in the limonene-1,2-epoxide (LE) isomerization over the ZSM-5 catalysts, namely *cis*-dihydrocarvone (**1a**), *trans*-dihydrocarvone (**1b**), carveol (**2**), 1,3,4-trimethyl-3-cyclohexen-1-carboxaldehyde (**3**, CAS number: 40702-26-9), fenchone (**4**), product **5**, 3-methyl-2-methylidene-bicyclo[3.2.1]oct-3-ene (**6**, CAS number: 49826-53-1), (2*S*,4*R*)-*p*-mentha-1(7),8-dien-2-ol (**7**, CAS number: 2102-62-7),

and limonene diol (**8**). Detailed information regarding retention times and mass spectra can be found in the Supporting Information (**Table 8.8** and **Figure 8.82**-**Figure 8.87**).

Repeatability of the experiments was investigated using d-ZSM-5/4d catalyst with the results demonstrating the reliability of the procedure (**Figure 8.74**). Additionally, **Figure 8.75** unequivocally confirms that the transformations follow a catalytic route, as evidenced by the linear dependence observed between the initial reaction rate and the catalyst mass.

4.4.2.2. Turnover frequency (TOF)

TOF values of limonene-1,2-epoxide (LE) have been correlated against the Brønsted/Lewis (BA/LA) molar ratio (**Figure 4.4.A**), the external/mesopore surface area (**Figure 4.4.B**), and the external Brønsted acid site concentration (**Figure 4.4.C**). The highest LE isomerization TOF was obtained with d-ZSM-5/4d catalyst, which exhibits the lowest BA/LA ratio (1.4), the largest mesoporosity contribution but also the highest share of external Brønsted acid sites. Thus, d-ZSM-5/4d sample exhibits a TOF value sevenfold higher than that of the conventional ZSM-5 material. The plots suggest a dependency between TOF and the external/mesopore surface area but the opposite effect with the BA/LA ratio. Moreover, a very good correlation is observed in **Figure 4.4.C** between the catalytic activity and the external Brønsted acid site population. This relevant finding confirms the high significance of steric and diffusional limitations due to the large molecular size of the different species involved in the reaction regarding the ZSM-5 micropores. Therefore, it can be concluded that the remarkable accessibility of the dendritic ZSM-5 materials contributes to overcoming those hindrances. In this way, **Table 8.6** illustrates a comparison based on TOF values for the four zeolites tested in this work with some recently reported heterogeneous systems, demonstrating the quite superior activity in the isomerization of limonene-1,2-epoxide obtained with both dendritic ZSM-5 zeolites (4.4 and 2.3 min^{-1} for d-ZSM-5/4d and d-ZSM-5/7d, respectively).

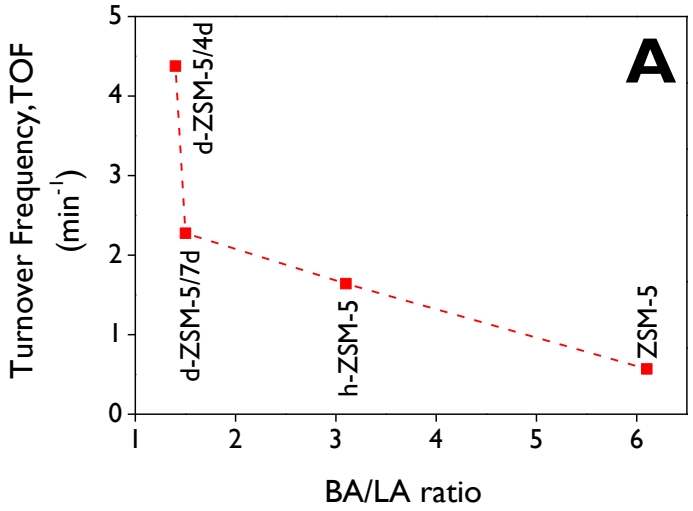

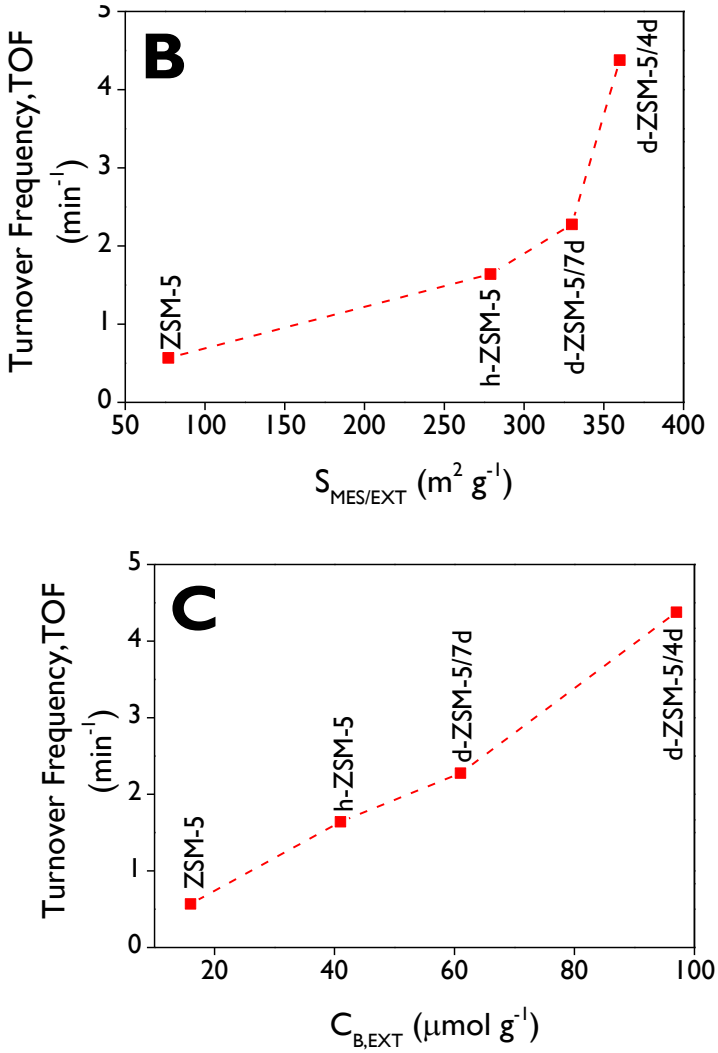

Figure 4.4. Turnover Frequency (TOF) of limonene-1,2-epoxide as a function of **(A)** BA/LA ratio, **(B)** external/mesopore surface area, and **(C)** external c acid site. **Reaction conditions:** $C_{LE,0}$ = 13 mmol L^{-1}, 75 mL of total volume, anhydrous ethyl acetate as a solvent, 115 mg of catalyst, 70 °C, 520-530 rpm, N_2 atmosphere.

4.4.2.3. Conversion after prolonged times and product distribution

The conversion and selectivity towards target products in the isomerization of LE significantly depend on the zeolite nanoarchitecture, as well as on their acidic and textural properties. **Figure 4.5.A** illustrates the conversion profiles for the commercial microporous zeolite (ZSM-5), the hierarchical zeolite (h-ZSM-5), and the two dendritic-based ZSM-5 catalysts. Furthermore, the reaction was conducted without a catalyst to demonstrate that it did not proceed solely due to the thermal effect (Blank, **Figure 4.5.A**), This is consistent with our earlier conclusions based on the linear dependence observed between the initial reaction rate and the catalyst mass. ZSM-5 exhibited limited reactivity for the transformation of LE, achieving only 20% conversion after 2 h, which could be assigned mainly to its small pore size (5.5 Å) since it is significantly lower than the LE kinetic diameter (8.35 Å, estimated by DFT). Accordingly, it can be assumed that LE is strongly hindered from entering the MFI micropores, hence the acid sites located on the external/mesopore surface area or at the pore mouths would be mainly responsible for the observed catalytic activity, which agrees well with the direct relationship between TOF and external Brønsted acidity shown earlier. Thus, when the external/mesopore surface area (**Table 4.1**) is increased by the creation of mesopores, the

conversion is significantly sharply enhanced, reaching around 90, 95 and 100% with h-ZSM-5, d-ZSM-5/7d and d-ZSM-5/4d catalysts, respectively, after 2 h.

The evolution of the *cis*/*trans*-LE molar ratio as a function of time is displayed in **Figure 4.5.B** for all catalysts, with an initial value around 0.65, corresponding to a molar composition of 38% *cis*-LE and 59% *trans*-LE in the commercial reagent. With the dendritic zeolites, values close to zero are obtained after 30 min while, with ZSM-5, a value of ca. 0.45 is reached after 2 h due to its low catalytic activity. Furthermore, the appreciable drop observed with dendritic zeolites in only 15 min allows to conclude that the reactivity of *cis*-LE is higher. The same conclusions can be drawn from the plots of the conversion of each isomer (*cis*-LE and *trans*-LE) as a function of reaction time, which are displayed in **Figure 8.79.A-B** in the Supporting Information. A larger steric hindrance of the oxygen atom in the *trans*-LE, in comparison with *cis*-LE, can explain the lower reactivity of *trans*-LE, as it is more difficult for this molecule to access the active sites of the catalyst [22].

The highest selectivity to DHC (*cis* + *trans*) was achieved with d-ZSM-5/4d (**Figure 4.5.C**), showing a small variation range (60-63%) during the reaction. Lower values were obtained with d-ZSM-5/7d (53-57%), h-ZSM-5 (40-50%), and conventional ZSM-5 samples. This is also an interesting fact as it indicates that the zeolite catalyst showing the highest activity is also the most selective for DHC formation. Selectivity to carveol (*cis* + *trans*) for all catalysts is displayed in **Figure 4.5.D**, with constant values around 10-12% over a wide conversion range for the hierarchical and the two dendritic zeolites. This suggests a minor effect of the BA/LA ratio and textural properties on carveol selectivity, in contrast to the selectivity for DHC. The low selectivities to carveol can be attributed to the absence of a bifunctional acid/base catalyst in the system, as reported for a catalytic mechanism converting an epoxide into an allylic alcohol by Raptis et al. [65].

No carveol was observed for ZSM-5 before 60 min of the reaction (up to 13% conversion). However, at the maximum conversion achieved under the tested conditions (20%), approximately 7.6% selectivity was reached. This behavior can be explained by the rapid decrease in the selectivity to product 3 (**Figure 4.5.E**) in the 0-20% conversion range, reaching about 28% at 20% conversion. This value is slightly higher than the selectivity range using the dendritic zeolites, which showed values of ca. 12-17% and 15-23% for d-ZSM-5/4d and d-ZSM-5/7d, respectively. The *cis*/*trans*-DHC molar ratio, depicted as a function of conversion in **Figure 4.5.F**, exhibited similar behavior across all catalysts. However, a slight preference for *cis*-DHC is observed with d-ZSM-5/4d compared to d-ZSM-5/7d. Moreover, with the dendritic zeolites, a final ratio (complete conversion) of ca. 0.53-0.60 is achieved.

The d-ZSM-5/4d catalyst exhibited a DHC yield of 63% after 2 h, significantly outperforming other catalytic systems based on amorphous silica-alumina (yield < 7% with toluene at room temperature after 1 h) [46], montmorillonite (yield < 20% under solvent-free conditions at 140 °C after 1 h) [47], and Fe/SBA-15 (yields < 10% using various solvents at 70 °C after 1 h) [49]. Moreover, the primary products with the first two catalysts were cyclopentanecarboxyaldehyde and carvenone, achieving yields of ca. 77% and 80%, respectively [46,47]. For Fe/SBA-15, conversions of limonene epoxide with any solvent did not exceed 21% after 1 h [49]. Although a combined selectivity to DHC and carvenone of ca. 85-90% over a heteropolyacid/SiO_2 has been reported [22], which describes two consecutive steps, including the fast production of DHC from LE and the slow isomerization of DHC into carvenone, the formation of carvenone was not observed in this work.

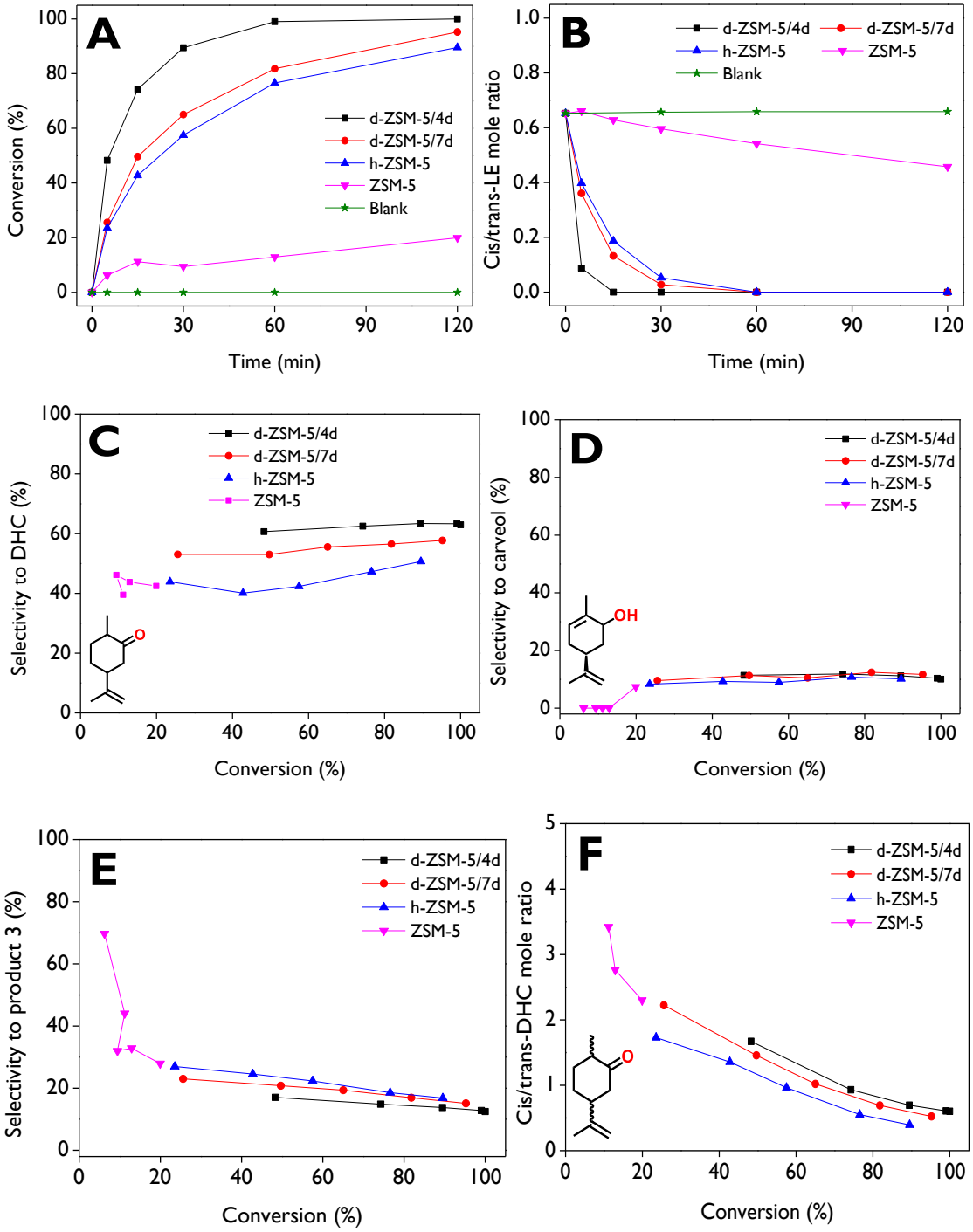

Figure 4.5. (A) Limonene-1,2-epoxide conversion and **(B)** *cis*/*trans* limonene-1,2-epoxide molar ratio as a function of the reaction time, **(C)** selectivity to dihydrocarvone, **(D)** selectivity to carveol, **(E)** selectivity to product **3**, and **(F)** *cis*/*trans* dihydrocarvone molar ratio, as a function of the conversion. **Reaction conditions:** $C_{LE,0}$ = 13 mmol L^{-1}, 75 mL of total volume, anhydrous ethyl acetate as a solvent, 115 mg of catalyst, 70 °C, 520-530 rpm, N_2 atmosphere.

To rationalize the results, the conversion of limonene epoxide after 2 h (**Figure 8.76.A-B**), the selectivity to DHC at 80% conversion (**Figure 8.76.C-D**), and the *cis*/*trans*-DHC molar ratio at 80% conversion (**Figure 8.76.E-F**) were plotted as functions of the external/mesopore surface area ($S_{MES/EXT}$) and BA/LA ratio. Conversion after 2 h was favored with an increase in $S_{MES/EXT}$ (**Figure 8.76.A**) and a decrease in the BA/LA ratio (**Figure**

8.76.B), achieving 100% with d-ZSM-5/4d. The highest selectivity to DHC at 80% conversion was reached with the same catalyst exhibiting a $S_{MES/EXT}$ of 360 m^2 g^{-1} (**Figure 8.76.C**) and a BA/LA ratio of 1.4 (**Figure 8.76.D**). Similarly, to the conversion, the selectivity to DHC increased with $S_{MES/EXT}$ and decreased with the BA/LA ratio. On the other hand, **Figure 8.76.E-F** illustrates the absence of a direct relationship between the *cis*/*trans*-DHC molar ratio with $S_{MES/EXT}$ and BA/LA ratio, but a minimum value of ca. 0.55 is achieved with h-ZSM-5 with a $S_{MES/EXT}$ of 279 m^2 g^{-1} and a BA/LA ratio of 3.1.

4.4.2.4. Effect of the substrate

Due to the commercial substrate used for assessing the limonene-1,2-epoxide isomerization is a mixture of *cis* and *trans* isomers (*cis*: *trans* molar ratio of 0.65:1), it is advisable to evaluate how the transformation proceeds starting with pure *cis* and *trans* isomers, utilizing the most active catalyst (d-ZSM-5/4d) at 70 °C, with anhydrous ethyl acetate as the solvent. Additionally, two main products, dihydrocarvone and carveol, were employed as starting substrates to investigate their stability or, conversely, to assess if they can be transformed under the tested reaction conditions. **Figure 4.6.A** illustrates the dependence of conversion as a function of time for five substrates, with complete conversions achieved after 2 h for the three LE sources. In contrast, no activity was observed with dihydrocarvone and L-carveol as starting reagents. This leads to the conclusion that the two main products during LE isomerization over dendritic zeolites are very stable. On the other hand, the reactivity order of the substrates is as follows: mixture-LE > *cis*-LE > *trans*-LE, with initial reaction rates of 0.92, 0.54, and 0.28 mmol min^{-1} g^{-1}, respectively. These results suggest a synergistic effect in the way that the mixture of isomers interacts in the catalyst surface, potentially enhancing the reaction rate and overall conversion, in comparison with the pure isomers as initial substrates [66,67]. The comparison of the initial reaction rates of neat isomers (*cis*-LE and *trans*-LE) with the analogous values of isomers present in the mixture-LE shows values of 0.62 and 0.30 mmol min^{-1} g^{-1} for *cis*-LE and *trans*-LE, respectively. These values are slightly higher than those of the neat isomers (0.54 and 0.28 mmol min^{-1} g^{-1}), confirming the synergistic effect of using the mixture-LE as raw material in the isomerization route.

Trans-LE exhibits high selectivity to DHC (**Figure 4.6.B**), maintaining values of ca. 80% across a wide conversion range. Surprisingly, our results suggest a high favorability of the formation of *trans*-DHC from *trans*-LE, as indicated in **Figure 4.6.E** and **Figure 4.6.F**. In contrast, when starting with *cis*-LE, only a maximum selectivity of ca. 45% to DHC is achieved, with *cis*-DHC being the primary configuration produced. **Figure 4.6.C** illustrates selectivities towards carveol, indicating no significant changes in this parameter when starting with mixture-LE and *cis*-LE, reaching maximum values of ca. 12%, while maximum values of approximately 4% are observed with *trans*-LE. Conversely, the significant formation of product **3** (**Figure 4.6.D**) is achieved with *cis*-LE as the substrate, reaching a maximum value of about 33%, whereas only maximum values of approximately 9% are reached when starting with *trans*-LE. Mixture-LE yields intermediate selectivity values ranging between 12% and 17%. *Trans*-DHC and *cis*-DHC are formed in a parallel pathway, as shown in **Figure 4.6.F**.

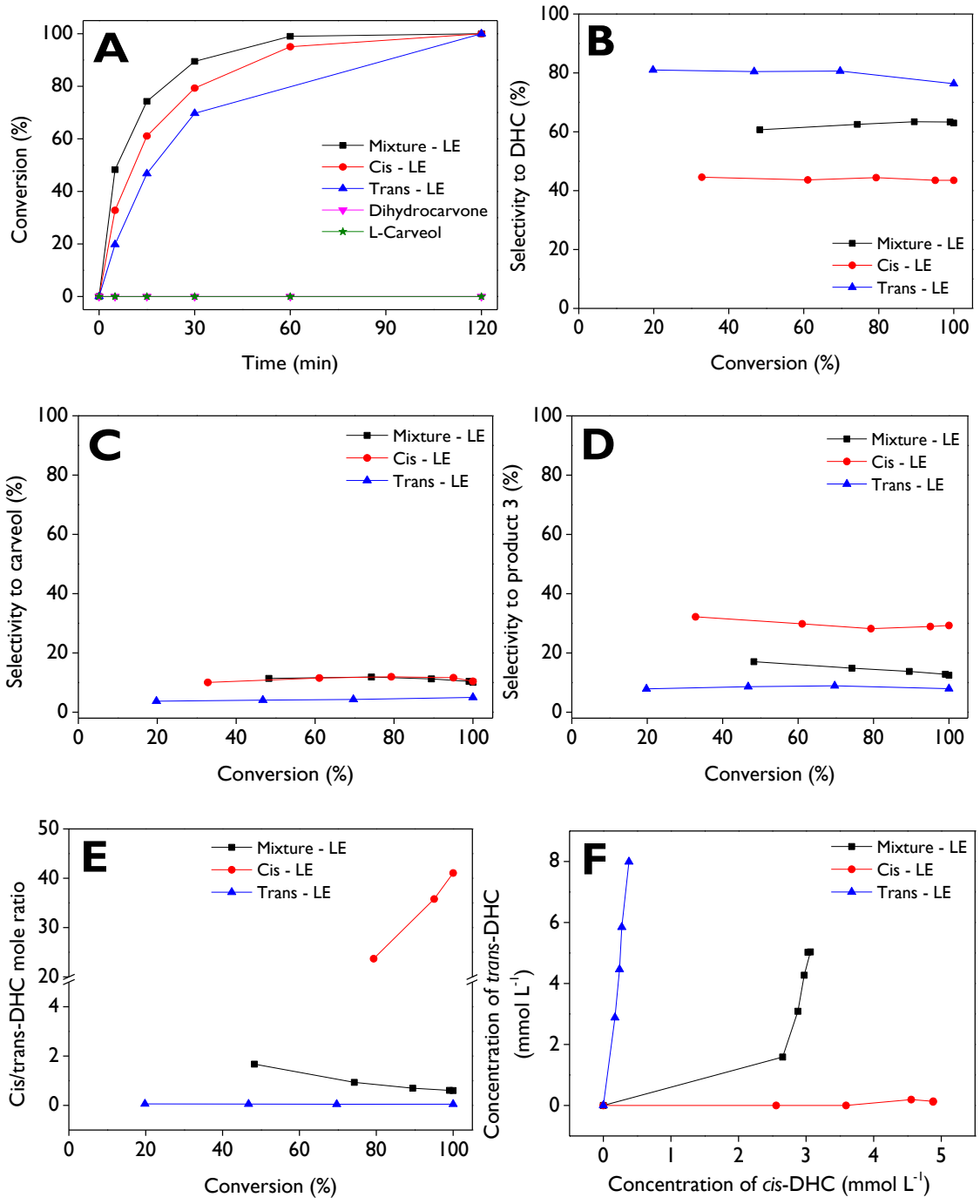

Figure 4.6. Effect of the substrate on its isomerization over d-ZSM-5/4d. **(A)** substrate conversion as a function of the reaction time; **(B)** selectivity to dihydrocarvone, **(C)** selectivity to carveol, **(D)** selectivity to product **3**, and **(E)** *cis*/*trans* dihydrocarvone molar ratio, as a function of the conversion; **(F)** concentration of *trans*-DHC vs. concentration of *cis*-DHC. **Reaction conditions:** $C_{substrate,0}$ = 13 mmol L^{-1}, 75 mL of total volume, anhydrous ethyl acetate as a solvent, 115 mg of d-ZSM-5/4d, 70 °C, 520-530 rpm, N_2 atmosphere.

4.4.2.5. Solvent effect

The solvent plays a critical role in the isomerization of limonene-1,2-epoxide, as reported in the literature [22,48,49] because it can control the stabilization of the charge of the intermediate carbocation during the reaction [22]. Solvents with dielectric constants between 2.2 and 3.1, such as 1,4-dioxane, toluene, and DMC, were earlier evaluated using Keggin

heteropolyacids-based materials [48] and Fe/SBA-15 as catalysts [49]. Therefore, the effect of the solvent is here assessed using a wide range of solvent polarity, represented by its values of dielectric constant. **Figure 4.7.A** shows the conversion profiles obtained with different solvents using the d-ZSM-5/4d sample, allowing to establish the reactivity order, which increases as follows: acetonitrile < ethyl acetate < DMC < toluene, exhibiting initial reaction rates of 0.10, 0.92, 1.2, and 1.7 mmol min^{-1} g^{-1}, respectively. Complete LE conversions were achieved after 15, 30, and 60 min with toluene, DMC, and ethyl acetate, respectively, whereas acetonitrile resulted in a low conversion of ca. 32% after 2 h. **Figure 4.7.B** shows that *cis*-LE is more reactive than *trans*-LE with solvents of low (toluene) and medium (DMC, ethyl acetate) polarity, given the *cis*/*trans*-LE ratio (**Figure 4.7.B**) achieved zero values at lower times compared to the complete conversion (**Figure 4.7.A**). In contrast, the most polar solvents, such as acetonitrile, exhibited a more competitive consumption of both *cis*-LE and *trans*-LE. The conversion profiles of the isomers, *cis*-LE and *trans*-LE, exhibit the expected behavior according to **Figure 4.7.B** and **Figure 8.79.C-D** in the Supporting Information.

A constant trend of DHC selectivity (**Figure 4.7.C**) is observed as the reaction progresses when using ethyl acetate and DMC as solvents, with values ranging from about 62% to 65%. In contrast, results with toluene indicate that LE isomerization is not favored towards DHC at high conversions, showing selectivity values between 40% and 44%. The highest (10-12%) and lowest (1-4%) selectivities to carveol (sum of *cis* and *trans*) are achieved with ethyl acetate and toluene as solvents, respectively (**Figure 4.7.D**). With DMC, selectivities to carveol are in the range of ca. 1 to 5%. The selectivity to product 3 (**Figure 4.7.E**) ranges between 10-20%, 15-20%, and 12-17% with toluene, DMC, and ethyl acetate, respectively.

Trans-DHC is favored over *cis*-DHC as the reaction proceeds with different solvents (**Figure 4.7.F**), stabilizing in a *cis*/*trans* molar ratio of about 0.5-0.6 at conversions above 80% with ethyl acetate and DMC, while toluene notably favors the formation of *trans*-DHC over *cis*-DHC, reaching ratios between 0.2-0.3. **Figure 4.7.G** shows that the LE conversion can be directly linked to low solvent polarity, while selectivity to DHC (*cis* + *trans*) reaches maximum values with moderately polar solvents such as ethyl acetate and DMC. However, *cis*-DHC is favored with ethyl acetate, whereas the formation of *trans*-DHC is promoted with DMC. On the other hand, carveol is most favored in solvents with medium polarity as ethyl acetate. A highly polar solvent, such as acetonitrile, is not suitable for LE isomerization leading to low conversions, and additionally, no formation of any of the 8 products in **Figure 8.73** was observed (**Table 4.3**). Contrarily, a main product was identified by GC-MS with low quality (35%) having the CAS number: 20662-85-5, its mass spectra being provided in **Figure 8.87**.

In summary, it can be concluded that the LE isomerization over the d-ZSM-5/4d catalyst is favored in non-polar solvents such as toluene, but its transformation is highly selective towards DHC in solvents with medium polarity, such as DMC and ethyl acetate. These results can be mechanistically explained by the dipolar orientations of solvents with the intermediate carbocation, facilitating the rearrangement of limonene-1,2-epoxide. The stability of this carbocation is influenced by solvent polarity, which plays a crucial role in determining product selectivity and favoring one specific route over others. Similar effects of solvent polarity have been reported for the rearrangement of other monoterpene epoxides, such as α-pinene epoxide, where it favors the formation of campholenic aldehyde and carveol as the major products [49]. The carbocation obtained after breaking the C-O bond can produce several thermodynamic products, as demonstrated in the literature [68]. These insights support the carbocations in the reaction mechanism of the rearrangement of limonene epoxide towards

dihydrocarvone over a heteropolyacid, proposed by Cotta et al. [22]. **Table 4.3** presents the detailed product distribution with the solvents, along with the initial reaction rate and TOF. It is worth mentioning that the formation of traces of limonene diol (product **8**) with DMC can be attributed to the low amount of water present as an impurity in commercial solvents.

Table 4.3. Product distribution on the isomerization of limonene-1,2-epoxide over d-ZSM-5/4d with different solvents. Notation for the different components is given in **Figure 8.73**.

Solvent	$-r_{LE,0}$ (mmol min^{-1} g^{-1})	TOF (min^{-1})	Conversion (%)	Selectivity (%)									
				1a	1b	2	3	4	5	6	7	8	Others
Toluene	1.7	7.9	100[a]	9.6	31.4	0.0	9.1	0.1	0.0	8.5	1.7	0.0	39.6
DMC	1.2	5.5	70	29.9	32.7	5.0	19.2	1.7	3.7	2.1	3.5	2.3	0.0
			100[a]	22.4	44.3	0.4	15.6	3.0	2.3	6.2	3.4	2.2	0.0
Ethyl acetate	0.9	4.4	70	30.2	32.4	11.9	14.9	1.6	3.0	1.9	4.2	0.0	0.0
			100[a]	23.7	39.3	10.1	12.5	3.3	2.3	4.9	4.0	0.0	0.0
Acetonitrile	0.1	0.5	32[a]	0.0	0.0	0.0	0.0	0.0	0.0	0.0	0.0	0.0	100.0

[a] Conversion values after 120 min. **Reaction conditions:** $C_{LE,0}$ = 13 mmol L^{-1}, 75 mL of total volume, 115 mg of d-ZSM-5/4d, 70 °C, 520-530 rpm, N_2 atmosphere.

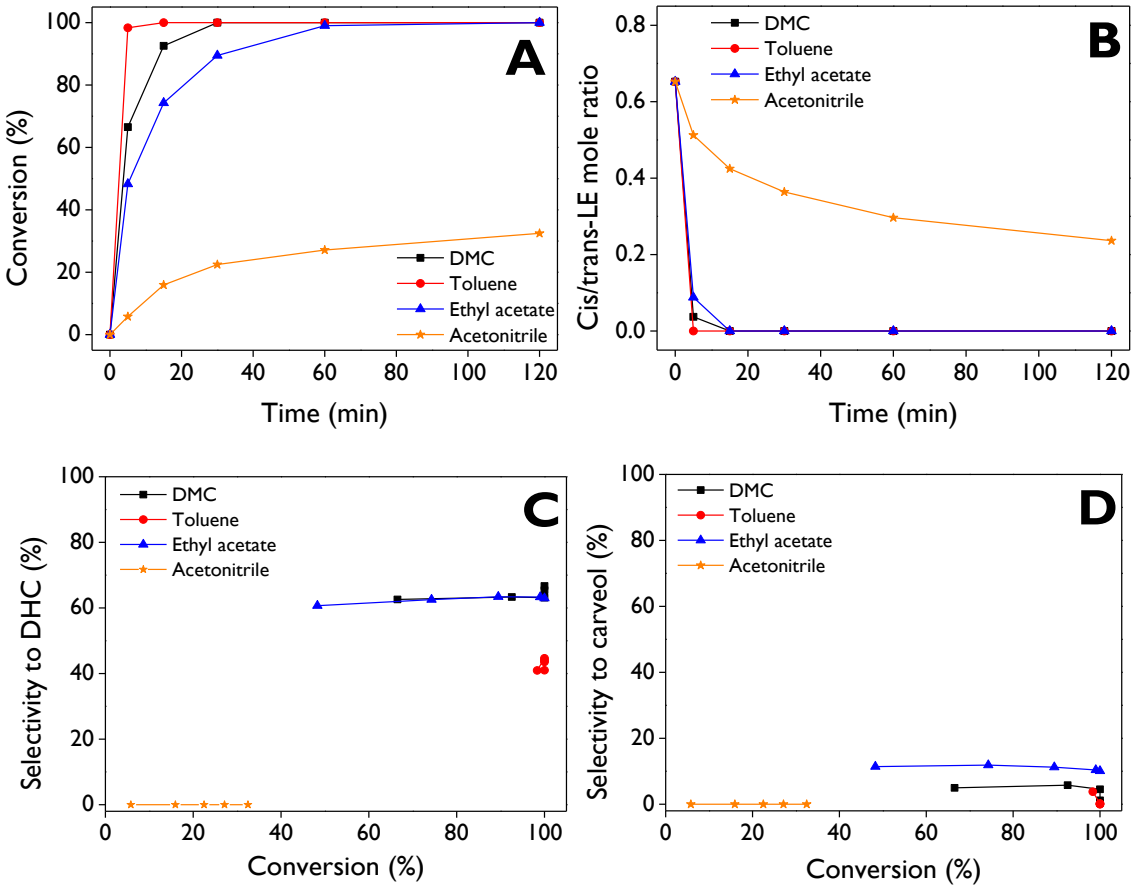

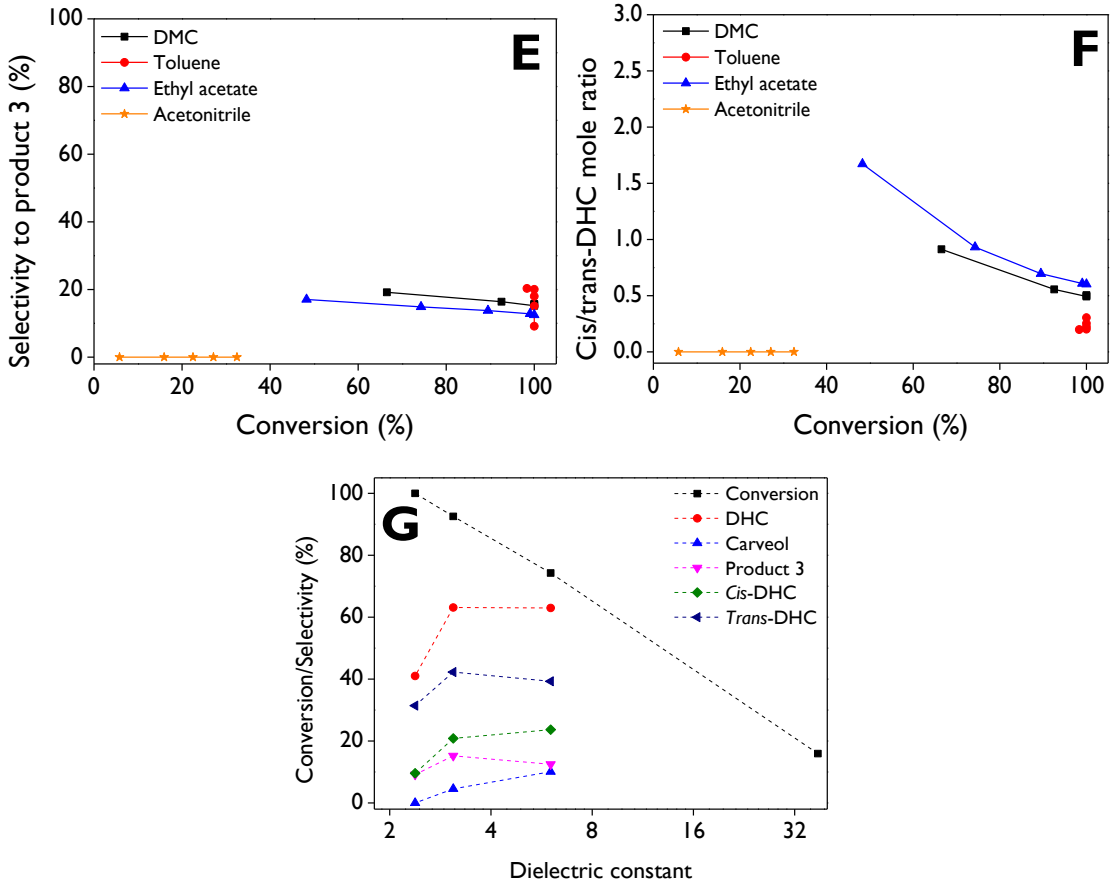

Figure 4.7. Effect of the solvent on the LE isomerization over d-ZSM-5/4d. **(A)** LE conversion and **(B)** *cis*/*trans*-LE molar ratio as a function of the reaction time; **(C)** selectivity to dihydrocarvone, **(D)** selectivity to carveol, **(E)** selectivity to product **3**, and **(F)** *cis*/*trans* dihydrocarvone molar ratio, as a function of the conversion; **(G)** conversion after 15 min or selectivity at 100% conversion as a function of the solvent dielectric constant: toluene (ε=2.38), dimethyl carbonate (ε=3.09), ethyl acetate (ε=6.02), acetonitrile (ε=37.5). **Reaction conditions:** $C_{LE,0}$ = 13 mmol L^{-1}, 75 mL of total volume, 115 mg of d-ZSM-5/4d, 70 °C, 520-530 rpm, N_2 atmosphere.

4.4.3. Robustness of the dendritic zeolites

The reuse of d-ZSM-5/4d was investigated with two procedures: i) filtration, washing with acetone, and drying at 100 °C (spent), and ii) regeneration of the spent catalyst through calcination at 550 °C, with the results shown in **Figure 4.8**. Upon reusing the spent catalyst, a significant loss of activity was observed (**Figure 4.8.A**), with only about 82% conversion achieved after 2 h, whereas the fresh run exhibited complete conversion after just 1 h. On the other hand, the decrease in selectivity towards DHC (**Figure 4.8.B**) with the spent catalyst suggests that the adsorbed species could block preferentially some types of active sites, in particular those responsible for the DHC formation, resulting in a significant change in the product distribution of the isomerization reaction. Conversely, when the spent catalyst was regenerated by air combustion, the catalytic activity was completely recovered, as it is evident in the conversion profile. Moreover, selectivity to DHC was slightly improved in comparison with the fresh catalyst (**Figure 4.8.B**). TPO-MS analysis (**Figure 8.77**) led to the conclusion that no coke formation occurred on the catalyst surface during the reaction, as evidenced by the absence of signals for CO and/or CO_2.

TGA-air analysis of the spent catalyst sample (**Figure 8.78**) evidence three main weight losses. The first one, which occurs at low temperatures, is also present in the parent zeolite, being assigned to the removal of physisorbed water. However, two other broad signals at about 280 and 560 °C can be observed in the TGA-DTG curves of the spent catalyst, being absent in the case of the parent zeolite. This fact denotes the accumulation of some organic matter on the spent catalyst, which is consistent with its light-yellow color. However, these weight losses suppose only 3 wt% (referred to the zeolite weight), which is significantly lower than the value corresponding to the complete filling of the zeolite micropores with organic matter (c.a 14 wt%). After regeneration by calcination at 550 °C, a completely white solid was obtained, indicating the total removal of these species. This is confirmed by the TGA-DTG profile of the regenerated sample (**Figure 8.78**), resembling that of the parent zeolite and agreeing with the full recovery of catalytic activity and selectivity towards DHC (**Figure 4.8**).

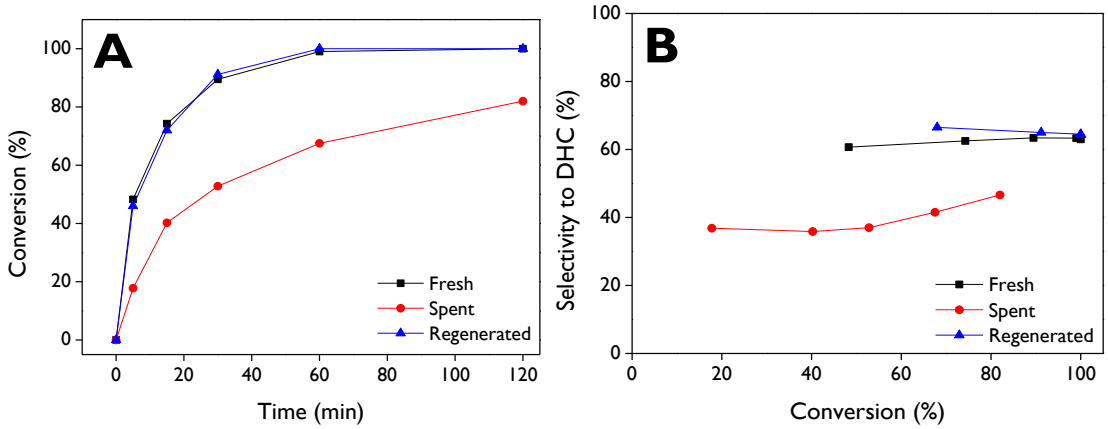

Figure 4.8. Reusability of d-ZSM-5/4d on the LE isomerization. **(A)** LE conversion as a function of reaction time and **(B)** selectivity to dihydrocarvone as a function of the conversion. **Reaction conditions:** $C_{LE,0}$ = 13 mmol L^{-1}, 75 mL of total volume, anhydrous ethyl acetate as a solvent, 115 mg of catalyst, 70 °C, 520-530 rpm, N_2 atmosphere.

4.4.4. Extending the scope of dendritic zeolite to the isomerization of α- and β-pinene epoxides

The application of dendritic zeolite d-ZSM-5/4d, identified as the most active material in the LE isomerization, was also assessed in the rearrangement of α- and β-pinene epoxides. These epoxides can be synthesized from the well-known corresponding pinenes through the epoxidation route. These catalytic tests were conducted under reaction conditions like those previously described for the LE isomerization, with anhydrous ethyl acetate as the solvent.

The main products obtained from the isomerization of α-pinene epoxide (**Figure 8.80.A**) are campholenic aldehyde (CA), fencholenic aldehyde (FA), *trans*-carveol (TC), pinocamphone (PC), and pinocarveol (PCOL), while *p*-cymene (PCY) can be obtained from dehydration of *trans*-carveol. In the case of β-pinene epoxide isomerization (**Figure 8.80.B**), the main products are myrtanal (*cis* + *trans*), myrtenol, and perillyl alcohol (PA). It is well-known that the production of campholenic aldehyde and myrtanal is favored with catalysts containing Lewis acid sites [69–71], as it the case of the dendritic ZSM-5 samples here investigated. Detailed information regarding retention times and mass spectra can be found in the Supporting Information (**Table 8.9**-**Table 8.10** and **Figure 8.88**-**Figure 8.92**).

Figure 4.9.A illustrates the complete conversion of α-pinene epoxide after 15 min, with selectivity values of 63%, 8%, 6%, 6%, and 2% for CA, TC, FA, PC, and PCY, respectively. **Figure 8.81** shows the profiles for the conversion of the epoxide and the yields of the products but using DMC as a solvent at 70 °C, resulting in complete conversion after 5 min and selectivity values of 72% (CA), 5% (TC), 5% (FA), 6% (PC), and 2% (PCY). With β-pinene epoxide (**Figure 4.9.B**), complete conversion was reached rapidly after 5 min, with selectivity values of 23%, 25%, 19%, and 3% for *cis*-myrtanal, *trans*-myrtanal, PA, and myrtenol, respectively.

The results demonstrate the promising catalytic activity of d-ZSM-5/4d in the isomerization of pinenes epoxides, leading to complete conversion in very short reaction times and mild reaction temperatures (50-70 °C). **Table 8.7** shows that our results with d-ZSM-5/4d and α-pinene epoxide (entries 1-2) generated higher yields of campholenic aldehyde (62.5% at 60 °C with ethyl acetate after 15 min, and 72.4% at 70 °C with DMC after 5 min) in comparison with entries 3, 5-6, 8-15. Entries 4 and 7 showed slightly higher yields (66% and 64%, respectively) but they were achieved at 70 °C for longer reaction times (2.5 h) and using toluene as the solvent. Moreover, our results with DMC also surpass those two entries. The higher selectivity achieved towards CA with DMC, compared to ethyl acetate, can be easily explained by the lower polarity of DMC (3.09 < 6.02). On the other hand, with β-pinene epoxide as a substrate, d-ZSM-5/4d (entry 16) demonstrated a higher yield of myrtanal (*cis* + *trans*) as the main product than other catalysts described in entries 17-18 and 20-24. A yield to myrtanal of ca. 47.5%, like that of d-ZSM-5/4d, was achieved with Sn-Beta-300 (entry 19) [72]. This catalyst exhibits a BA/LA acidity ratio of 0.75, close to the corresponding value of d-ZSM-5/4d (1.4). However, it is noteworthy that Sn-Beta-300 required a higher temperature and longer reaction time. Additionally, a less benign solvent, such as toluene, was used in comparison with ethyl acetate.

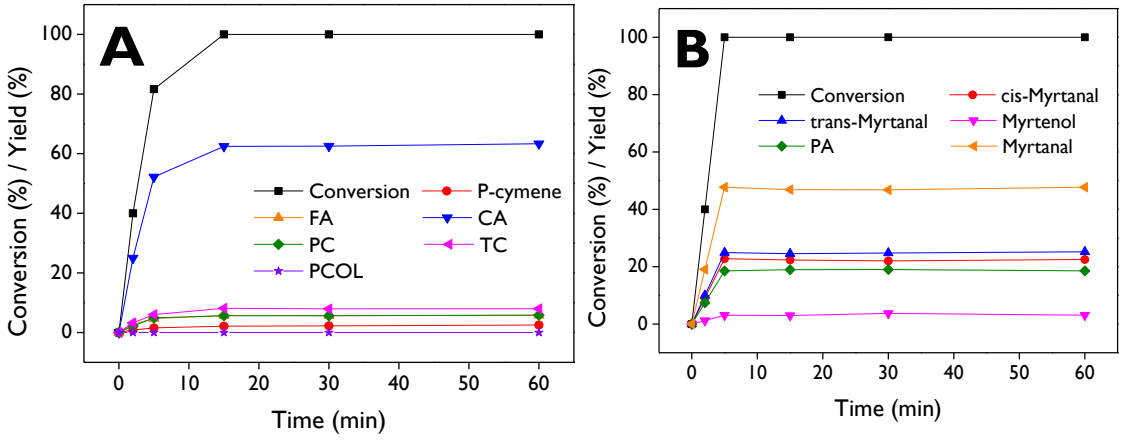

Figure 4.9. Conversion and product distribution of the isomerization of **(A)** α-pinene epoxide (60 °C) and **(B)** β-pinene epoxide (50 °C) over d-ZSM-5/4d. FA: Fencholenic aldehyde, CA: Campholenic aldehyde, PC: Pinocamphone, TC: *Trans*-carveol, PCOL: Pinocarveol, PA: Perillyl alcohol. **Reaction conditions:** C_0 = 13 mmol L^{-1}, 75 mL of total volume, anhydrous ethyl acetate as a solvent, 115 mg of catalyst, 520-530 rpm, N_2 atmosphere.

4.5. Conclusions

Dendritic ZSM-5 zeolites were tested in the isomerization of monoterpene epoxides such as limonene-1,2-epoxide, α-pinene epoxide, and β-pinene epoxide. The main products of the

epoxide rearrangement (dihydrocarvone, campholenic aldehyde, and myrtanal) are high-value compounds used for fragrances, cosmetics, and pharmaceuticals. The study included also conventional and hierarchical ZSM-5 samples as references.

Dendritic ZSM-5 zeolites exhibited a well-crystallized MFI zeolitic structure. The dendritic zeolite with a crystallization time of 4 days (d-ZSM-5/4d) presented a remaining mesoscopic ordering, formed during silanization of the synthesis gel, which disappeared when increasing the crystallization time to 7 days (d-ZSM-5/7d). Specifically, the isotherm shape of the dendritic zeolites exhibited a substantial contribution from mesopores, whereas TEM images denote a high degree of connectivity between the different levels of porosities.

The highest TOF (4.4 min^{-1}) for limonene-1,2-epoxide (LE) isomerization was achieved with d-ZSM-5/4d zeolite, which exhibited the lowest BA/LA ratio (1.4), the largest mesopore/external surface area (360 m^2 g^{-1}), the narrowest mesopore size distribution, and the highest concentration of external Brønsted acid sites (97 μmol g^{-1}). This material is significantly more active than catalysts earlier reported based on ordered mesoporous supports such as MCM-41 and SBA-15 with Fe and Cu as active phases. Additionally, this material demonstrated the highest selectivity (60-63%) for *cis*/*trans*-dihydrocarvone (DHC) during the reaction, enabling a DHC yield of 63% after 2 h, thereby surpassing recently reported catalysts for this application. A good correlation was found between the catalytic activity and the concentration of external Brønsted acid sites, showing the occurrence of strong steric/diffusional limitations that are mostly overcome when using the dendritic ZSM-5 samples due to their outstanding accessibility.

The reaction rate of LE isomerization is favored in non-polar solvents, while highly selective formation of DHC was observed in the solvents with medium polarity, such as dimethyl carbonate and ethyl acetate. d-ZSM-5/4d demonstrated to be a versatile catalyst for the isomerization of pinene epoxides, reaching 72% yield of campholenic aldehyde (70 °C, DMC, 5 min) and a 48% yield of myrtanal (50 °C, ethyl acetate, 5 min). These results either surpass or are equivalent to the recent heterogeneous catalysts reported for those routes.

Supporting Information

The Supporting Information File (**section 8.3**) contains details on the reaction setup, low-XRD patterns, repeatability test, confirmation of catalytic isomerization route, TOF calculations, rationalization of results with the properties of the catalysts, TPO-MS analysis, the performance of dendritic zeolite on the isomerization of α-pinene epoxide with DMC as solvent, and characterization of the substrate and reaction products by GC-MS.

4.6. Acknowledgments

Luis A. Gallego-Villada is grateful to Universidad de Antioquia for their support during his research internship through the project 2022-53000 as part of the "Convocatoria Programática 2021-2022: Ingeniería y Tecnología" program, as well as the "Beca Doctoral Universidad de Antioquia" scholarship. D.P.S., M.A-D., and J.C. are gratefully acknowledged to the European Research Council Horizon 2020 research and innovation program TODENZE project (ERC101021502).

4.7. References

[1] R.A. Sheldon, Green and sustainable manufacture of chemicals from biomass: state of the art, Green Chem. 16 (2014) 950–963. https://doi.org/10.1039/C3GC41935E.

[2] M. Golets, S. Ajaikumar, J.-P. Mikkola, Catalytic Upgrading of Extractives to Chemicals: Monoterpenes to "EXICALS," Chem. Rev. 115 (2015) 3141–3169. https://doi.org/10.1021/cr500407m.

[3] P. Sudarsanam, E. Peeters, E. V. Makshina, V.I. Parvulescu, B.F. Sels, Advances in porous and nanoscale catalysts for viable biomass conversion, Chem. Soc. Rev. 48 (2019) 2366–2421. https://doi.org/10.1039/C8CS00452H.

[4] J.E. Sánchez-Velandia, L.A. Gallego-Villada, P. Mäki-Arvela, A. Sidorenko, D. Yu. Murzin, Upgrading biomass to high-added value chemicals: synthesis of monoterpenes-based compounds using catalytic green chemical pathways, Catal. Rev. (2024) 1–126. https://doi.org/10.1080/01614940.2024.2329553.

[5] P.T. Anastas, J.C. Warner, Green Chemistry: Theory and Practice, Oxford University Press, 1998. https://books.google.fi/books?id=SrO8QgAACAAJ.

[6] A. Ludwiczuk, K. Skalicka-Woźniak, M.I. Georgiev, Terpenoids, in: Pharmacognosy, Elsevier, 2017: pp. 233–266. https://doi.org/10.1016/B978-0-12-802104-0.00011-1.

[7] L.A. Gallego-Villada, E.A. Alarcón, A.L. Villa, Evaluation of nopol production obtained from turpentine oil over Sn/MCM-41 synthesized by wetness impregnation using the Central Composite Design, Mol. Catal. 498 (2020) 111250. https://doi.org/10.1016/j.mcat.2020.111250.

[8] L.A. Gallego-Villada, E.A. Alarcón, A.L. Villa, Effect of Colombian raw materials on the Prins condensation reaction over Sn/MCM-41, Catal. Today. 372 (2021) 36–50. https://doi.org/10.1016/j.cattod.2020.10.040.

[9] J.E. Sánchez-Velandia, L.M. Valdivieso, F. Martínez O, S.M. Mejía, A.L. Villa, J. Wärnå, D.Y. Murzin, Synthesis of trans-pinocarveol from oxidation of β-pinene using multifunctional heterogeneous catalysts, Mol. Catal. 541 (2023) 113104. https://doi.org/10.1016/j.mcat.2023.113104.

[10] H. Martinez Q, Á.A. Amaya, E.A. Paez-Mozo, F. Martinez O, S. Valange, Photo-assisted O-atom transfer to monoterpenes with molecular oxygen and a dioxoMo(VI) complex immobilized on TiO2 nanotubes, Catal. Today. 375 (2021) 441–457. https://doi.org/10.1016/j.cattod.2020.07.053.

[11] H. Guo, X. Lu, J. He, H. Zhang, H. Zhang, Y. Dong, D. Zhou, Q. Xia, Co-MOF nanosheet supported on ZSM-5 with an improved catalytic activity for air epoxidation of olefins, Mater. Chem. Phys. 294 (2023) 127001. https://doi.org/10.1016/j.matchemphys.2022.127001.

[12] R. Hajian, E. Bahrami, Mn(III)-Porphyrin Immobilized on the Graphene Oxide-Magnetite Nanocomposite as an Efficient Heterogeneous Catalyst for the Epoxidation of Alkenes, Catal. Letters. 152 (2022) 2445–2456. https://doi.org/10.1007/s10562-021-03827-x.

[13] H. Zhang, X. Lu, L. Yang, Y. Hu, M. Yuan, C. Wang, Q. Liu, F. Yue, D. Zhou, Q. Xia,

Efficient air epoxidation of cycloalkenes over bimetal-organic framework ZnCo-MOF materials, Mol. Catal. 499 (2021) 111300. https://doi.org/10.1016/j.mcat.2020.111300.

[14] C. Wang, H. Zhan, X. Lu, R. Jing, H. Zhang, L. Yang, X. Li, F. Yue, D. Zhou, Q. Xia, A recyclable cobalt(<scp>iii</scp>)–ammonia complex catalyst for catalytic epoxidation of olefins with air as the oxidant, New J. Chem. 45 (2021) 2147–2156. https://doi.org/10.1039/D0NJ05466F.

[15] M. Vasconcellos-Dias, C.D. Nunes, V. Félix, P. Brandão, M.J. Calhorda, New heptacoordinate tungsten(II) complexes with α-diimine ligands in the catalytic oxidation of multifunctional olefins, Inorganica Chim. Acta. 519 (2021) 120263. https://doi.org/10.1016/j.ica.2021.120263.

[16] M.S. Nunes, D.M. Gomes, A.C. Gomes, P. Neves, R.F. Mendes, F.A.A. Paz, A.D. Lopes, A.A. Valente, I.S. Gonçalves, M. Pillinger, A 5-(2-Pyridyl)tetrazolate Complex of Molybdenum(VI), Its Structure, and Transformation to a Molybdenum Oxide-Based Hybrid Heterogeneous Catalyst for the Epoxidation of Olefins, Catalysts. 11 (2021) 1407. https://doi.org/10.3390/catal11111407.

[17] L.A. Gallego-Villada, E.A. Alarcón, A.L. Villa, Versatile Heterogeneous Catalytic System for the Selective Synthesis of Limonene Epoxide and Diepoxide, Ind. Eng. Chem. Res. 62 (2023) 20152–20169. https://doi.org/10.1021/acs.iecr.3c02633.

[18] L.A. Gallego-Villada, P. Mäki-Arvela, N. Kumar, E.A. Alarcón, Z. Vajglová, T. Tirri, I. Angervo, R. Lassfolk, M. Lastusaari, D.Y. Murzin, Zeolite Y-based catalysts for efficient epoxidation of R-(+)-Limonene: Insights into the structure-activity relationship, Microporous Mesoporous Mater. 372 (2024) 113098. https://doi.org/10.1016/j.micromeso.2024.113098.

[19] A. Rehman, F. Saleem, F. Javed, A. Ikhlaq, S.W. Ahmad, A. Harvey, Recent advances in the synthesis of cyclic carbonates via CO2 cycloaddition to epoxides, J. Environ. Chem. Eng. 9 (2021) 105113. https://doi.org/10.1016/j.jece.2021.105113.

[20] R. Mori, Replacing all petroleum-based chemical products with natural biomass-based chemical products: a tutorial review, RSC Sustain. 1 (2023) 179–212. https://doi.org/10.1039/D2SU00014H.

[21] A.B. Paninho, A.V.M. Nunes, Limonene carbonate synthesis from CO2: Continuous high-pressure flow catalysis with integrated product separation, J. Supercrit. Fluids. 193 (2023) 105827. https://doi.org/10.1016/j.supflu.2022.105827.

[22] R.F. Cotta, R.A. Martins, M.M. Pereira, K.A. da Silva Rocha, E.F. Kozhevnikova, I. V. Kozhevnikov, E. V. Gusevskaya, Heteropoly acid catalysis for the isomerization of biomass-derived limonene oxide and kinetic separation of the trans-isomer in green solvents, Appl. Catal. A Gen. 584 (2019) 117173. https://doi.org/10.1016/j.apcata.2019.117173.

[23] Foreverest, Dihydrocarvone, (n.d.). https://foreverest.net/products/turpentine-derivatives/dihydrocarvone.html (accessed November 12, 2023).

[24] J.M. Kouznetsov, Vladímir V Urbina G., E.E. Stashenko, N-Functionalization of dihydrocarvone: Obtainin aminocyclohexane derivatives and their spectrometric study,

J. Chil. Chem. Soc. 50 (2005) 559–563.

[25] J.R. Lowe, W.B. Tolman, M.A. Hillmyer, Oxidized Dihydrocarvone as a Renewable Multifunctional Monomer for the Synthesis of Shape Memory Polyesters, Biomacromolecules. 10 (2009) 2003–2008. https://doi.org/10.1021/bm900471a.

[26] Y. Dong, K.J. McCullough, S. Wittlin, J. Chollet, J.L. Vennerstrom, The structure and antimalarial activity of dispiro-1,2,4,5-tetraoxanes derived from (+)-dihydrocarvone, Bioorg. Med. Chem. Lett. 20 (2010) 6359–6361. https://doi.org/10.1016/j.bmcl.2010.09.113.

[27] J. Alarcon, C. Lamilla, C.L. Cespedes, Insecticidal activity of sesquiterpenes skeleton synthesized by the conventional Robinson annulations reaction on Drosophila melanogaster, Ind. Crops Prod. 42 (2013) 268–272. https://doi.org/10.1016/j.indcrop.2012.05.026.

[28] J.H. Advani, A.S. Singh, N.H. Khan, H.C. Bajaj, A. V. Biradar, Black yet green: Sulfonic acid functionalized carbon as an efficent catalyst for highly selective isomerization of α-pinene oxide to trans-carveol, Appl. Catal. B Environ. 268 (2020) 118456. https://doi.org/10.1016/j.apcatb.2019.118456.

[29] X. Feng, J. Hajek, H.S. Jena, G. Wang, S.K.P. Veerapandian, R. Morent, N. De Geyter, K. Leyssens, A.E.J. Hoffman, V. Meynen, C. Marquez, D.E. De Vos, V. Van Speybroeck, K. Leus, P. Van Der Voort, Engineering a Highly Defective Stable UiO-66 with Tunable Lewis- Brønsted Acidity: The Role of the Hemilabile Linker, J. Am. Chem. Soc. 142 (2020) 3174–3183. https://doi.org/10.1021/jacs.9b13070.

[30] L.D.B. Mandemaker, M. Rivera-Torrente, G. Delen, J.P. Hofmann, M. Lorenz, A. Belianinov, B.M. Weckhuysen, Nanoweb Surface-Mounted Metal–Organic Framework Films with Tunable Amounts of Acid Sites as Tailored Catalysts, Chem. – A Eur. J. 26 (2020) 691–698. https://doi.org/10.1002/chem.201903761.

[31] V.N. Panchenko, V.L. Kirillov, E.Y. Gerasimov, O.N. Martyanov, M.N. Timofeeva, Isomerization of α-pinene oxide to campholenic aldehyde in the presence of Al-SiO2 and magnetic Al-SiO2/Fe3O4 catalysts, React. Kinet. Mech. Catal. 130 (2020) 919–934. https://doi.org/10.1007/s11144-020-01811-x.

[32] C.J.A. Ribeiro, M.M. Pereira, E.F. Kozhevnikova, I. V. Kozhevnikov, E. V. Gusevskaya, K.A. da Silva Rocha, Heteropoly acid catalysts in upgrading of biorenewables: Synthesis of para-menthenic fragrance compounds from α-pinene oxide, Catal. Today. 344 (2020) 166–170. https://doi.org/10.1016/j.cattod.2018.12.023.

[33] A.S. Singh, J.H. Advani, A. V. Biradar, Phosphonate functionalized carbon spheres as Brønsted acid catalysts for the valorization of bio-renewable α-pinene oxide to trans - carveol, Dalt. Trans. 49 (2020) 7210–7217. https://doi.org/10.1039/D0DT00921K.

[34] E. Vrbková, E. Vyskočilová, M. Lhotka, L. Červený, Solvent Influence on Selectivity in α-Pinene Oxide Isomerization Using MoO3-Modified Zeolite BETA, Catalysts. 10 (2020) 1244. https://doi.org/10.3390/catal10111244.

[35] R. Barakov, N. Shcherban, P. Mäki-Arvela, P. Yaremov, I. Bezverkhyy, J. Wärnå, D.Y. Murzin, Hierarchical Beta Zeolites As Catalysts in α-Pinene Oxide Isomerization, ACS

Sustain. Chem. Eng. 10 (2022) 6642–6656. https://doi.org/10.1021/acssuschemeng.2c00441.

[36] A.S. Singh, D.R. Naikwadi, K. Ravi, A. V. Biradar, Chemoselective isomerization of α-Pinene oxide to trans-Carveol by robust and mild Brønsted acidic zirconium phosphate catalyst, Mol. Catal. 521 (2022) 112189. https://doi.org/10.1016/j.mcat.2022.112189.

[37] D. Makarouni, C. Dimitriadi Evgenidi, C. Kordulis, V. Dourtoglou, Catalytic conversion of biomass-derived compounds to high added value products using an acid treated natural mordenite, Sustain. Chem. Pharm. 33 (2023) 101125. https://doi.org/10.1016/j.scp.2023.101125.

[38] M.C. Cruz, J.E. Sánchez-Velandia, S. Causíl, A.L. Villa, Selective Synthesis of Perillyl Alcohol from β-Pinene Epoxide over Ti and Mo Supported Catalysts, Catal. Letters. 151 (2021) 2279–2290. https://doi.org/10.1007/s10562-020-03489-1.

[39] M. Chaves-Restrepo, A. Viloria, J.E. Sánchez-Velandia, A.L. Villa, Effect of reaction conditions and kinetics of the isomerization of β-pinene epoxide to myrtanal in the presence of Fe/MCM-41 and Fe/SBA-15, React. Kinet. Mech. Catal. 135 (2022) 2013–2029. https://doi.org/10.1007/s11144-022-02220-y.

[40] I. Paterova, B. Fidlerova, M. Vavra, E. Vyskocilova, L. Cerveny, Homogeneous Lewis and Brønsted acids as catalysts for β-pinene oxide rearrangement to prepare myrtenol and myrtanal, Mol. Catal. 492 (2020) 110945. https://doi.org/10.1016/j.mcat.2020.110945.

[41] H. Li, J. Liu, J. Zhao, H. He, D. Jiang, S.R. Kirk, Q. Xu, X. Liu, D. Yin, Selective Catalytic Isomerization of β-Pinene Oxide to Perillyl Alcohol Enhanced by Protic Tetraimidazolium Nitrate, ChemistryOpen. 10 (2021) 477–485. https://doi.org/10.1002/open.202000318.

[42] K. Ravi, D.R. Naikwadi, B.D. Bankar, A. V. Biradar, Sustainable Isomerization of α-Pinene Oxide to trans -Carveol using Formic Acid/Aniline System at Room Temperature, Adv. Sustain. Syst. 5 (2021) 1–6. https://doi.org/10.1002/adsu.202000212.

[43] S.M. Bruno, M. Pillinger, A.A. Valente, I.S. Gonçalves, Selective isomerization of α-pinene oxide to campholenic aldehyde by ionic liquid-supported indenyl-molybdenum(II)-bipyridine complexes, J. Organomet. Chem. 970–971 (2022) 122372. https://doi.org/10.1016/j.jorganchem.2022.122372.

[44] P.S. Löser, P. Rauthe, M.A.R. Meier, A. Llevot, Sustainable catalytic rearrangement of terpene-derived epoxides: towards bio-based biscarbonyl monomers, Philos. Trans. R. Soc. A Math. Phys. Eng. Sci. 378 (2020) 20190267. https://doi.org/10.1098/rsta.2019.0267.

[45] A. Corma, S. Iborra, A. Velty, Chemical Routes for the Transformation of Biomass into Chemicals, Chem. Rev. 107 (2007) 2411–2502. https://doi.org/10.1021/cr050989d.

[46] N. Ravasio, F. Zaccheria, M. Guidotti, R. Psaro, Mono- and Bifunctional Heterogeneous Catalytic Transformation of Terpenes and Terpenoids, Top. Catal. 27 (2004) 157–168. https://doi.org/10.1023/B:TOCA.0000013550.28170.6a.

[47] T.-T.T. Nguyen, D.-K.N. Chau, F. Duus, T.N. Le, Green Synthesis of Carvenone by

Montmorillonite-Catalyzed Isomerization of 1,2-Limonene Oxide, Int. J. Org. Chem. 03 (2013) 206–209. https://doi.org/10.4236/ijoc.2013.33027.

[48] V. V. Costa, K.A. da Silva Rocha, I. V. Kozhevnikov, E.F. Kozhevnikova, E. V. Gusevskaya, Heteropoly acid catalysts for the synthesis of fragrance compounds from biorenewables: isomerization of limonene oxide, Catal. Sci. Technol. 3 (2013) 244–250. https://doi.org/10.1039/C2CY20526B.

[49] J.E. Sánchez-Velandia, A.L. Villa, Selective synthesis of high-added value chemicals from α-pinene epoxide and limonene epoxide isomerization over mesostructured catalysts: Effect of the metal loading and solvent, Catal. Today. 394–396 (2022) 208–218. https://doi.org/10.1016/j.cattod.2021.09.011.

[50] J.E. Sánchez-Velandia, J.A. Castañeda-Olarte, C.F. Imbachí-Gamba, F. Martínez-Ortega, A.L. Villa, Hydrolysis of Limonene Epoxide over Hierarchical Zeolites, Catal. Letters. 153 (2023) 150–166. https://doi.org/10.1007/s10562-022-03963-y.

[51] A. Fihri, M. Bouhrara, U. Patil, D. Cha, Y. Saih, V. Polshettiwar, Fibrous Nano-Silica Supported Ruthenium (KCC-1/Ru): A Sustainable Catalyst for the Hydrogenolysis of Alkanes with Good Catalytic Activity and Lifetime, ACS Catal. 2 (2012) 1425–1431. https://doi.org/10.1021/cs300179q.

[51] C. Han, J. Yang, S. Dong, L. Ma, Q. Dai, J. Guo, Zeolite preparation from industrial solid waste: Current status, applications, and prospects, Sep. Purif. Technol. 354 (2025) 128957. https://doi.org/10.1016/j.seppur.2024.128957.

[52] N.S. Samanta, P.P. Das, P. Mondal, M. Changmai, M.K. Purkait, Critical review on the synthesis and advancement of industrial and biomass waste-based zeolites and their applications in gas adsorption and biomedical studies, J. Indian Chem. Soc. 99 (2022) 100761. https://doi.org/10.1016/j.jics.2022.100761.

[53] A. Maity, V. Polshettiwar, Dendritic Fibrous Nanosilica for Catalysis, Energy Harvesting, Carbon Dioxide Mitigation, Drug Delivery, and Sensing, ChemSusChem. 10 (2017) 3866–3913. https://doi.org/10.1002/cssc.201701076.

[54] M. del Mar Alonso-Doncel, C. Ochoa-Hernández, G. Gómez-Pozuelo, A. Oliveira, J. González-Aguilar, Á. Peral, R. Sanz, D.P. Serrano, Dendritic nanoarchitecture imparts ZSM-5 zeolite with enhanced adsorption and catalytic performance in energy applications, J. Energy Chem. 80 (2023) 77–88. https://doi.org/10.1016/j.jechem.2023.01.023.

[55] M. Alonso-Doncel, A. Peral, C. Ochoa-Hernández, R. Sanz, D.P. Serrano, Tracking the evolution of embryonic zeolites into hierarchical ZSM-5, J. Mater. Chem. A. 9 (2021) 13570–13587. https://doi.org/10.1039/D1TA01521D.

[56] M. Alonso-Doncel, A. Peral, M. Shamzhy, J. Čejka, R. Sanz, D.P. Serrano, Untangling the role of the organosilane functional groups in the synthesis of hierarchical ZSM-5 zeolite by crystallization of silanized protozeolitic units, Catal. Today. 345 (2020) 27–38. https://doi.org/10.1016/j.cattod.2019.11.031.

[57] D.P. Serrano, J. Aguado, Á. Peral, Controlling the generation of hierarchical porosity in ZSM-5 by changing the silanization degree of protozeolitic units, in: Stud. Surf. Sci.

Catal., Elsevier B.V., 2008: pp. 123–128. https://doi.org/10.1016/S0167-2991(08)80162-0.

[58] V. Zholobenko, C. Freitas, M. Jendrlin, P. Bazin, A. Travert, F. Thibault-Starzyk, Probing the acid sites of zeolites with pyridine: Quantitative AGIR measurements of the molar absorption coefficients, J. Catal. 385 (2020) 52–60. https://doi.org/10.1016/j.jcat.2020.03.003.

[59] K. Góra-Marek, K. Tarach, M. Choi, 2,6-Di- tert- butylpyridine Sorption Approach to Quantify the External Acidity in Hierarchical Zeolites, J. Phys. Chem. C. 118 (2014) 12266–12274. https://doi.org/10.1021/jp501928k.

[60] N. Kumar, P. Mäki-Arvela, S.F. Diáz, A. Aho, Y. Demidova, J. Linden, A. Shepidchenko, M. Tenhu, J. Salonen, P. Laukkanen, A. Lashkul, J. Dahl, I. Sinev, A. Leino, K. Kordas, T. Salmi, D.Y. Murzin, Isomerization of α-Pinene Oxide Over Iron-Modified Zeolites, Top. Catal. 56 (2013) 696–713. https://doi.org/10.1007/s11244-013-0029-y.

[61] D.Y. Murzin, T. Salmi, Catalytic Kinetics, 1st ed., ElSevier Science & Technology Books, 2005. http://link.springer.com/10.1007/s11244-013-0029-y.

[62] IZA Structure Commission, Database of Zeolite Structures, (n.d.). http://www.iza-structure.org/databases/ (accessed February 5, 2024).

[63] M. del M. Alonso-Doncel, E.A. Giner, D. de la Calle, J. Cueto, P. Horcajada, R.A. García-Muñoz, D.P. Serrano, Synthesis of Dendritic ZSM-5 Zeolite through Micellar Templating Controlled by the Amphiphilic Organosilane Chain Length, Cryst. Growth Des. 23 (2023) 5658–5670. https://doi.org/10.1021/acs.cgd.3c00326.

[64] M. Thommes, K. Kaneko, A. V. Neimark, J.P. Olivier, F. Rodriguez-Reinoso, J. Rouquerol, K.S.W. Sing, Physisorption of gases, with special reference to the evaluation of surface area and pore size distribution (IUPAC Technical Report), Pure Appl. Chem. 87 (2015) 1051–1069. https://doi.org/10.1515/pac-2014-1117.

[65] C. Raptis, H. Garcia, M. Stratakis, Selective Isomerization of Epoxides to Allylic Alcohols Catalyzed by TiO2 -Supported Gold Nanoparticles, Angew. Chemie Int. Ed. 48 (2009) 3133–3136. https://doi.org/10.1002/anie.200805838.

[66] D.Y. Murzin, P. Mäki-Arvela, E. Toukoniitty, T. Salmi, Asymmetric Heterogeneous Catalysis: Science and Engineering, Catal. Rev. 47 (2005) 175–256. https://doi.org/10.1081/CR-200057461.

[67] E.C. Schiesser, E. Blanco, A.B. Dongil, X. Zarate, M. Saavedra-Torres, E. Schott, R.I. Canales, N. Escalona, Insights into Hydrodeoxygenation of Furfural and Guaiacol Mixture: Experimental and Theoretical Studies, J. Phys. Chem. C. 125 (2021) 7647–7657. https://doi.org/10.1021/acs.jpcc.0c11415.

[68] J.E. Sánchez-Velandia, J.-A. Becerra, S.M. Mejía, A.L. Villa, F. Martínez O, Thermodynamics of the Isomerization of Monoterpene Epoxides, ACS Omega. 6 (2021) 34206–34218. https://doi.org/10.1021/acsomega.1c03049.

[69] M. Stekrova, N. Kumar, S.F. Díaz, P. Mäki-Arvela, D.Y. Murzin, H- and Fe-modified zeolite beta catalysts for preparation of trans-carveol from α-pinene oxide, Catal. Today. 241 (2015) 237–245. https://doi.org/10.1016/j.cattod.2013.12.004.

[70] M. Štekrová, M. Kubů, M. Shamzhy, Z. Musilová, J. Čejka, α-Pinene oxide isomerization: role of zeolite structure and acidity in the selective synthesis of campholenic aldehyde, Catal. Sci. Technol. 8 (2018) 2488–2501. https://doi.org/10.1039/C8CY00371H.

[71] M. Pitínová-Štekrová, P. Eliášová, T. Weissenberger, M. Shamzhy, Z. Musilová, J. Čejka, Highly selective synthesis of campholenic aldehyde over Ti-MWW catalysts by α-pinene oxide isomerization, Catal. Sci. Technol. 8 (2018) 4690–4701. https://doi.org/10.1039/C8CY01231H.

[72] P. Mäki-Arvela, N. Kumar, S.F. Diáz, A. Aho, M. Tenho, J. Salonen, A.-R. Leino, K. Kordás, P. Laukkanen, J. Dahl, I. Sinev, T. Salmi, D.Y. Murzin, Isomerization of β-pinene oxide over Sn-modified zeolites, J. Mol. Catal. A Chem. 366 (2013) 228–237. https://doi.org/10.1016/j.molcata.2012.09.028.

Chapter 5. Synthesis of Dihydrocarvone over Dendritic ZSM-5 Zeolite: A Comprehensive Study of Experimental, Kinetics, and Computational Insights

This chapter corresponds to an article published in ***Chemical Engineering Journal**, 2024, 498, 155377 – DOI: 10.1016/j.cej.2024.155377*

Luis A. Gallego-Villada[a,b,*], Wander Y. Perez-Sena[a], Julián E. Sánchez-Velandia[c], Jennifer Cueto[d], María del Mar Alonso-Doncel[d], Johan Wärmå[a], Päivi Mäki-Arvela[a], Edwin A. Alarcón[b], David P. Serrano[d,e*], Dmitry Yu. Murzin[a,*]

a. Laboratory of Industrial Chemistry and Reaction Engineering, Johan Gadolin Process Chemistry Centre, Åbo Akademi University, Henriksgatan 2, 20500 Turku/ Åbo, Finland
b. Environmental Catalysis Research Group, Chemical Engineering Faculty, Universidad de Antioquia, Medellín, Colombia
c. Sustainable and Supramolecular Research Group, Universidad Jaume I, Av. Vicent Sos Baynot, s/n, 12006, Castelló de la Plana, Spain
d. Thermochemical Processes Unit, IMDEA Energy Institute, Avda. Ramón de la Sagra, 3, 28935, Móstoles, Madrid, Spain
e. Chemical and Environmental Engineering Group, Rey Juan Carlos University, c/Tulipán s/n, 28933, Móstoles, Madrid, Spain

* Corresponding author, e-mail address: alfonso.gallego@udea.edu.co (Luis A. Gallego-Villada), david.serrano@imdea.org (David P. Serrano), dmitry.murzin@abo.fi (Dmitry Yu. Murzin)

Graphical Abstract

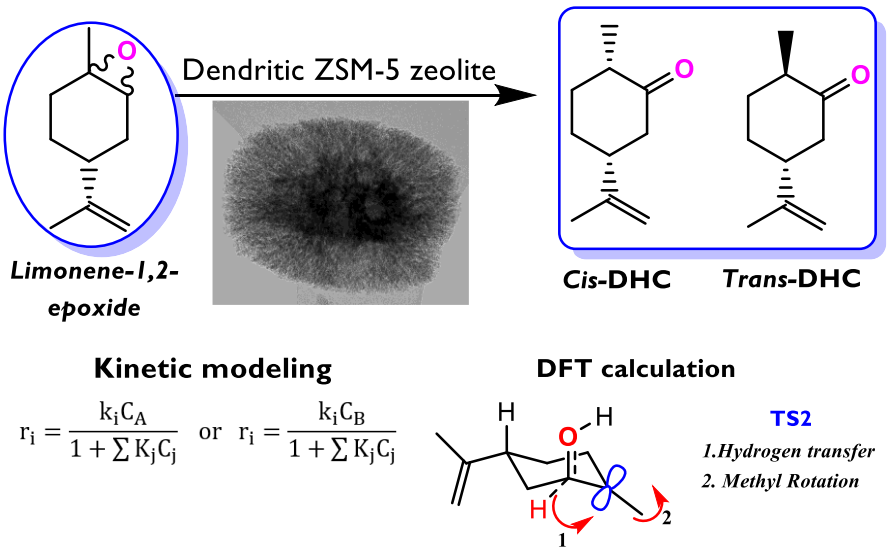

5.1. Abstract

This study explores the isomerization of limonene-1,2-epoxide (LE) from kinetic and mechanistic viewpoints, using a dendritic ZSM-5 zeolite (d-ZSM-5) as a highly selective catalyst for the formation of dihydrocarvone (DHC) in the form of diastereoisomers (*cis* + *trans*). Ethyl acetate, a green solvent, was used at mild reaction temperatures (50-70 °C). DHC, which can also be extracted from caraway oil, is widely used as an intermediate for epoxylactone production and as a constituent in flavors and perfumes. The d-ZSM-5 material exhibited remarkable activity with a turnover frequency (TOF) of 4.4 min^{-1}, significantly higher than other catalysts recently reported in the literature for this route. Kinetic modeling of LE isomerization was performed using a reaction network with eight parallel reactions and the corresponding rate equations, derived from the assumption of the rate-limiting surface reactions. The large standard errors in the statistical results of the initial data fitting suggested that three of those reactions can be neglected to describe the kinetic model more accurately. This refinement resulted in standard errors in the kinetic parameters lower than ca. 11%, confirming the statistical reliability of the modified kinetic model. Activation energies of 41.1 and 162 kJ mol^{-1} were estimated for the formation of *cis*-DHC and *trans*-DHC, respectively. Density Functional Theory (DFT) calculations revealed the preferred pathway for both *cis* and *trans*-LE conversion to DHC and carveol. The rate-determining step, carbocation formation ($\Delta Eact$ = 234 kJ mol^{-1}), precedes near-instantaneous dihydrocarvone formation under the studied conditions.

Keywords: ZSM-5, Dendritic zeolite, Limonene epoxide, Dihydrocarvone, Kinetic modeling, Density Functional Theory (DFT).

5.2. Introduction

Terpenes and terpenoids, such as e.g. dihydrocarvone (DHC), are useful as intermediates or final products in various application areas, including fragrances, cosmetics, and pharmaceuticals [1–3]. Monoterpenes, being among the most numerous and structurally diverse natural products, can be extracted by distillation of various biomass sources [4]. Limonene is a monocyclic terpene found in large quantities in numerous essential oils [5] and is the major constituent (91-96 wt%) of pressed orange-peel oil [6]. Oxidation of limonene gives epoxides, glycols, ketones, and alcohols, among other compounds of significant interest in green and sustainable chemistry [4,7–10]. Through isomerization of monoterpenes epoxides derived from biomass, many substances with potential pharmaceutical applications can be obtained.

1,2-Epoxy limonene (LE) is an attractive organic compound that, under acidic conditions, is isomerized into valuable fine chemicals, such as dihydrocarvone (*cis* + *trans*), carveol, and carvenone (**Figure 5.1**). Dihydrocarvone in turn is used in the synthesis of flavors and perfumes [11], providing numerous precursors like epoxylactones, which serve as intermediates in ring-opening polymerizations [12]. Additionally, this monoterpenoid is naturally found in caraway oil [13] and is used in the synthesis of dispiro-1,2,4,5-tetraoxanes, which exhibit potent anti-malarial activity [14], and α-cyperone, a eudesmane type sesquiterpenoid compound with potent insecticidal activity [15]. Furthermore, carveol exhibits chemopreventive properties against mammary carcinogenesis [16,17]. Carvenone is also widely used as a constituent in the synthesis of numerous flavors and fragrances [18].

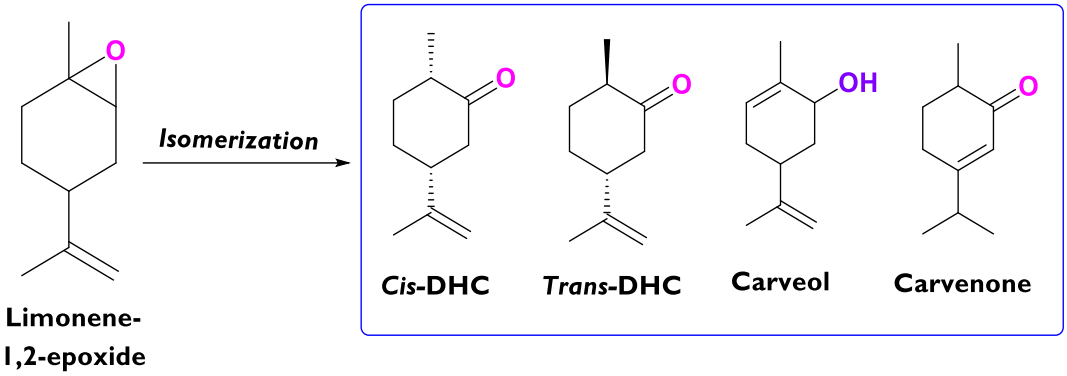

Figure 5.1. Rearrangement of limonene-1,2-epoxide into high added-value products.

In comparison to pinenes epoxides, isomerization of limonene epoxide has been scarcely studied. The conventional homogeneous catalyst reported for the isomerization of limonene epoxide is $ZnBr_2$, which results in cyclopentanecarboxyaldehyde (CPCA) and DHC as the main products [19]. Generally, LE can be converted in the presence of acidic heterogeneous catalysts [1], including amorphous silica-alumina [20], montmorillonite [18], Keggin-type heteropolyacids [1,21], Fe/SBA-15 [22], Au/TiO_2 [23], and SiO_2-Al_2O_3 [24]. According to these reports, the high reactivity and selectivity of the isomerization route depend strongly on the specific reaction conditions as well as on the catalyst and solvent type. The most critical factors influencing selectivity toward a specific target from limonene epoxide are the type of acid sites (Brønsted, Lewis, or their ratio) and the solvent (polar or non-polar).

Previous catalytic systems have used either toxic solvents such as toluene [20], 1,4-dioxane [21], dichloromethane [21], 1,2-dichloroethane [21], and acetonitrile [22], or very high temperatures (140 °C) [18]. Additionally, those systems exhibited limited yields to DHC as the major product, with the best result (80% yield) obtained with the Keggin-type heteropolyacid using 1,4-dioxane as the solvent [21]. In our recent study [25], dendritic ZSM-5 zeolites were found to be highly active catalysts for the valorization of monoterpene epoxides, such as internal limonene epoxide, α-pinene epoxide, and β-pinene epoxide, converting them into dihydrocarvone, campholenic aldehyde, and myrtanal, respectively. Notably, a remarkable yield of DHC (63%, 70 °C, 2 h) was achieved using a benign solvent like ethyl acetate and a relatively low temperature, with dendritic ZSM-5 zeolite (d-ZSM-5). **Table 5.1** presents a comparison based on turnover frequency (TOF) value for different heterogeneous catalysts, calculated based on the total acidity of the materials. Dendritic ZSM-5 zeolite exhibited superior activity in the isomerization route with a TOF of 4.4 min^{-1}, significantly higher than that of other catalysts.

Table 5.1. Comparison of TOF using several catalysts in the limonene-1,2-epoxide isomerization.

Catalyst	Solvent	Reaction conditions	TOF[b] (min^{-1})	Reference
ZSM-5	Ethyl acetate	13 mmol L^{-1}, 75 mL of total volume, 115 mg of catalyst, 70 °C, 520-530 rpm, N_2 atmosphere	0.6	[25]
h-ZSM-5	Ethyl acetate		1.6	
d-ZSM-5/4d	Ethyl acetate		4.4	
d-ZSM-5/7d	Ethyl acetate		2.3	
3.9Fe/SBA15[a]	Toluene	0.25 mmol of substrate, 1 mL of solvent, 70 °C, 750 rpm, 10 mg of catalyst	0.46	[22]
	Ethyl acetate		0.29	
	Acetonitrile		0.12	
	Acetone		0.35	
	THF		0.12	
	1,4-Dioxane		0.17	
	Tert-butanol		0.12	
	Cyclohexane		0.23	
	Hexane		0.23	

[a] The value represents the metal loading (% wt.). [b] TOF was calculated as $(n_{i,LE} - n_{f,LE})/(\Delta t \cdot TA \cdot W)$ where $n_{i,LE}$ and $n_{f,LE}$ correspond to moles of LE at time 0 min and 5 min, respectively, Δt is the time interval, W is the catalyst weight, and TA is the total acidity referred to the sum of Brønsted and Lewis acidity of the catalyst.

These findings validate the high interest and potential of dendritic zeolites due to their vast range of possible applications as catalysts [26]. These zeolites exhibit three-dimensional branched superstructures marked by exceptional accessibility, owing to a highly interconnected network of radially oriented mesopores [26,27], which facilitates the rearrangement of monoterpene epoxides into high-value-added products.

The opening of limonene epoxide is a crucial reaction for research from both catalytic and molecular perspectives due to its wide applications in fine chemistry. Despite the significance of this reaction, there is a lack of detailed information about key parameters necessary for understanding the reaction mechanism, including bonding interactions, transition states, formation of intermediates, and kinetics. Both experimental and theoretical reports in the open literature fail to provide a comprehensive description of the reaction mechanism or offer molecular-based explanations for the observed selectivity in limonene epoxide isomerization. This knowledge gap hinders the scaling up of the process and an in-depth understanding of its chemical nature.

Hence, the present study aims to perform the kinetic modeling and mechanistic exploration of the limonene-1,2-epoxide isomerization over dendritic ZSM-5 zeolite, selecting the catalyst sample that showed the best performance in our recent report on dendritic zeolites [25]. This material exhibited a high selectivity for *cis*/*trans*-dihydrocarvone, using mild reaction conditions and a green solvent, ethyl acetate. The current work focuses on successfully describing the reaction pathway through the proposed reaction network, explained by the very good accuracy of the kinetic model to fit the experimental data collected under varying substrates

(*cis*-LE, *trans*-LE, and mixture-LE) and temperatures. Density functional theory (DFT) calculations were also conducted to elucidate the mechanism of epoxide rearrangement.

5.3. Experimental section

5.3.1. Materials

Commercial reagents were used in the experiments without further processing. Reagents for the synthesis of dendritic material were aluminum isopropoxide (AlP, 98 wt.%, Sigma-Aldrich); tetrapropylammonium hydroxide (TPAOH, 40 wt.% in water, Sigma-Aldrich); tetraethyl orthosilicate (TEOS, 98 wt.%, Sigma-Aldrich); dimethyloctadecyl [3-(trimethoxysilyl) propil] ammonium chloride (TPOAC, 42 wt.% in methanol, Sigma-Aldrich); N-[3-(Trimethoxysilyl)propyl]aniline (Ph-A, 98%, Sigma-Aldrich). Reagents for the catalytic tests were (+)-limonene-1,2-epoxide (mixture of isomers *cis* + *trans*, ≥97 wt.%, Sigma-Aldrich), *cis*-(-)-limonene-1,2-epoxide (98 wt. %, Sigma-Aldrich), *trans*-limonene-1,2-epoxide (97.5 wt. %, Sigma-Aldrich), ethyl acetate (anhydrous, 99.8 wt.%, Sigma-Aldrich), and nitrogen (99.999%, Woikoski). Some standards utilized for the quantification through the multipoint calibration curves were D-dihydrocarvone (≥ 97 wt.%, mixture of isomers, Sigma-Aldrich), L-carveol (mixture of *cis* and *trans*, ≥ 95 wt.%, Sigma-Aldrich), (1*S*,2*S*,4*R*)-(+)-limonene-1,2-diol (≥ 97 wt.%, Sigma-Aldrich), and *p*-cymene (≥90 wt.%, Fluka).

5.3.2. Synthesis of dendritic ZSM-5 zeolite

The detailed methodology for the synthesis of dendritic ZSM-5 materials has been previously reported in our recent work [25]. The dendritic ZSM-5 sample was synthesized by initially mixing finely milled AlP with TPAOH and distilled water at 300 rpm and room temperature in a round bottom flask until AlP was completely dissolved. Subsequently, an appropriate amount of TEOS, was added dropwise while the flask was submerged in an ice bath. This mixture was then stirred at room temperature for 42 h to ensure complete hydrolysis of TEOS. The initial precursor solution had a molar composition of 1 Al_2O_3: 60 SiO_2: 11 TPAOH: 1500 H_2O. The hydrolysis by-products, primarily alcohols, were removed using a rotatory evaporator at 100 mbar and 50 °C. The clear precursor solution underwent pre-crystallization under reflux with stirring at 300 rpm and 90 °C for 20 h. Following this, the flask was cooled in an ice bath and a 5 mol% of TPOAC relative to the initial silicon content was added dropwise to the synthesis gel, which was then stirred in the ice bath for 6 h. Hydrothermal crystallization of the synthesis gel was conducted by transferring it to a Teflon-lined reactor, which was sealed and maintained at 150 °C for 4 days. Post-crystallization, the autoclaves were rapidly cooled in an ice bath to abruptly halt the process. This procedure yielded two solid phases from the dendritic synthesis gel after 4 days: a whitish supernatant gel and a white solid at the bottom of the Teflon container. The white solid, containing the dendritic zeolite sample, was mechanically separated, washed with distilled water, centrifuged at 11000 rpm three times, and dried at 100 °C overnight. The resulting solid was designated as d-ZSM-5. This material was calcined in a two-step process using Ar and synthetic air as carrier gases for the first and second steps, respectively, following a reported procedure [28].

5.3.3. Catalysts characterization

In our recent work [25], we extensively characterized the dendritic ZSM-5 zeolite using an arsenal of modern physico-chemical methods, including X-ray diffraction (XRD), argon physisorption, transmission electron microscopy (TEM), high resolution-TEM, inductively coupled plasma – optical emission spectrometry (ICP-OES), pyridine-FTIR, solid-state ^{27}Al

MAS NMR, DTBPy/FTIR, and TGA analyses. Additionally, temperature-programmed oxidation (TPO) coupled with mass spectrometry (MS) was employed to detect coke formation in the spent catalysts.

5.3.4. Catalytic tests

The isomerization of limonene-1-2-epoxide over a heterogeneous catalyst was conducted in a batch glass reactor (total liquid volume of 75 mL) under a nitrogen atmosphere. The reactor was equipped with a N_2 feeding system, a thermocouple, a sampling valve, and a condenser. Small catalyst particles (< 75 μm) were used to minimize internal mass transfer limitations. The catalytic tests were performed using a high liquid volume-to-catalyst mass ratio and vigorous agitation (530 rpm) to suppress external mass-transfer limitations [29,30].

In a typical run, 115 mg of catalyst was heated at 250 °C for 30 min under a nitrogen atmosphere to avoid the physisorption of water. Subsequently, 1 mmol of epoxide was added to the pre-heated ethyl acetate at 70 °C to reach a total liquid volume of 75 mL. The samples of 0.4 mL were collected at regular intervals using a syringe with 0.45 μm filters to analyze the reaction kinetics using an Agilent Technologies GC-6890N gas chromatograph equipped with a DB-1 column (30 m length x 250 μm internal diameter x 0.50 μm film thickness), an FID detector, and an autosampler.

Helium was used as the carrier gas at a pressure of 0.12 MPa and a flow rate of 1.5 mL min^{-1} with a split ratio of 10:1. The detector temperature was set to 280 °C, and the injection volume was 1 μL. The oven-temperature program started at 60 °C, ramping to 100 °C at a rate of 20 °C min^{-1}, followed by an increase to 200 °C at 10 °C min^{-1}, and holding for 1 min. The nature of the products was further confirmed using an Agilent GC/MS 6890N/5973N equipped with a DB-1 capillary column (30 m length x 250 μm internal diameter x 0.5 μm film thickness).

The limonene-1,2-epoxide conversion (X_{LE}), and selectivity to the product i (S_i) were calculated based on the **Eqs. (5.1)-(5.2)**.

$$X_{LE}(\%) = \frac{n_{LE,0} - n_{LE,t}}{n_{LE,0}} * 100 \quad \textbf{(5.1)}$$

$$S_i(\%) = \frac{n_{i,t}}{n_{LE,0} - n_{LE,t}} * 100 \quad \textbf{(5.2)}$$

Where $n_{LE,0}$, $n_{LE,t}$, and $n_{i,t}$ refer to the initial moles of LE, the moles of LE after time *t*, and the moles of the product i after time *t* in the reaction mixture, respectively. The concentrations of the species were determined from multipoint calibration curves. The initial reaction rate for limonene-1,2-epoxide was calculated using **Eq. (5.3)**, where $n_{LE,f}$ correspond to moles of LE after 5 min, Δt is the time interval, and W is the catalyst weight.

$$r_{0,LE} = \frac{n_{LE,0} - n_{LE,f}}{\Delta t * W} \quad \textbf{(5.3)}$$

5.3.5. Computational methodology

To optimize minimum structures and transition states, the DFT method was employed, specifically utilizing the hybrid functional B3LYP, known for its balance between accuracy and computational efficiency [31]. Additionally, Grimme's empirical dispersion correction (D3) was

incorporated to prevent the underestimation of energy [32,33]. The combination of the B3LYP hybrid functional and Grimme's dispersion correction (D3) has become a widely used approach in computational chemistry, owing to its ability to accurately describe various molecular properties [34]. While B3LYP is a well-established functional for predicting molecular geometries and energies, weak dispersion forces, crucial for numerous non-covalent interactions, tend to be underestimated [35]. This limitation is addressed by Grimme's D3 correction, which explicitly incorporates dispersion interactions into the calculation, significantly enhancing the accuracy of overall energy and structural predictions [32,33]. This combination of B3LYP and D3 has been demonstrated to be effective for diverse systems, including small molecules, polymers, and biological macromolecules. The 6-31++G(d,p) basis set was also used for these calculations. The effect of temperature (343 K) was considered during computational calculations.

To validate the calculated structures, frequency analysis was performed, checking for non-imaginary frequencies for stable geometries and a single imaginary frequency for transition states. This analysis was corroborated by calculating analytic second derivatives. The Intrinsic Reaction Coordinate (IRC) was employed to connect the transition state structures to the intermediates, products, and reactants. To consider solvent effects (ethyl acetate), the Conductor-like Polarizable Continuum Model (CPCM) was applied during optimization calculations. This model utilizes a set of overlapping spheres to represent the solute cavity and employs a continuous surface charge formalism to ensure reaction continuity and robustness [36]. In this study, H_3O^+ was used as the acid species instead of directly mimicking the structure of a dendritic zeolite. This decision was made because H_3O^+ serves as a representative model for the typical Brønsted acid site in the catalyst [37]. The initial reference was established as the sum of limonene epoxide (*cis* or *trans*) and the Brønsted acid H_3O^+. Topological analysis of the electronic density was conducted using the AIMALL software.

5.3.6. Kinetic modeling

5.3.6.1. Reaction network

The reaction network for the isomerization of limonene-1,2-epoxide over d-ZSM-5 is proposed according to our results (**Table 5.2** and **Table 8.11**) [25], as illustrated in **Figure 5.2**. Primarily, *cis*-limonene-1,2-epoxide (A) is transformed into *cis*-dihydrocarvone (C), and *trans*-limonene-1,2-epoxide (B) gives *trans*-dihydrocarvone (D). Additionally, A and B undergo parallel reactions, resulting in carveol (E) and 1,3,4-trimethyl-3-cyclohexen-1-carboxaldehyde (F). The formation of the alcohol (E) can be explained by a concerted mechanism of *cis*-LE and *trans*-LE over Au/TiO_2 as a catalyst [23]. Products 4, 5, 6, and 7 are collectively labeled as 'Others' due to their low concentrations relative to the previously mentioned products. This kinetic study aims to investigate the determining steps and possible reaction pathways of the isomerization of limonene-1,2-epoxide over the dendritic ZSM-5 zeolite. It is noteworthy that all routes primarily involve the isomerization of epoxides ($C_{10}H_{16}O$), except for their slow dehydration into product 6 ($C_{10}H_{14}$).

Table 5.2. Experimental conditions for the kinetic modeling over d-ZSM-5.[a]

Entry	Substrate	W (mg)	T (°C)
1	*Cis*-LE	115.8	70
2	*Trans*-LE	116.3	70
3	Mixture-LE	116.3	50
4	Mixture-LE	115.1	60
5	Mixture-LE	115.5	70

[a] 13 mmol L^{-1}, 75 mL of total volume, anhydrous ethyl acetate as a solvent, 520 rpm, N_2 atmosphere.

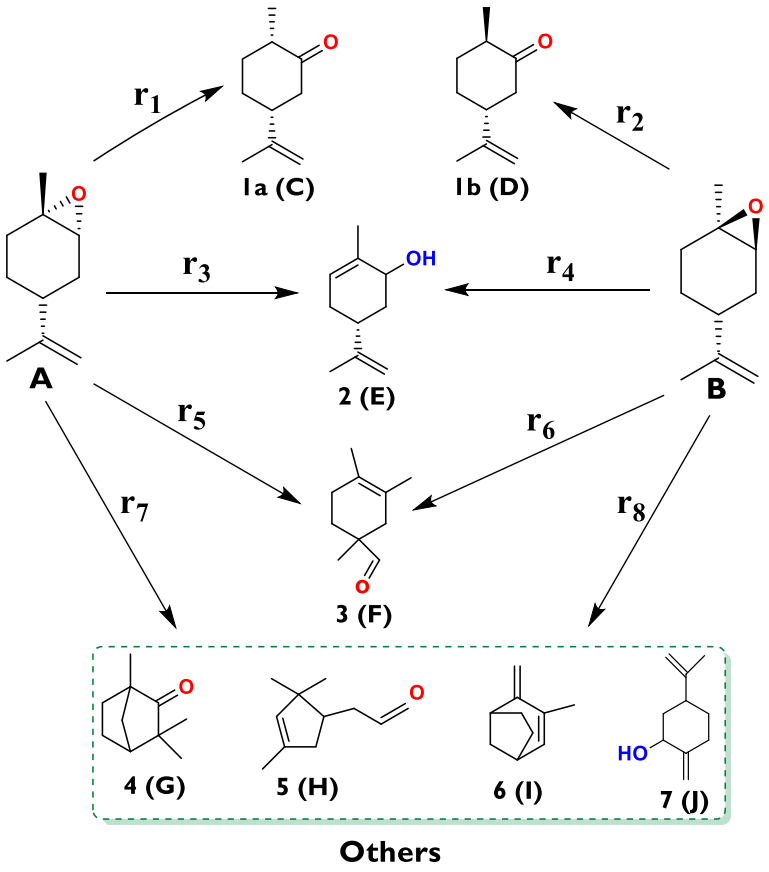

Figure 5.2. Reaction network for the isomerization of limonene-1,2-epoxide (**A:** *cis* configuration and **B:** *trans*-configuration) over d-ZSM-5.

5.3.6.2. Kinetic equations for a batch reactor

The reaction rate expressions are presented in **Eqs. (5.4)** and **(5.5)**, with detailed derivations available in the supporting information (**section 8.4.1**). The surface reactions are assumed to be irreversible, with k and K representing the reaction rate and adsorption equilibrium constants, respectively. Reaction constants are calculated using the modified Arrhenius equation, **Eq. (5.6)**, where k_{ref} refers to the reaction rate constant at an average temperature (T_{av} = 60 °C), E_a denotes the activation energy, and R represents the gas constant. On the other hand, the adsorption constants can be considered constant within the temperature range studied in this contribution (50-70 °C) [7,38,39].

$$r_i = \frac{k_i C_A}{1 + K_A C_A + K_B C_B + K_C C_C + K_D C_D + K_E C_E + K_F C_F} \quad (i = 1, 3, 5, 7) \tag{5.4}$$

$$r_j = \frac{k_j C_B}{1 + K_A C_A + K_B C_B + K_C C_C + K_D C_D + K_E C_E + K_F C_F} \quad (j = 2, 4, 6, 8) \tag{5.5}$$

$$k = k_{ref} e^{-\frac{E_a}{R}\left(\frac{1}{T} - \frac{1}{T_{av}}\right)} \tag{5.6}$$

The mole balance for the species in the liquid phase in the batch reactor is represented by **Eq. (5.7)**, where C_i is the concentration of species i, m_{cat} is the catalyst mass, V_R is the reaction volume, and R_i is the generation rate for species i, as shown in **Table 5.3**.

$$\frac{dC_i}{dt} = \frac{m_{cat}}{V_R} R_i \qquad (i = A, B, C, D, E, F, Others) \tag{5.7}$$

Table 5.3. Production rate for each species i.

Specie	Production rate (R_i)
Cis-limonene-1,2-epoxide (A)	$-(r_1 + r_3 + r_5 + r_7)$
Trans-limonene-1,2-epoxide (B)	$-(r_2 + r_4 + r_6 + r_8)$
Cis-dihydrocarvone (C)	r_1
Trans-dihydrocarvone (D)	r_2
Carveol (E)	$r_3 + r_4$
Product **3** (F)	$r_5 + r_6$
Others	$r_7 + r_8$

Product **3**: 1,3,4-trimethyl-3-cyclohexen-1-carboxaldehyde.

5.3.6.3. Parameters estimation

The estimation of parameters through nonlinear regression was conducted using the ModEst modeling and parameter estimation software (**section 8.4.3**) [40,41]. This process involved minimizing the objective function (O.F) by employing the Levenberg-Marquardt algorithm. O.F was formulated as the squared difference between the experimental and calculated values of the concentration of species [7,41], as illustrated in **Eq. (5.8)**. The determination coefficient (R^2) is a widely used metric for evaluating the goodness of fit, comparing the residual concentration values, as defined by **Eq. (5.9)**. Here, $C_{j,i,Exp}$ and $C_{j,i,Calc}$ refer to the experimental and modeled concentrations of the species j for each run i, respectively, while $\bar{C}_{j,i,Exp}$ refers to the mean of the experimental concentration data.

$$O.F = \sum_{j}^{N_{com}} \sum_{i=1}^{N_{obs}} \left(C_{j,i,Exp} - C_{j,i,Calc}\right)^2 \tag{5.8}$$

$$R^2(\%) = 100\left(1 - \frac{\sum_{j}^{N_{com}} \sum_{i=1}^{N_{obs}} \left(C_{j,i,Exp} - C_{j,i,Calc}\right)^2}{\sum_{j}^{N_{com}} \sum_{i=1}^{N_{obs}} \left(C_{j,i,Exp} - \bar{C}_{j,i,Exp}\right)^2}\right) \tag{5.9}$$

5.4. Results and Discussion

5.4.1. Catalyst properties

The dendritic ZSM-5 sample (d-ZSM-5) herein investigated corresponds with the material showing the best performance as reported in a separate article [25], in which its robustness and full recovery of the catalytic activity through regeneration by air calcination were demonstrated. The main physicochemical properties of this d-ZSM-5 sample are summarized in **Figure 5.3**. XRD pattern (**Figure 5.3.A**) shows the typical diffraction peaks of the MFI zeolitic structure, confirming the high crystallinity of the sample. Ar adsorption-desorption isotherm (**Figure 5.3.B**), and the derived NL-DFT pore size distribution, denote the presence of a well-defined mesoporosity with a peak maximum at about 5 nm, in addition to the peak corresponding to the MFI zeolitic structure micropores (0.55 nm) and a broad signal extending over the meso-macropore border. This singular and complex hierarchical porosity is a consequence of the presence of a dendritic nanostructure in this material.

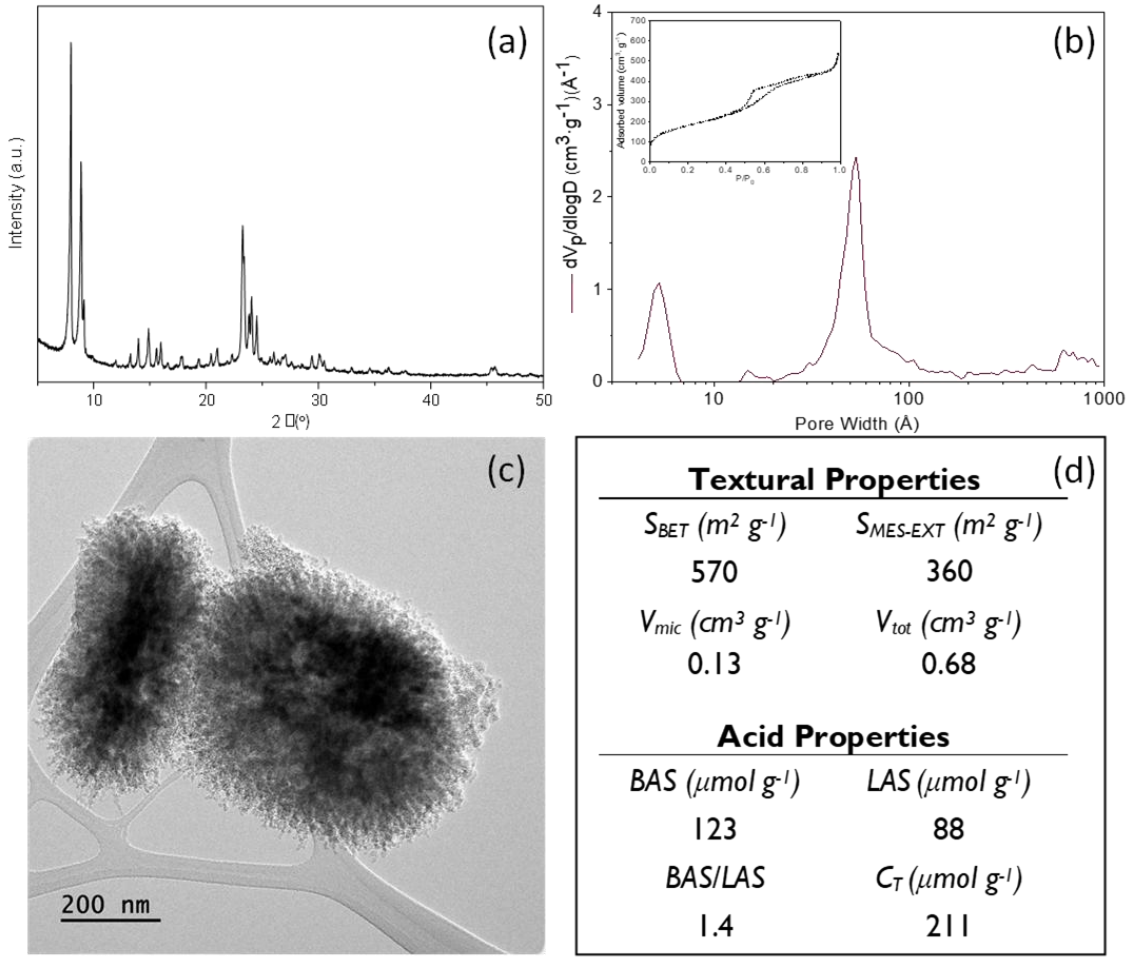

Figure 5.3. Summary of the characterization and physico-chemical properties of the calcined d-ZSM-5 sample: **(A)** XRD pattern, **(B)** Ar adsorption-desorption isotherm and NL-DFT pore size distribution (Ar, 87 K), **(C)** TEM image, **(D)** Textural properties and acid features (FTIR-pyridine, evacuation temperature: 250 °C).

As shown in the TEM image of **Figure 5.3.C**, and as earlier reported [26,27], the dendritic ZSM-5 is formed by particles with sizes between 0.2 – 0.8 mm that consist of branched and radially-oriented aggregates of very small zeolitic nanounits (5 – 10 nm size). Moreover, some vesicles inside the particles can be also appreciated. Therefore, the combination of micropores

inside the nanounits, voids existing between the nanounits, and vesicles generate a highly interconnected network of multilevel porosities. This nanoarchitecture provides d-ZSM-5 with outstanding accessibility, as denoted also by its large mesopore-external surface area (360 m^2 g^{-1}) and mesoporosity (about 80% of the total pore volume). These features have also an effect on the zeolite acidity that is formed by both Brønsted and Lewis acid sites in significant concentration (BAS/LAS = 1.4) with a high degree of accessibility [25].

5.4.2. Catalytic activity

In our recent study [25] the effects of the substrate (*cis*-LE, *trans*-LE, and mixture-LE), solvent polarity, and catalyst robustness were investigated. Herein the focus is on the effect of temperature which is crucial for determining the kinetic parameters, such as pre-exponential factors and activation energy, for all proposed reactions.

A wide range of values has been reported for the temperature of LE conversion over heterogeneous catalysts, such as room temperature [21], 40 °C [1], and 70 °C [22]. In this study, the temperature was investigated in the range of 50-70 °C using anhydrous ethyl acetate as a solvent. **Figure 5.4.A** clearly shows that LE conversion increases with the reaction temperature, reaching values of 60%, 80%, and 100% after 2 h at 50 °C, 60°C and 70 °C, respectively. Additionally, **Figure 5.4.B** demonstrates that *cis*-LE is more reactive at higher temperatures, with complete consumption observed after 15 and 60 min of the reaction at 70 and 60 °C, respectively. In the case of 50 °C, even after 2 h, *cis*-LE had not been completely converted.

These results indicate that the reaction proceeds at a low range of temperatures because of the high activity of the dendritic ZSM-5 catalyst. Moreover, both the substrate conversion and cis/trans ratio (**Figure 5.4.A** and **Figure 5.4.B**) very sharply when the temperature increases from 60 to 70 °C, evidencing the occurrence of a strongly activated process. The initial reaction rate of the epoxide ($-r_{LE,0}$), calculated under the same reaction conditions (initial molar concentration, agitation speed, and amount of catalyst), can be related to the absolute temperature, as shown in **Figure 5.4.G**, to estimate the activation energy (81.4 kJ mol^{-1}) of the epoxide isomerization. This value is very similar to a previously reported activation energy (82 kJ mol^{-1}) for the transformation of limonene epoxide to carvenone, using a Keggin-heteropolyacid catalyst [1].

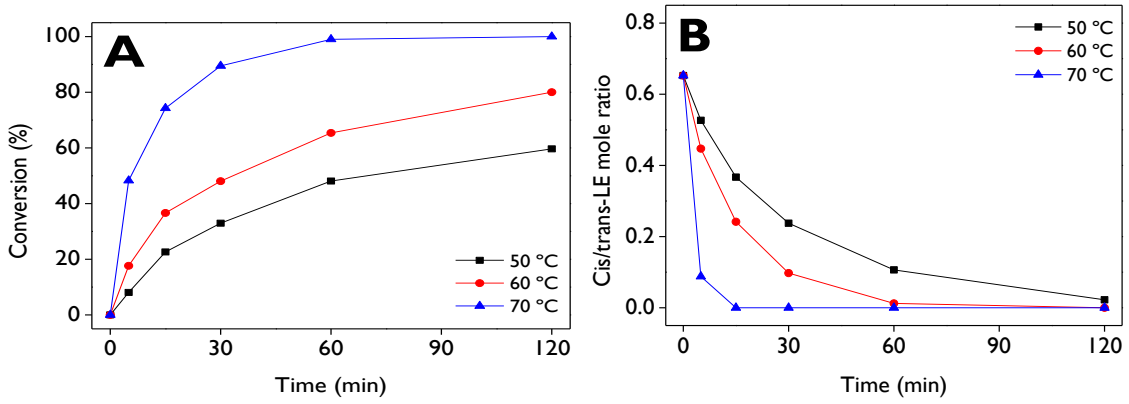

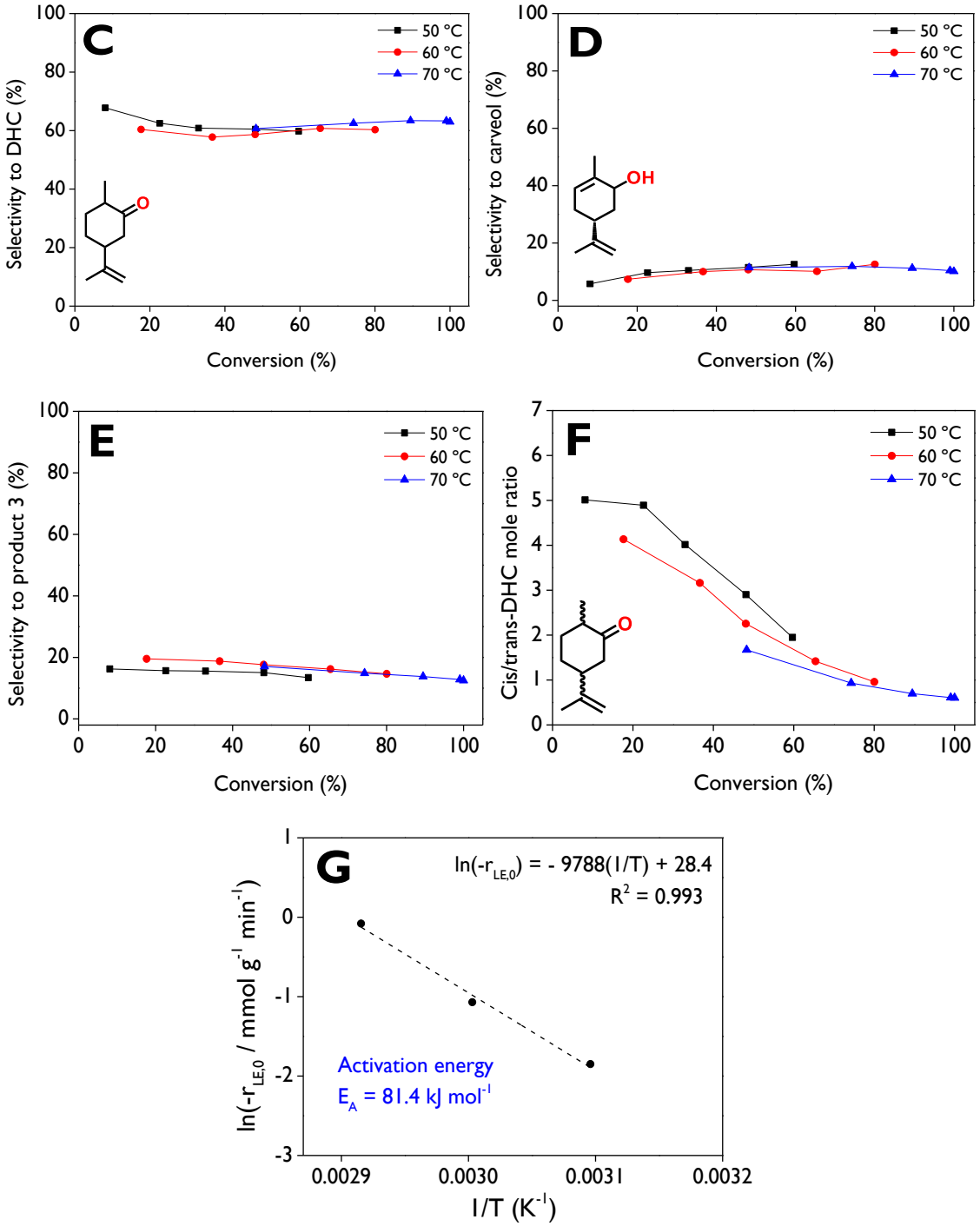

Figure 5.4. Effect of the temperature on the LE isomerization over d-ZSM-5. **(A)** LE conversion and **(B)** *cis*/*trans*-LE molar ratio as a function of the reaction time; **(C)** selectivity to dihydrocarvone, **(D)** selectivity to carveol, **(E)** selectivity to product **3**, and **(F)** *cis*/*trans* dihydrocarvone molar ratio, as a function of the conversion; **(G)** estimation of the activation energy. **Reaction conditions:** $C_{LE,0}$ = 13 mmol L^{-1}, 75 mL of total volume, anhydrous ethyl acetate as a solvent, 115 mg of d-ZSM-5, 520-530 rpm, N_2 atmosphere.

Selectivity to (*cis* + *trans*)-DHC (**Figure 5.4.C**) and carveol (**Figure 5.4.D**) is not significantly affected by the temperature given the values ranging between 60-67% and 7-12%, respectively. Selectivity of about 14-20% to product **3** (**Figure 5.4.E**) was reached at 60 and 70 °C, whereas a maximum value of 16% was achieved at a low temperature (50 °C). The *cis*/*trans*-

DHC molar ratio, shown in **Figure 5.4.F**, is reduced as the temperature increases. At 60% of conversion, values of ca. 1.9, 1.7, and 1.3 were reached at 50, 60, and 70°C, respectively.

The results with the dendritic zeolite demonstrate its superior activity for the isomerization of limonene-1,2-epoxide compared to other heterogeneous catalysts, such as 3.9 wt% Fe/SBA-15 [22], which exhibited only 15% conversion using ethyl acetate as a solvent at 70 °C after 1 h. This is significantly lower than the 99% conversion achieved with dendritic zeolite under the same temperature and at the same reaction time (**Figure 5.4.A**). The best conversion reported by the authors for Fe/SBA-15 was 21% using toluene as the solvent. In terms of selectivity, the values between 42-44% were achieved with these two solvents, while with d-ZSM-5, selectivity values exceeding 60% were obtained (**Figure 5.4.C**). On the other hand, when using a heteropolyacid as a catalyst with toluene as the solvent at 70 °C [1], complete conversion was reached, but with 46% selectivity to DHC and 34% selectivity to carvenone after 5 h of reaction. Using dimethyl carbonate as the solvent, the authors reported complete conversion, but with 20% selectivity to DHC and 68% selectivity to carvenone.

5.4.3. Computational calculations

DFT calculations revealed the typical reaction pathway for synthesizing *cis*/*trans*-dihydrocarvone and *trans*-carveol from *cis*/*trans*-limonene epoxide (**Figure 5.5**). At the assessed level of theory, no significant differences (~1 kJ mol^{-1}) were observed when the reaction started from either *cis* or *trans*-limonene epoxide. The presented calculations are interconnected, with the initial point of the DFT profile being *trans*-limonene epoxide.

As expected, the initial step in the reaction mechanism involves the approximation of oxygen to the acidic proton in H_3O^+. During this process, the energy decreases to -72 kJ mol^{-1}, indicating significant favorability. It is noteworthy that the C-O bond adjacent to the methylene group increases from 1.45 Å in the initial epoxide to 1.66 Å in **Int1**. This loss of covalence in **int1** is attributed to the formation of an oxonium ion, where the bond distances are slightly larger than the typical C-O bond. Subsequently, a transition state (**TS1**) is observed in which the C-O bond is partially broken, shifting from sp^3 to sp^2 hybridization. The adjacent carbon is minimally affected by **TS1;** however, the angles undergo slight changes, approaching 110°. The energy difference between **Int1** and **TS1** (ΔE_{act} TS1) increases to 234 kJ mol^{-1}. Utilizing the well-defined energies of TS1, the kinetic constant can be estimated.

The calculation of a thermal kinetic constant can be carried out using the Classical Transition State Theory, under the assumption that no trajectories recross the transition state [42]. While this assumption is suitable for systems employing classical mechanics, its application to chemical reactions is entirely invalid. An example illustrating this is the transfer reaction of light atoms, such as hydrogen, which can proceed via tunneling, as observed in both **TS1** and **TS2**. In such cases, the Wigner correction should be considered. A combination of both expressions yields **Eq. (5.10)**.

$$k = \frac{K_b T}{h} e^{-\frac{\Delta G}{RT}} * \left(1 + \frac{1}{24}\left|\frac{h\nu}{K_b T}\right|^2\right) \qquad \textbf{(5.10)}$$

Where k is the kinetic constant (in s^{-1}) of the transition state, K_b is the Boltzmann's constant (1.38×10^{-23} J K^{-1}), h is the Planck's constant (6.626×10^{-34} J s), R is the ideal gas constant (8.314 J mol^{-1} K^{-1}), T is the temperature, ΔG is the Gibbs free energy (in kJ mol^{-1}), and ν is the frequency of the transition state (in s^{-1}).

By using **Eq. (5.10)**, the kinetic constant of **TS1** (ν = - 472 cm^{-1}) yields a small value of 1.90×10^{-12} s^{-1}. Undoubtedly, the formation of the carbocation (**Int2**) by passing through **TS1** is the determining step in comparison with the upcoming steps. After **TS1**, a significant difference of 246 kJ mol^{-1} is observed concerning the tertiary carbocation (**Int2**). This intermediate is stabilized by hyperconjugation due to the methylene group. In comparison with the preceding **TS1** and **Int1**, the reactivity of the latter is higher because of the band-gap energy obtained as the difference between the HOMO-LUMO frontier orbitals (**Table 5.4**). In terms of stability and reactivity, the less stable specie (the most reactive) should be the one with the lowest HOMO-LUMO gap (Pearson's theory [43,44]). By using this well-known correlation for the isomerization of limonene epoxide, the reactivity of the most relevant structures decreases in the following order: **Int2** > **Int1**> ***Trans*/*cis*-limonene epoxide**.

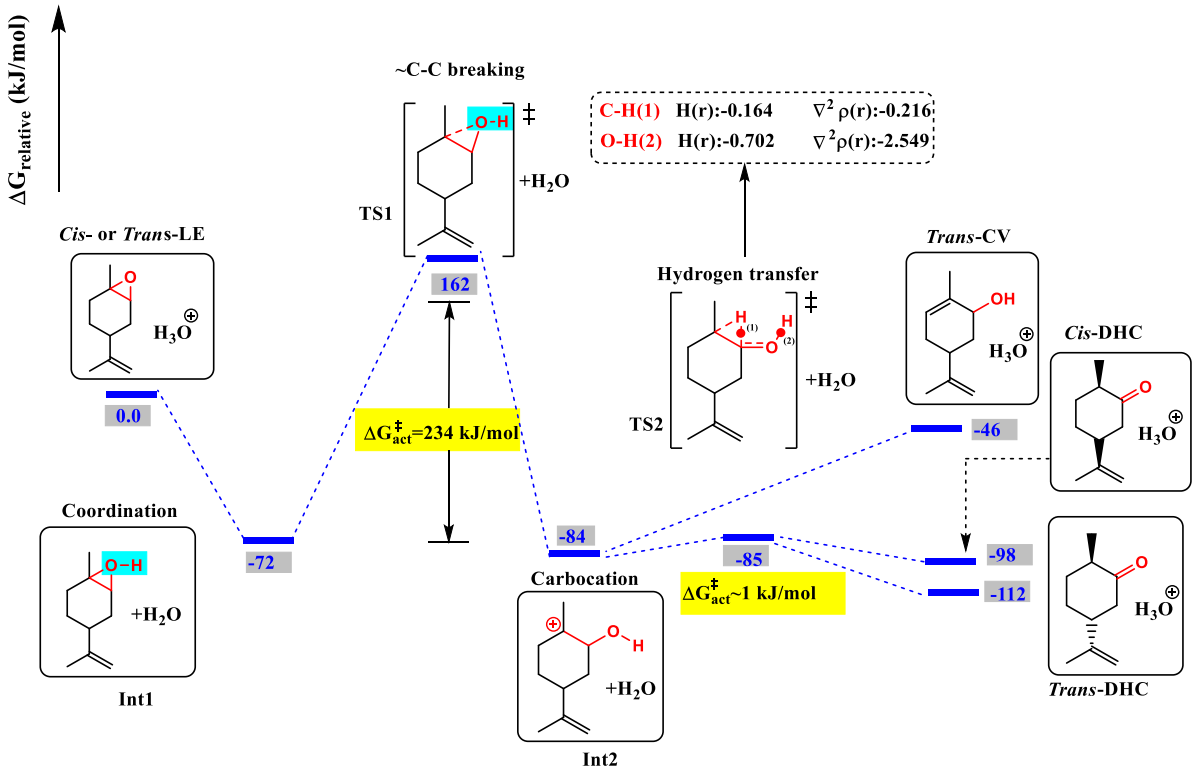

Figure 5.5. Calculated diagram for the isomerization of limonene epoxide into *trans*-carveol and *cis*/*trans*-dihydrocarvone.

Table 5.4. Band-gap HOMO-LUMO values of the calculated structures.

Structure	Band gap (eV)
Trans-limonene epoxide	6.7
Int1	5.7
Int2	3.2
Trans-carveol	6.3
Trans-DHC	6.0
Cis-DHC	6.0

After the formation of the intermediate carbocation (**Int2**), the elimination of the adjacent hydrogen results in *trans*-carveol with an overall Gibbs energy of -46 kJ mol^{-1}. In the case of both *cis* and *trans*-DHC, a second transition state (**TS2**) is observed. Specifically, in **TS2,** the hydrogen transfer occurs to the electron-deficient carbon adjacent to the alcohol group. The attached hydrogen to oxygen contributes its electronic pair to form the polarizable C=O bond. The energy difference between **TS2** (ν = -505 cm^{-1}) and I**nt2** is only 1 kJ mol^{-1}, yielding a kinetic constant of 1.03 s^{-1}, much faster than for **TS1,** indicating that the formation of **Int2** is evidently the determining step. The formation of both stereochemical configurations of DHC shows that they are thermodynamically favorable, even more so than the synthesis of *trans*-CV, aligning with our experimental results [25]. It is important to highlight that during the thermodynamic calculations, entropic effects were not considered due to their insignificance (< 0.042 kJ mol^{-1} K^{-1}).

The low level of *trans*-carveol formation [25] can be attributed to kinetic effects with a minor contribution of thermodynamics. It is evident that *trans*-carveol, on its own, is thermodynamically favorable from *trans*/*cis*-limonene epoxide. However, starting from the intermediate carbocation (**Int2**), achieving this alcohol becomes challenging due to the thermodynamics constraint of this step (ΔG = 38 kJ mol^{-1}). Additionally, elimination of the proton to form the C=C bond is not favored, likely due to the solvent used. Elimination reactions are generally favored in polar protic solvents compared to polar aprotic or non-polar solvents. Moreover, this bond is highly favored with hydrogen abstraction from the least hindered carbon [23]. This preference is the reason why *trans*/*cis*-DHC is favored over *trans*-CV, not only because of the thermodynamic contribution but also due to kinetic and solvent effects. These factors, together with the typical architecture/geometry of the dendritic zeolite (the latter not considered during the computational calculations), contribute to the observed experimental results [25]. Despite our proposed stepwise mechanism, the literature suggests that *trans*-CV synthesis over Au/TiO_2 can occur via a concerted pathway [23]. In this alternative mechanism, the axially oriented C-H bond on the geminal carbon of the epoxide preferentially reacts over the adjacent methylene group, leading primarily to the formation of this alcohol.

The exclusive formation of *trans*-DHC from *trans*-limonene epoxide and *cis*-DHC from cis-limonene epoxide can be explained as the methyl rotation in **TS2** (**Figure 5.6**) [23]. In *trans*-limonene epoxide, there is an equatorially oriented methyl group in the carbocation which after hydrogen transfer needs to rotate to keep both the stability and typical hybridization, leading exclusively to *trans*-DHC. Similarly, in *cis*-limonene epoxide, the methyl group in **TS2** rotates after the migration of hydrogen obtaining *cis*-DHC as the major product [23].

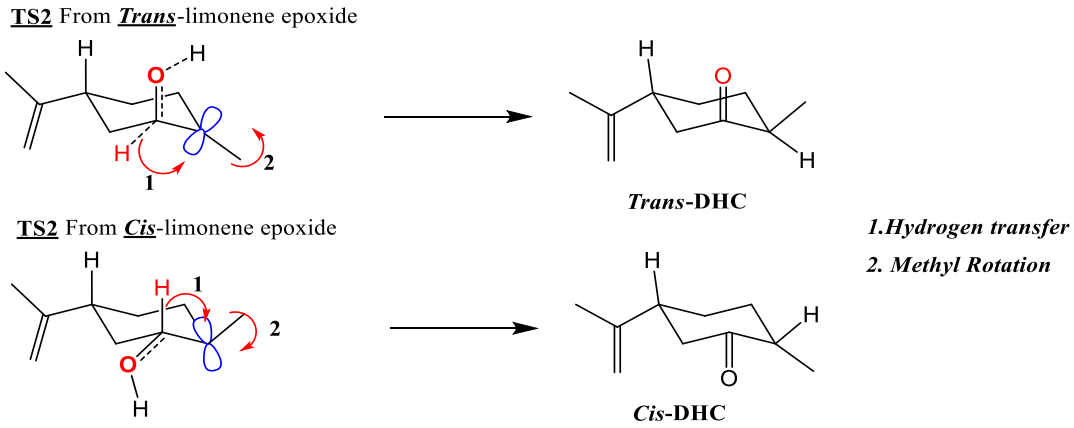

Figure 5.6. Explanation for the diastereomeric selectivity in both *trans*- and *cis*-limonene epoxide.

Additionally, an analysis of atoms in molecules was conducted for **TS2** to understand the nature of the hydrogen bond. For this purpose, the wavefunction was calculated, and various electronic variables (e.g., Laplacian of the electronic density ($\nabla^2 p(\mathbf{r})$) at the Bond Critical Point - BCP) were computed at the same level of theory. The positivity and negativity of the total energy density H(r) can indicate whether there is an ionic or covalent bond, circumventing issues with the Laplacian of the electronic density [45]. Furthermore, the combination of both $\nabla^2\rho(\mathbf{r})$ and H(**r**) can suggest the total or partial covalence of a bond. Depending on the signs of both, the interatomic distances in the compound can be categorized into three regions: Region I [$\nabla^2\rho(r) > 0$ and H(**r**)>0 (purely closed-shell interactions)], region II [$\nabla^2\rho(\boldsymbol{r}) > 0$ and H(**r**) <0 (closed-shell interactions with some covalent character)], and region III [$\nabla^2\rho(\boldsymbol{r}) < 0$ and H(**r**) <0 (strong hydrogen bond and covalent bond) [46]. As observed in **Figure 5.5** for **TS2** (and **Figure 8.94** and **Table 8.12** in supporting information), both $\nabla^2\rho(\mathbf{r})$ and H(**r**) are negative. This indicates that such interactions can be associated with the presence of covalence in both bonds with no closed-shell interactions.

5.4.4. Kinetics

The mechanistic details obtained from the computational calculations helped to elucidate the reaction kinetics. The preliminary kinetic analysis using **Eqs. (5.4)** and **(5.5)** revealed that adsorption of all species had no significant influence on fitting the experimental data, except for *cis*-dihydrocarvone (C). Therefore, the final fitting involved the omission of constants K_A, K_B, K_D, K_E, and K_F in the denominator terms of **Eqs. (5.4)** and **(5.5)**. **Table 8.13** presents the optimized kinetic parameters for the isomerization of limonene-1,2-epoxide. The reaction rate constants for reactions 4 and 6, estimated at 60 °C, exhibited the lowest values, consistent with the experimental results, where the primary reactions were identified as r_1 and r_2 involving the formation of stereoisomers of dihydrocarvone. Conversely, reactions 7, 3, and 1 demonstrated the lowest activation energies, while reactions 4 and 6 displayed the highest energy barriers. This indicates that reactions 4 and 6 are not favorable under the tested conditions. In addition, the analysis indicates that the formation of these dihydrocarvone isomers are the primary pathways which reinforce the notion that **int 2** formation is crucial (showed during the computational calculations). The adsorption equilibrium constant for *cis*-dihydrocarvone over d-ZSM-5 was estimated to be 220 L mol^{-1}. The high adsorption equilibrium constant for cis-DHC suggests it binds more strongly to the catalyst, potentially

affecting the final product distribution by influencing the conversion of the intermediate carbocation (Int2) to the specific DHC isomers. This aligns with the thermodynamic favorability discussed earlier. In summary, the kinetic analysis (reaction rates and activation energies from the previous section) suggests that the formation of both dihydrocarvone isomers (DHC) and *trans*-carveol (TC) is limited more by kinetic factors than by thermodynamics which is also evident from the values of kinetic constants achieved through numerical data fitting and discussed below.

A large difference in the values of the activation energies E_{A1} and E_{A2} reflects the experimental observations of the cis/trans ratio dependence on temperature and can be also in part explained by the apparent compensation effect (a lower value of the pre-exponential factor k_2 compared to k_1 compensating for a higher activation energy).

On the other hand, **Table 8.13** also indicates large errors for some of the parameters, which suggest that the associated catalytic reactions occur to a small extent (reactions 4, 6, and 7). The comparison between experimental concentration profiles and those calculated with the kinetic model is illustrated in **Figure 8.95**. The results demonstrate that the proposed kinetics can effectively capture the behavior of the experimental data, yielding a high R^2 of 96.09%. Furthermore, the statistical reliability of the constants was assessed through Markov Chain Monte Carlo (MCMC) analysis [40], as detailed in **section 8.4.6**. The correlation between some parameters is depicted in contour plots. These plots reveal strong mutual correlations among certain parameters, as indicated by the presence of a few elongated ovals.

Based on the previous results of the robust kinetic model, large errors were obtained for the parameters related to reactions 4, 6, and 7 (**Figure 5.2**). Therefore, the model was refined by suppressing these three reactions to achieve similar trends in the modeled kinetic curves shown in **Figure 8.95**, while reducing the number of parameters by six (3 k_i and 3 Ea_i). This adjustment aimed to lower the standard errors in the remaining kinetic parameters. The refined kinetic modeling was executed in ModEst considering $k_4 = k_6 = k_7 = 0$, resulting in almost the same quality of the fit (R^2 = 94.72%) maintaining very similar trends in the kinetic curves, as illustrated in **Figure 5.7**. **Table 5.5** details the optimized parameters for the refined model, which now only requires 11 parameters compared to the previous 17 (as shown in **Table 8.13**). The highest standard error was observed for Ea_2, with a relatively low value of 11.2%, indicating that the decision to suppress the three reactions was sound, leading to more accurate parameter values than previously obtained.

It is noteworthy to highlight that the kinetic parameters generally changed only slightly with the most significant change obtained for k_3. Additionally, note that the previously reported apparent activation energy (81 kJ mol^{-1}) was estimated using the initial rate of limonene epoxide consumption to all the products. Therefore, it cannot be directly compared with any of the values reported in **Table 5.5**, as each reaction has its own energy barrier.

Overall, in this work for isomers dihydrocarvone synthesis a robust kinetic model was developed that includes all experimentally observed transformation routes over dendritic ZSM-5 zeolite as a heterogeneous catalyst. This is fundamental for future studies in scaling up batch processes for the synthesis of this fine chemical, as well as for optimizing different reaction conditions such as reaction temperature, initial substrate concentration, the substrate source, and the reaction time.

To our knowledge, this contribution is the first one reporting detailed kinetic modeling for limonene-1,2-epoxide isomerization based on the reaction rate laws for a dendritic zeolite as a heterogeneous catalyst. Although the literature on this topic is scarce, most studies highlight the absence of kinetic studies [1,18,20-22]. Cortés and Elrod [47] reported the kinetics of the hydrolysis of some monoterpene epoxides with D_2O, including pinene epoxides, (*cis-endo*, *trans-endo*)-limonene epoxide, and (*cis-endo*, *trans-endo*, *exo*)-limonene epoxide. The authors derived the rate equation according to a homogeneous kinetic model, which depends on the general acid-catalyzed rate constant (k_{GA}), the Brønsted acid-catalyzed rate constant (k_{H+}), and the concentration of the epoxide. However, in this contribution, the hydrolysis route was not considered because it was avoided by using anhydrous ethyl acetate and performing thermal treatment on the catalyst before the beginning of the reaction.

Table 5.5. Optimized kinetic and statistical parameters for the refined kinetic model.

Parameter	Value	Units	Standard error (%)
k_1	2.49×10^{-5}	L mg^{-1} min^{-1}	9.3
k_2	4.35×10^{-6}	L mg^{-1} min^{-1}	6.1
k_3	9.38×10^{-6}	L mg^{-1} min^{-1}	7.0
k_5	1.35×10^{-5}	L mg^{-1} min^{-1}	7.7
k_8	5.26×10^{-6}	L mg^{-1} min^{-1}	7.3
Ea_1	41.1	kJ mol^{-1}	5.3
Ea_2	162.0	kJ mol^{-1}	11.2
Ea_3	35.5	kJ mol^{-1}	2.9
Ea_5	60.8	kJ mol^{-1}	5.8
Ea_8	80.2	kJ mol^{-1}	6.3
K_C	0.252	L $mmol^{-1}$	3.4

K_i values were estimated at 60 °C.

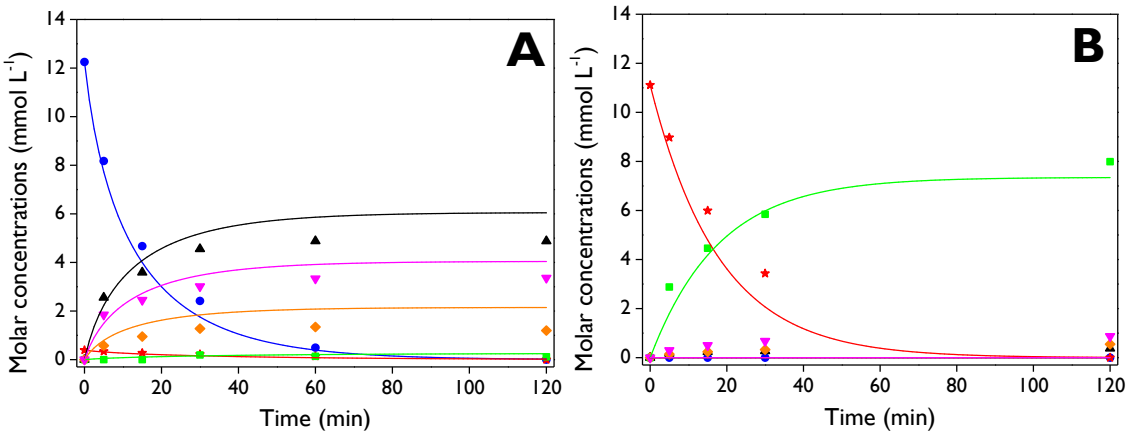

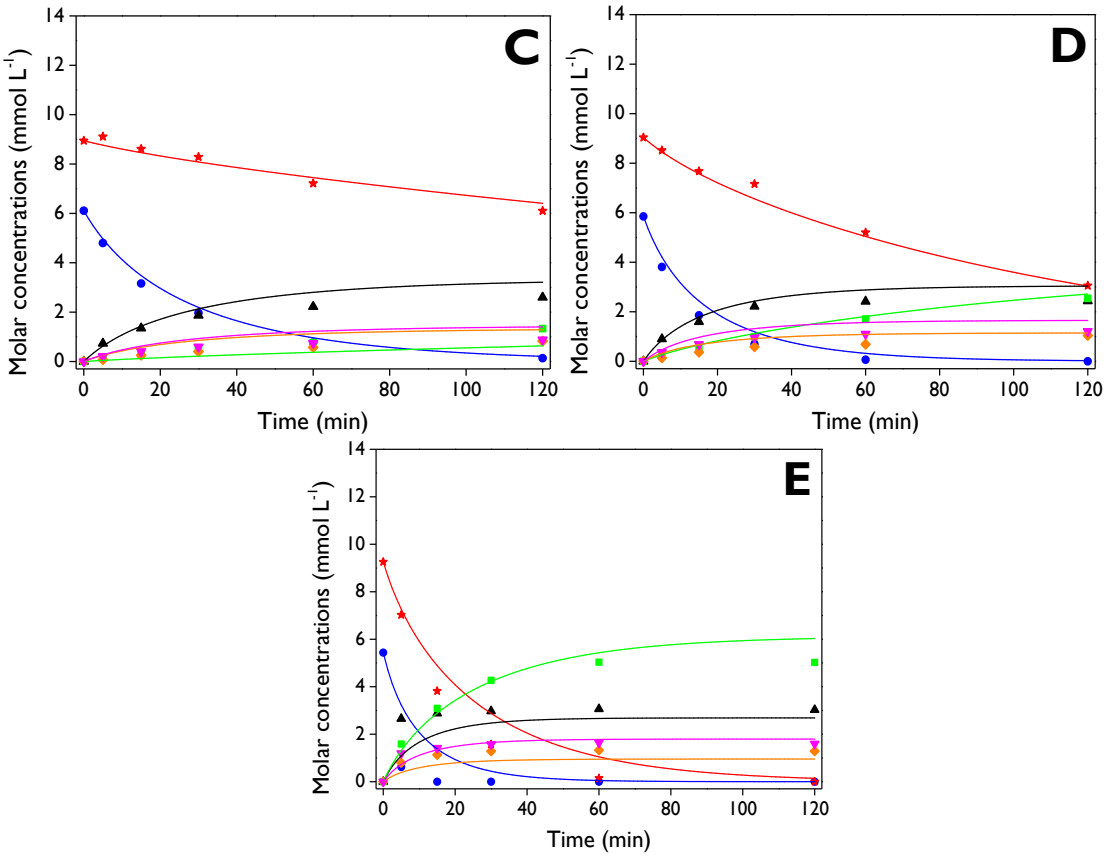

Figure 5.7. Concentration profiles of the species (C_A (—, ●), C_B (—, ✶), C_C (—, ▲), C_D (—, ■), C_E (—, ◆), C_F (—, ▼)) with the **refined model**, involved in the isomerization of limonene-1,2-epoxide over d-ZSM-5, with experimental values (symbols) and modeled values (solid lines). **Reaction conditions:** C_0 = 13 mmol L^{-1}, 75 mL total volume, anhydrous ethyl acetate as a solvent, 115 mg of catalyst, 520-530 rpm, N_2 atmosphere. **A)** *cis*-LE as the substrate at 70 °C, **B)** *trans*-LE as the substrate at 70 °C, **C)** mixture-LE as the substrate at 50 °C, **D)** mixture-LE as the substrate at 60 °C, **E)** mixture-LE as the substrate at 70 °C.

5.5. Conclusions

This study provides significant kinetic and mechanistic insights into the isomerization of limonene-1,2-epoxide over a dendritic ZSM-5 zeolite. This material demonstrated high selectivity and yield for forming dihydrocarvone (DHC) diastereoisomers due to its high accessibility, arising from its branched and radially oriented dendritic nanostructure and its balanced Brønsted/Lewis acidity. The use of anhydrous ethyl acetate as a green solvent at a mild reaction temperature further underscores the environmentally friendly approach of this process. The study examined the effect of reaction temperature on LE conversion, showing that higher temperatures increased sharply the catalytic activity, with complete conversion achieved at 70 °C within 2 h, denoting the occurrence of a strongly activated process. Interestingly, the selectivity to DHC and carveol was not significantly affected by temperature.

Kinetic modeling for the isomerization of limonene-1,2-epoxide over d-ZSM-5 was proposed based on the reaction network with parallel reactions from *cis*-LE and *trans*-LE, assuming surface reactions as the rate-limiting steps. In this reaction pathway, *cis*-DHC was formed from *cis*-LE, while *trans*-DHC was obtained from *trans*-LE. The statistical results of this robust kinetic modeling highlighted the necessity to refine the model by suppressing three reactions. This

adjustment led to a more accurate kinetic model with standard errors in all kinetic parameters reduced to below 11.2%. The activation energies were determined to be 41.1 and 162 kJ mol^{-1} for *cis*-DHC and *trans*-DHC formation, respectively.

This kinetic modeling was supported by DFT calculations, which revealed the preferred pathway for both *cis* and *trans*-limonene epoxide conversion to dihydrocarvone and carveol. Thermodynamics favors formation of dihydrocarvone (both isomers) over the spontaneous generation of carveol. The rate-determining step, carbocation formation ($\Delta Eact$ = 234 kJ mol^{-1}), precedes the nearly instantaneous formation of dihydrocarvone under the studied conditions. Analysis of the second transition state for DHC synthesis revealed closed-shell interactions with slight covalent character at the bond critical point. This finding is consistent with the experimental results, supporting the overall DFT profile.

Supporting Information

The Supporting Information (**section 8.4**) contains details on the derivation of the reaction rate laws for the kinetic modeling, the experimental data in terms of molar concentrations of species, the codes for kinetic parameters optimization in ModEst software, computational calculations, and Markov Chain Monte Carlo (MCMC) results.

5.6. Acknowledgments

Luis A. Gallego-Villada is grateful to Universidad de Antioquia for their support during his research internship through the project 2022-53000 as part of the "Convocatoria Programática 2021-2022: Ingeniería y Tecnología" program, as well as the "Beca Doctoral Universidad de Antioquia" scholarship. D.P.S., M.A-D., and J.C. are gratefully acknowledged to the European Research Council Horizon 2020 research and innovation program TODENZE project (ERC101021502). Julián E. Sánchez-Velandia is grateful to Universidad Jaume I for the postdoctoral position during 2022-2023 (programa Propi UJI) and the project (PID2020-11962RBC33),MCIN/AEI/10.13039/501100011033/European Union NextGeneration EU/PRTP.

5.7. References

[1] R.F. Cotta, R.A. Martins, M.M. Pereira, K.A. da Silva Rocha, E.F. Kozhevnikova, I. V. Kozhevnikov, E. V. Gusevskaya, Heteropoly acid catalysis for the isomerization of biomass-derived limonene oxide and kinetic separation of the trans-isomer in green solvents, Appl. Catal. A Gen. 584 (2019) 117173. https://doi.org/10.1016/j.apcata.2019.117173.

[2] Foreverest, Dihydrocarvone, (n.d.). https://foreverest.net/products/turpentine-derivatives/dihydrocarvone.html (accessed November 12, 2023).

[3] A.R. Alcántara, M.-J. Hernaiz, J.-V. Sinisterra, Biocatalyzed Production of Fine Chemicals, in: Compr. Biotechnol., Second Edi, Elsevier, 2011: pp. 309–331. https://doi.org/10.1016/B978-0-08-088504-9.00225-7.

[4] J.E. Sánchez-Velandia, L.A. Gallego-Villada, P. Mäki-Arvela, A. Sidorenko, D. Yu. Murzin, Upgrading biomass to high-added value chemicals: synthesis of monoterpenes-based compounds using catalytic green chemical pathways, Catal. Rev. (2024) 1–126. https://doi.org/10.1080/01614940.2024.2329553.

[5] V.M. Vaschetti, A.L. Cánepa, D. Barrera, K. Sapag, G.A. Eimer, S.G. Casuscelli, Limonene oxyfunctionalization over Cu-modified silicates employing hydrogen peroxide and t-Butyl hydroperoxide: Reaction pathway analysis, Mol. Catal. 481 (2020) 110234. https://doi.org/10.1016/j.mcat.2018.11.005.

[6] M. Caovilla, A. Caovilla, S.B.C. Pergher, M.C. Esmelindro, C. Fernandes, C. Dariva, K. Bernardo-Gusmão, E.G. Oestreicher, O.A.C. Antunes, Catalytic oxidation of limonene, α-pinene and β-pinene by the complex [FeIII(BPMP)Cl(μ-O)FeIIICl3] biomimetic to MMO enzyme, Catal. Today. 133–135 (2008) 695–698. https://doi.org/10.1016/j.cattod.2007.12.107.

[7] L.A. Gallego-Villada, E.A. Alarcón, A.L. Villa, Versatile Heterogeneous Catalytic System for the Selective Synthesis of Limonene Epoxide and Diepoxide, Ind. Eng. Chem. Res. 62 (2023) 20152–20169. https://doi.org/10.1021/acs.iecr.3c02633.

[8] L.A. Gallego-Villada, P. Mäki-Arvela, N. Kumar, E.A. Alarcón, Z. Vajglová, T. Tirri, I. Angervo, R. Lassfolk, M. Lastusaari, D.Y. Murzin, Zeolite Y-based catalysts for efficient epoxidation of R-(+)-Limonene: Insights into the structure-activity relationship, Microporous Mesoporous Mater. 372 (2024) 113098. https://doi.org/10.1016/j.micromeso.2024.113098.

[9] M. Vasconcellos-Dias, C.D. Nunes, V. Félix, P. Brandão, M.J. Calhorda, New heptacoordinate tungsten(II) complexes with α-diimine ligands in the catalytic oxidation of multifunctional olefins, Inorganica Chim. Acta. 519 (2021) 120263. https://doi.org/10.1016/j.ica.2021.120263.

[10] H. Zhang, X. Lu, L. Yang, Y. Hu, M. Yuan, C. Wang, Q. Liu, F. Yue, D. Zhou, Q. Xia, Efficient air epoxidation of cycloalkenes over bimetal-organic framework ZnCo-MOF materials, Mol. Catal. 499 (2021) 111300. https://doi.org/10.1016/j.mcat.2020.111300.

[11] Y.S. Demidova, E.V. Suslov, O.A. Simakova, K.P. Volcho, N.F. Salakhutdinov, I.L. Simakova, D.Y. Murzin, Selective one-pot carvone oxime hydrogenation over titania supported gold catalyst as a novel approach for dihydrocarvone synthesis, J. Mol. Catal. A Chem. 420 (2016) 142–148. https://doi.org/10.1016/j.molcata.2016.04.013.

[12] J.R. Lowe, W.B. Tolman, M.A. Hillmyer, Oxidized Dihydrocarvone as a Renewable Multifunctional Monomer for the Synthesis of Shape Memory Polyesters, Biomacromolecules. 10 (2009) 2003–2008. https://doi.org/10.1021/bm900471a.

[13] J.M. Kouznetsov, Vladímir V Urbina G., E.E. Stashenko, N-Functionalization of dihydrocarvone: Obtainin aminocyclohexane derivatives and their spectrometric study, J. Chil. Chem. Soc. 50 (2005) 559–563.

[14] Y. Dong, K.J. McCullough, S. Wittlin, J. Chollet, J.L. Vennerstrom, The structure and antimalarial activity of dispiro-1,2,4,5-tetraoxanes derived from (+)-dihydrocarvone, Bioorg. Med. Chem. Lett. 20 (2010) 6359–6361. https://doi.org/10.1016/j.bmcl.2010.09.113.

[15] J. Alarcon, C. Lamilla, C.L. Cespedes, Insecticidal activity of sesquiterpenes skeleton synthesized by the conventional Robinson annulations reaction on Drosophila melanogaster, Ind. Crops Prod. 42 (2013) 268–272. https://doi.org/10.1016/j.indcrop.2012.05.026.

[16] M. Stekrova, N. Kumar, S.F. Díaz, P. Mäki-Arvela, D.Y. Murzin, H- and Fe-modified zeolite beta catalysts for preparation of trans-carveol from α-pinene oxide, Catal. Today. 241 (2015) 237–245. https://doi.org/10.1016/j.cattod.2013.12.004.

[17] S.P. Bhatia, D. McGinty, C.S. Letizia, A.M. Api, Fragrance material review on carveol, Food Chem. Toxicol. 46 (2008) S85–S87. https://doi.org/10.1016/j.fct.2008.06.032.

[18] T.-T.T. Nguyen, D.-K.N. Chau, F. Duus, T.N. Le, Green Synthesis of Carvenone by Montmorillonite-Catalyzed Isomerization of 1,2-Limonene Oxide, Int. J. Org. Chem. 03 (2013) 206–209. https://doi.org/10.4236/ijoc.2013.33027.

[19] A. Corma, S. Iborra, A. Velty, Chemical Routes for the Transformation of Biomass into Chemicals, Chem. Rev. 107 (2007) 2411–2502. https://doi.org/10.1021/cr050989d.

[20] N. Ravasio, F. Zaccheria, M. Guidotti, R. Psaro, Mono- and Bifunctional Heterogeneous Catalytic Transformation of Terpenes and Terpenoids, Top. Catal. 27 (2004) 157–168. https://doi.org/10.1023/B:TOCA.0000013550.28170.6a.

[21] V. V. Costa, K.A. da Silva Rocha, I. V. Kozhevnikov, E.F. Kozhevnikova, E. V. Gusevskaya, Heteropoly acid catalysts for the synthesis of fragrance compounds from biorenewables: isomerization of limonene oxide, Catal. Sci. Technol. 3 (2013) 244–250. https://doi.org/10.1039/C2CY20526B.

[22] J.E. Sánchez-Velandia, A.L. Villa, Selective synthesis of high-added value chemicals from α-pinene epoxide and limonene epoxide isomerization over mesostructured catalysts: Effect of the metal loading and solvent, Catal. Today. 394–396 (2022) 208–218. https://doi.org/10.1016/j.cattod.2021.09.011.

[23] C. Raptis, H. Garcia, M. Stratakis, Selective Isomerization of Epoxides to Allylic Alcohols Catalyzed by TiO2 -Supported Gold Nanoparticles, Angew. Chemie Int. Ed. 48 (2009) 3133–3136. https://doi.org/10.1002/anie.200805838.

[24] K. Arata, S. Akutagawa, K. Tanabe, Isomerization of d-limonene oxide over solid acids and bases, J. Catal. 41 (1976) 173–179. https://doi.org/10.1016/0021-9517(76)90213-X.

[25] L.A. Gallego-Villada, J. Cueto, M. del M. Alonso-Doncel, P. Mäki-Arvela, E.A. Alarcón, D.P. Serrano, D.Y. Murzin, Dendritic ZSM-5 Zeolites as Highly Active Catalysts for the Valorization of Monoterpene Epoxides (Submitted), Green Chem. (2024).

[26] M. del Mar Alonso-Doncel, C. Ochoa-Hernández, G. Gómez-Pozuelo, A. Oliveira, J. González-Aguilar, Á. Peral, R. Sanz, D.P. Serrano, Dendritic nanoarchitecture imparts ZSM-5 zeolite with enhanced adsorption and catalytic performance in energy applications, J. Energy Chem. 80 (2023) 77–88. https://doi.org/10.1016/j.jechem.2023.01.023.

[27] M. del M. Alonso-Doncel, E.A. Giner, D. de la Calle, J. Cueto, P. Horcajada, R.A. García-Muñoz, D.P. Serrano, Synthesis of Dendritic ZSM-5 Zeolite through Micellar Templating Controlled by the Amphiphilic Organosilane Chain Length, Cryst. Growth Des. 23 (2023) 5658–5670. https://doi.org/10.1021/acs.cgd.3c00326.

[28] M. Alonso-Doncel, A. Peral, M. Shamzhy, J. Čejka, R. Sanz, D.P. Serrano, Untangling the role of the organosilane functional groups in the synthesis of hierarchical ZSM-5 zeolite by crystallization of silanized protozeolitic units, Catal. Today. 345 (2020) 27–38. https://doi.org/10.1016/j.cattod.2019.11.031.

[29] N. Kumar, P. Mäki-Arvela, S.F. Diáz, A. Aho, Y. Demidova, J. Linden, A. Shepidchenko, M. Tenhu, J. Salonen, P. Laukkanen, A. Lashkul, J. Dahl, I. Sinev, A. Leino, K. Kordas, T. Salmi, D.Y. Murzin, Isomerization of α-Pinene Oxide Over Iron-Modified Zeolites, Top. Catal. 56 (2013) 696–713. https://doi.org/10.1007/s11244-013-0029-y.

[30] D.Y. Murzin, T. Salmi, Catalytic Kinetics, 1st ed., ElSevier Science & Technology Books, 2005. http://link.springer.com/10.1007/s11244-013-0029-y.

[31] L. Lu, H. Hu, H. Hou, B. Wang, An improved B3LYP method in the calculation of organic thermochemistry and reactivity, Comput. Theor. Chem. 1015 (2013) 64–71. https://doi.org/10.1016/j.comptc.2013.04.009.

[32] S. Grimme, J. Antony, S. Ehrlich, H. Krieg, A consistent and accurate ab initio parametrization of density functional dispersion correction (DFT-D) for the 94 elements H-Pu, J. Chem. Phys. 132 (2010). https://doi.org/10.1063/1.3382344.

[33] W. Reckien, F. Janetzko, M.F. Peintinger, T. Bredow, Implementation of empirical dispersion corrections to density functional theory for periodic systems, J. Comput. Chem. 33 (2012) 2023–2031. https://doi.org/10.1002/jcc.23037.

[34] B. Civalleri, C.M. Zicovich-Wilson, L. Valenzano, P. Ugliengo, B3LYP augmented with an empirical dispersion term (B3LYP-D*) as applied to molecular crystals, CrystEngComm. 10 (2008) 405–410. https://doi.org/10.1039/B715018K.

[35] Y. Shao, Y. Mei, D. Sundholm, V.R.I. Kaila, Benchmarking the Performance of Time-Dependent Density Functional Theory Methods on Biochromophores, J. Chem. Theory Comput. 16 (2020) 587–600. https://doi.org/10.1021/acs.jctc.9b00823.

[36] Y. Takano, K.N. Houk, Benchmarking the Conductor-like Polarizable Continuum Model (CPCM) for Aqueous Solvation Free Energies of Neutral and Ionic Organic Molecules, J. Chem. Theory Comput. 1 (2005) 70–77. https://doi.org/10.1021/ct049977a.

[37] B. Lasne, P. Mäki-Arvela, A. Aho, Z. Vajglova, K. Eränen, N. Kumar, J.E. Sánchez-Velandia, M. Peurla, C. Mondelli, J. Pérez-Ramírez, D.Y. Murzin, Synthesis of Florol via Prins cyclization over heterogeneous catalysts, J. Catal. 405 (2022) 288–302. https://doi.org/10.1016/j.jcat.2021.12.008.

[38] L.A. Gallego-Villada, E.A. Alarcón, D.M. Ruiz, G.P. Romanelli, Kinetic study of the esterification of t-cinnamic acid over Preyssler structure acid, Mol. Catal. 528 (2022) 112507. https://doi.org/10.1016/j.mcat.2022.112507.

[39] L.A. Gallego-Villada, E.A. Alarcón, C. Cerrutti, G. Blustein, Á.G. Sathicq, G.P. Romanelli, Levulinic Acid Esterification with n -Butanol over a Preyssler Catalyst in a Microwave-Assisted Batch Reactor: A Kinetic Study, Ind. Eng. Chem. Res. 62 (2023) 10915–10929. https://doi.org/10.1021/acs.iecr.3c00893.

[40] D.Y. Murzin, J. Wärnå, H. Haario, T. Salmi, Parameter estimation in kinetic models of complex heterogeneous catalytic reactions using Bayesian statistics, React. Kinet. Mech. Catal. 133 (2021) 1–15. https://doi.org/10.1007/s11144-021-01974-1.

[41] H. Haario, ModEst User's guide, ProfMath Oy, Helsinki, 1994.

[42] W.H. Thompson, Quantum mechanical transition state theory and tunneling corrections, J. Chem. Phys. 110 (1999) 4221–4228. https://doi.org/10.1063/1.478304.

[43] R.G. Pearson, Hard and Soft Acids and Bases, J. Am. Chem. Soc. 85 (1963) 3533–3539. https://doi.org/10.1021/ja00905a001.

[44] R.G. Pearson, Recent advances in the concept of hard and soft acids and bases, J. Chem. Educ. 64 (1987) 561. https://doi.org/10.1021/ed064p561.

[45] D.K. Miller, C. Loy, S. V. Rosokha, Examining a Transition from Supramolecular Halogen Bonding to Covalent Bonds: Topological Analysis of Electron Densities and Energies in the Complexes of Bromosubstituted Electrophiles, ACS Omega. 6 (2021) 23588–23597. https://doi.org/10.1021/acsomega.1c03779.

[46] R. Bianchi, G. Gervasio, D. Marabello, The experimental charge density in transition metal compounds, Comptes Rendus Chim. 8 (2005) 1392–1399. https://doi.org/10.1016/j.crci.2004.12.015.

[47] Di.A. Cortés, M.J. Elrod, Kinetics of the Aqueous Phase Reactions of Atmospherically Relevant Monoterpene Epoxides, J. Phys. Chem. A. 121 (2017) 9297–9305. https://doi.org/10.1021/acs.jpca.7b09427.

Chapter 6. One-Pot Tandem Catalysis: Green Synthesis of β-Pinene Derivatives with MgO and Mesoporous catalysts

This chapter corresponds to an article published in ***Journal of Catalysis***, *2024, 438, 115698 – DOI: 10.1016/j.jcat.2024.115698*

Luis A. Gallego-Villada[a,*], Edwin A. Alarcón[a,*], Felipe Bustamante[a], Aída Luz Villa[a]

a. Environmental Catalysis Research Group, Chemical Engineering Department, Universidad de Antioquia, Medellín, Colombia

* Corresponding author: alfonso.gallego@udea.edu.co (Luis A. Gallego-Villada), edwin.alarcon@udea.edu.co (Edwin A. Alarcón)

Graphical Abstract

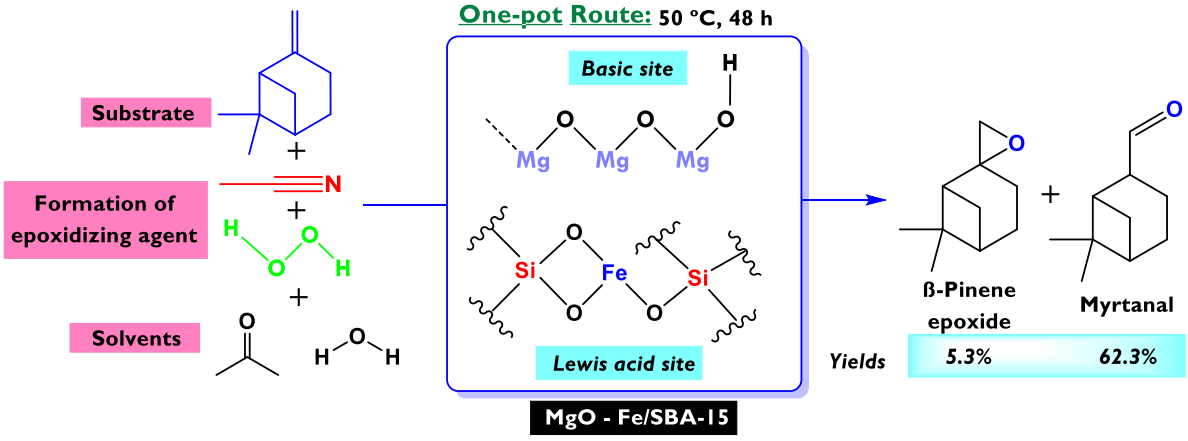

6.1. Abstract

Metal-modified heterogeneous catalysts based on mesoporous supports such as MCM-41 and SBA-15 were prepared and evaluated in the one-pot tandem transformation of β-pinene, along with MgO. This route involves epoxidation with H_2O_2 followed by the subsequent isomerization of the epoxide, yielding myrtanal as the major product; this aldehyde has wide-ranging applications as a fine chemical in fragrances, flavors, and as a precursor for pharmaceutical products. Several metals (Sn, Fe, Cu, and Co) were anchored onto the supports by wetness impregnation methodology and the solids were thoroughly characterized using ICP/OES, XRD, N_2 physisorption, TEM-EDX, pyridine-FTIR, NH_3-TPD, and XPS techniques. Among these catalysts, Fe (5.07 wt.%)/SBA-15 (FeS1) exhibited the highest yield to myrtanal (63%) with a H_2O_2 efficiency of up to 60%; this catalyst had a total acidity of 138 μmol g^{-1}, a surface area of 496 m^2 g^{-1}, a pore volume of 0.96 cm^3 g^{-1}, and an acid site density of 0.28 μmol m^{-2}. Myrtanal selectivity was also high with Sn-based catalysts, while it was poor with Cu-based materials and the null activity of Co catalysts. Total Lewis acidity and acid site density were identified as suitable kinetic descriptors of catalytic data, owing to their crucial role in the ring-opening of monoterpene epoxides. The most active catalyst showed reusability without considerable loss of substrate conversion or selectivity towards myrtanal. Additionally, no leaching of Fe was observed. Based on materials characterization and catalytic results, a plausible reaction pathway was proposed for the one-pot tandem transformation of β-pinene towards myrtanal.

Keywords

One-pot, Tandem, β-Pinene, Myrtanal, Fe/SBA-15, Mesoporous materials.

6.2. Introduction

The fine chemistry industry stands as a pivotal sector, crucial for the production of targeted molecules utilized as precursors in fragrances, pharmaceuticals, drugs, and related compounds [1,2]. Synthesizing these products entails working on small scales of production, typically around 10,000 metric tons per year. Despite their relatively modest volume, these chemicals command high unit prices compared to others, owing to their exceptional purity, exceeding 99% with less than 10 ppm of metal residues, and stringent quality requirements, with pharmaceuticals often requiring an enantiomeric excess exceeding 98% [3]. Terpenes and terpenoids represent the most abundant and diverse class of natural products, exceeding 75000 variants, often found within essential oils (EOs), which are volatile and concentrated liquids extracted from various plant parts [4,5]. Monoterpenes and sesquiterpenes typically dominate the composition of EOs; for instance, turpentine oil, predominantly comprising α-pinene and β-pinene, is extracted from the raw resin obtained through steam distillation of pine trees [6]. Notably, the chemical composition of turpentine varies significantly based on factors such as wood species, biomass growth region, pulping process or mill, and even harvesting season [7].

The oxidation of monoterpenes over heterogeneous catalysts has been widely investigated, focusing on two competitive routes; the first one corresponds to typical oxidation by radical pathways using oxidizing agents, while the second one is associated with the epoxidation of the C=C bond to achieve the corresponding cyclic ether [3]. The predominance of each reaction pathway depends on the olefin nature, the oxidizing agent, the catalyst, and the reaction conditions. Bioderived biomass such as β-pinene monoterpene has gained tremendous

importance nowadays as it can be converted to β-pinene epoxide (**Figure 6.1**), which is an important chemical used in the production of polymers, fragrances, formulations in manufacturing, pharmaceuticals, and cosmetics, among others [8,9]. However, as β-pinene epoxide is a highly strained molecule, it can be rearranged under mild conditions into thermodynamically more stable compounds such as myrtanal, myrtenol, or perillyl alcohol (**Figure 6.1**). These products have a wide variety of applications in the fine chemistry industry such as fragrances, flavors, precursors of pharmaceutical products, and diesel additives [10,11].

Table 6.1 presents some heterogeneous catalysts that have been reported for the oxidation/epoxidation of β-pinene using different oxidizing agents such as molecular oxygen (O_2), hydrogen peroxide (H_2O_2), *tert*-butyl hydroperoxide (TBHP), cumene hydroperoxide (CHP), and urea hydroperoxide (UHP). Particularly, O_2 is considered a very attractive oxidizing agent because it is the cheapest and most desirable for selective oxidation in terms of environmental issues; however, controlling the high-efficiency dissociation of molecular O_2 with a triplet ground state into a singlet state is a significant challenge in the epoxidation process [8]. Entries 1-5 (**Table 6.1**) show that air or O_2 was the oxidizing agent in the epoxidation with catalysts such as ZnCo-MOF [8], CoO_X/mordenite [12], $MoCl_2O_2Bipy/TiO_2$-NT [13], ZSM-5/Co-MOF [14], and $[Co(NH_3)_6]Cl_3$ [15]. The highest yield to β-pinene epoxide (56.8 %), using O_2 as an oxidant and CHP as the initiator, was achieved with the ZSM-5/Co-MOF composite catalyst (entry 4), resulting also in a highly active material for the epoxidation of α-pinene and R-(+)-limonene with yields to the epoxides of 94.5% and 47.1%, respectively. These results suggest a dependence of the reactivity on the monoterpene structure, due to the presence of a bicyclic structure in pinenes, favoring the reactivity in comparison with limonene.

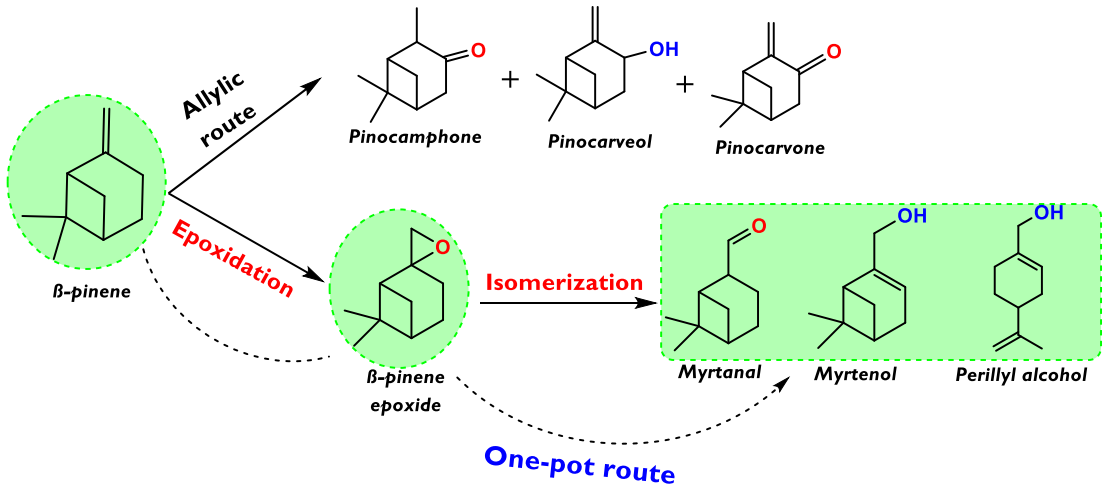

Figure 6.1. Reaction pathways of the β-pinene transformation towards isomers of β-pinene epoxide.

On the other hand, from an environmental point of view, H_2O_2 is convenient because it generates water as a byproduct [9]. However, for safety reasons, H_2O_2 is often available commercially in aqueous solutions (30 wt. %), whose water content can have a significant effect as a real inhibitor of catalysts by metals, slowing down the reaction. In general, the epoxide selectivity is poor in the presence of water or protic solvents due to the ring-opening secondary reaction leading to the formation of glycol compounds [16]. Therefore, it is an important challenge to investigate optimal reaction conditions to avoid undesirable reactions

and maximize the selectivity to the target molecules. Many systems have used H_2O_2 as the oxidizing agent (entries 6-12, **Table 6.1**), with MgO (entry 12) standing out as the significantly superior catalyst for the epoxidation of β-pinene, achieving complete conversion and 74% selectivity to the epoxide after 2 h and at a very low temperature (50 °C) [17]. This catalyst is used in a Payne system consisting of the formation of an epoxidizing agent like peroxyacetimidic acid from H_2O_2 using acetonitrile as the activator, acetone as solvent, and water as an improver [17]. This catalytic system has also been employed for the versatile epoxidation of R-(+)-limonene, yielding either limonene epoxides (endo and exo) or limonene diepoxide, depending on the reaction conditions [18]. With UHP as an oxidizing agent and an organotin-oxometalate coordination polymer, $[(nBu_3Sn)_2MoO_4]$, as catalyst (entry 13), a significantly low conversion (40%) was achieved after a long reaction time (10 h).

Table 6.1. Catalytic systems for the oxidation/epoxidation of β-pinene.

Entry	Catalyst	Reaction conditions	Oxidizing agent	X_β (%)	S_i (%)	Ref.
1	ZnCo-MOF	30 mg catalyst, 3 mmol substrate, 10 g DMF, 90 °C, 5 h	40 mL min^{-1} air	70.8	62.5 Epoxide	[8]
2	CoO_X/mordenite	100 mg of catalyst, 6 mmol of substrate, 10 g of DMF, 90 °C, 4 h	40 mL min^{-1} air and 0.6 mmol CHP	36.8	93.3 Epoxide	[12]
3	$MoCl_2O_2Bipy/TiO_2$-NT	15 mg catalyst, 0.1 mmol substrate, 10 mL CH_3CN, 19 °C, 18 h, light λ = 360 nm.	O_2	46	72 Epoxide 18 Myrtenal	[13]
4	ZSM-5/Co-MOF	10 mg catalyst, 3 mmol substrate, 10 g DMF, 90 °C, 5 h	40 mL min^{-1} air and 0.3 mmol CHP	72.6	78.3 Epoxide	[14]
5	$[Co(NH_3)_6]Cl_3$	5 mg catalyst, 3 mmol substrate, 10 g, 90 °C, 5 h,	40 mL min^{-1} air and 0.3 mmol TBHP	43	55 Epoxide	[15]
6	$FeCl_3 \cdot 6H_2O$	25 mg catalyst, 0.5 mmol substrate, 9 mL t-amyl alcohol, 25 °C	1.5 mmol H_2O_2	91.0	>50 Epoxide	[19]
7	$PdCl_2$	100 μmol catalyst, 2.5 mmol substrate, 10 mL CH_3CN, 60 °C, 8 h	3 mmol H_2O_2	58	19 Epoxide 57 Pinocarveol 24 Pinocarvone	[20]
8			9 mmol H_2O_2	55	4 Epoxide 47 Pinocarveol 49 Pinocarvone	
9	$[LMn(O)_3MnL](PF_6)_2$	1.25 μmol catalyst, 1.25 mmol substrate, 5 mL CH_3CN, 25 °C, 0.5 h	6.25 mmol H_2O_2	NR	10 Epoxide [a]	[21]
10	Pd/HPA-300/SBA-15	15 mg catalyst, 1 mmol substrate, 1 mL acetone, 50 °C, 18 h	6.8 mmol H_2O_2	99	63 Pinocarveol 12 Pinocamphone 16 Myrtenol	[22]
11	Pd(0.5)/HPA-SBA-15			90	67 Pinocarveol 13 Pinocamphone 15 Myrtenol	
12	MgO	1: 1.2: 30.2: 19.7: 3.2: 15.6 weight ratios for β-pinene: MgO: H_2O: acetone: H_2O_2: acetonitrile, 50 °C, 2 h.	H_2O_2	100	74 Epoxide	[17]
13	$[(nBu_3Sn)_2MoO_4]$	30 mg catalyst, 5 mmol substrate, 10 mL CH_3CN, 50 °C, 10 h	10 mmol UHP	40	70 Epoxide 11 Pinocamphone 9 Pinocarveol	[23]

X_β: β-Pinene conversion. **S_i:** Selectivity to product i. **DMF:** Dimethylformamide. **CHP:** Cumene hydroperoxide. **UHP:** Urea hydroperoxide. **Bipy:** 2,2′ -bipyridine-4,4′ -dicarboxylato. **NR:** Not reported. [a]Value corresponds to the yield.

In the context of β-pinene epoxide isomerization, various heterogeneous catalysts have been investigated. Among them, one notable catalyst is a microporous and crystalline material characterized by pores with a diameter of at least 0.52 nm [24,25], whose empirical formula is $H_w(M_wTi_xSn_yZr_zSi_{1-w-x-z})O_2$; this catalyst exhibited a remarkable 98% conversion and 94% selectivity towards myrtanal (80 °C, 1 h, acetonitrile as solvent). In addition, mesoporous catalysts based on Me/MCM-41 (Me = Sn, Ti, Zr, Al, and Si) have been also explored. Notably, Sn/MCM-41 emerged as the most effective catalyst, achieving complete conversion with 82% selectivity towards myrtanal, 4% to myrtenol, and 5% to perillyl alcohol (80 °C, 1 h, nitromethane as solvent) [11]. It has been suggested that Sn enhances acidity strength and Lewis behavior required for myrtanal synthesis. Other catalysts reported in the literature include Sn-β [26], supported ionic liquid [27], Sn-MCM-41 [28], Fe-β zeolite [29], and tetraimidazolium nitrate ($[PEimi][HNO_3]_4$) [30]. Therefore, experimental findings have indicated that myrtanal formation is favored by Lewis acidity, particularly in non-polar solvents like toluene.

Consequently, the production of myrtanal using β-pinene as a starting material has been carried out through two independent stages. Firstly, β-pinene epoxide is obtained in one reactor, which is then purified to obtain high-purity epoxide. Subsequently, it is used as a substrate for the epoxide rearrangement in another reaction vessel to obtain the target molecules, either myrtanal, myrtenol, or perillyl alcohol. However, a significant contemporary challenge in organic chemistry is the search for alternative cleaner, safer, and environmentally friendly technologies [31], which are aimed at contributing to the goals of sustainable development and the principles of green chemistry. Therefore, the reduction of waste, together with the use of renewable feedstock, environmentally friendly reagents, and catalysts, is significant to achieving more sustainable processes [31]. An effective approach is to synthesize myrtanal as the target molecule in a single reaction vessel, which is directly related to the 'one-pot' concept, being able to apply to a multi-step reaction, method, or synthesis. This approach is promising and effective because the two involved transformations (β-pinene epoxidation and epoxide isomerization) can be carried out in a single pot, avoiding several intermediate purification processes, minimizing chemical waste, saving time, and simplifying practical aspects [32].

To our knowledge, as of the current date, there have been no reports found in open literature regarding one-pot reactions for the transformation of β-pinene into myrtanal, myrtenol, or perillyl alcohol as the main products. Few reports exist regarding the one-pot reaction of a similar monoterpene, α-pinene, into campholenic aldehyde primarily. However, these systems are not highly selective towards the aldehyde; instead, the route is quite competitive, yielding various products. Selectivity towards the aldehyde was increased over the bifunctional PrAlPO-5 catalyst [33] by decreasing the (Al + P)/Pr ratio that enhanced Lewis acidity, reaching up to 90% at complete conversion (70°C, 12 h, chloroform as solvent, and air as the oxidizing agent). Zeolite Y encaged Ru (III) and Fe(III) complexes [34], prepared by the flexible ligand method, showed complete conversion of α-pinene towards campholenic aldehyde (35.9%), α-pinene epoxide (34.1%), and verbenone (20.7%) after 18 h at 80 °C, using H_2O_2 as the oxidizing agent and acetonitrile as solvent.

V-MCM-41 [35] synthesized via direct hydrothermal method, exhibited an α-pinene conversion of 12.8% with selectivities up to 13.4% for campholenic aldehyde, 15.9% for 1,2 pinanediol,

36.3% for *trans*-sobrerol, and 11.4% for verbenol (70 °C, 7 h, H_2O_2 as the oxidizing agent, and acetonitrile as solvent). A report on the effect of vanadium content in nickel phosphate molecular sieve (V-VSB-5) on α-pinene epoxide isomerization [36] showed that an increase in V content enhanced the strength of Brønsted acid sites and increased isomerization of α-pinene epoxide to *trans*-carveol and decreased conversion to campholenic aldehyde. Specifically, 12% of α-pinene conversion was reached with selectivities of 21%, 8%, and 9% for epoxide, campholenic aldehyde, and *trans*-carveol, respectively (60 °C, 5 h, molecular oxygen as the oxidant, and acetonitrile as the solvent). Outdated papers reported Co/SiO_2 [37] and Ti-HMS [38,39] as catalysts that exhibited low α-pinene conversions, typically below 40%, under the tested reaction conditions.

Although significant progress has been evidenced in the field of one-pot catalytic reactions over the past decades, these reactions have not yet found general application in the production of fine chemicals due to the difficulty of reaction control [40]. Hence, this study aims to utilize the catalysis-in-tandem approach [41], which involves using multiple catalysts combined in a single reaction vessel, undergoing a sequence of precisely staged catalytic steps, specifically monoterpene epoxidation and epoxide rearrangement. This research focus was to investigate the catalytic system composed of MgO, for promoting the β-pinene epoxidation through a Payne system with H_2O_2, and a Lewis acid catalyst based on Me/Support (Me = Sn, Fe, Cu, Co; Support = MCM-41, SBA-15), favoring the rearrangement of β-pinene epoxide, under compatible and mild reaction conditions. The aim was to establish optimal reaction conditions for the selective synthesis of myrtanal from a biomass-derived source like β-pinene.

6.3. Experimental Section

6.3.1. Materials

Commercial reagents were used as received unless stated otherwise. Reagents for the synthesis of mesoporous catalysts were myristyltrimethylammonium bromide (MTAB, 99 wt.%, Sigma Aldrich), tetraethyl orthosilicate (TEOS, 98 wt.%, Sigma-Aldrich), ammonium hydroxide (NH_4OH, 29 wt.%, Merck), poly(ethylene glycol)-block-poly(propylene glycol)-block-poly(ethylene glycol) (P123, PEG 30 wt.%, Sigma-Aldrich, molecular weight of 5800), hydrochloric acid fuming (HCl, 37 wt.%, Merck), iron(III) nitrate nonahydrate ($Fe(NO_3)_3 \cdot 9H_2O$, 99.5 wt.%, PanReac AppliChem), copper(II) nitrate trihydrate ($Cu(NO_3)_2 \cdot 3H_2O$, 99.5 wt.%, Carlo Erba), cobalt(II) nitrate hexahydrate ($Co(NO_3)_2 \cdot 6H_2O$, 100 wt.%, J.T. Baker), and stannous chloride dihydrate ($SnCl_2 \cdot 2H_2O$, 100 wt.%, AlfaAesar). Reagents for catalytic tests were β-pinene (99 wt.%, Sigma-Aldrich), hydrogen peroxide (H_2O_2, 30 % w/v, PanReac AppliChem), acetone (99.9 wt.%, PanReac AppliChem), acetonitrile (99.5 wt.%, Merck), and magnesium oxide (MgO, 99.6 wt.%, J.T. Baker). Reagents for the quantification of H_2O_2 were cerium (IV) sulfate solution ($Ce(SO_4)_2 \cdot 4H_2O$, 0.1 mol L^{-1}, Titripur, Merck), and manganese (IV) oxide (MnO_2, > 99 wt.%, Sigma-Aldrich).

6.3.2. Synthesis of Mesoporous Supports

MCM-41 and SBA-15 supports were synthesized following the procedures reported by Grün et al. [42] and Shah et al. [43], respectively. In the case of MCM-41, the template MTAB was dissolved in deionized water under magnetic stirring (750 rpm) to achieve a concentration of 0.055 mol L^{-1}. The pH was adjusted with NH_4OH, and TEOS was then added dropwise using a Masterflex model 77200-60 peristaltic pump (0.7 mL min^{-1}). The molar ratio of the mixture was 1 TEOS: 0.1380 MTAB: 1.6280 NH_4OH: 147.0995 H_2O. The resulting suspension was

stirred at room temperature for 1 h, and the precipitate was filtered, dried overnight at 100 °C, and calcined at 550 °C for 5 h at a heating rate of 1 °C min^{-1}. Typical synthesis conditions included 22.43 g MTAB, 101.71 g TEOS, 104.60 mL NH_4OH, and 1.2 L of deionized water.

For SBA-15, P123 was dissolved in a mixture of deionized water and HCl (2 M) under magnetic stirring (450 rpm) at room temperature for 1 h. Subsequently, TEOS was slowly added using a peristaltic pump (0.42 mL min^{-1}). The molar ratio of the mixture was 1 TEOS: 0.0058 P123: 5.7757 HCl: 195.9030 H_2O. The mixture was stirred at 40 °C and 500 rpm for 24 h, then transferred to a Teflon flask for hydrothermal treatment at 100 °C for 48 h. The precipitated solid was filtered, washed with abundant deionized water, dried for 24 h at room temperature, and finally calcined for 24 h at 550 °C with a heating rate of 1 °C min^{-1}. Typical synthesis conditions included 2.2450 g P123, 4.2687 g TEOS, 60.0182 g HCl (2 M), and 15.0185 g of deionized water. Schemes of the experimental methodology are presented in **Figure 8.97** and **Figure 8.98**.

6.3.3. Synthesis of Metal-Modified Catalysts

The anchoring of the metals as the active phases onto supports was conducted through the wetness impregnation procedure (**Figure 8.99**). In this method, 40 mL of an aqueous solution of the salt precursor with a specified loading, was added to 1 g of the previously dried support. The resulting mixture was stirred continuously at 750 rpm for 2 h at room temperature and subsequently dried overnight at 80 °C. Then, the synthesized materials (**Table 6.2**) were activated by calcination at 550 °C for 5 h at a heating rate of 1 °C min^{-1}.

Table 6.2. Description of the prepared catalysts.

Entry	Support	Metal	Nominal loading (% wt.)[a]	Catalyst
1	MCM-41	Sn	2.96	SnM1
2	MCM-41	Sn	5.16	SnM2
3	MCM-41	Fe	5.06	FeM1
4	MCM-41	Cu	5.06	CuM1
5	MCM-41	Co	5.07	CoM1
6	SBA-15	Sn	4.95	SnS1
7	SBA-15	Sn	10.10	SnS2
8	SBA-15	Fe	3.08	FeS1
9	SBA-15	Fe	5.11	FeS2
10	SBA-15	Cu	5.04	CuS1
11	SBA-15	Co	5.27	CoS1

[a] Calculated as the ratio of metal mass to support mass.

6.3.4. Catalyst Characterization

The metal-modified mesoporous catalysts were thoroughly analyzed by several techniques. The concentration of the metals (Sn, Fe, Cu, and Co) in the catalysts was determined using inductively coupled plasma optical emission spectroscopy (ICP/OES) with a spectrometer coupled to Plasma iCAP XP (Thermo Scientific). A microwave digestor (Ethos Easy model, Milestone) equipped with 24 positions, along with an acid purifier (Duopur model, Milestone) was used for sample preparation. Powder X-ray Diffraction patterns (XRD) were obtained using a Malvern-PANalytical Empyrean 2012 diffractometer equipped with a PIXcel3D detector and a copper source (λ = 1.541874 Å). The measurements were conducted at 45 kV and 40

mA, with a low Bragg range of 2θ = 0.5–10°. The goniometer was configured for omega/2theta scans, employing reflection transmission spinner mode with a 4s rotation period. The scan step size was 0.02°, and each step took 80 s.

The textural properties were investigated by nitrogen physisorption isotherms at 77 K acquired using a Micromeritics ASAP 2020 PLUS instrument. Before analysis, the samples underwent pretreatment at 350 °C for 8 h under a high vacuum for degassing. Surface areas were determined utilizing the BET model, while the pore size distribution was calculated using the BJH model for the desorption isotherm, incorporating the Harkins and Jura correction [44]. This correction accounts for surface tension and capillary forces influencing nitrogen desorption in small pores. The morphology of the catalysts was examined via transmission electron microscopy (TEM) using a TECNAI F20 Super Twin microscope operating at a resolution of 0.1 nm with an acceleration voltage of 200 kV. The microscope was equipped with a GATAN US 1000XP-P chamber. The samples were dispersed in an ethanol mixture using an ultrasonic bath for 10 min at room temperature and subsequently placed on the Cu lacey carbon grid of 200 mesh and allowed to dry. For determining the elemental composition in the materials, an Oxford Instruments XMAX EDX detector was employed. To calculate the average size of metal particles, the diameter of approximately 250 particles was measured using ImageJ software.

The acidity type of mesoporous catalysts was assessed through infrared spectroscopy using a Frontier FT-IR spectrometer (PerkinElmer, spectrum 65 model) with pyridine (≥ 99%) as a probe molecule. This method enabled both qualitative and quantitative determination of Brønsted and Lewis acid sites. The spectrometer was equipped with a high-resolution Mercury Cadmium Telluride (MCT) detector and a diffuse reflectance cell (DRIFT). Spectra were recorded with a resolution of 4 cm min^{-1}, ranging from 1750 to 1350 cm^{-1}, over 40 sweeps; the samples were pressed into thin pellets (5-10 mg). Before analysis, the sample underwent pretreatment, gradually reaching 550 °C at a rate of 1 °C min^{-1} and held at that temperature for 5 h. Subsequently, the DRIFT cell's sample holder was heated to 400 °C (10 °C min^{-1}) in a helium flow, capturing spectra at 10 °C intervals (blanks). The pyridine adsorption process was initiated at 40 °C for 30 min, followed by the removal of excess pyridine from the solid surface using a helium flow for 30 min. Desorption started up to 400 °C (10 °C min^{-1}), with spectra recorded every 10 °C. Finally, the difference between the spectra with pyridine and blanks was calculated; Brønsted acid sites (BAS) and Lewis acid sites (LAS) were determined using spectral bands at 1545 cm^{-1} and 1450 cm^{-1}, respectively [45].

The determination of total acidity strength was performed using ammonia-temperature programmed desorption (NH_3-TPD) on a Micromeritics Autochem 2920 instrument. Initially, around 100 mg of the sample underwent *in-situ* activation at 550 °C for 30 min (10 °C min^{-1}). Subsequently, the sample was cooled to 50 °C under helium flow of 50 mL min^{-1} and saturated with a gas mixture containing 0.3 vol% NH_3/He (50 mL min^{-1}) for 90 min. The physisorbed NH_3 was then flushed with helium (50 mL min^{-1}) at 50 °C for 1 h; lastly, the sample underwent heating to 600 °C (10 °C min^{-1}) under a helium flow of 50 mL min^{-1} for the desorption of NH_3. **Eq. (6.1)** was used to quantify the acidity strength based on the calibration of the TCD signal and the NH_3 concentration, where C_{Des} corresponds to NH_3 acidity (mol NH_3 g^{-1}), m_{cat} is the mass of the catalyst, $\dot{V}_{He}$ is the volumetric flow of the carrier gas (50 mL He min^{-1}), V_m is the molar volume of one mole of an ideal gas at standard conditions (22.4 L mol^{-1}), β is the heating rate (10 °C min^{-1}), and C_i is the ammonia concentration (% vol).

$$C_{Des} = \frac{1}{m_{cat}} \frac{\dot{V}_{He}}{V_m} \frac{1}{\beta} \int_{T_0}^{T_f} C_i dT \quad \textbf{(6.1)}$$

X-ray photoelectron spectroscopy (XPS) analyses were conducted utilizing a Specs X-ray photoelectron spectrometer (NAP-XPS) equipped with a PHOIBOS 150 1D-DLD analyzer. A monochromatic Al-Kα source (1486.7 eV, 13 kV) was employed, and the step energy for general spectra was set at 85.36 eV, while for high-resolution spectra, it was 20 eV. 20 scans were performed for the high-resolution spectra and 5 scans for general spectra. Charge compensation was applied during sample measurements with an energy of 3 eV and 20 μA. All spectra were calibrated using the adventitious carbon 1s peak at 285.0 eV. A Shirley-type background was subtracted from the spectra, and CasaXPS software was utilized for processing the XPS data.

In our recent work [18], MgO was thoroughly characterized using various techniques, including XRD, nitrogen adsorption-desorption isotherms, thermogravimetric analysis (TGA), Fourier transform-infrared spectroscopy (FTIR), and scanning electron microscopy-energy dispersive X-ray spectroscopy (SEM-EDX).

6.3.5. Catalytic Measurements

The one-pot catalytic reactions were performed in 2 mL batch reactors, capped vials covered with silicone septa. The reaction temperature was maintained by immersing the vials in a well-stirred oil bath controlled by an EKT Hei-Con Heidolph controller. Catalytic tests were carried out using a sufficiently high liquid volume-to-catalyst mass ratio and vigorous agitation (1000 rpm) to overcome external mass-transfer limitations. Additionally, small catalyst particles (<75 μm) were utilized to suppress internal mass-transfer limitations. Reactions were stopped by cooling the vials in an ice bath, followed by separating catalysts from the reaction mixture through centrifugation at 3000 rpm for 8 min. Two catalysts were employed in the heterogeneous system, MgO, renowned for its excellent catalytic activity in the epoxidation of monoterpenes [17,18], and acidic mesoporous materials (**Table 6.2**) to promote the isomerization of epoxide. In a typical experiment, 0.1 mmol of β-pinene was loaded into the reactor, with weight ratios of 1: 0.72: 1.2: 30.3: 19.7: 15.7: 0.8 for β-pinene: acidic catalyst: MgO: H_2O: acetone: acetonitrile: H_2O_2, the suspension was stirred at 1000 rpm at 50 °C. An aliquot of the centrifuged mixture was utilized for quantifying H_2O_2, while MnO_2 was added to the rest of the mixture for oxidant decomposition before GC-MS analysis.

The reaction products were identified using gas chromatography coupled with mass spectrometry, employing a GC-MS Agilent 7890N equipped with a DB-1 column (30 m, 320 μm, 0.25 μm), a FID detector, and an autosampler. The carrier gas was He (30.462 cm s^{-1}, 2.2912 mL min^{-1}), with a split ratio of 15:1. The detector temperature was set at 250 °C, with an injection volume of 1 μL. The oven temperature was initially kept at 70 °C for 2 min, followed by heating up to 130 °C (10 °C min^{-1}) for 1 min, and finally, an increase to 180 °C (20 °C min^{-1}). The β-pinene conversion (X_β), the selectivity (S_j), and the yield to the product j (Y_j) were calculated using **Eqs. (6.2)-(6.4)**.

$$X_\beta(\%) = \frac{C_{\beta,0} - C_{\beta,t}}{C_{\beta,0}} * 100 \quad \textbf{(6.2)}$$

$$S_j(\%) = \frac{C_{j,t}}{C_{\beta,0} - C_{\beta,t}} * 100 \quad \textbf{(6.3)}$$

$$Y_j(\%) = \frac{C_{j,t}}{C_{\beta,0}} * 100 \quad \textbf{(6.4)}$$

$C_{\beta,0}$, $C_{\beta,t}$, and $C_{j,t}$ denote the initial molar concentration of β-pinene, the molar concentration of β-pinene after time t, and the molar concentration of the product j after time t in the reaction mixture, respectively; concentrations were calculated with the area normalization method.

6.3.6. Quantification of Oxidizing Agent

The H_2O_2 concentration was monitored via cerimetric titration, as reported previously in our work [18]. Briefly, the yellow cerium (IV) sulfate reacts with H_2O_2 to produce colorless cerium (III) sulfate, sulfuric acid, and oxygen. A 100 µL sample was placed into a beaker with 5 mL of deionized water and titrated using a Metrohm 775 Dosimat equipment. The endpoint was reached when the solution changed from colorless to yellow, indicating an excess of titrant agent in the medium. The concentration in wt. % was calculated using **Eq. (6.5)**, where θ_{SF} is the stoichiometric factor (1/2 for H_2O_2/$Ce(SO_4)_2$), C_T is the concentration of the titrant agent, V_s is the spent volume for the sample titration, V_b is the spent volume of the titrant for the blank test (5 mL of deionized water), $MW_{H_2O_2}$ is the molecular weight of H_2O_2, and W_s is the weight of the sample. The H_2O_2 conversion, as defined in **Eq. (6.6)**, was calculated using the initial molar concentration ($C_{H_2O_2,0}$).

$$C_{H_2O_2} = \frac{\theta_{SF} C_T (V_T - V_b) MW_{H_2O_2}}{W_s} * 100 \quad \textbf{(6.5)}$$

$$X_{H_2O_2}(\%) = \frac{C_{H_2O_2,0} - C_{H_2O_2}}{C_{H_2O_2,0}} * 100 \quad \textbf{(6.6)}$$

6.4. Results and Discussion

6.4.1. Catalyst Characterization

6.4.1.1. Chemical Analysis

The quantification of metals in the catalysts, determined by ICP/OES, is presented in **Table 6.3**. Values ranging from 0.0% (unmodified supports) up to 8.5 wt.% (FeM1) were obtained; clearly, these values differ from the nominal metal loadings reported in **Table 6.2**.

Table 6.3. Metal loading, unit cell parameters, and textural properties of catalysts based on MCM-41 and SBA-15.

Catalyst	% Metal[a]	2θ (°)	d_{100}[b] (nm)	a_0[c] (nm)	ACS[d] (nm)	BET area (m^2 g^{-1})	Pore volume (cm^3 g^{-1})	APS[e] (nm)	MC[f] (molec nm^{-2})
MCM-41	0.00	2.76	3.20	3.69	19.29	1394	0.49	2.31	0.00
SnM1	1.25	2.82	3.13	3.61	24.40	1188	0.47	1.66	0.05
SnM2	2.17	2.85	3.10	3.58	22.86	1113	0.42	1.66	0.10
FeM1	8.50	2.87	3.07	3.55	20.24	954	0.26	1.66	0.96
CuM1	5.59	2.98	2.96	3.42	18.04	610	0.25	3.37	0.87
CoM1	4.55	3.01	2.93	3.39	15.96	1803	0.96	3.39	0.26
SBA-15	0.00	0.96	9.19	10.61	62.98	860 [46]	n.r	n.r	0.00
SnS1	2.32	0.88	10.03	11.58	165.89	611	1.23	7.70	0.19
SnS2	2.24	n.a	n.a	n.a	n.a	628	1.22	7.55	0.18
FeS1	5.07	0.93	9.49	10.96	123.98	496	0.96	6.37	1.10
FeS2	5.14	0.91	9.70	11.20	96.22	617	1.09	6.42	0.90
CuS1	4.54	0.91	9.70	11.20	150.81	555	1.08	6.44	0.78
CoS1	5.35	0.90	9.80	11.32	165.89	533	1.17	7.69	1.03

[a] The weight percentage of the metal was determined by ICP/OES. [b] The interplanar spacing for the plane (100) (d_{100}) was calculated using the Bragg equation, **Eq. (6.7)**. [c]The unit cell parameter (a_0) was calculated using **Eq. (6.8)**. [d] The average crystal size (ACS) was calculated with the Scherrer equation, **Eq. (6.9)**. [e]The average pore size (APS) was estimated from the pore size distributions (**Figure 6.3.C** and **Figure 6.3.D**).
[f]Metal coverage (MC) = (% metal/100)*(N_A/MW)*(1/BET), where N_A is Avogadro's number and MW is the molecular weight of metal. n.a: Not available because the (100) Bragg reflection was not observed. n.r: Not reported.

6.4.1.2. X-Ray Diffraction

Figure 6.2 presents the XRD patterns for the prepared catalysts based on MCM-41 (**Figure 6.2.A**) and SBA-15 supports (**Figure 6.2.B**). Three diffraction peaks corresponding to reflections (100), (110), and (200) are observed in all the catalysts, which are characteristic of the typical hexagonal arrangement of these two materials [6,47–50]. The main diffraction peaks for the MCM-41 series of catalysts are located at 2θ = 2.8°, 4.8°, and 5.4°, corresponding to the crystallographic planes (100), (110), and (200), respectively. It is noteworthy that in all materials, the main peak associated with the (100) crystallographic plane can be clearly observed, but in the metal-modified MCM-41 catalysts, the intensity of the other two peaks decreased compared to the support. Furthermore, slight shifts (Δ2θ) were observed in the (100) peak in the catalysts after the impregnation of metals, with a maximum shift of 0.25° for CoM1. Additionally, XRD of the materials that contained Co, Cu, or Fe indicates a decrease in the well arrangement of the hexagonal pores due to a decrease in the intensity of the main diffraction peak, while materials with Sn exhibit an XRD like the support.

For the SBA-15 series of catalysts, the same three crystallographic planes are located at 2θ = 1.0°, 1.6°, and 1.8°, respectively. Notably, the intensity of SnS2 significantly decreased in comparison with the SBA-15 support and the other metal-modified catalysts. This decrease can be attributed to the high Sn loading. Similar results regarding the high loading of Fe anchored on SBA-15 have been reported, where the intensity of the (100) plane almost

completely disappeared [46]. On the other hand, the catalyst with Co (CoS1) exhibited an appreciable loss of hexagonal rearrangement, as suggested by the low intensity of the main diffraction peak. Co-supported on MCM-41 (CoM1) also showed the lowest crystallinity due to a broad peak and low intensity.

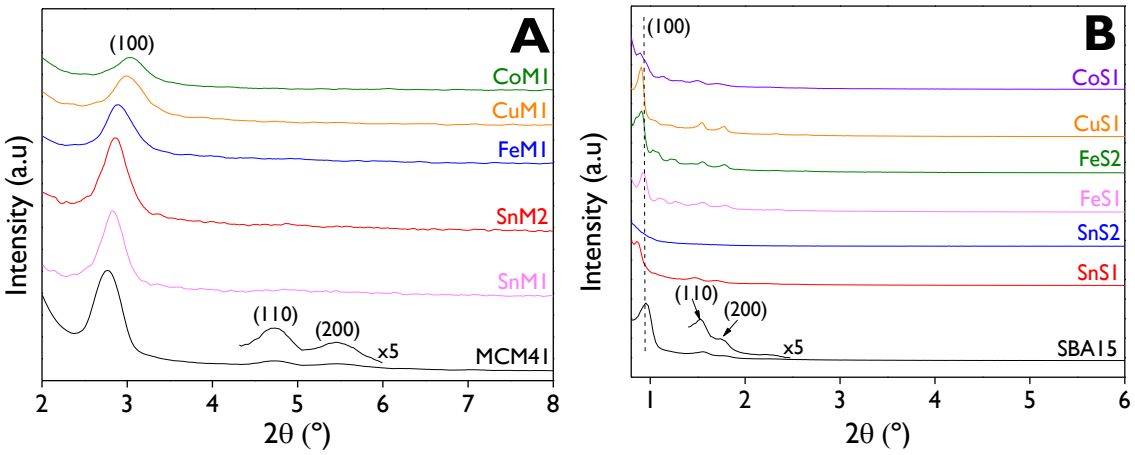

Figure 6.2. XRD patterns of catalysts based on **(A)** MCM-41 and **(B)** SBA-15.

The indexing of the diffraction peaks [51,52] can be performed using Bragg's law, **Eq. (6.7)**, and the interplanar spacing (d) for the hexagonal structure can be calculated with **Eq. (6.8)**, where d represents the interplanar spacing for the plane (h k l), with h, k, and l being the Miller indices. θ denotes the diffraction angle, λ is the wavelength of the incident X-ray beam (0.154 nm for a copper lamp), and a_0 is the unit cell parameter in the hexagonal structure.

$$n\lambda = 2d\sin(\theta) \quad \textbf{(6.7)}$$

$$a_0 = \frac{2d}{\sqrt{3}}\sqrt{h^2 + hk + k^2} \quad \textbf{(6.8)}$$

Additionally, the average crystal size (ACS) can be calculated using the Scherrer equation [53], described by **Eq. (6.9)**, where K is the shape factor constant (0.94), and β (in radians) is the full width at half maximum (FWHM) of the most intense diffraction peak (100).

$$ACS = \frac{K\lambda}{\beta\cos(\theta)} \quad \textbf{(6.9)}$$

The results of the unit cell parameters (d_{100} and a_0) and the ACS are presented in **Table 6.3**. The values of d_{100} and a_0 for the metal-modified MCM-41 catalysts decreased compared to the MCM-41 support, as expected from the shift in the diffraction peak associated with the (100) plane. In contrast, for the catalysts based on SBA-15, these values increased with respect to the SBA-15 support, which is evidenced with a shift to the left of the main diffraction peak. It is noteworthy that the corresponding values of d_{100} and a_0 for catalysts based on SBA-15 are around three times those for catalysts based on MCM-41. Additionally, the loading of Sn onto MCM-41 (SnM1 and SnM2) and Fe onto SBA-15 (FeS1 and FeS2) seems to have no significant influence on d_{100} and a_0.

Among the MCM-41 catalysts, SnM1 and SnM2 exhibited the highest ACS values (24.4 and 22.9 nm, respectively) showing a narrower main diffraction peak at the lowest Bragg angle (**Eq. (6.9)** and **Figure 6.2.A**). Conversely, the lowest ACS value (16.0 nm) was obtained for CoM1, based on its wider peak and the most rightward shift (2θ = 3.01°). For the SBA-15

catalysts, all materials exhibited values of at least 63 nm; SnS1 showed the highest value (165.9 nm).

6.4.1.3. Textural Properties

The N_2 adsorption-desorption isotherms (**Figure 6.3.A** and **Figure 6.3.B**) of the catalysts were measured to determine the textural properties, such as the BET surface area, pore volume, and average pore size (APS), as illustrated in **Table 6.3**. The presence of mesopores in catalysts based on MCM-41 and SBA-15 is confirmed by **Figure 6.3.A** and **Figure 6.3.B**, respectively. All materials exhibit type IV-like isotherms according to the IUPAC classification [54–56]. However, notice that the MCM-41 support and the catalysts based on MCM-41, such as SnM1, SnM2, and FeM1, did not exhibit the hysteresis loop, which can be attributed to the low pore sizes of those materials (**Table 6.3**), practically at the boundary of micropores and mesopores, as has been previously reported [49,57]. All materials in **Figure 6.3.A** show strong adsorption at around a relative pressure of 0.2. Contrarily, isotherms of all materials based on SBA-15 (**Figure 6.3.B**) exhibited a typical hysteresis loop of type H1 with steep condensation and evaporation branches between relative pressures of 0.7 and 0.75, indicating a narrow mesopore size distribution and demonstrating the good quality of the materials [58]. In addition, the further increase in the adsorbed volume at the end of the isotherm can be associated with the adsorption on the external surface of the porous materials [58]. The isotherms for SBA-15 materials allow the conclusion that they belong to porous systems that consist of cylindrical geometry pores opened on both sides [59].

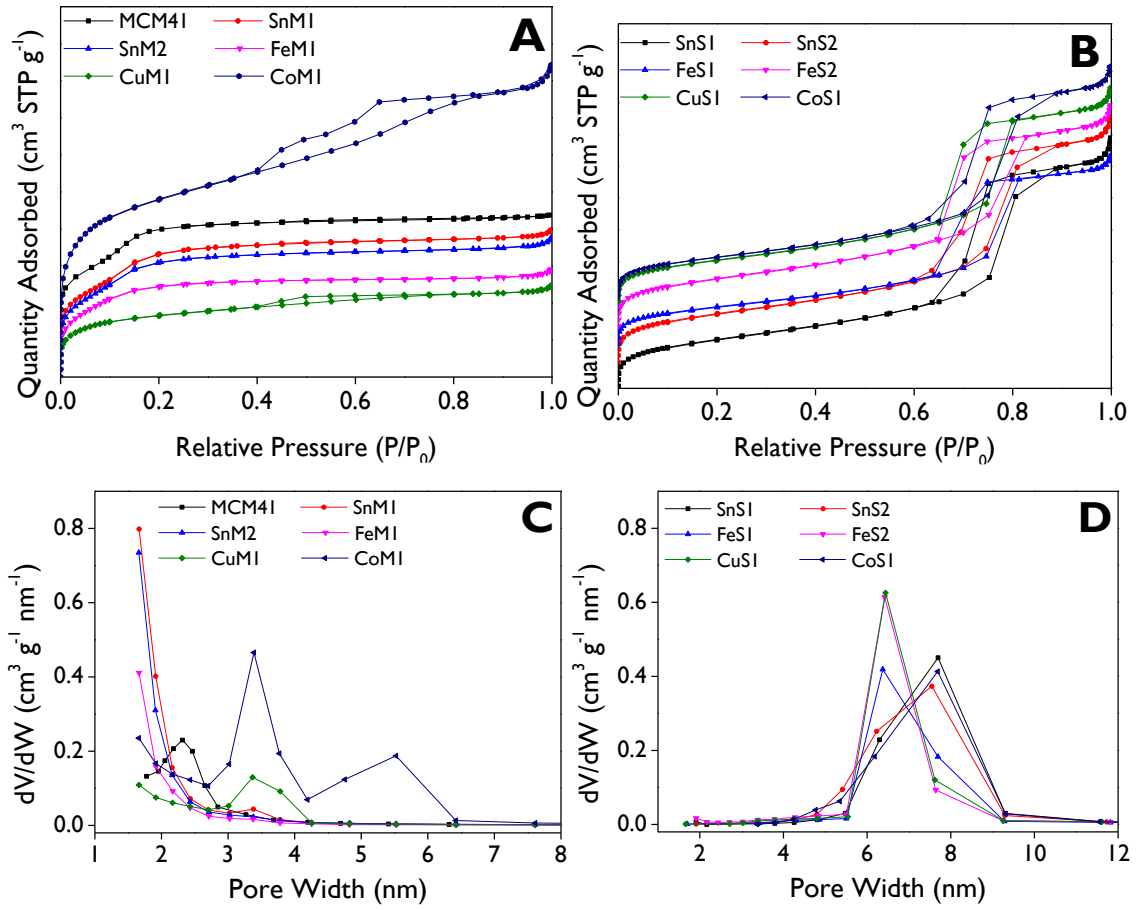

Figure 6.3. N_2 adsorption-desorption isotherms **(A, B)** and pore size distributions **(C, D)** for catalysts based on MCM-41 **(A, C)** and SBA-15 **(B, D)**.

The BET areas (**Table 6.3**) of the catalysts based on MCM-41 show that the support exhibited a very high BET area (1394 $m^2 g^{-1}$) and this value decreased along with the incorporation of different metals like Sn, Fe, and Cu, obtaining a value below 50% for CuM1 (610 $m^2 g^{-1}$), suggesting possible pore blocking or clogging in those materials. For catalysts based on SBA-15, the surface area of the support is 860 $m^2 g^{-1}$ [46]. When the metals were anchored onto the support by wetness impregnation, like catalysts with MCM-41, a decrease in the surface areas was observed, reaching the lowest value for the FeS1 catalyst (496 $m^2 g^{-1}$) signifying a loss of about 42% of the area concerning the support. In this way, it is clear that the incorporation of metals significantly affects the catalyst surface, reducing their BET area, as reported in similar catalysts for Prins condensation and isomerization reactions [46,49]. On the other hand, the Sn loading did not exhibit an effect on the BET area for MCM-41 and SBA-15 catalysts, while appreciable differences were observed with different Fe loadings onto SBA-15. The BET surface area was utilized in conjunction with the metal percentage determined by ICP-OES to determine the metal coverage (MC), as reported in **Table 6.3**. This parameter represents the number of metal entities per unit area of the catalyst.

Furthermore, notice that the pore volume (**Table 6.3**) can be directly related to the BET area, reaching the highest values for the MCM-41 support (0.49 $cm^3 g^{-1}$) and SnS1 (1.23 $cm^3 g^{-1}$), among each series of catalysts. However, although the BET areas for catalysts based on MCM-41 were larger than those for SBA-15 materials, the pore diameter and the pore volume of SBA-15 catalysts are much larger than for MCM-41 catalysts [60], which can be attributed to the cylindrical shape of the pores in the SBA-15 which allows low packing density, existing more space between the pores, resulting in a larger total pore volume. These characteristics are useful for the fabrication of electrochemical sensors [61] and dental applications [62].

The pore size distributions for catalysts based on MCM-41 and SBA-15 are presented in **Figure 6.3.C** and **Figure 6.3.D**, respectively. **Figure 6.3.C** shows that the average pore size (APS) for the materials MCM-41, SnM1, SnM2, and FeM1 is very close to 2 nm, limiting between micropores and mesopores, while distributions for CuM1 and CoM1 are shifted to the right, with APS values of 3.37 and 3.39 nm, respectively. This observation aligns with the behavior of the N_2 isotherms. For SBA-15 catalysts (**Figure 6.3.D**), SnS1, SnS2, and CoS1 exhibit closer values between 7.55 and 7.70 nm, while FeS1, FeS2, and CuS1 show lower values between 6.37 and 6.44 nm. Therefore, it can be concluded that the loading of Sn and Fe onto the mesoporous supports did not significantly affect the pore size of the catalysts.

6.4.1.4. TEM-EDX Analysis

The TEM images for the prepared catalysts are shown in **Figure 6.4** and **Figure 8.100-Figure 8.111**. **Figure 6.4.a-f** and **Figure 8.100-Figure 8.105** depict the morphology of the catalysts based on MCM-41, where the characteristic channels with a typical ordered hexagonal array mesostructure for these materials are observed in most of them [49,63]. However, **Figure 6.4.f** and **Figure 8.105** show the morphology for cobalt-modified MCM-41 (CoM1), which does not clearly exhibit the ordered structure. This aligns with the previous results of XRD (**Figure 6.2.A**), which showed a low intensity of the main diffraction peak, which suggested the absence of a well-arranged structure in that material. Conversely, **Figure 6.4.a** and **Figure 8.100** show a very high and uniform distribution of hexagonal rearrangement of pores in the unmodified support (MCM-41), validating the successful synthesis of the support. For catalysts based on SBA-15, the TEM images are shown in **Figure 6.4.g-l** and **Figure 8.106-Figure 8.111**, revealing excellent ordering in the channels with well-defined and uniform pores, typical of SBA-15 materials [64,65].

The materials modified with Sn in either MCM-41 (**Figure 6.4.b-c**, **Figure 8.101**, **Figure 8.102**) and SBA-15 (**Figure 6.4.g-h**, **Figure 8.106**, **Figure 8.107**) exhibit well-dispersed metal particles over the supports, as has been detected for Sn nanoparticles in heterogeneous catalysts based on microporous and hierarchical zeolite Y-based catalysts [66,67]. The images of mesoporous catalysts with Fe (**Figure 6.4.d,i,j**, **Figure 8.103**, **Figure 8.108**, **Figure 8.109**) and Cu (**Figure 6.4.e,k**, **Figure 8.104**, **Figure 8.110**) suggest that metal nanoparticles are located inside the channels. These results differ significantly from those previously reported for different loadings of Fe and Cu supported onto MCM-41 and SBA-15 [46], where the authors observed Cu nanoparticles in the TEM images of all materials and also Fe nanoparticles in some of the synthesized materials. These notable differences are attributed to the post-grafting procedure utilized by them, which used incipient wetness impregnation with the same salt precursors with a defined volume of salt precursor depending on the support (5.4 mL g^{-1} MCM-41 and 3.0 mL g^{-1} SBA-15), while in this study, wetness impregnation was used, characterized by an excess of the salt precursor solution, which is a more reproducible method and easier to scale-up for the synthesis of a bigger batch of catalysts. Therefore, it is concluded that the post-impregnation procedure in the preparation of the catalysts for the metal nanoparticles is of great importance and influences the location of the active phase in the mesoporous supports.

The elemental maps of silicon, oxygen, and the corresponding metal (Sn, Fe, Cu, and Co) for four catalysts, namely FeM1, SnS1, CuS1, and CoS1, are presented in **Figure 8.112**-**Figure 8.115**. These maps indicate the excellent distribution of metals in the support achieved through wetness impregnation. This conclusion is drawn from the similarity in the physical form of the elemental maps for the metals to the elemental maps of oxygen and silicon in each mesoporous catalyst. Additionally, there is no presence of concentrated or agglomerated regions, further supporting the effective distribution of metals throughout the catalysts.

As previously mentioned for the four Sn-modified catalysts, and despite the qualitative information concluded from the TEM images, the distribution of Sn particle sizes can be obtained from at least 250 measurements from the TEM micrographs for each catalyst, as shown in **Figure 6.5**. The two catalysts based on MCM-41, SnM1 and SnM2, exhibited a lower average particle size with values of 4.1 and 7.3 nm, respectively, in comparison with values for the SBA-15 catalysts, SnS1 and SnS2, with values of 7.6 and 8.4 nm, respectively. Notice that values for materials based on MCM-41 differ significantly, which can be associated with the notable difference in Sn loadings (**Table 6.3**). In contrast, no appreciable difference in loading was observed in materials based on SBA-15. The average particle size for several catalysts based on Sn and K-Sn dealuminated zeolite Y was reported [67], showing values ranging from 4.9 nm to 6.1 nm, using $SnCl_4 \cdot 5H_2O$ as the salt precursor, and different materials Sn-zeolite Y (SiO_2/Al_2O_3 molar ratio = 5.1, 30, and 80, and the corresponding dealuminated zeolites) using $SnCl_4 \cdot 5H_2O$ and $SnCl_2$ as salt precursors [66], which exhibited average values between 7.3 and 10.4 mm. Interestingly, higher average particle size was observed with higher metal loading in the catalysts in those studies, similar to our findings.

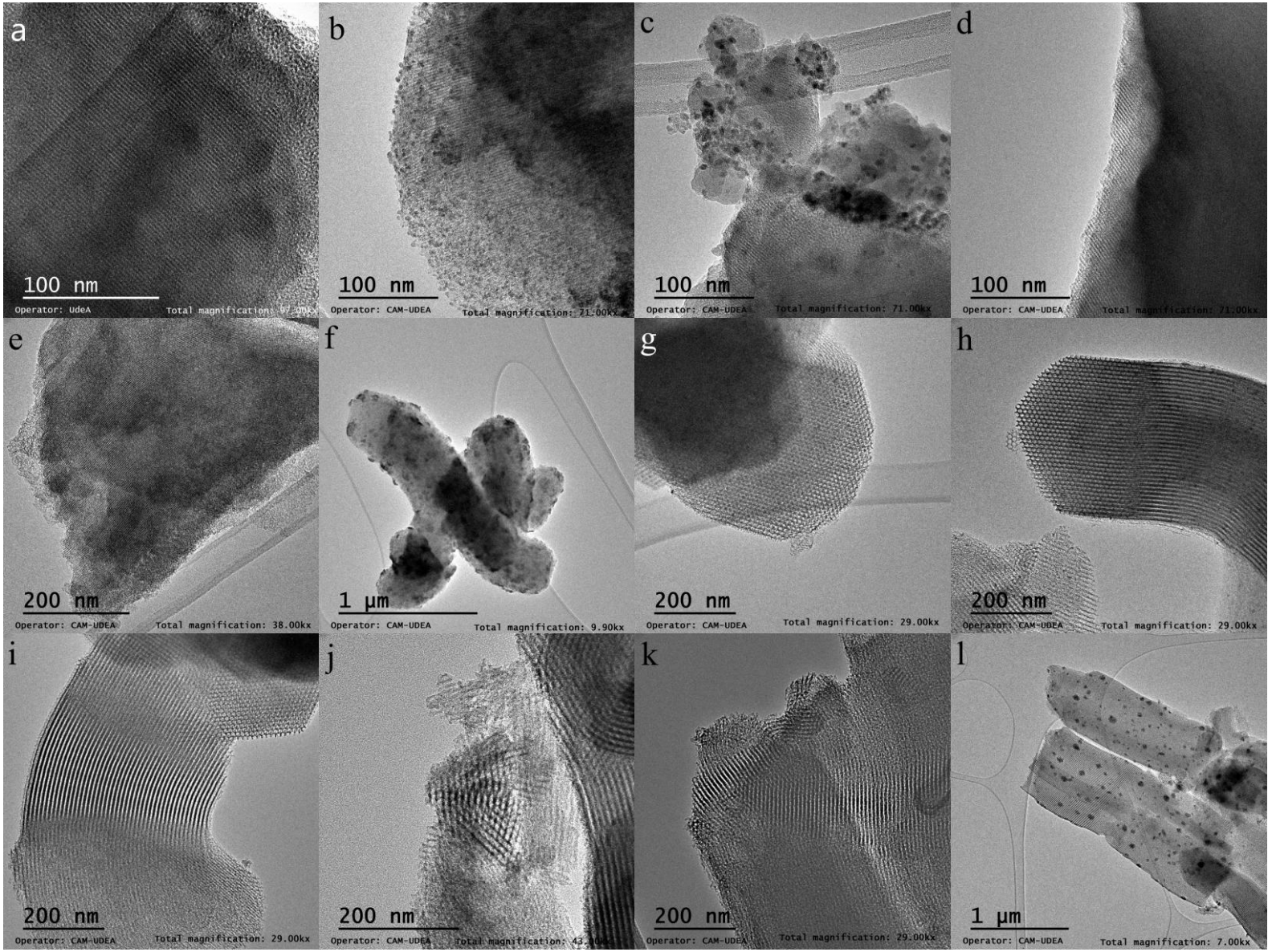

Figure 6.4. Transmission Electron Microscopy (TEM) images of **a.** MCM-41, **b.** SnM1, **c.** SnM2, **d.** FeM1, **e.** CuM1, **f.** CoM1, **g.** SnS1, **h.** SnS2, **i.** FeS1, **j.** FeS2, **k.** CuS1, **l.** CoS1.

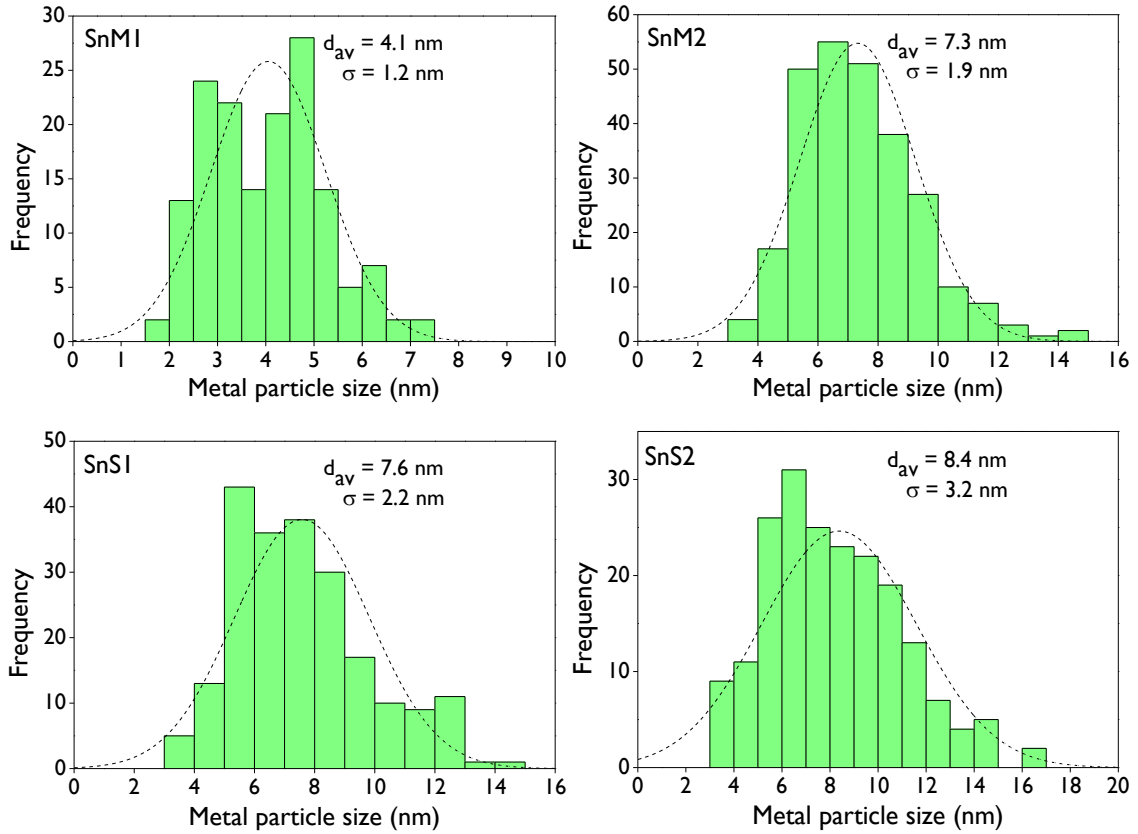

Figure 6.5. Tin size distribution of tin-modified catalysts.

The elemental composition of the catalysts was determined using EDX, and the results are presented in **Table 6.4** as atomic weight percentages. All materials exhibit the presence of Si, O, and the respective metal, with no detectable impurities (weight balance totaling 100%). The differences in the weight percentages of metals, as compared to the values determined by ICP/OES (**Table 6.3**), can be readily explained. EDX in TEM micrographs provides point analysis, meaning that the composition depends on the specific region where the analysis was conducted. On the other hand, ICP/OES is a more robust technique for quantification across the entire sample.

Table 6.4. Elemental composition of the prepared catalysts using TEM-EDX analysis.

Catalyst	Weight %		
	Si	O	Metal
SnM1	39.50	46.59	13.91
SnM2	42.99	51.50	5.51
FeM1	45.94	49.94	4.12
CuM1	45.78	51.45	2.77
CoM1	47.25	52.33	0.42
SnS1	47.21	51.02	1.77
SnS2	54.07	40.93	5.00
FeS1	46.96	52.36	0.68
FeS2	47.81	51.31	0.88
CuS1	53.37	44.09	2.54
CoS1	47.58	50.38	2.04

6.4.1.5. Catalyst Acidity

The quantification through adsorption-desorption FTIR analysis of pyridine as a probe molecule for the prepared catalysts is presented in **Table 6.5** and **Figure 8.116**. This analysis plays a crucial role in identifying the strength of acid sites (weak, medium, and strong), as well as the type of acidity (Brønsted and Lewis), which needs to be performed at various temperatures (100 °C, 200 °C, and 300 °C). Typical FTIR spectra for the materials are depicted in **Figure 8.116**, where the band around 1545 cm^{-1} associated with Brønsted acidity was not observed [66,67]. On the contrary, a well-defined band associated with Lewis acidity was observed around 1450 cm^{-1} in all materials [46,49]. The very slight band around 1480-1490 cm^{-1} has been associated with the presence of Brønsted + Lewis sites [68], indicating only Lewis acid sites for these materials. The intense band around 1595 cm^{-1} corresponds to the interaction of pyridine with hydrogen linked to silanol groups [69]. Therefore, the reported values in **Table 6.5** for the prepared catalysts correspond entirely to the Lewis acidity type. This aligns with previous reports based on Fe, Cu, and Sn-supported mesoporous materials [46,49,64,70,71].

All FTIR spectra of materials show appreciable absorbance changes, decreasing as the temperature increases, indicating no very significant strong acidity in the mesoporous catalysts, as evidenced by the values presented in **Table 6.5**. CoM1 exhibited the highest % of strong acidity with a value of 22.2%, followed by SnM1 with 16.7%; the other catalysts presented strong acidity < 10%. On the contrary, FeM1 presented the highest % of weak acidity (91.6%) followed by CuS1 (90.3%). SnM1 exhibited the lowest % of weak acidity (36.7%) and the highest % of medium acidity (46.7%). SnS1 and FeS1 exhibited the highest total acidity with values of ca. 138 μmol g^{-1}. It is noteworthy that total acidity increases with the metal loading, as observed for SnM1 and SnM2 with values of 30 and 81 μmol g^{-1} corresponding to Sn loadings of 1.25 and 2.17 % (**Table 6.3**), respectively. In contrast, the pairs SnS1 and SnS2, and FeS1 and FeS2 differ in the values of total acidity, although these materials have similar metal loadings, as evidenced In **Table 6.3**. These differences in the distribution of acid site strengths

can be explained by the silanol group environments, as it is well-known that the acidity of mesoporous materials such as MCM-41 and SBA-15 is caused by the silanol groups on the structure [72,73]. Furthermore, **Table 6.5** shows the density of acid sites for each metal-modified catalyst.

Table 6.5. Acidic properties of the catalysts by pyridine-FTIR.

Catalyst	Acidity[a] (μmol g^{-1})				Acid sites density[b] (μmol m^{-2})
	Weak	Medium	Strong	Total	
SnM1	11	14	5	30	0.025
SnM2	68	8	5	81	0.073
FeM1	87	5	3	95	0.100
CuM1	81	15	7	103	0.169
CoM1	27	1	8	36	0.020
SnS1	101	24	13	138	0.226
SnS2	93	8	5	106	0.169
FeS1	113	13	12	138	0.278
FeS2	83	11	7	101	0.164
CuS1	102	7	4	113	0.204
CoS1	99	6	9	114	0.214

[a] Measurements at 100 °C: weak + medium + strong; measurements at 200 °C: medium + strong; measurements at 300 °C: strong.
[b] Calculated as total acidity/ BET area.

The strength of acidity in the catalysts was also investigated using NH_3-TPD, which can be classified according to the deconvoluted signals as very weak, weak, medium, and strong acidity with a maximum band in the range <150 °C, < 250 °C, < 330 °C, and 330-500 °C [49,74], respectively. **Figure 6.6** shows that none of the materials exhibit deconvoluted signals above 330 °C, associated with strong acidity, verifying the low values previously reported using pyridine-FTIR analysis. **Table 8.14** displays the quantification through NH_3 as a probe molecule for all the catalysts.

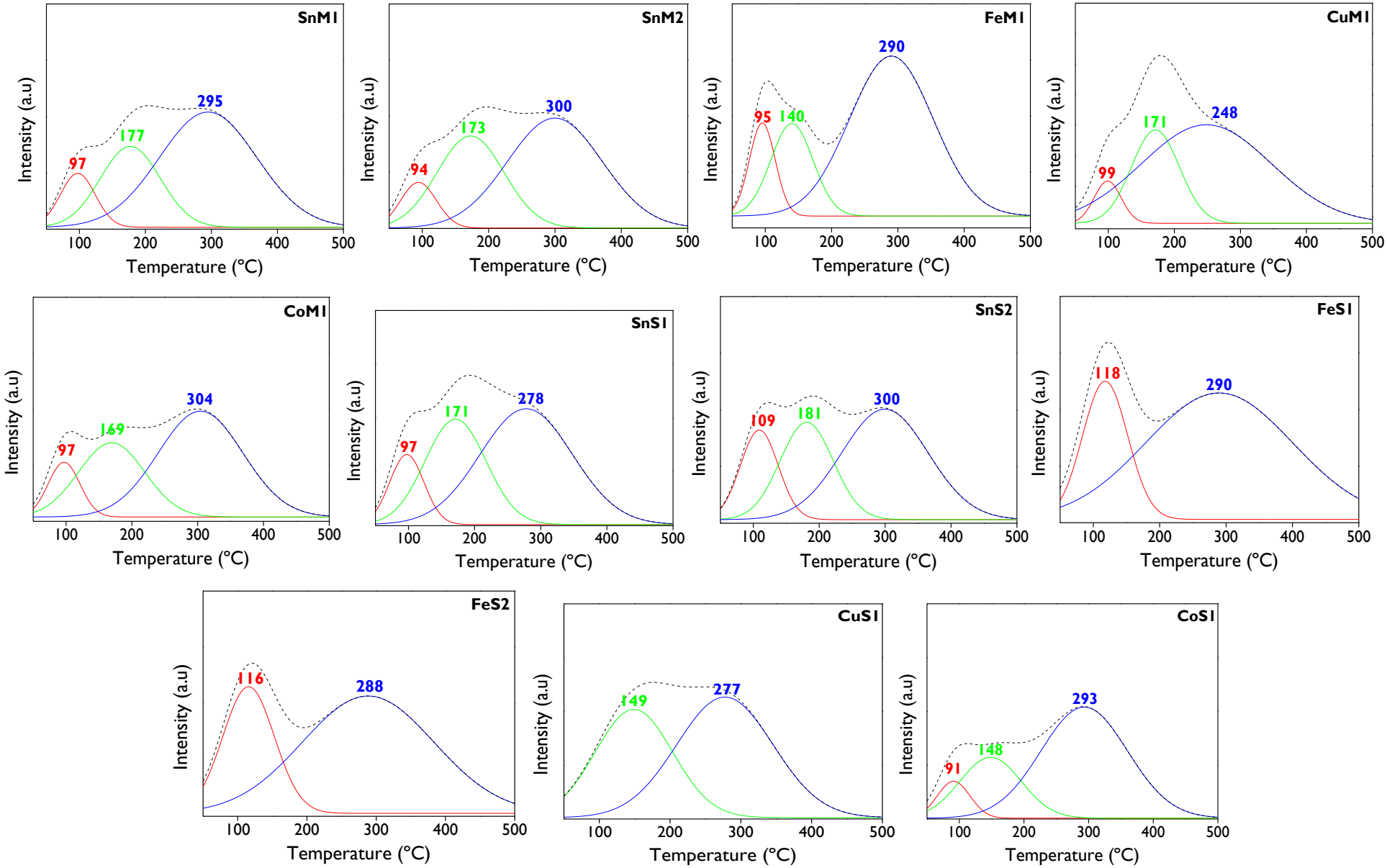

Figure 6.6. NH_3-TPD profiles for the metal-modified catalysts.

6.4.1.6. Surface Chemistry

The investigation into the oxidation states on catalytic surfaces and surface chemical composition was conducted using X-ray photoelectron spectroscopy (XPS), employing survey scans in wide scan and high-resolution spectra modes for all metal-modified catalysts based on MCM-41 and SBA-15 supports. The wide spectra for catalysts with Sn, Fe, Cu, and Co are presented in **Figure 8.117**-**Figure 8.120**, respectively. All materials exhibited characteristic peaks at around 26, 104, 155, 285, 533, and 977 eV binding energy, corresponding to O2s, Si2p, Si2S, C1s, O1s, and oxygen KLL Auger transition, respectively [49,75]. Peaks associated with $Sn3d_{5/2}$ and $Sn3d_{3/2}$ were observed in **Figure 8.117** at around 487 and 496 eV [49], respectively; while peaks linked to $Co2p_{3/2}$ and $Co2p_{1/2}$ were evident in **Figure 8.120** at approximately 780.8 and 795.9 eV [76], respectively. In contrast, peaks associated with Fe (**Figure 8.118**) and Cu (**Figure 8.119**) were not discernible in the wide XPS spectra. However, **Figure 6.7** displays high-resolution XPS spectra for Sn3d, Fe2p, Cu2p, and Co2p for all the catalysts. Additionally, **Figure 8.121** depicts high-resolution spectra of all catalysts for Si2p, showing a peak around 104 eV attributed to Si-O-Si of the silica network, while **Figure 8.122** exhibits O1s spectra with two deconvoluted signals around 533 and 534 eV, attributed to oxygen from the silica framework and silanol groups on the surface, respectively [49].

The Sn3d spectra (**Figure 6.7**) exhibit well-defined spin-orbit doublet peaks at around 487.6 eV and 496.1 eV, associated with Sn^{4+} $3d_{5/2}$ and Sn^{4+} $3d_{3/2}$, respectively [64,77], with a separation of ca. ΔV = 8.4 - 8.5 eV [78,79]. In the Fe-supported MCM-41 catalyst (FeM1), peaks at around 710.4 eV and 725.8 eV binding energies correspond to Fe $2p_{3/2}$ and Fe $2p_{1/2}$, respectively, indicating the Fe^{3+} oxidation state [78,80]. However, the presence of Fe^{2+} can be inferred after deconvolution of the Fe 2p3/2 signal to a lesser extent compared to Fe^{3+}, as reported in the literature [81]. Fe-supported SBA-15 catalysts (FeS1 and FeS2) did not exhibit clear signals, suggesting the absence of Fe species on the catalyst surface, as indicated by morphology analysis (**Figure 6.4**) that showed their presence within the channels.

Catalysts impregnated with Cu showed clear signals for both Cu $2p_{3/2}$ and $2p_{1/2}$ at around 934 eV and 953.7 eV, respectively [78,81,82]. The low-energy peaks of Cu $2p_{3/2}$ (933.8 eV) are typically attributed to Cu^{2+} in octahedral sites, while high-energy peaks (936.5 eV) correlate with Cu^{2+} in tetrahedral sites [83]. However, the binding energy for Cu^{+} is quite similar ($\approx$ 933 eV). Therefore, the absence of a strong Cu^{2+} satellite peak around 943 eV led to the conclusion of the presence of only Cu^{+} species on the catalyst surface (CuS1). Notably, no signals were observed for CuM1, similarly to FeS1 and FeS2 [78,81,83].

XPS spectra for catalysts containing Co displayed spin-orbit components Co $2p_{3/2}$ and Co $2p_{1/2}$ at around 780.1 and 795.4 eV [76,84], respectively. The doublet of $2p_{3/2}$ can be deconvoluted into two peaks at around 780.7 and 782.1 eV, attributed to Co^{3+} and Co^{2+} species, respectively. Furthermore, the presence of a satellite peak in the vicinity of the $2p_{3/2}$ region around 788 eV further demonstrates the existence of cobalt oxides [76].

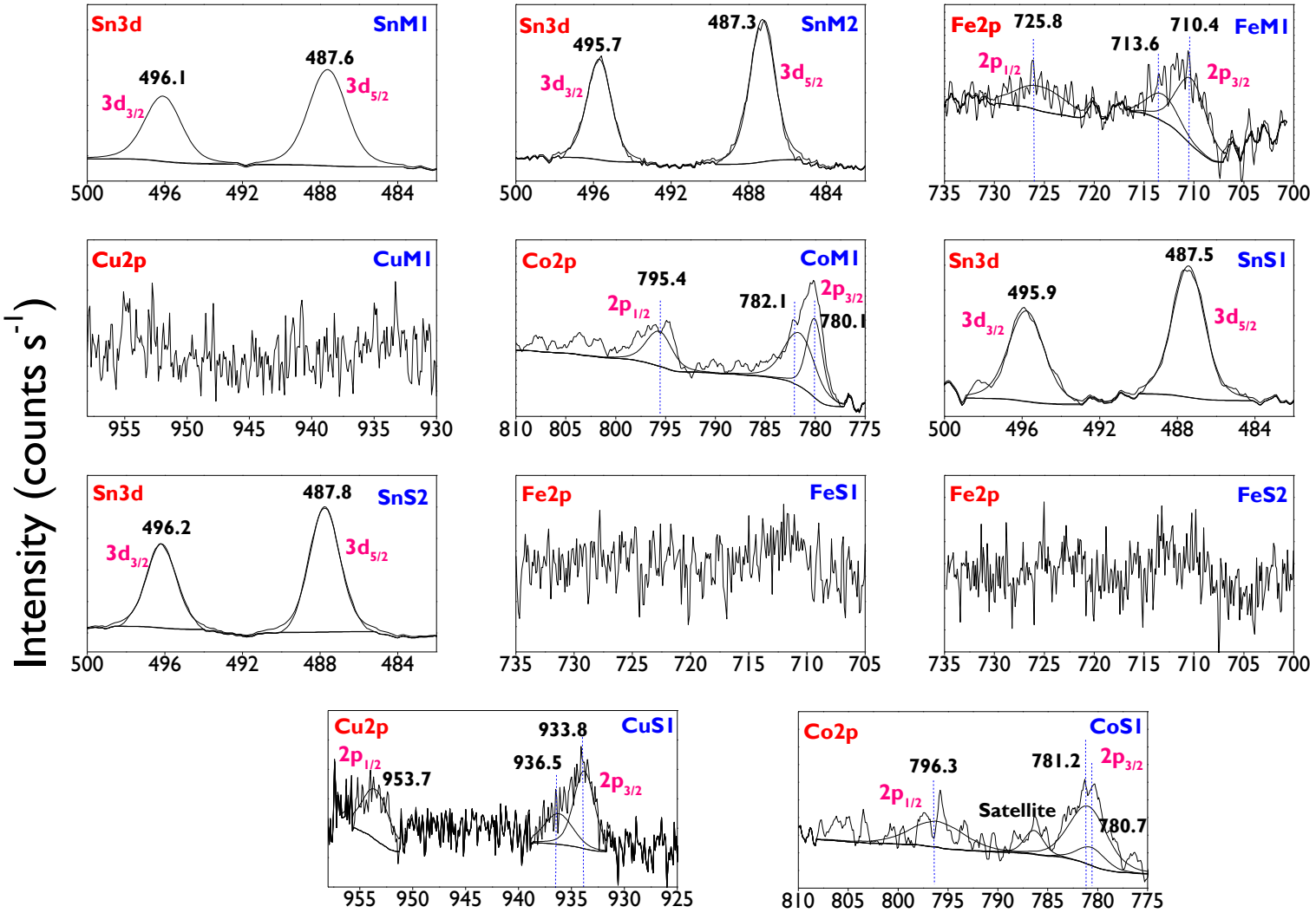

Figure 6.7. High-resolution XPS spectra of Sn, Fe, Cu, and Co over MCM-41 and SBA-15.

The surface composition of the catalysts is presented in **Table 6.6**. All materials exhibited oxygen content ranging from 61.30 to 64.77 wt. % and silicon content ranging from 35.23 to 38.32 wt. %, resulting in O/Si ratios between 1.60 and 1.84. These values are consistent with those previously reported for catalysts based on ordered silica materials [49]. SnM1 showed the highest metal species composition, with 1.28 wt. % Sn^{4+}. It is noteworthy that this surface composition of metal species is notably lower than the elemental composition previously reported by TEM-EDX (**Table 6.4**), suggesting that active species are also present within the channels, as it was shown by the TEM images and the lack of defined signals in the high-resolution XPS spectra for some catalysts based on Fe and Cu.

Table 6.6. Surface composition of all catalysts.

Catalyst	Weight %							
	O	Si	Sn^{4+}	Fe^{3+}	Fe^{2+}	Cu^{1+}	Co^{3+}	Co^{2+}
SnM1	62.32	36.41	1.28	0.00	0.00	0.00	0.00	0.00
SnM2	61.66	37.11	1.22	0.00	0.00	0.00	0.00	0.00
FeM1	61.30	38.32	0.00	0.27	0.11	0.00	0.00	0.00
CuM1	64.77	35.23	0.00	0.00	0.00	0.00*	0.00	0.00
CoM1	62.03	37.00	0.00	0.00	0.00	0.00	0.42	0.55
SnS1	62.15	37.56	0.29	0.00	0.00	0.00	0.00	0.00
SnS2	62.37	36.62	1.02	0.00	0.00	0.00	0.00	0.00
FeS1	62.23	37.77	0.00	0.00*	0.00*	0.00	0.00	0.00
FeS2	61.94	38.06	0.00	0.00*	0.00*	0.00	0.00	0.00
CuS1	61.91	37.89	0.00	0.00	0.00	0.20	0.00	0.00
CoS1	63.20	36.55	0.00	0.00	0.00	0.00	0.05	0.20

The quantification was performed using the equation $C_x = \frac{I_x/S_x}{\sum I_i/S_i}$, where I_x represents the area of the relative peak of the photoelectrons of element x, and S_x denotes the relative sensitivity factor (RSF) [79], as reported by Scofield [85]: RSF (O1s) = 2.93, RSF(Si2p) = 0.817, RSF($Sn3d_{5/2}$) = 14.8, RSF($Fe2p_{3/2}$) = 10.82, RSF($Cu2p_{3/2}$) = 16.73, and RSF($Co2p_{3/2}$) = 12.62. * These values were taken as 0 due to the absence of defined signals in **Figure 6.7**.

6.4.2. Catalytic Performance

6.4.2.1. General aspects

Figure 6.1 depicts the general scheme of the products obtained in the rearrangement of β-pinene epoxide, including *cis*-myrtanal, *trans*-myrtanal, myrtenol, and perillyl alcohol. However, additional products are yielded in this contribution, with their retention times and mass spectra outlined in **section 8.5.7** of the Supporting Information. Suggestions for the corresponding compounds of some of these products are also provided. Additionally, the repeatability of the experiments was investigated using the FeS1 catalyst as presented in **Figure 8.136**. Results demonstrated the reliability of the experimental setup.

6.4.2.2. Conversion and product distribution: Role of the acidic catalyst

The role of the acidic catalyst (**Figure 6.8** and **Figure 6.9**) was evaluated in the conversion and product distribution in the one-pot tandem transformation of β-pinene with H_2O_2. The first step consists of synthesizing β-pinene epoxide through a Payne system with MgO as a catalyst, achieving complete conversion after 2 h under the tested reaction conditions [17].

The second step corresponds to rearranging the epoxide towards target products like myrtanal (*cis* + *trans*) as the major product, which is greatly influenced by the type of acidic catalyst, as will be evaluated below.

The effect of the prepared catalysts on the β-pinene conversion and yield of products based on MCM-41 is illustrated in **Figure 6.8**, while the results with catalysts based on SBA-15 are displayed in **Figure 6.9**. The blank test (without acidic material, **Figure 6.8.A** and **Figure 6.9.A**) resulted in complete conversion after 2 h of reaction, as reported for β-pinene [17] and limonene [18] under similar reaction conditions in a Payne system. Additionally, those studies demonstrated that the catalytic epoxidation of both monoterpenes did not proceed in the absence of MgO because it is a heterogeneous reaction. With the MCM-41 support and some metal-modified catalysts such as SnM1, SnM2, and FeM1 (**Figure 6.8.A**), complete conversion can also be reached after 2 h, demonstrating no existence of an antagonistic effect of the acidic material in the first step of the epoxidation of the substrate. Conversely, the catalyst modified with Cu exhibited a maximum conversion of ca. 73% after 48 h, while null activity was reached with CoM1. In the case of catalysts based on SBA-15 (**Figure 6.9.A**), complete conversion was reached after 2 h with the support, and the Sn- and Cu-modified materials, while catalysts modified with Fe exhibited conversion values between 42 and 51% at the same time. However, with these two catalysts, the complete conversion was reached later. Similarly, the CoS1 catalyst exhibited no reactivity of β-pinene in the epoxidation route as CoM1.

The decrease in β-pinene conversion at 2 h with some metal-modified catalysts (CuM1, FeS1, FeS2, CoM1, and CoS1) could suggest blocking of the active sites of MgO caused by the metallic agglomerates, resulting in inhibition of the formation of β-pinene epoxide. However, it can also be explained by the rapid consumption of H_2O_2 through decomposition caused by metals, as reported previously in the literature [86,87], with cobalt being a more active phase for decomposition. The H_2O_2 efficiency will be discussed later.

The yield of β-pinene epoxide with all catalysts based on MCM-41 (**Figure 6.8.B**), except CuM1 and CoM1, exhibited maximum values of ca. 80-83% at 2 h, whereas CuM1 showed a maximum value of 49% at 24 h. On the other hand, **Figure 6.9.B** shows similar maximum values of the yield of epoxide with all materials, except Fe-modified catalysts (FeS1 and FeS2) which showed their maximum yields at 7 h corresponding to 76% and 80%, respectively. Cobalt-based catalysts are not active in the reaction, which causes the yield of epoxide to be zero. The blank test (**Figure 6.8.B** and **Figure 6.9.B**) demonstrated a 50% yield of epoxide at 48 h, explaining the necessity of using an acidic material, either MCM-41, SBA-15, or metal-modified support to promote the rearrangement of the epoxide towards isomers. In the case of catalysts based on MCM-41 (**Figure 6.8.B**), yield of epoxide of ca. 2.5%, 6.4%, 10.2%, and 16.0% were reached at 48 h with MCM-41, SnM2, SnM1, and FeM1, respectively, whereas with catalysts based on SBA-15 (**Figure 6.9.B**), yield of epoxide of 0%, 5.3%, 7.3%, 12.2%, and 20.5% were achieved with SBA-15, FeS1, FeS2, SnS2, and CuS1, respectively. Surprisingly, the yield to epoxide at 48 h with SnS1 catalyst is like the blank test. It is noteworthy that the yield (or selectivity) to epoxide decreases as the reaction progresses, explained by the formation of its main isomers like *cis*/*trans*-myrtanal and perillyl alcohol, and suggested hydration of the epoxide to a diol ($C_{10}H_{18}O_2$) represented by the product 6 (**section 8.5.7**, Supporting Information).

With MCM-41 prepared catalysts (**Figure 6.8.C**), the materials MCM-41, SnM1, SnM2, and FeM1 exhibited higher yields of myrtanal ranging from 50 to 53% after 48 h, compared with 38%, 29%, and 0% associated with the blank, CuM1, and CoM1, respectively. In the case of SBA-15 materials (**Figure 6.9.C**), catalysts impregnated with Fe (FeS1 and FeS2) significantly demonstrated the highest yields of myrtanal at 48 h with values of 62.3% and 59.0%, respectively, in comparison with the other catalysts with values between 35% and 45% for SnS2, FeS1, and SBA-15. Notice that CuS1 presented a very low yield of myrtanal of ca. 15%, lower than the analogous material based on MCM-41. These results are consistent with previous yields of β-pinene epoxide, which means the yield of myrtanal increases as the yield to epoxide decreases, intrinsically explained by the consecutive isomerization reaction of the epoxide (**Figure 6.1**). Additionally, the findings underscore the limitations of Cu and Co as active phases for achieving highly selective transformation towards myrtanal as the target molecule. However, an active phase is required to further enhance the yield of myrtanal, observing favoring this target product with Fe and Sn materials.

The yield of perillyl alcohol, another typical product resulting from the rearrangement of β-pinene epoxide, varies between 0% and 10%, as depicted in **Figure 6.8.D** and **Figure 6.9.D**. The highest yields (6-10%) are attained with longer reaction times using materials containing Sn (SnM1, SnM2, SnS2) and Fe (FeM1, FeS1, FeS2) as active phases. Conversely, Cu-modified catalysts yield perillyl alcohol in amounts lower than 5% throughout the entire reaction time. Some literature reports using heterogeneous catalysts based on Fe and Sn have shown the production of perillyl alcohol. For instance, Sn-MCM-41 achieved a yield of 65% at 70 °C over 24 h using dimethylsulfoxide (DMSO) as a solvent [28], while Fe-β zeolite yielded 63% at 70 °C over 3 h, also in DMSO [29]. The authors attributed the enhanced selectivity to perillyl alcohol to the presence of a strong basic polar solvent like DMSO.

The *cis*/*trans*-myrtanal molar ratio reaches a maximum of ca. 2.0 in the absence of a catalyst (Blank) after 24 h, as depicted in **Figure 6.8.E** and **Figure 6.9.E**. Similarly, with mesoporous materials such as MCM-41 (**Figure 6.8.E**) and SBA-15 (**Figure 6.9.E**), a very similar maximum was achieved within the same time. With Sn and Fe-modified catalysts, a positive trend is observed over time, resulting in molar ratios between 1.5 and 2.0 at 48 h with MCM-41-based catalysts (**Figure 6.8.E**) and between 1.8 and 2.3 at 48 h with SBA-15-based catalysts (**Figure 6.9.E**). Conversely, Cu-modified catalysts exhibited molar ratios between 2.5 and 2.9 at 48 h. Our results demonstrate that *cis*-myrtanal is preferred over *trans*-myrtanal, regardless of the heterogeneous catalyst used. Although, typically in aldehydes, the *trans* configuration can be more stable than the *cis* configuration due to steric hindrance and electronic effects, as the larger groups in the *trans* configuration are farther apart, our results indicate that under the reaction conditions, the *cis* isomer is more kinetically favored than the *trans* isomer. These findings are novel, as there is no existing knowledge of other studies reporting the preference of myrtanal isomers.

Figure 6.8.F and **Figure 6.9.F** illustrate the yield of myrtanal as a function of the yield of β-pinene epoxide for materials based on MCM-41 and SBA-15, respectively. From those results is concluded the consecutive reactions of epoxidation and isomerization, as the yield of myrtanal increases with the decrease in the yield of epoxide, signifying its ring opening. Similarly, **Figure 6.8.G** and **Figure 6.9.G** show that diol (product 6, $C_{10}H_{18}O$) is formed as β-pinene epoxide disappears in the reaction. The investigation to determine precisely whether diol is obtained from the hydration of epoxide, as previously reported for limonene-1,2-

epoxide [67,88], or from an intermediate like the other products mentioned in the Supporting Information, is beyond the scope of our study.

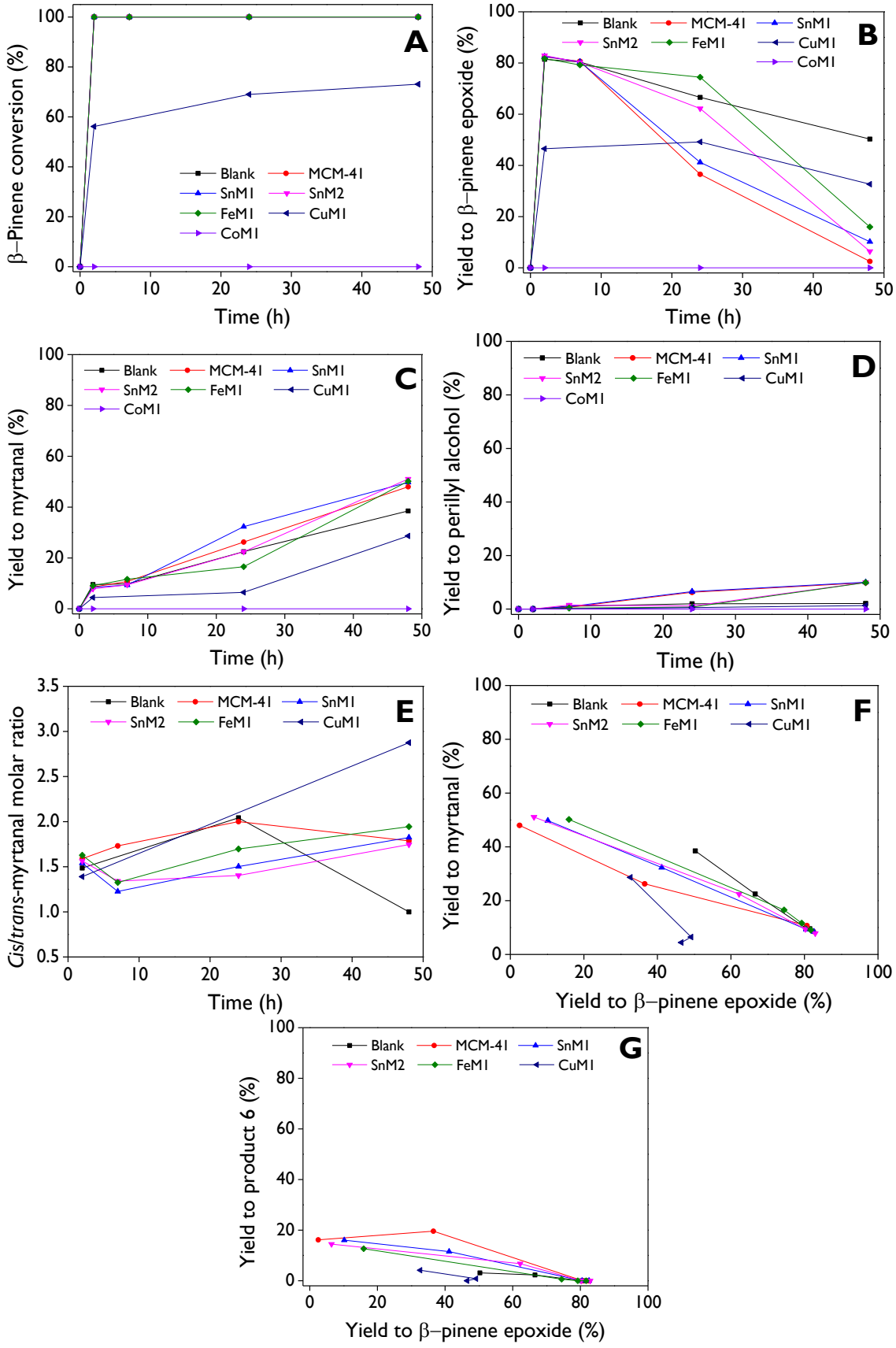

Figure 6.8. Role of acidic catalysts based on MCM-41 support in the one-pot transformation of β-pinene: **(A)** β-Pinene conversion, **(B)** yield of β-pinene epoxide, **(C)** yield of myrtanal, **(D)** yield of perillyl alcohol, **(E)** *cis*/*trans*-myrtanal molar ratio, **(F)** yield of myrtanal vs. yield of β-pinene epoxide, and **(G)** yield of product 6 vs. yield of β-pinene epoxide. **Reaction conditions:** 0.1 mmol of β-pinene with weight ratios of 1: 0.72: 1.2: 30.3: 19.7: 15.7: 0.8 for β-pinene: acidic catalyst: MgO: H_2O: acetone: acetonitrile: H_2O_2, 50 °C, 1000 rpm.

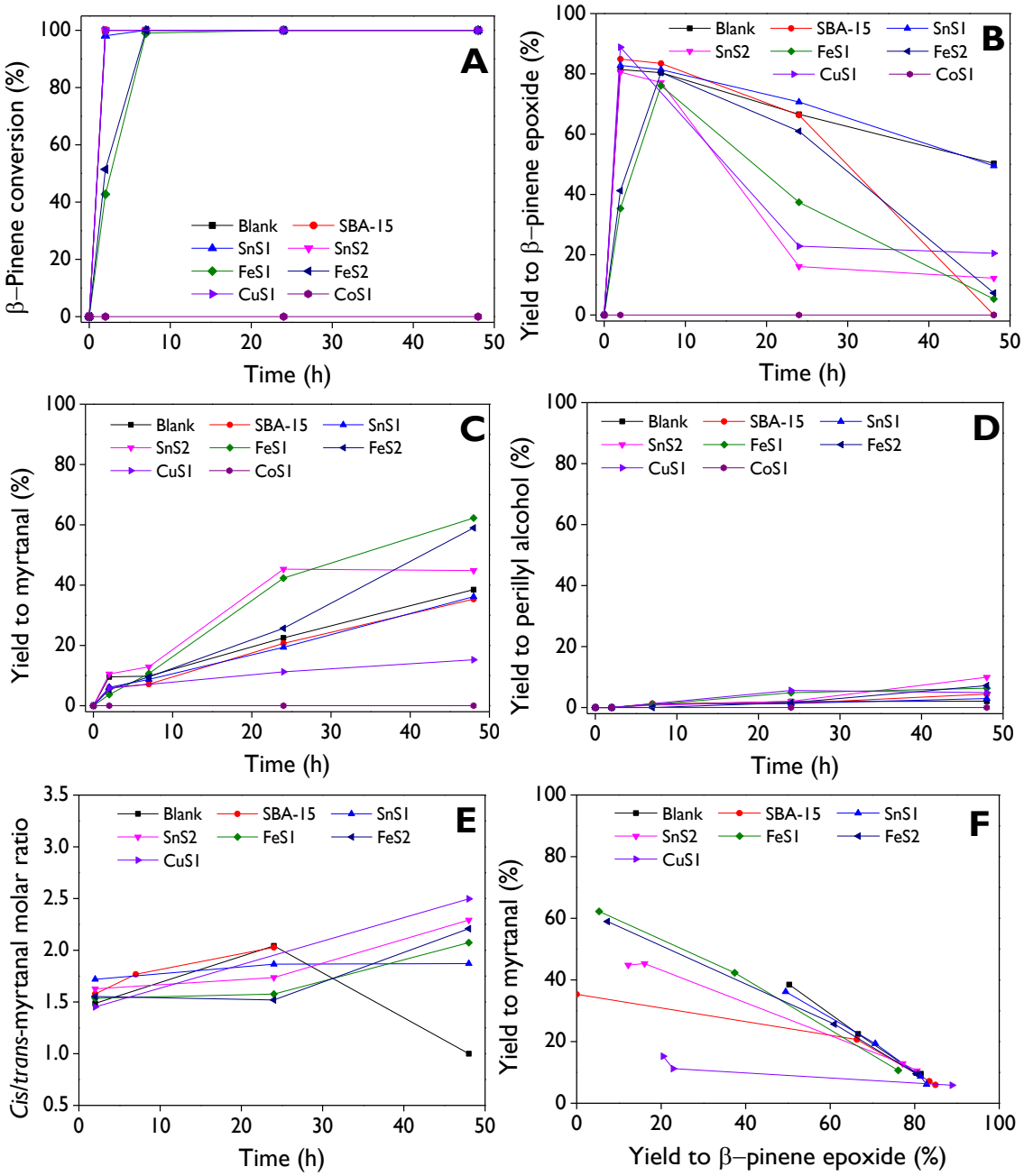

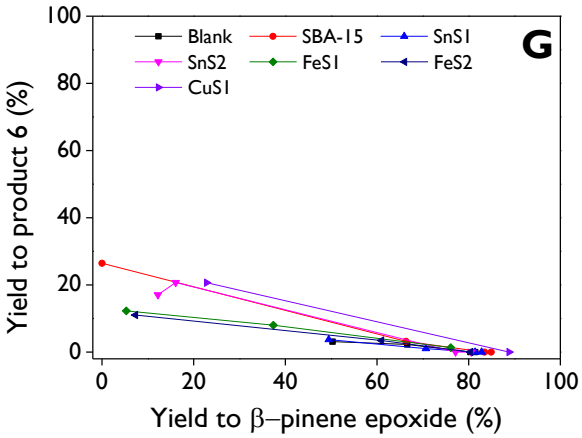

Figure 6.9. Role of acidic catalysts based on SBA-15 support in the one-pot transformation of β-pinene: **(A)** β-Pinene conversion, **(B)** yield of β-pinene epoxide, **(C)** yield of myrtanal, **(D)** yield of perillyl alcohol, **(E)** *cis*/*trans*-myrtanal molar ratio, **(F)** yield of myrtanal vs. yield of β-pinene epoxide, and **(G)** yield of product 6 vs. yield of β-pinene epoxide. **Reaction conditions:** 0.1 mmol of β-pinene with weight ratios of 1: 0.72: 1.2: 30.3: 19.7: 15.7: 0.8 for β-pinene: acidic catalyst: MgO: H_2O: acetone: acetonitrile: H_2O_2, 50 °C, 1000 rpm.

6.4.2.3. Conversion and efficiency of the oxidizing agent

The profiles of H_2O_2 conversion (**Figure 8.137**) were determined using the mathematical procedure outlined in our recent work [67], employing the global conversion of H_2O_2 calculated via cerimetric titration. These profiles effectively demonstrate that the reaction rate of H_2O_2 decomposition follows the sequence: Co > Cu > Fe > Sn, whether supported on MCM-41 (**Figure 8.137.B**) or SBA-15 (**Figure 8.137.D**). Additionally, the H_2O_2 efficiency [67] for materials based on MCM-41 (**Figure 6.10.A**) and SBA-15 (**Figure 6.10.B**) indicates that efficiency is null for cobalt-based catalysts, whereas for Sn-modified catalysts, nearly 100% efficiency can be achieved within 2 h, albeit decreasing with an increase in the reaction time. Therefore, Sn emerges as a promising metal for substantially mitigating the decomposition of H_2O_2, consistent with recent studies utilizing Sn-dealuminated zeolite Y for the efficient epoxidation of R-(+)-limonene [67], reaching efficiency values up to 85%, demonstrating that most of the consumption of H_2O_2 is directed towards the production of the corresponding epoxide. It is noteworthy that with the blank test, efficiency remains consistently high throughout the entire reaction time, as expected due to the absence of metal species promoting decomposition. On the other hand, although Sn yielded the highest efficiency among the various active phases, the results with Fe are also promising. This is particularly notable considering that catalysts based on Fe anchored on SBA-15 showed the highest yields of myrtanal.

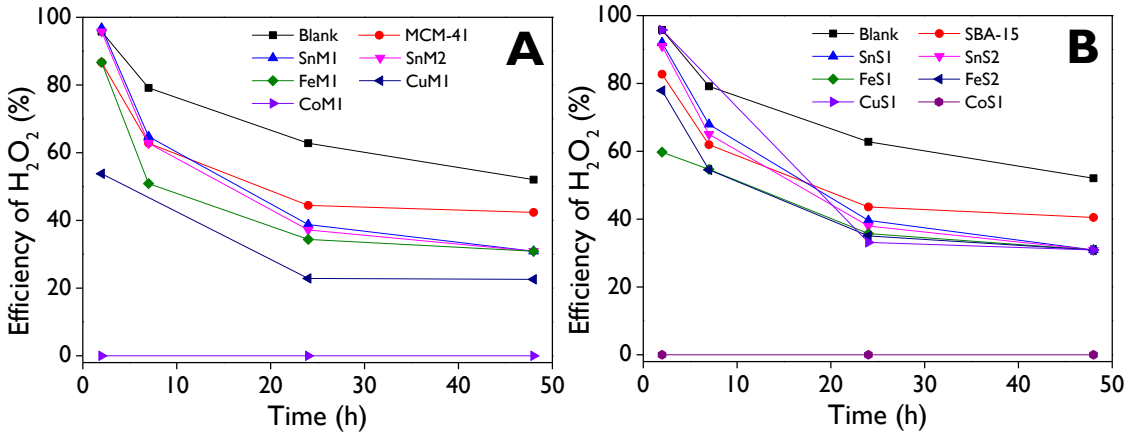

Figure 6.10. Efficiency of H_2O_2 in the one-pot transformation of β-pinene with the catalysts based on MCM-41 **(A)** and SBA-15 **(B)**. **Reaction conditions:** 0.1 mmol of β-pinene with weight ratios of 1: 0.72: 1.2: 30.3: 19.7: 15.7: 0.8 for β-pinene: acidic catalyst: MgO: H_2O: acetone: acetonitrile: H_2O_2, 50 °C, 1000 rpm. Efficiency was calculated as $X_{H2O2,epox}/X_{H2O2,global}$ [67], where the numerator represents the partial conversion of H_2O_2 through the epoxidation reaction, and the denominator represents the overall conversion of H_2O_2 determined by cerimetric titration.

6.4.2.4. Acidity-based properties as descriptors of the catalytic activity

The Lewis acid sites play a crucial role in the highly selective synthesis of target products such as myrtanal through the ring-opening of β-pinene epoxide. Therefore, understanding the dependency of catalytic data, such as activity in terms of conversion and selectivity to rearrange products, on total acidity (specifically, Lewis acidity) and acid site density is of great interest. Recently, acid site density has been identified as a suitable kinetic descriptor for catalytic reactions employing microporous materials like zeolites [89] and mesoporous materials [90]. **Figure 6.11.A** shows that the yield of β-pinene epoxide increases as total acidity increases for Sn-modified catalysts, reaching a yield of ca. 49% after 48 h with the SnS1 catalyst possessing a total acidity of 138 μmol g^{-1}. Conversely, with Fe-modified catalysts, epoxide yield decreases as total acidity increases, reaching a minimum value of 5.3 % with FeS1, which has a similar acidity to SnS1. These results suggest the critical role of the active phase in the one-pot tandem route, as the catalytic behavior is entirely dependent on the impregnated metal on the mesoporous supports. Cu-based catalysts exhibit a similar inverse relationship between the yield of epoxide and total acidity, resembling the behavior of Fe-based catalysts. However, Co-based catalysts show no activity in the catalytic reaction, as evidenced by the null efficiency of H_2O_2 shown in **Figure 6.10**.

The relationship between the yield of myrtanal at 48 h and total acidity (**Figure 6.11.B**) shows an opposite profile to the yield of epoxide for materials impregnated with Sn and Fe. This can be explained by the consecutive reactions where the epoxide is formed first and subsequently myrtanal is obtained from the ring-opening of the epoxide. It is noteworthy that the yield of myrtanal decreases as the concentration of acid sites increases with Sn-based catalysts, consistent with previous reports on Sn-modified beta zeolites [26]. Conversely, authors using Fe-based catalysts [46] starting from β-pinene epoxide reported no significant differences in selectivity to myrtanal, whereas in our contribution clear differences can be observed in **Figure 6.11.B**. Surprisingly, Cu-based catalysts show a decrease in the yield of myrtanal as total acidity increases, similar to the behavior of epoxide yield. The low yield of myrtanal with these materials, as depicted in **Figure 6.8.C** and **Figure 6.9.C**, can explain the

behaviors observed in **Figure 6.11.A** and **Figure 6.11.B**. Furthermore, these results suggest that Cu materials may not be promising for the proposed one-pot tandem system, as it was previously proposed for a typical isomerization system starting from high-purity epoxide as substrate [46].

The yield of diol at 48 h (**Figure 6.11.C**) shows slight dependence on total acidity in Fe-based catalysts, with values between 11-12.5%; while values between 14 and 17% are observed with Sn catalysts in the range of 30-100 μmol pyridine g^{-1}. When the total acidity increases within this range, the yield of diol decreases to 3.7%. With Cu catalysts, yields between 4 and 7% were achieved with total acidity between 100 and 120 μmol g^{-1}. The *cis*/*trans*-myrtanal molar ratio at 48 h (**Figure 6.11.D**) showed the maximum value for all materials at very similar total acidity levels of 100-110 μmol g^{-1}, resulting in a ratio of 2.88 for CuM1 as the global maximum.

Although total acidity in mesoporous catalysts is significant, surface area is also a crucial textural property in heterogeneous catalytic reactions, as it directly relates to the availability of active sites for the reaction to proceed. The surface area is often affected by the type of impregnated metal and the loading, as previously discussed. Therefore, correlating this property with total acidity to calculate a robust kinetic descriptor factor like acid site density (μmol m^{-2}), as reported in **Table 6.5**, could be very insightful. **Figure 6.11.E–H** exhibit the yield of epoxide, myrtanal, and diol, and the *cis*/*trans*-myrtanal molar ratio after 48 h as a function of the acid site density, resulting in similar trends as reported in **Figure 6.11.A-D**. FeS1, the catalyst with the highest yield of myrtanal (63%), presented an acid site density of 0.28 μmol m^{-2}; furthermore, this catalyst presented a total acidity of 138 μmol g^{-1}, a Fe loading of 5.07%, a BET surface area of 496 m^2 g^{-1}, a pore volume of 0.96 cm^3 g^{-1}, an average pore size of 6.37 nm, and a metal coverage (MC) of 1.10 entities nm^{-2}. It is noteworthy that this material presented the highest MC (**Table 6.3**) and total acidity (**Table 6.5**), and the lowest BET surface area (**Table 6.3**).

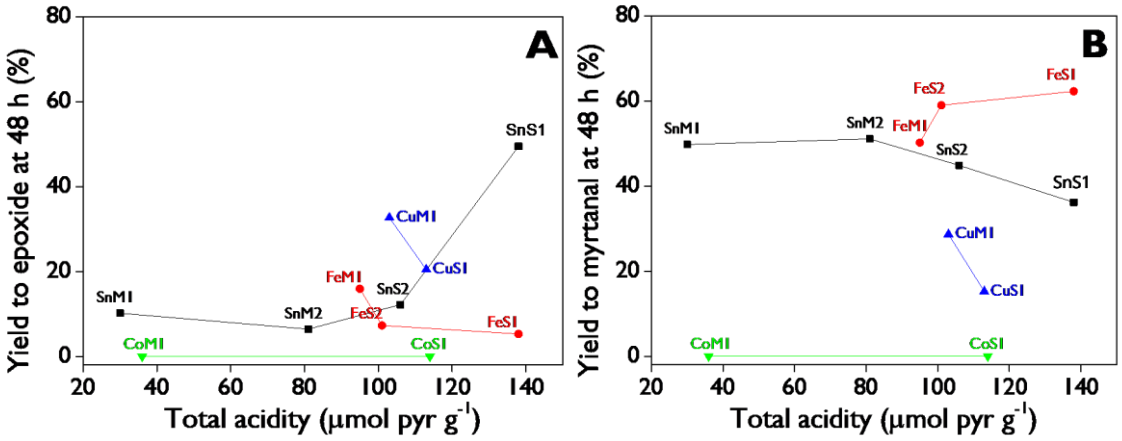

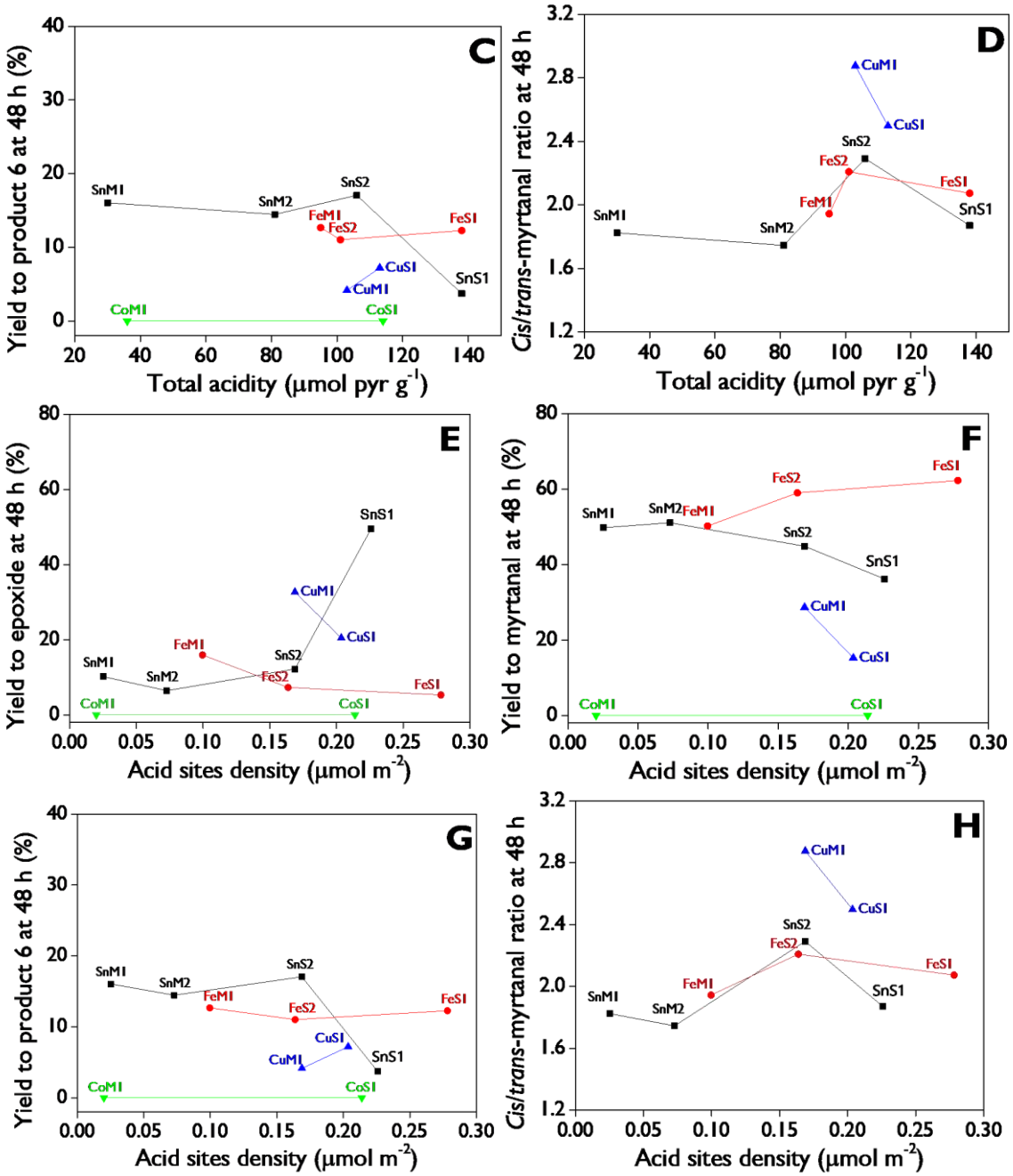

Figure 6.11. Total acidity (**A, B, C, D**) and acid sites density (**E, F, G, H**) as descriptors of yield of epoxide (**A, E**), yield of myrtanal (**B, F**), yield of product 6 (**C, G**), and *cis/trans*-myrtanal molar ratio (**D, H**). **Reaction conditions:** 0.1 mmol of β-pinene with weight ratios of 1: 0.72: 1.2: 30.3: 19.7: 15.7: 0.8 for β-pinene: acidic catalyst: MgO: H_2O: acetone: acetonitrile: H_2O_2, 50 °C, 1000 rpm.

6.4.2.5. Effect of the reaction conditions

The reaction conditions, based on weight ratios for substrate: MgO: H_2O: acetone: acetonitrile: H_2O_2, have been previously investigated using β-pinene [17] and limonene [18] as substrates. Therefore, the best conditions for those parameters have been employed in this contribution. Here, the amount of FeS2 in the one-pot reaction of β-pinene is evaluated by varying the FeS2: β-pinene weight ratio between 0.36 and 1.45. **Figure 6.12.A** confirms that the presence of a large amount of the acid catalyst in the reaction medium hampers the

substrate conversion, attributed to favoring the decomposition of H_2O_2 (**Figure 6.10**), obtaining complete conversions more rapidly with only 0.36 of weight ratio. **Figure 8.138.A** demonstrates that the overall conversion of H_2O_2 increases with the increase in the amount of FeS2. Additionally, **Figure 8.138.B** shows a linear trend between the initial reaction rate of H_2O_2 and the catalyst mass, confirming the absence of mass transfer limitations. The yield of epoxide (**Figure 6.12.B**) reaches its maximum at short reaction times for the different ratios, with complete consumption of epoxide at long times. During this extended period, it is principally converted to myrtanal (**Figure 6.12.C**) but also to diol (product 6, **Figure 6.12.D**). Diol is slightly favored with high amounts of acid catalyst (high weight ratios), which, in turn, reduces the selectivity towards myrtanal as the target molecule. **Figure 6.12.E** and **Figure 6.12.F** illustrate the yield of myrtanal and the yield of diol as a function of the yield of β-pinene epoxide, respectively. They demonstrate the consecutive reactions of epoxidation and isomerization.

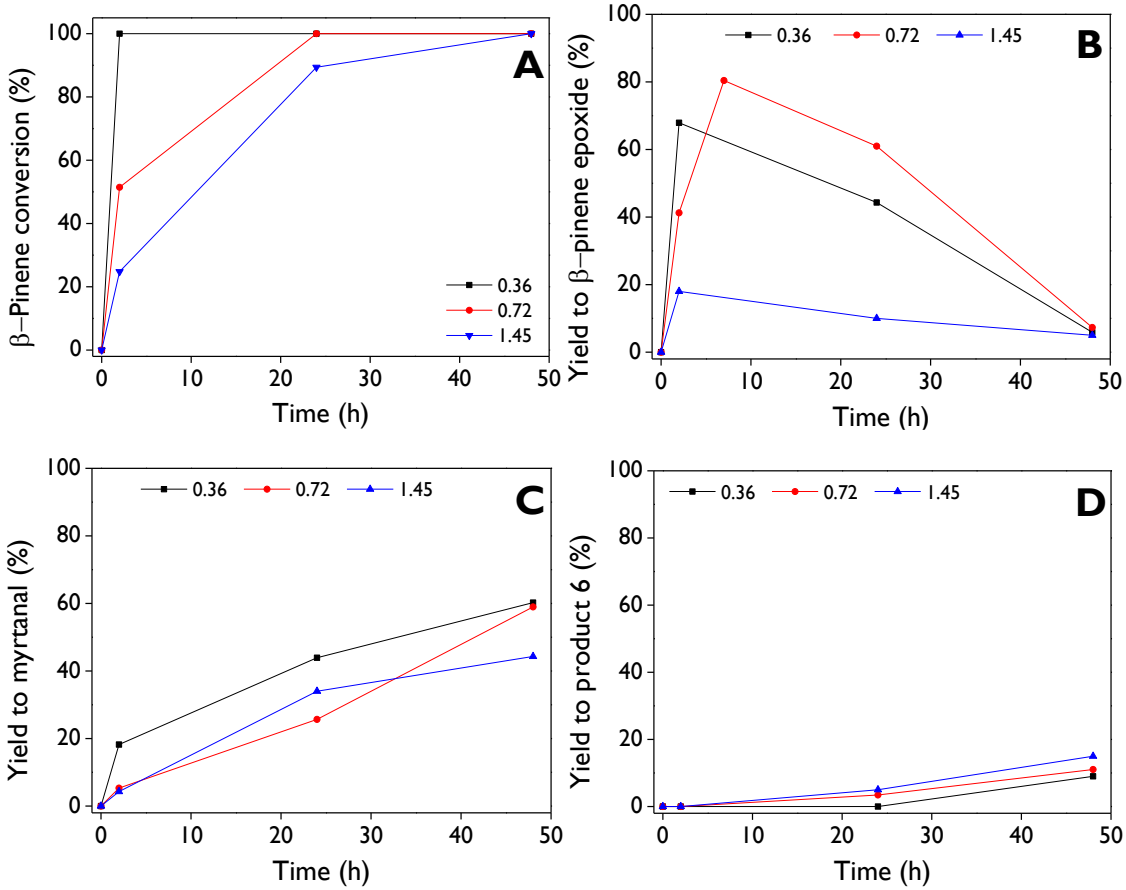

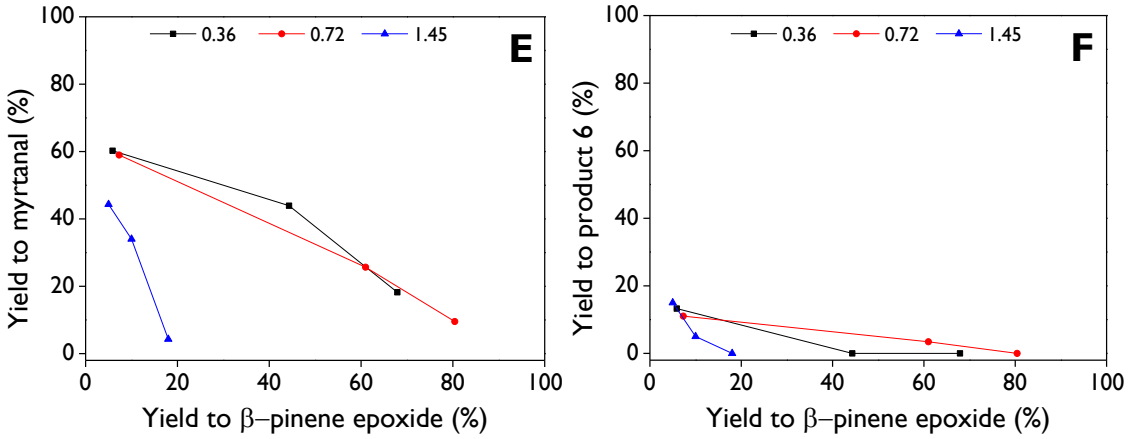

Figure 6.12. Effect of amount of FeS2 in the one-pot transformation of β-pinene: **(A)** β-Pinene conversion, **(B)** yield of β-pinene epoxide, **(C)** yield of myrtanal, **(D)** yield of product 6, **(E)** yield of myrtanal vs. yield of β-pinene epoxide, and **(F)** yield of product 6 vs. yield of β-pinene epoxide. **Reaction conditions:** 0.1 mmol of β-pinene with weight ratios of 1: (0.36, 0.72, 1.45): 1.2: 30.3: 19.7: 15.7: 0.8 for β-pinene: acidic catalyst: MgO: H_2O: acetone: acetonitrile: H_2O_2, 50 °C, 1000 rpm.

The effect of H_2O_2 concentration (H_2O_2/β-pinene weight ratio) has been previously investigated in our research group for this system [91], demonstrating that 0.80 is the most suitable ratio, favoring the yield of myrtanal. Additionally, the effect of temperature was evaluated, showing the inherent behavior of increasing catalytic activity (conversion) with temperature. However, results showed that the best selectivity to myrtanal was achieved at 50 °C, which avoids the formation of many products compared to higher temperatures such as 60 and 70 °C. This is advantageous due to the low energy requirements in the system.

6.4.2.6. Scope of the one-pot tandem catalytic system

The results of this contribution demonstrated the significance of the proposed one-pot tandem catalytic system for the highly selective synthesis of myrtanal as the major product, forming a mixture of *cis* + *trans* isomers, in comparison with other heterogeneous catalysts (**Table 6.7**) utilized solely for the second step of the epoxide isomerization. With the one-pot tandem system (entry 1), a yield of 62.3% of myrtanal can be achieved starting from β-pinene, which markedly surpasses previous catalysts reported, including dendritic material based on ZSM-5 zeolite such as d-ZSM-5/4d (entry 2) and Sn-Beta-300 (entry 5), which yielded myrtanal at approximately 47.5%. This promising catalytic activity achieved with our one-pot tandem system is noteworthy as it demonstrates the establishment of compatible and mild reaction conditions for the one-pot transformation of β-pinene, including very low temperature (50 °C), benign solvents and reagents like acetone and acetonitrile, and a green oxidizing agent such as H_2O_2. Conversely, very poor yields of myrtanal were obtained with the other catalysts (entries 3-4, 6-12). These results lead to the conclusion regarding the synergistic effect between the Payne system for the synthesis of β-pinene epoxide and subsequent isomerization, selectively promoting myrtanal formation by acidic catalysts like FeS1 (Fe/SBA-15).

Table 6.7. Heterogeneous catalysts for the isomerization of β-pinene epoxide.

Entry	Catalyst	Solvent	Reaction conditions	Conversion (%)	Selectivity (%)	Ref
1*	MgO – FeS1	Acetone + water	0.1 mmol of β-pinene, weight ratios of 1: 0.72: 1.2: 30.3: 19.7: 15.7: 0.8 for β-pinene: acidic catalyst: MgO: H_2O: acetone: acetonitrile: H_2O_2, 50 °C, 1000 rpm	100	5.3 epoxide 42.0 *cis*-myrtanal 20.3 *trans*-myrtanal 2.8 myrtenol 6.3 PA 12.3 diol	This work
2	d-ZSM-5/4d	Ethyl acetate	13 mmol L^{-1}, 115 mg catalyst, 50 °C, 5 min	100	47.7 myrtanal 3.1 myrtenol 18.5 PA	[88]
3	Fe/MCM-41	Acetonitrile	0.25 mmol substrate, 26% of catalyst, 1 mL solvent, 70 °C, 1 h	23	90 myrtanal 8 PA 2 myrtenol	[92]
4	Fe/SBA-15	Hexane		27	68 myrtanal 26 PA 6 myrtenol	
5	Sn-Beta-300	Toluene	0.012 mol L^{-1}, 75 mg of catalyst, 150 mL total, 70 °C, 6 h	72	66 myrtanal 10 PA 2 myrtenol	[26]
6	Zeolite beta 25	DMSO	0.8 mL substrate, 25 wt% of catalyst (based on the substrate), volume ratio substrate: solvent = 1:5, 70 °C, 2 h	100	19 myrtanal 36 PA 10 myrtenol 9 p-Menth-1-en-7,8-diol	[93]
7	Ti/SBA-15	Hexane	0.25 mmol substrate, 10 mg catalyst, 0.5 mL solvent, 80 °C, 1 h	> 99	20 myrtanal 45 PA	[94]
8	Mo/SBA-15	Hexane		> 99	63 PA	
9	Mo/MCM-41	Hexane		98	2 myrtanal 20 PA 5 myrtenol	
10	Mo/SiO_2	Hexane		99	12 myrtanal 32 PA 2 myrtenol	
11	Sn-MCM-41	DMSO	1.4 mol L^{-1}, 10 wt% of catalyst, volume ratio epoxide: solvent = 1:8, 70 °C, 24 h	98.4	8.2 myrtanal 66.1 PA 12 myrtenol	[28]
12	Fe-β zeolite	DMSO	1.6 mol L^{-1}, 10 wt% of catalyst, volume ratio epoxide: solvent = 1:8, 70 °C, 3 h	100	63.1 PA	[29]

PA: Perillyl alcohol. * This system corresponds to the one-pot transformation of β-pinene towards myrtanal as the major product.

6.4.3. Catalyst stability

The robustness of the FeS2 catalyst was explored through reusability and leaching tests. For the reuse tests, the catalyst was separated from the reaction medium by centrifugation (3000 rpm, 8 min) for subsequent washing with acetone at 50 °C and drying at 100 °C [18]. The β-pinene conversion and selectivity to products after 20 h of reaction are shown in **Figure**

6.13.A. The results demonstrated that catalytic activity is completely recovered after washing and drying, showing complete conversion. Selectivity to target products remains approximately constant between the fresh and reuse runs, with values ranging between 41-44% for epoxide and 38-40% for myrtanal.

The leaching test was conducted using the hot-filtration method to remove the mixture of catalysts (MgO + FeS2) after 4 h of reaction. **Figure 6.13.B** shows that profiles, when catalysts were removed (dashed lines), did not significantly change between 4 and 48 h, demonstrating the heterogeneity of the reaction.

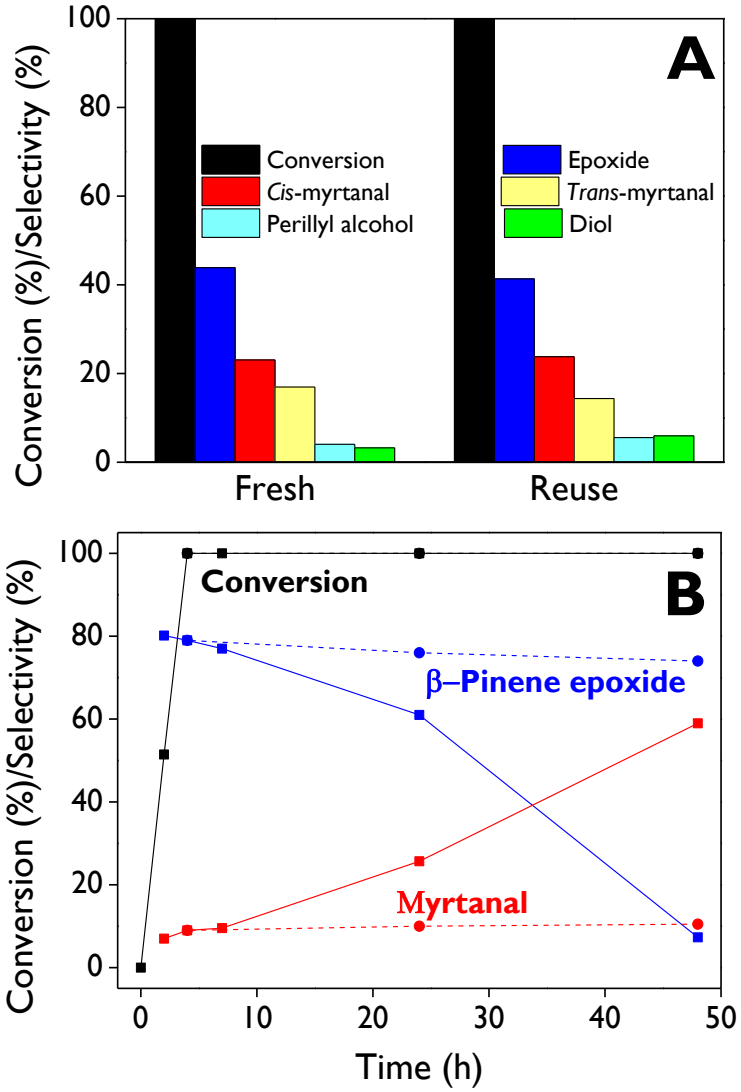

Figure 6.13. Stability of FeS2 catalyst in the one-pot transformation of β-pinene: **(A)** β-Pinene conversion and selectivity for the fresh and reuse runs after 20 h, **(B)** β-Pinene conversion and selectivity as function of time for fresh run (solid lines) and leaching test (dashed lines), where catalyst was removed at 4 h. **Reaction conditions:** 0.1 mmol of β-pinene with weight ratios of 1: 0.72: 1.2: 30.3: 19.7: 15.7: 0.8 for β-pinene: acidic catalyst: MgO: H_2O: acetone: acetonitrile: H_2O_2, 50 °C, 1000 rpm.

6.4.4. Plausible reaction pathway

The Payne system has been successfully reported for the epoxidation route of monoterpenes [17,18] which involves the formation of an active intermediate oxidant like peroxyacetimidic acid, which is formed by activating H_2O_2 with acetonitrile through a nucleophilic attack by perhydroxyl anion species (HOO^-) on the nitrile [95,96]. Furthermore, the MgO material contains medium-strength basic sites, which favors the epoxidation route of β-pinene [17]. **Figure 6.14** shows the proposed reaction pathway for the one-pot tandem transformation of β-pinene using two heterogeneous catalysts: MgO and Fe/support, based on a mechanism previously reported by our research group [17].

Initially, the presence of basic sites in MgO, along with deprotonation - favored by a basic pH in the system - and the rehydration of MgO, facilitate the formation of the epoxidation agent, namely peroxyacetimidic acid. Subsequently, the substrate undergoes activation on Mg^{2+} sites via the exocyclic carbon-carbon double bond and reacts with the epoxidation agent, resulting in the formation of β-pinene epoxide and acetamide. Furthermore, a relatively low yield of myrtanal was observed, attributed to the thermal effect in the rearrangement of the epoxide. Then, the exo-epoxide adsorbs and coordinates onto the Lewis acid site (Fe^{3+}) of Fe/MCM-41 or Fe/SBA-15 materials, which are widely known to favor the ring opening towards myrtanal, leading to iron reduction, cleavage of the C-O bond, and formation of the tertiary carbocation. Subsequently, hydrogen transfer facilitates the formation of the secondary carbocation at the exo-carbon until the lone pair of electrons from the oxygen coordinated to iron neutralizes the carbocation charge, resulting in the formation of a C=O bond [46]. Finally, myrtanal, the desired product, is synthesized, and the acid catalyst is regenerated.

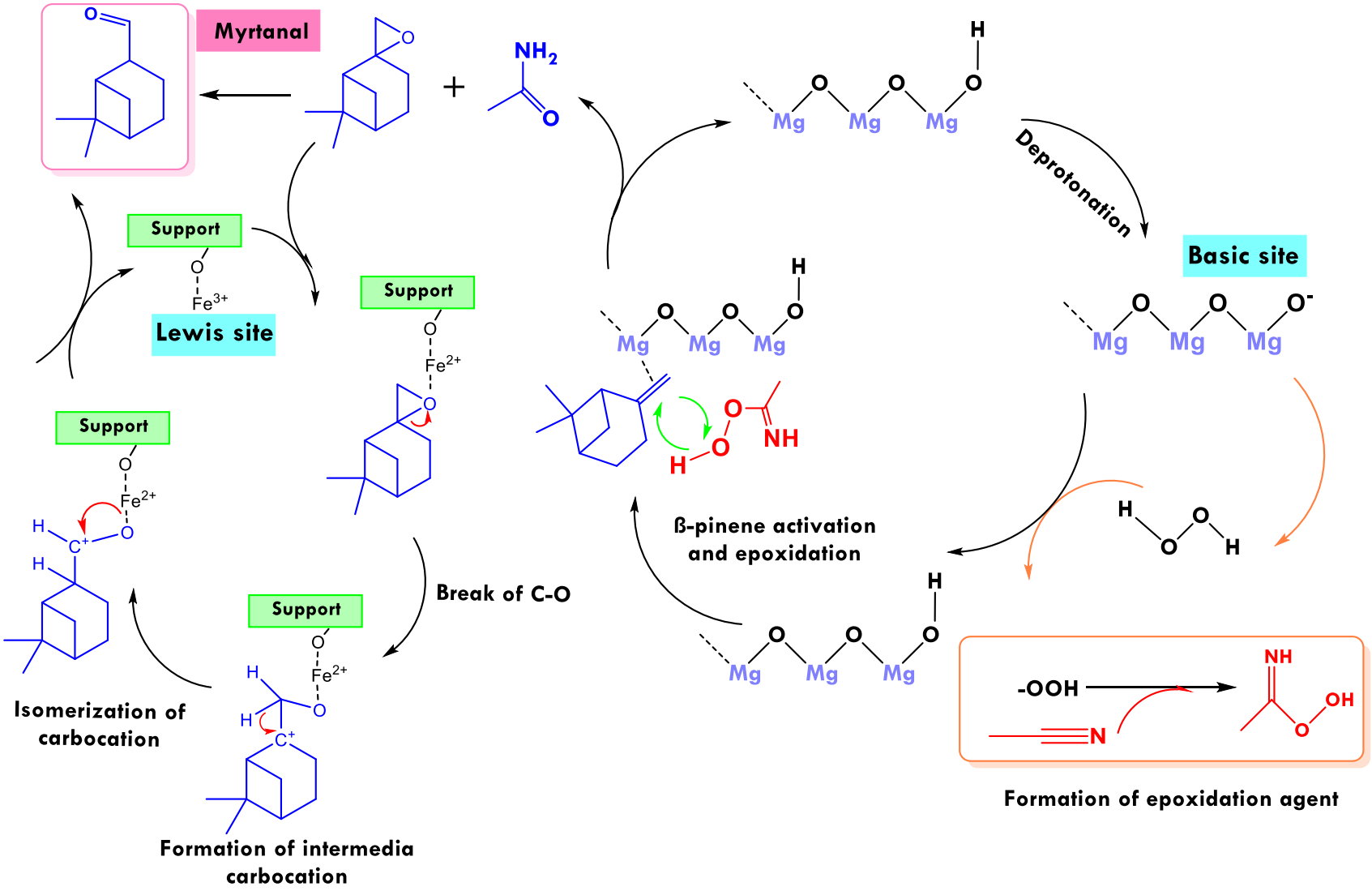

Figure 6.14. Plausible reaction pathway for the synthesis of myrtanal through a one-pot tandem route of β-pinene.

6.5. Conclusions

A Payne system consisting of commercial MgO with an acid catalyst was used to evaluate the one-pot transformation of β-pinene using a catalysis-in-tandem approach. The aim was to synthesize β-pinene epoxide through the oxidation of β-pinene with H_2O_2, followed by isomerization towards a mixture of myrtanal isomers as the target products. The acid catalysts were based on mesoporous supports such as MCM-41 and SBA-15, modified with various metals (Sn, Fe, Cu, and Co) using the wetness impregnation method. The synthesized products are widely employed as fine chemicals in fragrances, flavors, and precursors for pharmaceuticals.

The synthesized catalysts exhibited typical ordered mesoporous structures, as confirmed by XRD, although some degree of loss in crystallinity was noted after the anchoring of metals. All catalysts showed typical type-IV isotherms; however, some lacked the characteristic hysteresis loop, specifically based on MCM-41, attributed to low pore sizes at the boundary between micro- and mesopores. The BET surface area decreased as the metal loading increased in all materials. Channels with ordered hexagonal arrays were observed for all catalysts through TEM, except for cobalt-modified MCM-41, which correlated with a low-intensity peak in XRD. TEM micrographs suggested the presence of Sn on the support surface, while for Fe- and Cu-based catalysts, the metal nanoparticles were located inside the channels. The wetness impregnation method achieved excellent distribution of metals on the supports, as demonstrated by the metal mapping. All materials exhibited solely Lewis acid sites, as indicated by the band at 1450 cm^{-1} in pyridine-FTIR analysis.

The highest yields of myrtanal (59.0-62.3%) were obtained with Fe-SBA-15 materials after 48 h at 50 °C, using weight ratios of 1: 0.72: 1.2: 30.3: 19.7: 15.7: 0.8 for β-pinene: Fe-SBA-15: MgO: H_2O: acetone: acetonitrile: H_2O_2. High concentrations of H_2O_2, high amounts of acid catalysts, and high temperatures favored the formation of other products over myrtanal. The total acidity and the acid site density were proposed as suitable descriptors of the catalytic activity, highlighting the crucial role of acidity in the ring opening and selectivity of target products. Fe-SBA-15, with the highest total acidity of 138 μmol g^{-1} and the highest acid density of 0.28 μmol m^{-2}, exhibited the best yield to myrtanal (62.3%). This material also presented the highest metal coverage of 1.10 entities nm^{-2}. Cu and Co catalysts showed poor or no activity in the catalytic reaction due to their high activity in the decomposition of H_2O_2. The robustness of the Fe/SBA-15 catalyst was tested through reusability and leaching tests, resulting in no significant loss of activity and selectivity for myrtanal, nor leaching of Fe as the active phase.

In this study, a plausible reaction pathway was proposed considering MgO for the epoxidation route and Lewis acid site (Fe^{3+}) for the selective ring opening of the epoxide towards myrtanal. Finally, this is the first study of a one-pot tandem system for the synthesis of myrtanal from β-pinene under mild reaction conditions.

6.6. Acknowledgments

The authors extend their gratitude to the Universidad de Antioquia for providing financial support for this research through the Foundation for the Promotion of Research and Technology, Project 2022-56550, as well as Project 2022-53000 as a part of the 2021-2022 Programmatic Call: Engineering and Technology. Luis A. Gallego-Villada would like to express his gratitude to the Universidad de Antioquia for its support of his Ph.D. studies through the "Beca Doctoral Universidad de Antioquia" scholarship.

6.7. References

[1] H.-U. Blaser, Heterogeneous catalysis for fine chemicals production, Catal. Today. 60 (2000) 161–165. https://doi.org/10.1016/S0920-5861(00)00332-1.

[2] C. Lucarelli, A. Vaccari, Examples of heterogeneous catalytic processes for fine chemistry, Green Chem. 13 (2011) 1941. https://doi.org/10.1039/c0gc00760a.

[3] J.E. Sánchez-Velandia, L.A. Gallego-villada, P. Mäki-Arvela, A. Sidorenko, D.Y. Murzin, Upgrading Biomass to High-Added Value Chemicals: Synthesis of Monoterpenes-based Compounds using Catalytic Green Chemical Pathways, Catal. Rev. (2024).

[4] A. Masyita, R. Mustika Sari, A. Dwi Astuti, B. Yasir, N. Rahma Rumata, T. Bin Emran, F. Nainu, J. Simal-Gandara, Terpenes and terpenoids as main bioactive compounds of essential oils, their roles in human health and potential application as natural food preservatives, Food Chem. X. 13 (2022) 100217. https://doi.org/10.1016/j.fochx.2022.100217.

[5] V. Karuppiah, K.E. Ranaghan, N.G.H. Leferink, L.O. Johannissen, M. Shanmugam, A. Ní Cheallaigh, N.J. Bennett, L.J. Kearsey, E. Takano, J.M. Gardiner, M.W. van der Kamp, S. Hay, A.J. Mulholland, D. Leys, N.S. Scrutton, Structural Basis of Catalysis in the Bacterial Monoterpene Synthases Linalool Synthase and 1,8-Cineole Synthase, ACS Catal. 7 (2017) 6268–6282. https://doi.org/10.1021/acscatal.7b01924.

[6] L.A. Gallego-Villada, E.A. Alarcón, A.L. Villa, Evaluation of nopol production obtained from turpentine oil over Sn/MCM-41 synthesized by wetness impregnation using the Central Composite Design, Mol. Catal. 498 (2020) 111250. https://doi.org/10.1016/j.mcat.2020.111250.

[7] M. Golets, S. Ajaikumar, J.-P. Mikkola, Catalytic Upgrading of Extractives to Chemicals: Monoterpenes to "EXICALS," Chem. Rev. 115 (2015) 3141–3169. https://doi.org/10.1021/cr500407m.

[8] H. Zhang, X. Lu, L. Yang, Y. Hu, M. Yuan, C. Wang, Q. Liu, F. Yue, D. Zhou, Q. Xia, Efficient air epoxidation of cycloalkenes over bimetal-organic framework ZnCo-MOF materials, Mol. Catal. 499 (2021) 111300. https://doi.org/10.1016/j.mcat.2020.111300.

[9] A. Corma, S. Iborra, A. Velty, Chemical Routes for the Transformation of Biomass into Chemicals, Chem. Rev. 107 (2007) 2411–2502. https://doi.org/10.1021/cr050989d.

[10] D. García, F. Bustamante, A.L. Villa, M. Lapuerta, E. Alarcón, Oxyfunctionalization of Turpentine for Fuel Applications, Energy & Fuels. 34 (2020) 579–586. https://doi.org/10.1021/acs.energyfuels.9b03742.

[11] A. Corma, M. Renz, M. Susarte, Transformation of Biomass Products into Fine Chemicals Catalyzed by Solid Lewis- and Brønsted-acids, Top. Catal. 52 (2009) 1182–1189. https://doi.org/10.1007/s11244-009-9266-5.

[12] P. Tao, X. Lu, H. Zhang, R. Jing, F. Huang, S. Wu, D. Zhou, Q. Xia, Enhanced activity of microwave-activated CoOx/MOR catalyst for the epoxidation of α-pinene with air, Mol. Catal. 463 (2019) 8–15. https://doi.org/10.1016/j.mcat.2018.11.006.

[13] H. Martinez Q, Á.A. Amaya, E.A. Paez-Mozo, F. Martinez O, S. Valange, Photo-assisted O-atom transfer to monoterpenes with molecular oxygen and a dioxoMo(VI) complex immobilized on TiO2 nanotubes, Catal. Today. 375 (2021) 441–457. https://doi.org/10.1016/j.cattod.2020.07.053.

[14] H. Guo, X. Lu, J. He, H. Zhang, H. Zhang, Y. Dong, D. Zhou, Q. Xia, Co-MOF nanosheet supported on ZSM-5 with an improved catalytic activity for air epoxidation of olefins, Mater. Chem. Phys. 294 (2023) 127001.

https://doi.org/10.1016/j.matchemphys.2022.127001.

[15] C. Wang, H. Zhan, X. Lu, R. Jing, H. Zhang, L. Yang, X. Li, F. Yue, D. Zhou, Q. Xia, A recyclable cobalt(III)–ammonia complex catalyst for catalytic epoxidation of olefins with air as the oxidant, New J. Chem. 45 (2021) 2147–2156. https://doi.org/10.1039/D0NJ05466F.

[16] Y. Mahamat Ahmat, S. Madadi, L. Charbonneau, S. Kaliaguine, Epoxidation of Terpenes, Catalysts. 11 (2021) 847. https://doi.org/10.3390/catal11070847.

[17] D. García, M. Jaramillo, F. Bustamante, A.L. Villa, E. Alarcón, Epoxidation of β-pinene with a highly-active and low-cost catalyst, Brazilian J. Chem. Eng. 38 (2021) 89–100. https://doi.org/10.1007/s43153-020-00078-y.

[18] L.A. Gallego-Villada, E.A. Alarcón, A.L. Villa, Versatile Heterogeneous Catalytic System for the Selective Synthesis of Limonene Epoxide and Diepoxide, Ind. Eng. Chem. Res. 62 (2023) 20152–20169. https://doi.org/10.1021/acs.iecr.3c02633.

[19] K. Schröder, K. Junge, A. Spannenberg, M. Beller, Design of a bio-inspired imidazole-based iron catalyst for epoxidation of olefins: Mechanistic insights, Catal. Today. 157 (2010) 364–370. https://doi.org/10.1016/j.cattod.2010.04.034.

[20] A.A. de Oliveira, M.L. da Silva, M.J. da Silva, Palladium-Catalysed Oxidation of Bicycle Monoterpenes by Hydrogen Peroxide in Acetonitrile Solutions: A Metal Reoxidant-Free and Environmentally Benign Oxidative Process, Catal. Letters. 130 (2009) 424–431. https://doi.org/10.1007/s10562-009-9970-6.

[21] C.B. Woitiski, Y.N. Kozlov, D. Mandelli, G. V. Nizova, U. Schuchardt, G.B. Shul'pin, Oxidations by the system "hydrogen peroxide–dinuclear manganese(IV) complex–carboxylic acid," J. Mol. Catal. A Chem. 222 (2004) 103–119. https://doi.org/10.1016/j.molcata.2004.08.003.

[22] J.E. Sánchez-Velandia, L.M. Valdivieso, F. Martínez O, S.M. Mejía, A.L. Villa, J. Wärnå, D.Y. Murzin, Synthesis of trans-pinocarveol from oxidation of β-pinene using multifunctional heterogeneous catalysts, Mol. Catal. 541 (2023) 113104. https://doi.org/10.1016/j.mcat.2023.113104.

[23] A. Bordoloi, F. Lefebvre, S.B. Halligudi, Organotin-oxometalate coordination polymer catalyzed oxyfunctionalization of monoterpenes, J. Mol. Catal. A Chem. 270 (2007) 177–184. https://doi.org/10.1016/j.molcata.2007.02.004.

[24] O. de la Torre, M. Renz, A. Corma, Applied Catalysis A : General Biomass to chemicals : Rearrangement of ᴺʟ -pinene epoxide into myrtanal with well-defined single-site substituted molecular sieves as reusable solid Lewis-acid catalysts, "Applied Catal. A, Gen. 380 (2010) 165–171. https://doi.org/10.1016/j.apcata.2010.03.056.

[25] A. Corma, M. Renz, O. De La Torre, Production of myrtanal from beta-pinene epoxide, US 8,633,338 B2, 2014.

[26] P. Mäki-Arvela, N. Kumar, S.F. Diáz, A. Aho, M. Tenho, J. Salonen, A.-R. Leino, K. Kordás, P. Laukkanen, J. Dahl, I. Sinev, T. Salmi, D.Y. Murzin, Isomerization of β-pinene oxide over Sn-modified zeolites, J. Mol. Catal. A Chem. 366 (2013) 228–237. https://doi.org/10.1016/j.molcata.2012.09.028.

[27] E. Salminen, L. Rujana, P. Mäki-Arvela, P. Virtanen, T. Salmi, J.-P. Mikkola, Biomass to value added chemicals: Isomerisation of β-pinene oxide over supported ionic liquid catalysts (SILCAs) containing Lewis acids, Catal. Today. 257 (2015) 318–321. https://doi.org/10.1016/j.cattod.2014.05.024.

[28] E. Vyskočilová, M. Malý, A. Aho, J. Krupka, L. Červený, The solvent effect in β-pinene oxide rearrangement, React. Kinet. Mech. Catal. 118 (2016) 235–246. https://doi.org/10.1007/s11144-016-0994-9.

[29] E. Vyskočilová, J. Dušek, M. Babirádová, J. Krupka, I. Paterová, L. Červený, Perillyl alcohol preparation from β-pinene oxide using Fe-modified zeolite beta, Res. Chem. Intermed. 44 (2018) 3971–3984. https://doi.org/10.1007/s11164-018-3335-y.

[30] H. Li, J. Liu, J. Zhao, H. He, D. Jiang, S.R. Kirk, Q. Xu, X. Liu, D. Yin, Selective Catalytic Isomerization of β-Pinene Oxide to Perillyl Alcohol Enhanced by Protic Tetraimidazolium Nitrate, ChemistryOpen. 10 (2021) 477–485. https://doi.org/10.1002/open.202000318.

[31] M.J. Climent, A. Corma, S. Iborra, Heterogeneous Catalysts for the One-Pot Synthesis of Chemicals and Fine Chemicals, Chem. Rev. 111 (2011) 1072–1133. https://doi.org/10.1021/cr1002084.

[32] Y. Hayashi, Pot economy and one-pot synthesis, Chem. Sci. 7 (2016) 866–880. https://doi.org/10.1039/C5SC02913A.

[33] B. Sundaravel, C.M. Babu, R. Vinodh, W.S. Cha, H.-T. Jang, Synthesis of campholenic aldehyde from α-pinene using bi-functional PrAlPO-5 molecular sieves, J. Taiwan Inst. Chem. Eng. 63 (2016) 157–165. https://doi.org/10.1016/j.jtice.2016.02.028.

[34] D.R. Godhani, H.D. Nakum, D.K. Parmar, J.P. Mehta, N.C. Desai, Zeolite Y encaged Ru(III) and Fe(III) complexes for oxidation of styrene, cyclohexene, limonene, and α-pinene: An eye-catching impact of H2SO4 on product selectivity, J. Mol. Catal. A Chem. 426 (2017) 223–237. https://doi.org/10.1016/j.molcata.2016.11.020.

[35] C.M. Chanquía, A.L. Cánepa, E.L. Winkler, E. Rodríguez-Castellón, S.G. Casuscelli, G.A. Eimer, Nature of active vanadium nanospecies in MCM-41 type catalysts for olefins oxidation, Mater. Chem. Phys. 175 (2016) 172–179. https://doi.org/10.1016/j.matchemphys.2016.03.014.

[36] M.N. Timofeeva, Z. Hasan, V.N. Panchenko, I.P. Prosvirin, S.H. Jhung, Vanadium-containing nickel phosphate molecular sieves as catalysts for α-pinene oxidation with molecular oxygen: A study of the effect of vanadium content on activity and selectivity, J. Mol. Catal. A Chem. 363–364 (2012) 328–334. https://doi.org/10.1016/j.molcata.2012.07.008.

[37] P.A. Robles-Dutenhefner, M.J. da Silva, L.S. Sales, E.M.B. Sousa, E. V. Gusevskaya, Solvent-free liquid-phase autoxidation of monoterpenes catalyzed by sol–gel Co/SiO2, J. Mol. Catal. A Chem. 217 (2004) 139–144. https://doi.org/10.1016/j.molcata.2004.03.007.

[38] Y.-W. Suh, N.-K. Kim, W.-S. Ahn, H.-K. Rhee, Redox-mesoporous molecular sieve as a bifunctional catalyst for the one-pot synthesis of campholenic aldehyde from α-pinene, J. Mol. Catal. A Chem. 174 (2001) 249–254. https://doi.org/10.1016/S1381-1169(01)00192-3.

[39] Y.-W. Suh, N.-K. Kim, W.-S. Ahn, H.-K. Rhee, One-pot synthesis of campholenic aldehyde from α-pinene over Ti-HMS catalyst II: effects of reaction conditions, J. Mol. Catal. A Chem. 198 (2003) 309–316. https://doi.org/10.1016/S1381-1169(02)00733-1.

[40] M.J. Climent, A. Corma, S. Iborra, M.J. Sabater, Heterogeneous Catalysis for Tandem Reactions, ACS Catal. 4 (2014) 870–891. https://doi.org/10.1021/cs401052k.

[41] T.L. Lohr, T.J. Marks, Orthogonal tandem catalysis, Nat. Chem. 7 (2015) 477–482. https://doi.org/10.1038/nchem.2262.

[42] M. Grün, K.K. Unger, A. Matsumoto, K. Tsutsumi, Novel pathways for the preparation of mesoporous MCM-41 materials: control of porosity and morphology, Microporous Mesoporous Mater. 27 (1999) 207–216. https://doi.org/10.1016/S1387-1811(98)00255-8.

[43] P. Shah, A. V. Ramaswamy, K. Lazar, V. Ramaswamy, Synthesis and characterization of tin oxide-modified mesoporous SBA-15 molecular sieves and catalytic activity in trans-esterification reaction, Appl. Catal. A Gen. 273 (2004) 239–248. https://doi.org/10.1016/j.apcata.2004.06.039.

[44] G. Jura, W.D. Harkins, Surfaces of Solids. XI. Determination of the Decrease (π) of Free Surface Energy of a Solid by an Adsorbed Film, J. Am. Chem. Soc. 66 (1944) 1356–1362. https://doi.org/10.1021/ja01236a046.

[45] C.A. Emeis, Determination of Integrated Molar Extinction Coefficients for Infrared Absorption Bands of Pyridine Adsorbed on Solid Acid Catalysts, J. Catal. 141 (1993) 347–354. https://doi.org/10.1006/jcat.1993.1145.

[46] J.E. Sánchez-Velandia, A.L. Villa, Isomerization of α- and β- pinene epoxides over Fe or Cu supported MCM-41 and SBA-15 materials, Appl. Catal. A Gen. 580 (2019) 17–27. https://doi.org/10.1016/j.apcata.2019.04.029.

[47] J.S. Beck, J.C. Vartuli, W.J. Roth, M.E. Leonowicz, C.T. Kresge, K.D. Schmitt, C.T.W. Chu, D.H. Olson, E.W. Sheppard, S.B. McCullen, J.B. Higgins, J.L. Schlenker, A new family of mesoporous molecular sieves prepared with liquid crystal templates, J. Am. Chem. Soc. 114 (1992) 10834–10843. https://doi.org/10.1021/ja00053a020.

[48] A. Galarneau, H. Cambon, F. Di Renzo, R. Ryoo, M. Choi, F. Fajula, Microporosity and connections between pores in SBA-15 mesostructured silicas as a function of the temperature of synthesis, New J. Chem. 27 (2003) 73–79. https://doi.org/10.1039/b207378c.

[49] L.A. Gallego-Villada, E.A. Alarcón, A.L. Villa, Effect of Colombian raw materials on the Prins condensation reaction over Sn/MCM-41, Catal. Today. 372 (2021) 36–50. https://doi.org/10.1016/j.cattod.2020.10.040.

[50] X. Dong, Y. Wang, H. Dan, Z. Hong, K. Song, Q. Xian, Y. Ding, A facile route to synthesize mesoporous SBA-15 silica spheres from powder quartz, Mater. Lett. 204 (2017) 97–100. https://doi.org/10.1016/j.matlet.2017.05.115.

[51] N.A. Razik, Frecise lattice constant determination of hexagonal, rhombohedral, and tetragonal crystals from X-ray powder diffractometric data, Phys. Status Solidi. 90 (1985) K125–K128. https://doi.org/10.1002/pssa.2210900247.

[52] Y. Ishii, Y. Nishiwaki, A. Al-zubaidi, S. Kawasaki, Pore Size Determination in Ordered Mesoporous Materials Using Powder X-ray Diffraction, J. Phys. Chem. C. 117 (2013) 18120–18130. https://doi.org/10.1021/jp4057362.

[53] R.J. Farrauto, M.C. Hobson, Catalyst Characterization, in: Encycl. Phys. Sci. Technol., Elsevier, 2003: pp. 501–526. https://doi.org/10.1016/B0-12-227410-5/00087-9.

[54] G. Ertl, H. Knozinger, F. Schuth, J. Weitkamp, Handbook of Heterogeneous Catalysis, Wiley-VCH Verlag GmbH, Germany, 2008. https://doi.org/10.1002/9783527610044.

[55] K.S.W. Sing, Reporting physisorption data for gas/solid systems with special reference to the determination of surface area and porosity (Recommendations 1984), Pure Appl. Chem. 57 (1985) 603–619. https://doi.org/10.1351/pac198557040603.

[56] F. Rouquerol, J. Rouquerol, K. Sing, CHAPTER 1 - Introduction, in: F. Rouquerol, J.

Rouquerol, K.B.T.-A. by P. and P.S. Sing (Eds.), Academic Press, London, 1999: pp. 1–26. https://doi.org/https://doi.org/10.1016/B978-012598920-6/50002-6.

[57] T. Miyata, A. Endo, T. Ohmori, T. Akiya, M. Nakaiwa, Evaluation of pore size distribution in boundary region of micropore and mesopore using gas adsorption method, J. Colloid Interface Sci. 262 (2003) 116–125. https://doi.org/10.1016/S0021-9797(02)00254-0.

[58] A. Grosman, C. Ortega, Nature of Capillary Condensation and Evaporation Processes in Ordered Porous Materials, Langmuir. 21 (2005) 10515–10521. https://doi.org/10.1021/la051030o.

[59] K. Quiroz-Estrada, M. Esparza-Schulz, C. Felipe, A Better Understanding of the SBA-15 Pores Filling through Textural Changes in CMK-3 Carbon Synthesis and Its CO2:CH4 Adsorption Selectivity, J. Compos. Sci. 6 (2022) 344. https://doi.org/10.3390/jcs6110344.

[60] T. Heikkilä, J. Salonen, J. Tuura, N. Kumar, T. Salmi, D.Y. Murzin, M.S. Hamdy, G. Mul, L. Laitinen, A.M. Kaukonen, J. Hirvonen, V.-P. Lehto, Evaluation of Mesoporous TCPSi, MCM-41, SBA-15, and TUD-1 Materials as API Carriers for Oral Drug Delivery, Drug Deliv. 14 (2007) 337–347. https://doi.org/10.1080/10717540601098823.

[61] F. Khanmohammadi, B.M. Razavizadeh, E. Fooladi, Application of electrochemical sensor modified by SBA-15 /Fe3O4/polyaniline nanocomposite for determination of tyrosine in milk samples, Sens. Bio-Sensing Res. 42 (2023) 100602. https://doi.org/10.1016/j.sbsr.2023.100602.

[62] D. Gkiliopoulos, I. Tsamesidis, A. Theocharidou, G.K. Pouroutzidou, E. Christodoulou, E. Stalika, K. Xanthopoulos, D. Bikiaris, K. Triantafyllidis, E. Kontonasaki, SBA-15 Mesoporous Silica as Delivery Vehicle for rhBMP-2 Bone Morphogenic Protein for Dental Applications, Nanomaterials. 12 (2022) 822. https://doi.org/10.3390/nano12050822.

[63] Y. Liu, S. Yang, C. Shi, L. Pan, X. Zhang, J.-J. Zou, HPW/MCM-41 catalytic Simmons-Smith cyclopropanation of olefins for synthesis of high-energy–density fuel, Chem. Eng. Sci. 283 (2024) 119366. https://doi.org/10.1016/j.ces.2023.119366.

[64] I. Aguas, M.J. Hidalgo, A.L. Villa, E.A. Alarcón, Homolimonenol synthesis over Sn supported mesoporous materials, Catal. Today. 394–396 (2022) 403–413. https://doi.org/10.1016/j.cattod.2021.07.025.

[65] A. Nuri, A. Bezaatpour, M. Amiri, N. Vucetic, J.-P. Mikkola, D.Y. Murzin, Pd Nanoparticles Stabilized on the Cross-Linked Melamine-Based SBA-15 as a Catalyst for the Mizoroki–Heck Reaction, Catal. Letters. 152 (2022) 991–1002. https://doi.org/10.1007/s10562-021-03691-9.

[66] P. Demuth, L.A. Gallego-Villada, P. Mäki-Arvela, R. Majidov, Z. Vajglová, N. Kumar, I. Angervo, M. Lastusaari, K. Eränen, D.Y. Murzin, Micro and mesoporous materials based on zeolite Y for the florol synthesis via the prins cyclization of isoprenol, Catal. Today. 433 (2024) 114695. https://doi.org/10.1016/j.cattod.2024.114695.

[67] L.A. Gallego-Villada, P. Mäki-Arvela, N. Kumar, E.A. Alarcón, Z. Vajglová, T. Tirri, I. Angervo, R. Lassfolk, M. Lastusaari, D.Y. Murzin, Zeolite Y-based catalysts for efficient epoxidation of R-(+)-Limonene: Insights into the structure-activity relationship, Microporous Mesoporous Mater. 372 (2024) 113098. https://doi.org/10.1016/j.micromeso.2024.113098.

[68] B. Chakraborty, B. Viswanathan, Surface acidity of MCM-41 by in situ IR studies of pyridine adsorption, Catal. Today. 49 (1999) 253–260. https://doi.org/10.1016/S0920-5861(98)00431-3.

[69] A. Ramírez, B.L. Lopez, L. Sierra, Study of the Acidic Sites and Their Modifications in Mesoporous Silica Synthesized in Acidic Medium under Quiescent Conditions, J. Phys. Chem. B. 107 (2003) 9275–9280. https://doi.org/10.1021/jp0351472.

[70] J.M. Ramos, J.A. Wang, S.O. Flores, L.F. Chen, N. Nava, J. Navarrete, J.M. Domínguez, J.A. Szpunar, Ultrasound-assisted synthesis and catalytic activity of mesostructured FeOx/SBA-15 and FeOx/Zr-SBA-15 catalysts for the oxidative desulfurization of model diesel, Catal. Today. 349 (2020) 198–209. https://doi.org/10.1016/j.cattod.2018.04.059.

[71] M. Stekrova, N. Kumar, P. Mäki-Arvela, O. Ardashov, K. Volcho, N. Salakhutdinov, D. Murzin, Selective Preparation of trans-Carveol over Ceria Supported Mesoporous Materials MCM-41 and SBA-15, Materials (Basel). 6 (2013) 2103–2118. https://doi.org/10.3390/ma6052103.

[72] A.A. El-Rayyes, A.A. Al-Arfaj, U.K.A. Klein, S.A.I. Barri, Acidity of All-Silica MCM-41—Studied by Laser Spectroscopy of Adsorbed Fluorescent Probe Compounds, Catal. Letters. 97 (2004) 83–90. https://doi.org/10.1023/B:CATL.0000034292.46628.15.

[73] P.R.S. Braga, A.A. Costa, J.L. de Macedo, G.F. Ghesti, M.P. de Souza, J.A. Dias, S.C.L. Dias, Liquid phase calorimetric-adsorption analysis of Si-MCM-41: Evidence of strong hydrogen-bonding sites, Microporous Mesoporous Mater. 139 (2011) 74–80. https://doi.org/10.1016/j.micromeso.2010.10.020.

[74] F. Arena, R. Dario, A. Parmaliana, A characterization study of the surface acidity of solid catalysts by temperature programmed methods, Appl. Catal. A Gen. 170 (1998) 127–137. https://doi.org/10.1016/S0926-860X(98)00041-6.

[75] J. Baltrusaitis, C.R. Usher, V.H. Grassian, Reactions of sulfur dioxide on calcium carbonate single crystal and particle surfaces at the adsorbed water carbonate interface, Phys. Chem. Chem. Phys. 9 (2007) 3011. https://doi.org/10.1039/b617697f.

[76] M. Smyrnioti, T. Ioannides, Synthesis of Cobalt-Based Nanomaterials from Organic Precursors, in: Cobalt, InTech, 2017. https://doi.org/10.5772/intechopen.70947.

[77] W. Xia, H. Wang, X. Zeng, J. Han, J. Zhu, M. Zhou, S. Wu, High-efficiency photocatalytic activity of type II SnO/Sn 3 O 4 heterostructures via interfacial charge transfer, CrystEngComm. 16 (2014) 6841–6847. https://doi.org/10.1039/C4CE00884G.

[78] ThermoFisher, Thermo Fisher Scientific, X-Ray Photoelectron Spectroscopy Learning Center, (n.d.). https://www.thermofisher.com/co/en/home/materials-science/learning-center/surface-analysis.html (accessed March 25, 2024).

[79] C.D. Wagner, W.M. Riggs, L.E. Davis, J.F. Moulder, Handbook of Xray Photoelectron Spectroscopy.pdf, Perkin-Elmer corporation, 1979.

[80] M. Stekrova, N. Kumar, A. Aho, I. Sinev, W. Grünert, J. Dahl, J. Roine, S.S. Arzumanov, P. Mäki-Arvela, D.Y. Murzin, Isomerization of α-pinene oxide using Fe-supported catalysts: Selective synthesis of campholenic aldehyde, Appl. Catal. A Gen. 470 (2014) 162–176. https://doi.org/10.1016/j.apcata.2013.10.044.

[81] J.E. Sánchez-Velandia, A.L. Villa, Selective synthesis of high-added value chemicals from α-pinene epoxide and limonene epoxide isomerization over mesostructured catalysts: Effect of the metal loading and solvent, Catal. Today. 394–396 (2022) 208–218. https://doi.org/10.1016/j.cattod.2021.09.011.

[82] J.M. Lázaro Martínez, E. Rodríguez-Castellón, R.M.T. Sánchez, L.R. Denaday, G.Y. Buldain, V. Campo Dall' Orto, XPS studies on the Cu(I,II)–polyampholyte heterogeneous catalyst: An insight into its structure and mechanism, J. Mol. Catal. A Chem. 339 (2011) 43–51. https://doi.org/10.1016/j.molcata.2011.02.010.

[83] L. Sun, J. Liu, W. Luo, Y. Yang, F. Wang, C. Weerakkody, S.L. Suib, Preparation of amorphous copper - chromium oxides catalysts for selective oxidation of cyclohexane, Mol. Catal. 460 (2018) 16–26. https://doi.org/10.1016/j.mcat.2018.09.007.

[84] A.M. Venezia, X-ray photoelectron spectroscopy (XPS) for catalysts characterization, Catal. Today. 77 (2003) 359–370. https://doi.org/10.1016/S0920-5861(02)00380-2.

[85] J.H. Scofield, Theoretical Photoionization Cross Sections from 1 to 1500 keV, University of California, Livermore, California, 1973.

[86] J.F. Perez-Benito, Copper(II)-Catalyzed Decomposition of Hydrogen Peroxide: Catalyst Activation by Halide Ions, Monatshefte Für Chemie/Chemical Mon. 132 (2001) 1477–1492. https://doi.org/10.1007/s007060170004.

[87] N. Danyliuk, V. Mandzyuk, Hydrogen peroxide decomposition using cobalt ferrite catalyst activated by induction heating, Mol. Cryst. Liq. Cryst. 766 (2023) 100–110. https://doi.org/10.1080/15421406.2023.2222256.

[88] L.A. Gallego-Villada, Dendritic ZSM-5 Zeolites as Highly Active Catalysts for the Valorization of Monoterpene Epoxides (Submitted - In Peer Review), Green Chem. (2024).

[89] D.Y. Murzin, Acid Site Density as a Kinetic Descriptor of Catalytic Reactions over Zeolites, Chemistry (Easton). 4 (2022) 1609–1623. https://doi.org/10.3390/chemistry4040105.

[90] D.Y. Murzin, Catalytic kinetics in nanoconfined space of acidic micro/mesoporous materials, Chem. Eng. Sci. 294 (2024) 120078. https://doi.org/10.1016/j.ces.2024.120078.

[91] L.A. Gallego-Villada, E.A. Alarcón, Transformation of monoterpenes through one-pot pathways over heterogeneous catalysts, in: Eng. Transform., 2022: pp. 36–42.

[92] M. Chaves-Restrepo, A. Viloria, J.E. Sánchez-Velandia, A.L. Villa, Effect of reaction conditions and kinetics of the isomerization of β-pinene epoxide to myrtanal in the presence of Fe/MCM-41 and Fe/SBA-15, React. Kinet. Mech. Catal. 135 (2022) 2013–2029. https://doi.org/10.1007/s11144-022-02220-y.

[93] K. Zítová, E. Vyskočilová, L. Červený, Preparation of α-terpineol and perillyl alcohol using zeolites beta, Res. Chem. Intermed. 47 (2021) 4297–4310. https://doi.org/10.1007/s11164-021-04515-6.

[94] M.C. Cruz, J.E. Sánchez-Velandia, S. Causíl, A.L. Villa, Selective Synthesis of Perillyl Alcohol from β-Pinene Epoxide over Ti and Mo Supported Catalysts, Catal. Letters. 151 (2021) 2279–2290. https://doi.org/10.1007/s10562-020-03489-1.

[95] I. Kirm, F. Medina, X. Rodríguez, Y. Cesteros, P. Salagre, J. Sueiras, Epoxidation of styrene with hydrogen peroxide using hydrotalcites as heterogeneous catalysts, Appl. Catal. A Gen. 272 (2004) 175–185. https://doi.org/10.1016/j.apcata.2004.05.039.

[96] K. Yamaguchi, K. Mori, T. Mizugaki, K. Ebitani, K. Kaneda, Epoxidation of α,β-Unsaturated Ketones Using Hydrogen Peroxide in the Presence of Basic Hydrotalcite Catalysts, J. Org. Chem. 65 (2000) 6897–6903. https://doi.org/10.1021/jo000247e.

Chapter 7. Conclusions and Future Work

General conclusions

This doctoral thesis systematically investigated new routes of heterogeneous catalytic systems based on mesoporous materials for the highly selective synthesis of fine chemicals from biomass-derived substrates such as β-pinene and limonene. The focus was primarily on tandem routes of epoxidation/isomerization, which represent a challenging one-pot approach in green organic synthesis, aligning with the principles of green chemistry and contributing to sustainable development goals. These one-pot pathways show promise but also pose significant challenges due to the need for compatible reaction conditions using benign reactants and solvents under mild conditions. While each chapter included conclusions, the general findings of this thesis are summarized as follows:

Commercial magnesium oxide, comprising periclase and brucite crystalline phases, has proven to be a robust heterogeneous catalyst with basic sites for the epoxidation of R-(+)-limonene into a mixture of limonene epoxides and limonene diepoxide using a Payne system. While our research group previously utilized this catalyst for the epoxidation of other monoterpenes like β-pinene, this work introduces a novel approach: reducing the amount of H_2O_2 in the Payne system, which minimizes the competitive hydration of internal limonene epoxide into limonene glycol, which is caused by water present in the commercial H_2O_2 and the generated during H_2O_2 decomposition, thereby enhancing selectivity towards epoxydic products. Furthermore, this thesis presents, for the first time, a detailed kinetic modeling of a Payne-type catalytic route in fine chemistry. The modeling includes a pseudo-homogeneous reversible model for the formation of peroxyacetimidic acid (PA) as the epoxidizing agent using acetonitrile and H_2O_2. Additionally, heterogeneous models consider surface reactions as rate-limiting steps for H_2O_2 decomposition and the formation of limonene epoxide from limonene and PA. These findings underscore the potential for optimizing reaction conditions to improve the selectivity and yield of limonene epoxides. The kinetic study provides valuable insights that lay a foundation for scaling up these fine chemical processes, thereby making significant contributions to the advancement of catalysis science and engineering.

Metal-modified catalysts based on hierarchical zeolite Y were successfully evaluated as selective materials for the valorization of R-(+)-limonene via the epoxidation route. These catalysts were primarily modified with varying loadings of tin using $SnCl_4 \cdot 5H_2O$ as the precursor salt. The study provides detailed insights into the relationship between the physicochemical properties of these materials and their catalytic performance. It was demonstrated that conversion and selectivity to the main products depend strongly on the Brønsted to Lewis acidity (BAS/LAS) ratio and mesoporosity fraction. As anticipated, increasing metal loading led to a reduction in surface area due to pore-blocking effects. The most active catalyst, achieving the highest turnover frequency, was found to be K-Sn modified hierarchical zeolite Y. This catalyst exhibited the lowest BAS/LAS ratio (0.1), the highest mesoporosity fraction (43%), and the lowest total surface area (465 $m^2\ g^{-1}$). The study highlighted the crucial role of solvent choice, favoring the epoxidation route when using aprotic polar solvents with high polarity and

medium donor capacity. The mechanistic study proposed that superficial Sn-OH groups on the zeolites serve as the most active sites, offering lower steric hindrance compared to the bulk Sn network. In contrast, while some materials were modified with potassium, the results did not indicate the presence of basic sites, suggesting that potassium modifications primarily influenced the textural properties of the materials.

Dendritic ZSM-5 zeolites, considered highly promising mesoporous materials, have demonstrated superior activity in the valorization of monoterpene epoxides such as α-pinene epoxide, β-pinene epoxide, and limonene-1,2-epoxide, yielding major products like campholenic aldehyde, myrtanal, and dihydrocarvone. These materials feature well-defined MFI zeolitic structures with unique morphologies, which enhance accessibility and reactivity compared to traditional ZSM-5 zeolite. The specific textural properties of dendritic zeolitic surpass the catalytic performance of recent heterogeneous systems based on other mesoporous materials such as MCM-41 and SBA-15 impregnated with various metals. These findings provide a comprehensive understanding of the key aspects of the epoxide isomerization route, crucial for designing catalytic systems suitable for one-pot transformations of monoterpenes. Additionally, kinetic modeling for the isomerization of limonene-1,2-epoxide was successfully conducted using a reaction network considering parallel reactions starting from *cis*-LE and *trans*-LE, with mathematical expressions derived from heterogeneous kinetics models. DFT calculations were employed to support the experimental findings and the proposed kinetics model. To date, no previous studies have reported on the use of these catalysts for the valorization of this type of biomass.

Based on solid findings from previous catalytic systems in both the epoxidation and isomerization routes, a one-pot tandem system is proposed for transforming β-pinene into myrtanal. This system utilizes two heterogeneous catalysts: commercial magnesium oxide and acidic materials with Lewis acidity supported on mesoporous solids such as MCM-41 and SBA-15, modified with various metals (Sn, Fe, Cu, and Co) via wetness impregnation. The substrate conversion and yield to the main products were successfully correlated with two kinetic descriptors suitable for such routes: total Lewis acidity and acid site density. While there are limited reports on the one-pot reaction of a monoterpene, existing systems of α-pinene to campholenic aldehyde are not highly selective towards aldehyde and often use rare elements like Praseodymium along with non-benign reagents or solvents in their synthesis. In contrast, this one-pot system for myrtanal production represents the first reported instance, contributing significantly to the ongoing advancement in organic synthesis and biomass valorization through environmentally friendly processes. The highest yield of myrtanal was achieved using Fe/SBA-15 in the Payne system at 50 °C with a minimal excess of H_2O_2, which helps mitigate water presence favoring secondary reactions.

Finally, a clear description is provided of how each specific objective (**section 1.4.2**) was achieved, correlating the chapters of this thesis that contributed to meeting those objectives.

Objective 1: A wide variety of mesoporous materials were evaluated, including MgO (**Chapter 2** and **Chapter 6**), hierarchical Y-type zeolites (**Chapter 3**), dendritic zeolites (with mesoporosity) of the ZSM-5 type (**Chapter 4** and **Chapter 5**), and mesostructured materials such as MCM-41 and SBA-15 (**Chapter 6**). These materials were assessed either for their performance in the independent routes of epoxidation or isomerization or the one-pot tandem route (using two heterogeneous catalysts simultaneously).

Objective 2: **Chapter 6** reports suitable reaction conditions for the one-pot transformation of β-pinene using a tandem catalysis approach. MgO was employed as the catalyst to promote the epoxidation of β-pinene, while acidic catalysts based on MCM-41 and SBA-15 were used to facilitate the isomerization of the epoxide, primarily to myrtanal. These reaction conditions were developed based on significant findings from the previous chapters (**Chapter 2** to **Chapter 5**).

Objective 3: The effect of different reaction conditions and the role of the catalyst were studied in **Chapter 2** and **Chapter 3** for the epoxidation route of R-(+)-limonene, in **Chapter 4** for the isomerization of monoterpene epoxides, and **Chapter 6** for the one-pot catalytic system.

Objective 4: **Chapter 3** provides a detailed correlation between the physicochemical properties of Y-type zeolite-based catalysts and their catalytic activity for the epoxidation of limonene. **Chapter 4** demonstrates how the catalytic activity of dendritic ZSM-5 zeolite-based catalysts is significantly influenced by their textural and acidic properties in the isomerization of monoterpene epoxides. Finally, **Chapter 6** demonstrated that total acidity and acid site density are effective kinetic descriptors for explaining the catalytic data on the one-pot transformation of β-pinene into myrtanal.

Future work

Future work recommendations can be derived from this doctoral thesis, including:

- Conduct kinetic modeling for limonene epoxidation over K-Sn-hierarchical zeolite Y presented in Chapter 3. Consider most products reported in this thesis to establish kinetic expressions for potential reactor design.

- Evaluate heterogeneous catalytic systems for transforming monoterpenes using materials based on hierarchical zeolite Y with varying SiO_2/Al_2O_3 ratios, and anchored metals other than Sn such as Fe, Cu, and Zn. Additionally, explore alternative methods for introducing metal as active phases, as evidenced in Chapter 3 by minimal loss of catalytic activity due to slight Sn leaching, including incipient wetness impregnation, precipitation, and hydrothermal methods.

- Perform kinetic modeling for the isomerization of α-pinene epoxide and β-pinene epoxide to optimize conditions favoring the production of campholenic aldehyde and myrtanal, respectively, using dendritic ZSM-5 zeolites.

- Evaluate kinetic modeling to describe pathways for the one-pot tandem system proposed in Chapter 6 for myrtanal production from β-pinene.

- Considering findings in chapters 2 and 3 indicating the nearly obligatory use of acetonitrile, a highly polar solvent, for monoterpenes epoxidation route, and preferences in chapters 4 and 5 for isomerization in apolar or medium-polarity solvents like toluene, ethyl acetate, or dimethyl carbonate, suggest employing a methodology using catalysts like metal-hierarchical zeolite Y with a solvent mixture: acetonitrile + (ethyl acetate, toluene, or dimethyl carbonate), evaluating suitability based on chemical compatibility and miscibility.

- Implement flow reactors in the most promising catalytic routes studied to improve control over reaction parameters such as residence time, temperature, pressure, and mixing, and to achieve scalability in fine chemical processes.

Chapter 8. Supporting Information

8.1. Chapter 2

8.1.1. Reaction rate equations deduction

The transformation of R-(+)-limonene with H_2O_2 over MgO as a heterogeneous catalyst is described in **Figure 8.1**.

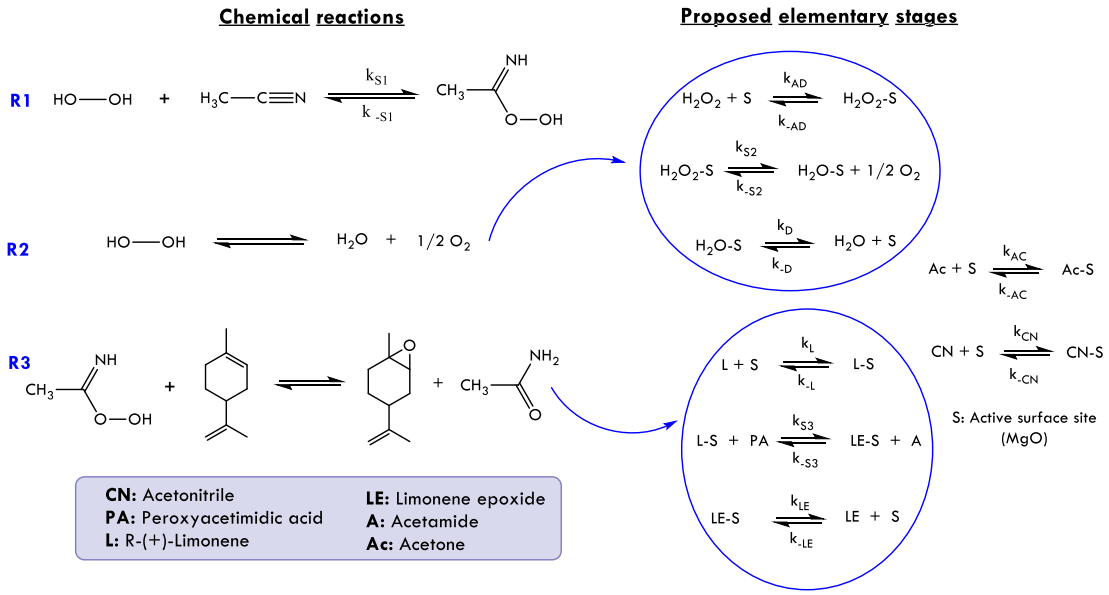

Figure 8.1. Set of reactions and proposed reaction pathway to produce limonene epoxide through a Payne system with water and acetone, and MgO as a heterogeneous catalyst.

S: surface site on catalyst
C_i: concentration of specie i in the bulk of the solution
C_v: concentration of available surface site on catalyst
C_{is}: concentration of specie i adsorbed at the surface site
C_t: total number of sites available on the catalyst surface.
k_i: Reaction rate constant of direct reaction i
k_{-i}: Reaction rate constant of reverse reaction i
K_i: Equilibrium constant for step i

The reaction rate law for reactions R2 and R3 using heterogeneous kinetic models is deduced as follows, considering the steps illustrated in **Figure 8.1** and elementary reactions in both directions of each step.

Reaction R2 (Decomposition of H_2O_2)

$$r_{AD} = k_{AD}\left[C_{H_2O_2}C_V - \frac{C_{H_2O_2\cdot S}}{K_{AD}}\right] \qquad (8.1)$$

$$r_{S2} = ks_2 \left[C_{H_2O_2 \cdot S} - \frac{C_{H_2O \cdot S} C_{O_2}^{\frac{1}{2}}}{K_{S2}} \right] \quad (8.2)$$

$$r_D = k_D \left[C_{H_2O \cdot S} - \frac{C_{H_2O} C_V}{K_D} \right] \quad (8.3)$$

Reaction R3 (Formation of limonene epoxide)

$$r_L = k_L \left[C_L C_V - \frac{C_{L \cdot S}}{K_L} \right] \quad (8.4)$$

$$r_{S3} = k_{S3} \left[C_{L \cdot S} C_{PA} - \frac{C_{LE \cdot S} C_A}{K_{S3}} \right] \quad (8.5)$$

$$r_{LE} = k_{LE} \left[C_{LE \cdot S} - \frac{C_{LE} C_V}{K_{LE}} \right] \quad (8.6)$$

Species that do not participate in the reactions but are adsorbed

$$r_{Ac} = k_{Ac} \left[C_{Ac} C_V - \frac{C_{Ac \cdot S}}{K_{Ac}} \right] \quad (8.7)$$

$$r_{CN} = k_{CN} \left[C_{CN} C_V - \frac{C_{CN \cdot S}}{K_{CN}} \right] \quad (8.8)$$

The **Eqs. (8.1)**, **(8.3)**, **(8.4)**, **(8.6)**, **(8.7)** and **(8.8)** are solved to find the concentrations of adsorbed species (C_{is}) when these are equal to zero, assuming the surface reactions (**Eqs. (8.2)** and **(8.5)**) as the rate-limiting steps.

$$C_{H_2O_2 \cdot S} = K_{AD} C_{H_2O_2} C_V \quad (8.9)$$

$$C_{H_2O \cdot S} = \frac{C_{H_2O} C_V}{K_D} \quad (8.10)$$

$$C_{L \cdot S} = K_L C_L C_V \quad (8.11)$$

$$C_{LE \cdot S} = \frac{C_{LE} C_V}{K_{LE}} \quad (8.12)$$

$$C_{Ac \cdot S} = K_{Ac} C_{Ac} C_V \quad (8.13)$$

$$C_{CN \cdot S} = K_{CN} C_{CN} C_V \quad (8.14)$$

The balance of sites is defined by **Eq. (8.15)**:

$$C_t = C_V + C_{H_2O_2 \cdot S} + C_{H_2O \cdot S} + C_{L \cdot S} + C_{LE \cdot S} + C_{Ac \cdot S} + C_{CN \cdot S} \quad \textbf{(8.15)}$$

By replacing **Eqs. (8.9) – (8.14)** in **Eq. (8.15)** and simplifying, **Eq. (8.16)** is obtained:

$$C_t = C_V + K_{AD} C_{H_2O_2} C_V + \frac{C_{H_2O} C_V}{K_D} + K_L C_L C_V + \frac{C_{LE} C_V}{K_{LE}} + K_{Ac} C_{Ac} C_V + K_{CN} C_{CN} C_V$$

$$C_V = \frac{C_t}{1 + K_{AD} C_{H_2O_2} + \frac{C_{H_2O}}{K_D} + K_L C_L + \frac{C_{LE}}{K_{LE}} + K_{Ac} C_{Ac} + K_{CN} C_{CN}} \quad \textbf{(8.16)}$$

Replacing **Eq. (8.16)** in **Eqs. (8.2)** and **(8.5)**, the final expressions for the reaction rates of R2 and R3 are obtained:

$$r_{S2} = ks_2 \left[K_{AD} C_{H_2O_2} - \frac{C_{H_2O} C_{O_2}^{\frac{1}{2}}}{K_D K_{S2}} \right] C_V$$

$$r_{S2} = \frac{ks_2 C_t \left[K_{AD} C_{H_2O_2} - \frac{C_{H_2O} C_{O_2}^{\frac{1}{2}}}{K_D K_{S2}} \right]}{\left[1 + K_{AD} C_{H_2O_2} + \frac{C_{H_2O}}{K_D} + K_L C_L + \frac{C_{LE}}{K_{LE}} + K_{Ac} C_{Ac} + K_{CN} C_{CN} \right]} \quad (k_2 = k_{S2} C_t) \quad \textbf{(8.17)}$$

$$r_{S3} = k_{S3} \left[K_L C_L C_{PA} - \frac{C_{LE} C_A}{K_{LE} K_{S3}} \right] C_V$$

$$r_{S3} = \frac{k_{S3} C_t \left[K_L C_L C_{PA} - \frac{C_{LE} C_A}{K_{LE} K_{S3}} \right]}{\left[1 + K_{AD} C_{H_2O_2} + \frac{C_{H_2O}}{K_D} + K_L C_L + \frac{C_{LE}}{K_{LE}} + K_{Ac} C_{Ac} + K_{CN} C_{CN} \right]} \quad (k_3 = k_{S3} C_t) \quad \textbf{(8.18)}$$

8.1.2. Reaction rate calculations

For the determination of the reaction rate of both limonene and H_2O_2 for the 7 entries of the set of experimental tests (**Table 2.2** of **Chapter 2**), the data of experimental concentrations were fitted to mathematical functions using Matlab software. The adjustment for each test is presented in **Figure 8.2** to **Figure 8.8** and **Figure 8.9** to **Figure 8.15** for limonene and H_2O_2, respectively, which corresponds to a rational expression of the molar concentration as a function of time, given by **Eq. (8.19)**.

$$C_i(t) = \frac{p_1 t + p_2}{t + q_1} \quad (i = \text{Limonene}, H_2O_2) \qquad \textbf{(8.19)}$$

Limonene

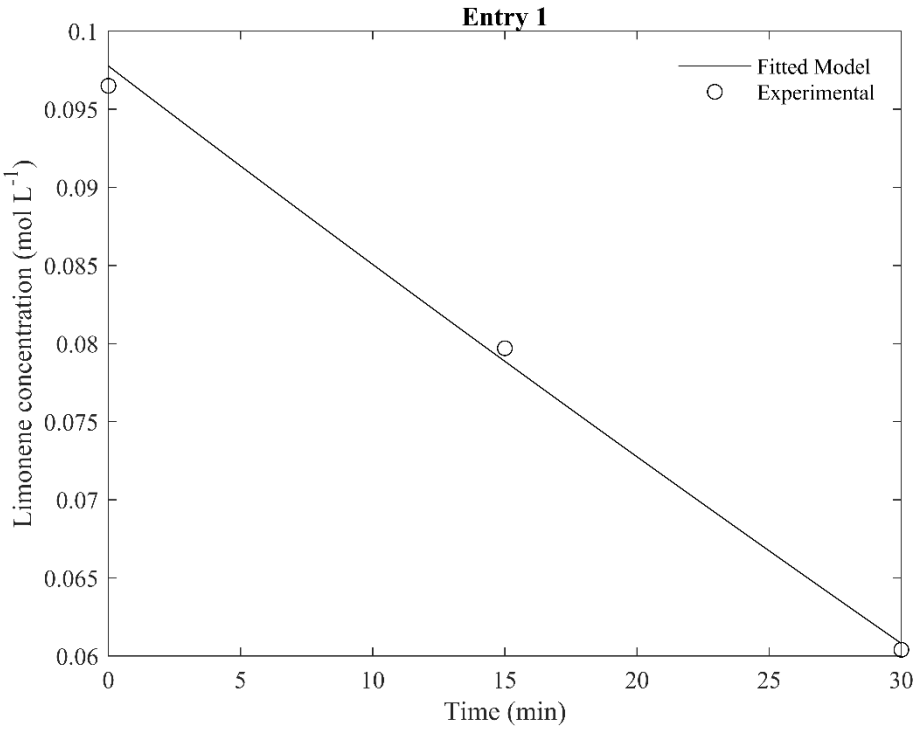

Figure 8.2. Fitting of limonene concentration for **entry 1** in the oxidation route with H_2O_2 over MgO as catalyst. **Reaction conditions:** 0.10 mmol of R-(+)-limonene and 1: 1.20: 30.3: 19.7: 15.7: 0.8 as weight ratios for R-(+)-limonene: MgO: H_2O: acetone: acetonitrile: H_2O_2, at 50 °C.

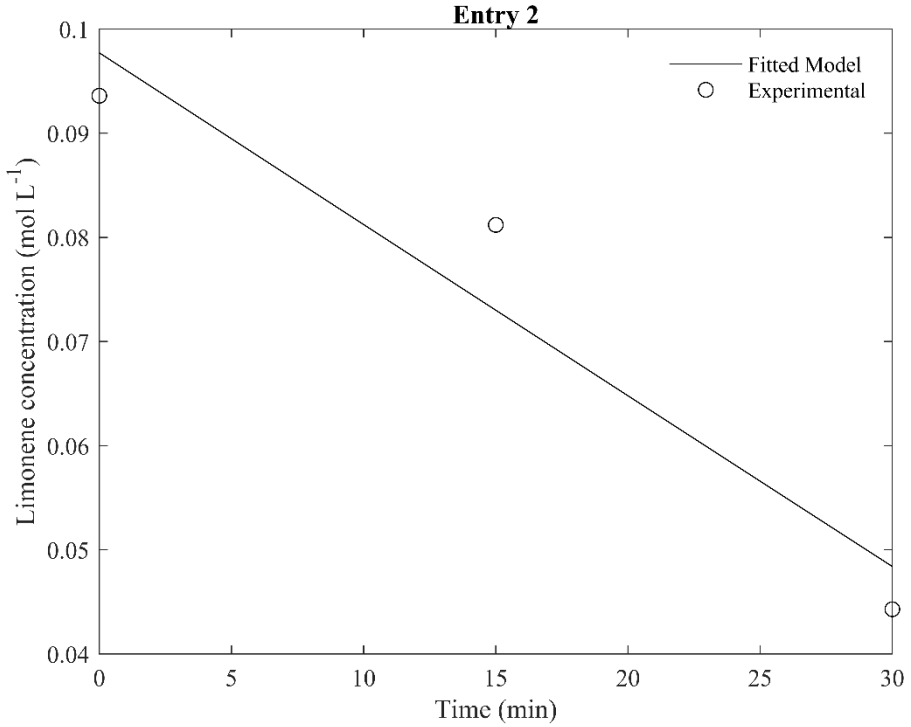

Figure 8.3. Fitting of limonene concentration for **entry 2** in the oxidation route with H_2O_2 over MgO as catalyst. **Reaction conditions:** 0.10 mmol of R-(+)-limonene and 1: 0.90: 30.3: 19.7: 15.7: 0.8 as weight ratios for R-(+)-limonene: MgO: H_2O: acetone: acetonitrile: H_2O_2, at 50 °C.

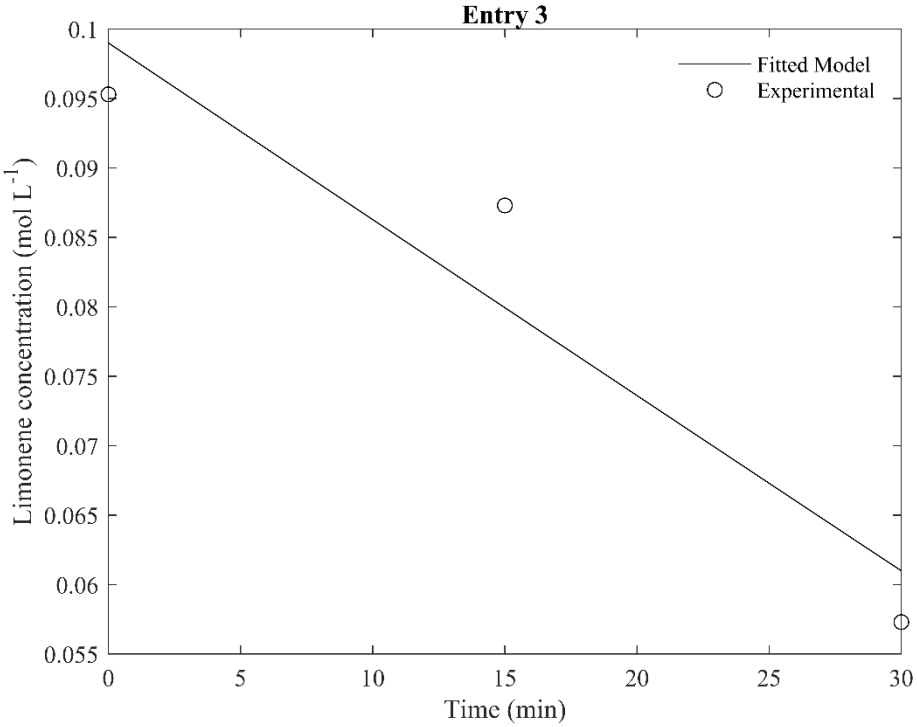

Figure 8.4. Fitting of limonene concentration for **entry 3** in the oxidation route with H_2O_2 over MgO as catalyst. **Reaction conditions:** 0.10 mmol of R-(+)-limonene and 1: 0.60: 30.3: 19.7: 15.7: 0.8 as weight ratios for R-(+)-limonene: MgO: H_2O: acetone: acetonitrile: H_2O_2, at 50 °C.

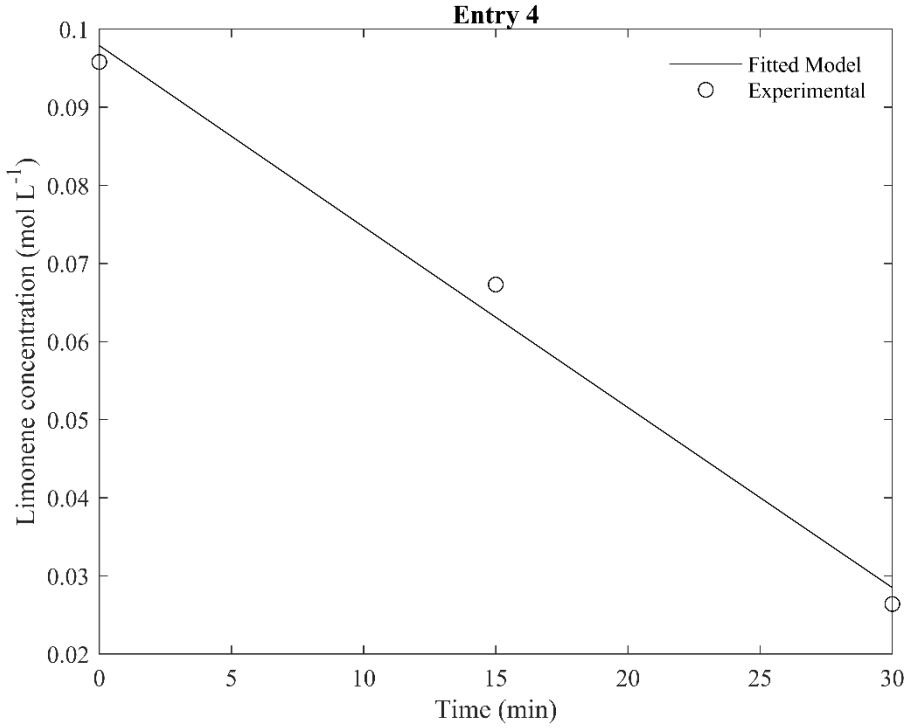

Figure 8.5. Fitting of limonene concentration for **entry 4** in the oxidation route with H_2O_2 over MgO as catalyst. **Reaction conditions:** 0.10 mmol of R-(+)-limonene and 1: 1.20: 30.3: 19.7: 15.7: 1.20 as weight ratios for R-(+)-limonene: MgO: H_2O: acetone: acetonitrile: H_2O_2, at 50 °C.

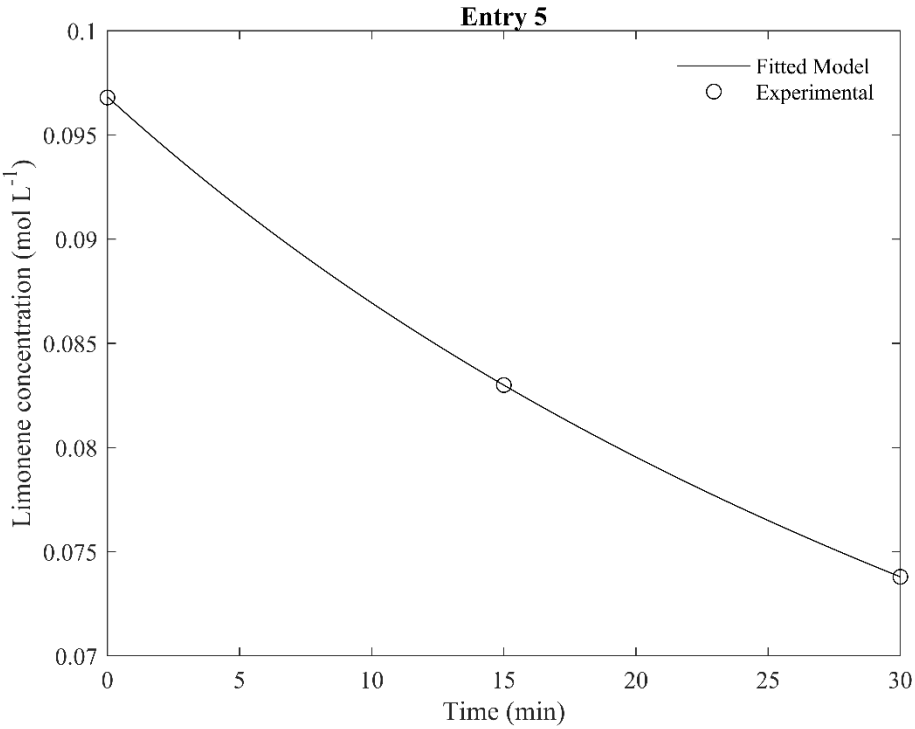

Figure 8.6. Fitting of limonene concentration for **entry 5** in the oxidation route with H_2O_2 over MgO as catalyst. **Reaction conditions:** 0.10 mmol of R-(+)-limonene and 1: 1.20: 30.3: 19.7: 15.7: 0.8 as weight ratios for R-(+)-limonene: MgO: H_2O: acetone: acetonitrile: H_2O_2, at 40 °C.

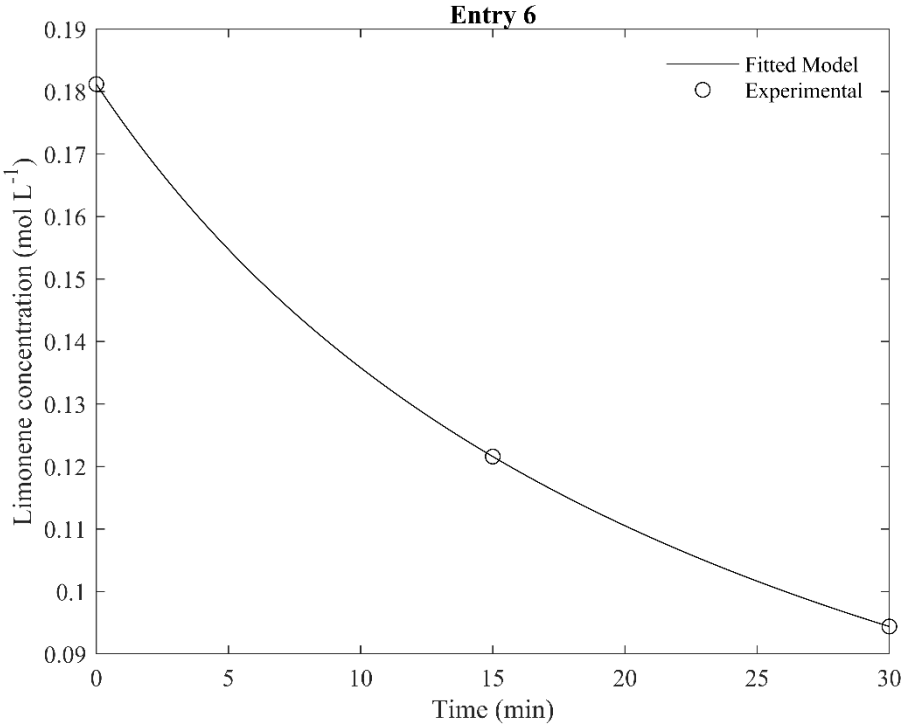

Figure 8.7. Fitting of limonene concentration for **entry 6** in the oxidation route with H_2O_2 over MgO as catalyst. **Reaction conditions:** 0.20 mmol of R-(+)-limonene and 1: 0.60: 16.22: 9.85: 7.85: 0.8 as weight ratios for R-(+)-limonene: MgO: H_2O: acetone: acetonitrile: H_2O_2, at 50 °C.

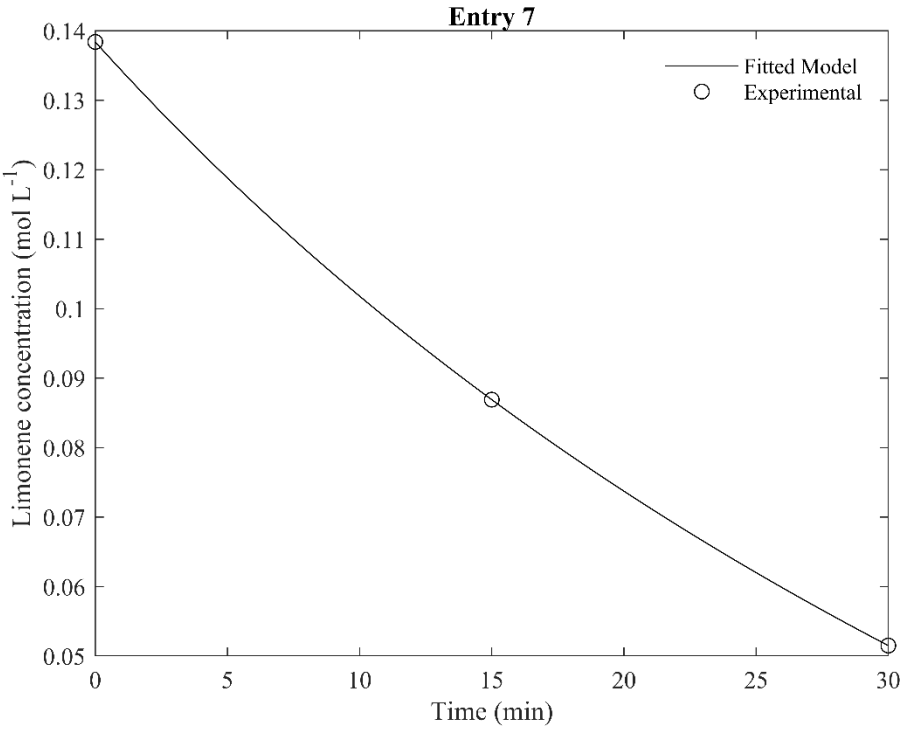

Figure 8.8. Fitting of limonene concentration for **entry 7** in the oxidation route with H_2O_2 over MgO as catalyst. **Reaction conditions:** 0.15 mmol of R-(+)-limonene and 1: 0.80: 20.91: 13.13: 10.47: 0.8 as weight ratios for R-(+)-limonene: MgO: H_2O: acetone: acetonitrile: H_2O_2, at 50 °C.

H_2O_2

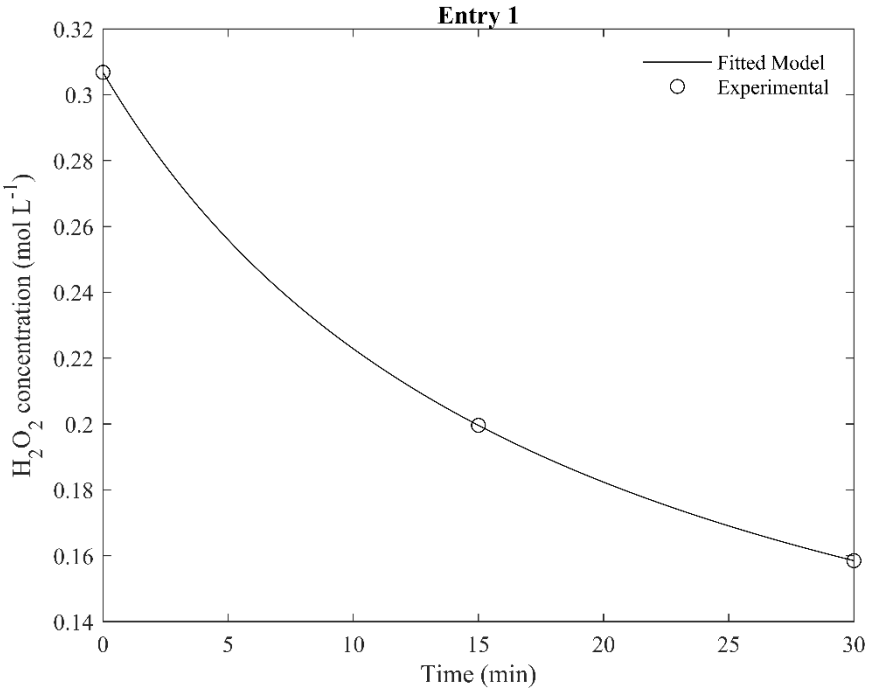

Figure 8.9. Fitting of H_2O_2 concentration for **entry 1** in the oxidation route with limonene over MgO as catalyst. **Reaction conditions:** 0.10 mmol of R-(+)-limonene and 1: 1.20: 30.3: 19.7: 15.7: 0.8 as weight ratios for R-(+)-limonene: MgO: H_2O: acetone: acetonitrile: H_2O_2, at 50 °C.

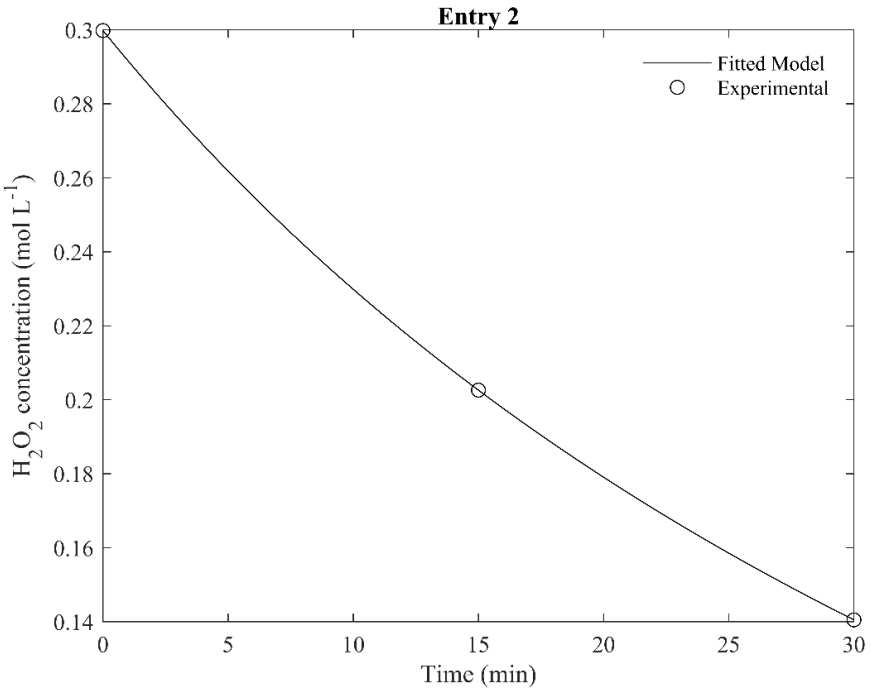

Figure 8.10. Fitting of H_2O_2 concentration for **entry 2** in the oxidation route with limonene over MgO as catalyst. **Reaction conditions:** 0.10 mmol of R-(+)-limonene and 1: 0.90: 30.3: 19.7: 15.7: 0.8 as weight ratios for R-(+)-limonene: MgO: H_2O: acetone: acetonitrile: H_2O_2, at 50 °C.

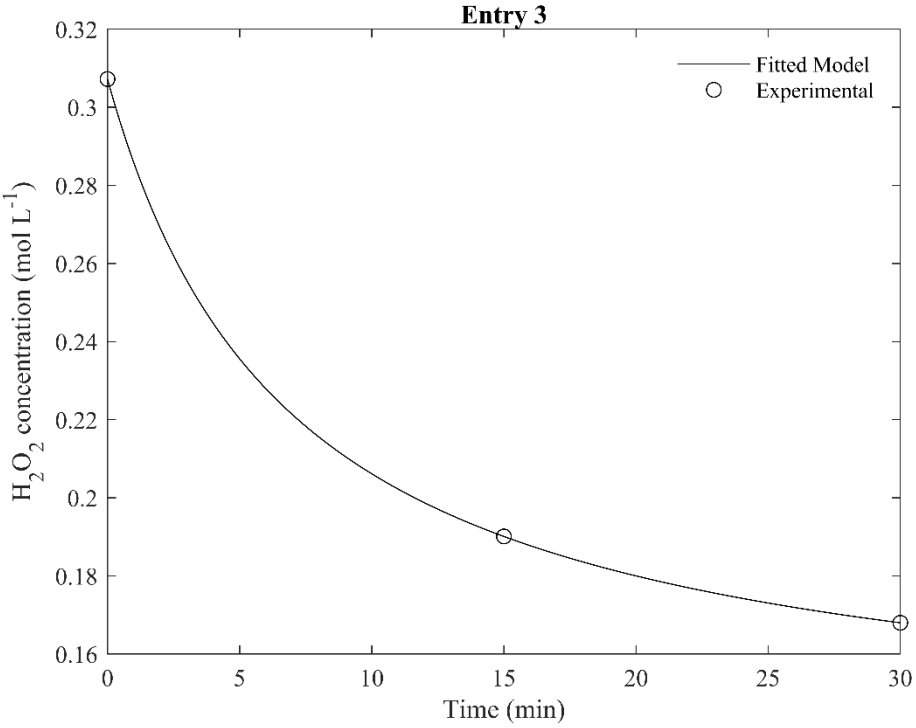

Figure 8.11. Fitting of H_2O_2 concentration for **entry 3** in the oxidation route with limonene over MgO as catalyst. **Reaction conditions:** 0.10 mmol of R-(+)-limonene and 1: 0.60: 30.3: 19.7: 15.7: 0.8 as weight ratios for R-(+)-limonene: MgO: H_2O: acetone: acetonitrile: H_2O_2, at 50 °C.

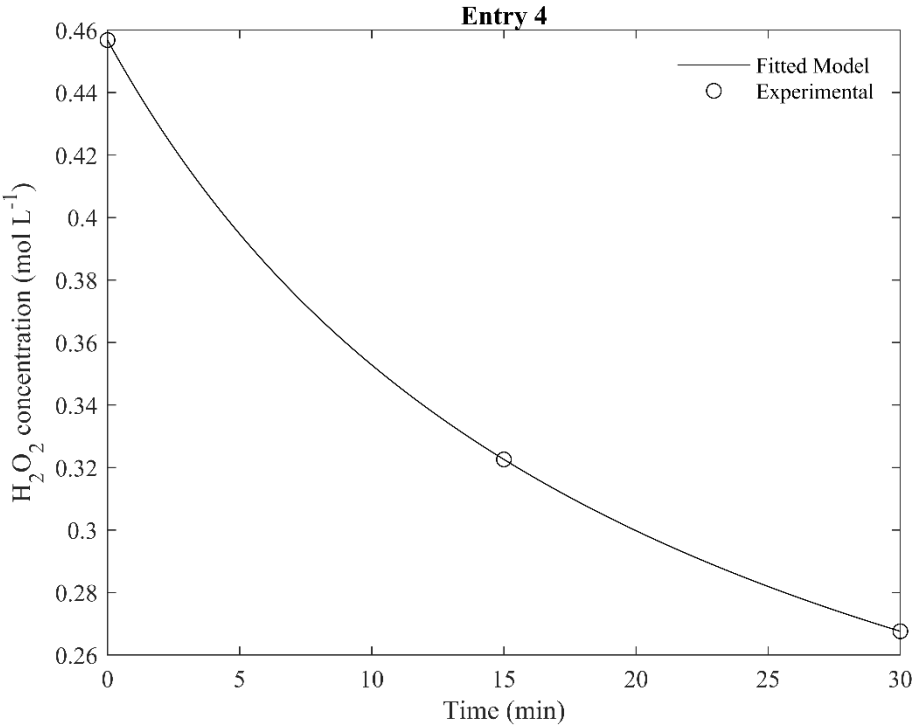

Figure 8.12. Fitting of H_2O_2 concentration for **entry 4** in the oxidation route with limonene over MgO as catalyst. **Reaction conditions:** 0.10 mmol of R-(+)-limonene and 1: 1.20: 30.3: 19.7: 15.7: 1.20 as weight ratios for R-(+)-limonene: MgO: H_2O: acetone: acetonitrile: H_2O_2, at 50 °C.

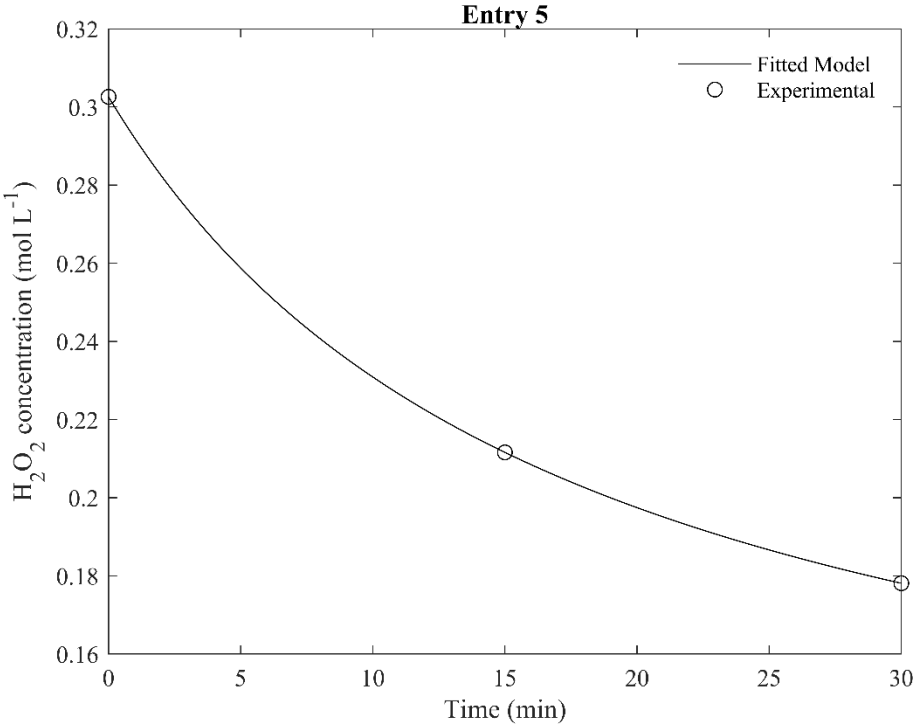

Figure 8.13. Fitting of H_2O_2 concentration for **entry 5** in the oxidation route with limonene over MgO as catalyst. **Reaction conditions:** 0.10 mmol of R-(+)-limonene and 1: 1.20: 30.3: 19.7: 15.7: 0.8 as weight ratios for R-(+)-limonene: MgO: H_2O: acetone: acetonitrile: H_2O_2, at 40 °C.

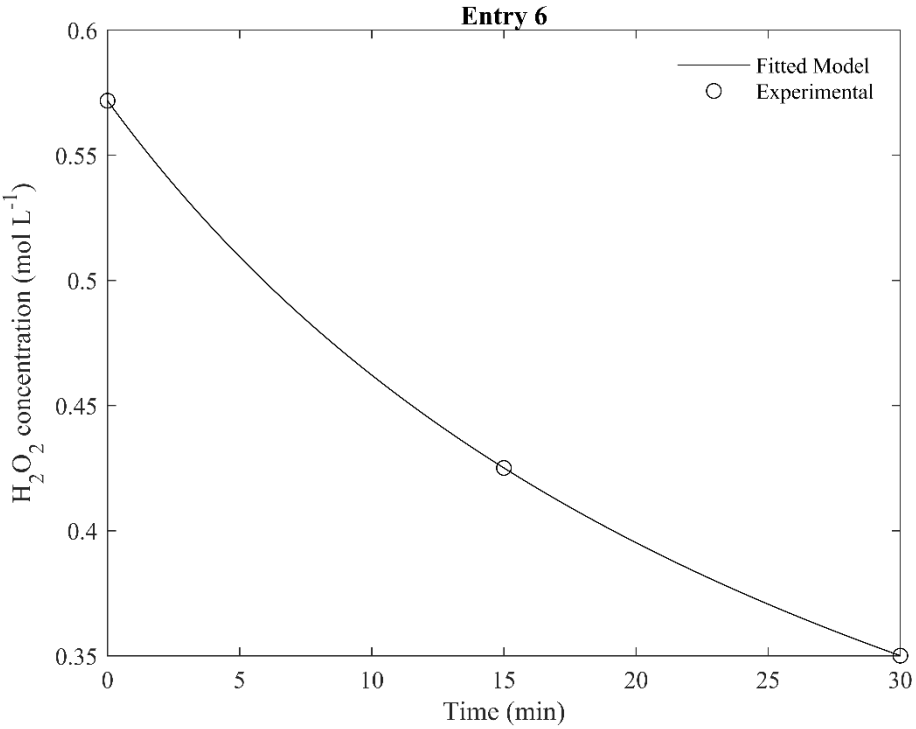

Figure 8.14. Fitting of H_2O_2 concentration for **entry 6** in the oxidation route with limonene over MgO as catalyst. **Reaction conditions:** 0.20 mmol of R-(+)-limonene and 1: 0.60: 16.22: 9.85: 7.85: 0.8 as weight ratios for R-(+)-limonene: MgO: H_2O: acetone: acetonitrile: H_2O_2, at 50 °C.

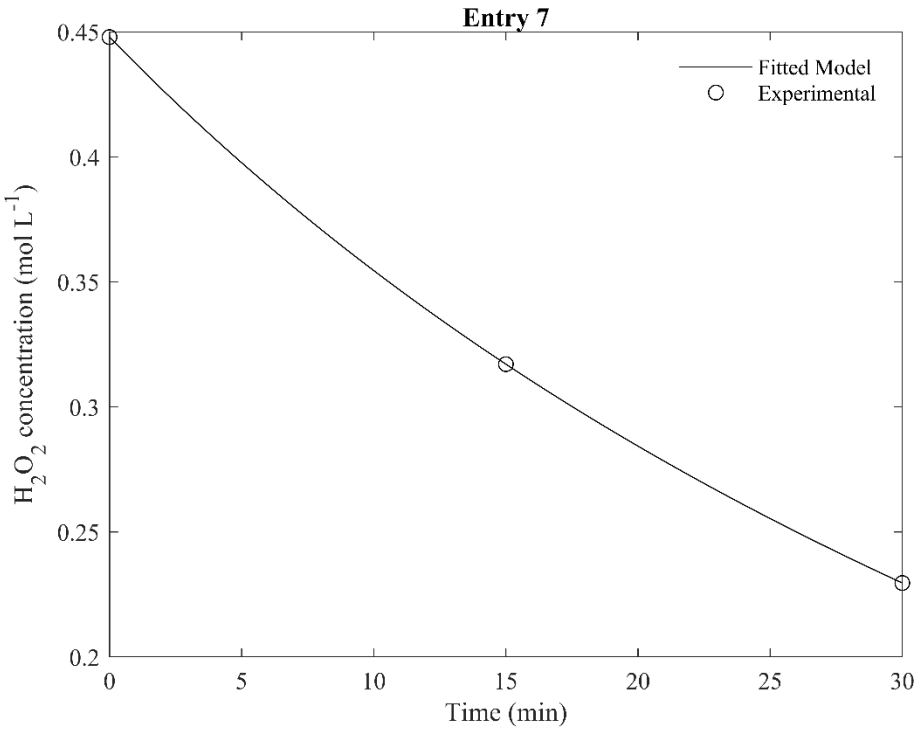

Figure 8.15. Fitting of H_2O_2 concentration for **entry 7** in the oxidation route with limonene over MgO as catalyst. **Reaction conditions:** 0.15 mmol of R-(+)-limonene and 1: 0.80: 20.91: 13.13: 10.47: 0.8 as weight ratios for R-(+)-limonene: MgO: H_2O: acetone: acetonitrile: H_2O_2, at 50 °C.

Table 8.1 and **Table 8.2** show the values of the three parameters for fitting the experimental concentrations of limonene and H_2O_2, respectively, to the mathematical model, and two stats parameters for evaluating the goodness of fits such as determination coefficient (R^2), and the sum of squared errors (SSE).

Table 8.1. Parameters associated with the mathematical model for fitting limonene molar concentration as a function of time for the 7 experimental runs.

Entry	p_1	p_2	q_1	R^2	SSE
1	-0.7297	62.73	641.70	0.996	2.47E-06
2	-11.4900	686.00	7020.00	0.923	1.01E-04
3	-6.3970	504.60	5097.00	0.898	8.15E-05
4	-13.2200	560.50	5725.00	0.989	2.64E-05
5	0.0281	5.76	59.49	1.000	1.29E-09
6	0.0215	4.56	25.18	1.000	5.69E-14
7	-0.1396	9.13	65.95	1.000	2.96E-12

Table 8.2. Parameters associated with the mathematical model for fitting H_2O_2 molar concentration as a function of time for the 7 experimental runs.

Entry	p_1	p_2	q_1	R^2	SSE
1	0.06629	5.723	18.65	1.00	1.89E-13
2	-0.1413	15.91	53.08	1.00	9.01E-14
3	0.1356	2.144	6.979	1.00	1.12E-11
4	0.1362	9.517	20.83	1.00	5.03E-17
5	0.1056	5.289	17.48	1.00	7.34E-13
6	0.1182	17.94	31.37	1.00	3.29E-10
7	-0.2115	27.15	60.62	1.00	2.86E-13

By differentiation of **Eq. (8.19)**, r_i^{exp} can be calculated according to **Eq. (8.20)**. **Figure 8.16** to **Figure 8.22** and **Figure 8.23** to **Figure 8.29** show the profiles of the reaction rate of limonene and H_2O_2, respectively, for each one of the 7 tests.

$$R_i^{exp} = \frac{V}{W}\frac{dC_i^{exp}}{dt} \quad (i = \text{Limonene}, H_2O_2) \tag{8.20}$$

Limonene

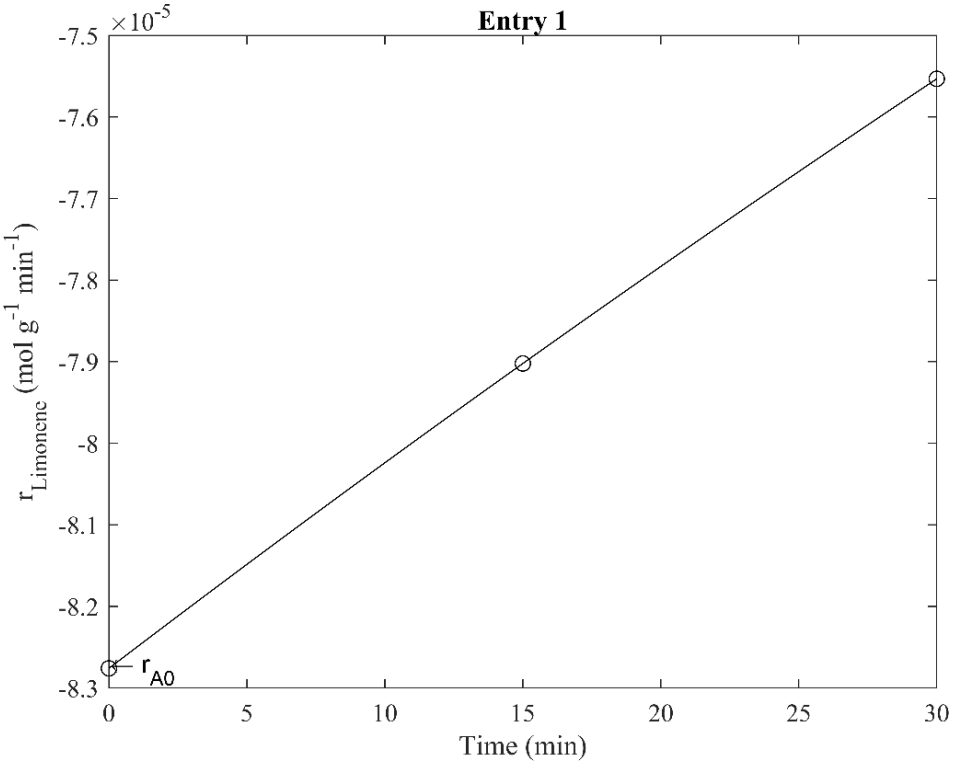

Figure 8.16. Reaction rate of limonene as a function of time for **entry 1** in the oxidation route with H_2O_2 over MgO as catalyst.

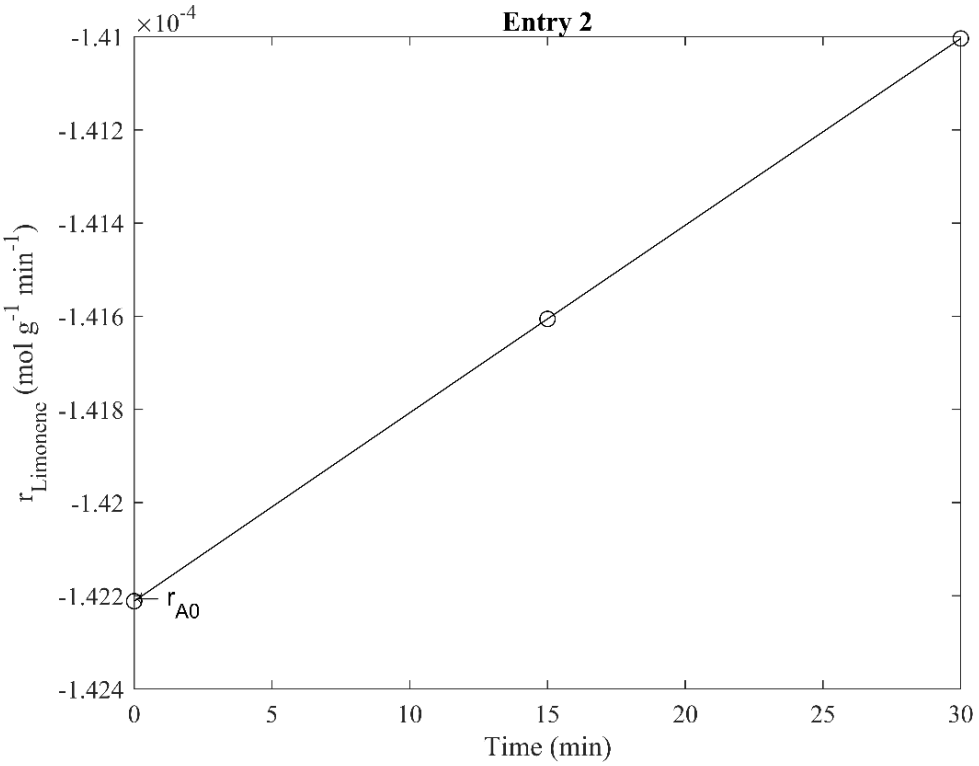

Figure 8.17. Reaction rate of limonene as a function of time for **entry 2** in the oxidation route with H_2O_2 over MgO as catalyst.

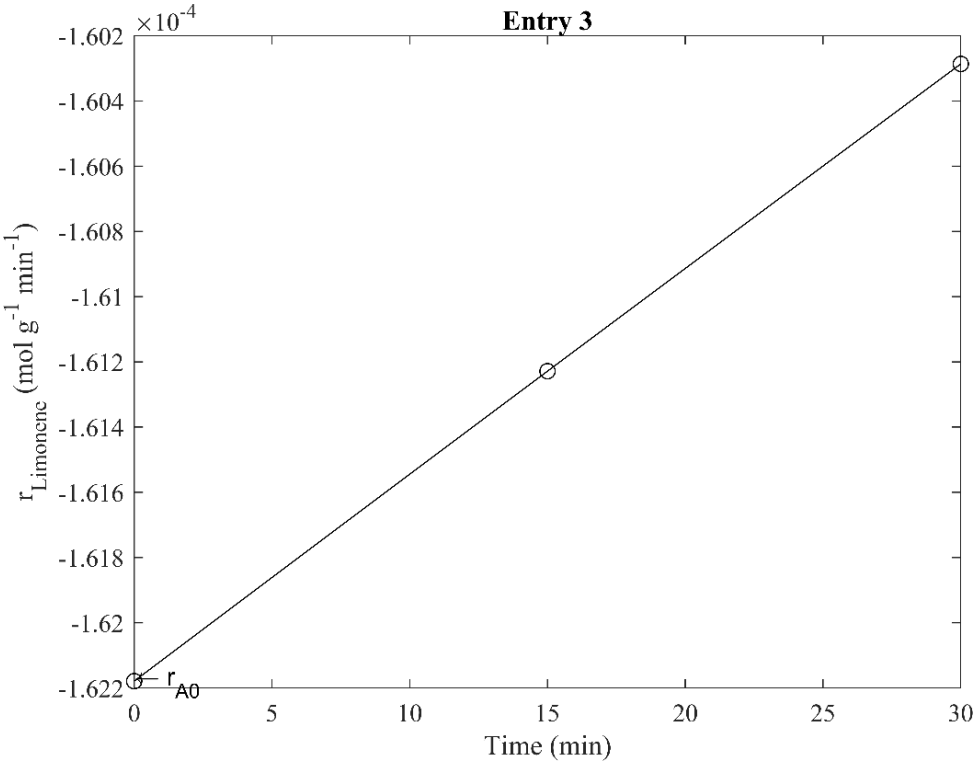

Figure 8.18. Reaction rate of limonene as a function of time for **entry 3** in the oxidation route with H_2O_2 over MgO as catalyst.

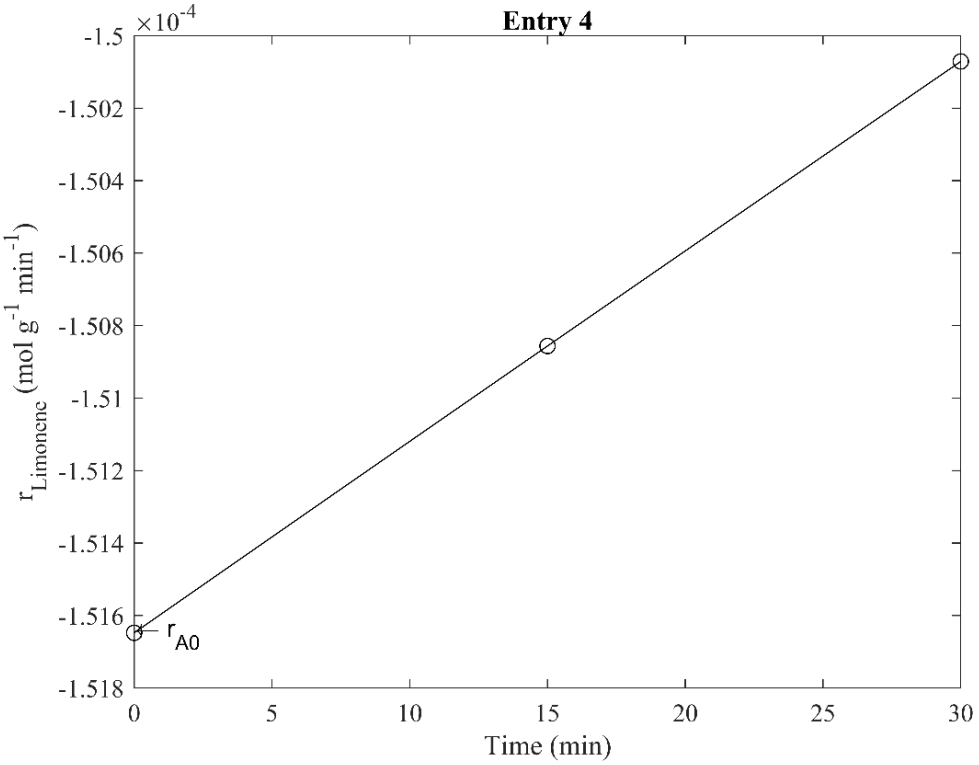

Figure 8.19. Reaction rate of limonene as a function of time for **entry 4** in the oxidation route with H_2O_2 over MgO as catalyst.

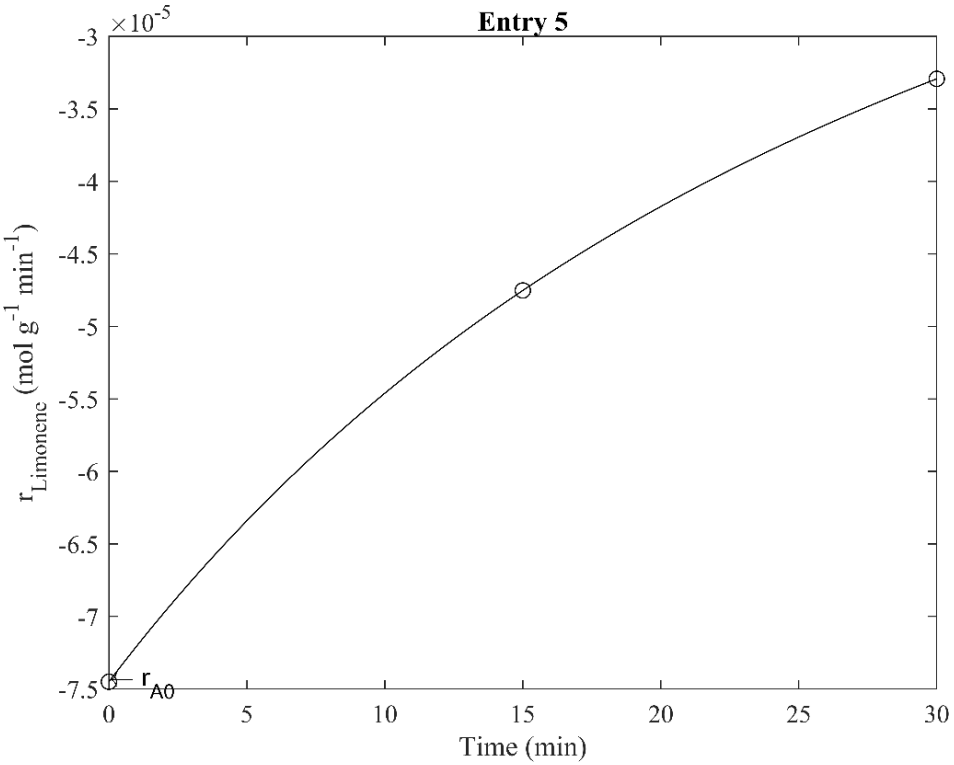

Figure 8.20. Reaction rate of limonene as a function of time for **entry 5** in the oxidation route with H_2O_2 over MgO as catalyst.

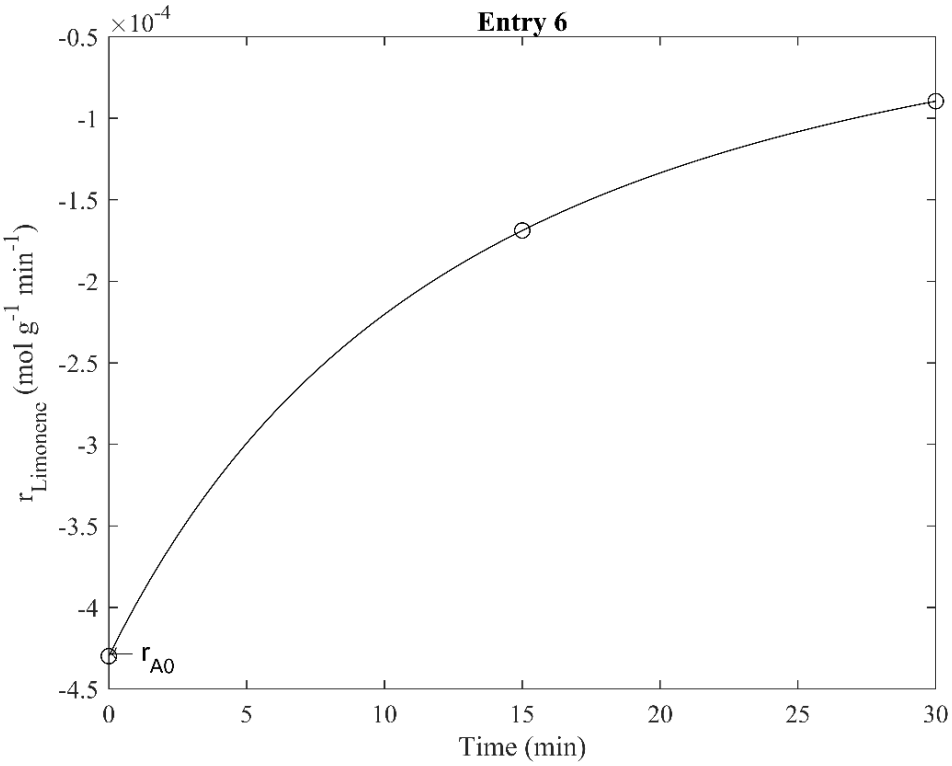

Figure 8.21. Reaction rate of limonene as a function of time for **entry 6** in the oxidation route with H_2O_2 over MgO as catalyst.

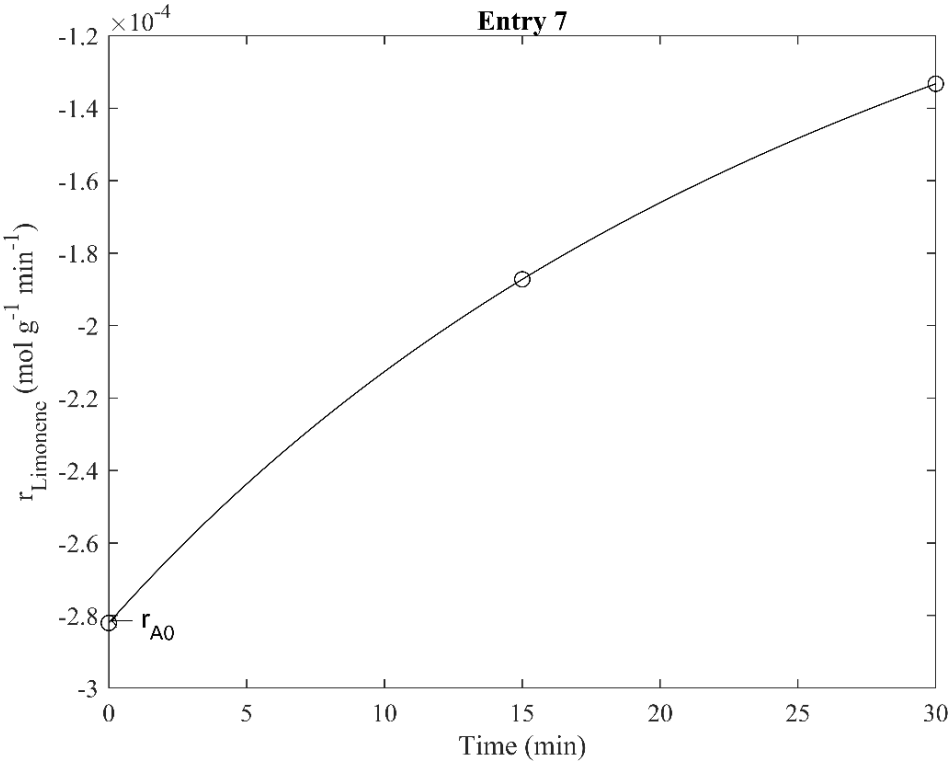

Figure 8.22. Reaction rate of limonene as a function of time for **entry 7** in the oxidation route with H_2O_2 over MgO as catalyst.

H_2O_2

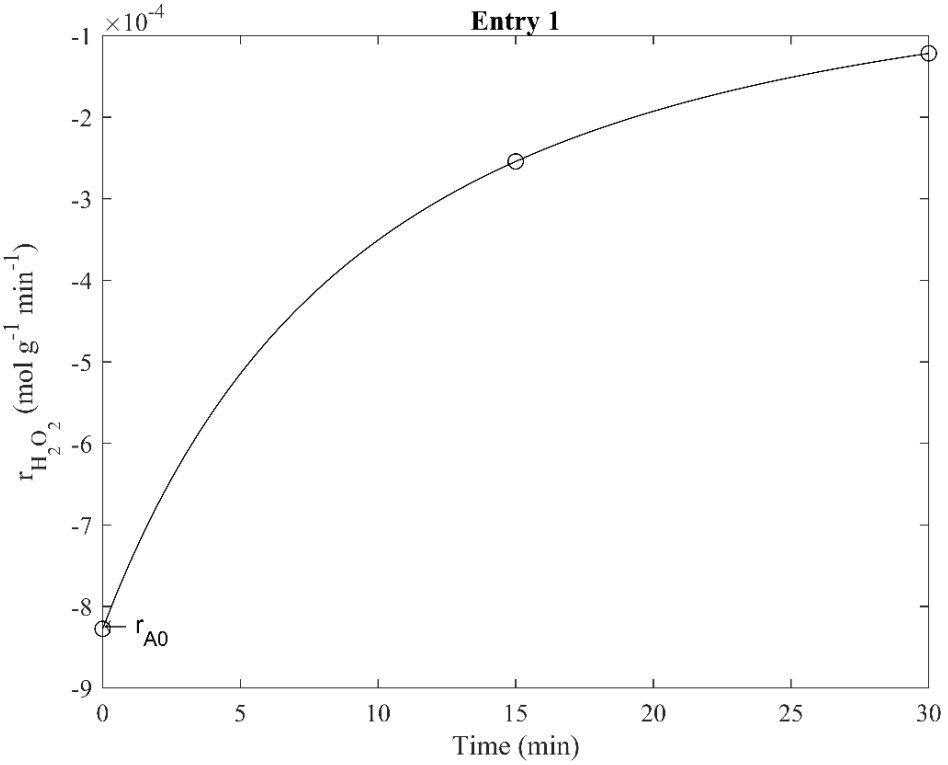

Figure 8.23. Reaction rate of H_2O_2 as a function of time for **entry 1** in the oxidation route with limonene over MgO as catalyst.

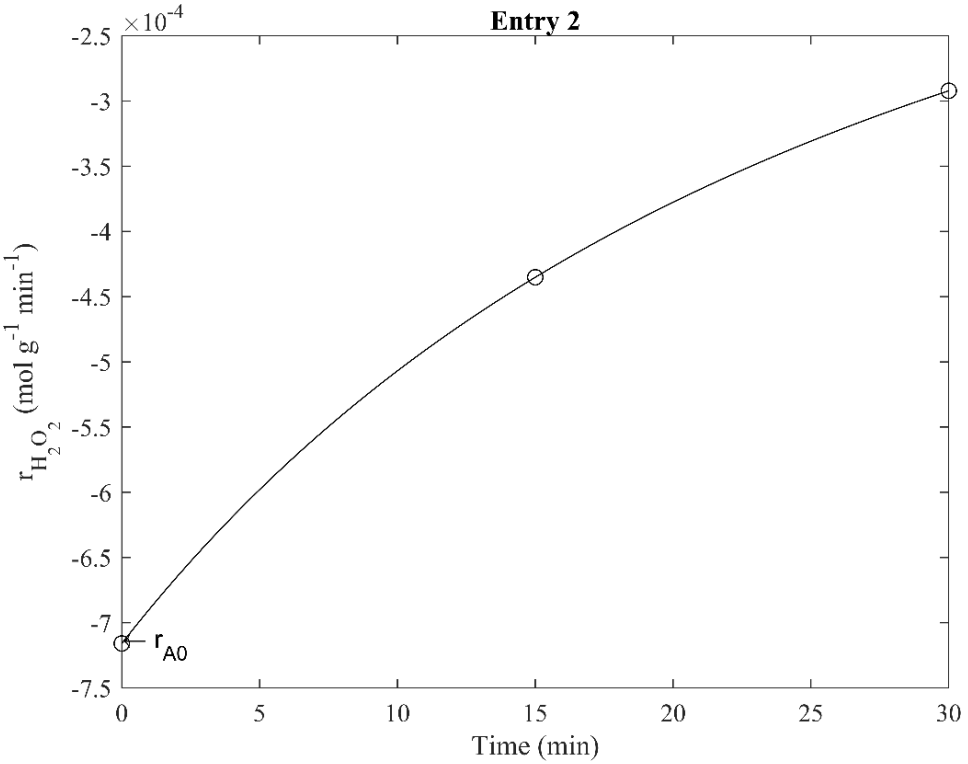

Figure 8.24. Reaction rate of H_2O_2 as a function of time for **entry 2** in the oxidation route with limonene over MgO as catalyst.

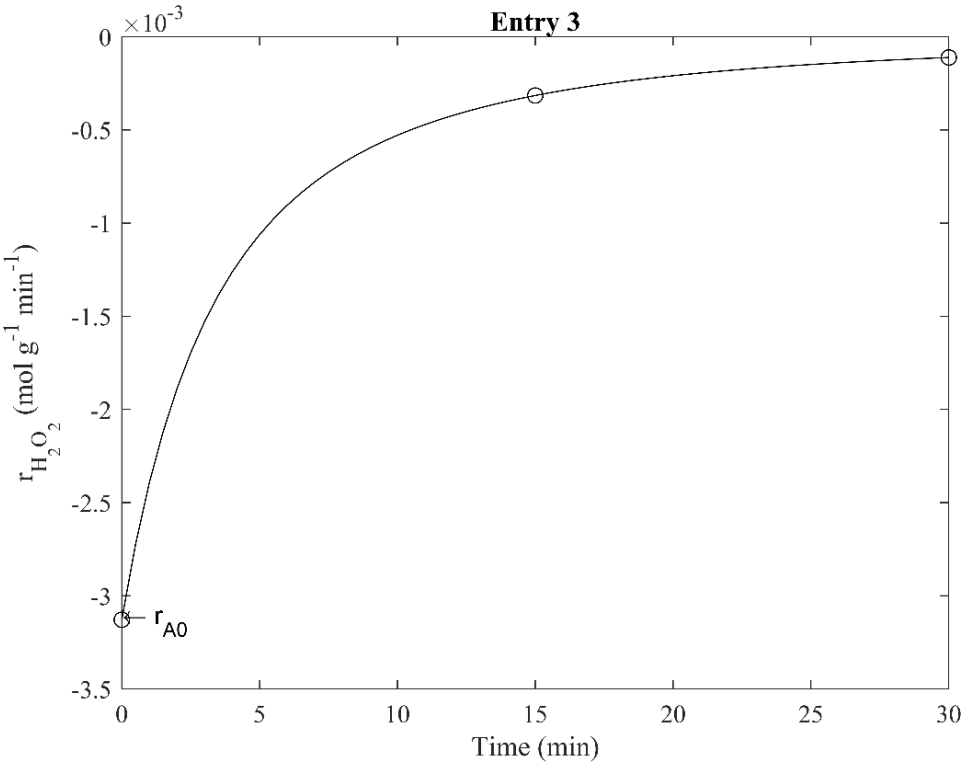

Figure 8.25. Reaction rate of H_2O_2 as a function of time for **entry 3** in the oxidation route with limonene over MgO as catalyst.

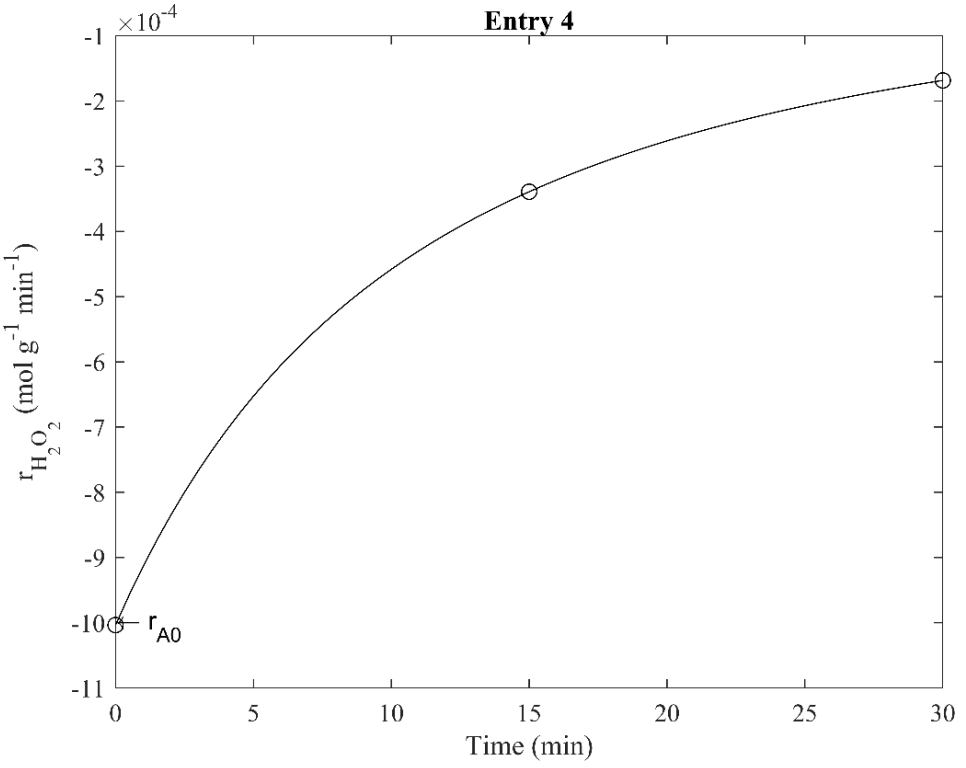

Figure 8.26. Reaction rate of H_2O_2 as a function of time for **entry 4** in the oxidation route with limonene over MgO as catalyst.

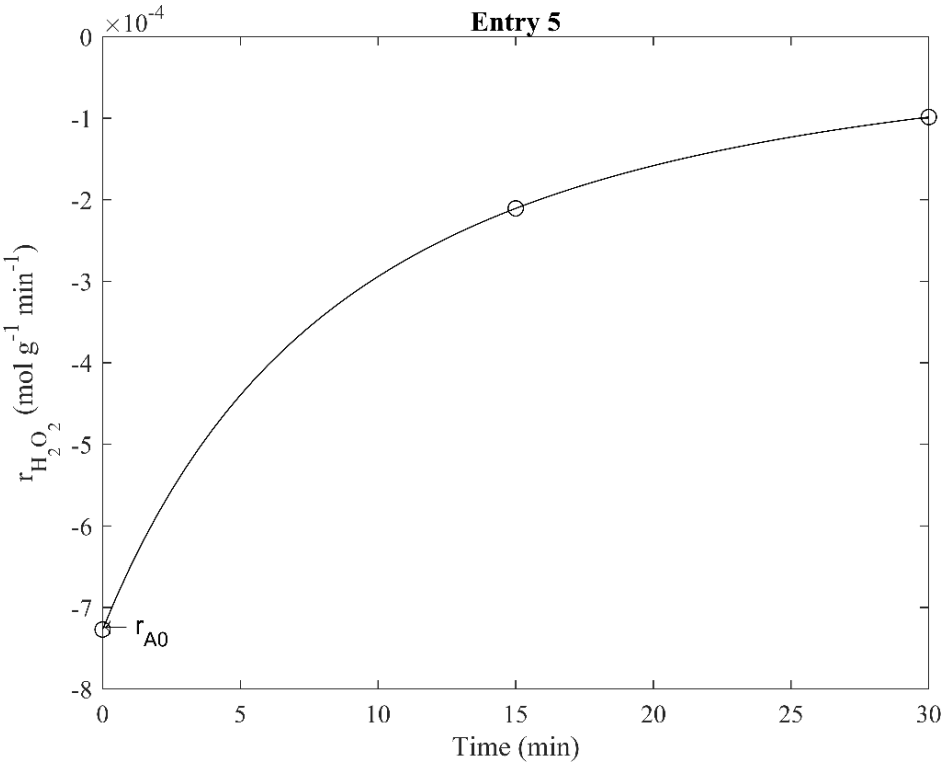

Figure 8.27. Reaction rate of H_2O_2 as a function of time for **entry 5** in the oxidation route with limonene over MgO as catalyst.

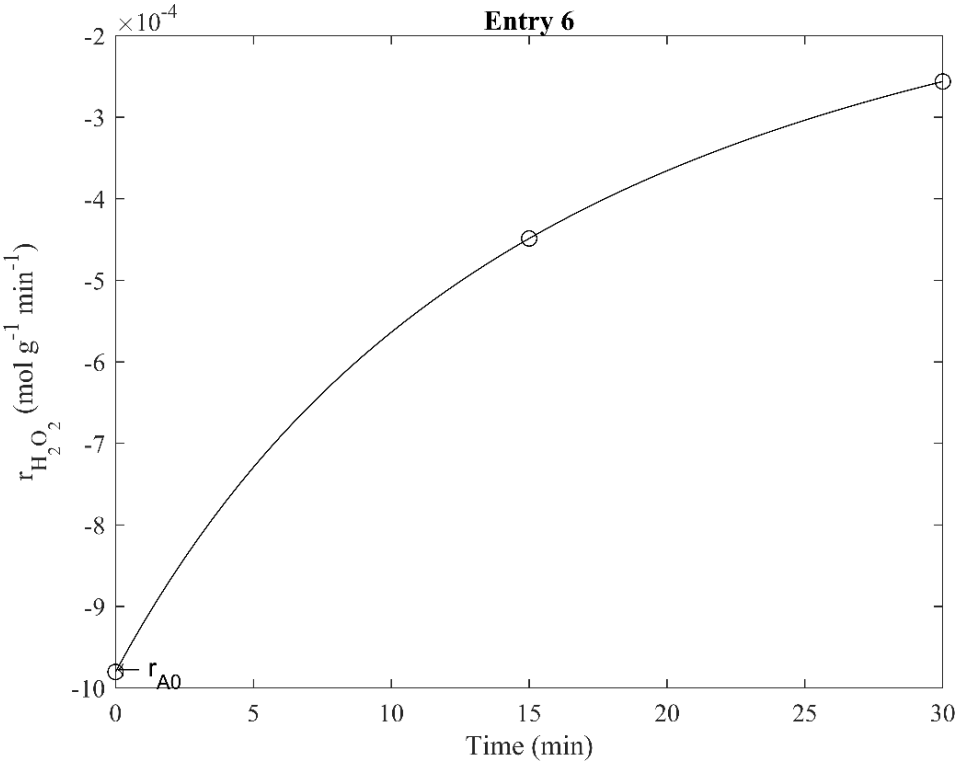

Figure 8.28. Reaction rate of H_2O_2 as a function of time for **entry 6** in the oxidation route with limonene over MgO as catalyst.

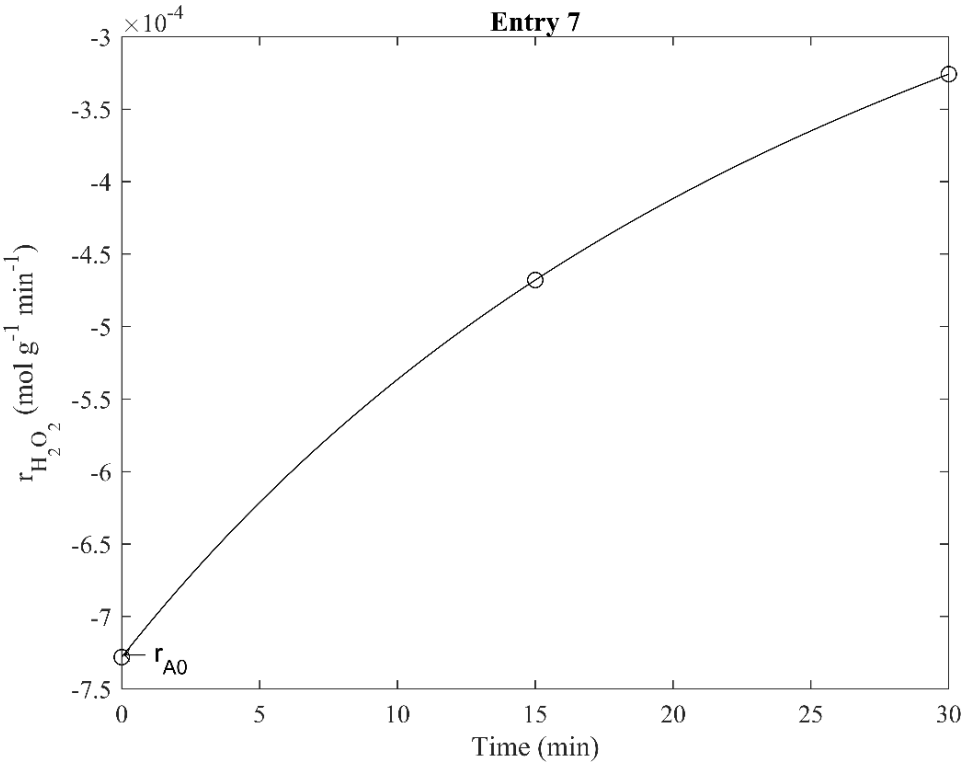

Figure 8.29. Reaction rate of H_2O_2 as a function of time for **entry 7** in the oxidation route with limonene over MgO as catalyst.

8.1.3. SEM-EDS analysis

$Mg(OH)_2$

Spectrum processing :
Peaks possibly omitted : 1.665, 2.149, 2.431, 9.703, 11.464 keV

Processing option : All elements analyzed (Normalised)
Number of iterations = 3

Standard :
O SiO2 1-Jun-1999 12:00 AM
Mg MgO 1-Jun-1999 12:00 AM

Element	App Conc.	Intensity Corrn.	Weight%	Weight% Sigma	Atomic%
O K	54.75	1.4791	51.00	0.24	61.26
Mg K	30.96	0.8704	49.00	0.24	38.74
Totals			100.00		

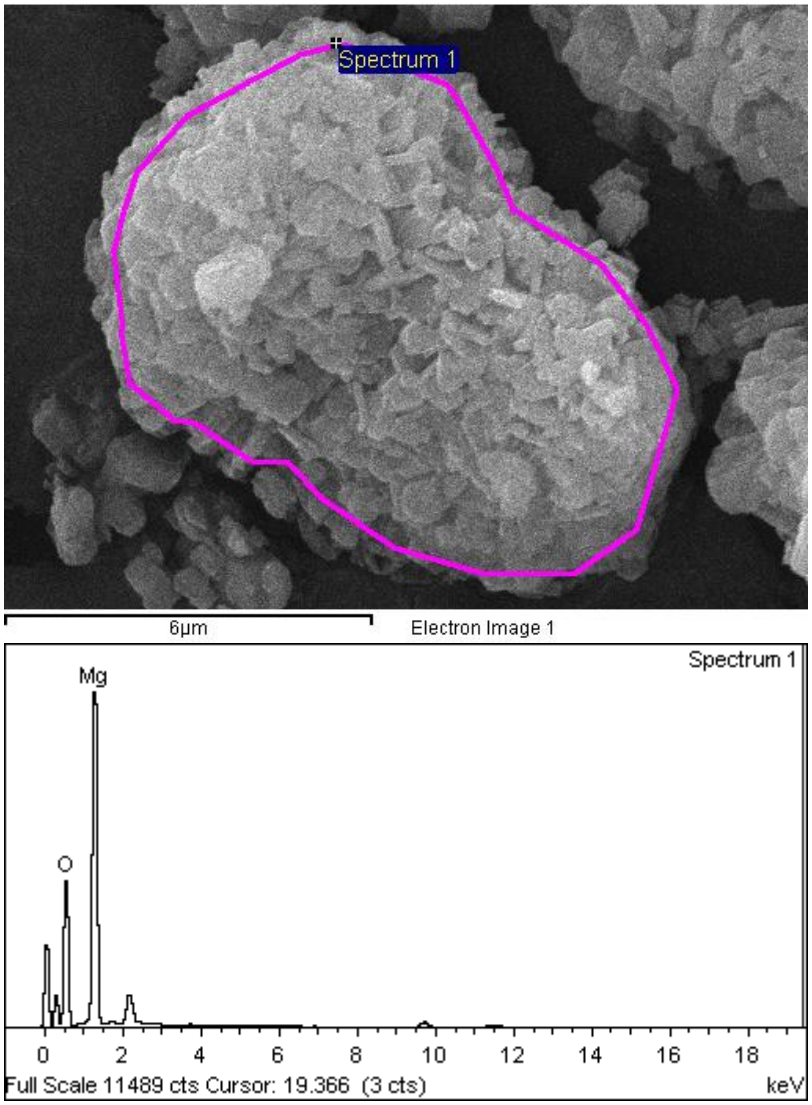

Figure 8.30. SEM-EDS of $Mg(OH)_2$.

MgO calcined at 600 °C (10 °C min^{-1} for 1 h)

Spectrum processing :
Peaks possibly omitted : 2.150, 2.435, 6.300, 9.704, 11.475, 13.360 keV

Processing option : All elements analyzed (Normalised)
Number of iterations = 3

Standard :
O SiO2 1-Jun-1999 12:00 AM
Mg MgO 1-Jun-1999 12:00 AM

Element	App Conc.	Intensity Corrn.	Weight%	Weight% Sigma	Atomic%
O K	60.93	1.3092	38.81	0.20	49.08
Mg K	71.57	0.9757	61.19	0.20	50.92
Totals			100.00		

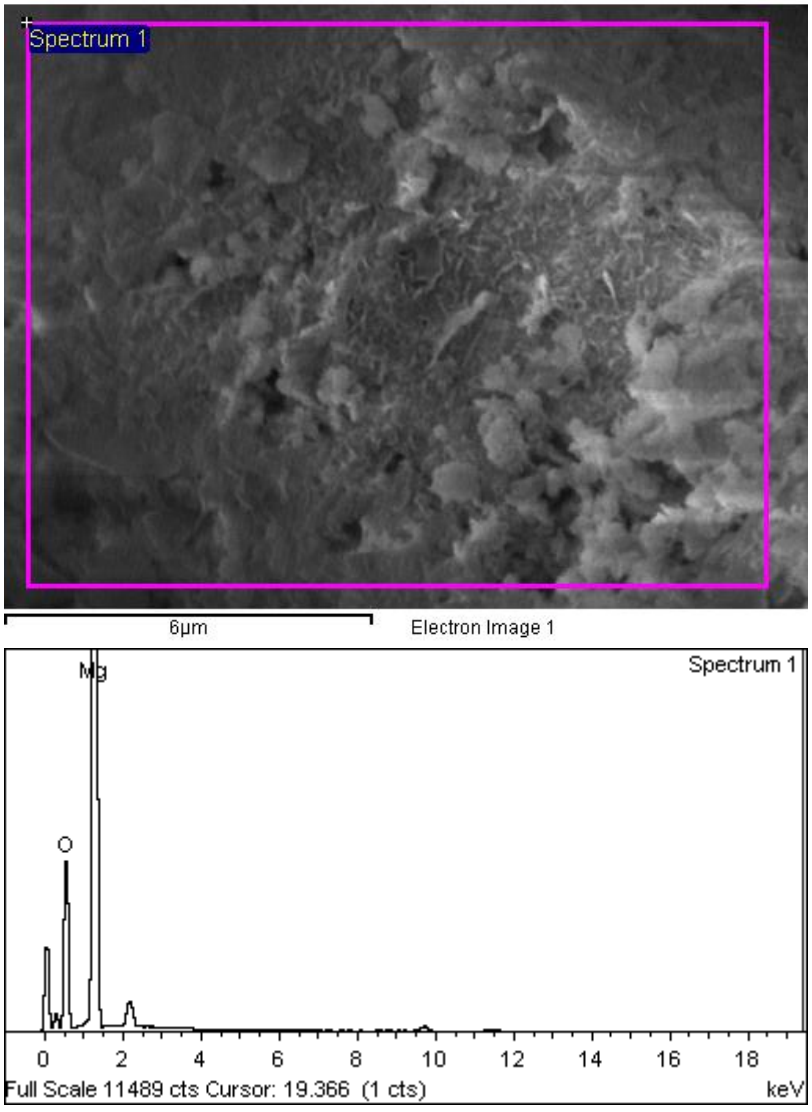

Figure 8.31. SEM-EDS of MgO calcined at 600 °C.

MgO fresh catalyst

Spectrum processing :
Peaks possibly omitted : 1.669, 2.149, 2.438, 8.494, 9.702, 11.477, 13.365, 13.710 keV

Processing option : All elements analyzed (Normalised)
Number of iterations = 2

Standard :
O SiO2 1-Jun-1999 12:00 AM
Mg MgO 1-Jun-1999 12:00 AM

Element	App Conc.	Intensity Corrn.	Weight%	Weight% Sigma	Atomic%
O K	11.61	1.4901	51.59	0.26	61.82
Mg K	6.34	0.8648	48.41	0.26	38.18
Totals			100.00		

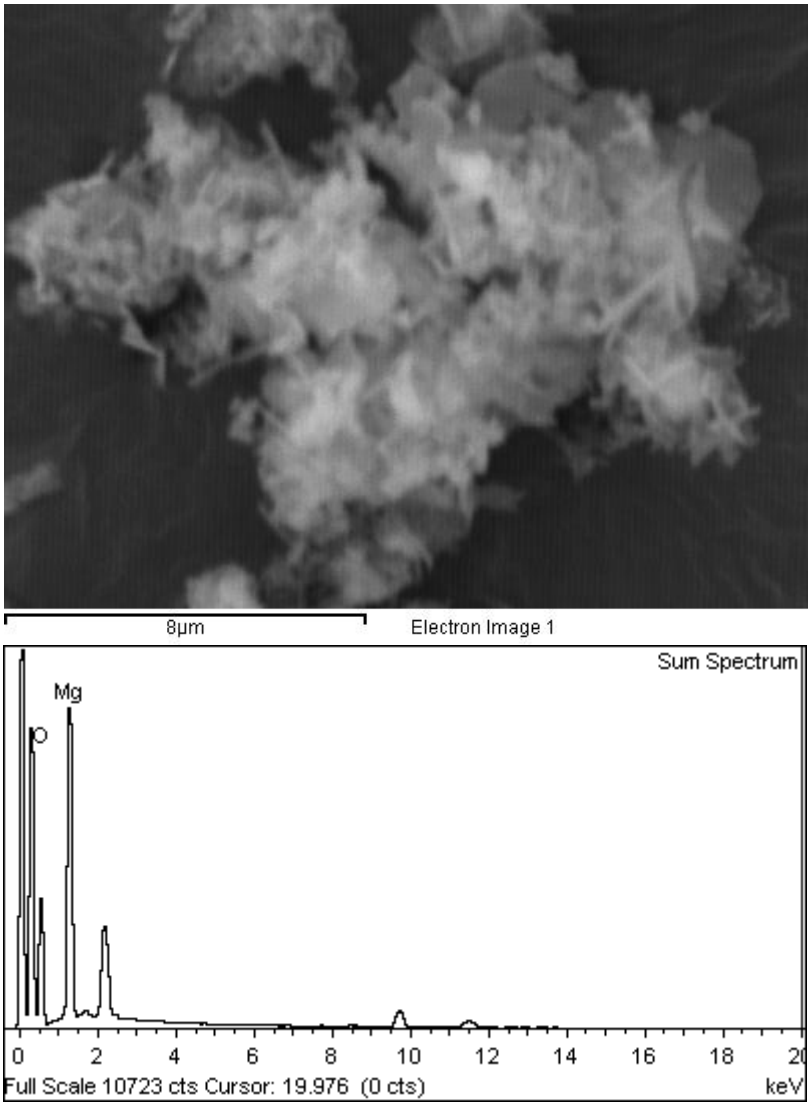

Figure 8.32. SEM-EDS of MgO fresh catalyst.

MgO spent catalyst

Spectrum processing :
Peaks possibly omitted : 1.671, 2.147, 2.435, 2.825, 4.513, 6.400, 9.704, 11.472, 13.358 keV

Processing option : All elements analyzed (Normalised)
Number of iterations = 2

Standard :
O SiO2 1-Jun-1999 12:00 AM
Mg MgO 1-Jun-1999 12:00 AM

Element	App Conc.	Intensity Corrn.	Weight%	Weight% Sigma	Atomic%
O K	20.45	1.4057	45.85	0.18	56.26
Mg K	15.71	0.9111	54.15	0.18	43.74
Totals			100.00		

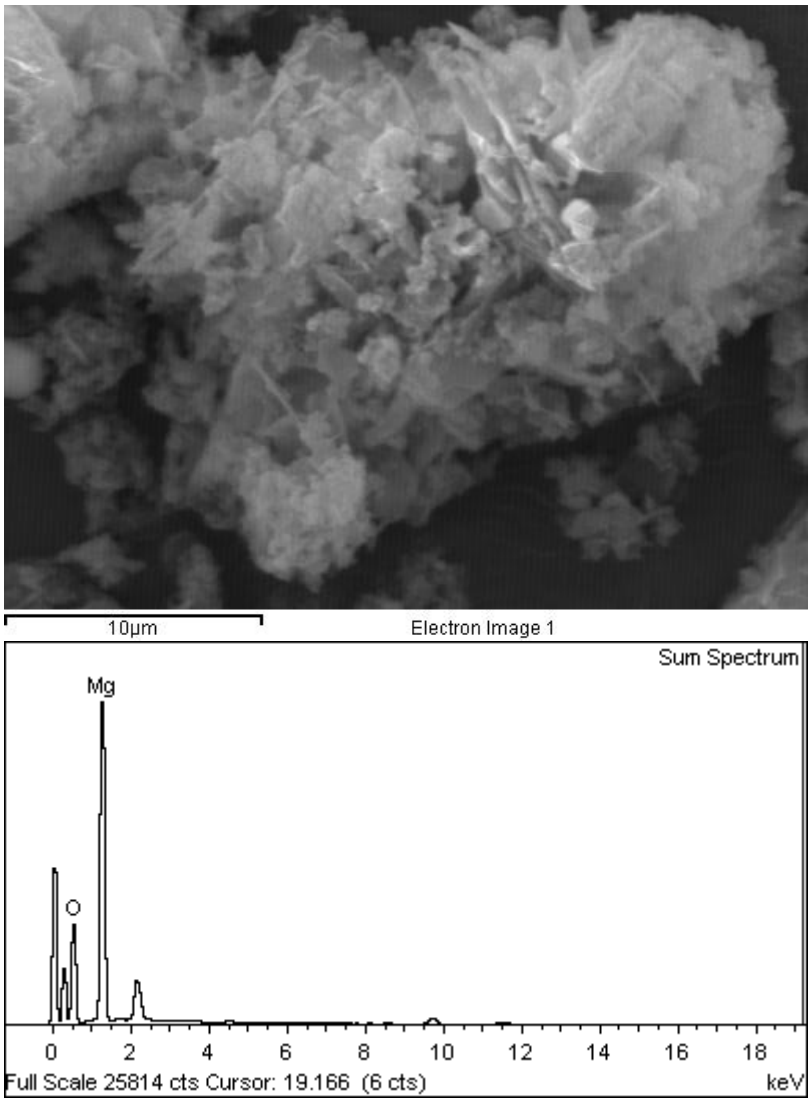

Figure 8.33. SEM-EDS of MgO spent catalyst.

8.1.4. Estimation of diffusion coefficient using Aspen Plus software

The aspen Physical Property System has seven built-in diffusivity models: Chapman-Enskog-Wilke-Lee (Binary) and Chapman-Enskog-Wilke-Lee (Mixtury) for low pressure vapor, Dawson-Khoury-Kobayashi (Binary) and Dawson-Khoury-Kobayashi (Mixture) for vapor, Nernst-Hartley for electrolyte, and Wilke-Chang (Binary) and Wilke-Chang (Mixture) for liquid. In this work, the last model was employed by Aspen for calculating the diffusion coefficients, which is described by **Eqs. (8.21)** and **(8.22)**:

$$D_i^l(m^2\ s^{-1}) = 1.17282x10^{-16}\frac{(\varphi M)^{1/2}T}{n^l\left(V_{bi}{}^l\right)^{0.6}} \quad \textbf{(8.21)}$$

$$\varphi M = \frac{\sum_{j\neq i} x_j \varphi_j M_j}{\sum_{j\neq i} x_j} \quad \textbf{(8.22)}$$

Where:

φ_j: Association factor of solvent: 2.26 for water, 1.90 for methanol, 1.50 for ethanol, 1.20 for propyl alcohols and n-butanol, and 1.00 for all other solvents.
n^l: Mixture liquid viscosity of all no diffusing components (kg m^{-1} s^{-1}).
x_j: mole fraction of specie i in the liquid mixture.
M_j: Molecular weight of specie i.
T: Absolute temperature (K).
$V_{bi}{}^l$: Liquid molar volume at the normal boiling point of specie i (m^3 $kmol^{-1}$).

8.1.5. Weisz-Prater criterion

Table 8.3. Weisz-Prater criterion for limonene.

Entry	V (mL)	W (mg)	r_{L0} (mol g^{-1} min^{-1})	C_{L0} (mol L^{-1})	$D_{L,L}$ (cm^2 s^{-1})	$D_{L,eff}$ (cm^2 s^{-1})	$N_{W-P\ (L)}$
1	1.06	16.52	-0.000083	0.096463	1.52310E-05	3.34685E-06	0.1518
2	1.06	12.28	-0.000142	0.093637	1.52310E-05	3.34685E-06	0.2687
3	1.05	8.28	-0.000162	0.095346	1.52310E-05	3.34685E-06	0.3009
4	1.06	16.30	-0.000152	0.095809	1.52833E-05	3.35834E-06	0.2791
5	1.06	16.45	-0.000074	0.096774	1.26807E-05	2.78645E-06	0.1635
6	1.11	16.40	-0.000430	0.181233	1.51279E-05	3.32419E-06	0.4227
7	1.09	16.30	-0.000282	0.138396	1.51795E-05	3.33553E-06	0.3618

Table 8.4. Weisz-Prater criterion for H_2O_2.

Entry	V (mL)	W (mg)	$r_{H2O2,0}$ (mol g^{-1} min^{-1})	$C_{H2O2,0}$ (mol L^{-1})	$D_{H2O2,L}$ (cm^2 s^{-1})	$D_{H2O2,eff}$ (cm^2 s^{-1})	$N_{W-P\ (H2O2)}$
1	1.06	16.52	-0.000828	0.306766	5.03541E-05	1.10648E-05	0.1444
2	1.06	12.28	-0.000716	0.299842	5.03541E-05	1.10648E-05	0.1277
3	1.05	8.28	-0.003129	0.307183	5.03541E-05	1.10648E-05	0.5451
4	1.06	16.30	-0.001004	0.456835	5.07188E-05	1.11449E-05	0.1167
5	1.06	16.45	-0.000727	0.302644	4.19265E-05	9.21290E-06	0.1543
6	1.11	16.40	-0.000981	0.571777	5.04527E-05	1.10864E-05	0.0916
7	1.09	16.30	-0.000728	0.447910	5.04036E-05	1.10757E-05	0.0869

8.1.6. Chromatograms of the reusability tests

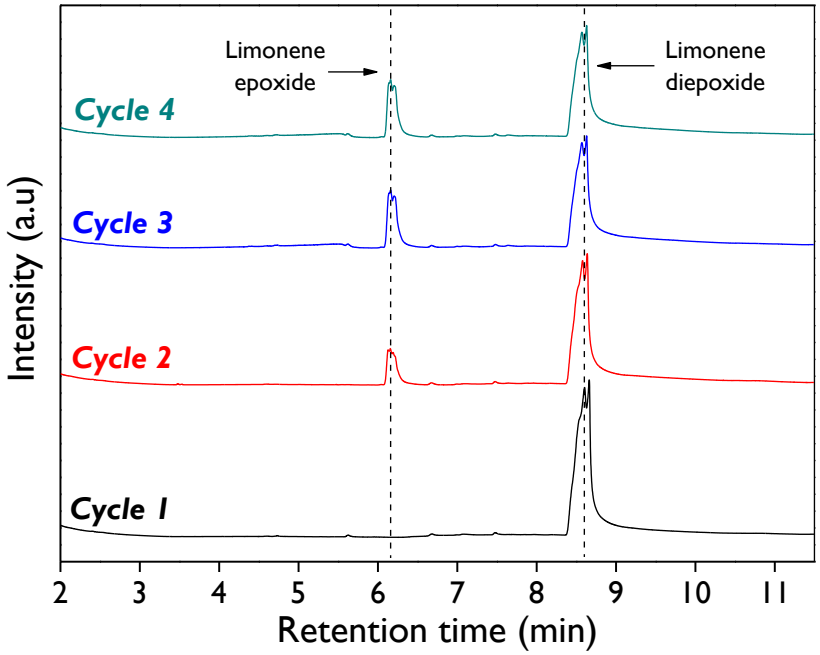

Figure 8.34. Chromatograms of the reusability tests for commercial MgO.

8.2. Chapter 3

8.2.1. XRD patterns

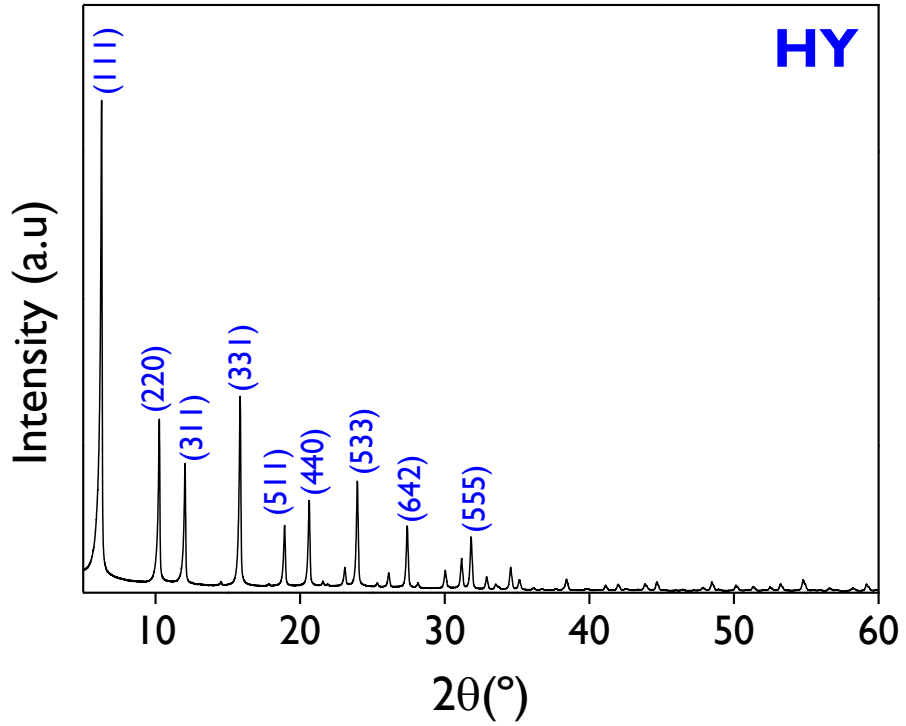

Figure 8.35. XRD pattern of the HY material.

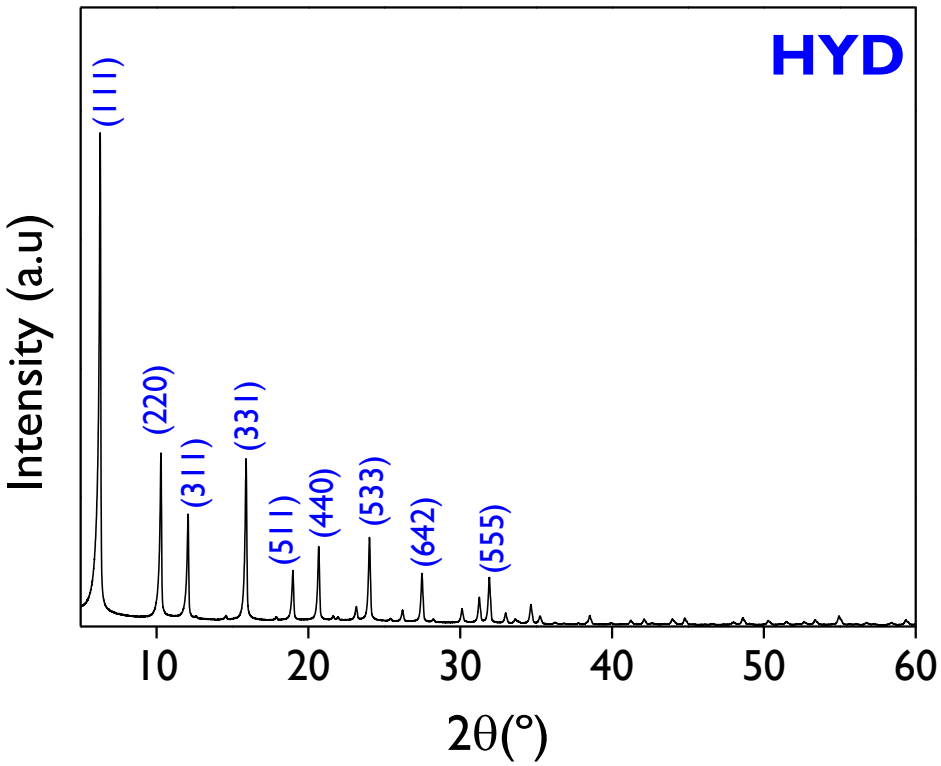

Figure 8.36. XRD pattern of the HYD material.

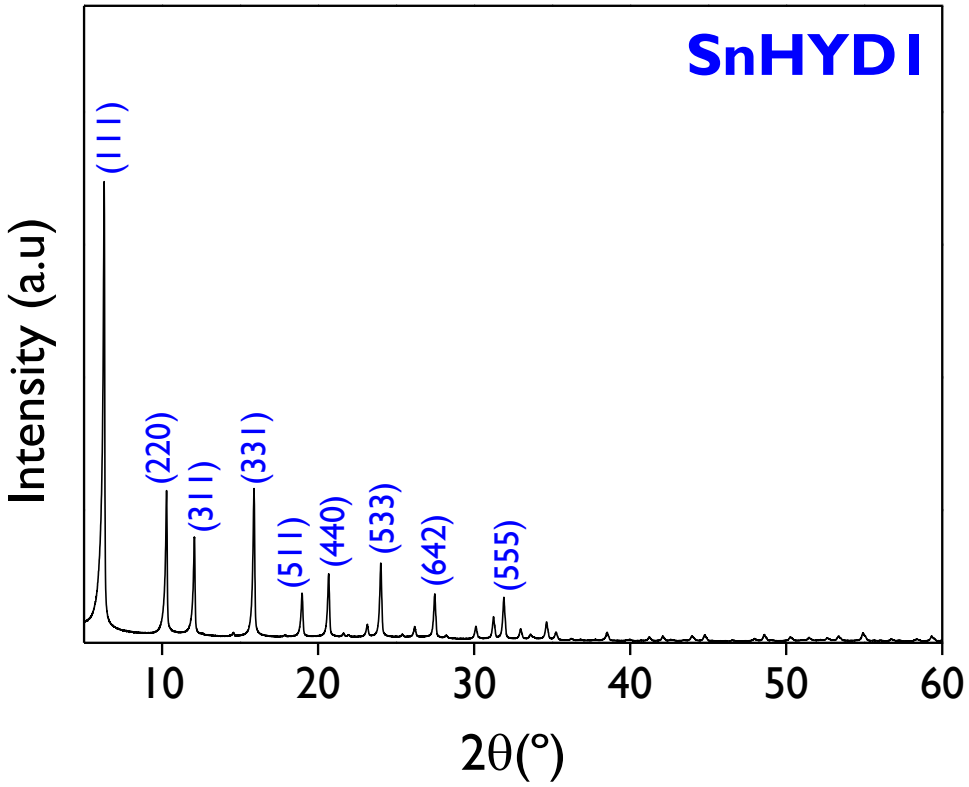

Figure 8.37. XRD pattern of the SnHYD1 material.

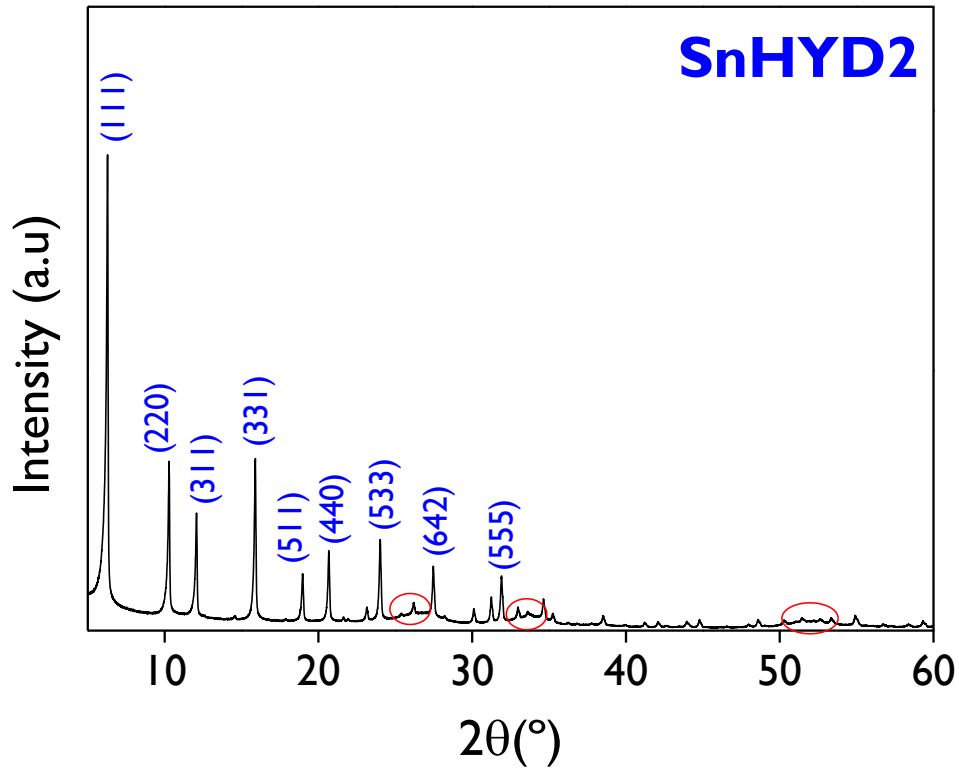

Figure 8.38. XRD pattern of the SnHYD2 material.

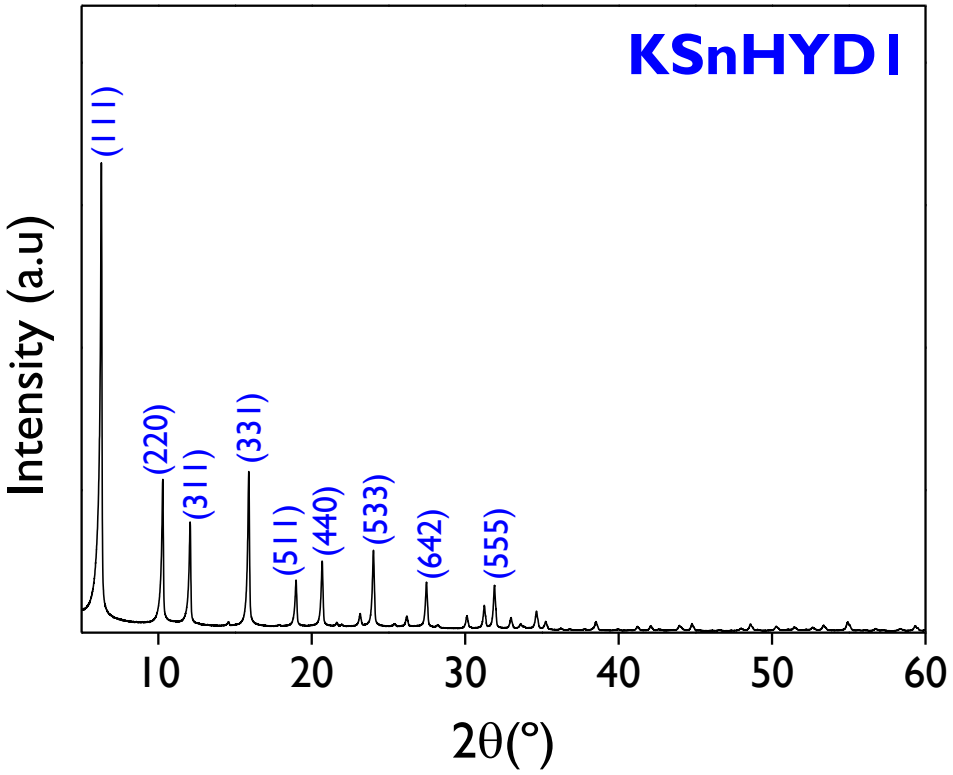

Figure 8.39. XRD pattern of the KSnHYD1 material.

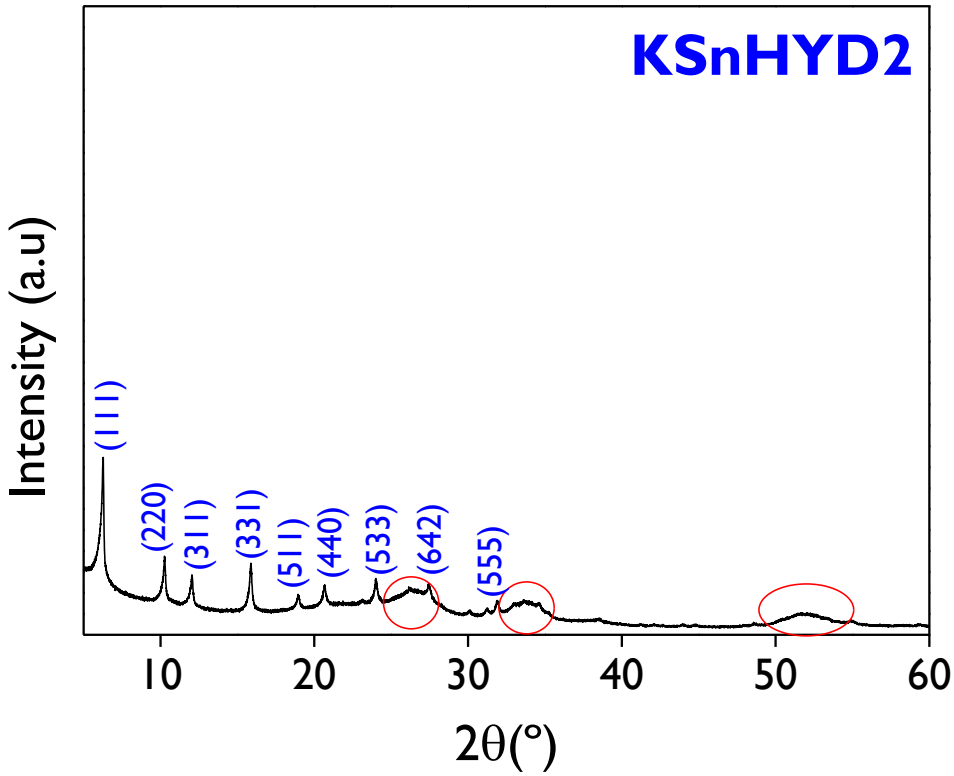

Figure 8.40. XRD pattern of the KSnHYD2 material.

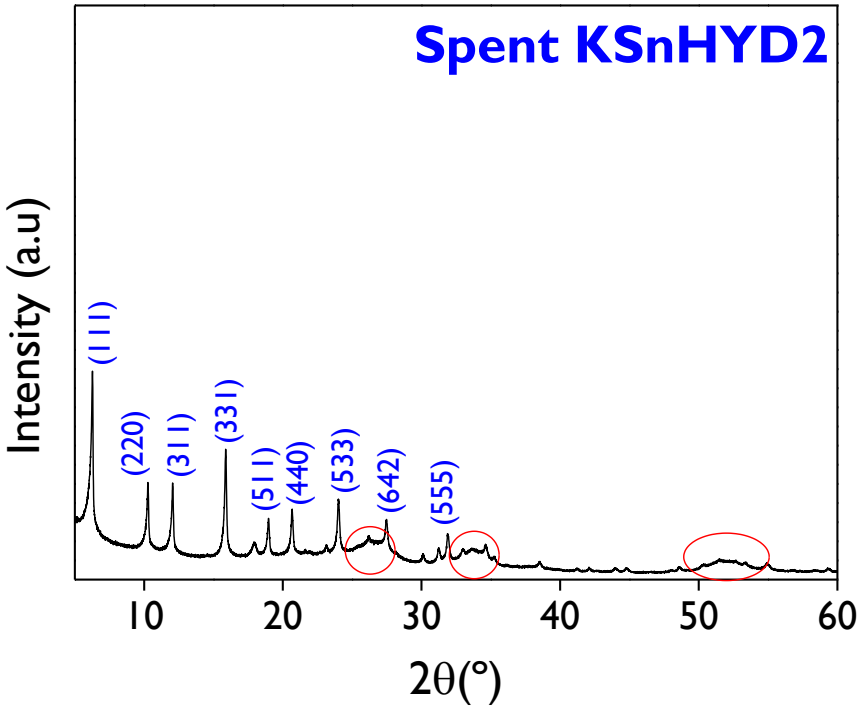

Figure 8.41. XRD pattern of the spent KSnHYD2 material.

8.2.2. TEM images

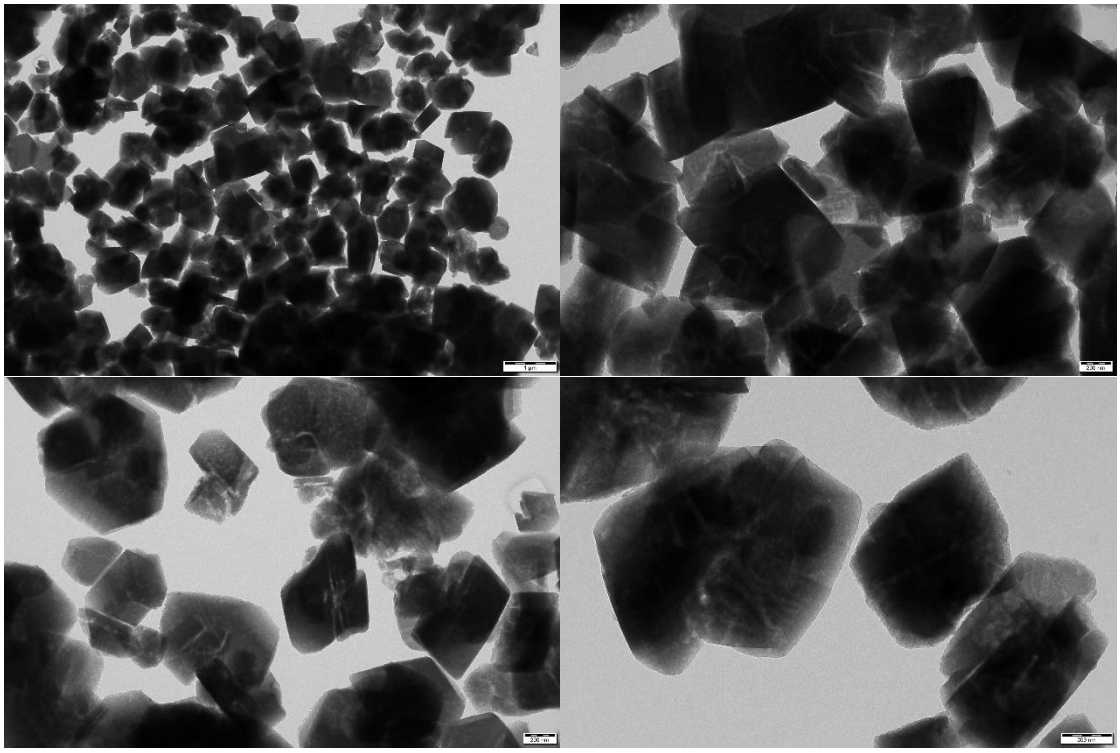

Figure 8.42. TEM images of HY material.

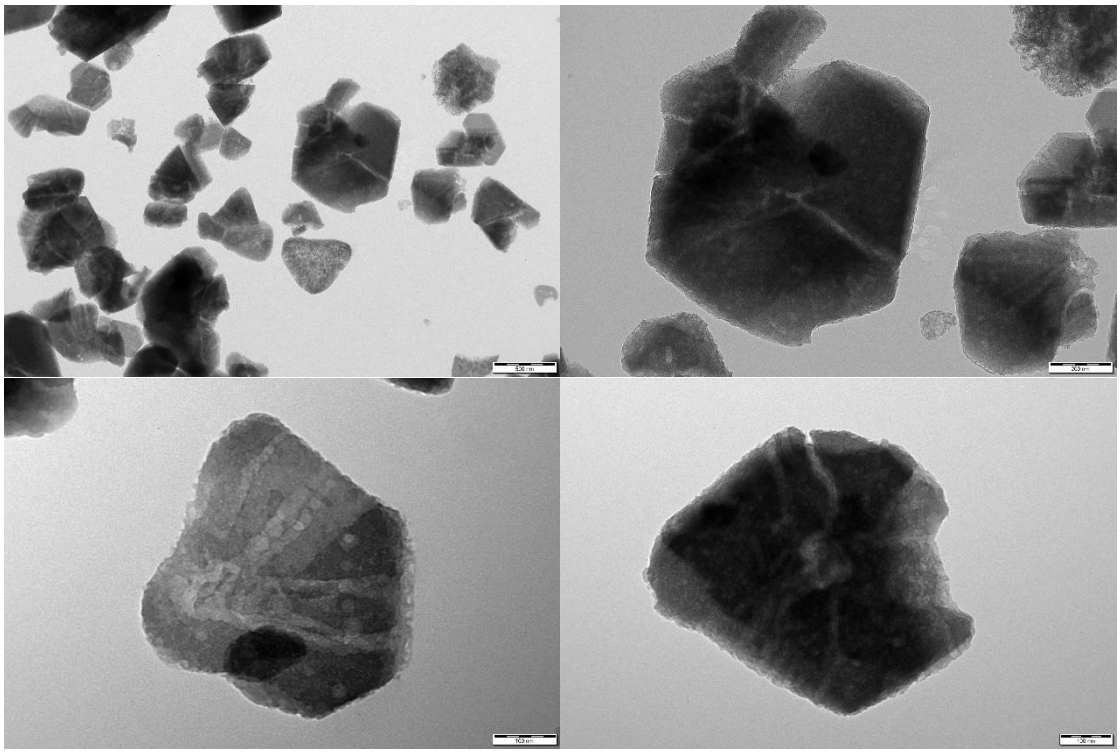

Figure 8.43. TEM images of HYD material.

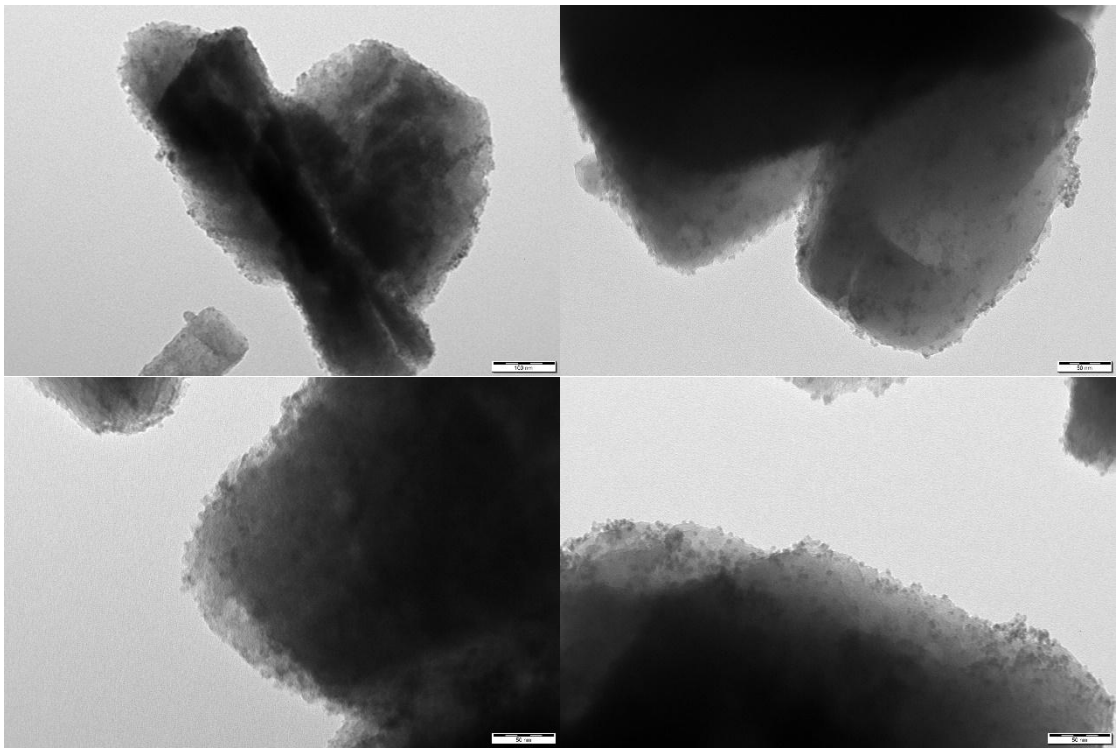

Figure 8.44. TEM images of SnHYD1 material.

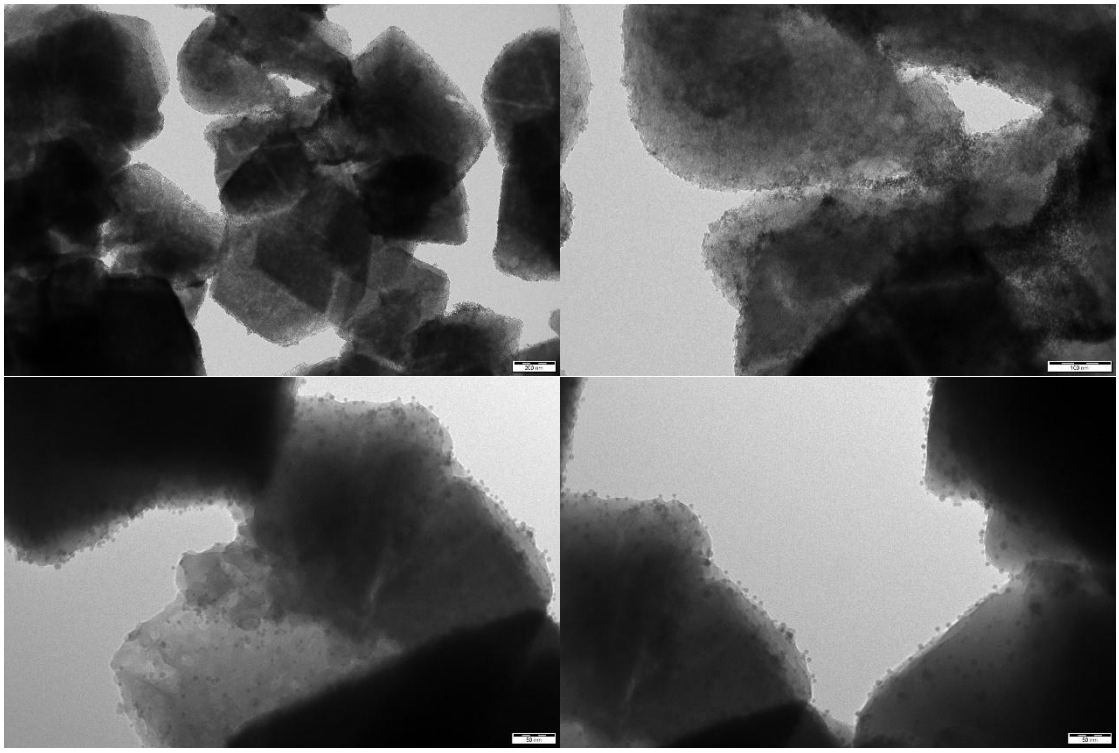

Figure 8.45. TEM images of KSnHYD1 material.

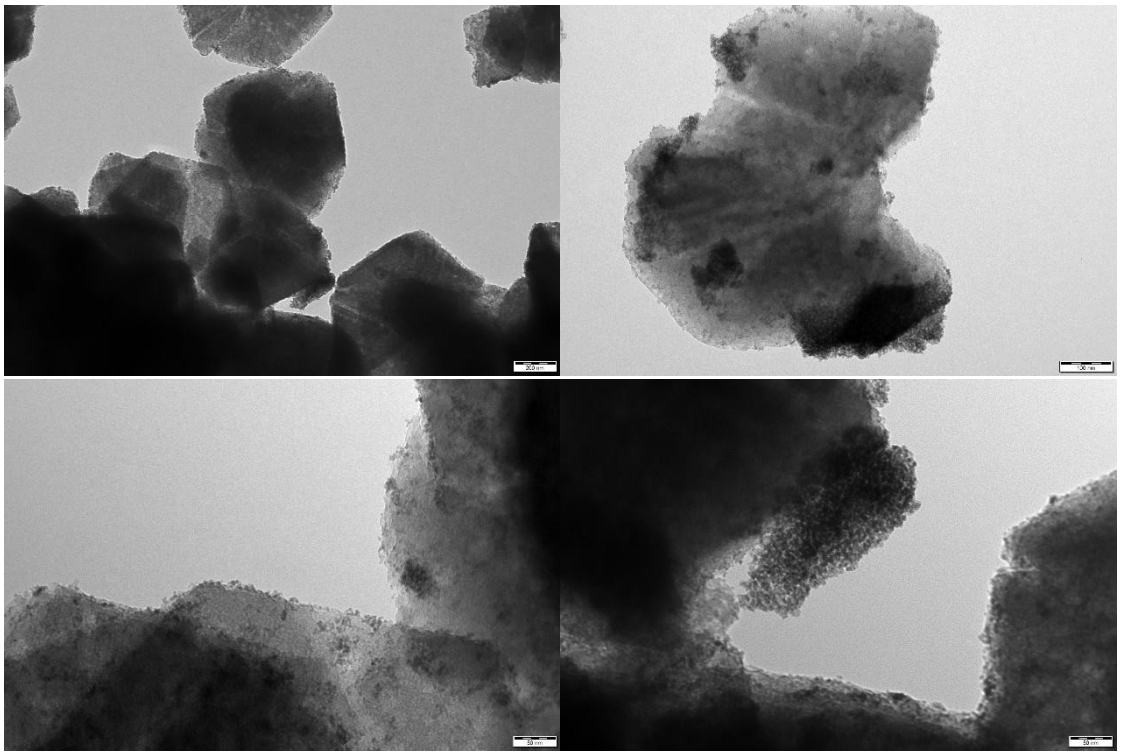

Figure 8.46. TEM images of SnHYD2 material.

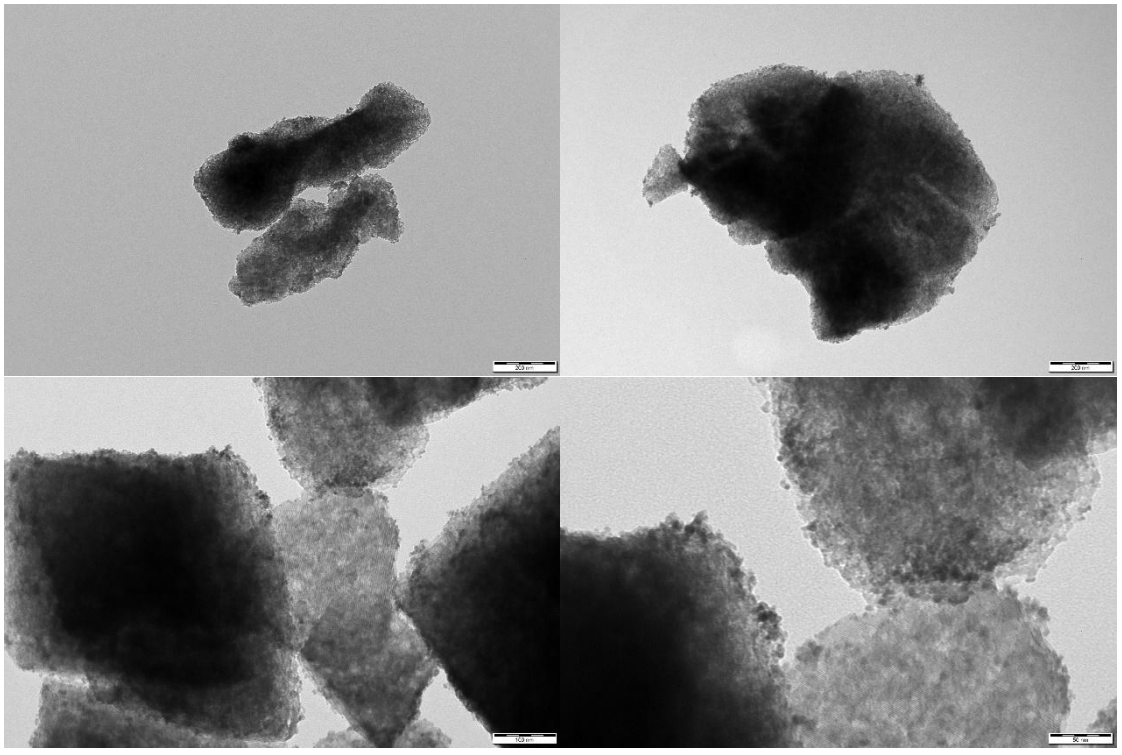

Figure 8.47. TEM images of KSnHYD2 material.

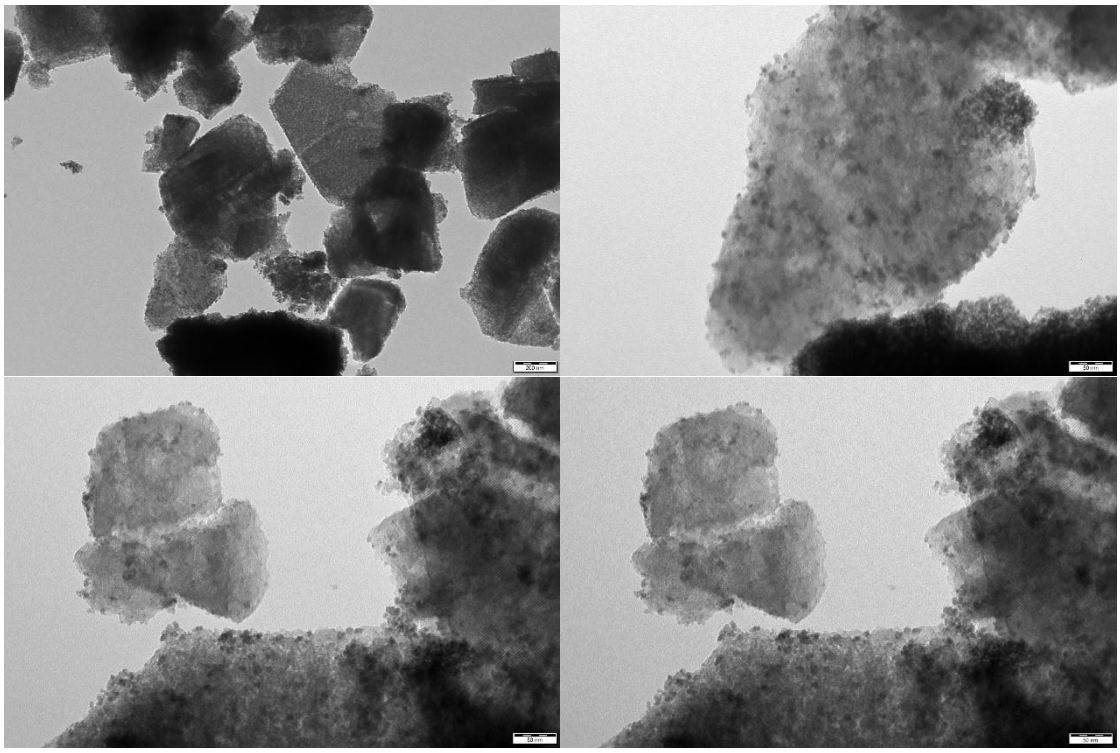

Figure 8.48. TEM images of spent KSnHYD2 material.

8.2.3. SEM images

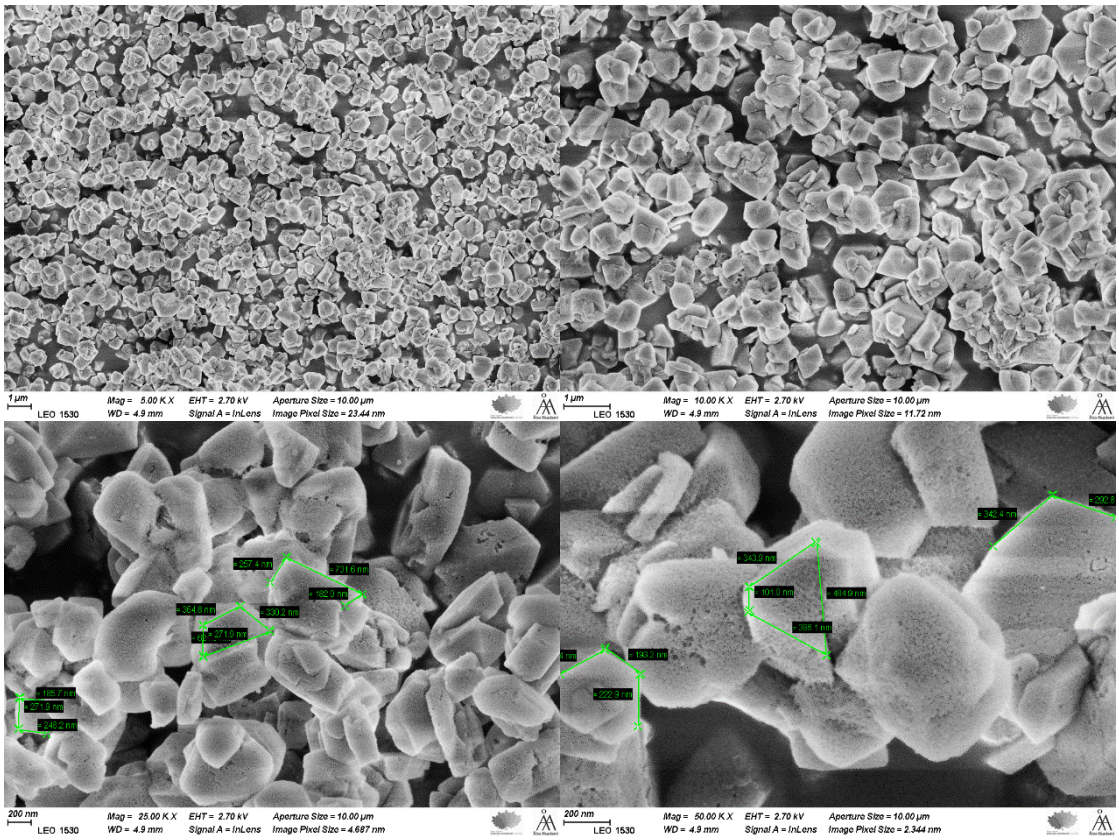

Figure 8.49. SEM images of HY material.

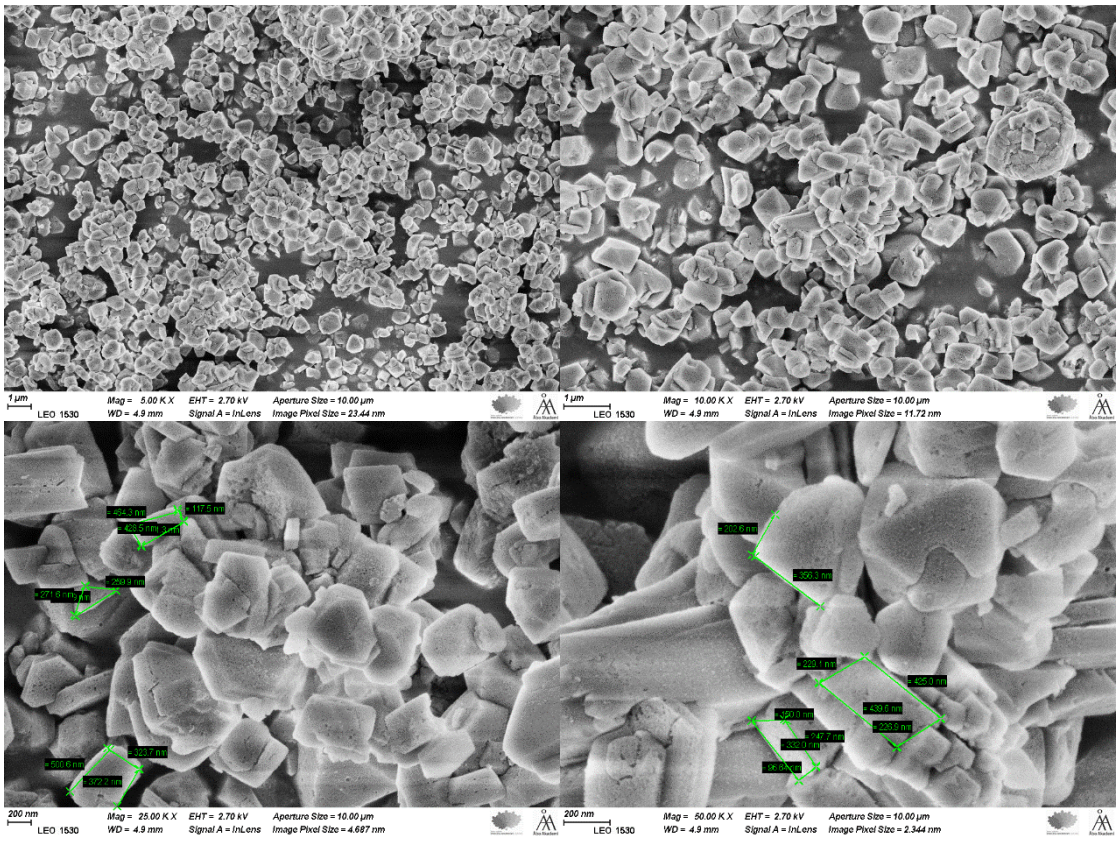

Figure 8.50. SEM images of HYD material.

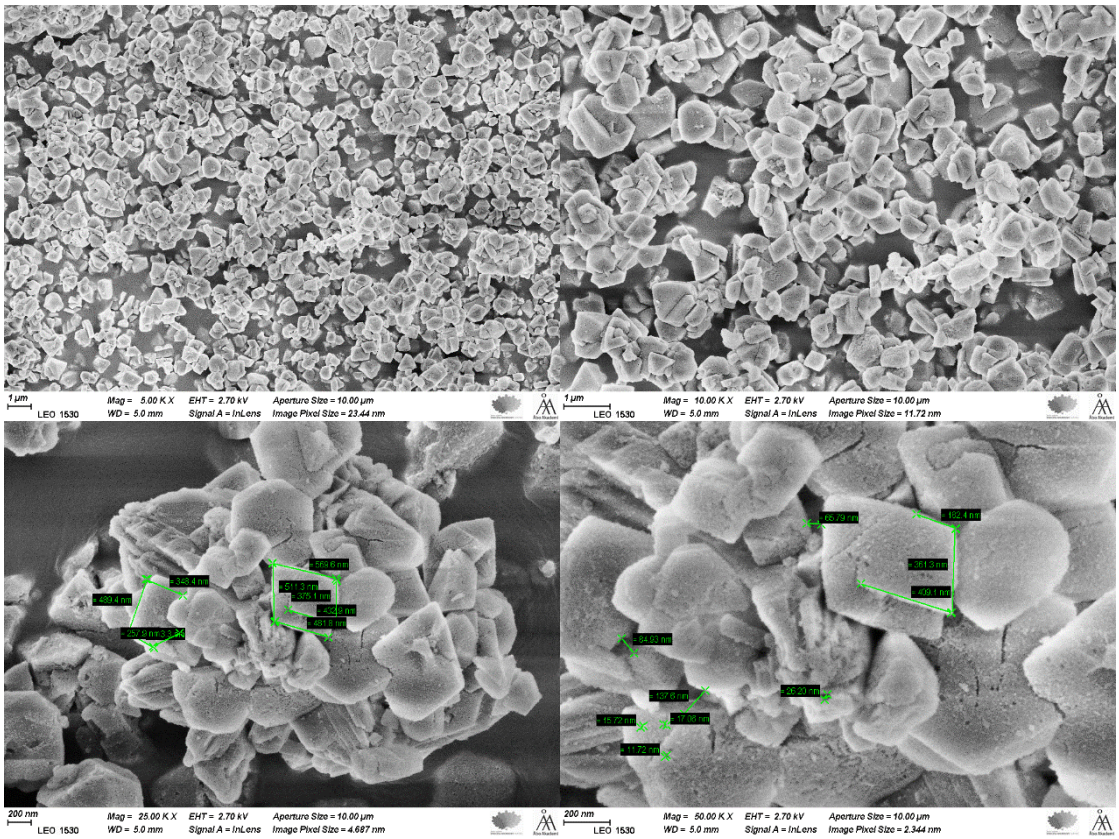

Figure 8.51. SEM images of SnHYD1 material.

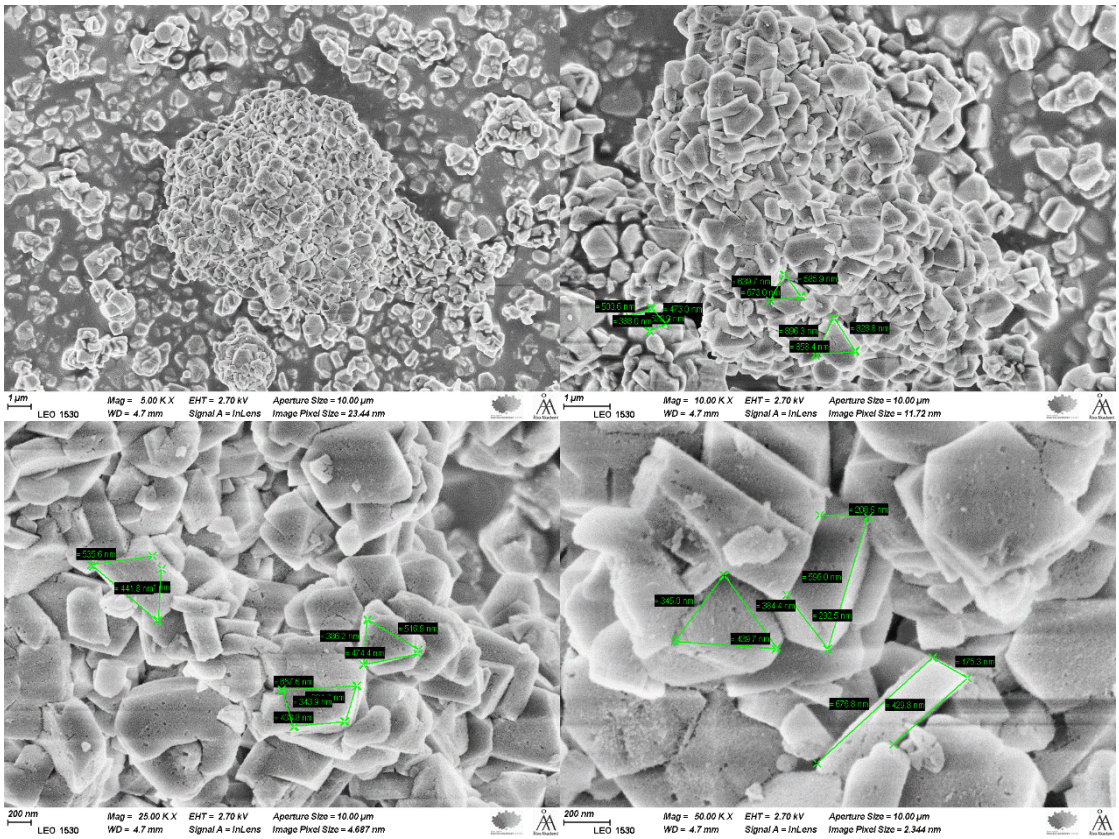

Figure 8.52. SEM images of KSnHYD1 material.

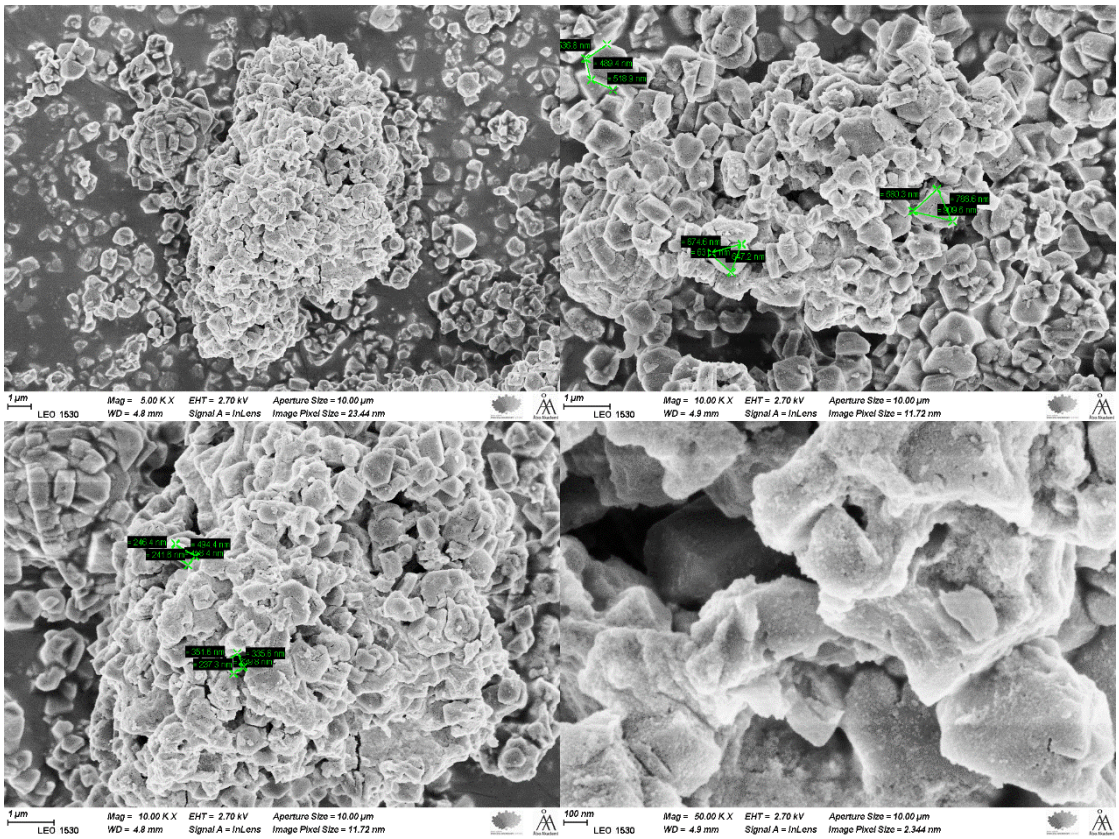

Figure 8.53. SEM images of SnHYD2 material.

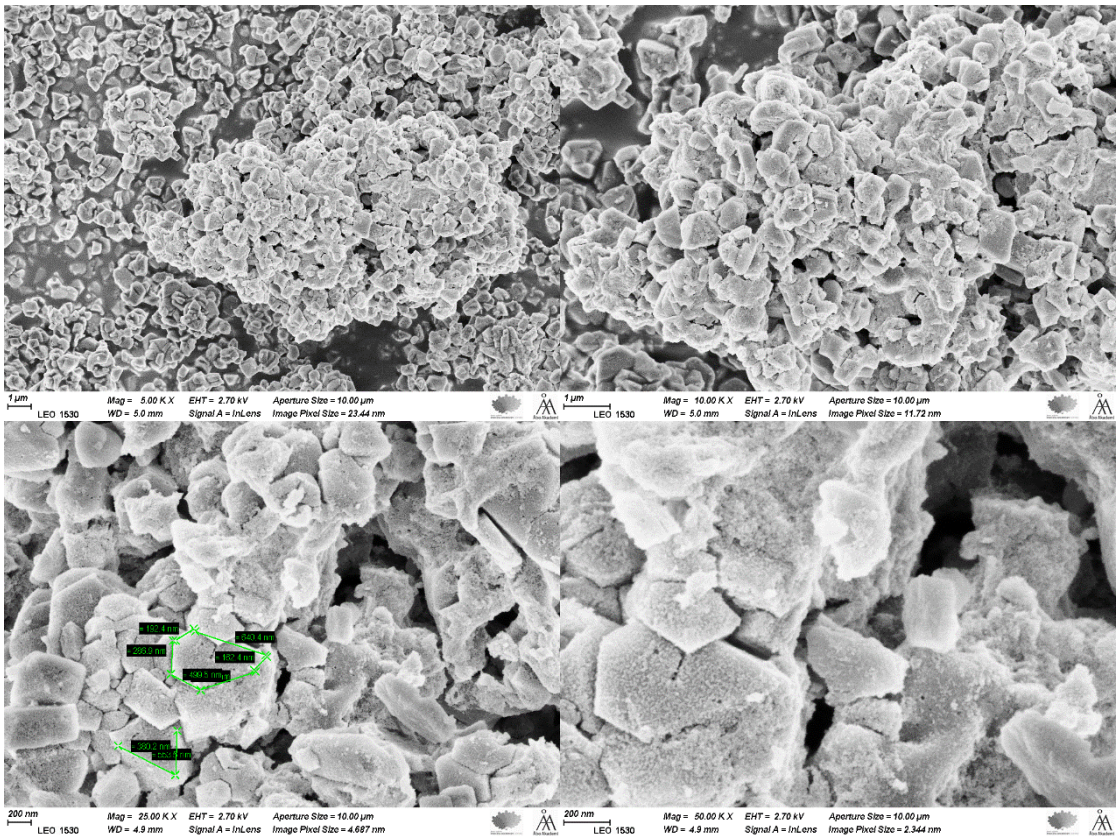

Figure 8.54. SEM images of KSnHYD2 material.

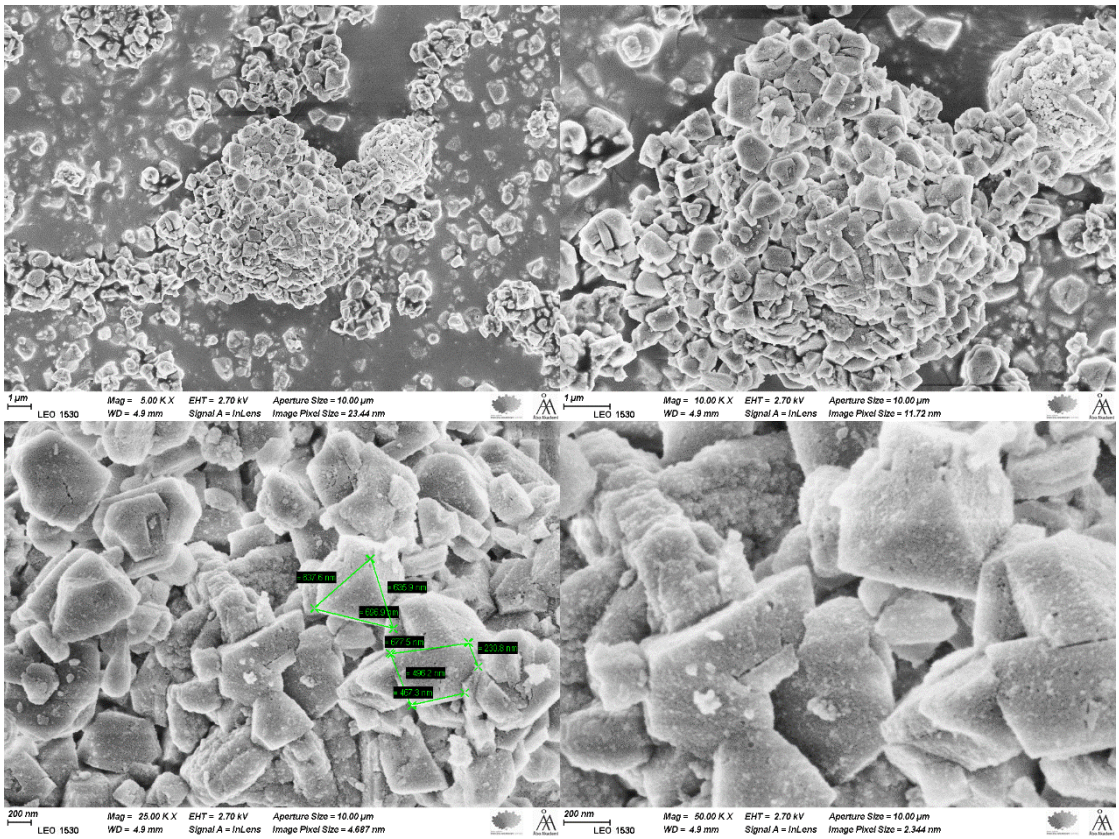

Figure 8.55. SEM images of spent KSnHYD2 material.

8.2.4. Pyridine-FTIR spectra

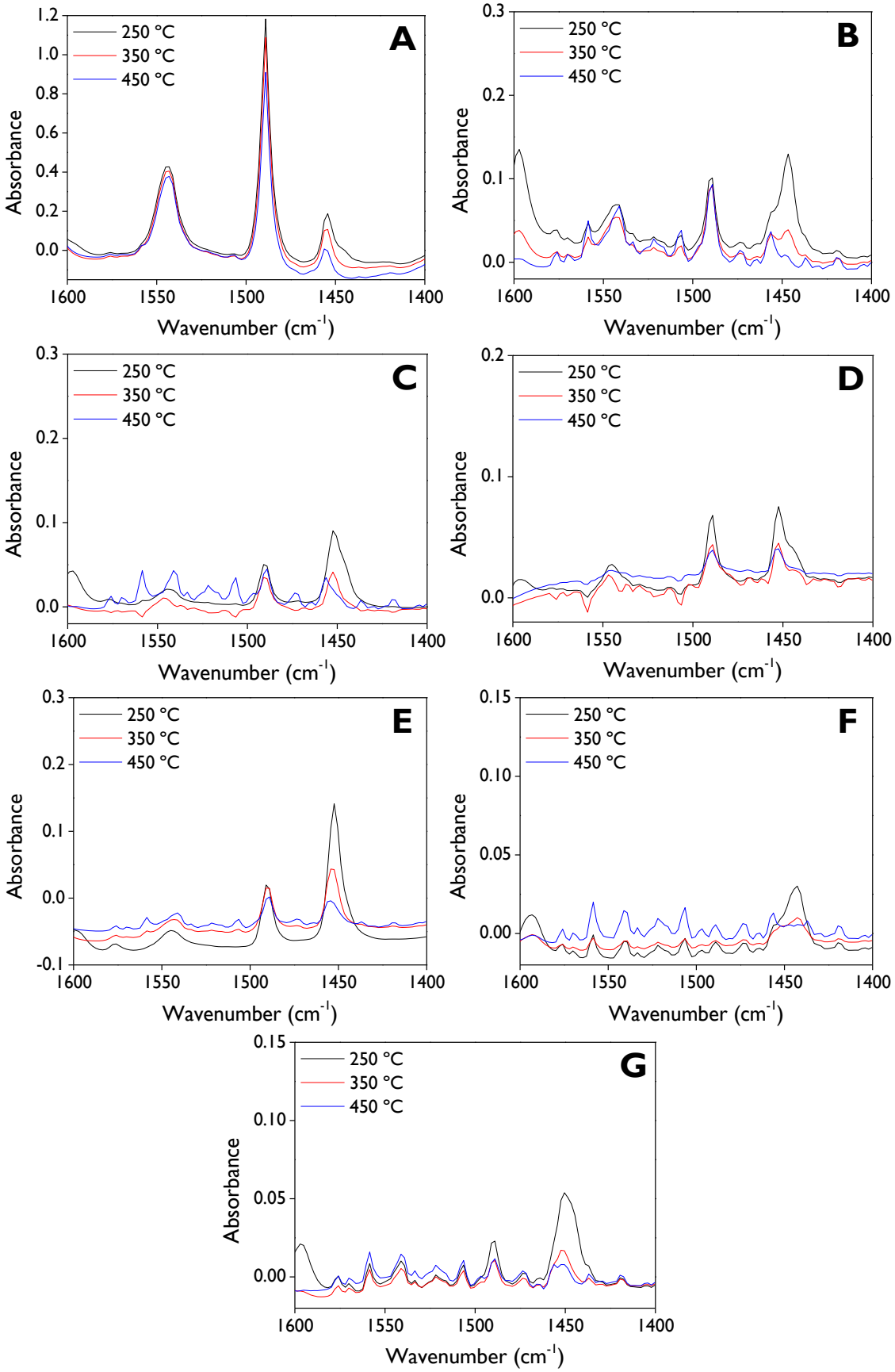

Figure 8.56. Pyridine-FTIR spectra of **(A)** HY, **(B)** HYD, **(C)** SnHYD1, **(D)** KSnHYD1, **(E)** SnHYD2, **(F)** KSnHYD2, **(G)** KSnHYD2-Spent.

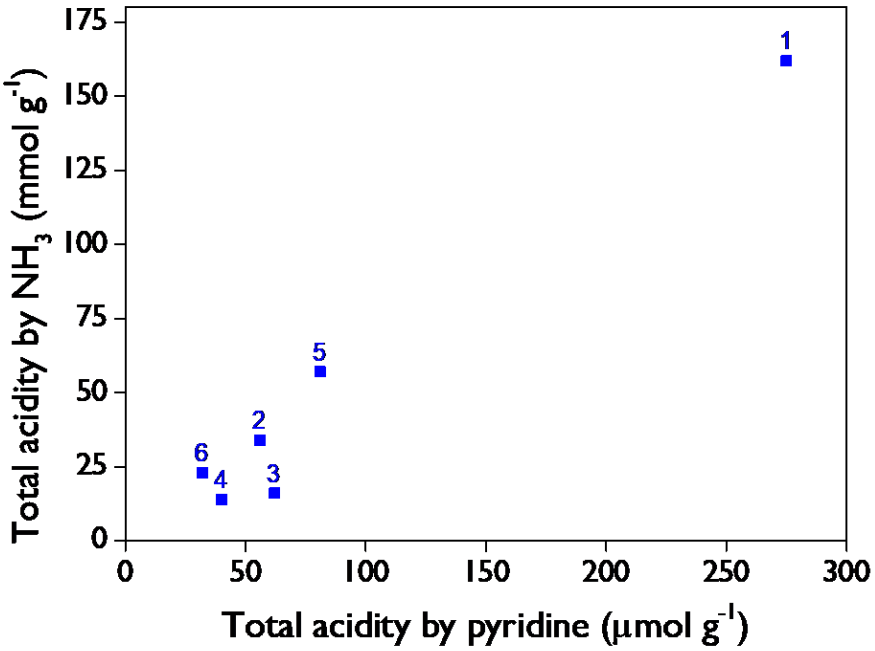

Figure 8.57. Relationship between the total acidity measured by pyridine-FTIR and NH3-TPD. **(1)** HY, **(2)** HYD, **(3)** SnHYD1, **(4)** KSnHYD1, **(5)** SnHYD2, **(6)** KSnHYD2.

8.2.5. CO_2-TPD analysis

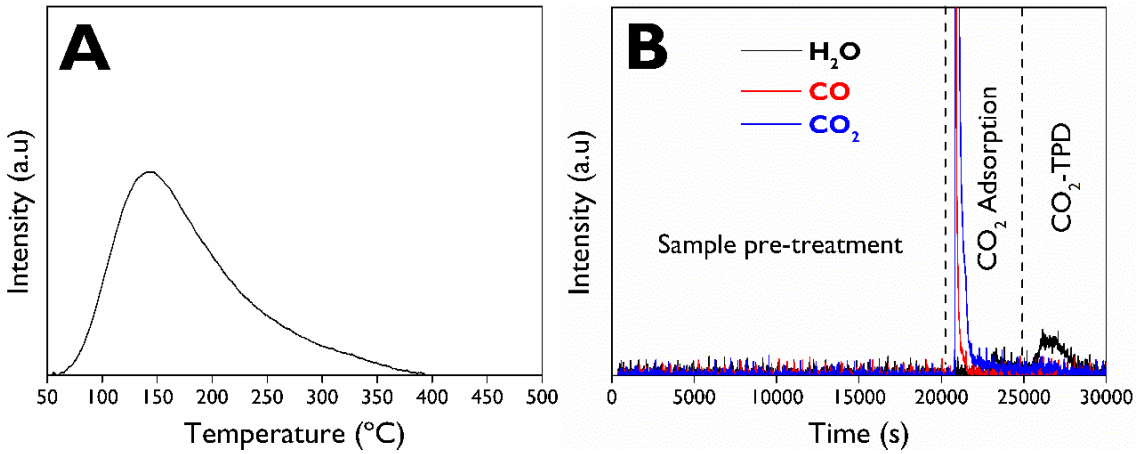

Figure 8.58. Basicity measurement by CO_2-TPD of the KSnHYD2 catalyst: **(A)** CO_2-TPD profile, and **(B)** *In-situ* mass spectrometry.

8.2.6. Screening of catalysts

Reagents

Zeolitic materials purchased to Zeolyst International: Zeolites Y such as CBV 400 (SiO_2/Al_2O_3 mole ratio = 5.1, hydrogen cation form), CBV 720 (SiO_2/Al_2O_3 mole ratio = 30, hydrogen cation form), and CBV 780 (SiO_2/Al_2O_3 mole ratio = 80, hydrogen cation form); Zeolites Beta such as CP814E (SiO_2/Al_2O_3 mole ratio = 25, ammonium cation form), and CP811C-300 (SiO_2/Al_2O_3 mole ratio = 300, hydrogen cation form).

Synthesis of catalysts using the Evaporation Impregnation Method (EIM)

Initially, NH_4-Beta-25 was transformed to H-Beta-25 in a muffle oven using a step calcination procedure (entry 1, **Table 8.5**), which involves heating from room temperature to temperature T_1 for time t_1 and maintaining this temperature for time t_2. Next, the temperature was raised to T_2 within time t_3 and held for time t_4. Finally, the catalyst was cooled down to 25 °C over 100 min.

A specific amount of the precursor (**Table 8.5**) was dissolved in 250 mL of distilled water and the pH of the aqueous solution was measured. Then, 10 g of hydrogen form zeolite (H-Beta or H-Y) was added slowly into the 500 mL flask containing the aqueous solution of the metal precursor. The resulting mixture was attached to a Rotavapor (Büchi Instrument R-114), where it was rotated for 24 h at a speed of 50-60 rpm at room temperature. After the completion of the synthesis, the aqueous phase was evaporated at 70 °C in the rotavapor. Then, the catalyst was carefully removed from the flask and placed in a crucible. Subsequently, the catalyst was dried in an oven at 100 °C for 7 h. The catalyst was calcined in static air using the step calcination procedure reported in **Table 8.5** for each catalyst. The resulting solids were coded as xMe-H-Zeolite-MR-EIM, where x is the nominal loading of metal (Me), Zeolite is H-BETA or H-Y, and MR is the SiO_2/Al_2O_3 mole ratio.

Table 8.5. Description of synthesized catalysts based on zeolites Y and Beta.

Entry	Catalyst	Zeolite	Metal precursor (g)	Step calcination procedure
1	5Ni-H-Beta-25-EIM	H-Beta-25	$Ni(NO_3)_2 \cdot 6H_2O$ (2.56)	T_1 = 250 °C, t_1 = 50 min t_2 = 40 min, T_2 = 400 °C t_3 = 60 min, t_4 = 180 min
2	5Ni-H-Beta-300-EIM	H-Beta-300		
3	10Ni-H-Beta-25-EIM	H-Beta-25	$Ni(NO_3)_2 \cdot 6H_2O$ (5.12)	
4	Mg-H-Y-80-EIM	H-Y-80	$Mg(NO_3)_2 \cdot 6H_2O$ (3.5)	T_1 = 250 °C, t_1 = 75 min t_2 = 50 min, T_2 = 400 °C t_3 = 60 min, t_4 = 180 min
5	Ca-H-Y-30-EIM	H-Y-30	$CaSO_4 \cdot 2H_2O$ (4.58)	T_1 = 200 °C, t_1 = 85 min t_2 = 70 min, T_2 = 450 °C t_3 = 60 min, t_4 = 180 min

Results

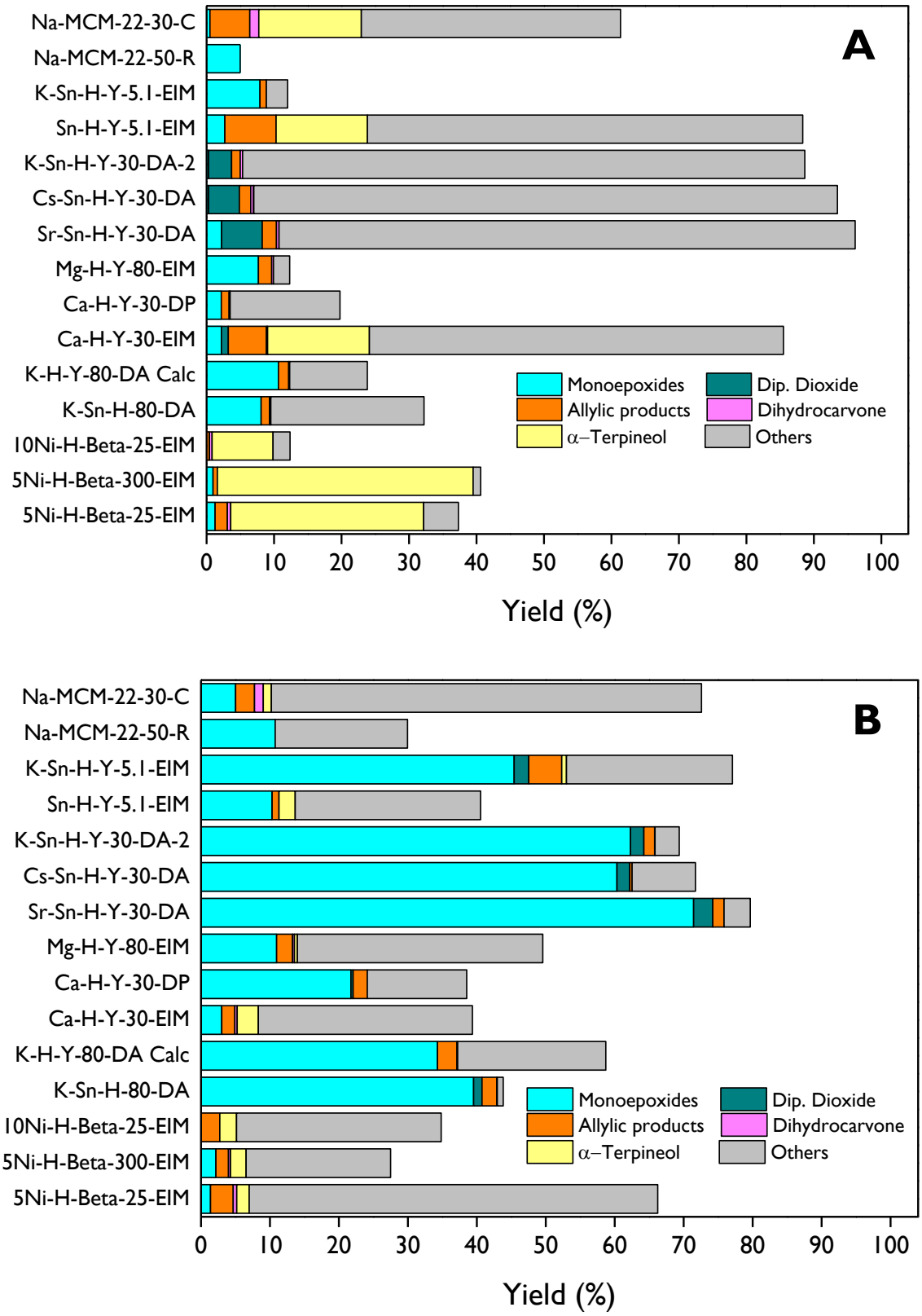

Figure 8.59. Yield to products of R-(+)-limonene oxidation over different heterogeneous catalysts. **Reaction conditions:** 2.02 mmol of limonene, H_2O_2/limonene mole ratio = 3:1, 6 mL of **(A)** ethyl acetate or **(B)** acetonitrile, 90.7 mg of catalyst, 70 °C, 24 h.

8.2.7. Repeatability test

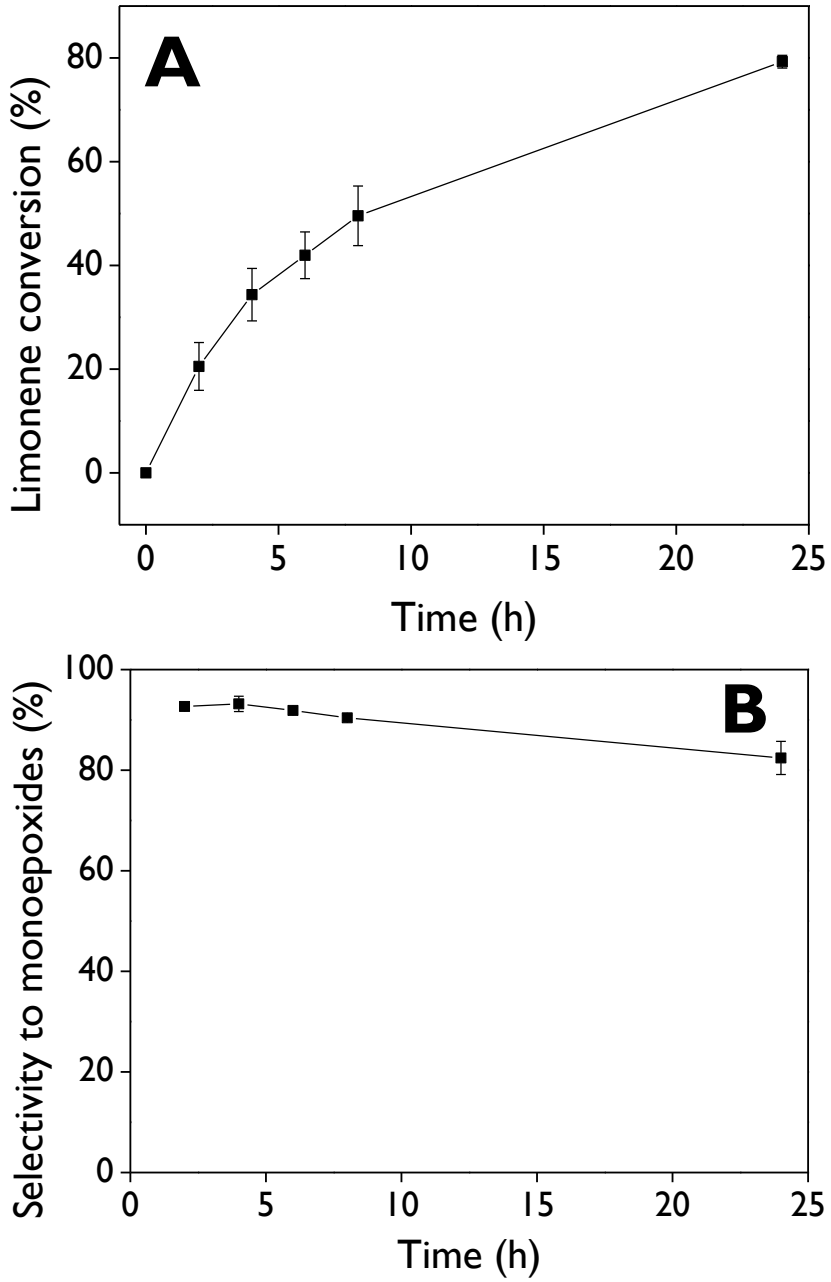

Figure 8.60. Repeatability test in the R-(+)-limonene epoxidation over KSnHYD2 as a catalyst using three experimental runs: **(A)** Limonene conversion and **(B)** Selectivity to monoepoxides. **Reaction conditions:** $C_{L,0}$ = 0.27 M, acetonitrile as a solvent, 648 mg of catalyst, 70 °C, 800 rpm. Figures were constructed with error bars (standard deviation), which were obtained from three experimental runs under the same conditions.

8.2.8. Initial reaction rate and turnover frequency

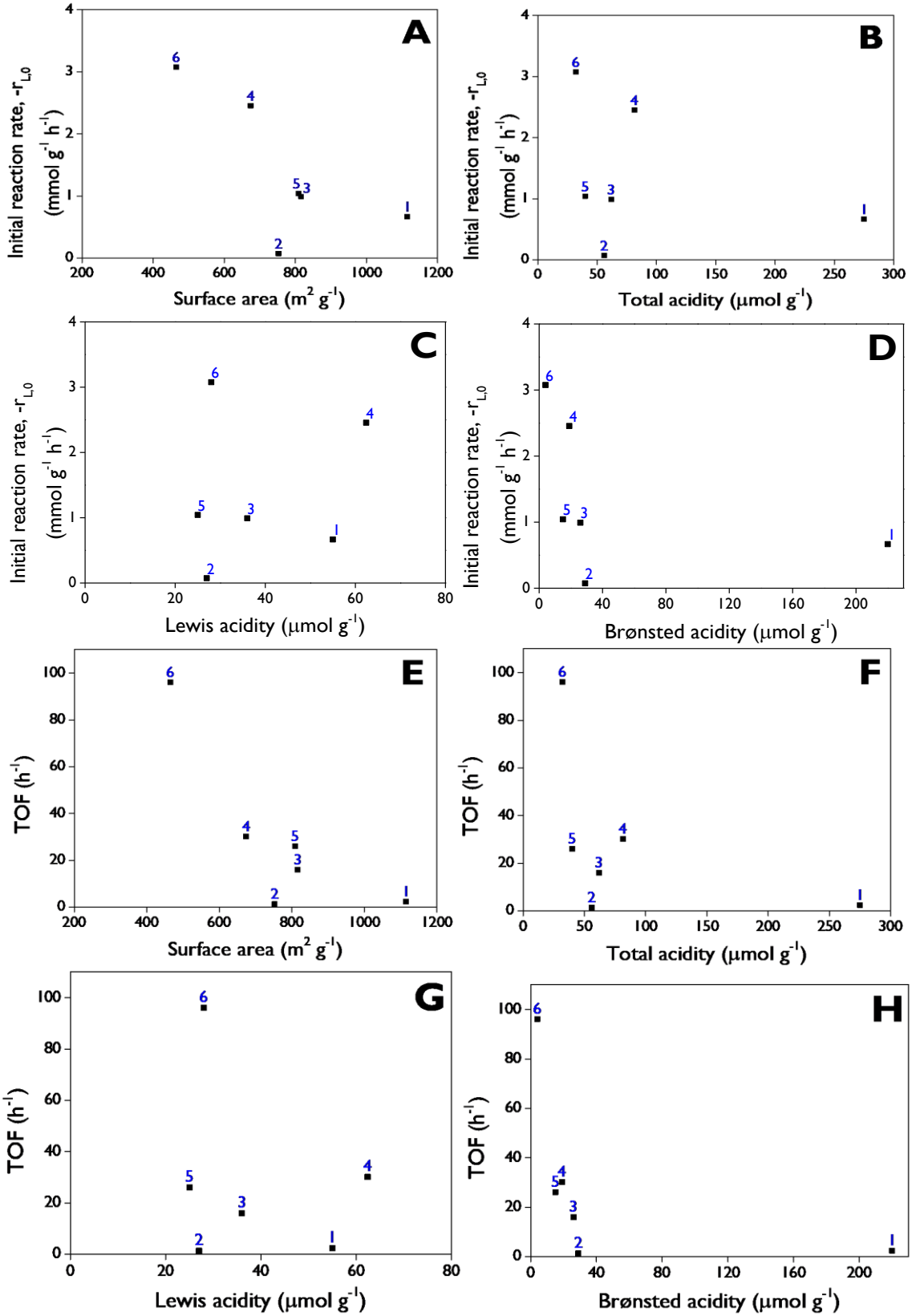

Figure 8.61. Initial reaction rate and turnover frequency as functions of the total surface area, total pyridine acidity, Lewis acidity, and Brønsted acidity. (1) HY, (2) HYD, (3) SnHYD1, (4) SnHYD2, (5) KSnHYD1, (6) KSnHYD2.

8.2.9. Concentration of limonene-1,2-epoxide vs. concentration of diol

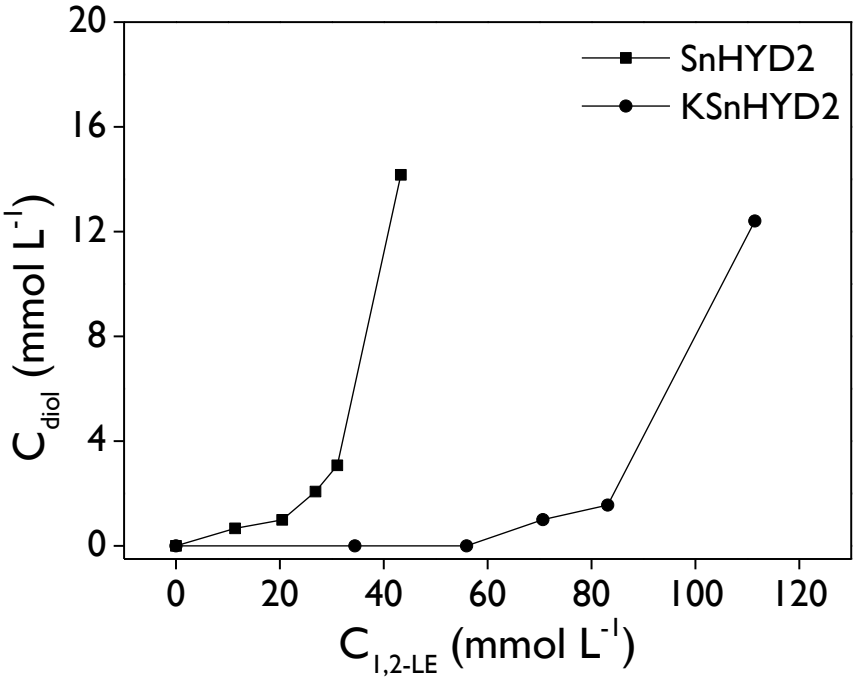

Figure 8.62. Concentration of limonene diol as a function of the concentration of limonene-1,2-epoxide. **Reaction conditions:** $C_{L,0}$ = 0.27 M, acetonitrile as a solvent, H_2O_2/limonene molar ratio = 5:1, 432 mg of catalyst, 70 °C, 800 rpm.

8.2.10. Initial reaction rates vs. concentrations

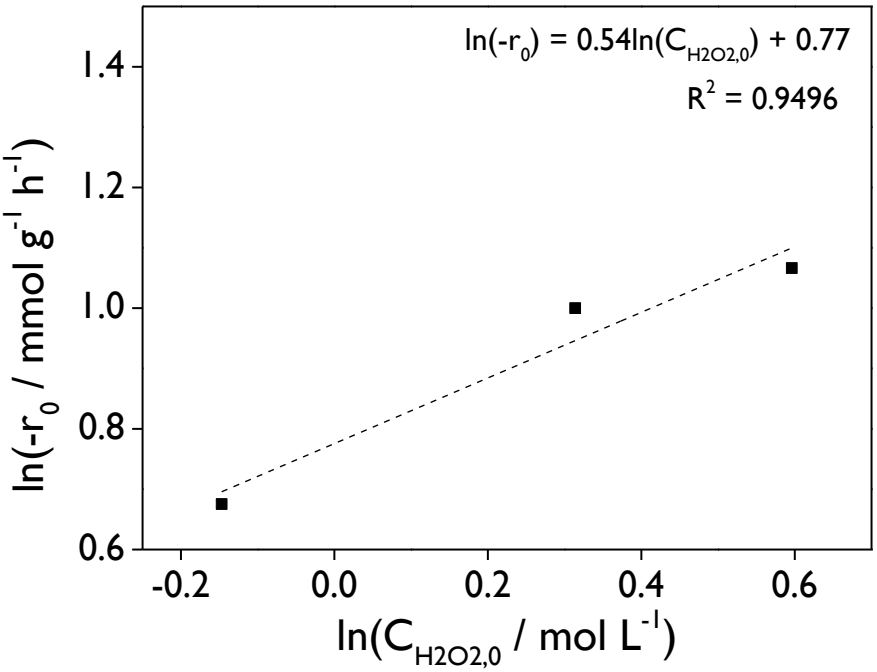

Figure 8.63. $\ln(-r_0)$ vs. $\ln(C_{H2O2,0})$ for the epoxidation of R-(+)-limonene over KSnHYD2 as a catalyst. **Reaction conditions:** $C_{L,0}$ = 0.27 M, acetonitrile as a solvent, 648 mg of catalyst, 70 °C, 800 rpm.

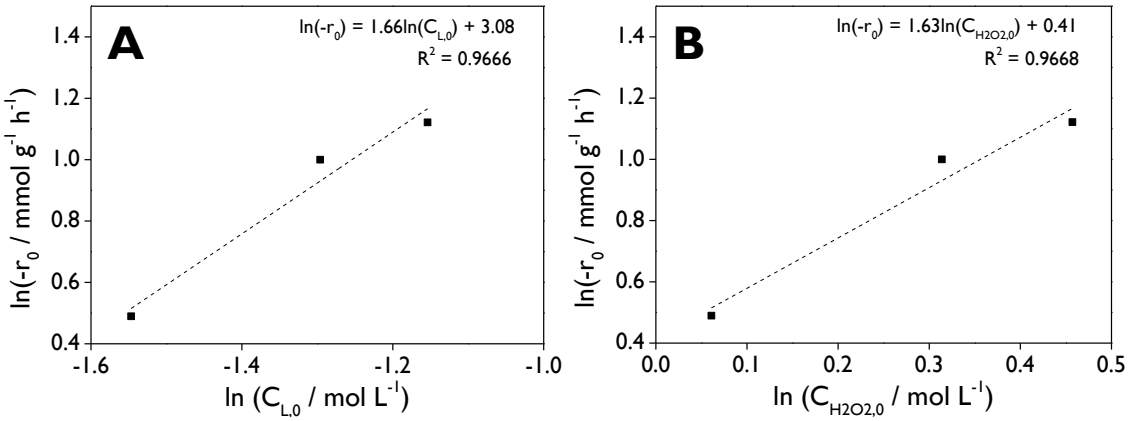

Figure 8.64. A) $\ln(-r_0)$ vs. $\ln(C_{L,0})$ and **B)** $\ln(-r_0)$ vs. $\ln(C_{H2O2,0})$ for the epoxidation of R-(+)-limonene over KSnHYD2 as a catalyst. **Reaction conditions:** H_2O_2/limonene molar ratio = 5:1, acetonitrile as a solvent, 648 mg of catalyst, 70 °C, 800 rpm.

8.2.11. Conversion profiles of H_2O_2

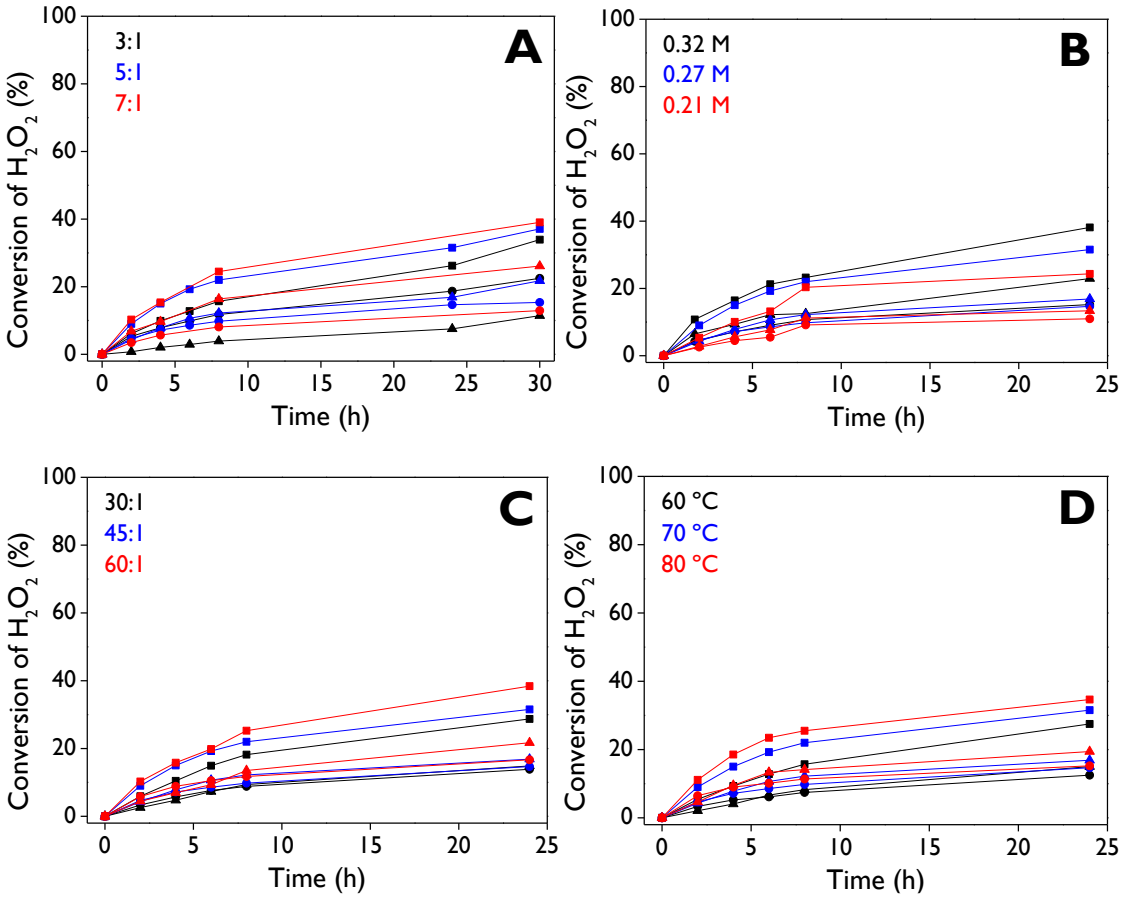

Figure 8.65. Profiles of the H_2O_2 conversion: **(A)** effect of the H_2O_2/limonene mole ratio, **(B)** effect of the limonene initial concentration, **(C)** effect of the catalyst (mg): limonene (mmol) ratio, and **(D)** effect of the reaction temperature. The reaction conditions were reported in the labels of **Figure 3.12** to **Figure 3.15**. **Notation:** X_{H2O2}: global conversion (squares), X_{ep}: conversion through the epoxidation reaction (circles), X_{dec}: conversion through the decomposition reaction (triangles).

8.2.12. TPO-MS analysis

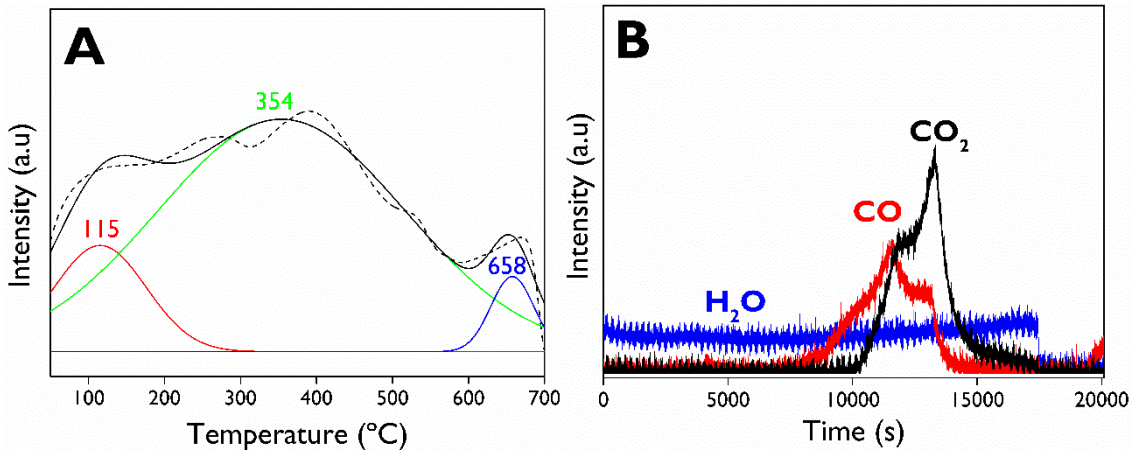

Figure 8.66. Characterization of the spent SnHYD1 catalyst: **(A)** O_2-TPO profile, and **(B)** *In-situ* mass spectrometry.

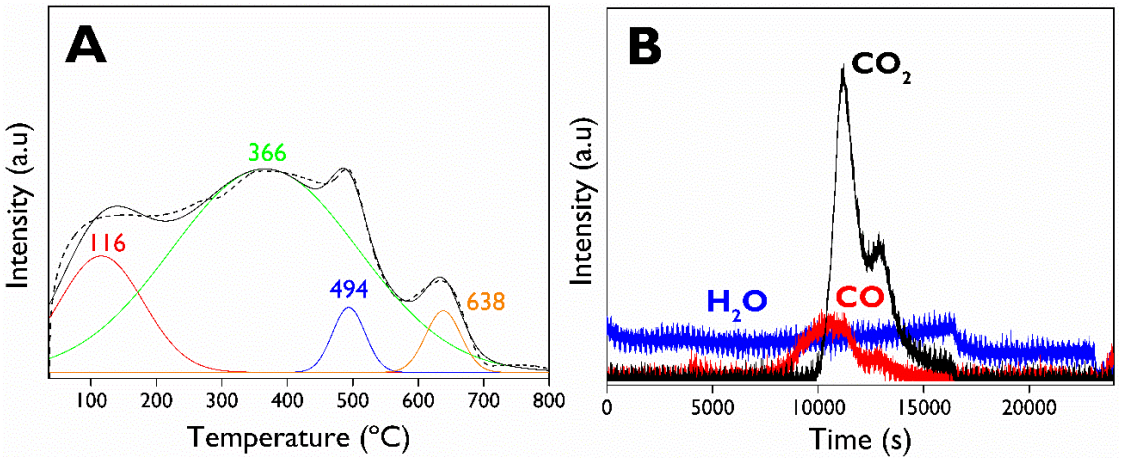

Figure 8.67. Characterization of the spent SnHYD2 catalyst: **(A)** O_2-TPO profile, and **(B)** *In-situ* mass spectrometry.

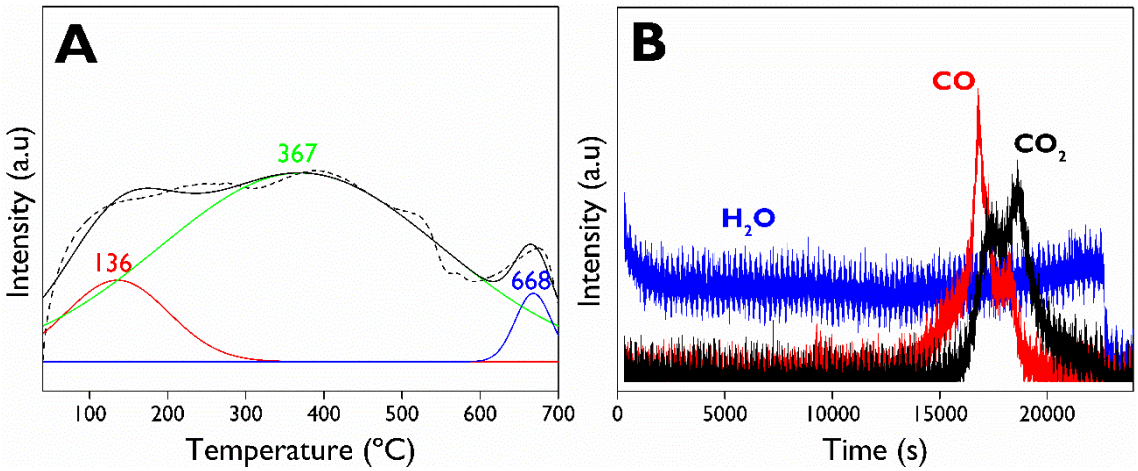

Figure 8.68. Characterization of the spent KSnHYD1 catalyst: **(A)** O_2-TPO profile, and **(B)** *In-situ* mass spectrometry.

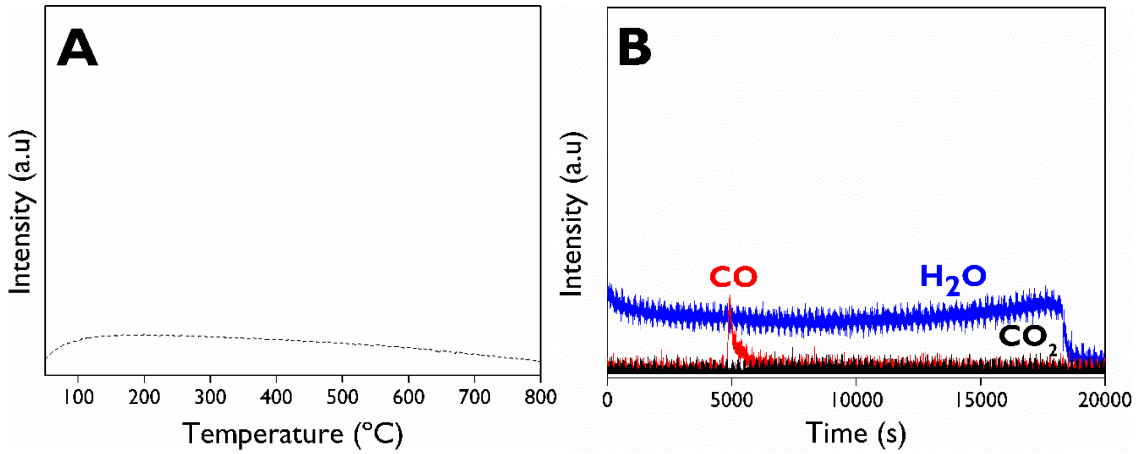

Figure 8.69. Characterization of the regenerated KSnHYD2 catalyst: **(A)** O_2-TPO profile, and **(B)** *In-situ* mass spectrometry.

8.3. Chapter 4

8.3.1. Scheme of the reaction setup

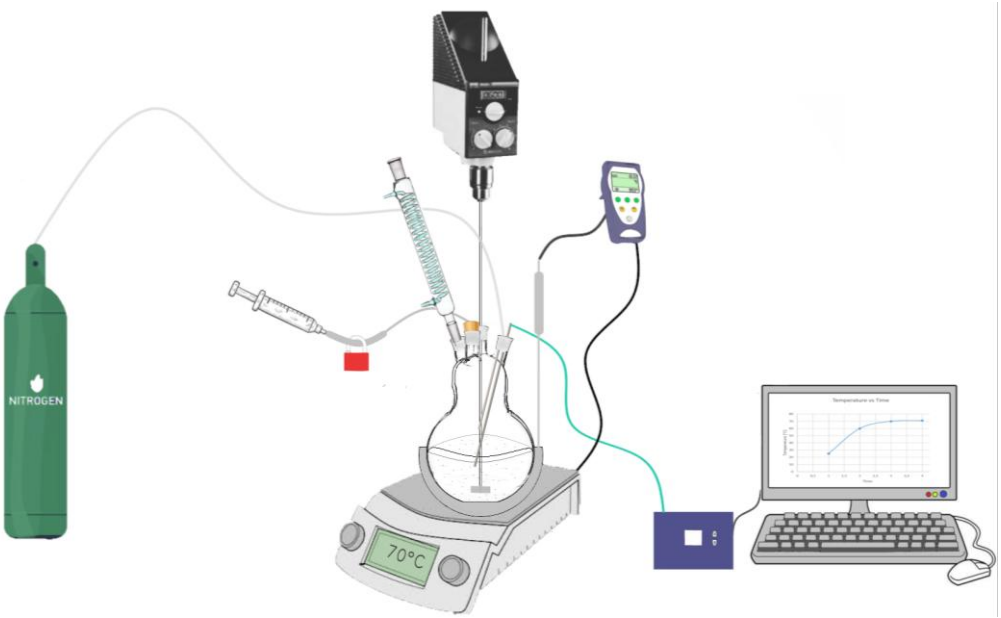

Figure 8.70. Reaction setup equipped with a mechanical stirrer, a condenser, a thermocouple, an N_2 feeding, and a sampling valve.

8.3.2. Low-angle XRD patterns

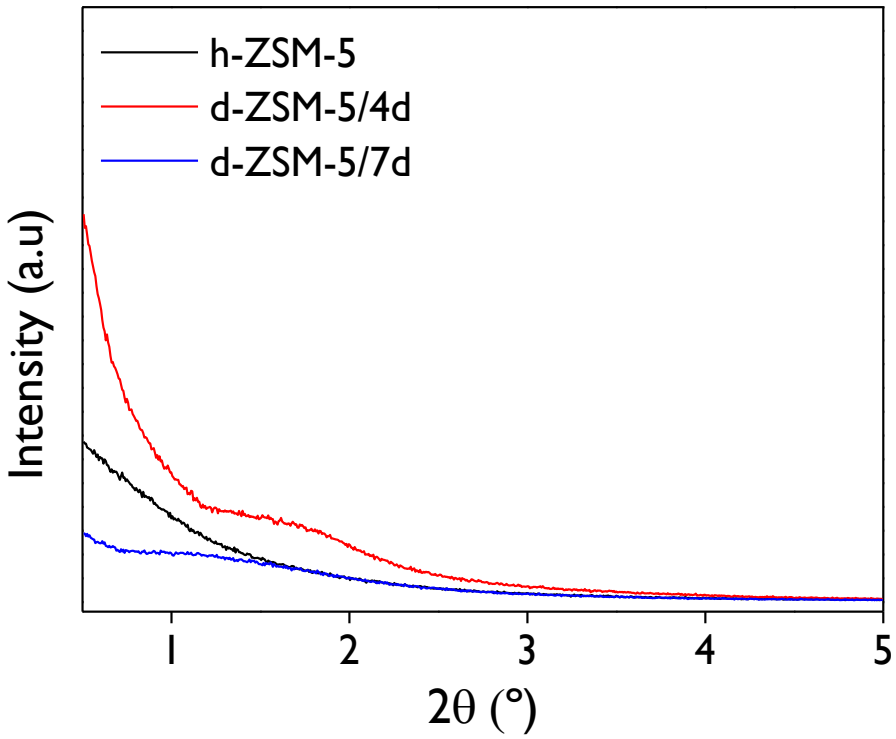

Figure 8.71. Low-angle XRD patterns of the zeolite samples.

8.3.3. SEM Analysis

The SEM images provide a more detailed insight into the surface morphology of zeolitic particles. In contrast to the smooth surface of ZSM-5 particles (**Figure 8.72.A**), modified zeolites like h-ZSM-5 (**Figure 8.72.B**) exhibit distinct characteristics. Specifically, voids are observed between the nanocrystal aggregates of the globular particle, as depicted in **Figure 4.3**. Furthermore, **Figure 8.72.C** and **Figure 8.72.D** illustrate the oval-shaped particles of the dendritic samples. Notably, the central 50 nm voids are evident in the d-ZSM-5/4d particle (**Figure 8.72.C**), and the distinctive morphology of the d-ZSM-5/7d particle in **Figure 8.72.D** highlights these voids even more prominently.

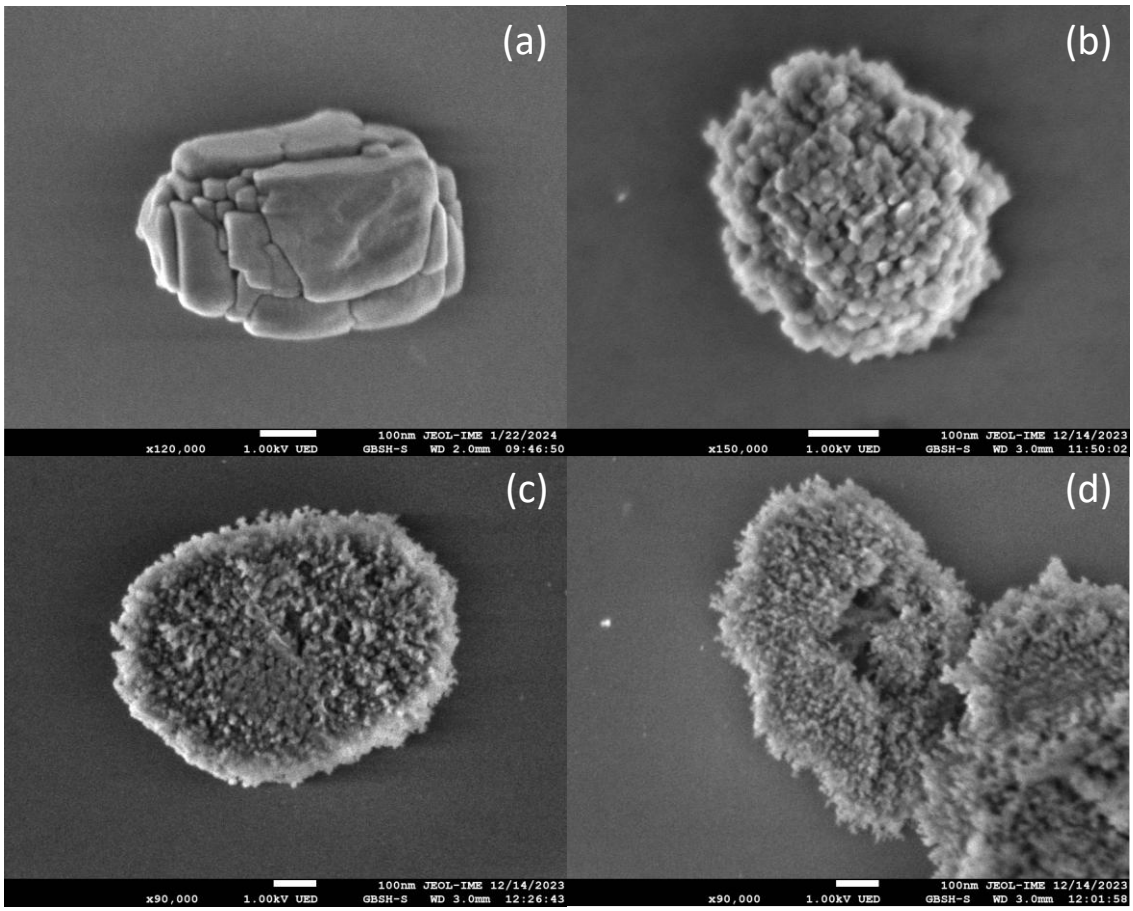

Figure 8.72. SEM images of (a) ZSM-5, (b) h-ZSM-5, (c) d-ZSM-5/4d, and (d) d-ZSM-5/7d zeolites.

8.3.4. Scheme of reaction products of limonene-1,2-epoxide isomerization

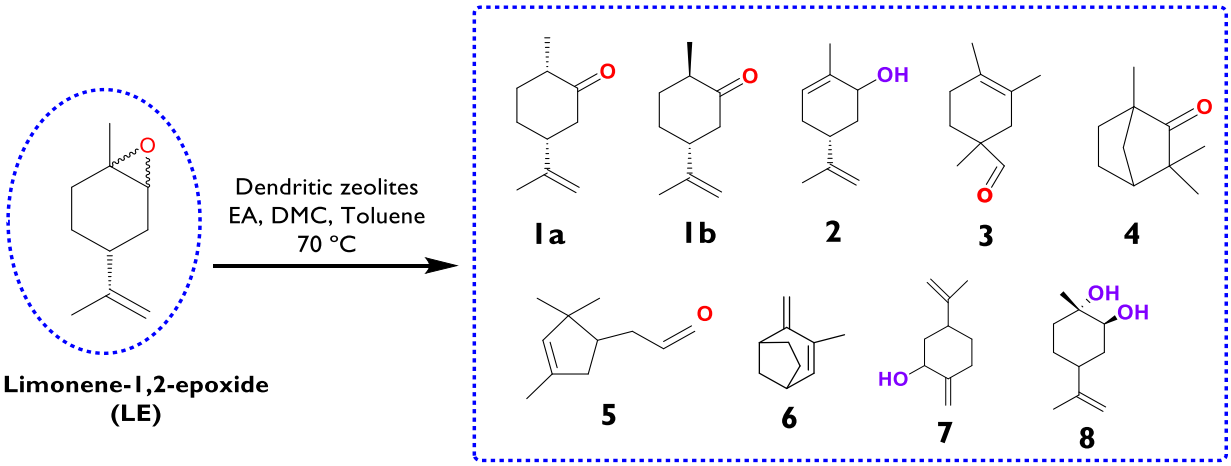

Figure 8.73. Reaction products of limonene-1,2-epoxide transformations over heterogeneous catalysts based on zeolite ZSM-5.

8.3.5. Repeatability test

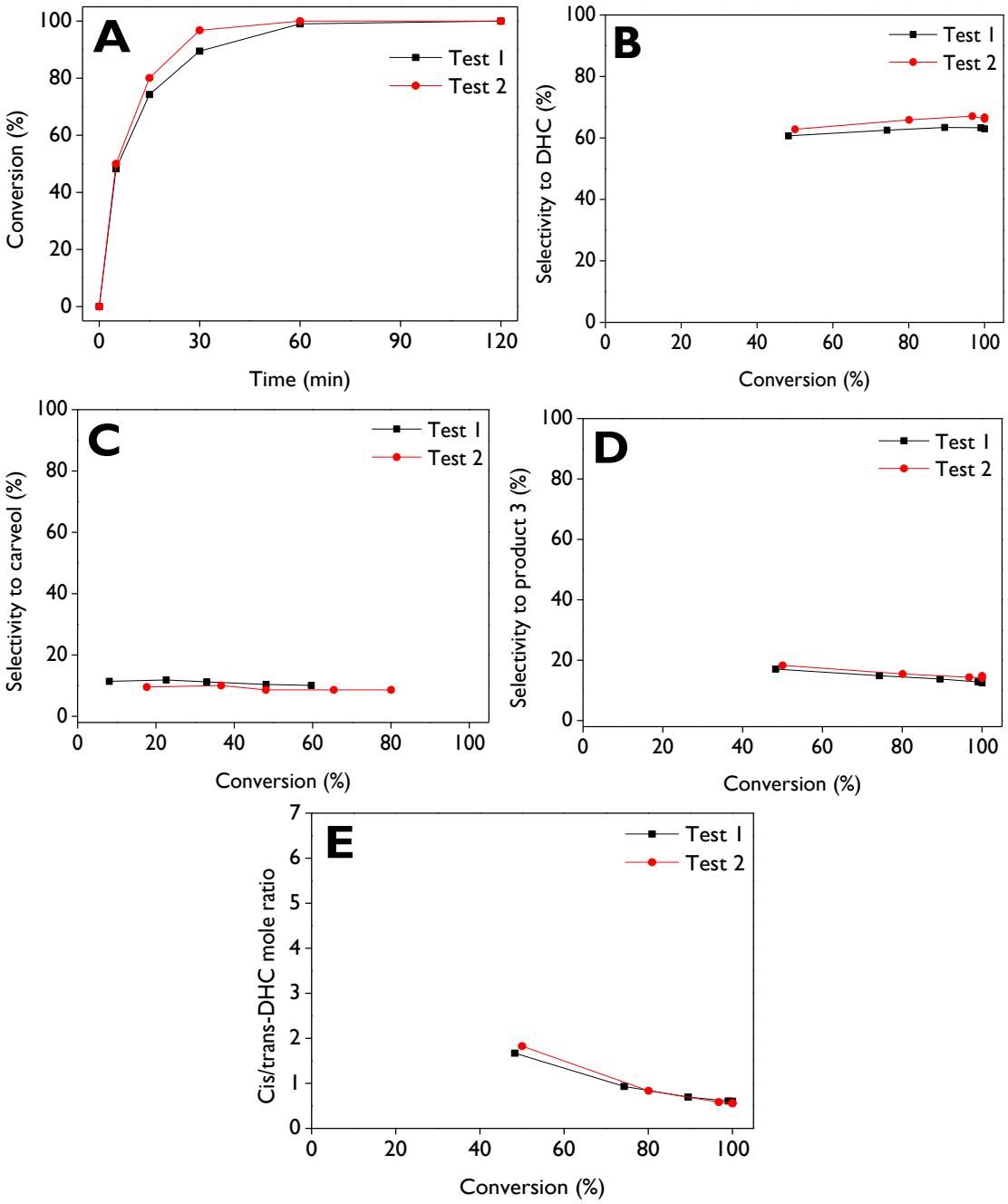

Figure 8.74. Repeatability test of d-ZSM-5/4d in the isomerization of LE. **(A)** LE conversion as a function of the reaction time, **(B)** selectivity to dihydrocarvone, **(C)** selectivity to carveol, **(D)** selectivity to product **3**, and **(E)** cis/trans dihydrocarvone mole ratio, as a function of the conversion. **Reaction conditions:** $C_{LE,0}$ = 13 mmol L^{-1}, 75 mL of total volume, anhydrous ethyl acetate as a solvent, 115 mg of catalyst, 70 °C, 520-530 rpm, N_2 atmosphere.

8.3.6. Confirmation of catalytic route

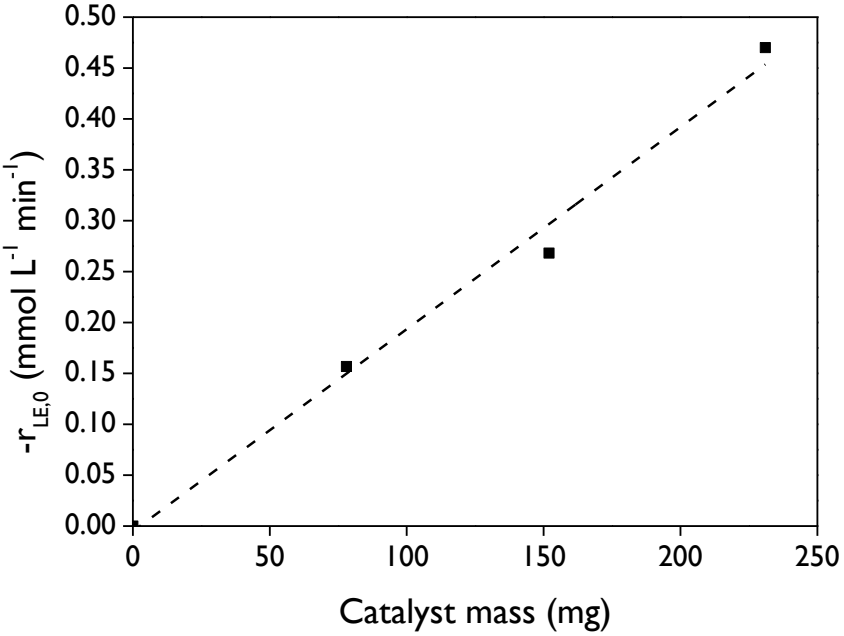

Figure 8.75. Initial reaction rate of limonene-1,2-epoxide as a function of catalyst mass over d-ZSM-5/7d. **Reaction conditions:** $C_{substrate,0}$ = 13 mmol L^{-1}, 150 mL of total volume, anhydrous ethyl acetate as a solvent, 70 °C, 520-530 rpm, N_2 atmosphere.

8.3.7. Turnover Frequency (TOF)

Table 8.6. Comparison of turnover of frequency (TOF) for various heterogeneous catalysts in the limonene-1,2-epoxide isomerization.

Catalyst	Solvent	Reaction conditions	TOF[b] (min^{-1})	Selectivity to target (%)[d]	Reference
ZSM-5	Ethyl acetate	13 mmol L^{-1}, 75 mL of total volume, 115 mg of catalyst, 70 °C, 520-530 rpm, N_2 atmosphere	0.6	42 (20)	This work
h-ZSM-5	Ethyl acetate		1.6	43 (60)	
d-ZSM-5/4d	Ethyl acetate		4.4	62 (60)	
d-ZSM-5/7d	Ethyl acetate		2.3	55 (60)	
3.9Fe/SBA15[a]	Toluene	0.25 mmol of substrate, 1 mL of solvent, 70 °C, 750 rpm, 10 mg of catalyst	0.46	42 (21)	[1]
	Ethyl acetate		0.29	44 (15)	
	Acetonitrile		0.12	50 (5)	
	Acetone		0.35	0 (17)	
	THF		0.12	48 (5)	
	1,4-Dioxane		0.17	0 (8)	
	Tert-butanol		0.12	13 (5)	
	Cyclohexane		0.23	7 (12)	
	Hexane		0.23	2 (10)	
8.6Fe/MCM41[a,c]	Toluene	0.25 mmol of substrate, 1 mL of solvent, 70 °C, 750 rpm, 25 mg of catalyst	0.8	62 (100)	[1]
	Ethyl acetate		0.8	56 (100)	
	tert-Butanol		0.8	56 (100)	
5.4Cu/MCM4 [a,c]	Toluene		0.2	69 (38)	[1]
	Ethyl acetate		0.01	96 (<1)	
	tert-Butanol		0.00	0 (0)	
9.2Fe/SBA15 [a,c]	Toluene		0.2	65 (100)	[1]
	Ethyl acetate		0.2	56 (100)	
	tert-Butanol		0.2	50 (100)	
7.2Cu/SBA15 [a,c]	Toluene		0.1	67 (41)	[1]
	Ethyl acetate		0.02	80 (6)	
	tert-Butanol		0.04	63 (11)	

[a] The values represent the metal loading (% wt.). [b] TOF was calculated with **Eq. (4.5)**. [c] Substrate corresponds to α-pinene epoxide. [d] Values in parenthesis indicate the conversion and target corresponds to dihydrocarvone or campholenic aldehyde if the substrate is limonene-1,2-epoxide or α-pinene epoxide, respectively.

8.3.8. Rationalization of results with the properties of the catalysts

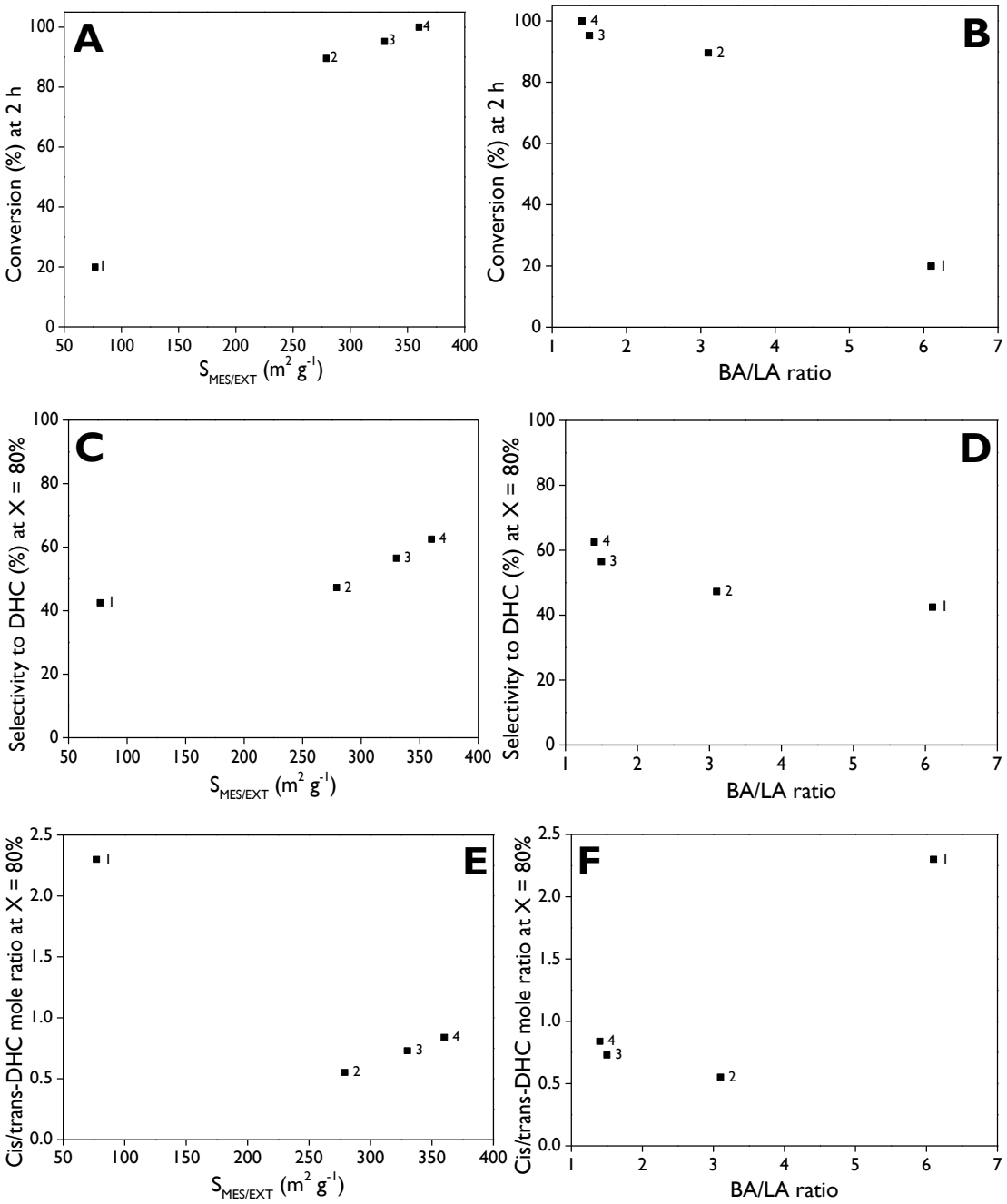

Figure 8.76. Conversion of limonene epoxide at 2 h as a function of the external/mesopore surface area **(A)** and the Brønsted-to-Lewis acidity ratio **(B)**, selectivity to dihydrocarvone at 80% conversion (20% for ZSM-5) as a function of the external/mesopore surface area **(C)** and the Brønsted-to-Lewis acidity ratio **(D)**, and *cis*/*trans* dihydrocarvone molar ratio at 80% conversion (20% for ZSM-5) as a function of the external/mesopore surface area **(E)** and the Brønsted-to-Lewis acidity ratio **(F)**, for (1) ZSM-5, (2) h-ZSM-5, (3) d-ZSM-5/7d, (4) d-ZSM-5/4d. **Reaction conditions:** $C_{LE,0}$ = 13 mmol L^{-1}, 75 mL of total volume, anhydrous ethyl acetate as a solvent, 115 mg of catalyst, 70 °C, 520-530 rpm, N_2 atmosphere.

8.3.9. Temperature Programmed Oxidation – Mass Spectrometry (TPO-MS)

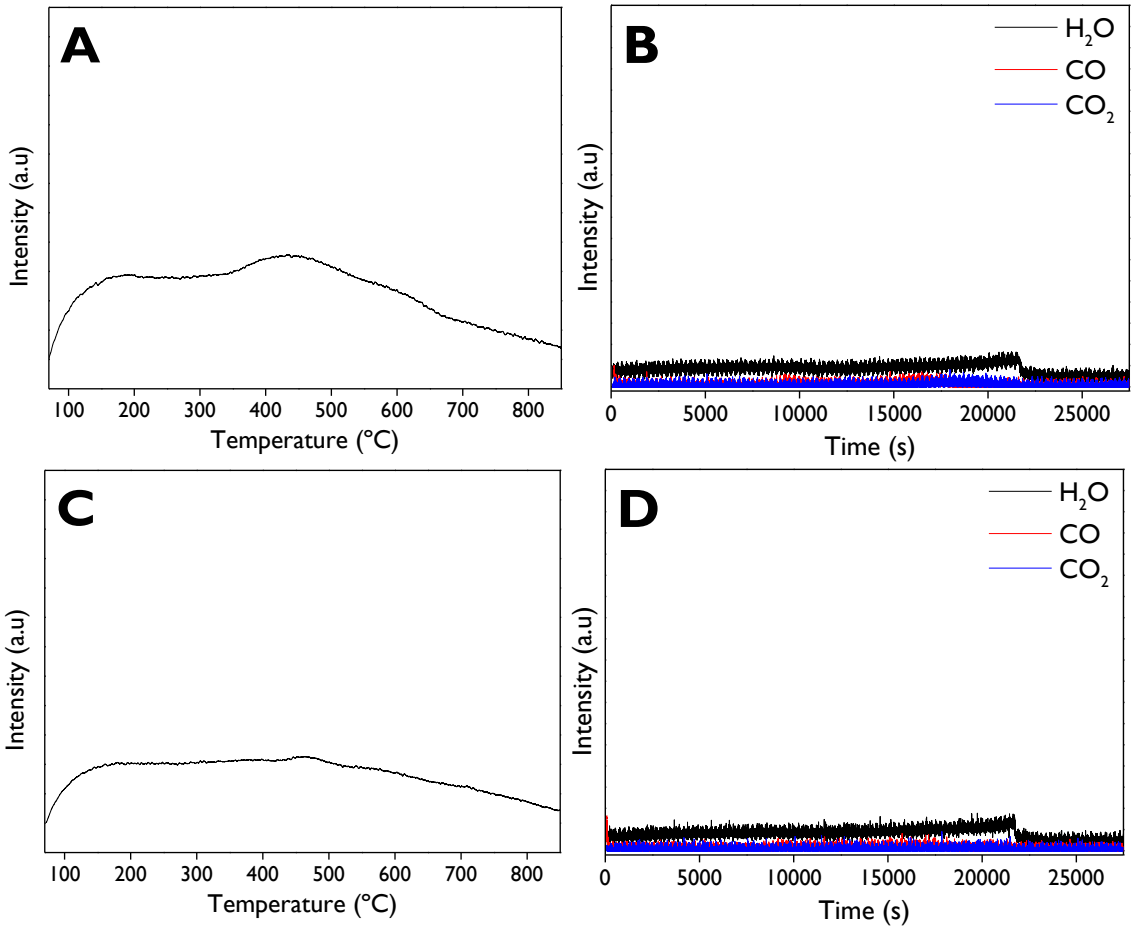

Figure 8.77. TPO profiles (**A, C**) and *in-situ* mass spectrometry (**B, D**) for the spent (**A, B**) and regenerated catalyst d-ZSM-5/4d (**C, D**).

8.3.10. TGA-Air analyses

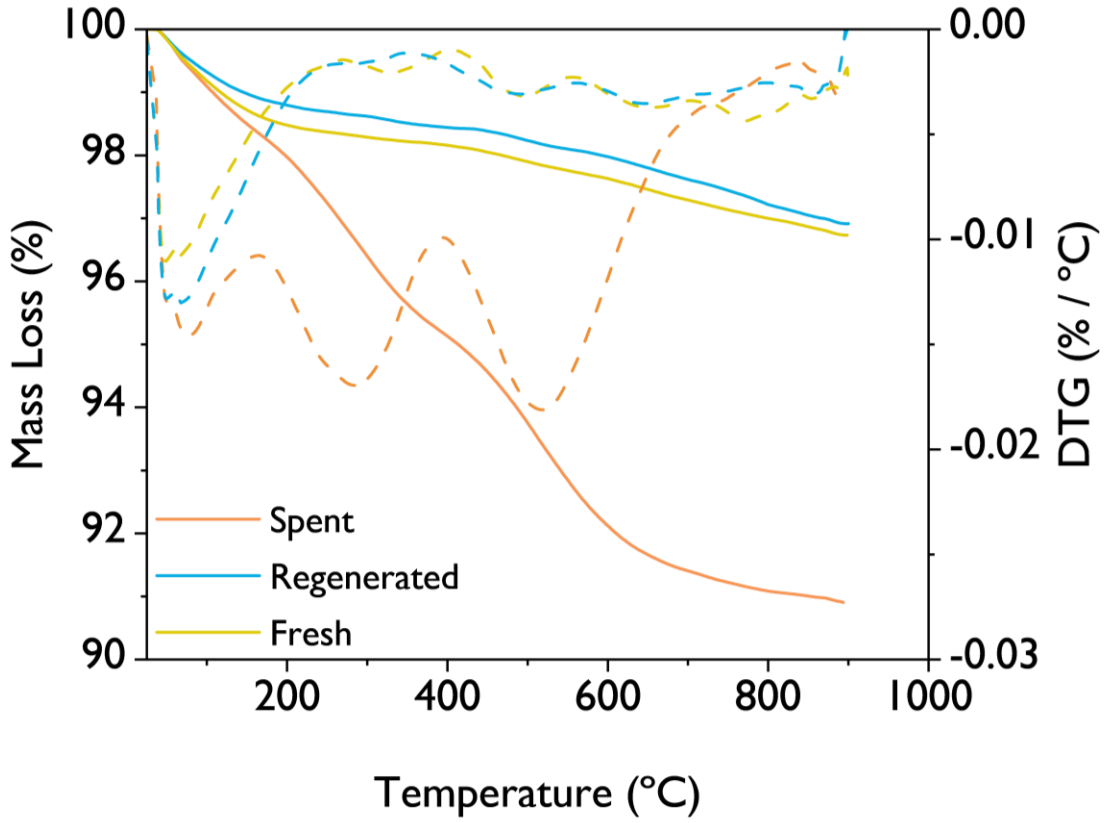

Figure 8.78. TGA-DTG (air) analyses of the fresh, spent, and regenerated catalysts of sample d-ZSM-5/4d.

8.3.11. Conversion of limonene-1,2-epoxide isomers

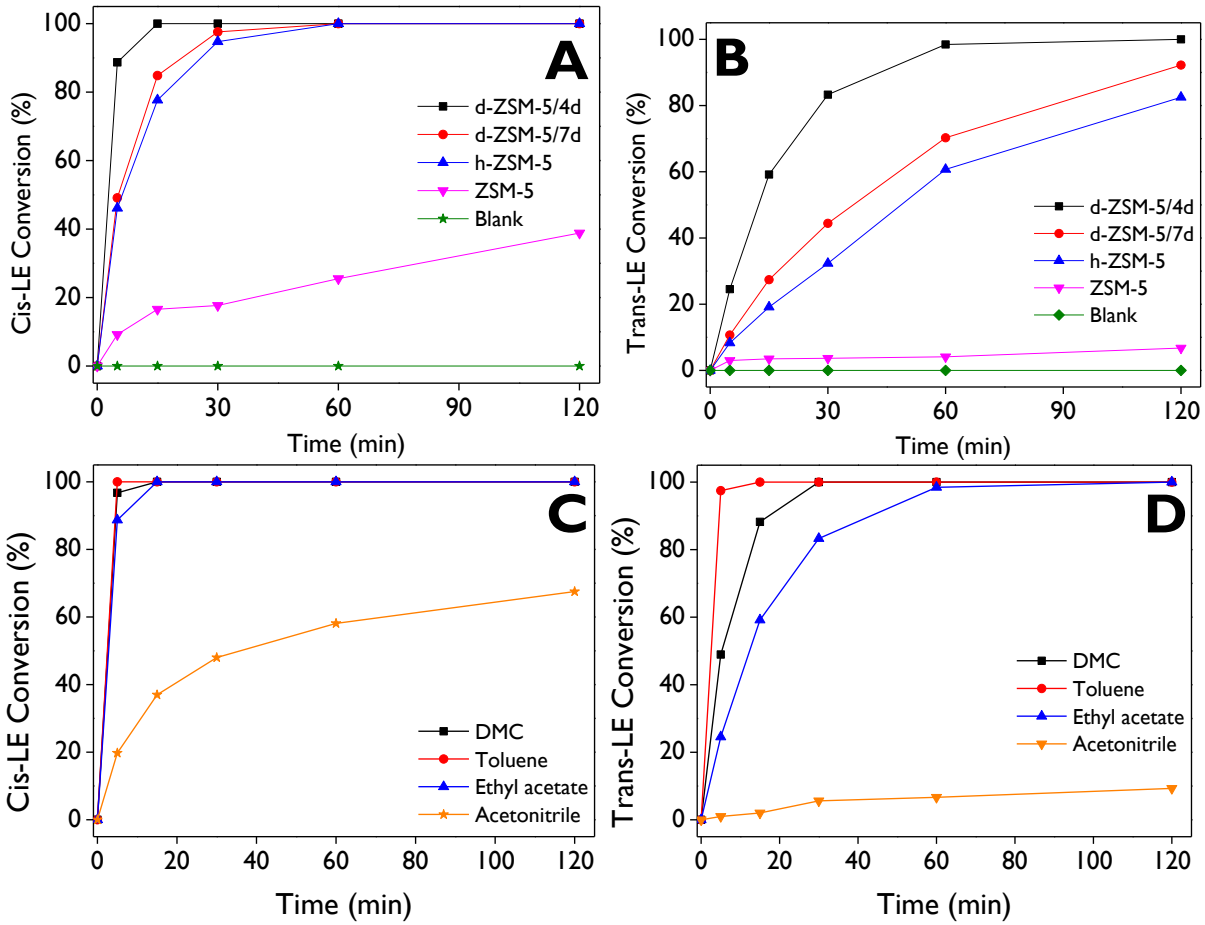

Figure 8.79. Conversion of cis-limonene-1,2-epoxide (**A, C**) and trans-limonene-1,2-epoxide (**B, D**) as a function of reaction time, evaluating the effect of the catalyst (**A, B**) and the solvent (**C, D**). Reaction conditions for Figures A and B are described in **Figure 4.5**, and those for Figures C and D are described in **Figure 4.7**.

8.3.12. Isomerization of pinene epoxides

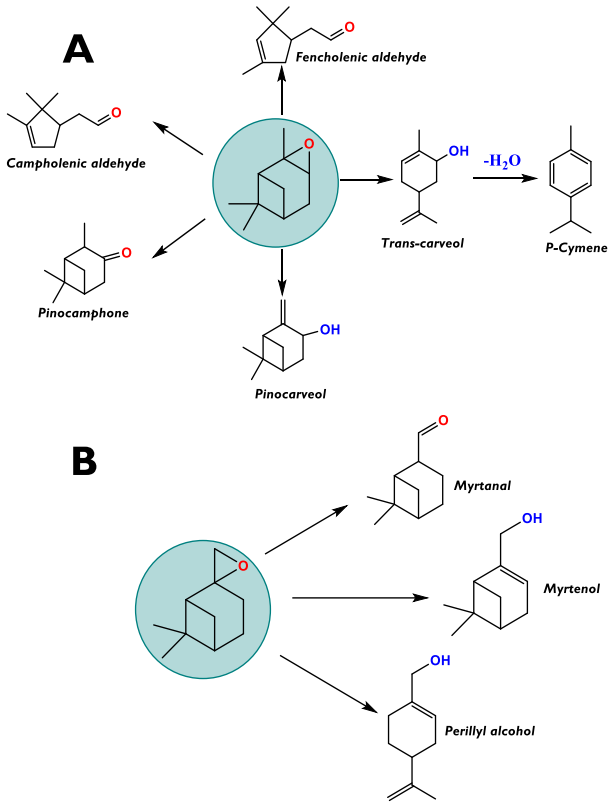

Figure 8.80. Main products of **(A)** α-pinene epoxide and **(B)** β-pinene epoxide rearrangement.

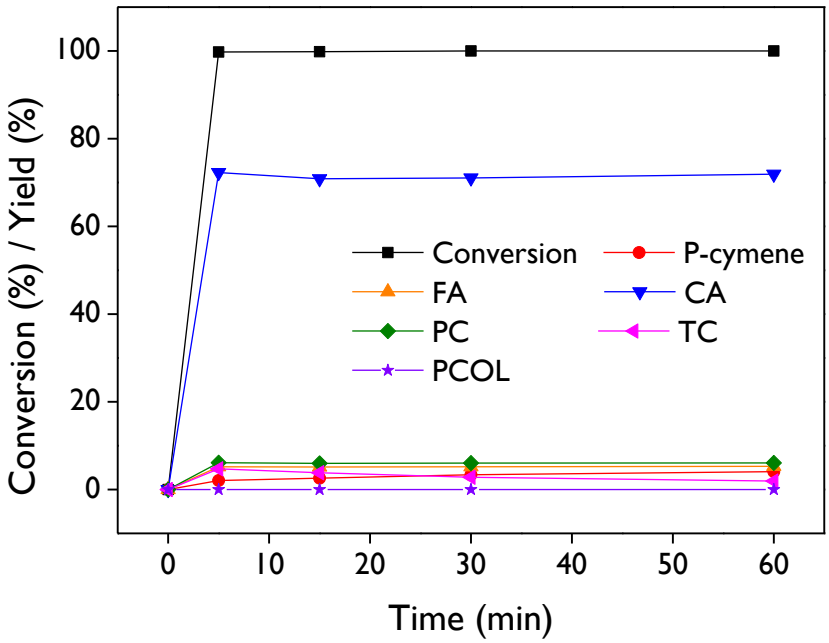

Figure 8.81. Conversion and product distribution of the isomerization of α-pinene epoxide over d-ZSM-5/4d. FA: Fencholenic aldehyde, CA: Campholenic aldehyde, PC: Pinocamphone, TC: *Trans*-carveol, PCOL: Pinocarveol, PA: Perillyl alcohol. **Reaction conditions:** C_0 = 13 mmol L^{-1}, 75 mL of total volume, dimethyl carbonate as a solvent, 115 mg of catalyst, 70 °C, 520-530 rpm, N_2 atmosphere.

8.3.13. Comparison of catalytic systems for the isomerization of pinene epoxides.

Table 8.7. Comparison of catalytic systems for the isomerization of α- and β-pinene epoxides.

Entry	Substrate	Catalyst	Solvent	Reaction conditions	Conversion (%)	Selectivity (%)	Ref
1	α-Pinene epoxide	d-ZSM-5/4d	Ethyl acetate	13 mmol L^{-1}, 115 mg catalyst, 60 °C, 15 min	100	62.5 CA 8.1 TC 5.7 FA 5.6 PC 2 PCY	This work
2			Dimethyl carbonate	13 mmol L^{-1}, 115 mg catalyst, 70 °C, 5 min	100	72.4 CA 4.7 TC 5.2 FA 6.1 PC 2.1 PCY	This work
3		ZrP[a] (2.4 M)	N, N-Dimethylacetamide	3.28 mmol substrate, 50 mg catalyst, 2 mL solvent, 160 °C, 5 h	100	19 CA 73 TC	[2]
4		Fe/MCM-41 (1.7 wt%)	Toluene	0.25 mmol substrate, 10 mg catalyst, 1 mL solvent, 70 °C, 2.5 h	100	66 CA	[1]
5			Ethyl acetate		100	58 CA	
6		Cu/MCM-41 (1.3 wt%)	Toluene		20	82 CA	
7		Fe/SBA-15 (3.9 wt%)	Toluene		100	64 CA	
8			Ethyl acetate		100	58 CA	
9		Cu/SBA-15 (1.2 wt%)	Toluene		46	71 CA	
10		MZ-5[b] (1.5)	N, N-Dimethylacetamide	2 mmol substrate, 75 mg catalyst, 100 mL solvent, 140 °C, 3 h	92	27 CA 45 TC	[3]
11		MoO_3-Modified beta zeolite	Toluene	1.25 g substrate, 125 mg catalyst, 6 mL solvent, 70 °C, 3 h	100	34.2 CA 14.8 TC 14.0 PMD	[4]
12			Ethyl acetate		97	37.1 CA 15.8 TC 13.9 PMD	
13		$Cs_{2.5}H_{0.5}PW_{12}0_{40}$	Acetone	0.75 mmol substrate, 7.50 µmol catalyst, 5 mL total, 40 °C, 5 min	100	17 CA 11 TS 62 Pinol	[5]
14		Al-SiO_2 (12 wt%)	Dichloroethane	0.25 mmol substrate, 5 mg catalyst, 2 mL solvent, 30 °C, 30 min	80	72 CA 2 FA 15 TC 8 TS	[6]
15		Phosphonate/Carbon	DMF	3.28 mmol substrate, 50 mg catalyst, 2 mL solvent, 140 °C, 1 h	100	22 CA 67 TC 9 TPC	[7]
16	β-Pinene epoxide	d-ZSM-5/4d	Ethyl acetate	13 mmol L^{-1}, 115 mg catalyst, 50 °C, 5 min	100	47.7 myrtanal 3.1 myrtenol 18.5 PA	This work
17		Fe/MCM-41	Acetonitrile	0.25 mmol substrate, 26% of	23	90 myrtanal 8 PA	[8]

			catalyst, 1 mL solvent, 70 °C, 1 h		2 myrtenol	
18	Fe/SBA-15	Hexane		27	68 myrtanal 26 PA 6 myrtenol	
19	Sn-Beta-300	Toluene	0.012 mol L^{-1}, 75 mg of catalyst, 150 mL total, 70 °C, 6 h	72	66 myrtanal 10 PA 2 myrtenol	[9]
20	Zeolite beta 25	DMSO	0.8 mL substrate, 25 wt% of catalyst (based on the substrate), volume ratio substrate: solvent = 1:5, 70 °C, 2 h	100	19 myrtanal 36 PA 10 myrtenol 9 p-Menth-1-en-7,8-diol	[10]
21	Ti/SBA-15	Hexane	0.25 mmol substrate, 10 mg catalyst, 0.5 mL solvent, 80 °C, 1 h	> 99	20 myrtanal 45 PA	[11]
22	Mo/SBA-15	Hexane		> 99	63 PA	
23	Mo/MCM-41	Hexane		98	2 myrtanal 20 PA 5 myrtenol	
24	Mo/SiO_2	Hexane		99	12 myrtanal 32 PA 2 myrtenol	

[a]Value in parenthesis refer to the concentration of H_3PO_4 utilized in the synthesis of the catalyst. [b] Selectivities at 70 % conversion. **ZrP:** Zirconium phosphate. **MZ:** Mesoporous beta zeolite where the value in parenthesis denotes the Brønsted-to-Lewis acidity ratio. **CA:** Campholenic aldehyde**. TC:** *Trans*-Carveol. **FA:** Fencholenic aldehyde. **PC**: Pinocamphone. **PCY:** *p*-Cymene. **PMD:** *p*-Methadien-2-ol. **TS:** *trans*-Sobrerol. **TPC:** *Trans*-Pinocarveol. **PA:** Perillyl alcohol.

8.3.14. Characterization of substrate and reaction products

8.3.14.1. Isomerization of limonene-1,2-epoxide

Table 8.8. Retention times for the compounds involved in the isomerization of limonene-1,2-epoxide.

Compound	Retention time (min)
Cis limonene-1,2-epoxide	7.17
Trans limonene-1,2-epoxide	7.22
Cis dihydrocarvone (1a)	7.99
Trans dihydrocarvone (1b)	8.10
Carveol (2)	8.32 and 8.49
Product 3	6.81
Fenchone (4)	7.75
Product 5	7.82
Product 6	5.15
Product 7	7.91
Limonene glycol (8)	9.92

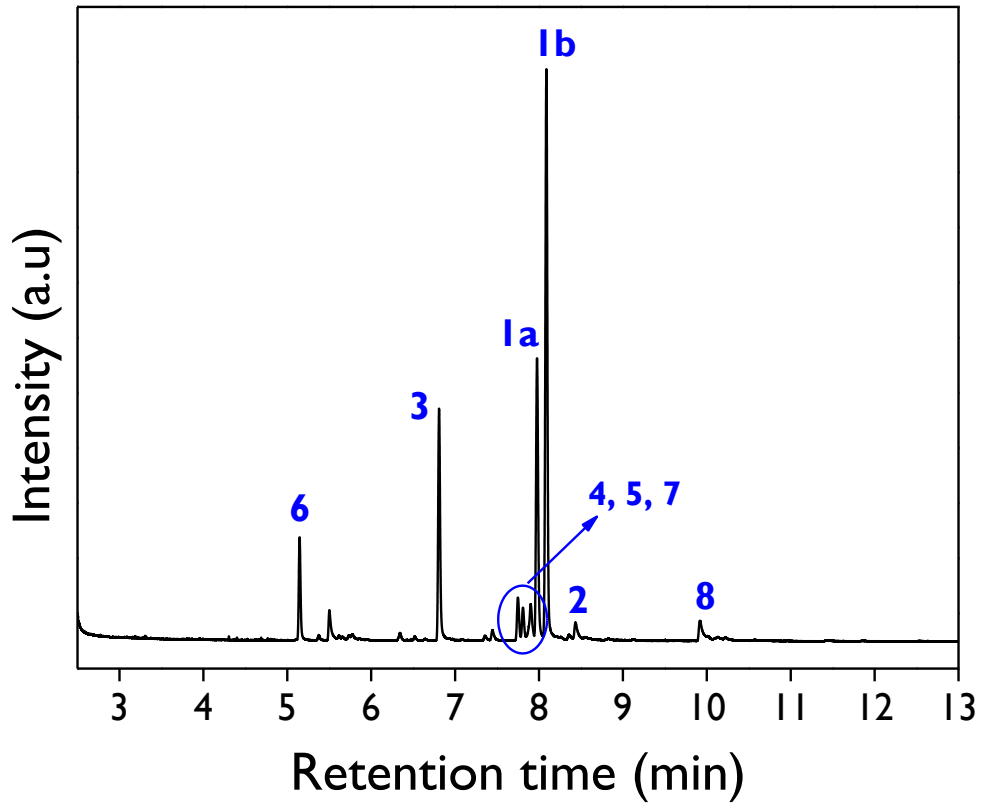

Figure 8.82. Representative chromatogram of a reaction sample after 2 h in the isomerization of limonene-1,2-epoxide. **Reaction conditions:** $C_{substrate,0}$ = 13 mmol L^{-1}, 75 mL of total volume, DMC as a solvent, 115 mg of d-ZSM-5/4d, 70 °C, 520-530 rpm, N_2 atmosphere.

❖ **Product 3**

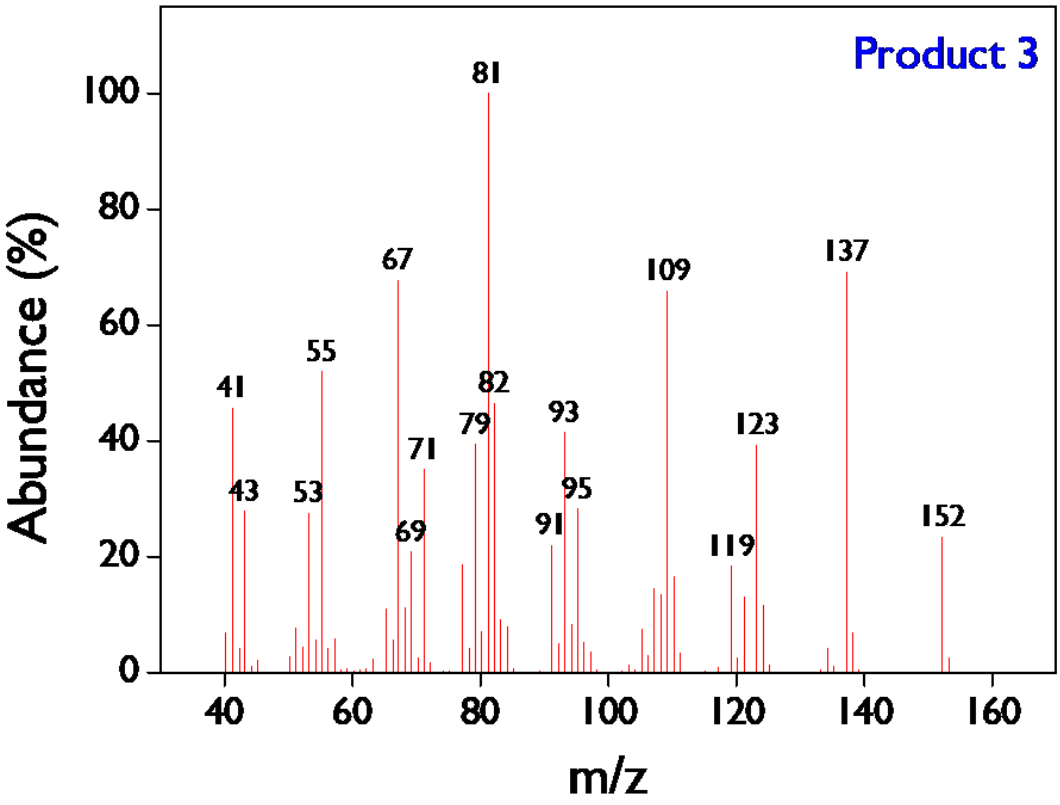

Figure 8.83. Mass spectrum of product 3.

❖ **Product 5**

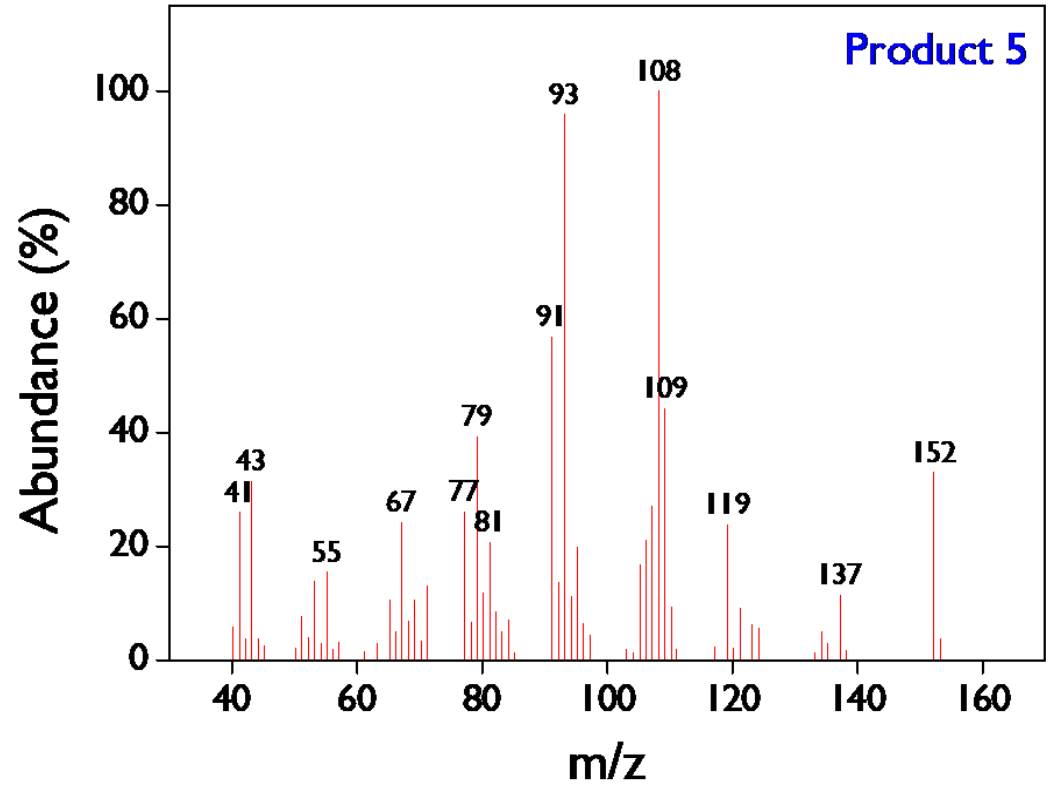

Figure 8.84. Mass spectrum of product 5.

❖ **Product 6**

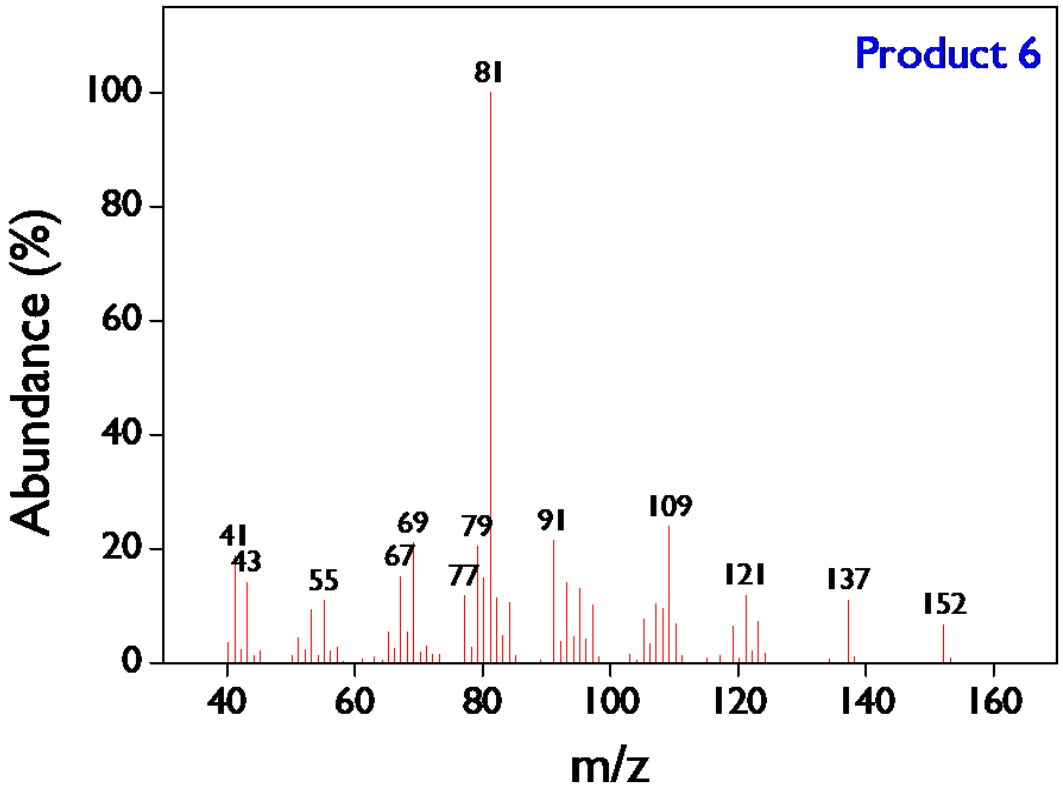

Figure 8.85. Mass spectrum of product 6.

❖ **Product 7**

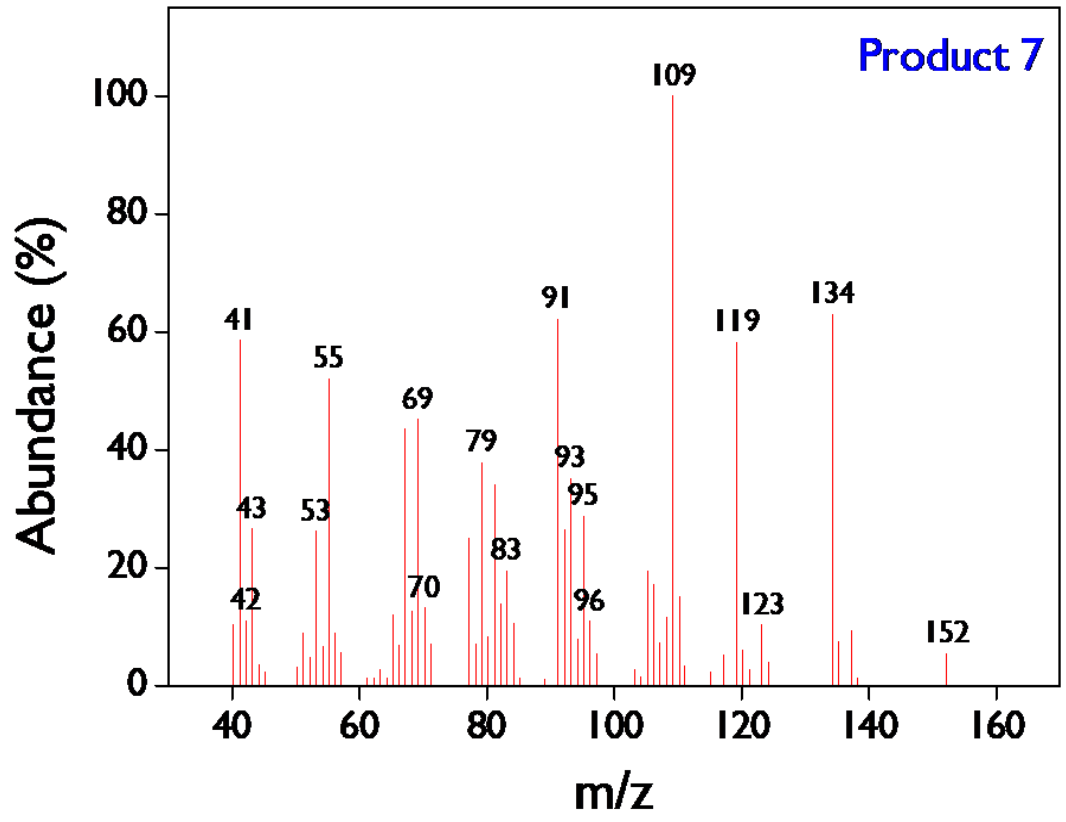

Figure 8.86. Mass spectrum of product 7.

❖ **Product obtained with acetonitrile as solvent**

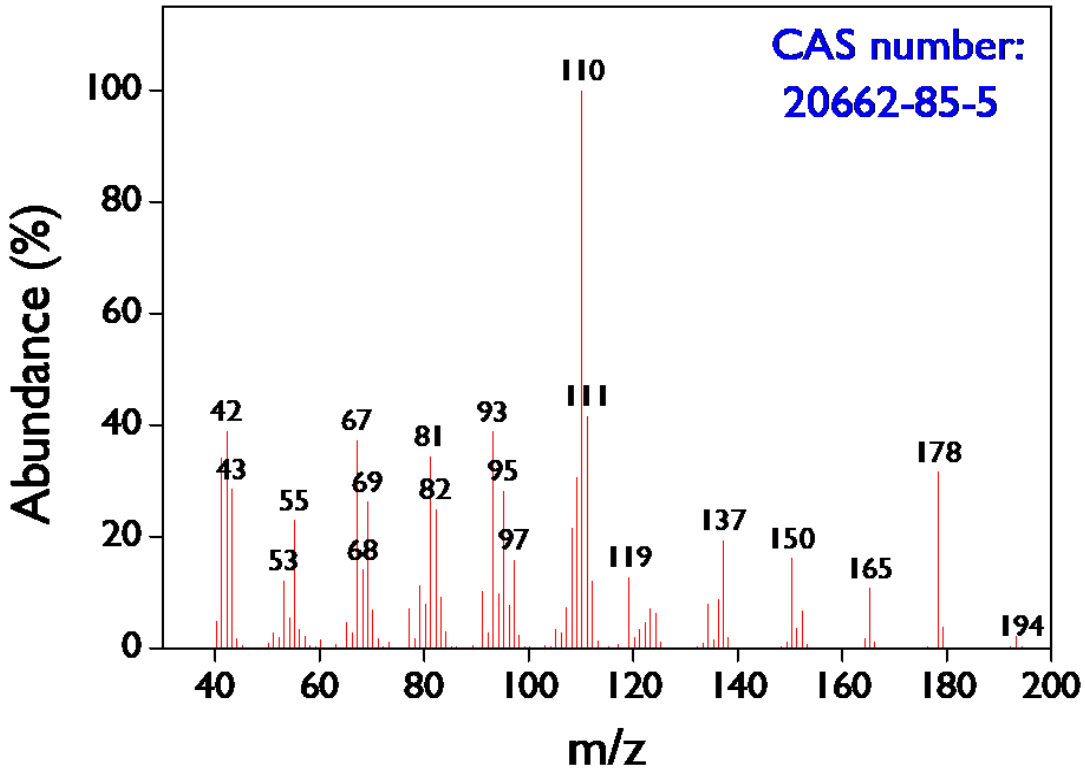

Figure 8.87. Mass spectrum of the main product obtained with acetonitrile as solvent.

8.3.14.2. Isomerization of α-pinene epoxide

Table 8.9. Retention times for the compounds involved in the isomerization of α-pinene epoxide.

Compound	Retention time (min)
α-Pinene epoxide	6.78
Campholenic aldehyde (1)	7.02
Fencholenic aldehyde (2)	6.47
P-Cymene (3)	5.72
Trans-pinocarveol (4)	7.43
Pinocamphone (5)	7.54
Trans-Carveol (6)	8.32

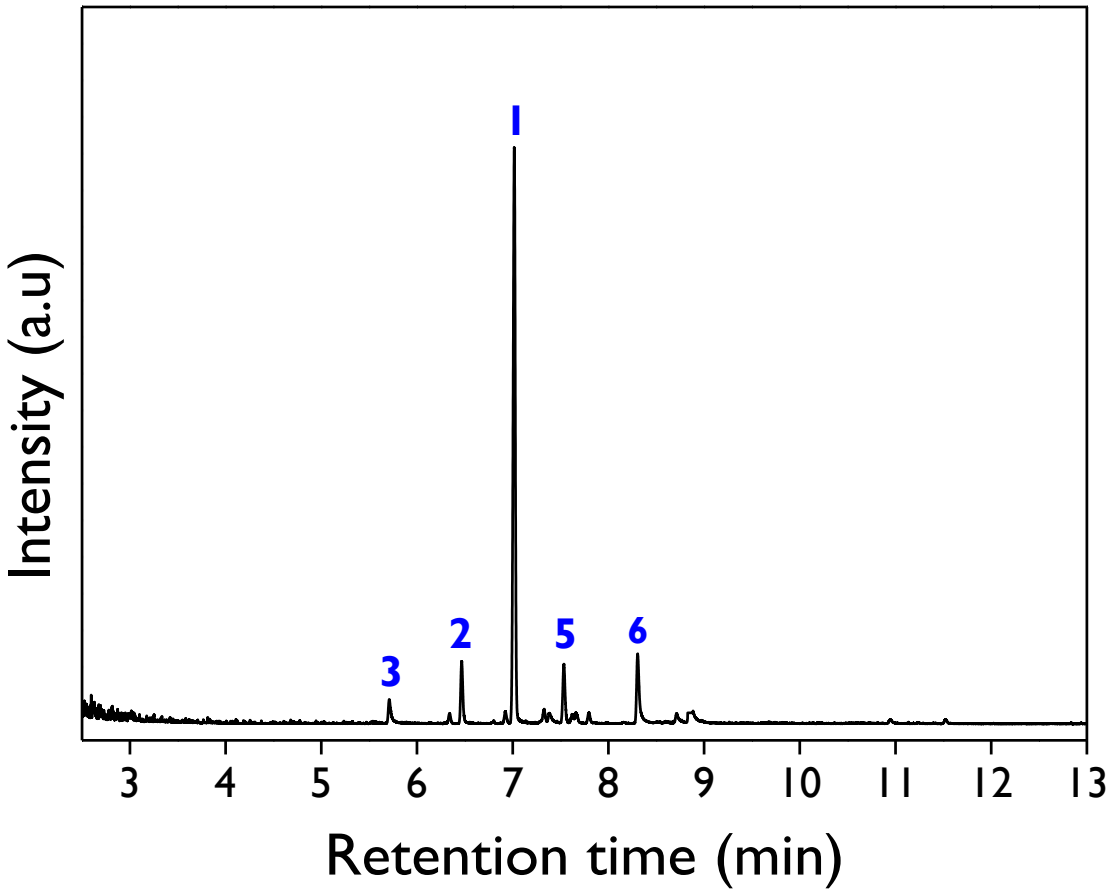

Figure 8.88. Representative chromatogram of a reaction sample after 60 min in the isomerization of α-pinene epoxide. **Reaction conditions:** $C_{substrate,0}$ = 13 mmol L^{-1}, 75 mL of total volume, ethyl acetate as a solvent, 115 mg of d-ZSM-5/4d, 60 °C, 520-530 rpm, N_2 atmosphere.

8.3.14.3. Isomerization of β-pinene epoxide

Table 8.10. Retention times for the compounds involved in the isomerization of β-pinene epoxide.

Compound	Retention time (min)
β-pinene epoxide	7.55
Product 1 (1)	7.11
Product 2 (2)	7.79
Cis-myrtanal (3a)	7.87
Trans-myrtanal (3b)	7.96
Myrtenol (4)	8.08
Perillyl alcohol (5)	9.45
Product 3 (6)	9.84

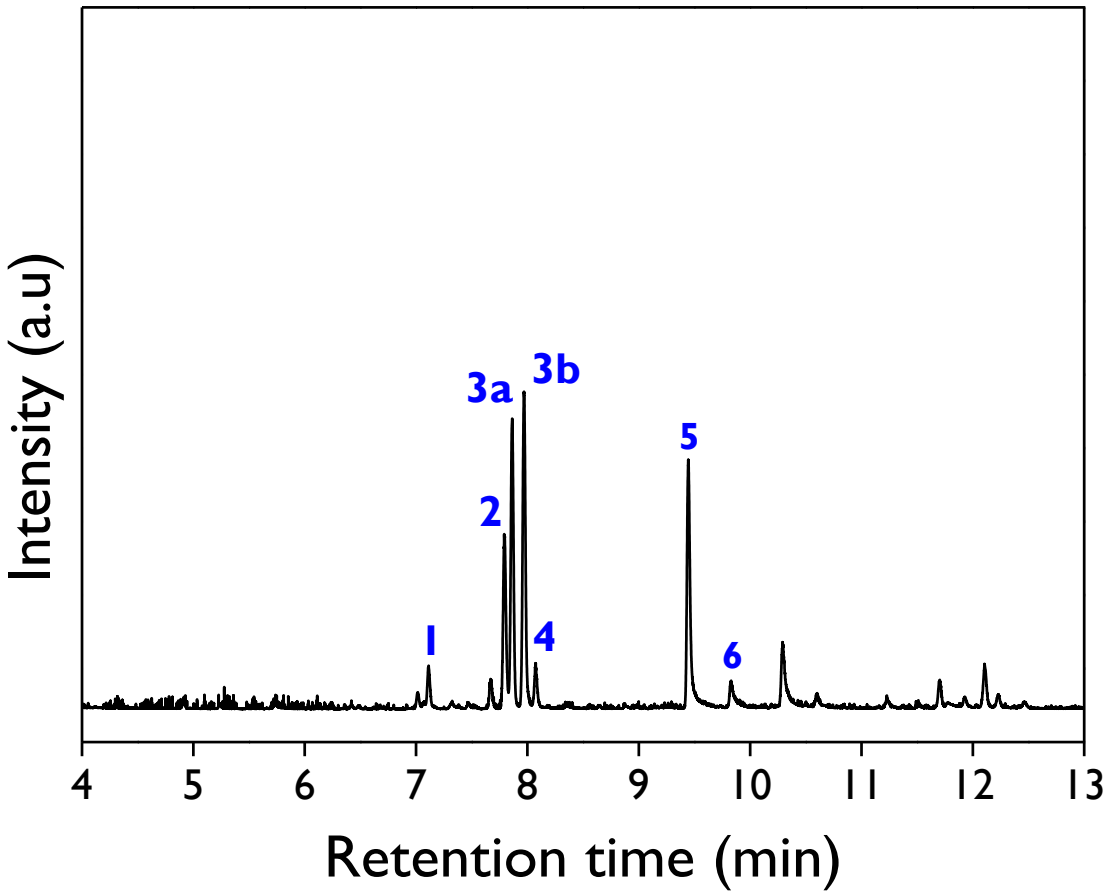

Figure 8.89. Representative chromatogram of a reaction sample after 60 min in the isomerization of β-pinene epoxide. **Reaction conditions:** $C_{substrate,0}$ = 13 mmol L^{-1}, 75 mL of total volume, ethyl acetate as a solvent, 115 mg of d-ZSM-5/4d, 50 °C, 520-530 rpm, N_2 atmosphere.

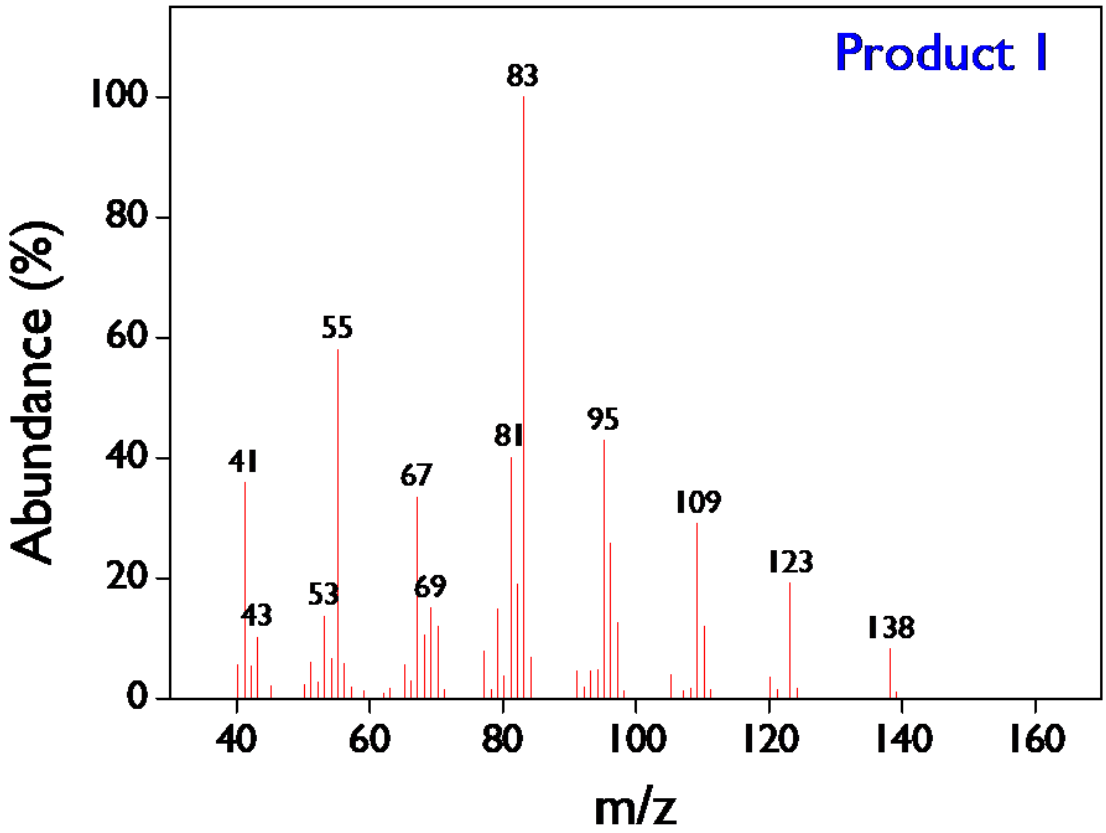

Figure 8.90. Mass spectrum of product 1.

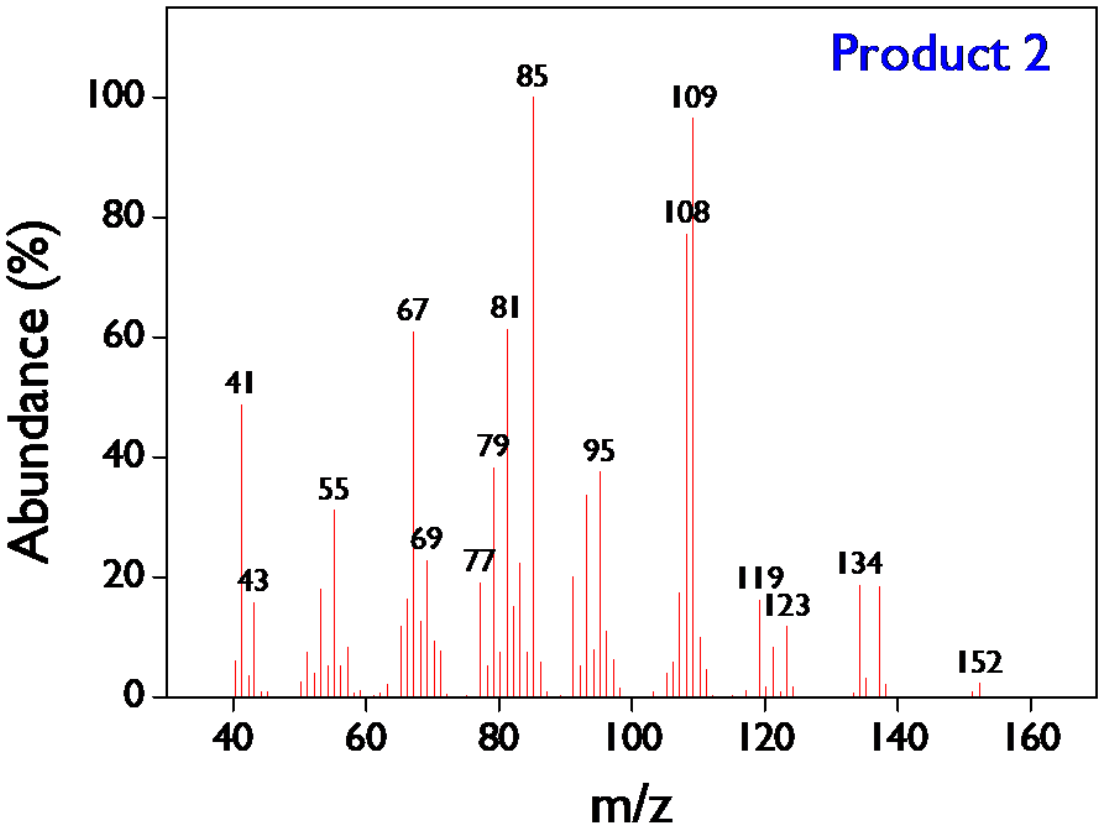

Figure 8.91. Mass spectrum of product 2.

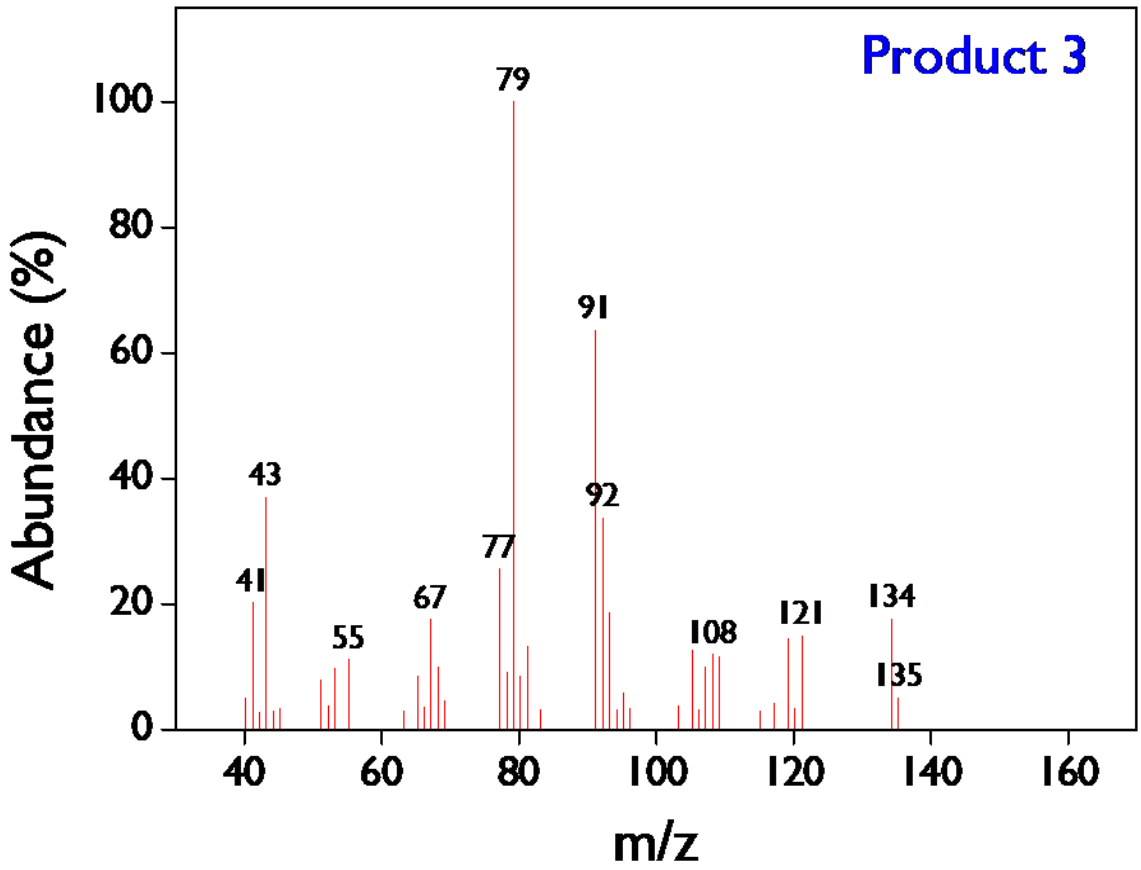

Figure 8.92. Mass spectrum of product 3.

8.3.15. References

[1] J. E. Sánchez-Velandia and A. L. Villa, "Selective synthesis of high-added value chemicals from α-pinene epoxide and limonene epoxide isomerization over mesostructured catalysts: Effect of the metal loading and solvent," *Catal. Today*, vol. 394–396, no. 52, pp. 208–218, Jul. 2022, doi: 10.1016/j.cattod.2021.09.011.

[2] A. S. Singh, D. R. Naikwadi, K. Ravi, and A. V. Biradar, "Chemoselective isomerization of α-Pinene oxide to trans-Carveol by robust and mild Brønsted acidic zirconium phosphate catalyst," *Mol. Catal.*, vol. 521, no. October 2021, p. 112189, Mar. 2022, doi: 10.1016/j.mcat.2022.112189.

[3] R. Barakov *et al.*, "Hierarchical Beta Zeolites As Catalysts in α-Pinene Oxide Isomerization," *ACS Sustain. Chem. Eng.*, vol. 10, no. 20, pp. 6642–6656, May 2022, doi: 10.1021/acssuschemeng.2c00441.

[4] E. Vrbková, E. Vyskočilová, M. Lhotka, and L. Červený, "Solvent Influence on Selectivity in α-Pinene Oxide Isomerization Using MoO3-Modified Zeolite BETA," *Catalysts*, vol. 10, no. 11, p. 1244, Oct. 2020, doi: 10.3390/catal10111244.

[5] C. J. A. Ribeiro, M. M. Pereira, E. F. Kozhevnikova, I. V. Kozhevnikov, E. V. Gusevskaya, and K. A. da Silva Rocha, "Heteropoly acid catalysts in upgrading of biorenewables: Synthesis of para-menthenic fragrance compounds from α-pinene oxide," *Catal. Today*, vol. 344, no. December 2018, pp. 166–170, Mar. 2020, doi: 10.1016/j.cattod.2018.12.023.

[6] V. N. Panchenko, V. L. Kirillov, E. Y. Gerasimov, O. N. Martyanov, and M. N. Timofeeva, "Isomerization of α-pinene oxide to campholenic aldehyde in the presence of Al-SiO2 and magnetic Al-SiO2/Fe3O4 catalysts," *React. Kinet. Mech. Catal.*, vol. 130, no. 2, pp. 919–934, Aug. 2020, doi: 10.1007/s11144-020-01811-x.

[7] A. S. Singh, J. H. Advani, and A. V. Biradar, "Phosphonate functionalized carbon spheres as Brønsted acid catalysts for the valorization of bio-renewable α-pinene oxide to trans - carveol," *Dalt. Trans.*, vol. 49, no. 21, pp. 7210–7217, 2020, doi: 10.1039/D0DT00921K.

[8] M. Chaves-Restrepo, A. Viloria, J. E. Sánchez-Velandia, and A. L. Villa, "Effect of reaction conditions and kinetics of the isomerization of β-pinene epoxide to myrtanal in the presence of Fe/MCM-41 and Fe/SBA-15," *React. Kinet. Mech. Catal.*, vol. 135, no. 4, pp. 2013–2029, Aug. 2022, doi: 10.1007/s11144-022-02220-y.

[9] P. Mäki-Arvela *et al.*, "Isomerization of β-pinene oxide over Sn-modified zeolites," *J. Mol. Catal. A Chem.*, vol. 366, pp. 228–237, Jan. 2013, doi: 10.1016/j.molcata.2012.09.028.

[10] K. Zítová, E. Vyskočilová, and L. Červený, "Preparation of α-terpineol and perillyl alcohol using zeolites beta," *Res. Chem. Intermed.*, vol. 47, no. 10, pp. 4297–4310, Oct. 2021, doi: 10.1007/s11164-021-04515-6.

[11] M. C. Cruz, J. E. Sánchez-Velandia, S. Causíl, and A. L. Villa, "Selective Synthesis of Perillyl Alcohol from β-Pinene Epoxide over Ti and Mo Supported Catalysts," *Catal. Letters*, vol. 151, no. 8, pp. 2279–2290, Aug. 2021, doi: 10.1007/s10562-020-03489-1.

8.4. Chapter 5

8.4.1. Kinetic modeling

The reaction rate laws for the eight reactions of the reaction network (**Figure 5.2**) are obtained, using heterogeneous kinetic models as deduced from the steps illustrated in **Figure 8.93**.

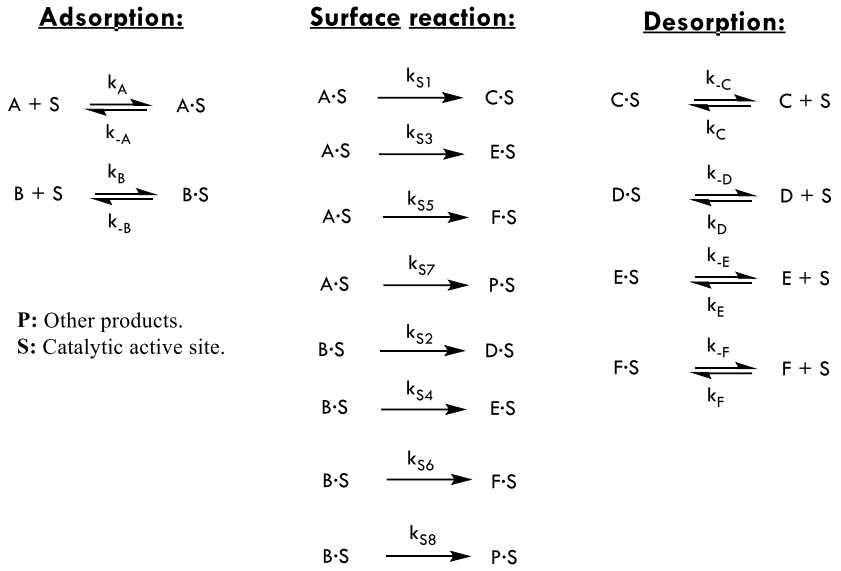

Figure 8.93. Elemental steps proposed for the reaction network of the isomerization of limonene-1,2-epoxide.

S: Surface site on catalyst.
C_i: Concentration of specie i in the bulk of the solution.
C_v: Concentration of available surface site on the catalyst surface.
C_{is}: Concentration of specie i adsorbed at the surface site.
C_t: Total number of sites available on the catalyst surface.
k_i: Reaction rate constant of direct reaction i.
k_{-i}: Reaction rate constant of reverse reaction i.
K_i: Equilibrium constant for step i.

$$r_{A,ads} = k_A \left[C_A C_V - \frac{C_{A\cdot S}}{K_A} \right] \quad \textbf{(8.23)}$$

$$r_{B,ads} = k_B \left[C_B C_V - \frac{C_{B\cdot S}}{K_B} \right] \quad \textbf{(8.24)}$$

$$r_1 = k_{s1} C_{A\cdot S} \quad \textbf{(8.25)}$$

$$r_2 = k_{s2} C_{B\cdot S} \quad \textbf{(8.26)}$$

$$r_3 = k_{s3} C_{A\cdot S} \quad \textbf{(8.27)}$$

$$r_4 = k_{s4}\mathrm{C_{B\cdot S}} \quad \textbf{(8.28)}$$

$$r_5 = k_{s5}\mathrm{C_{A\cdot S}} \quad \textbf{(8.29)}$$

$$r_6 = k_{s6}\mathrm{C_{B\cdot S}} \quad \textbf{(8.30)}$$

$$r_7 = k_{s7}\mathrm{C_{A\cdot S}} \quad \textbf{(8.31)}$$

$$r_8 = k_{s8}\mathrm{C_{B\cdot S}} \quad \textbf{(8.32)}$$

$$r_{C,des} = k_{-C}\left[C_{C\cdot S} - \frac{C_C C_V}{K_{C,d}}\right] \quad \textbf{(8.33)}$$

$$r_{D,des} = k_{-D}\left[\mathrm{C_{D\cdot S}} - \frac{C_D C_V}{K_{D,d}}\right] \quad \textbf{(8.34)}$$

$$r_{E,des} = k_{-E}\left[\mathrm{C_{E\cdot S}} - \frac{C_E C_V}{K_{E,d}}\right] \quad \textbf{(8.35)}$$

$$r_{F,des} = k_{-F}\left[\mathrm{C_{F\cdot S}} - \frac{C_F C_V}{K_{F,d}}\right] \quad \textbf{(8.36)}$$

The **Eqs. (8.23)**, **(8.24)**, and **(8.33)-(8.36)** are solved to find the concentrations of adsorbed species (C_{is}) when these are equal to zero, assuming the surface reactions (**Eqs. (8.25)-(8.32)**) as the rate-limiting steps.

$$\mathrm{C_{A\cdot S}} = \mathrm{K_A C_A C_V} \quad \textbf{(8.37)}$$

$$\mathrm{C_{B\cdot S}} = \mathrm{K_B C_B C_V} \quad \textbf{(8.38)}$$

$$\mathrm{C_{C\cdot S}} = \frac{C_C C_V}{K_{C,d}} = K_C C_C C_V \quad \textbf{(8.39)}$$

$$\mathrm{C_{D\cdot S}} = \frac{C_D C_V}{K_{D,d}} = K_D C_D C_V \quad \textbf{(8.40)}$$

$$\mathrm{C_{E\cdot S}} = \frac{C_E C_V}{K_{E,d}} = K_E C_E C_V \quad \textbf{(8.41)}$$

$$\mathrm{C_{F\cdot S}} = \frac{C_F C_V}{K_{F,d}} = K_F C_F C_V \quad \textbf{(8.42)}$$

The balance of sites is defined by **Eq. (8.43)**:

$$C_t = C_V + C_{A\cdot S} + C_{B\cdot S} + C_{C\cdot S} + C_{D\cdot S} + C_{E\cdot S} + C_{F\cdot S} \quad \textbf{(8.43)}$$

By replacing **Eqs. (8.37) – (8.42)** in **Eq. (8.43)** and simplifying, **Eq. (8.44)** is obtained:

$$C_t = C_V + K_A C_A C_V + K_B C_B C_V + K_C C_C C_V + K_D C_D C_V + K_E C_E C_V + K_F C_F C_V$$

$$C_V = \frac{C_t}{1 + K_A C_A + K_B C_B + K_C C_C + K_D C_D + K_E C_E + K_F C_F} \quad \textbf{(8.44)}$$

Replacing **Eq. (8.44)** in **Eqs. (8.37)** and **(8.38)**:

$$C_{A\cdot S} = \frac{K_A C_A C_t}{1 + K_A C_A + K_B C_B + K_C C_C + K_D C_D + K_E C_E + K_F C_F} \quad \textbf{(8.45)}$$

$$C_{B\cdot S} = \frac{K_B C_B C_t}{1 + K_A C_A + K_B C_B + K_C C_C + K_D C_D + K_E C_E + K_F C_F} \quad \textbf{(8.46)}$$

The final expressions for the reaction rates of r_1-r_8 are shown below, where $k_i = k_{si} K_i C_t$:

$$r_1 = \frac{k_1 C_A}{1 + K_A C_A + K_B C_B + K_C C_C + K_D C_D + K_E C_E + K_F C_F} \quad \textbf{(8.47)}$$

$$r_2 = \frac{k_2 C_B}{1 + K_A C_A + K_B C_B + K_C C_C + K_D C_D + K_E C_E + K_F C_F} \quad \textbf{(8.48)}$$

$$r_3 = \frac{k_3 C_A}{1 + K_A C_A + K_B C_B + K_C C_C + K_D C_D + K_E C_E + K_F C_F} \quad \textbf{(8.49)}$$

$$r_4 = \frac{k_4 C_B}{1 + K_A C_A + K_B C_B + K_C C_C + K_D C_D + K_E C_E + K_F C_F} \quad \textbf{(8.50)}$$

$$r_5 = \frac{k_5 C_A}{1 + K_A C_A + K_B C_B + K_C C_C + K_D C_D + K_E C_E + K_F C_F} \quad \textbf{(8.51)}$$

$$r_6 = \frac{k_6 C_B}{1 + K_A C_A + K_B C_B + K_C C_C + K_D C_D + K_E C_E + K_F C_F} \quad \textbf{(8.52)}$$

$$r_7 = \frac{k_7 C_A}{1 + K_A C_A + K_B C_B + K_C C_C + K_D C_D + K_E C_E + K_F C_F} \quad \textbf{(8.53)}$$

$$r_8 = \frac{k_8 C_B}{1 + K_A C_A + K_B C_B + K_C C_C + K_D C_D + K_E C_E + K_F C_F} \quad \textbf{(8.54)}$$

8.4.2. Experimental data

Table 8.11. Experimental data for five entries (**Table 5.2**).

Concentrations (mmol L^{-1}) - Entry 1										
Time (min)	**A**	**B**	**C**	**D**	**E**	**F**	**G**	**H**	**I**	**J**
0	12.25035	0.391386	0.00000	0	0	0	0	0	0	0
5	8.175433	0.340825	2.55695	0	0.576582	1.846867	0	0.295413	0	0.460803
15	4.670978	0.276649	3.59123	0	0.949243	2.452585	0	0.491995	0.101546	0.639374
30	2.416241	0.221549	4.55546	0.192321	1.277328	3.0131	0.084902	0.594946	0.159072	0.808615
60	0.493175	0.138682	4.88088	0.136366	1.342556	3.334137	0.116398	0.644153	0.21732	0.855694
120	0	0	4.87827	0.118789	1.196238	3.360986	0.162482	0.636463	0.288565	0.840628
Concentrations (mmol L^{-1}) - Entry 2										
Time (min)	**A**	**B**	**C**	**D**	**E**	**F**	**G**	**H**	**I**	**J**
0	0	11.1144	0	0	0	0	0	0	0	0
5	0	8.971172	0.171649	2.879587	0.14000	0.296878	0.097957	0.056501	0.124615	0
15	0	5.993082	0.239275	4.460625	0.238327	0.503389	0.147129	0.072447	0.180834	0
30	0	3.432805	0.272488	5.845286	0.327046	0.676072	0.213139	0.00339	0.249476	0
120	0	0	0.378855	7.989785	0.547031	0.870578	0.497457	0	0.679019	0
Concentrations (mmol L^{-1}) - Entry 3										
Time (min)	**A**	**B**	**C**	**D**	**E**	**F**	**G**	**H**	**I**	**J**
0	6.108932	8.945104	0	0	0	0	0	0	0	0
5	4.799300	9.111212	0.732329	0.146161	0.074622	0.210545	0	0.045744	0	0.086399
15	3.161466	8.612688	1.349758	0.275916	0.251710	0.407730	0.018222	0.108248	0	0.189008
30	1.968829	8.286401	1.867082	0.464872	0.400199	0.59586	0.029754	0.163486	0.029113	0.281429
60	0.767211	7.215008	2.222586	0.765867	0.570286	0.743413	0.049114	0.188992	0.055936	0.342854
120	0.13582	6.103274	2.598271	1.332841	0.827384	0.883472	0.115393	0.286947	0.079729	0.452211
Concentrations (mmol L^{-1}) - Entry 4										
Time (min)	**A**	**B**	**C**	**D**	**E**	**F**	**G**	**H**	**I**	**J**
0	5.851357	9.037603	0	0	0	0	0	0	0	0
5	3.809269	8.51795	0.900368	0.217757	0.136455	0.361606	0	0.088357	0.014514	0.132204
15	1.856026	7.678723	1.59539	0.504498	0.364595	0.682448	0.023952	0.157649	0.039757	0.265831
30	0.697334	7.161304	2.218446	0.983868	0.583549	0.96205	0.049728	0.232713	0.048851	0.379125
60	0.063724	5.199296	2.418621	1.70608	0.687199	1.099821	0.086861	0.257291	0.091396	0.440464
120	0	3.054952	2.436383	2.541658	1.039105	1.21036	0.154517	0.261546	0.161353	0.44751
Concentrations (mmol L^{-1}) - Entry 5										
Time (min)	**A**	**B**	**C**	**D**	**E**	**F**	**G**	**H**	**I**	**J**
0	5.437472	9.260068	0	0	0	0	0	0	0	0
5	0.617526	7.024891	2.652738	1.586881	0.796826	1.19208	0.071522	0.267844	0.073935	0.344678
15	0	3.822	2.878806	3.088456	1.132462	1.418247	0.151253	0.290416	0.184536	0.399529
30	0	1.57173	2.972405	4.269705	1.283957	1.573629	0.254321	0.305177	0.325563	0.436342
60	0	0.146626	3.063548	5.035164	1.328376	1.639575	0.389552	0.293647	0.542354	0.496938
120	0	0	3.026907	5.02392	1.289662	1.596416	0.422709	0.290982	0.620866	0.514407

8.4.3. Codes for optimization of kinetic parameters using ModEst software

8.4.3.1. Project definition

```
&project
 projectname = 'le'
/
 &files
nsets = 5
datafile(1) = 'Exp1.txt'
datafile(2) = 'Exp2.txt'
datafile(3) = 'Exp3.txt'
datafile(4) = 'Exp4.txt'
datafile(5) = 'Exp5.txt'

dumpfile = 'le3.bin'
resultfile  = 'le3.est'
reportfile = 'le3.sta'
optfile  = 'le3.res'
ndumpp      = 100
!restartfile  = 'le3.res'

/

&problem
task  = 'est'
model = 'ode'
odesolver = 'odessa'
optimizer = 'simlev'
objfun = 'lsq'
/

&modelpar
nstates = 11
nsaux   = 10

modelvar = 'Tmean  global 60
          k1 global   2.29e-5
          k2 global 4.06e-5
          k3 global 5.95e-6
          k4 global 2.72e-7
          k5 global 1.03e-5
          k6 global 1.43e-7
          k7 global 1.22e-5
          k8 global 4.14e-6
          Ea1 global 42900
          Ea2 global 167000
          Ea3 global 42200
          Ea4 global 207000
          Ea5 global 71600
```

```
        Ea6 global 250000
        Ea7 global 8550
        Ea8 global 60600
        KA  global 0
        KB  global 0
        KC  global 0.22
        KD  global 0
        KE  global 0
        KF  global 0
        KG  global 0
        KH  global 0
        KI  global 0
        KJ  global 0

        Vr     global   0.075
        Temp   local    70 70 50 60 70
        Mcat   local    115.8 116.3 116.3 115.1 115.5
        time     Odevar   file;

        s0(1:10)  initval   file;
                        file;
                        file;
                        file;
                        file;
                        file;
                        0;

                      '

target  = '
        k1  0 10
        k2  0 10
        k3  0 10
        k4  0 10
        k5  0 10
        k6  0 10
        k7  0 10
        k8  0 10
        Ea1   1e3 1.5e5
        Ea2   1e3 2.5e5
        Ea3   1e3 1.5e5
        Ea4   1e3 2.5e5
        Ea5   1e3 1.5e5
        Ea6   1e3 2.5e5
        Ea7   1e3 1.5e5
        Ea8   1e3 2.5e5
        KC     0 10
```

```
          '

/

dstep = 1e-6

 &filepar
combined = 0
usew =0
nobs(1)   = 6 5 6 6 6
ncolxy(1) = 14
nydata(1) = 6
indx(1,1) = 1
indy(1,1) = 2 3 4 5 6 7
 /

&print
echo = 1
echodata = 1
optmonit = 1
stats = 1
debug = 1
jacout = 1
/

&design
/

&simflex
abstols = 1.00E-16
reltols = 1.00E-16
sizes = .1
itmaxs = 600
/

&levmar
 reltollm=1.0d-10
 iterdflm=100

/


&newton
/


&odessa
 satol = 1.0e-9
```

```
 srtol = 1.0e-9
 /

 &euler
 stpeul = 1e-3
 /


&mcmc
 nsimu       = 80000   ! length of the chain
 doadapt     = 0       ! do we adapt
 adaptint    = 200     ! intervall for adaptation
 burnintime  = 5000    ! initial burn in time
 doburnin    = 1
 drscale     = 5       ! scaling factor for second stage DR
! sstype      = 0       ! how SS is calculated: 0 = normal, 1 = sqrt, 2 = lognormal
 sstrans     = 1
 printint    = 1000    ! interval to print statistics
 filepars    = 0       ! read initial values from files instead of modest? (1=yes)
 updatesigma = 1       ! update error variance? (1=yes)
 N0          = 1       ! prior for error variance,
 S02         = 0       !    1/s^2 ~ Gamma(N0/2,2/N/S02)
 chainfile   = 'chain.mat'    ! file to save the chain
 s2file      = 's2chain.mat'  ! file to save sigma2 chain
 dumpint     = 50
/
```

8.4.3.2. Method subroutine

```
      subroutine fode(ns,t,s,ds,
     &           xdata,nx,nobs,
     &           nsaux,nstatea,
     &           states0,
     &           gpar,ngpar,
     &           lpar,nlpar,
     &           iobs,iset)

      implicit none

c     arguments

      integer*4 ns,nsaux,nstatea    !n of state variables
      real*8    t           !time
      real*8    s(nstatea) !state variables
      real*8    ds(ns)      !derivatives
      integer*4 nx,nobs,ngpar,nlpar
      real*8    xdata(nx,nobs)
      real*8    states0(nstatea)
```

```
      real*8    gpar(ngpar)
      real*8    lpar(nlpar)
      integer*4 iobs,iset

c     local variables (all user defined variables must be declared here!)
          real*8 CA,CB,CC,CD,CE,CF,CG,CH,CI,COthers,Z,Rho, D
          real*8 r1,r2,r3,r4,r5,r6,r7,r8

     include 'le.inc'

c     user code:
     where (s.lt.0.0d0) s=0.0d0
      CA=s(1)
      CB=s(2)
      CC=s(3)
      CD=s(4)
      CE=s(5)
      CF=s(6)
      CG=s(7)
      CH=s(8)
      CI=s(9)
      COthers=s(10)


     Temp = Temp + 273.15
     Tmean = Tmean + 273.15
     z = 1.0/Temp - 1.0/Tmean
     Rho = Mcat/Vr

     k1 = k1*exp(-Ea1*z/8.3143)
     k2 = k2*exp(-Ea2*z/8.3143)
     k3 = k3*exp(-Ea3*z/8.3143)
     k4 = k4*exp(-Ea4*z/8.3143)
     k5 = k5*exp(-Ea5*z/8.3143)
     k6 = k6*exp(-Ea6*z/8.3143)
     k7 = k7*exp(-Ea7*z/8.3143)
     k8 = k8*exp(-Ea8*z/8.3143)

     D = 1.0+KA*cA+KB*cB+KC*cC+KD*cD+KE*cE+KF*cF
     r1 = k1*CA/D
     r2 = k2*CB/D
     r3 = k3*CA/D
     r4 = k4*CB/D
     r5 = k5*CA/D
     r6 = k6*CB/D
     r7 = k7*CA/D
     r8 = k8*CB/D
```

```
      ds(1) = (-r1-r3-r5-r7)*Rho
      ds(2) = (-r2-r4-r6-r8)*Rho
      ds(3) = r1*Rho
      ds(4) = r2*Rho
      ds(5) = (r3 + r4)*Rho
      ds(6) = (r5 + r6)*Rho
      ds(7) = (0)*Rho
      ds(8) = (0)*Rho
      ds(9) = (0)*Rho
      ds(10) = (r7 + r8)*Rho
      return
      end
```

8.4.3.3. Definition of initial conditions

```
      subroutine inits0(ns,t,s,
     &          xdata,nx,nobs,
     &          nsaux,nstatea,
     &          states0,
     &          gpar,ngpar,
     &          lpar,nlpar,
     &          iobs,iset)

      implicit none

c     arguments

      integer*4 ns,nsaux,nstatea   !n of state variables
      real*8    t          !time
      real*8    s(nstatea) !state variables

      integer*4 nx,nobs,ngpar,nlpar
      real*8    xdata(nx,nobs)
      real*8    states0(ns)
      real*8    gpar(ngpar)
      real*8    lpar(nlpar)
      integer*4 iobs,iset

* local variables (all user defined variables must be declared here!)

      include 'le.inc'

* user code:
      s = states0
      t=xdata(1,1)
      return
      end
```

8.4.3.4. Definition of output variables

```
      subroutine observations(s,ns,yest,ny,
     &           xdata,nx,nobs,
     &           nsaux,nstatea,
     &           states0,
     &           gpar,ngpar,
     &           lpar,nlpar,
     &           iobs,iset)

      implicit none

c     arguments

      integer*4 ns,nsaux,nstatea    !n of state variables
      real*8    s(nstatea) !state variables
      integer*4 ny          !n of obs. vars
      real*8    yest(ny)    !observed variables

      integer*4 nx,nobs,ngpar,nlpar
      real*8    xdata(nx,nobs)
      real*8    states0(nstatea)
      real*8    gpar(ngpar)
      real*8    lpar(nlpar)
      integer*4 iobs,iset

* local variables (all user defined variables must be declared here!)

      include 'le.inc'

c     user code:
      yest(1)=s(1)
      yest(2)=s(2)
      yest(3)=s(3)
      yest(4)=s(4)
      yest(5)=s(5)
      yest(6)=s(6)

      return
      end
```

8.4.4. Computational calculations

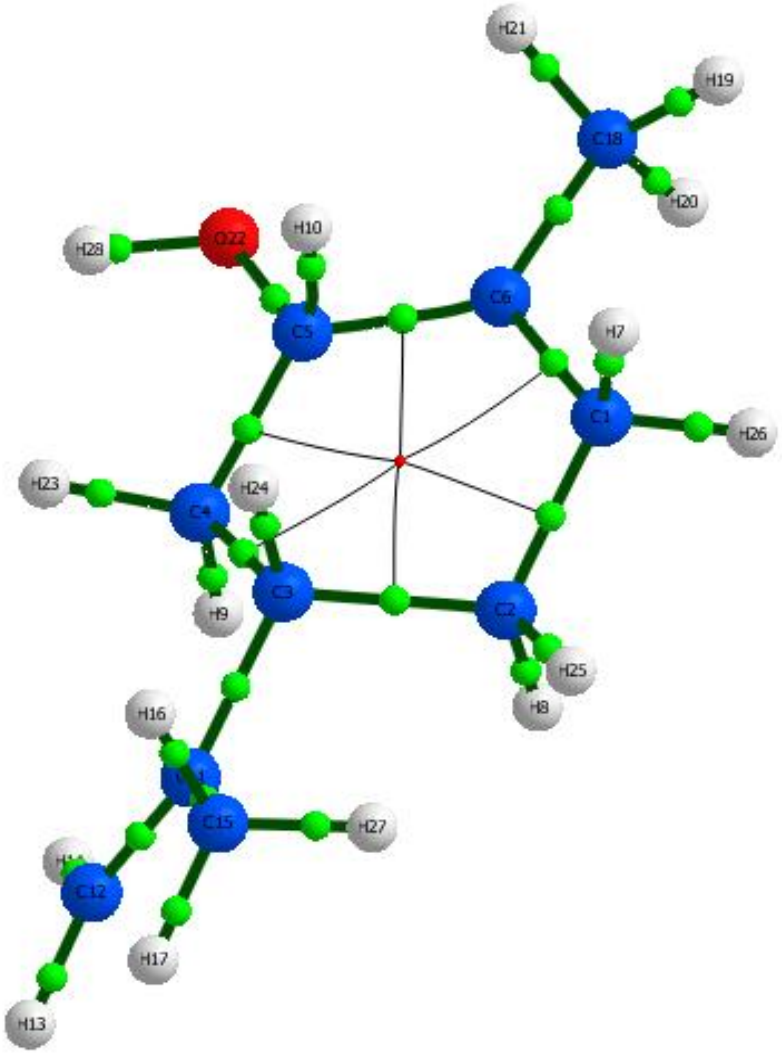

Figure 8.94. Molecular graph of TS2 obtained in AIMALL after topological analysis. Blue: carbon, white: hydrogen, red: oxygen, green: BCP.

Table 8.12. Selected data obtained from Topological analysis of **TS2**.

BCP	*Atoms**	$\rho(r)$	$\nabla^2\rho(r)$	*G*	*V*
1	C1 - C2	+0.239686	-0.537449	+0.056573	-0.247508
2	C2 - C3	+0.236367	-0.513421	+0.055448	-0.239251
3	C3 - C4	+0.239685	-0.534842	+0.056413	-0.246537
4	C1 - C6	+0.258474	-0.633951	+0.072454	-0.303395
5	C4 - C5	+0.246142	-0.571975	+0.065448	-0.273890
6	C5 - C6	+0.300912	-0.821227	+0.092532	-0.390371
7	C1 - H7	+0.271233	-0.895213	+0.040775	-0.305353
8	C2 - H8	+0.277078	-0.927031	+0.040975	-0.313708
9	C4 - H9	+0.276923	-0.928145	+0.040232	-0.312501
10	C5 - H10	+0.203398	-0.446703	+0.052100	-0.215877
11	C3 - C11	+0.247472	-0.573135	+0.057260	-0.257804
12	C11 - C15	+0.250182	-0.589003	+0.059465	-0.266181
13	C11 - C12	+0.339788	-0.990061	+0.138161	-0.523837
14	C12 - H14	+0.279552	-0.951519	+0.040852	-0.319584
15	C12 - H13	+0.280217	-0.959466	+0.037565	-0.314996
16	C15 - H17	+0.276307	-0.926757	+0.040142	-0.311974
17	C3 - H24	+0.274435	-0.906365	+0.043358	-0.313308
18	C15 - H16	+0.271345	-0.892345	+0.042828	-0.308742
19	C18 - H21	+0.279426	-0.954740	+0.037157	-0.312998
20	C6 - C18	+0.264606	-0.665584	+0.075710	-0.317816
21	C18 - H19	+0.277574	-0.939275	+0.038580	-0.311980
22	C18 - H20	+0.265257	-0.864707	+0.040222	-0.296620
23	C5 - O22	+0.292490	-0.550260	+0.278979	-0.695523
24	C4 - H23	+0.277543	-0.933586	+0.040162	-0.313720
25	C2 - H25	+0.279829	-0.947334	+0.040093	-0.317020
26	C1 - H26	+0.273795	-0.912335	+0.039977	-0.308038
27	C15 - H27	+0.271815	-0.894332	+0.043665	-0.310914
28	O22 - H28	+0.359820	-2.546994	+0.065506	-0.767760

*The numbers are indicated in **Figure 8.94**.

8.4.5. Kinetics

Table 8.13. Kinetic and statistical parameters for the kinetic study.

Parameter	Value	Units	Standard error (%)
k_1	2.29×10^{-5}	L mg^{-1} min^{-1}	9.9
k_2	4.06×10^{-6}	L mg^{-1} min^{-1}	14.3
k_3	5.95×10^{-6}	L mg^{-1} min^{-1}	24.6
k_4	2.72×10^{-7}	L mg^{-1} min^{-1}	> 100
k_5	1.03×10^{-5}	L mg^{-1} min^{-1}	18.1
k_6	1.43×10^{-7}	L mg^{-1} min^{-1}	> 100
k_7	1.22×10^{-5}	L mg^{-1} min^{-1}	19.2
k_8	4.14×10^{-6}	L mg^{-1} min^{-1}	15.2
Ea_1	42.9	kJ mol^{-1}	17.9
Ea_2	167	kJ mol^{-1}	7.6
Ea_3	42.2	kJ mol^{-1}	53.2
Ea_4	207	kJ mol^{-1}	97.4
Ea_5	71.6	kJ mol^{-1}	23.0
Ea_6	250	kJ mol^{-1}	> 100
Ea_7	8.55	kJ mol^{-1}	> 100
Ea_8	60.6	kJ mol^{-1}	22.5
K_C	0.22	L $mmol^{-1}$	30.7

k_1-k_8 values were estimated at 60 °C.

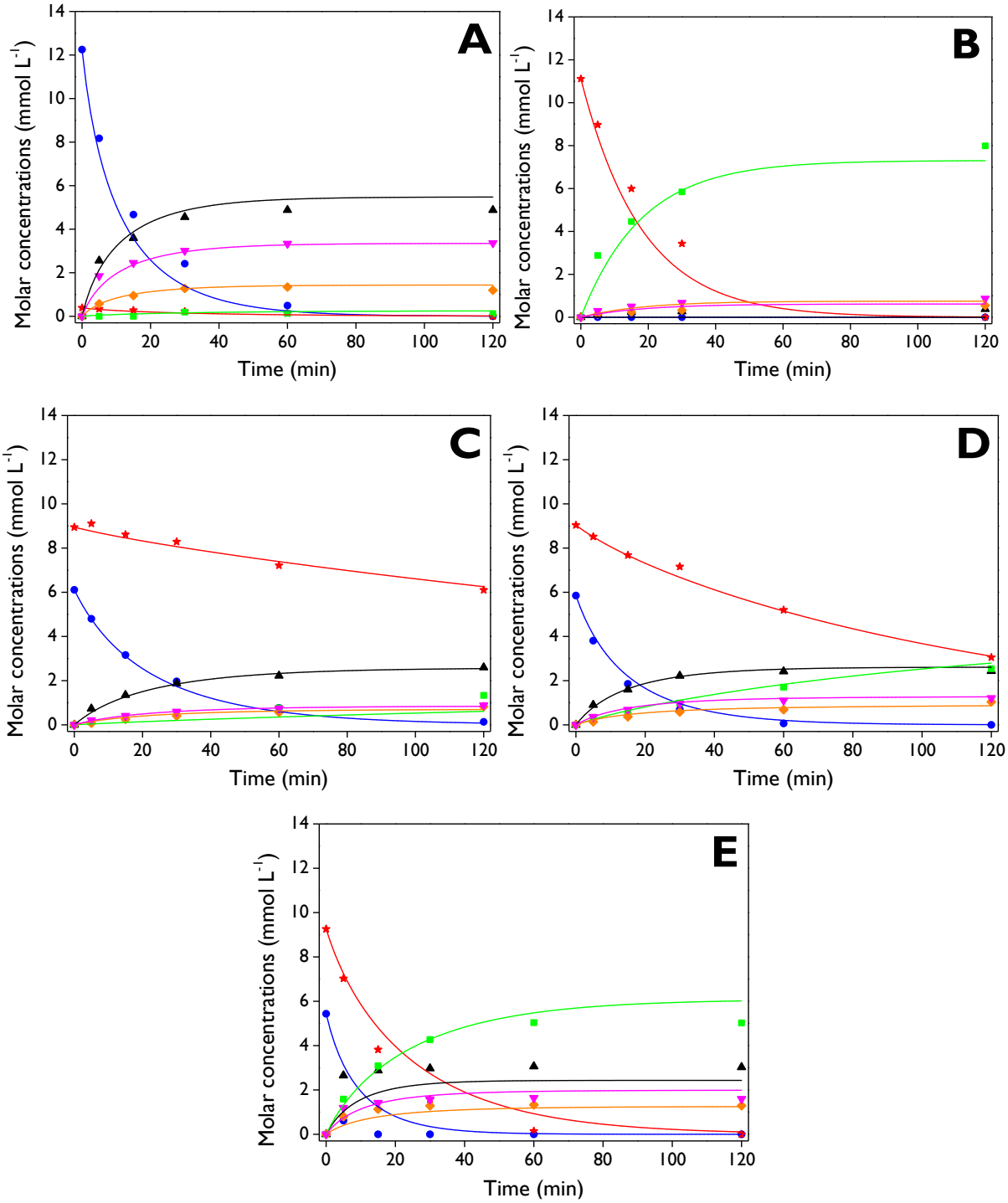

Figure 8.95. Concentration profiles of the species (C_A (—, ●), C_B (—, ✶), C_C (—, ▲), C_D (—, ■), C_E (—, ◆), C_F (—, ▼)) involved in the isomerization of limonene-1,2-epoxide over d-ZSM-5, with experimental values (symbols) and modeled values (solid lines). **Reaction conditions:** C_0 = 13 mmol L^{-1}, 75 mL total volume, anhydrous ethyl acetate as a solvent, 115 mg of catalyst, 520-530 rpm, N_2 atmosphere. **A)** *cis*-LE as the substrate at 70 °C, **B)** *trans*-LE as the substrate at 70 °C, **C)** mixture-LE as the substrate at 50 °C, **D)** mixture-LE as the substrate at 60 °C, **E)** mixture-LE as the substrate at 70 °C.

8.4.6. Markov Chain Monte Carlo (MCMC) results

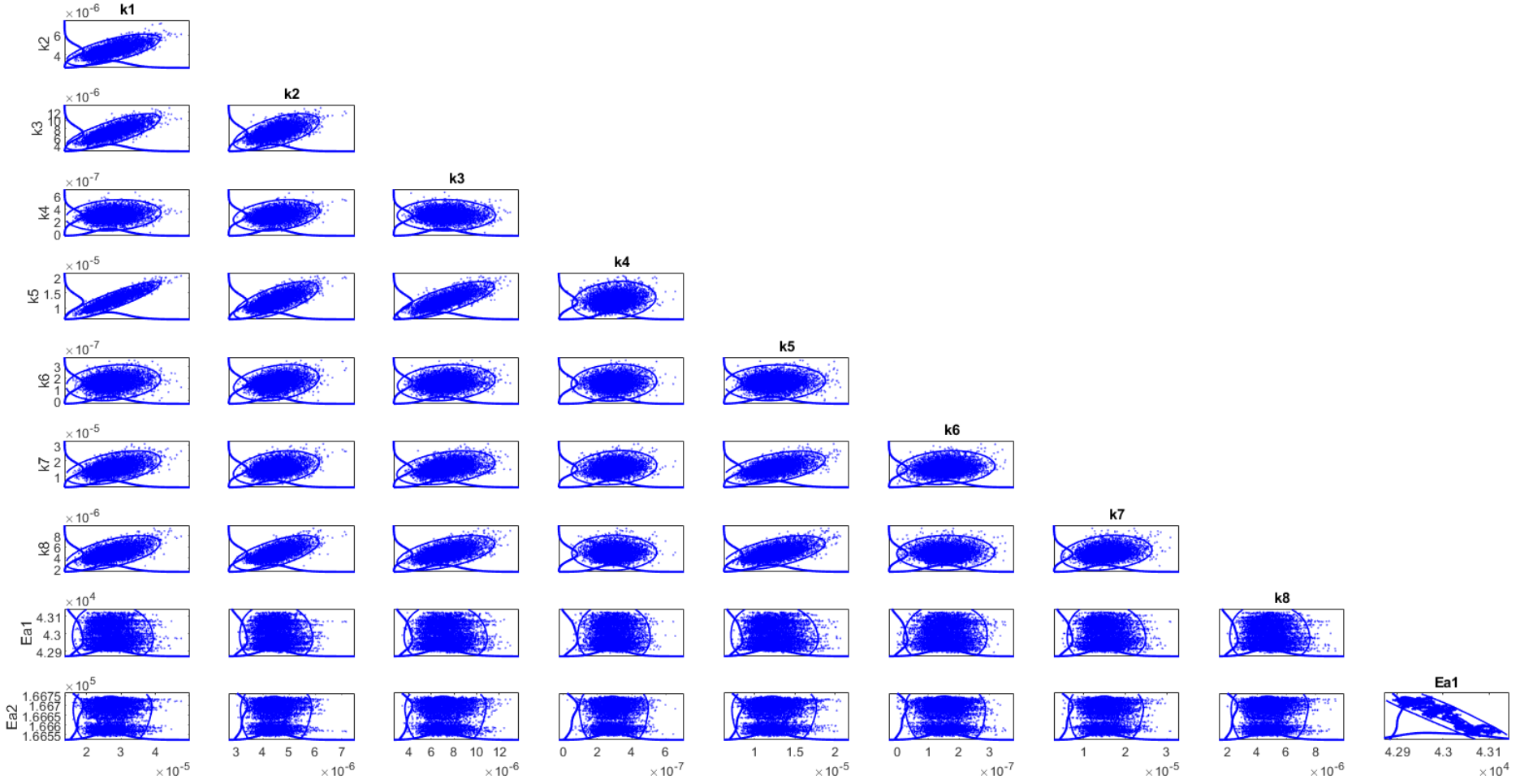

Figure 8.96. Markov Chain Monte Carlo (MCMC) results.

8.5. Chapter 6

8.5.1. Synthesis of materials

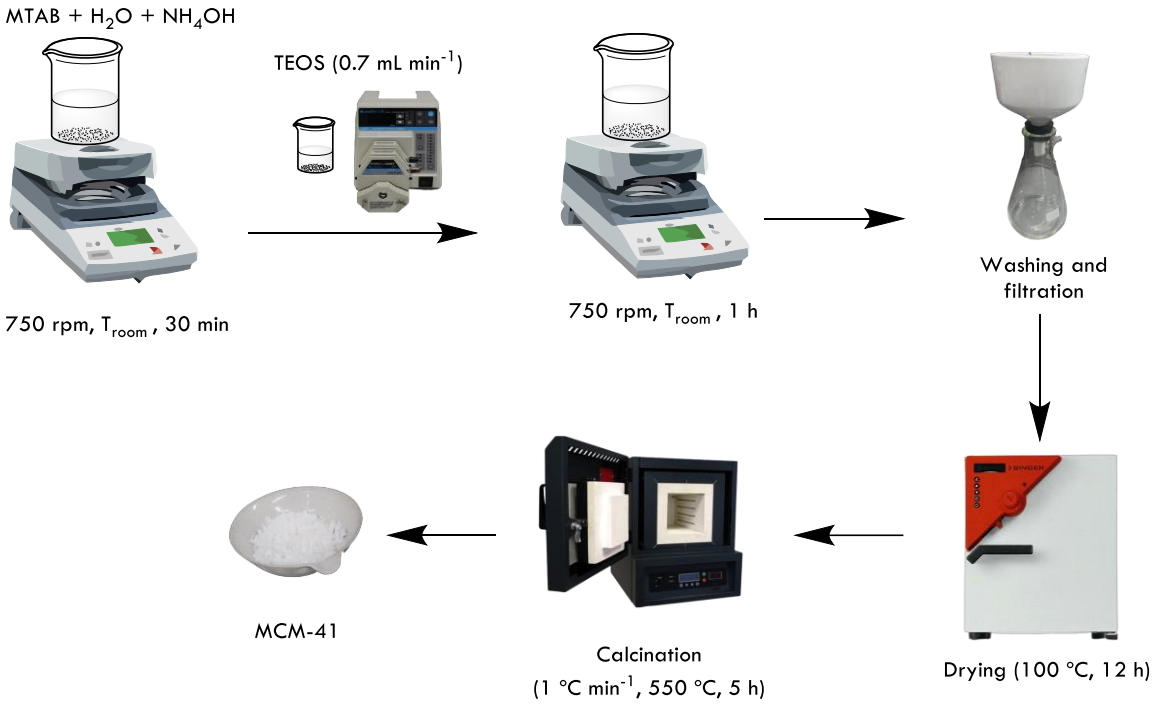

Figure 8.97. Scheme of the synthesis of MCM-41 support.

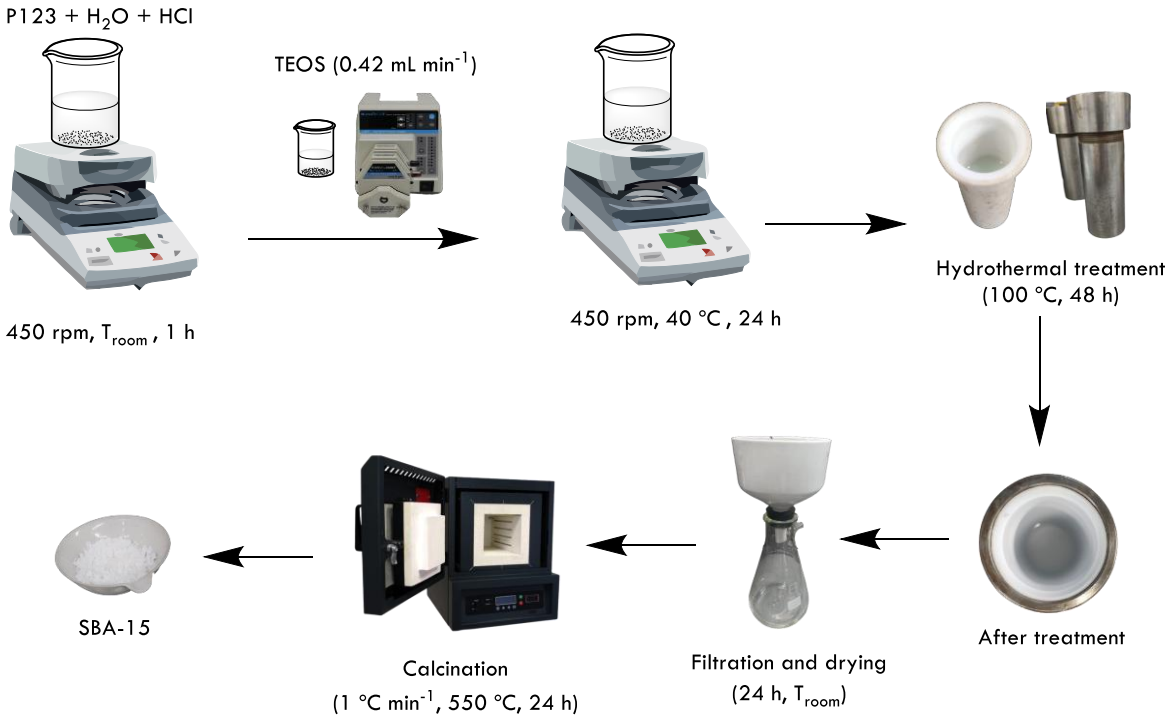

Figure 8.98. Scheme of the synthesis of SBA-15 support.

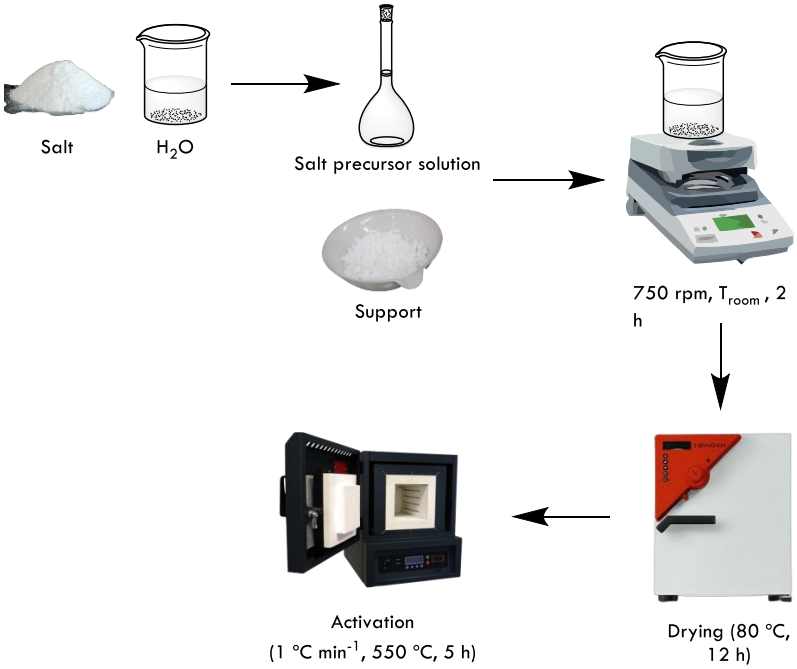

Figure 8.99. Scheme of the wetness impregnation procedure.

8.5.2. TEM images

MCM-41

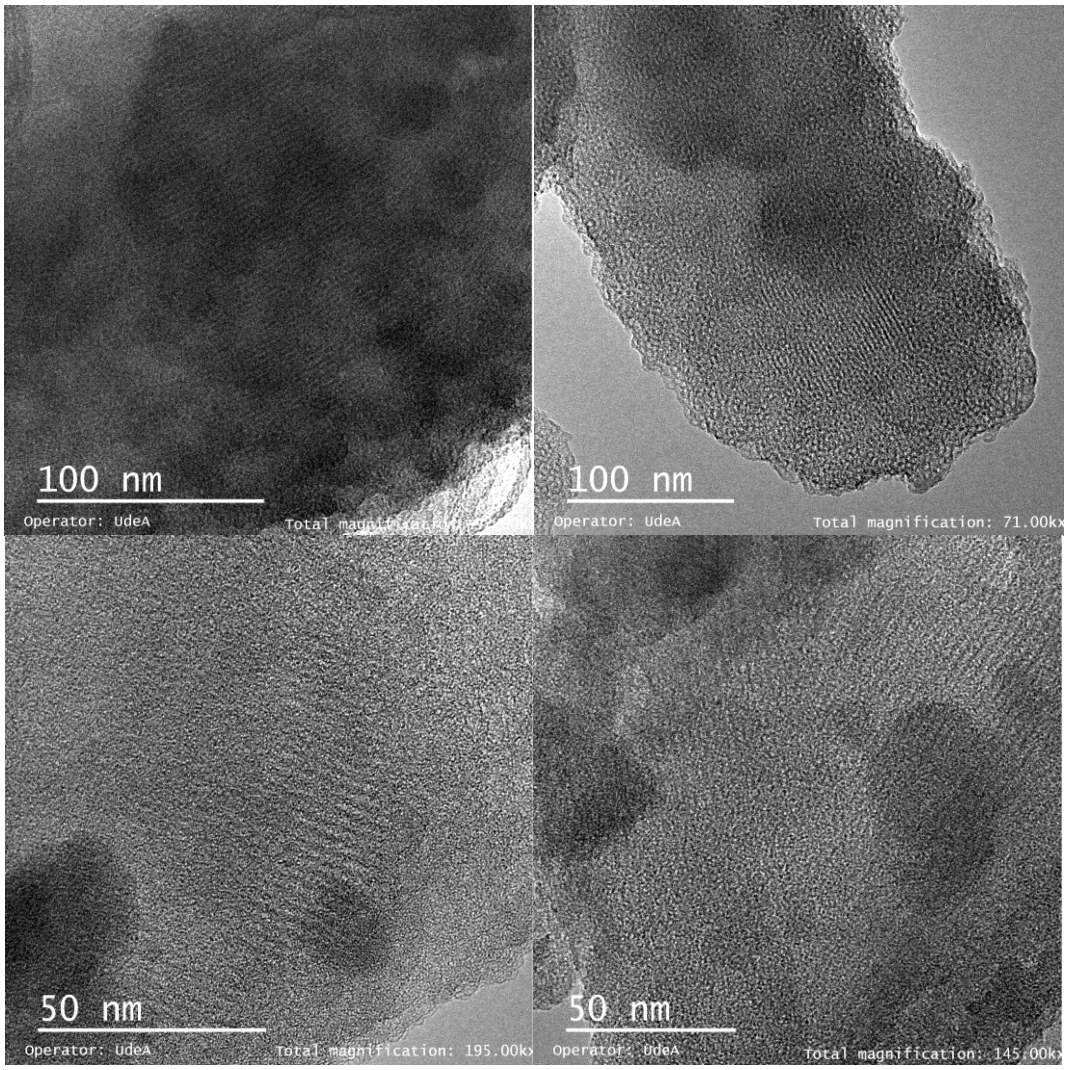

Figure 8.100. TEM images of MCM-41 support.

SnM1

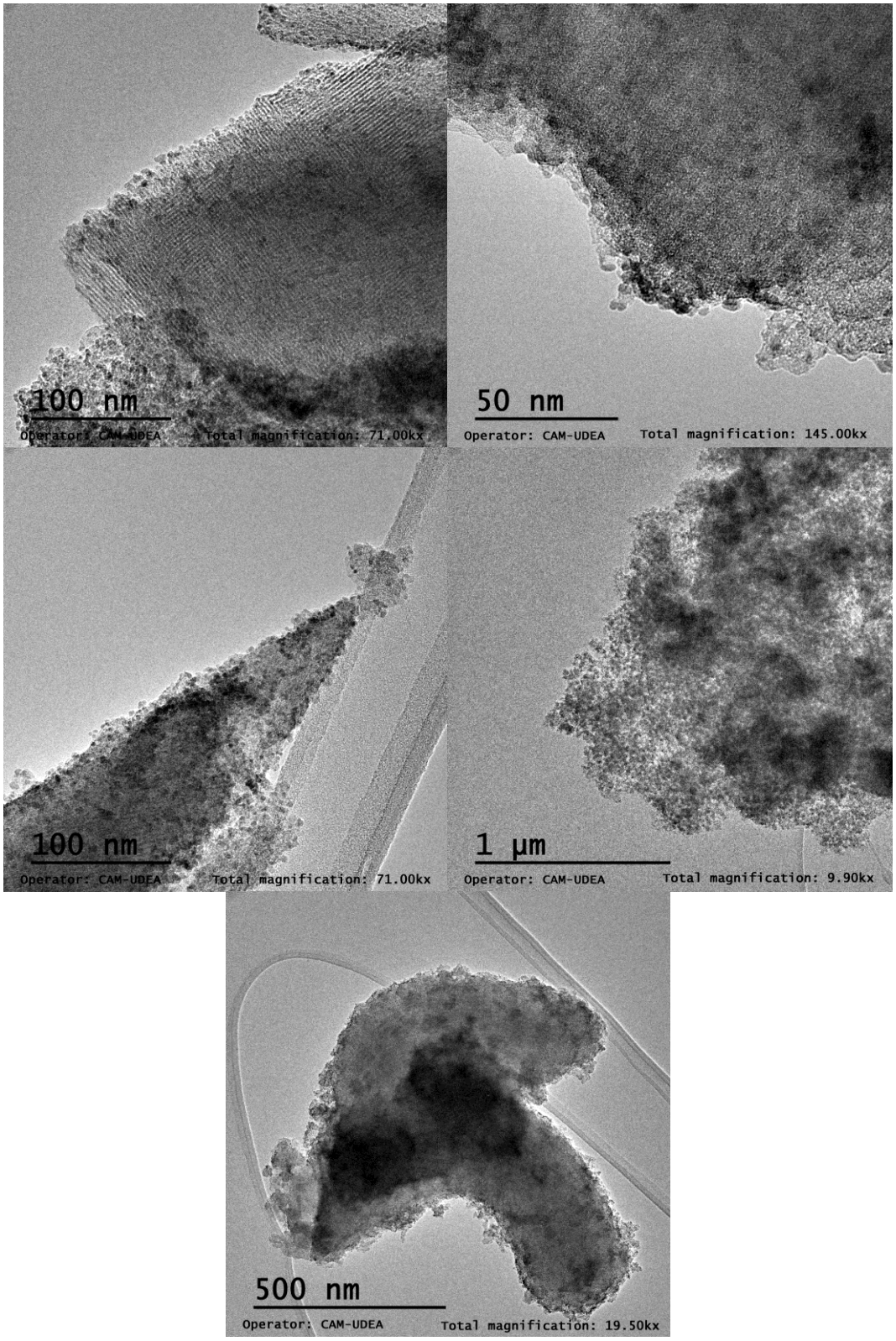

Figure 8.101. TEM images of SnM1 catalyst.

SnM2

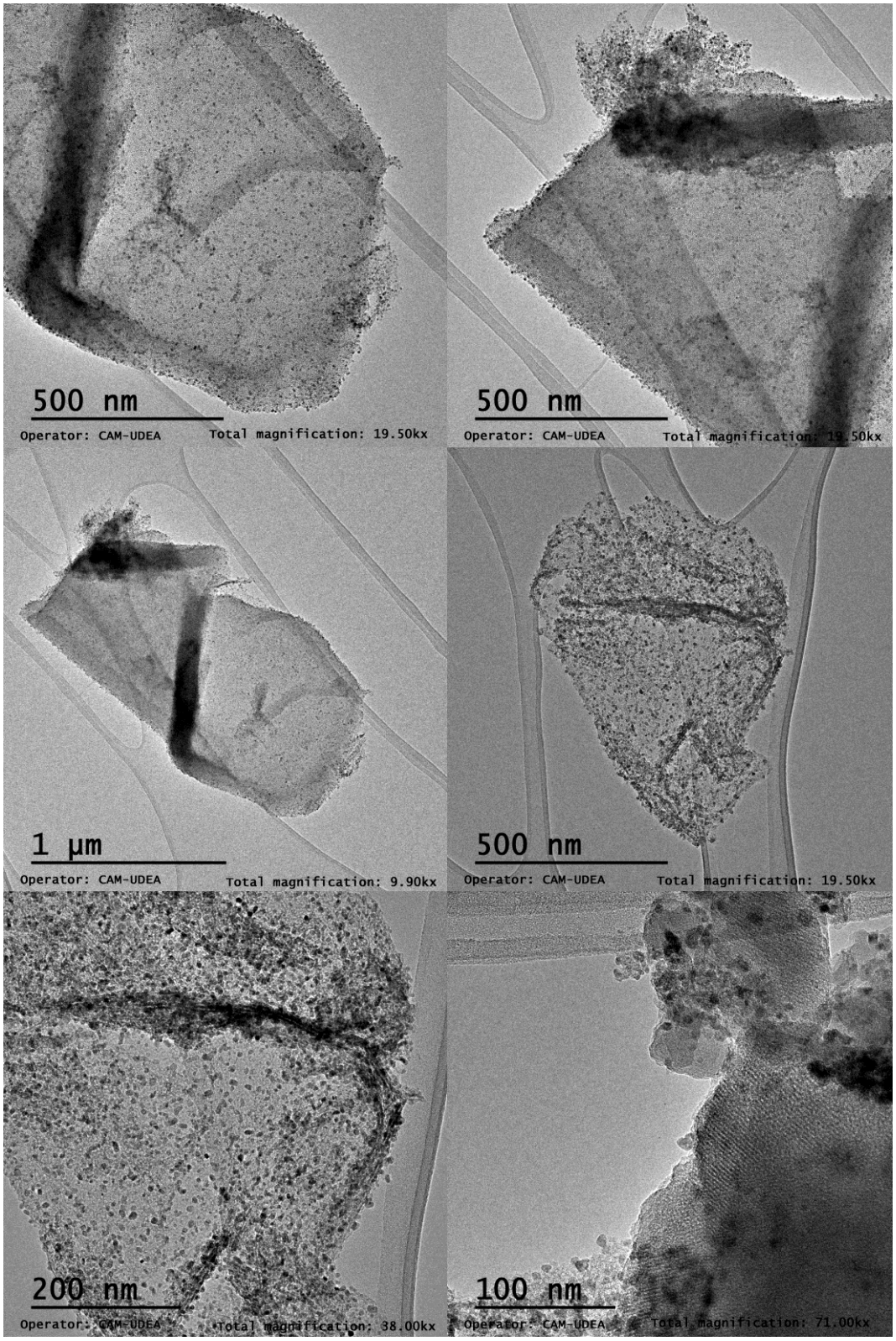

Figure 8.102. TEM images of SnM2 catalyst.

FeM1

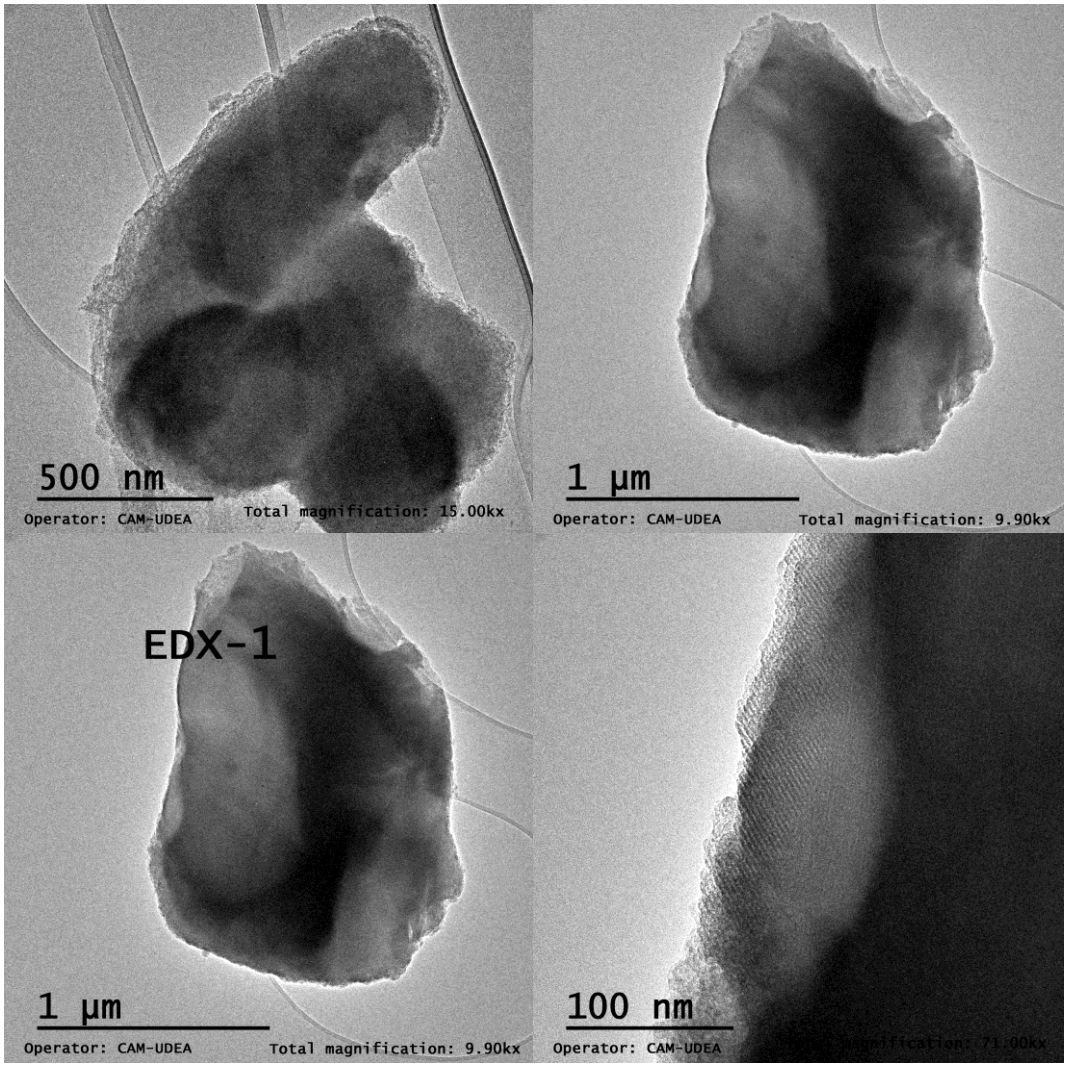

Figure 8.103. TEM images of FeM1 catalyst.

CuM1

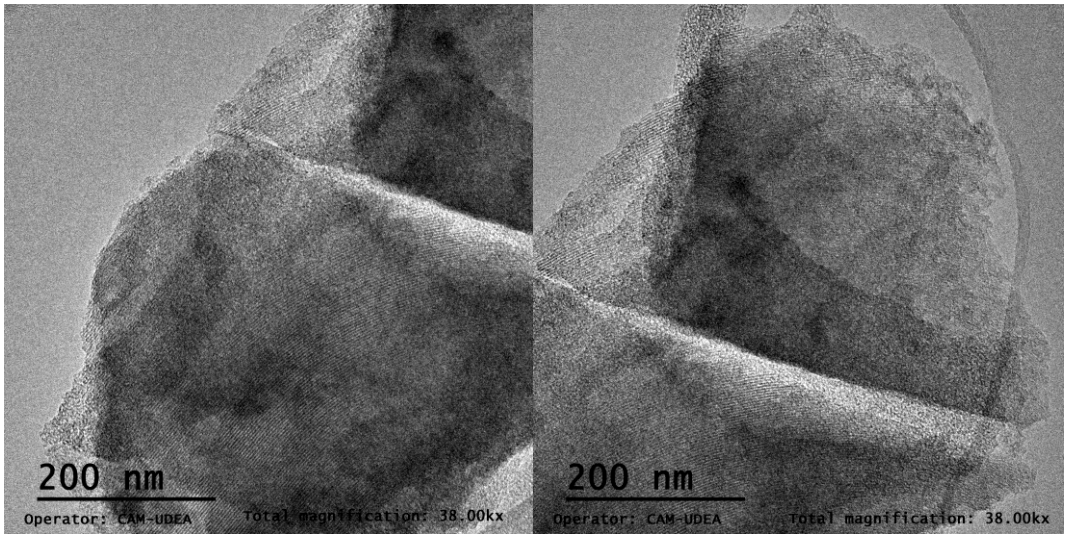

Figure 8.104. TEM images of CuM1 catalyst.

CoM1

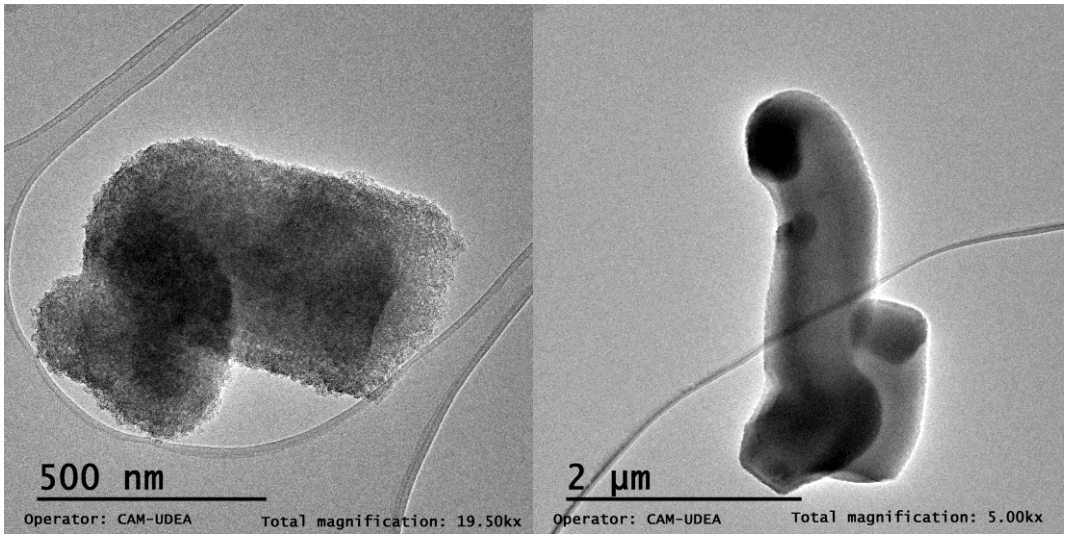

Figure 8.105. TEM images of CoM1 catalyst.

SnS1

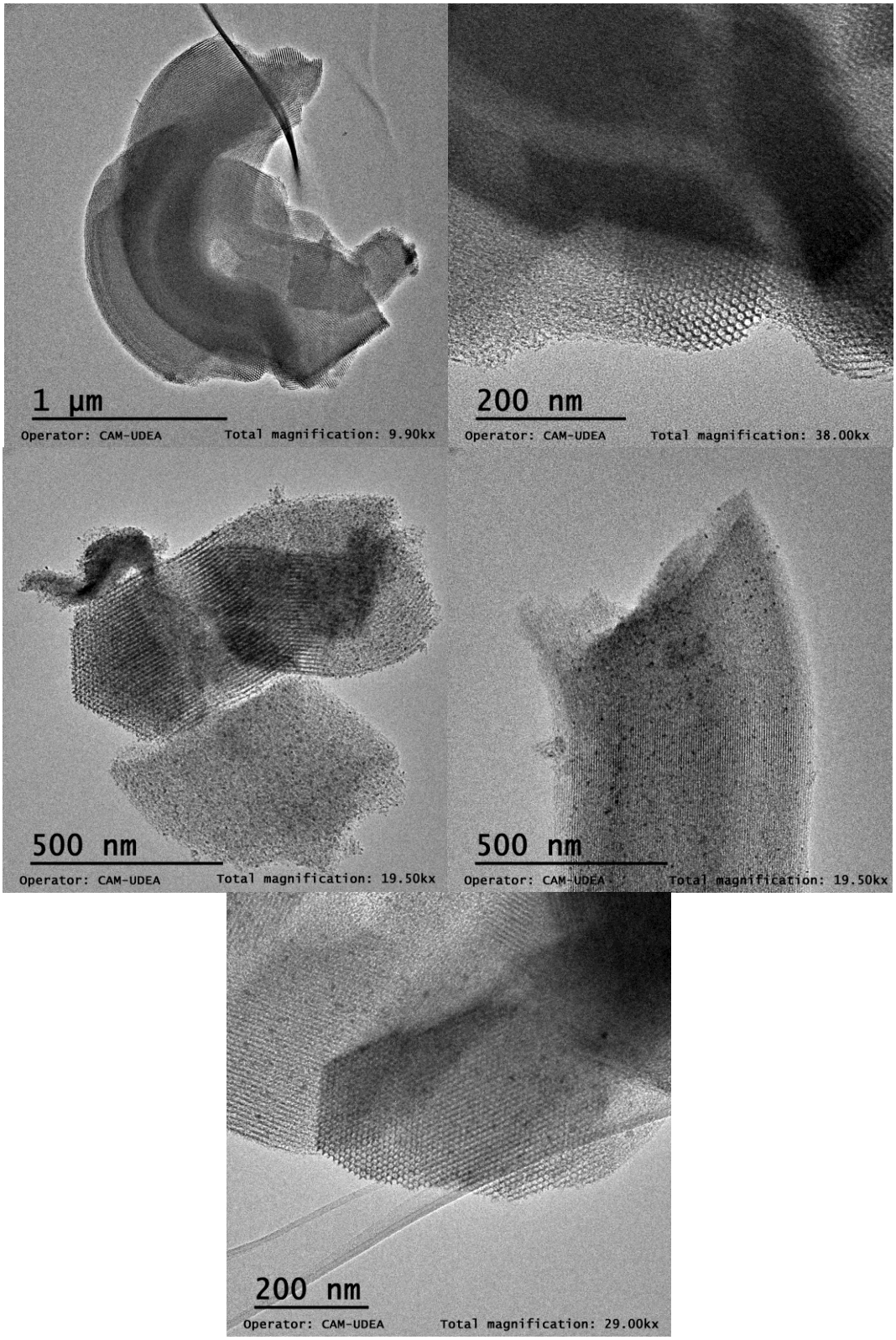

Figure 8.106. TEM images of SnS1 catalyst.

SnS2

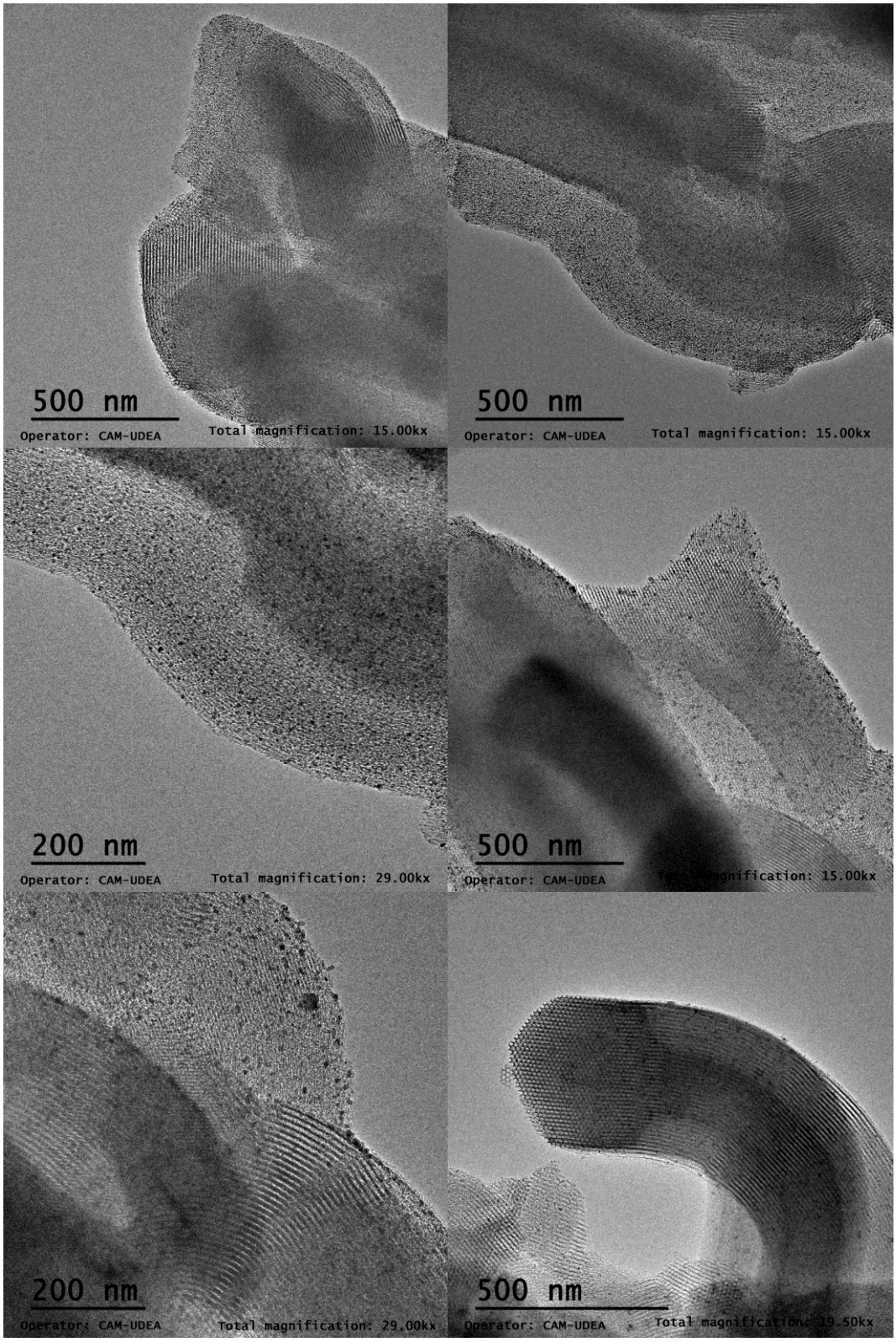

Figure 8.107. TEM images of SnS2 catalyst.

FeS1

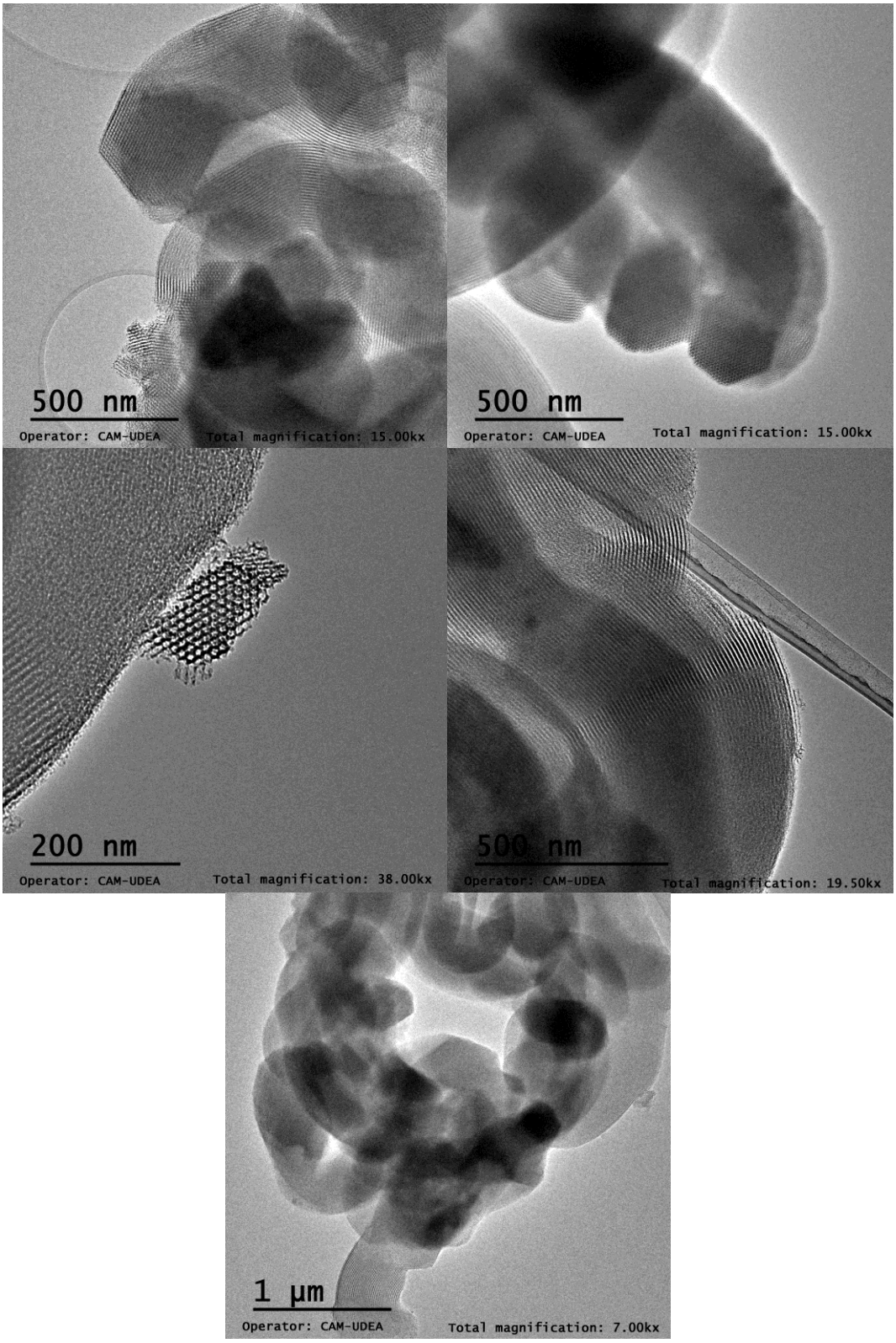

Figure 8.108. TEM images of FeS1 catalyst.

FeS2

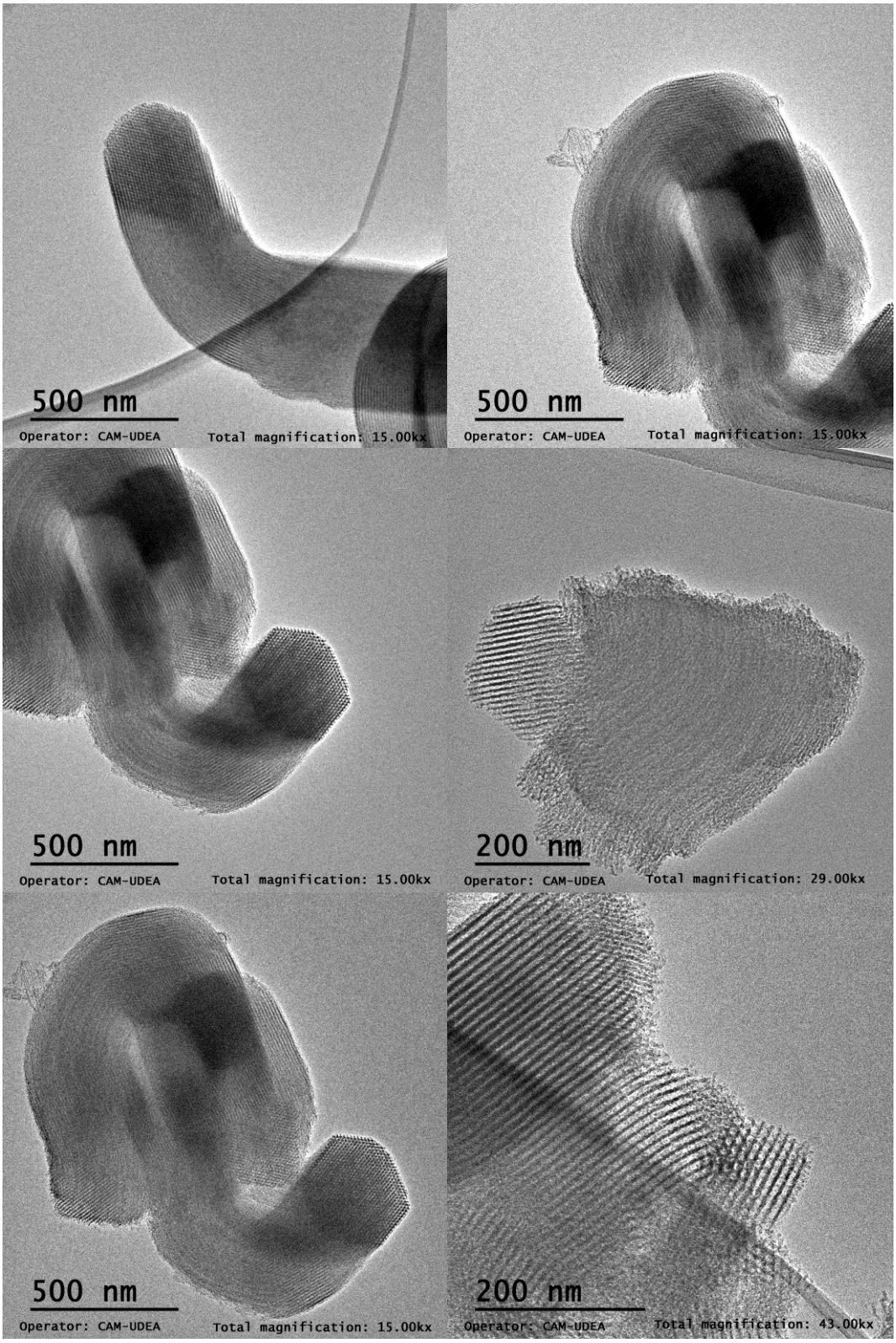

Figure 8.109. TEM images of FeS2 catalyst.

CuS1

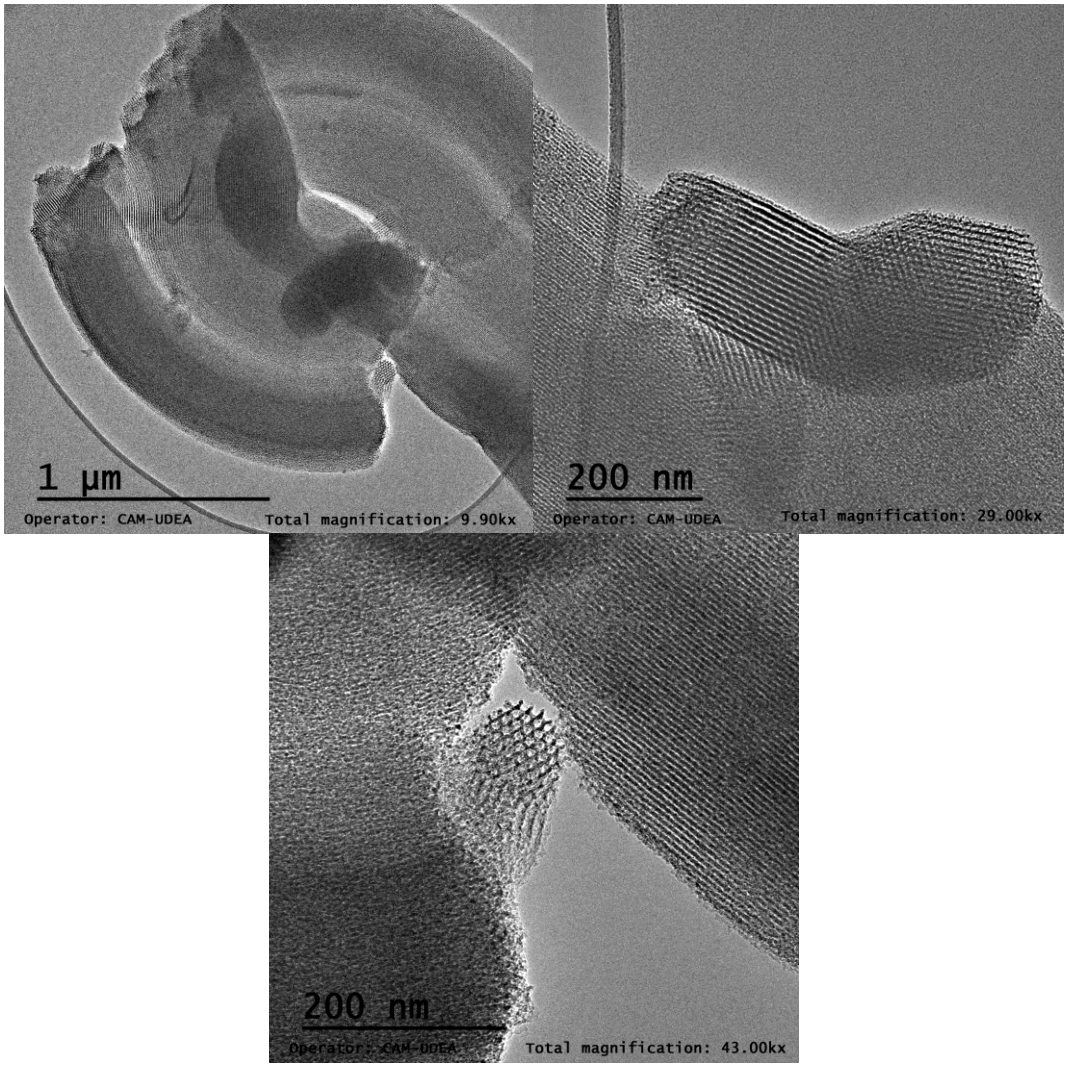

Figure 8.110. TEM images of CuS1 catalyst.

CoS1

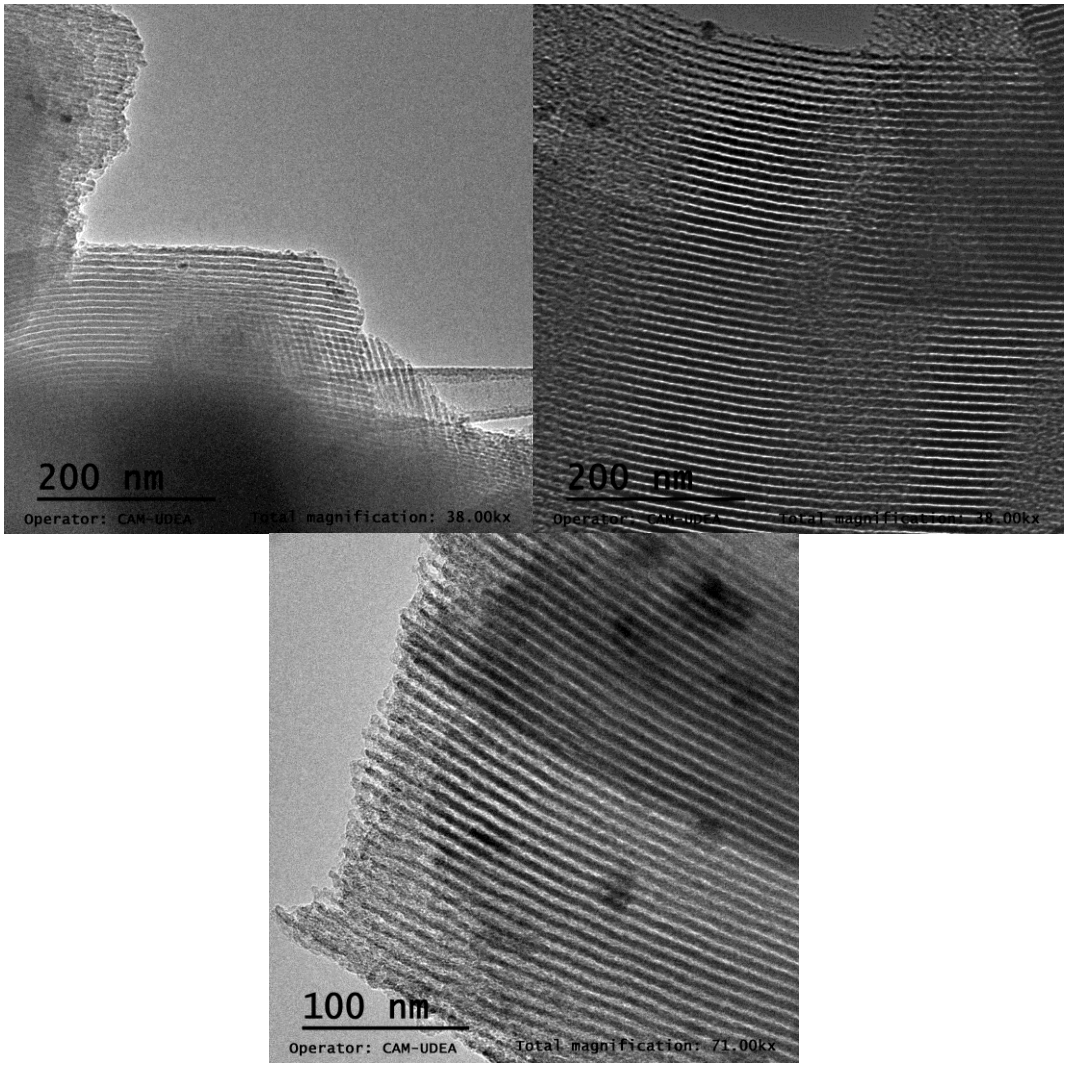

Figure 8.111. TEM images of CoS1 catalyst.

8.5.3. Elemental maps

FeM1

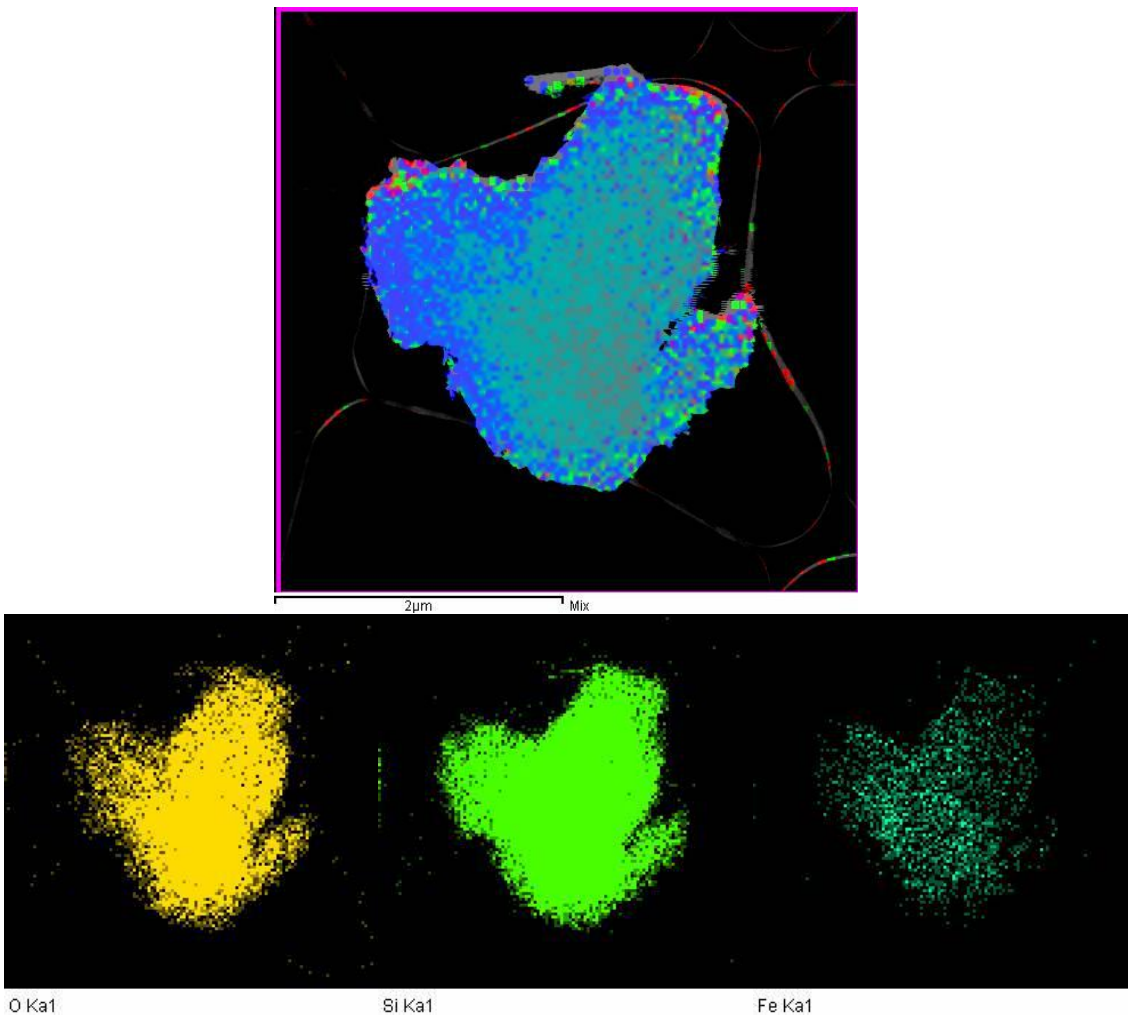

Figure 8.112. Elemental maps of the FeM1 catalyst.

SnS1

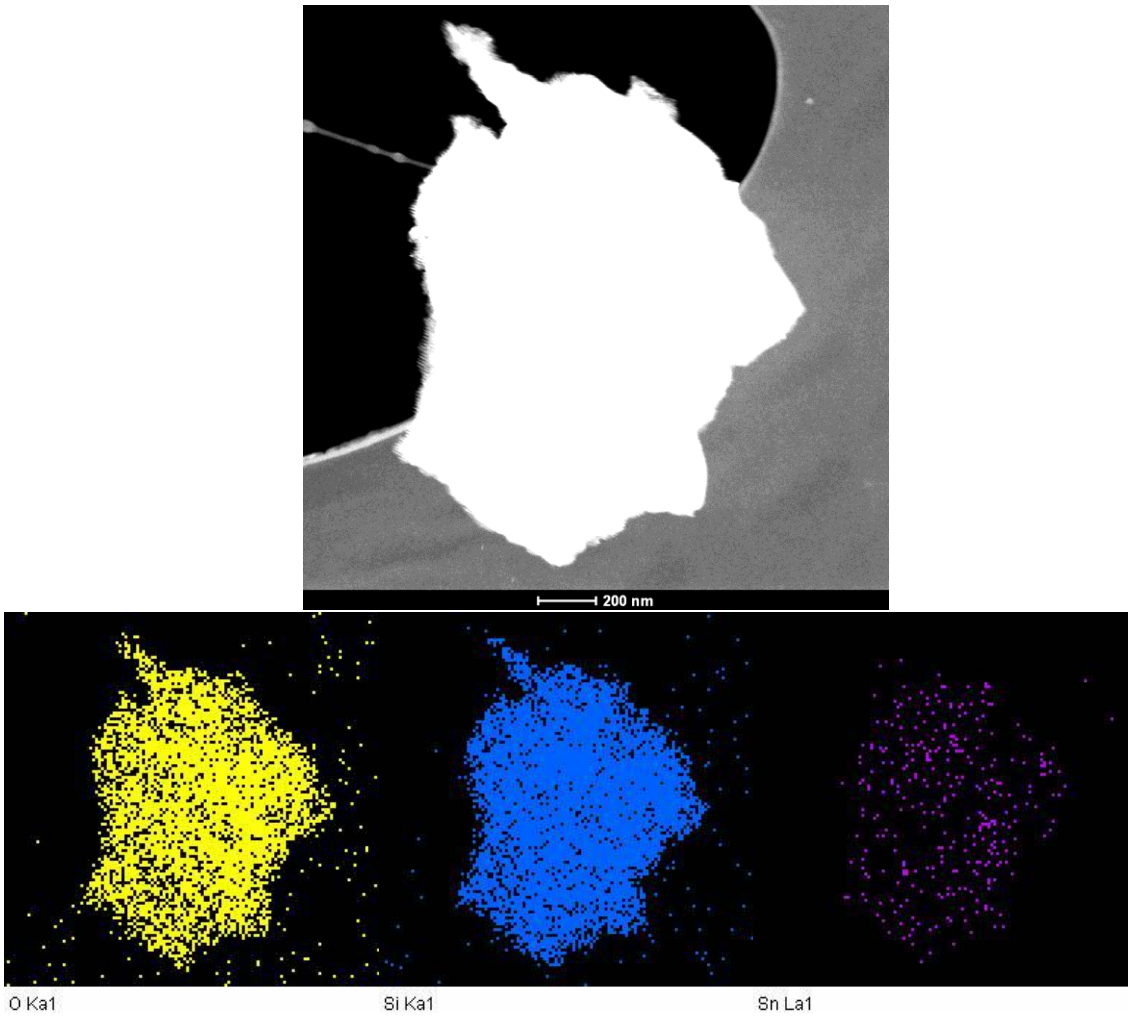

Figure 8.113. Elemental maps of the SnS1 catalyst.

CuS1

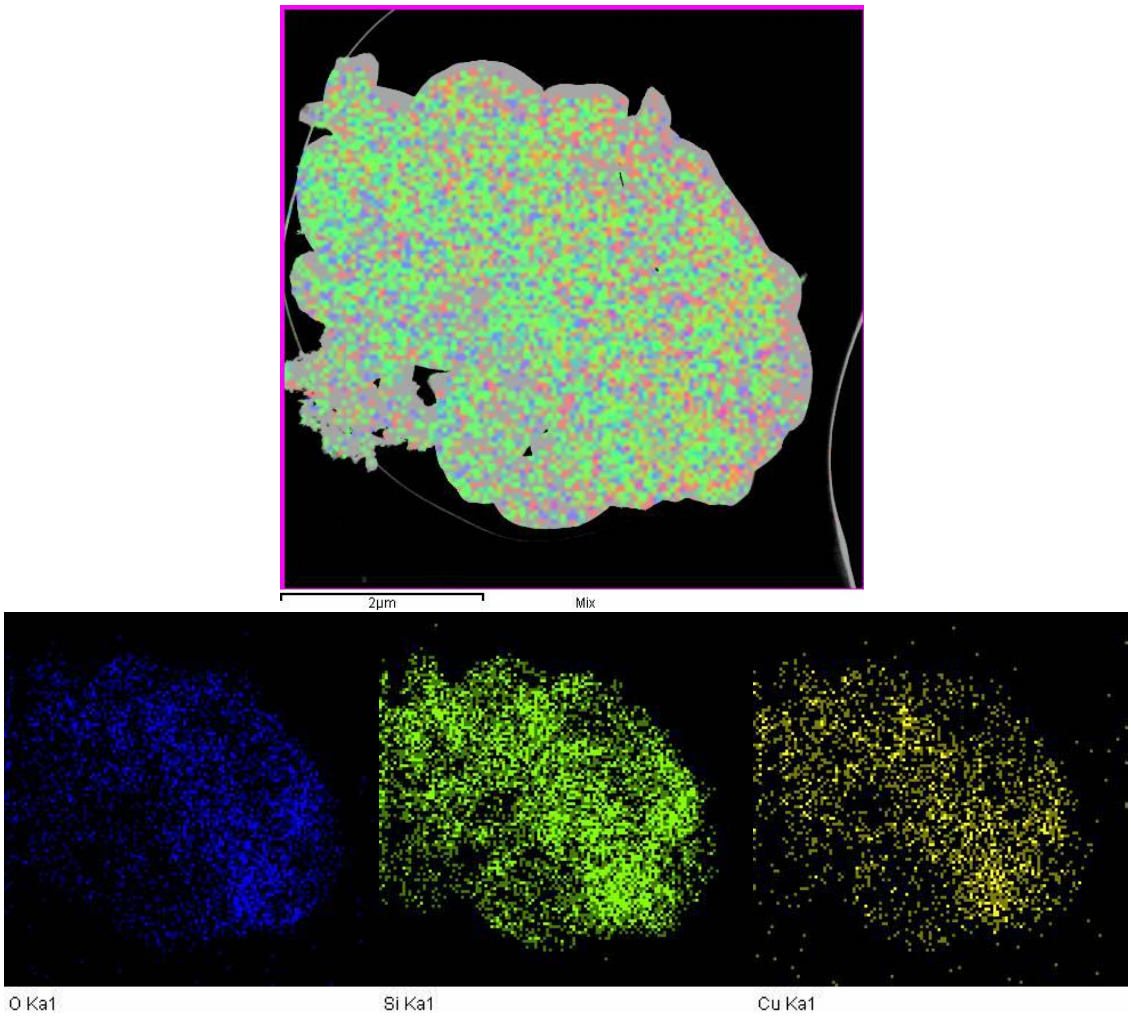

Figure 8.114. Elemental maps of the CuS1 catalyst.

CoS1

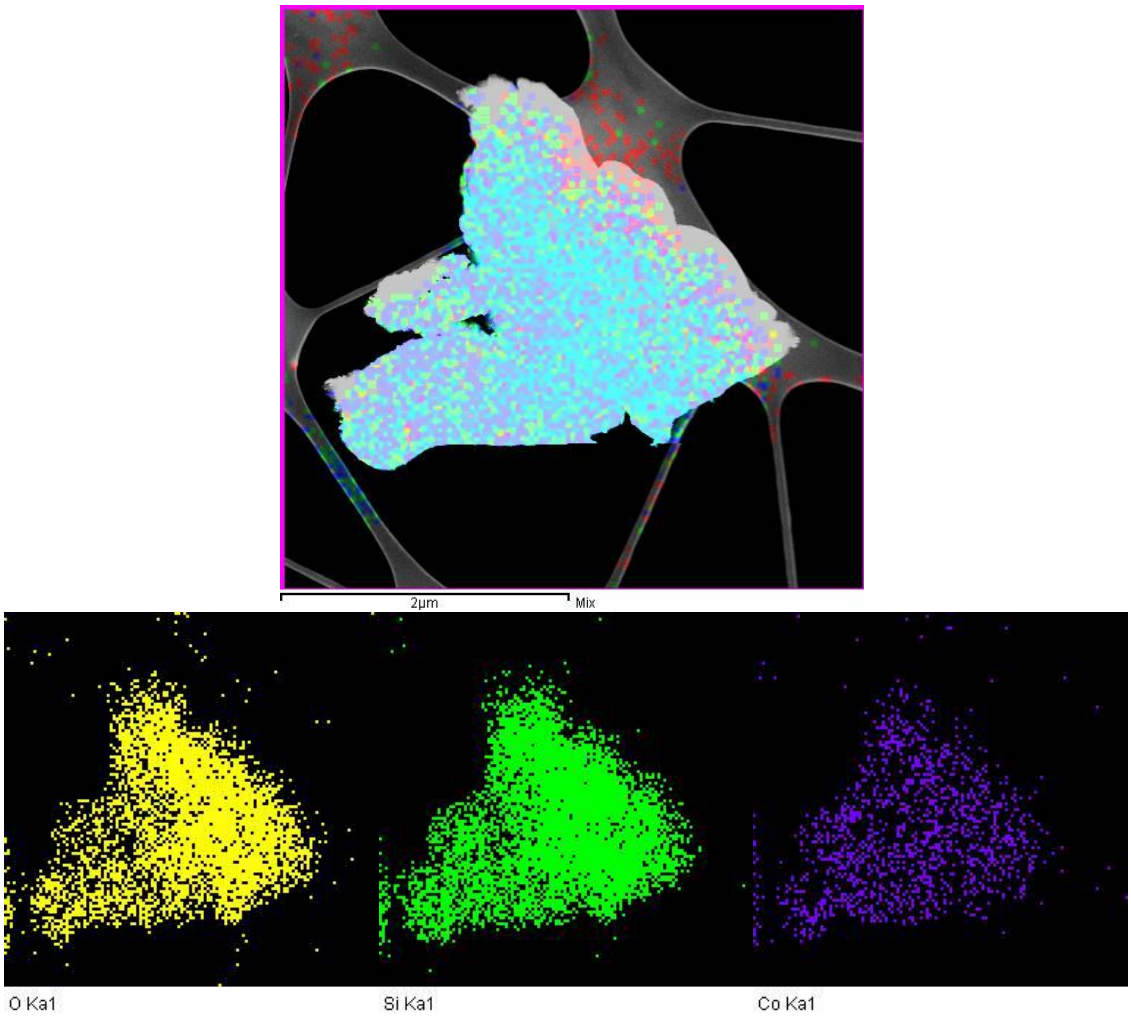

Figure 8.115. Elemental maps of the CoS1 catalyst.

8.5.4. Pyridine-FTIR

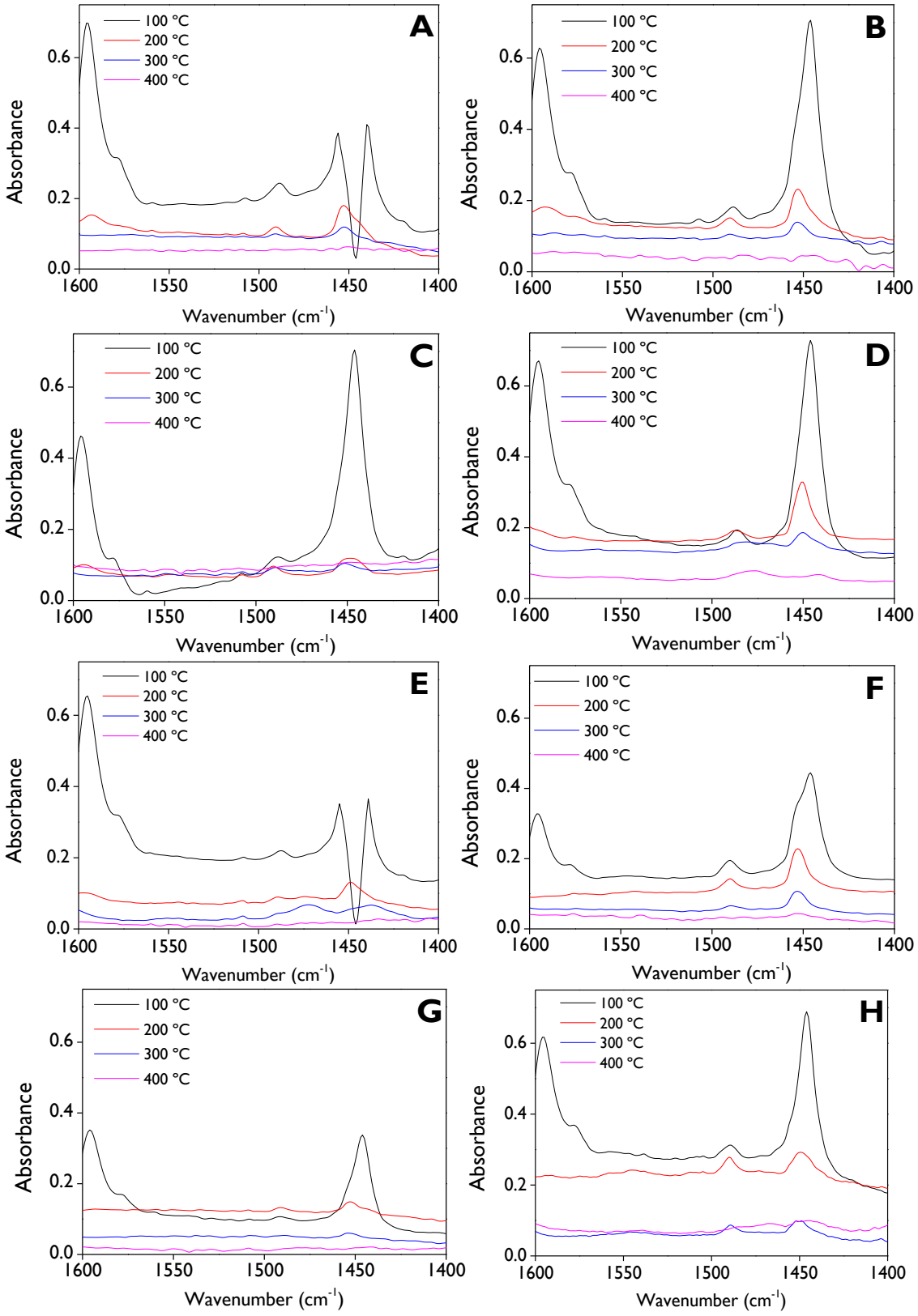

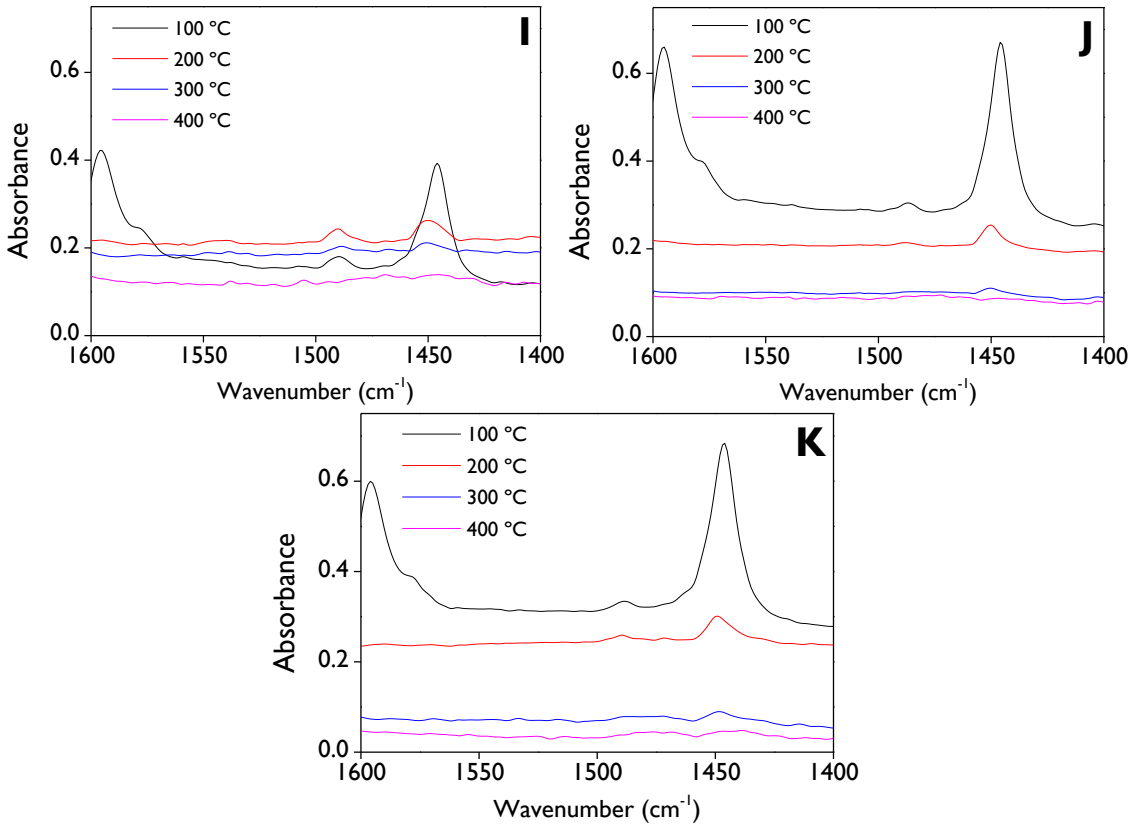

Figure 8.116. Pyridine-FTIR spectra of **(A)** SnM1, **(B)** SnM2, **(C)** FeM1, **(D)** CuM1, **(E)** CoM1, **(F)** SnS1, **(G)** SnS2, **(H)** FeS1, **(I)** FeS2, **(J)** CuS1, **(K)** CoS1.

8.5.5. NH_3-TPD Analysis

Table 8.14. Acidic properties of the catalysts using NH_3-TPD.

Catalyst	Acidity (μmol g^{-1})			
	Very weak	Weak	Medium	Total
SnM1	15	39	89	143
SnM2	13	48	81	141
FeM1	19	31	106	156
CuM1	16	63	180	259
CoM1	14	39	70	123
SnS1	20	54	90	164
SnS2	26	40	74	141
FeS1	49	0	146	195
FeS2	48	0	114	162
CuS1	0	67	92	159
CoS1	10	30	78	118

8.5.6. XPS Analysis

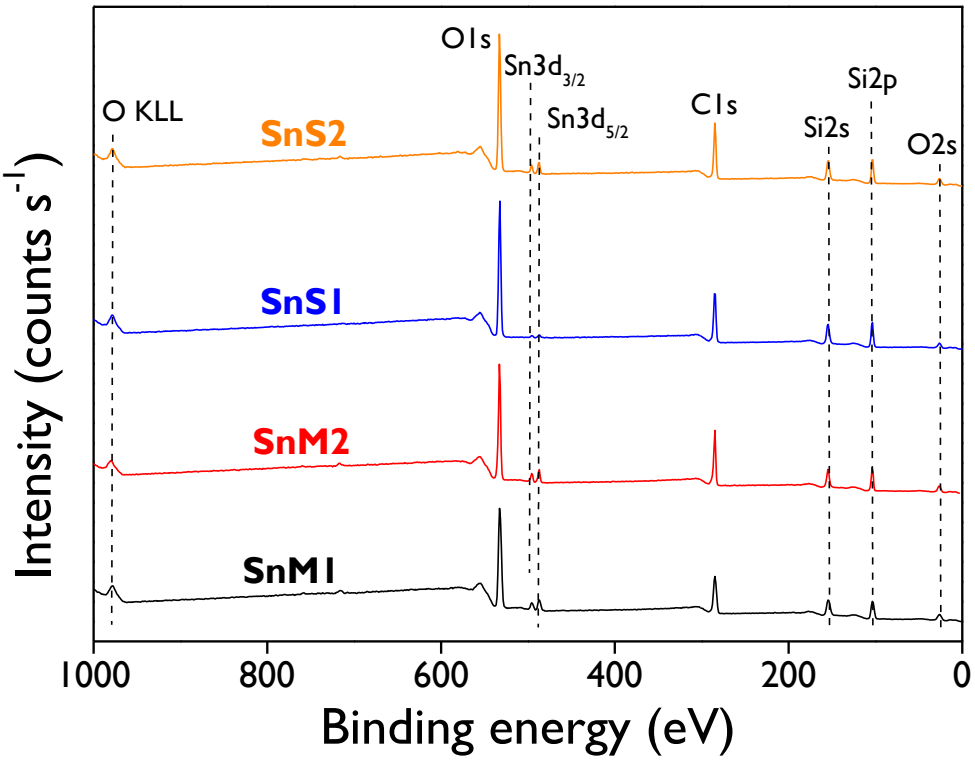

Figure 8.117. Wide scan XPS spectra of catalysts modified with Sn.

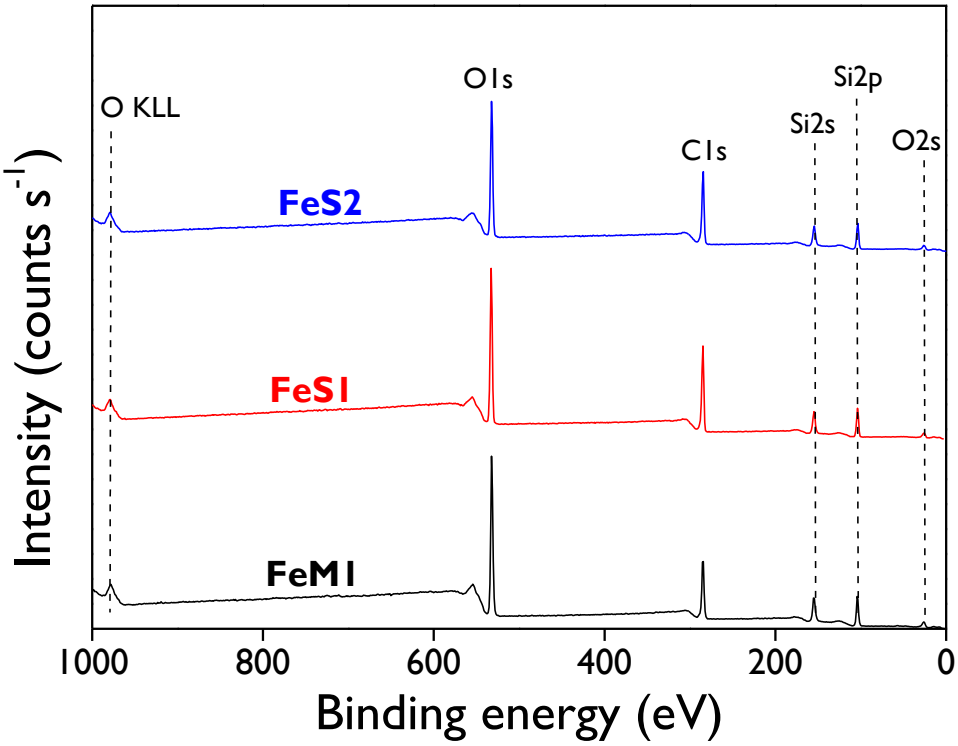

Figure 8.118. Wide scan XPS spectra of catalysts modified with Fe.

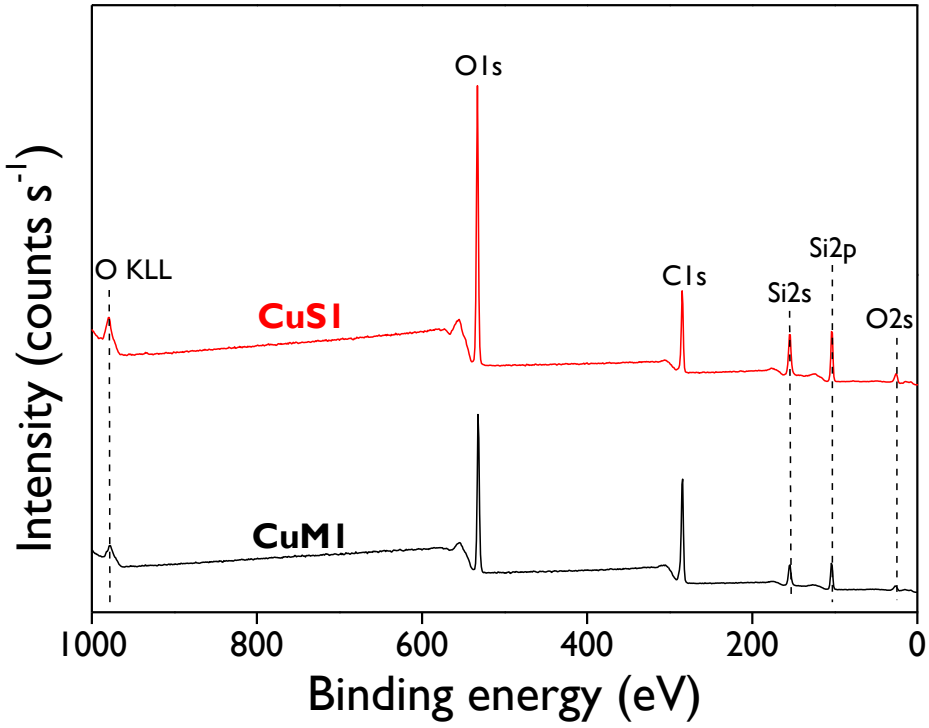

Figure 8.119. Wide scan XPS spectra of catalysts modified with Cu.

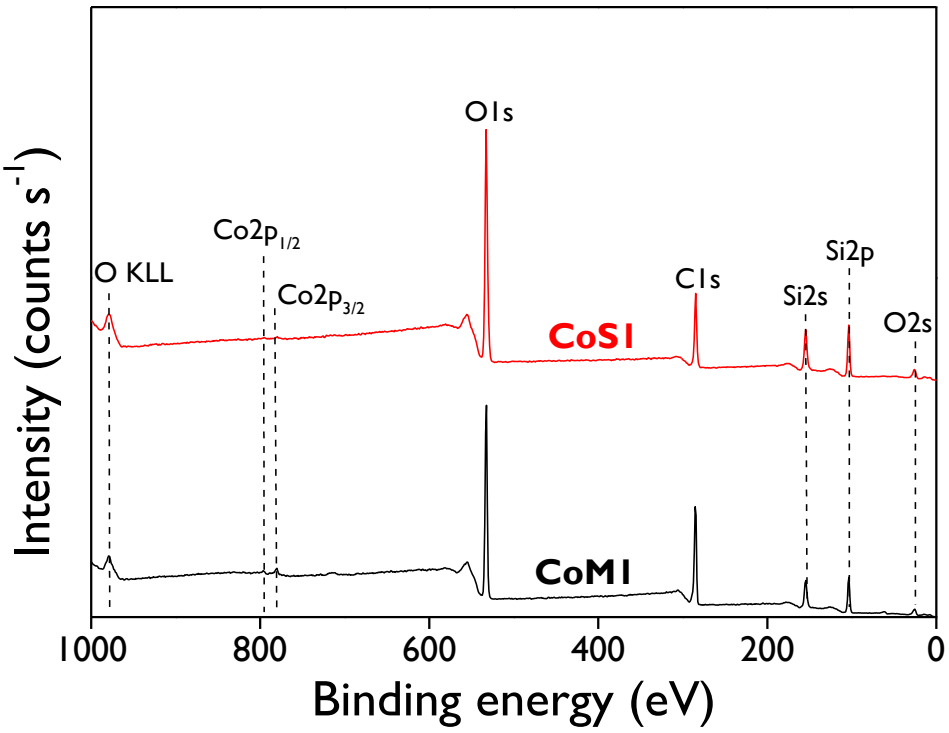

Figure 8.120. Wide scan XPS spectra of catalysts modified with Co.

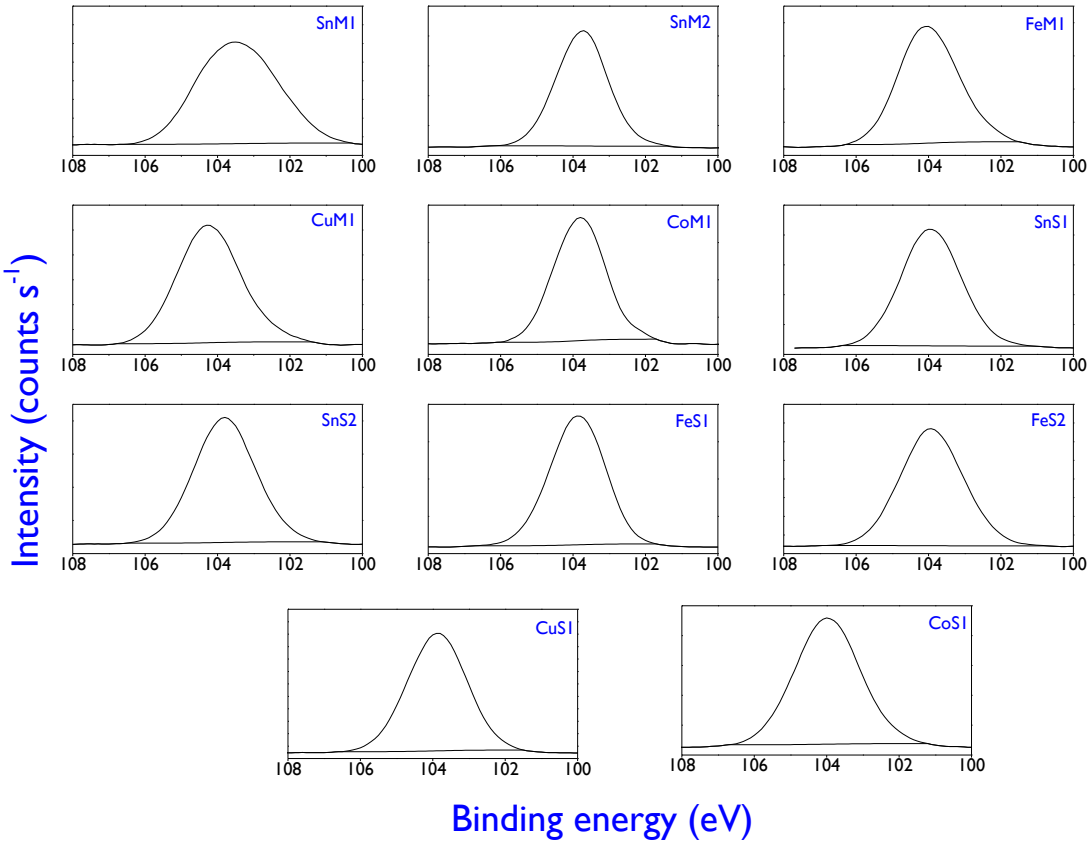

Figure 8.121. High-resolution XPS spectra for the Si2p region of all catalysts.

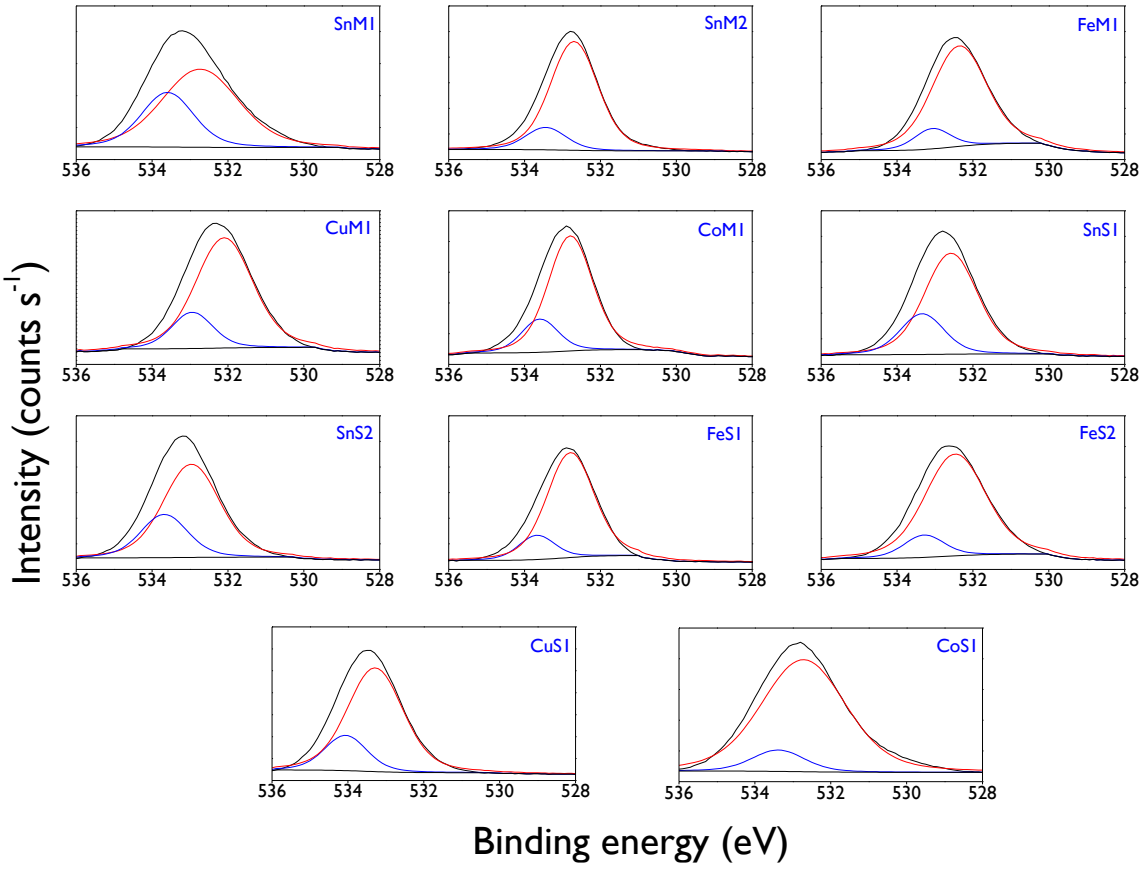

Figure 8.122. High-resolution XPS spectra for the O1s region of all catalysts.

8.5.7. Characterization of substrate and reaction products

Table 8.15. Retention times for the compounds involved in the one-pot transformation of β-pinene.

Compound	Retention time (min)	Chemical formula
β-Pinene (a)	3.95	$C_{10}H_{16}$
Product 1	5.60	$C_{10}H_{16}O$
Product 2	6.05	$C_{10}H_{16}O$
Product 3	6.23	$C_{10}H_{16}O$
β-Pinene epoxide (b)	6.45	$C_{10}H_{16}O$
Product 4	6.60	$C_{10}H_{16}O$
Product 5	6.67	$C_{10}H_{16}O$
Cis-Myrtanal (c_1)	6.76	$C_{10}H_{16}O$
Trans-Myrtanal (c_2)	6.85	$C_{10}H_{16}O$
Myrtenol (d)	7.20	$C_{10}H_{16}O$
Perillyl alcohol (e)	8.69	$C_{10}H_{16}O$
Product 6	9.94	$C_{10}H_{18}O_2$

Possible identification of the products:

Product 1: α-Pinene epoxide (CAS number: 72936-74-4) with quality GC-MS = 60%.
Product 2: Artemiseole (CAS number: 60485-46-3) with low-quality GC-MS = 28%.
Product 4: Bicyclo[2.2.1]heptane-2,5-diol, 1, 7, 7-trimethyl-, (2-endo, 5-exo)- (CAS number: 10359-41-8) with low-quality GC-MS = 40%.
Product 6: Bicyclo[3.1.0]hexane-6-methanol,2-hydroxy-1,4,4-trimethyl (CAS number: 58795-41-8) with low-quality GC-MS = 25%.

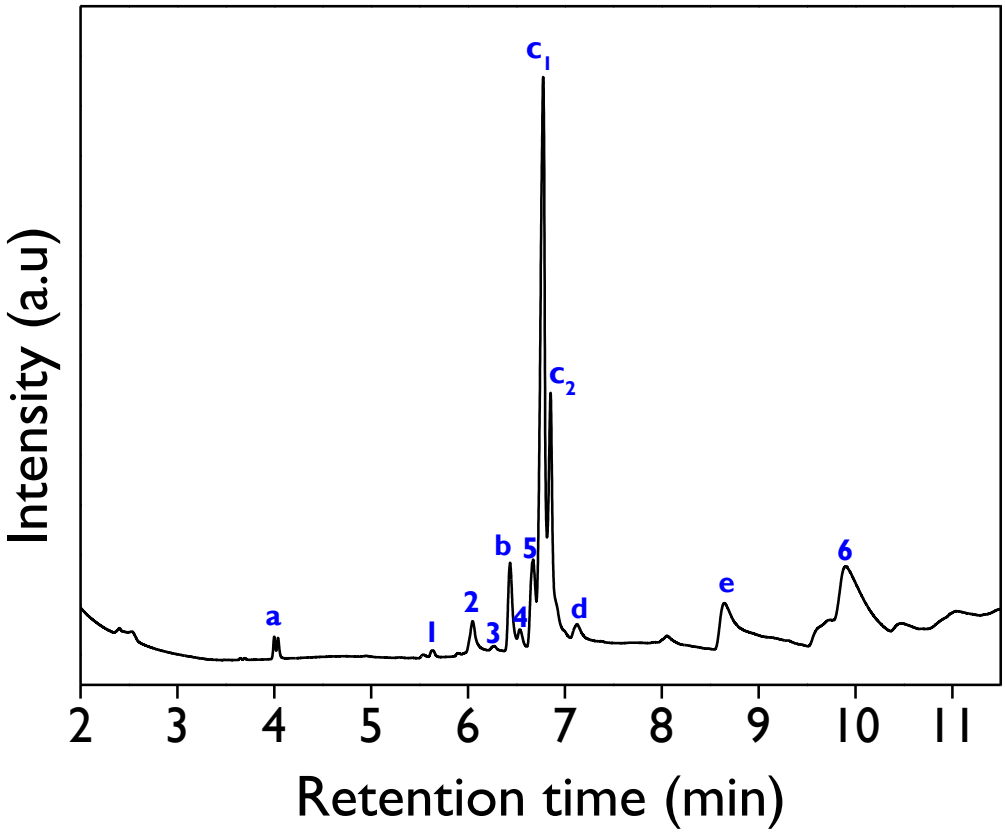

Figure 8.123. Representative chromatogram of a reaction sample after 48 h in the one-pot transformation of β-pinene. **Reaction conditions:** 0.10 mmol β-pinene, 1: 1.2: 0.72: 30.3: 19.7: 0.8: 15.7 as weight ratios for β-pinene: MgO: acid catalyst: H_2O: acetone: H_2O_2: acetonitrile, 50 °C, 1000 rpm.

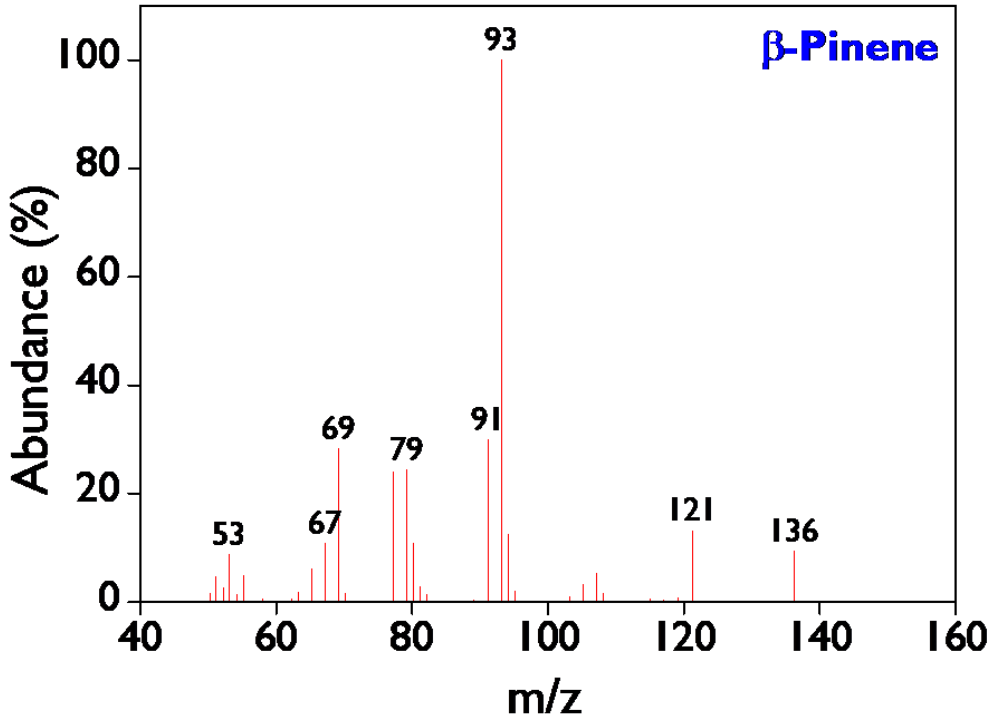

Figure 8.124. Mass spectrum of the β-pinene.

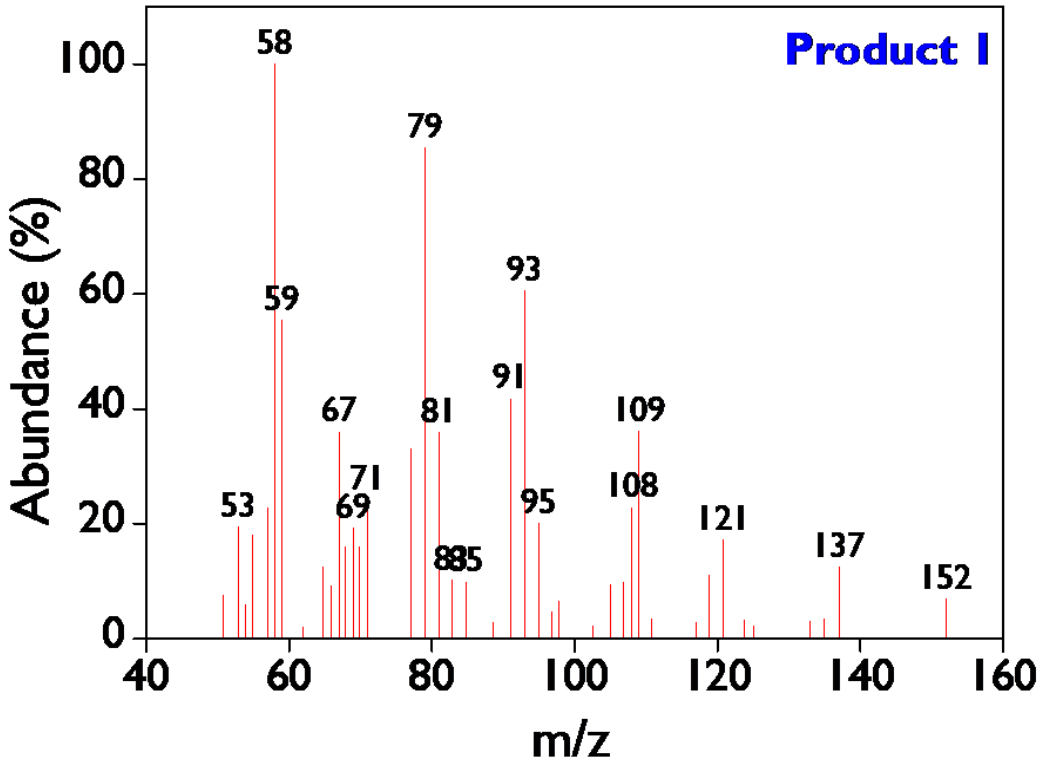

Figure 8.125. Mass spectrum of the product 1.

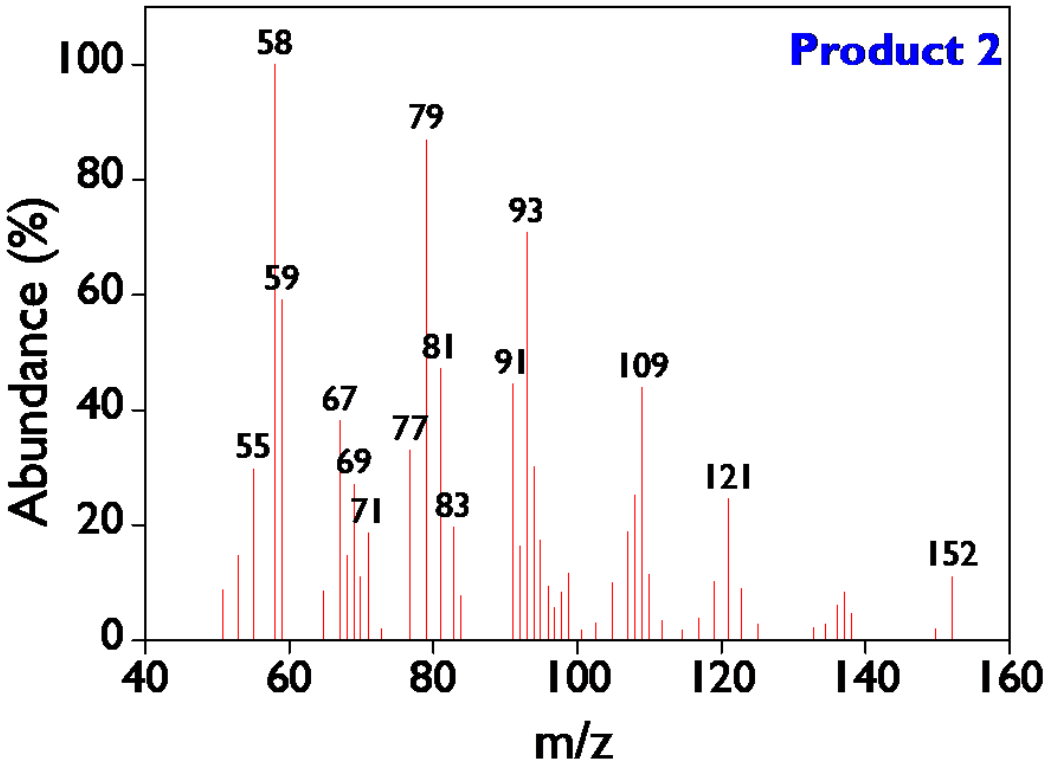

Figure 8.126. Mass spectrum of the product 2.

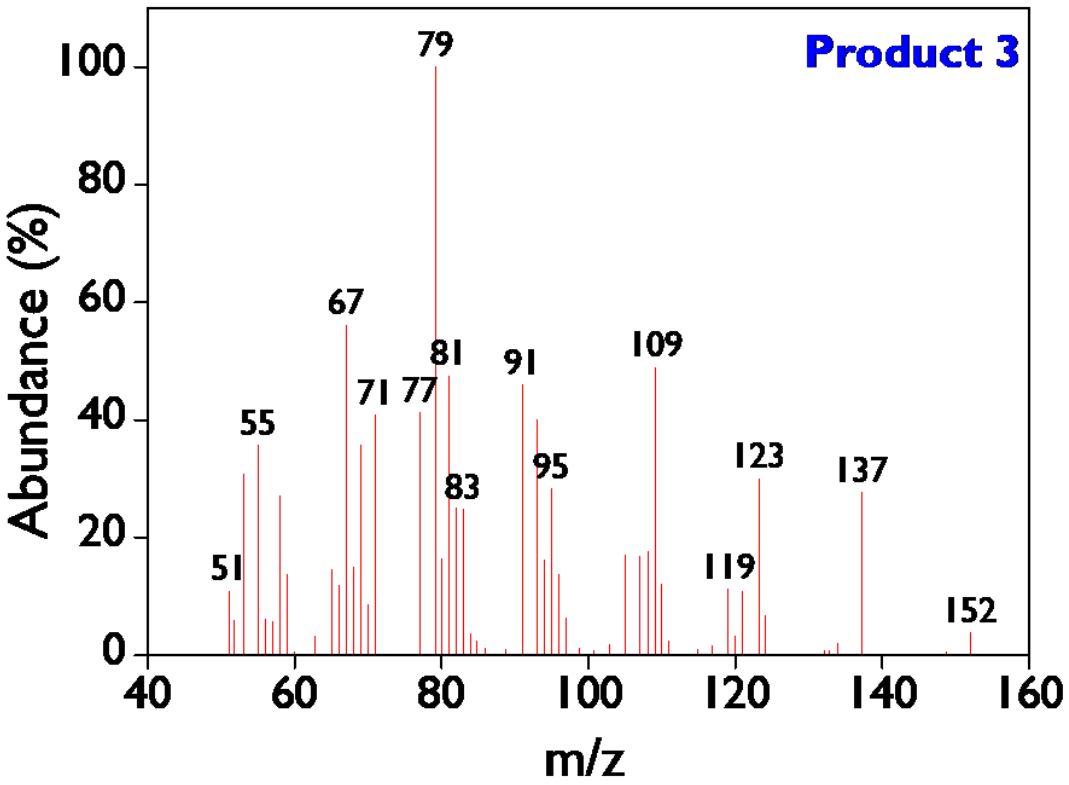

Figure 8.127. Mass spectrum of the product 3.

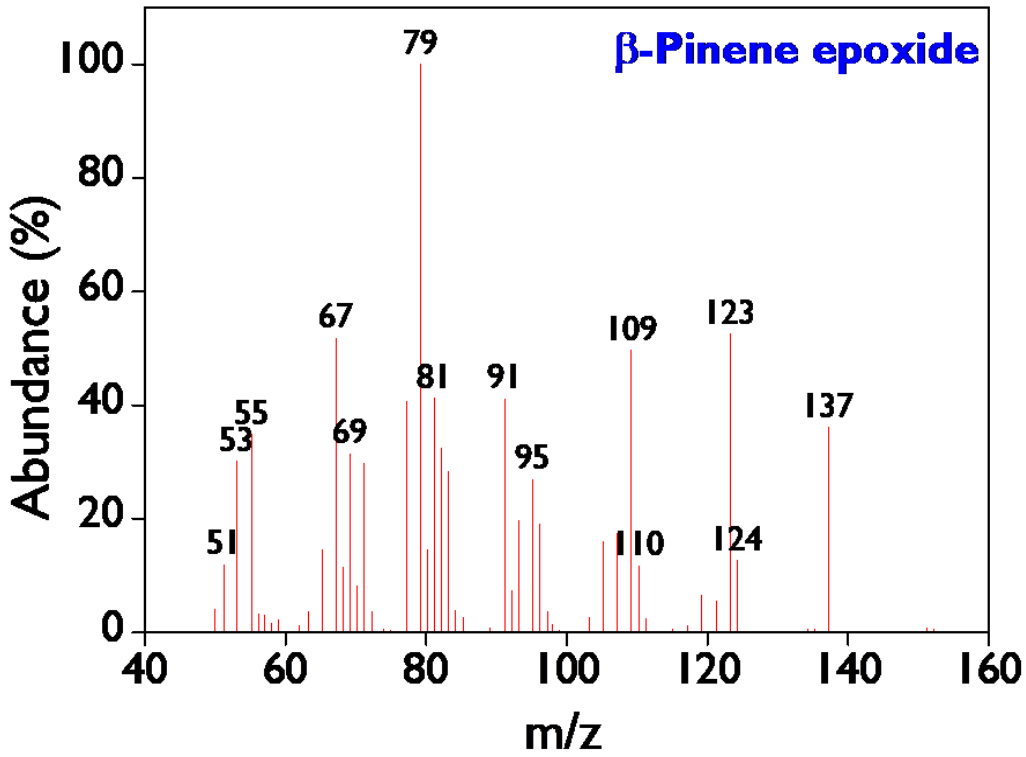

Figure 8.128. Mass spectrum of the β-pinene epoxide.

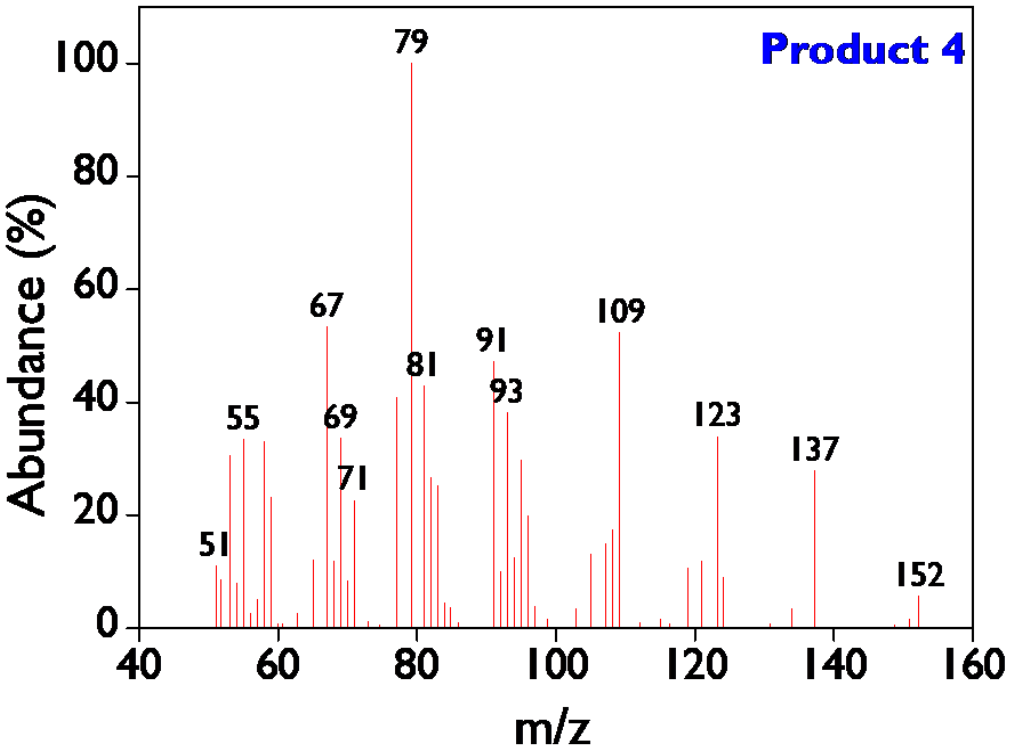

Figure 8.129. Mass spectrum of the product 4.

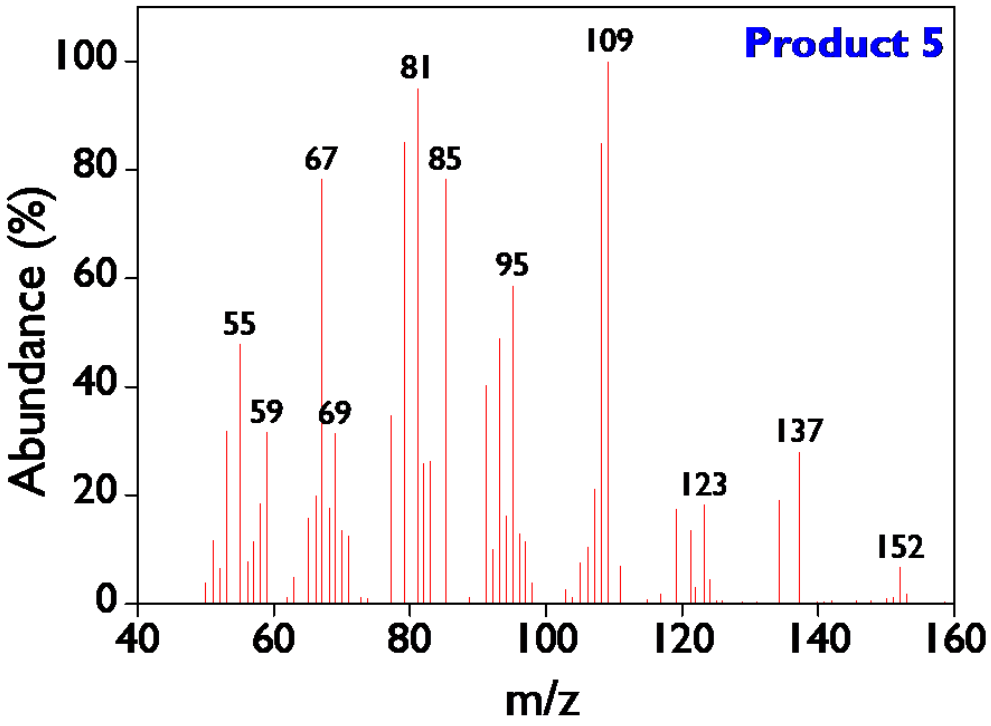

Figure 8.130. Mass spectrum of the product 5.

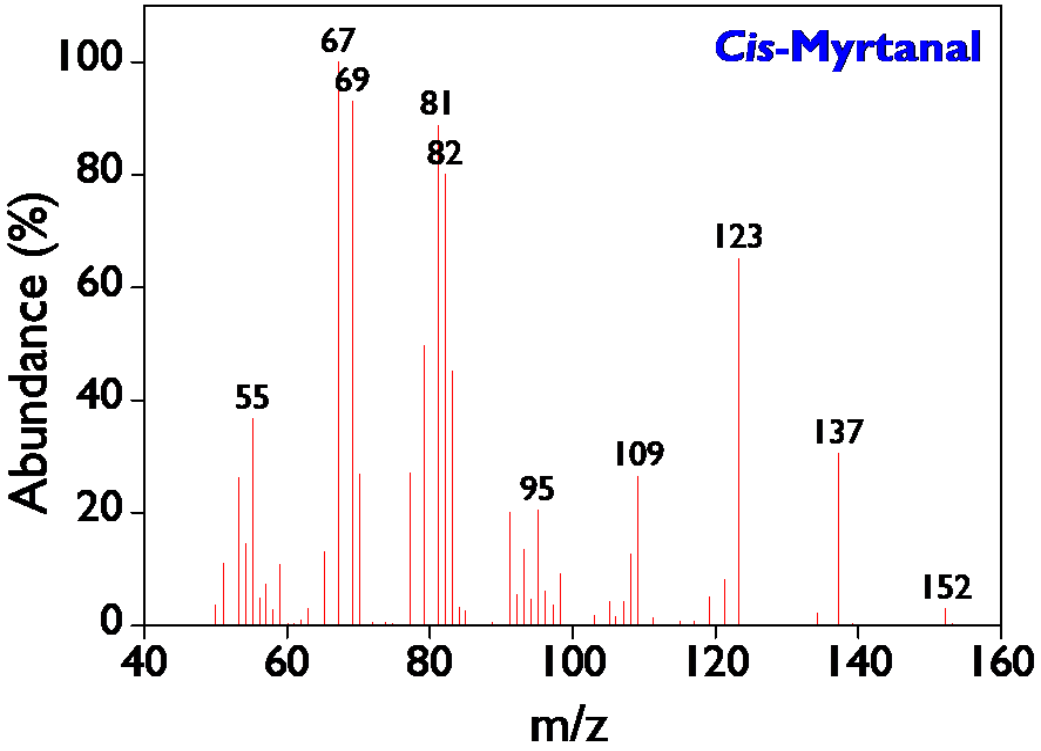

Figure 8.131. Mass spectrum of the *cis*-myrtanal.

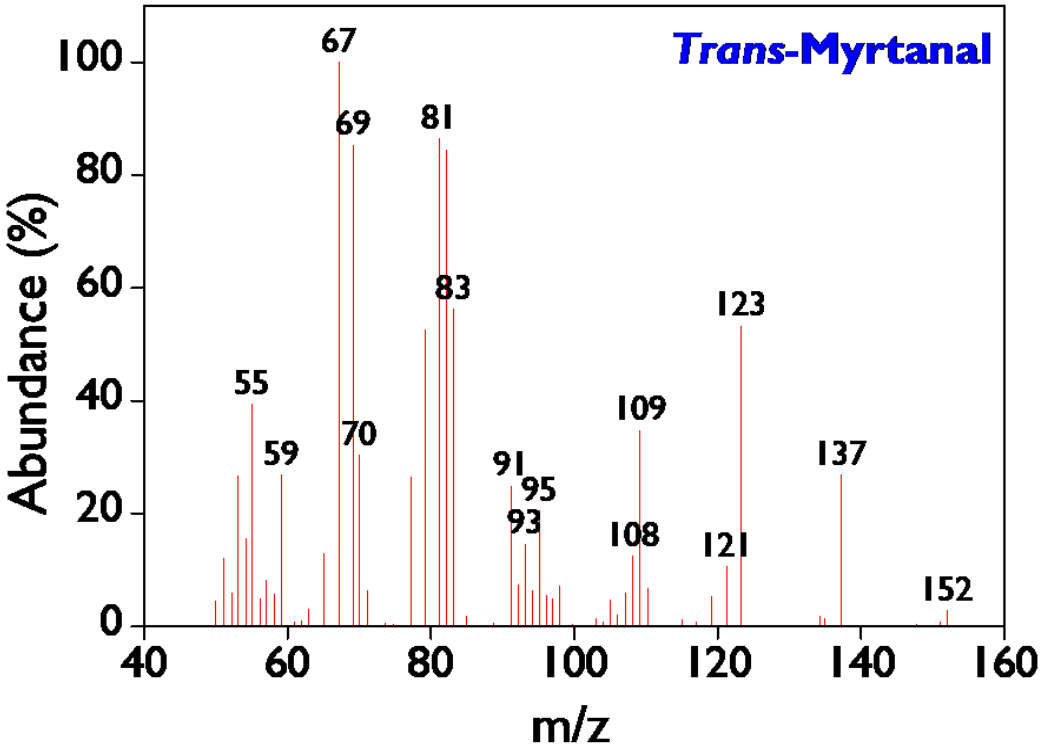

Figure 8.132. Mass spectrum of the *trans*-myrtanal.

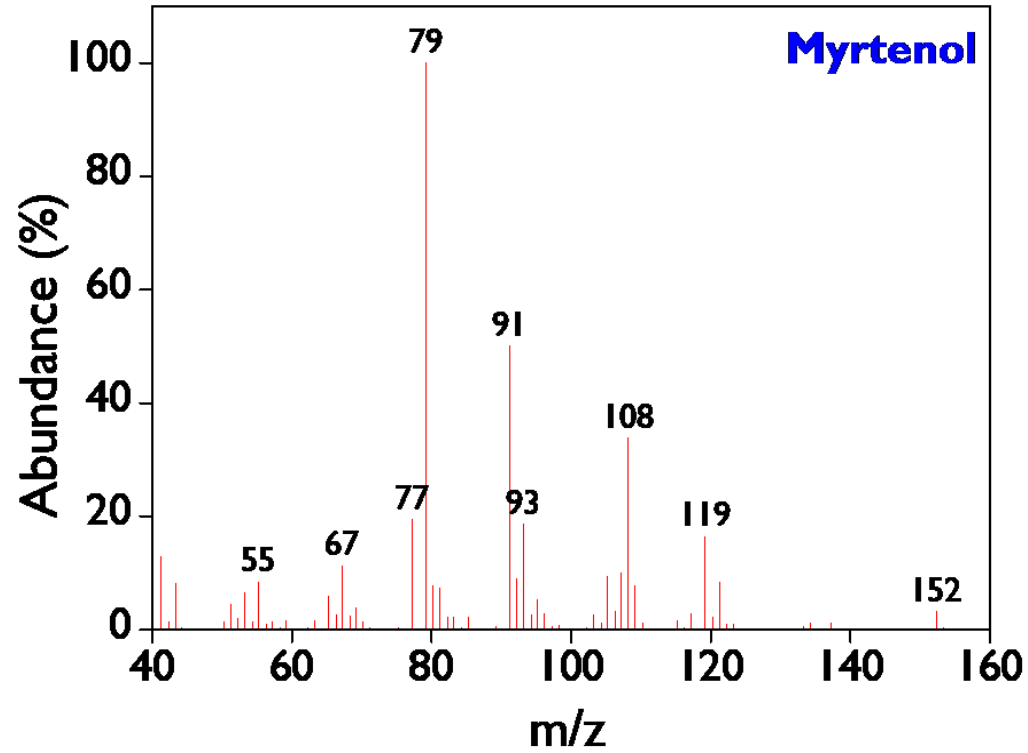

Figure 8.133. Mass spectrum of the myrtenol.

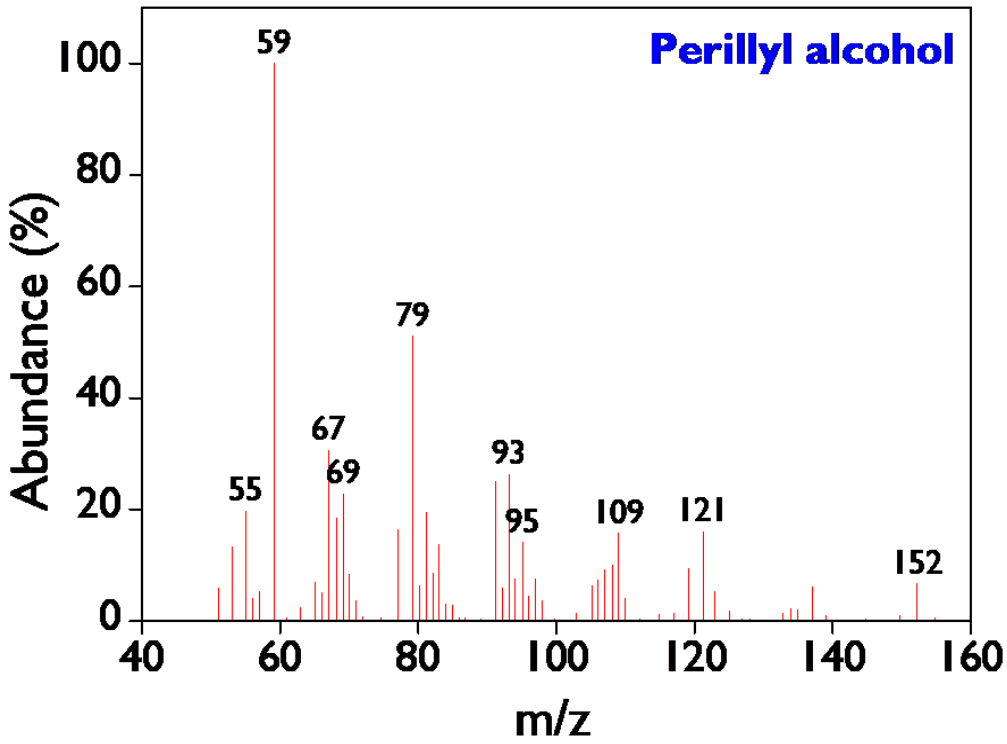

Figure 8.134. Mass spectrum of the perillyl alcohol.

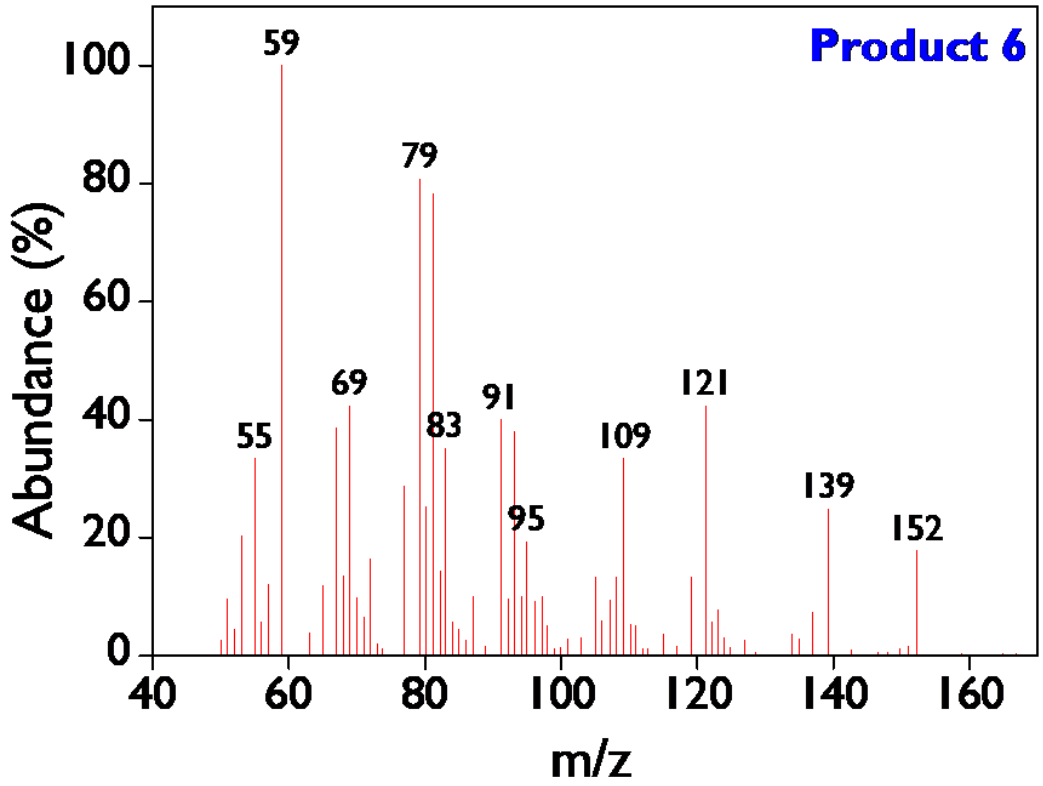

Figure 8.135. Mass spectrum of the product 6.

8.5.8. Repeatability test

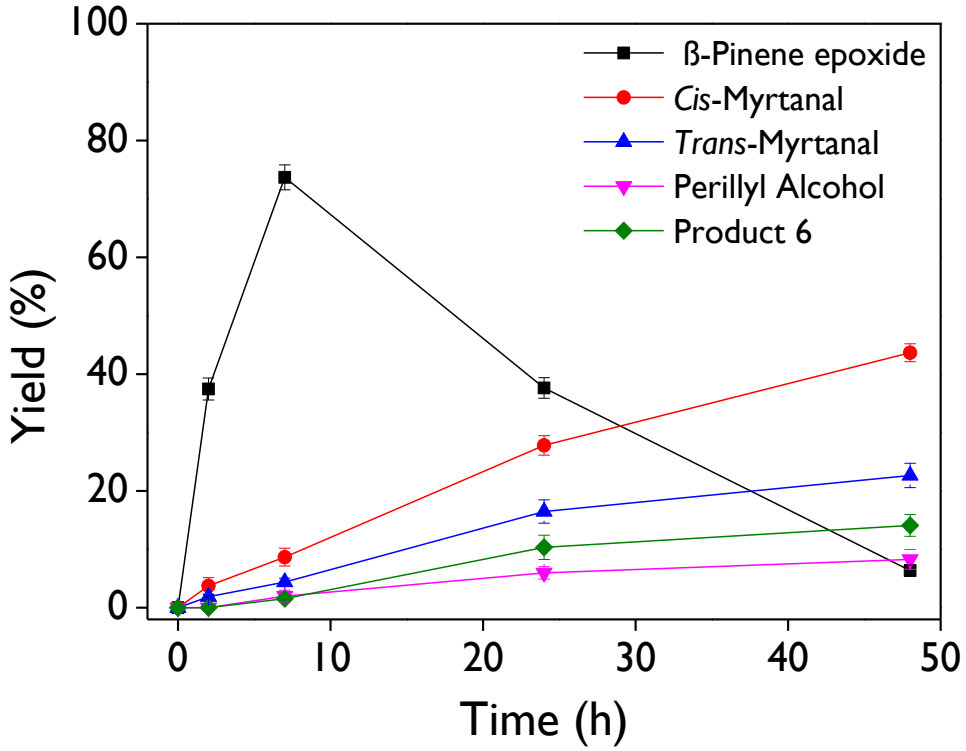

Figure 8.136. Repeatability test in the one-pot transformation of β-pinene over FeS1 as a catalyst. **Reaction conditions:** 0.1 mmol of β-pinene with weight ratios of 1: 0.72: 1.2: 30.3: 19.7: 15.7: 0.8 for β-pinene: acidic catalyst: MgO: H_2O: acetone: acetonitrile: H_2O_2, 50 °C, 1000 rpm. Figures were constructed with error bars (standard deviation), which were obtained from three experimental runs under the same conditions.

8.5.9. Conversion profiles of H_2O_2

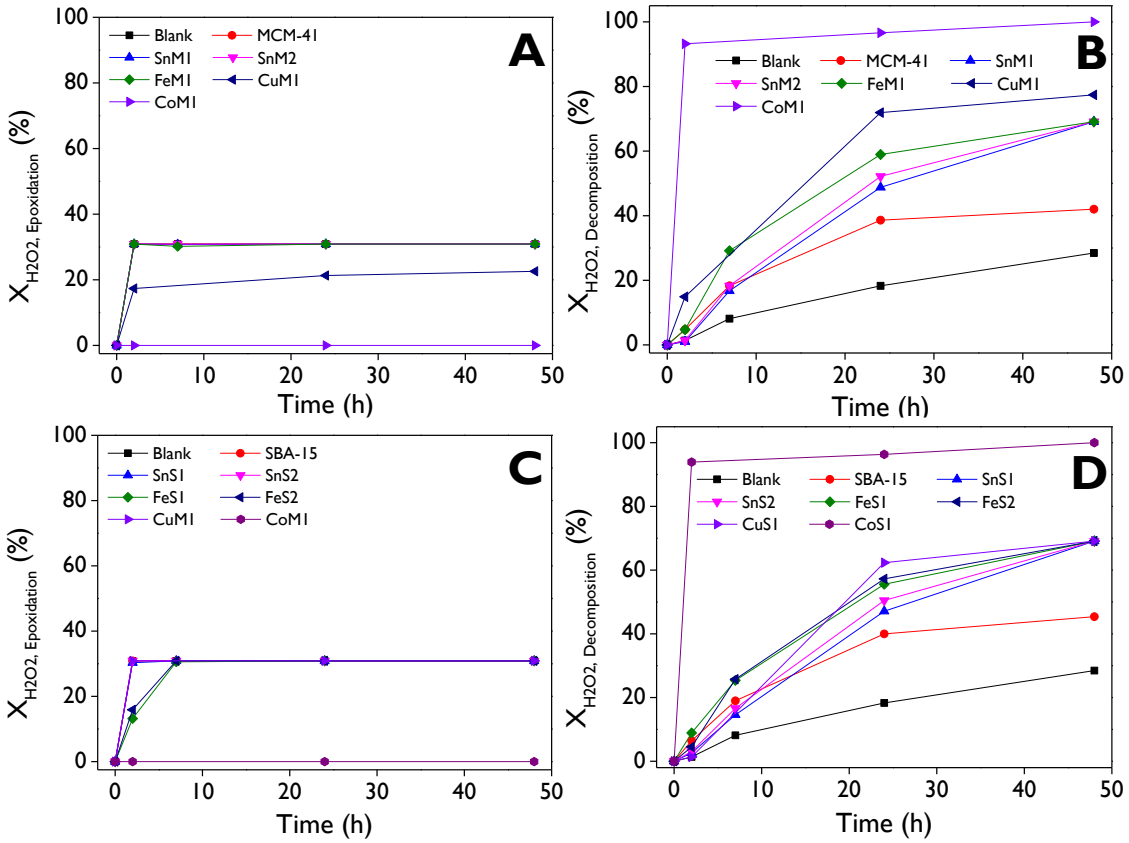

Figure 8.137. Profiles of the H_2O_2 conversion into the epoxidation reaction (**A, C**) and the decomposition route **(B, D)** with the catalysts based on MCM-41 **(A, B)** and SBA-15 **(C, D)**. **Reaction conditions:** 0.1 mmol of β-pinene with weight ratios of 1: 0.72: 1.2: 30.3: 19.7: 15.7: 0.8 for β-pinene: acidic catalyst: MgO: H_2O: acetone: acetonitrile: H_2O_2, 50 °C, 1000 rpm. Calculations were performed based on a recent contribution [1].

8.5.10. Effect of the amount of acid catalyst on the overall conversion of H_2O_2

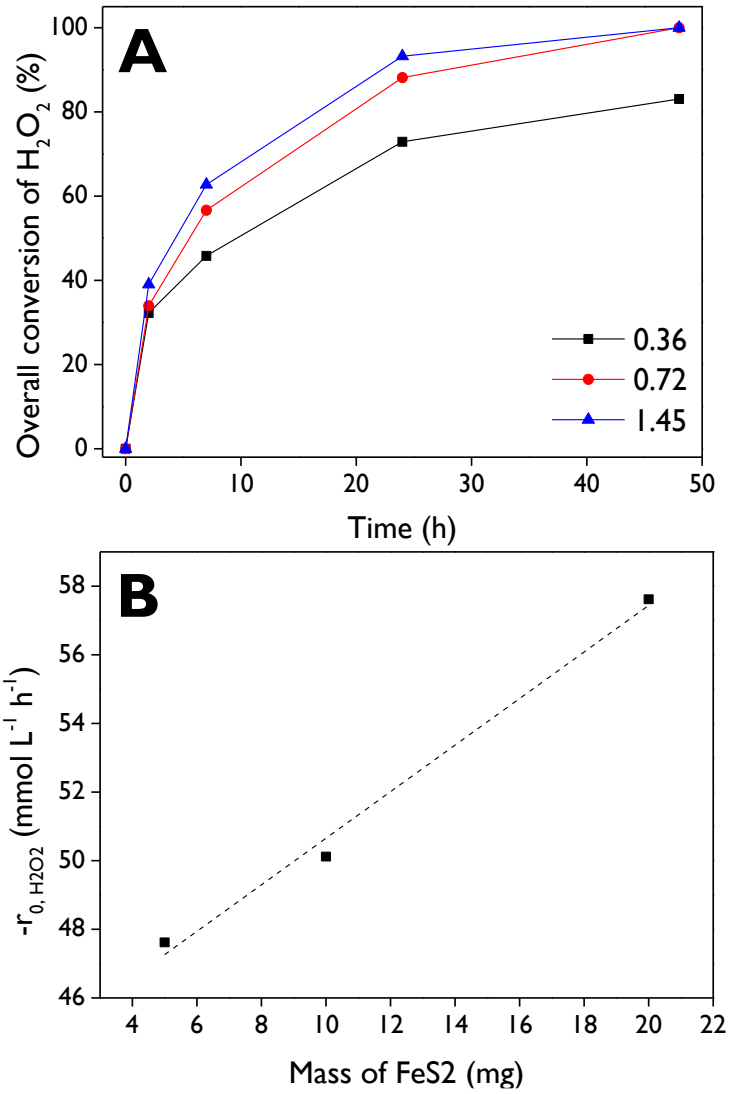

Figure 8.138. Effect of amount of FeS2 in the one-pot transformation of β-pinene: **(A)** Global conversion of H_2O_2, and **(B)** initial reaction rate of H_2O_2 as a function of mass of FeS2. **Reaction conditions:** 0.1 mmol of β-pinene with weight ratios of 1: (0.36, 0.72, 1.45): 1.2: 30.3: 19.7: 15.7: 0.8 for β-pinene: acidic catalyst: MgO: H_2O: acetone: acetonitrile: H_2O_2, 50 °C, 1000 rpm.

8.5.11. References

[1] L.A. Gallego-Villada, P. Mäki-Arvela, N. Kumar, E.A. Alarcón, Z. Vajglová, T. Tirri, I. Angervo, R. Lassfolk, M. Lastusaari, D.Y. Murzin, Zeolite Y-based catalysts for efficient epoxidation of R-(+)-Limonene: Insights into the structure-activity relationship, Microporous Mesoporous Mater. 372 (2024) 113098. https://doi.org/10.1016/j.micromeso.2024.113098.